Lecture Notes in Networks and Systems 165

Soumen Banerjee
Jyotsna Kumar Mandal *Editors*

Advances in Smart Communication Technology and Information Processing

OPTRONIX 2020

Springer

Lecture Notes in Networks and Systems

Volume 165

The series "Lecture Notes in Networks and Systems" publishes the latest developments in Networks and Systems—quickly, informally and with high quality. Original research reported in proceedings and post-proceedings represents the core of LNNS.

Volumes published in LNNS embrace all aspects and subfields of, as well as new challenges in, Networks and Systems.

The series contains proceedings and edited volumes in systems and networks, spanning the areas of Cyber-Physical Systems, Autonomous Systems, Sensor Networks, Control Systems, Energy Systems, Automotive Systems, Biological Systems, Vehicular Networking and Connected Vehicles, Aerospace Systems, Automation, Manufacturing, Smart Grids, Nonlinear Systems, Power Systems, Robotics, Social Systems, Economic Systems and other. Of particular value to both the contributors and the readership are the short publication timeframe and the world-wide distribution and exposure which enable both a wide and rapid dissemination of research output.

The series covers the theory, applications, and perspectives on the state of the art and future developments relevant to systems and networks, decision making, control, complex processes and related areas, as embedded in the fields of interdisciplinary and applied sciences, engineering, computer science, physics, economics, social, and life sciences, as well as the paradigms and methodologies behind them.

Indexed by SCOPUS, INSPEC, WTI Frankfurt eG, zbMATH, SCImago.

All books published in the series are submitted for consideration in Web of Science.

More information about this series at http://www.springer.com/series/15179

Soumen Banerjee · Jyotsna Kumar Mandal
Editors

Advances in Smart Communication Technology and Information Processing

OPTRONIX 2020

Springer

Editors
Soumen Banerjee
Department of Electronics
and Communication Engineering
University of Engineering & Management
Kolkata, India

Jyotsna Kumar Mandal
Department of Computer Science
and Engineering
University of Kalyani
Kalyani, West Bengal, India

ISSN 2367-3370 ISSN 2367-3389 (electronic)
Lecture Notes in Networks and Systems
ISBN 978-981-15-9432-8 ISBN 978-981-15-9433-5 (eBook)
https://doi.org/10.1007/978-981-15-9433-5

This Springer imprint is published by the registered company Springer Nature Singapore Pte Ltd.
The registered company address is: 152 Beach Road, #21-01/04 Gateway East, Singapore 189721, Singapore

Conference Committees

A. Organizing Committee

Patron

Prof. Dr. Satyajit Chakrabarti, Chancellor, University of Engineering and Management (UEM), Kolkata
Founder Director, Institute of Engineering and Management (IEM), Kolkata

Chair

Prof. Dr. Sajal Dasgupta, Vice-Chancellor, University of Engineering and Management (UEM), Kolkata

Co-Chair

Prof. Dr. Satyajit Chakrabarti, Pro-Vice-Chancellor, University of Engineering and Management, UEM, Kolkata Director, Institute of Engineering and Management, IEM, Salt Lake, Kolkata

Convener

Prof. Dr. Soumen Banerjee, HOD, Department of Electronics & Communication Engineering
University of Engineering and Management, Kolkata

Treasurer

Mr. Indranil Banerjee, Accounts Officer, University of Engineering and Management, Kolkata

B. Advisory Committee

Prof. Biplab Sanyal, Uppsala University, Sweden
Prof. Haricharan S. Reehal, London South Bank University, UK

Prof. Vasudevan Lakshminarayanan, University of Waterloo, Canada
Prof. Detlef Streitferdt, Technical University of Germany, Germany
Prof. Takaaki Goto, Toyo University, Saitama, Japan
Prof. Amlan Chatterjee, California State University, USA
Prof. Tarun Kumar Gangopadhyay, Former Scientist, CSIR-CGCRI, Kolkata
Prof. Arup Lal Chakrabarty, IIT, Gandhinagar
Prof. D. K. Banwet, Ex-Professor, IIT Delhi
Prof. D. S. Chauhan, Vice-Chancellor, GLA University, Mathura
Prof. Amlan Chakraborty, University of Calcutta
Prof. Sanatan Chattopadhyay, University of Calcutta
Prof. Nikhil Ranjan Das, University of Calcutta
Prof. Susanta Sen, Ex-Professor, CU. Emeritus Professor - NIT, Durgapur
Prof. Bhaskar Gupta, Jadavpur University
Prof. Subir Sarkar, Jadavpur University
Prof. Chandan Kumar Sarkar, Ex-Professor, Jadavpur University
Prof. Monojit Mitra, IIEST, Shibpur
Prof. Susanta Kumar Parui, IIEST, Shibpur
Prof. Ajit Kumar Panda, NIST, Behrampur
Prof. Debaprasad Das, Assam University
Dr. Tirtha Pratim Das, Deputy Director, DTDI, ISRO
Dr. Pradipta Roy, Scientist-F, ITR Chandipur, DRDO

C. Technical Committee

Prof. Soumen Banerjee (Chair), UEM, Kolkata
Prof. J. K. Mandal (Chair), University of Kalyani
Dr. Arnab Roy, Inter Digital Communications, USA
Dr. Archita Banerjee, Carlisle Interconnect Technologies, USA
Prof. Babusena Paul, University of Johannesburg, South Africa
Dr. Bappaditya Mandal, Uppsala University, Sweden
Prof. Mrinal Kanti Mandal, IIT, Kharagpur
Prof. Somak Bhattacharya, IIT, BHU
Prof. Abhirup Das Barman, University of Calcutta
Prof. Soumya Pandit, University of Calcutta
Prof. Soumya Sen, University of Calcutta
Prof. Sunit Kumar Sen, Ex-Professor, University of Calcutta
Prof. Subal Kar, Ex-Professor, University of Calcutta
Prof. Sheli Sinha Chaudhuri, Jadavpur University
Prof. Sudhabindu Roy, Jadavpur University
Prof. D. R. Poddar, Ex-Professor, Jadavpur University
Prof. Debashis Mitra, IIEST, Shibpur
Prof. Surojit Roy, IIEST, Shibpur
Prof. Sujit Mandal, NIT, Durgapur

Prof. Sanjay Dhar Roy, NIT, Durgapur
Prof. Ayan Chatterjee, NIT, Sikkim
Prof. T. R. Lenka, NIT, Silchar
Mr. Alinjar Bhowmick, IBM, Kolkata
Prof. Gautam Saha, NEHU, Shillong
Prof. Arindam Biswas, Kazi Nazrul University, WB
Prof. Atanu Kundu, Secretary, IEEE Kolkata Section
Prof. Sushanta Kumar Mandal, Sardha University
Prof. Shubhabrata Dutta, SRM University
Prof. K. P. Ghatak, UEM, Kolkata
Prof. Rajiv Ganguly, UEM, Kolkata
Prof. Abir Chattopadhyay, UEM, Kolkata
Prof. Rajarshee Paul, UEM, Kolkata
Prof. Sankhadeep Chatterjee, UEM, Kolkata

Preface

Optics/Photonics and Optoelectronics are indispensable in almost all spheres of life, ranging from everyday life requirements such as communication and biomedicine to advanced science and technology. Starting from basic classical geometric and physical optics to quantum optics, there has been tremendous technological advancement as a result of which we have areas such as optical communication networks, optical information processing, space optics, electro-optics, optomechatronics, organic photonics, and so forth.

In today's era of communication, a modern society is totally crippled without the use of communication technology. The enormous applications of communication have rendered immense service to mankind and played a pivotal role in bringing radical change in life and society, thereby helping in uniting people across the globe. With the emergence of data centric computing, scientific and engineering disciplines have gone through drastic changes. The availability of redundant data from different sources has made it possible to use artificial intelligence, machine learning, computer vision, cloud computing, big data solutions, and Internet-of-Things (IoT) in day-to-day activities.

Keeping the present scenario in mind, the 6th International Conference on Opto-Electronics and Applied Optics (OPTRONIX—2020) was organized by the University of Engineering & Management (UEM), Kolkata, India from June 8–10th, 2020 in association with Springer. This conference showcased and highlighted the recent trends in research and development in areas of Optoelectronics with particular emphasis on communication technology and its different kinds. The first Optronix conference (Optronix-2014) was held in the year 2014 in Kolkata, India, in technical collaboration with OSI—SPIE Student Chapter, Kolkata, and supported by DST, Govt. of India and CSIR. Its proceedings were published by Springer in the form of a book titled "Advances in Optical Science and Engineering (Proceedings of the First International Conference, OPTRONIX-2014)"—Editors: V. Lakshminarayanan and I. Bhattacharya (Springer Proceedings in Physics). The second in the series Optronix-2015 was held at the University of British Columbia, Vancouver, Canada, in technical collaboration with IEEE Photonics Society supported by IEEE Vancouver Section. Its papers were published in IEEE Xplore Digital Library. The third in the series Optronix-2015 was held in Kolkata, India, with technical collaboration from OSI, India and American Journal of Electronics and Communication Technology (AJECT), Canada. Its proceedings were also published by Springer in the book titled "Advances in Optical Science and Engineering (Proceedings of the Third International Conference, OPTRONIX-2016)"—Editors: I. Bhattacharya, S. Chakrabarti, H. S. Reehal, and V. Lakshminarayanan (Springer Proceedings in Physics). The fourth and fifth conferences, Optronix-2017 and Optronix-2019, were held in Kolkata, India in technical collaboration with IEEE with its research papers being published in IEEE Xplore Digital Library. For the Optronix-2019 conference, a book titled "Intelligent Computing: Image Processing based Applications" was published by Springer, covering book chapters related to many selected papers from the conference along with others as well. Also, the extended versions of some of the selected papers were published in SCI Indexed Journal from Springer.

The theme of the present conference Optronix-2020 was chosen as "Advances in Smart Communication Technology and Information Processing." The current conference focused on various applications of such technologies so as to make intelligent information processing systems transform the landscape of human civilization. The conference also encouraged the students, scholars, academicians, and researchers to take up more projects in the relevant area so as to get more intellectual involvement in the said field. The purpose of this conference was to inform the scientists and researchers of this field in India and abroad about the latest developments in the relevant domain and to raise awareness among the academic fraternity to get them involved in different activities in the years ahead—an effort to realize Knowledge-Based Society. The conference proceedings are all inside this book titled "Advances in Smart Communication Technology and Information Processing" in the Book Series "Lecture Notes in Networks and Systems (LNNS)" by Springer and the extended versions of some of the selected papers are to be published in SCI Indexed Journal from Springer.

Many scientist and academicians from India and abroad were invited to deliver their invited talks. However, as the entire world during the conference period was engulfed by the novel corona virus, and the COVID-19 disease declared as pandemic by WHO, the entire conference was organized ONLINE through the Google Meet platform which resulted in many speakers being unable to attend the conference physically to deliver their speeches. We express our sincere thanks and gratitude to all the eminent speakers from academia and R & D organizations for delivering their valuable and informative speeches online amid such pandemic situation prevailing worldwide. The distinguished Chief Guest and Keynote Speaker for Optronix-2020 conference was Dr. Binoy K. Das, Director, Integrated Test Range (ITR), Chandipur, DRDO, Govt. of India, and we are very much thankful to him for kindly accepting our invitation, gracing the inaugural function, and delivering such an enlightening Keynote Address, all in online. The eminent national invited speakers were Prof. Dr. Amlan Chakraborty (Professor and Director, AKCSIT, University of Calcutta), Prof. Dr. Sheli Sinha Chaudhuri (Professor and Head, Dept. of Electronics & Telecommunication Engineering, Jadavpur University), Prof. Dr. J. K. Mandal (Professor, Dept. of Computer Science & Engineering, University of Kalyani), Dr. Pradipta Roy

(Scientist-F, Integrated Test Range (ITR), Chandipur, DRDO, Govt. of India), Prof. Dr. Bhaskar Gupta (Professor, Dept. of Electronics & Tele-communication Engineering, Jadavpur University), and Prof. Dr. Nikhil Ranjan Das (Professor, Institute of Radio Physics & Electronics, University of Calcutta).

I thank the University authorities for holding Optronix-2020 conference online in such critical condition. A special thanks to the Hon'ble Chancellor and Hon'ble Pro-Vice-Chancellor for continuous support toward successful organization of the conference. I sincerely thank all the Members of the Advisory and Technical Committee for their valuable suggestions and necessary guidance. I express my heartfelt thanks to Hon'ble Vice-Chancellor for his advice, inspiring mentorship, and for providing us with all possible logistic support for smooth conduction of the conference.

I thank all the session chairs and the delegates for their enthusiastic participation in this conference. I take this opportunity to thank all the reviewers and technical committee members for providing their valuable comments on time and helping toward the improvement of quality of papers presented in the conference. I thank our publishing house Springer, for kindly agreeing to publish the conference proceedings. I thank all my colleagues for their relentless support and cooperation in organizing the conference and making it a grand success. I thank everyone else whose contribution has made this conference possible and look forward to organizing next year the seventh conference in the next year, Optronix-2021.

Kolkata, India — Prof. (Dr.) Soumen Banerjee
Convener, Optronix-2020

West Bengal, India — Jyotsna Kumar Mandal

Message from Conference Chair

Let me congratulate Dr. Soumen Banerjee, HOD and all faculty members in the Department of Electronics and Communication Engineering of our university for organizing this 6th International Conference on Opto-Electronics and Applied Optics (OPTRONIX-2020) from June 8–10th, 2020.

Optoelectronics and Applied Optics/Photonics are indispensable in almost all spheres of life covering Optical communication networks, Optical information processing, Space optics, Electro optics, Optomechatronics, Organic photonics, and many other applications. Optoelectronic devices include Laser diodes, Solar cells, LEDs, and Optical fibers. These devices are used in different electronic project kits as well as in Telecommunications, Military services, and Medical applications.

About 48 students of our university are the members of students' chapters of OPTICAL SOCIETY OF AMERICA (OSA) and SOCIETY OF PHOTO-OPTICAL INSTRUMENTATION ENGINEERS (SPIE). The Presidents of these two chapters travel once a year to the USA for about 7–10 days at the costs of the societies and present the chapter activities and meet international experts and professors in the USA.

Our first OPTRONIX International conference was held in 2014, at IEM, Kolkata, under the technical collaboration of Optical Society of India & SPIE Students Chapter, Kolkata and financially supported by DST and CSIR, GOI. The papers presented were published by Springer.

Our second OPTRONIX International conference was held in 2015 at the University of British Columbia, Vancouver, Canada under the technical collaboration of IEEE Photonics society. The papers presented were published by IEEE.

From the third international OPTRONIX conference, held in 2016 onwards, our university is hosting this event every year. All these conferences were very successful. The papers presented were published either by Springer or by IEEE.

Till 5th OPTRONIX 2019 conference, IEM-UEM group organized these events in the institution premises where all national and international eminent speakers, participants, and students were physically present and interacted and enjoyed the conferences within the tranquil academic ambience of the institution.

Only this year, due to COVID-19 pandemic situation prevailing worldwide, OPTRONIX-2020 is being held virtually through GOOGLE MEET in order to maintain physical distancing.

The theme of this 6th international OPTRONIX-2020 conference commencing from today is *Advances in Smart Communication Technology and Information Processing*. The current conference focuses on the various applications of such technologies in making intelligent information processing systems which are transforming the landscape of human civilization.

Dr. Binoy K. Das—Director, Integrated Test Range, Chandipur, DRDO, GOI, graced this Inaugural function digitally as our Chief Guest cum Keynote speaker. I am thankful to all our distinguished session Chairmen and invited speakers in this conference.

I came to know out of about 70 papers submitted, only 45 very good papers were finally accepted by the scrutiny committee. All accepted and presented papers will be published as Book Chapters in Springer Conference Proceedings.

I wish this OPTRONIX-2020 conference will give rise to many new concepts and research ideas, in which our students of relevant disciplines will be interested. Our students will get the rare opportunities to interact with the subject experts to enrich their knowledge for real-life application.

I wish this conference a great success.

Prof. (Dr.) Sajal Dasgupta
Vice-Chancellor
University of Engineering & Management, Kolkata
and
Conference Chair, Optronix-2020

Optronix-2020: Speakers

Chief Guest & Keynote Speaker

Dr. Binoy K. Das *Outstanding Scientist, Director, Integrated Test Range (ITR) Chandipur, DRDO, Govt. of India.*

Topic: *Recent Trends in Electro-Optics*

Invited Speakers

No.	Speakers	Affiliation	Topic
1.	**Prof. Dr. Amlan Chakraborty**	*Former Dean, University of Calcutta* *Professor and Director, A. K. Choudhury School of Information Technology, CU*	*Quantum Internet: The Next Global Network*
2.	**Prof. Dr. Sheli Sinha Chaudhuri**	*Professor and Head* *Dept. of Electronics & Telecommunication Engg.* *Jadavpur University*	*Deep Learning and Medical Image Analysis*
3.	**Prof. Dr. J. K. Mandal**	*Professor, Department of Computer Science & Engineering,* *University of Kalyani*	*Chaos Based Security and Authentication in Public Domain Networks*

(continued)

No.	Speakers	Affiliation	Topic
4.	**Dr. Pradipta Roy**	*Scientist-F, Integrated Test Range (ITR) Chandipur, DRDO, Govt. of India*	*Object Detection and Tracking*
5.	**Prof. Dr. Bhaskar Gupta**	*Professor, Department of Electronics & Tele-communication Engineering Jadavpur University*	*Effect of Electro-magnetic Radiation on Indian Flora*
6.	**Prof. Dr. Nikhil Ranjan Das**	*Professor, Institute of Radio Physics & Electronics, University of Calcutta*	*Quantum Dot SLEDs as Broadband Optical Sources for Sub-cellular OCT*

Contents

Advances in Modern Communication Engineering

A Dielectric Resonator MIMO Antenna for Intelligent Transportation Systems 3
Goffar Ali Sarkar, Susanta Kumar Parui, and Soumen Banerjee

Some Studies on Microstrip Patch Antennas for Wearable Applications 11
Sandipan Mitra, Subhadip Santra, Anuplab Chatterjee, Surjya Prakash Saha, and Aditya Brahmachari

Ultra Wide Band Planar Inverted F Antenna Design 19
Priyanka Das, S. Navyashri, Diya Chatterjee, Reeju Ray, and Pooja Mukherjee

A Novel Design of Circularly Polarized Antenna with Asymmetric Slots 27
Priyanka Das, Shubhadeep Dey, and Saswata Banerjee

Novel Design of a Wideband Microstrip Antenna for 5G Applications 37
Priyanka Das, Mouli Ghosh, Sayani Banik, Subhodeep Mondal, and Sudhanshu Shekhar

Performance Analysis of an Electrostatic Doping Assisted Dual Parallel Mach-Zehnder Modulator 47
Soumi Saha, Rohan Roy, and Subhradeep Pal

Semi-hexagonal Half Mode SIW Antennas and Arrays for Vehicular Communication Systems 59
Soumen Banerjee, Sampoorna Das Mazumdar, Sombuddha Chatterjee, and Susanta Kumar Parui

Designing a Framework for Real-Time WiFi-Based Indoor Positioning 71
Ayan Kumar Panja, Chandreyee Chowdhury, Priya Roy, Sakil Mallick, Sukanto Mondal, Soumik Paul, and Sarmistha Neogy

CPW Wide-Band Bandpass Filter Using Combination of Series Open and Folded Shunt Short Stubs 83
P. Mondal, R. Bera, B. Mandal, Soumen Banerjee, A. Ghosh, and Susanta Kumar Parui

Design of Circularly Polarized On-Chip Slot Antenna with Enhanced Gain Using Micromachining 91
Harshavardhan Singh, Sachin Kumar, Biki Raj Hazarika, and Sujit Kumar Mandal

Synthesis of Unequally Spaced Time-Modulated Linear Arrays Through Optimized Position and On-Time Using Differential Evolution 99
S. Patra, Sujit Kumar Mandal, G. K. Mahanti, and N. Pathak

Meta Sensing Ovarian Cancer Cells at THz from C Band Radiation Biophysics 111
Abhirupa Saha, Sanjib Sil, Srikanta Pal, Bhaskar Gupta, and Piyali Basak

Intelligent Systems and Information Processing

A Metaheuristic Approach for Image Segmentation Using Genetic Algorithm 125
Joy Bhattacharjee, Soumen Santra, and Arpan Deyasi

Improved Twitter Sarcasm Detection by Addressing Imbalanced Class Problem 135
Kushankur Ghosh, Arghasree Banerjee, Mayukh Bhattacharjee, and Sankhadeep Chatterjee

Classification of Citrus Fruits and Prediction of Their Largest Producer Based on Deep Learning Architectures 147
Kyamelia Roy, Sheli Sinha Chaudhuri, Soumi Bhattacharjee, and Srijita Manna

Unsupervised Machine Learning Algorithm Based Rotten Fruit Segmentation 157
Kyamelia Roy, Sayan Pramanik, and Sheli Sinha Chaudhuri

Capsule Neural Network Architecture Based Multi-class Fruit Image Classification 171
Kyamelia Roy, Probhakar Roy, and Sheli Sinha Chaudhuri

Effects of Class Imbalance Problem in Convolutional Neural Network Based Image Classification 181
Arghasree Banerjee, Kushankur Ghosh, Arya Sarkar, Mayukh Bhattacharjee, and Sankhadeep Chatterjee

Smart Plant Monitoring System Using BLYNK Application 193
Abhinandan Mohanty and Sreyashi Roy

Performance Improvement of Convolutional Neural Network Using Random Under Sampling 207
Kushankur Ghosh, Arya Sarkar, Arghasree Banerjee, and Sankhadeep Chatterjee

Robust and Atomic Technique for Edge Detection to Identify Edges Present in Digital Image Using DSCTHS Method 219
Debkumar Chowdhury, Sanjukta Mishra, Sujoy Paul, Sreejit Bagchi, Hazim Ahmed, Trisha Das, and Chinmoy Mandal

Performance Improvement of Artificial Neural Networks by Addressing Class Overlapping Problem 229
Sankhadeep Chatterjee, Asit Kumar Das, Kushankur Ghosh, Arghasree Banerjee, Mayukh Bhattacharjee, and Soumen Banerjee

Multilabel Sentiment Prediction by Addressing Imbalanced Class Problem Using Oversampling 239
Mayukh Bhattacharjee, Kushankur Ghosh, Arghasree Banerjee, and Sankhadeep Chatterjee

Image Segmentation Based on Galactic Swarm Optimization 251
Shouvik Chakraborty, Kalyani Mali, Arghasree Banerjee, Mayukh Bhattacharjee, and Sankhadeep Chatterjee

A Biomedical Image Segmentation Approach Using Darwinian Particle Swarm Optimization and Thresholding 259
Shouvik Chakraborty, Kalyani Mali, Kushankur Ghosh, Arya Sarkar, and Sankhadeep Chatterjee

An Image Security Method Based on Low Dimensional Chaotic Environment and DNA Encoding 267
Mousomi Roy, Shouvik Chakraborty, Kalyani Mali, Deepayan Roy, and Sankhadeep Chatterjee

Penalized Fuzzy C-Means Coupled Level Set Based Biomedical Image Segmentation 279
Shouvik Chakraborty, Kalyani Mali, Kushankur Ghosh, and Arya Sarkar

Utilization of Hyperchaotic Environment and DNA Sequences for Digital Image Security 289
Mousomi Roy, Shouvik Chakraborty, Kalyani Mali, and Deepayan Roy

A Biomedical Image Segmentation Approach Using Fractional Order Darwinian Particle Swarm Optimization and Thresholding 299
Shouvik Chakraborty, Kalyani Mali, Arghasree Banerjee, and Mayukh Bhattacharjee

An Intelligent and Smart Belt for the Blind People 307
Souvik Chakraborty, Avishek Bhadra, Samrat Mondal, Suraj Prasad, and Shouvik Chakraborty

Spam Detection Using Threshold Method on Whatsapp Image Data 317
Arunabha Tarafdar, Hrittika Paul, Shubhojit Gupta, Labani Acharjee, Akash Sah, and Soham Ganguly

Skin Lesion Classification Using Deep Convolutional Neural Network and Transfer Learning Approach 327
Pravin Kumar Samanta and Nirmal Kumar Rout

Susceptibility Analysis of Novel Corona Virus Using Hadoop Distributed File System 337
Pravin Kumar Samanta, Soumyadev Mukherjee, and Nirmal Kumar Rout

Latest Trends in Semiconductor and Electronics Industry

Computing Photocurrent in Heterojunction Solar Cell with Gaussian Diffusion Profile 349
Purbasha Ray, Swarnav Mukhopadhyay, and Arpan Deyasi

A Low Energy and Area Efficient Switching Scheme for a Charge Redistribution SAR ADC Architecture 361
Pranati Ghoshal, Chanchal Dey, and Sunit Kumar Sen

A Survey on Lee Filter and Its Improved Variants 371
Sriparna Banerjee, Sheli Sinha Chaudhuri, Raghav Mehra, and Arundhati Misra

Design and Optimization of Single Junction GaSb Solar Cell for Maximum Utilization of IR Solar Spectrum 385
Bubai Maji and Rik Chattopadhyay

A Comprehensive Review of Median Filter, Hybrid Median Filter and Their Proposed Variants 393
Sriparna Banerjee, Sheli Sinha Chaudhuri, Raghav Mehra, and Arundhati Misra

Dual-Axis Solar Tracker Without Microcontroller 407
Sohom Chakraborty, Anusua Roy, and Sukanya Dey

Inter-subband Photoresponse Analysis of CdS/ZnSe QWIP 417
Md Aref Billaha, Biplab Bhowmick, and Santosh Kumar Choudhary

Fire Extinguishing Robot Using Arduino and DTMF Controller 425
Susmita Chaki, Didhiti Nandi, and Juhita Das

Studies on al and Mg Co-Doped ZnO Thin Films Grown by Sol-Gel Technique 433
Arpita Das and Sohom Chakraborty

Grid Connected Rooftop Solar Photo-Voltaic Power Plants Programme in India: A Review of State Solar Rooftop Policies, Net Metering Regulations, Challenges and Way Forward 443
Arvind Kumar, Hiren Chandra Borah, and Utpal Goswami

Design of a Microring Resonator Having High Sensitivity for Biosensing Applications 459
Piyali Mukherjee and N. R. Das

Technical Assessment for Implementation of Agricultural Solar Pump in West Bengal to Reduce AT&C Loss of Discom—A Case Study 471
Utpal Goswami, Arnab Ganguly, Prabir Kumar Dash, Suprava Chakraborty, and Arvind Kumar

Author Index 483

Editors and Contributors

About the Editors

Prof. Dr. Soumen Banerjee is Head of the Department of Electronics & Communication Engineering at the University of Engineering & Management (UEM), Kolkata. He was also the Guest-Faculty at the Department of Applied Physics, Science College (Razabazar Campus), University of Calcutta and also Ex-Faculty of Institute of Engineering & Management (IEM), Kolkata.

He has a teaching experience of 18+ years. He obtained B.Sc. degree with Honours in Physics from University of Calcutta and both B.Tech. and M.Tech. degrees from the Institute of Radio Physics & Electronics, University of Calcutta, India. He obtained his Ph.D. degree in Engineering from Indian Institute of Engineering Science and Technology (IIEST), Shibpur. His research interest includes wide band gap semiconductor based Impatt diodes design, fabrication and characterization in D-band, W-band and THz frequencies, SIW technology based antennas, printed antennas and arrays, FSS, Dielectric Resonator antennas and Body wearable antennas. He has published 80+ research papers in International Journals and International/National Conferences.

Dr. Banerjee has authored 10 books and 3 book chapters in fields of Communication Engineering, Electromagnetic Field Theory, Microwave and Antenna. He is a corporate member of IEEE (USA) and IEEE AP Society, IETE (New Delhi, India) and IE (India). He is reviewer of several International Journals like IEEE Sensors Letter, Microwave and Optical Technology Letters

(MOTL-Wiley), Journal of Electromagnetic Waves and Applications (Taylor & Francis), Radioengineering Journal (Czech and Slovak Technical Univ.), Journal of Computational Electronics (Springer-Nature), Journal of Renewable and Sustainable Energy (American Institute of Physics-AIP), Journal of Infrared, Millimeter, and Terahertz Waves (Springer-Nature), etc.

Website: www.uem.edu.in
Linkedin: www.linkedin.com/in/soumencu
e-mail: prof.sbanerjee@gmail.com

Prof. Dr. Jyotsna Kumar Mandal did his M.Tech. in Computer Science from University of Calcutta in 1987 and was awarded Ph.D. (Engineering) in Computer Science and Engineering by Jadavpur University in 2000. Presently he is working as Professor, Computer Science & Engineering Department, University of Kalyani. He was the Former Dean, Faculty of Engineering, Technology & Management, Kalyani University for two consecutive terms during 2008–2012; Director-IQAC, Kalyani University and Chairman-CIRM and Placement Cell. He served as Professor of Computer Applications, Kalyani Government Engineering College for two years, Associate Professor of Computer Science for eight years at North Bengal University, Assistant Professor of Computer Science, North Bengal University for seven years and Lecturer at NERIST, Itanagar for one year.

He has 32 years of teaching and research experience in Coding theory, Data and Network Security & authentication; Remote Sensing & GIS based Applications, Data Compression, Error Correction, Visual Cryptography and Steganography. He has successfully guided 23 Ph.Ds, 1 submitted and 8 are pursuing. He had supervised 3 M.Phils, more than 70 M.Techs and more than 125 MCA Dissertations. He is the Guest Editor of Microsystems Technologies Journal (SCI indexed) of Springer. He had published more than 400 research articles out of which 170 articles are in International Journals. He had published 7 books from LAP Germany, IGI Global etc. and had organized 31 International Conferences. He is the Corresponding Editor of edited volumes

and conference proceedings of Springer, IEEE, Elsevier etc. and have edited 32 volumes as volume editor.

Website: www.jkmandal.com
e-mail: jkmandal@klyuniv.ac.in;
jkm.cse@gmail.com

Contributors

Labani Acharjee Computer Science & Engineering, University of Engineering and Management, Kolkata, India

Hazim Ahmed University of Engineering and Management, Kolkata, India

Sreejit Bagchi University of Engineering and Management, Kolkata, India

Arghasree Banerjee Department of Computer Science & Engineering, University of Engineering & Management, Kolkata, India

Saswata Banerjee University of Engineering and Management, Kolkata, India

Soumen Banerjee Department of Electronics and Communication Engineering, University of Engineering & Management, Kolkata, West Bengal, India

Sriparna Banerjee Jadavpur University, Kolkata, India

Sayani Banik University of Engineering and Management, Kolkata, India

Piyali Basak Jadavpur University, Kolkata, India

R. Bera Department of Electronics and Communication Engineering, Gayatri Vidya Parishad College of Engineering, Visakhapatnam, India

Avishek Bhadra M.B.C. Institute of Engineering & Technology, Bardhaman, West Bengal, India

Joy Bhattacharjee Department of Electronic Science, A.P.C College, Barasat, India

Mayukh Bhattacharjee Department of Computer Science & Engineering, University of Engineering & Management, Kolkata, India

Soumi Bhattacharjee University of Engineering and Management, Kolkata, India

Biplab Bhowmick Department of Electronics and Communication Engineering, Asansol Engineering College, Asansol, India

Md Aref Billaha Department of Electronics and Communication Engineering, Asansol Engineering College, Asansol, India

Hiren Chandra Borah Ministry of New and Renewable Energy, Government of India, New Delhi, India

Aditya Brahmachari Department of Electronics & Communication Engineering, University of Engineering & Management, Kolkata, India

Susmita Chaki University of Engineering & Management, Kolkata, India

Shouvik Chakraborty University of Kalyani, Kalyani, West Bengal, India

Sohom Chakraborty University of Engineering and Management, Kolkata, India

Souvik Chakraborty M.B.C. Institute of Engineering & Technology, Bardhaman, West Bengal, India

Suprava Chakraborty MNIT, Jaipur, India

Anuplab Chatterjee Department of Electronics & Communication Engineering, University of Engineering & Management, Kolkata, India

Diya Chatterjee University of Engineering and Management, Kolkata, India

Sankhadeep Chatterjee Department of Computer Science & Engineering, University of Engineering & Management, Kolkata, India;
Indian Institute of Engineering Science & Technology, Shibpur, India

Sombuddha Chatterjee Institute of Engineering and Management, Kolkata, India

Rik Chattopadhyay Dept. of Electronics and Telecommunication Engineering, Indian Institute of Engineering Science and Technology, Shibpur, Howrah, India

Sheli Sinha Chaudhuri Jadavpur University, Kolkata, West Bengal, India

Santosh Kumar Choudhary Department of Electronics and Communication Engineering, VNR Vignana Jyothi Institute of Engineering and Technology, Hyderabad, India

Chandreyee Chowdhury Jadavpur University, Kolkata, India

Debkumar Chowdhury University of Engineering and Management, Kolkata, India

Arpita Das University of Engineering and Management, Kolkata, India

Asit Kumar Das Department of Computer Science & Technology, Indian Institute of Engineering Science and Technology, Shibpur, India

Juhita Das University of Engineering & Management, Kolkata, India

N. R. Das Institute of Radio Physics & Electronics, University of Calcutta, Kolkata, India

Priyanka Das University of Engineering and Management, Kolkata, India

Trisha Das University of Engineering and Management, Kolkata, India

Prabir Kumar Dash Ministry of New and Renewable Energy, New Delhi, India

Chanchal Dey Instrumentation Engineering, Department of Applied Physics, University College of Technology, Kolkata, India

Shubhadeep Dey University of Engineering and Management, Kolkata, India

Sukanya Dey University of Engineering and Management, Kolkata, India

Arpan Deyasi Department of Electronics and Communication Engineering, RCC Institute of Information Technology, Kolkata, India

Arnab Ganguly CUTS International, Jaipur, India

Soham Ganguly Computer Science & Engineering, University of Engineering and Management, Kolkata, India

A. Ghosh Department of Electronics and Telecommunication Engineering, Indian Institute of Engineering Science and Technology, Howrah, India

Kushankur Ghosh Department of Computer Science & Engineering, University of Engineering & Management, Kolkata, India

Mouli Ghosh University of Engineering and Management, Kolkata, India

Pranati Ghoshal Applied Electronics and Instrumentation Engineering Department, Techno Main, Kolkata, India

Utpal Goswami West Bengal Renewable Energy Development Agency, Kolkata, West Bengal, India

Bhaskar Gupta Jadavpur University, Kolkata, India

Shubhojit Gupta Computer Science & Engineering, University of Engineering and Management, Kolkata, India

Biki Raj Hazarika Department of Electronics and Communication engineering, National Institute of Technology Durgapur, Durgapur, India

Arvind Kumar Ernst & Young LLP, Gurugram, Haryana, India;
World Bank-MNRE-SBI Technical Assistance Programme, New Delhi, India

Sachin Kumar Department of Electronics and Communication engineering, National Institute of Technology Durgapur, Durgapur, India

G. K. Mahanti Department of ECE, NIT Durgapur, Durgapur, WB, India

Bubai Maji Dept. of Electronics and Telecommunication Engineering, Indian Institute of Engineering Science and Technology, Shibpur, Howrah, India

Kalyani Mali University of Kalyani, Kalyani, West Bengal, India

Sakil Mallick Jadavpur University, Kolkata, India

B. Mandal Division of Solid State Electronics, Department of Engineering Sciences, Angstrom Laboratory, Uppsala University, Uppsala, Sweden

Chinmoy Mandal University of Engineering and Management, Kolkata, India

Sujit Kumar Mandal Department of Electronics and Communication engineering, National Institute of Technology Durgapur, Durgapur, India

Srijita Manna University of Engineering and Management, Kolkata, India

Sampoorna Das Mazumdar Institute of Engineering and Management, Kolkata, India

Raghav Mehra Indian Space Research Organization, Ahmedabad, India

Sanjukta Mishra Brainware University, Kolkata, India

Arundhati Misra Indian Space Research Organization, Ahmedabad, India

Sandipan Mitra Department of Electronics & Communication Engineering, University of Engineering & Management, Kolkata, India

Abhinandan Mohanty School of Electronics Engineering, (Deemed To Be University), Kalinga Institute of Industrial Technology, Bhubaneswar, Odisha, India

P. Mondal Department of Electronics and Communication Engineering, Gayatri Vidya Parishad College of Engineering, Visakhapatnam, India

Samrat Mondal M.B.C. Institute of Engineering & Technology, Bardhaman, West Bengal, India

Subhodeep Mondal University of Engineering and Management, Kolkata, India

Sukanto Mondal Jadavpur University, Kolkata, India

Piyali Mukherjee University of Engineering & Management, Kolkata, India; Institute of Radio Physics & Electronics, University of Calcutta, Kolkata, India

Pooja Mukherjee University of Engineering and Management, Kolkata, India

Soumyadev Mukherjee School of Computer Science Engineering, KIIT Deemed to Be University, Bhubaneswar, India

Swarnav Mukhopadhyay Department of Electronics and Telecommunication Engineering, Jadavpur University, Kolkata, India

Didhiti Nandi University of Engineering & Management, Kolkata, India

S. Navyashri University of Engineering and Management, Kolkata, India

Sarmistha Neogy Jadavpur University, Kolkata, India

Srikanta Pal Birla Institute of Technology, Ranchi, India

Subhradeep Pal Department of EEE, Birla Institute of Technology and Sciece, Pilani (BITS Pilani), Hyderabad, Telangana, India

Ayan Kumar Panja Jadavpur University, Kolkata, India;
Institute of Engineering & Management, Kolkata, India

Susanta Kumar Parui Department of Electronics and Telecommunication Engineering, Indian Institute of Engineering Science and Technology, Shibpur, Howrah, West Bengal, India

N. Pathak Department of ECE, Dr. B.C. Roy Engineering College, Durgapur, WB, India

S. Patra Department of ECE, SMIT-TIG, Guptipara, Hooghly, WB, India;
Department of ECE, NIT Durgapur, Durgapur, WB, India

Hrittika Paul Computer Science & Engineering, University of Engineering and Management, Kolkata, India

Soumik Paul Jadavpur University, Kolkata, India

Sujoy Paul University of Engineering and Management, Kolkata, India

Sayan Pramanik University of Engineering & Management, Kolkata, West Bengal, India

Suraj Prasad M.B.C. Institute of Engineering & Technology, Bardhaman, West Bengal, India

Purbasha Ray Department of Electronics and Telecommunication Engineering, Jadavpur University, Kolkata, India

Reeju Ray University of Engineering and Management, Kolkata, India

Nirmal Kumar Rout School of Electronics Engineering, KIIT Deemed to be University, Bhubaneswar, India

Anusua Roy University of Engineering and Management, Kolkata, India

Deepayan Roy University of Kalyani, West Bengal, Kalyani, India;
Department of Computer Science & Engineering, University of Engineering & Management, Kolkata, India

Kyamelia Roy Jadavpur University, Jadavpur, Kolkata, West Bengal, India

Mousomi Roy University of Kalyani, Kalyani, West Bengal, India

Priya Roy Jadavpur University, Kolkata, India

Probhakar Roy University of Engineering and Management, Kolkata, India

Rohan Roy School of Electronics Engineering, Kalinga Institute of Industrial Technology (KIIT), Bhubaneswar, Odisha, India

Sreyashi Roy School of Electronics Engineering, (Deemed To Be University), Kalinga Institute of Industrial Technology, Bhubaneswar, Odisha, India

Akash Sah Computer Science & Engineering, University of Engineering and Management, Kolkata, India

Abhirupa Saha Jadavpur University, Kolkata, India

Soumi Saha Department of Electronics and Communication Engineering, University of Engineering & Management (UEM), Newtown, Kolkata, India

Surjya Prakash Saha Department of Electronics & Communication Engineering, University of Engineering & Management, Kolkata, India

Pravin Kumar Samanta School of Electronics Engineering, KIIT Deemed to be University, Bhubaneswar, India

Soumen Santra Department of Computer Application, Techno International Newtown, Rajarhat, India

Subhadip Santra Department of Electronics & Communication Engineering, University of Engineering & Management, Kolkata, India

Arya Sarkar Department of Computer Science & Engineering, University of Engineering & Management, Kolkata, India

Goffar Ali Sarkar Department of Electronics and Telecommunication Engineering, Indian Institute of Engineering Science and Technology, Shibpur, Howrah, West Bengal, India

Sunit Kumar Sen Instrumentation Engineering, Department of Applied Physics, University College of Technology, Kolkata, India

Sudhanshu Shekhar University of Engineering and Management, Kolkata, India

Sanjib Sil Calcutta Institute of Engineering and Management, Calcutta, India

Harshavardhan Singh Department of Electronics and Communication engineering, National Institute of Technology Durgapur, Durgapur, India

Arunabha Tarafdar Computer Science & Engineering, University of Engineering and Management, Kolkata, India

Advances in Modern Communication Engineering

A Dielectric Resonator MIMO Antenna for Intelligent Transportation Systems

Goffar Ali Sarkar, Susanta Kumar Parui, and Soumen Banerjee

Abstract A two element multi-input-multi-output (MIMO) antenna system based on dielectric resonator antenna (DRA) is proposed in this work for application in IEEE 802.11p band dedicated to intelligent transportation system (ITS). The antenna element of rectangular shape is designed with dielectric constant (ε_r) value of 20. The antenna elements are arranged in orthogonal fashion to achieve polarization diversity. The S-parameters, radiation patterns and several MIMO diversity matrices have been studied. Impedance bandwidth is observed as 5.6%. Over the operating band, the MIMO antenna system gives an isolation of 18 dB. Peak gain for the antenna is obtained as 5.7 dBi. The correlation coefficient and diversity gain have been noticed as nearly 0 and 10 dB respectively.

Keywords Dielectric resonator antenna (DRA) · Envelope correlation coefficient (ECC) · Multiple-input-multiple-output (MIMO) · Impedance bandwidth · Isolation · Peak gain

G. A. Sarkar (✉) · S. K. Parui
Department of Electronics and Telecommunication Engineering, Indian Institute of Engineering Science and Technology, Shibpur, Howrah, West Bengal, India
e-mail: goffar.ali@gmail.com

S. K. Parui
e-mail: arkapv@yahoo.com

S. Banerjee
Department of Electronics and Communication Engineering, University of Engineering & Management, Kolkata, West Bengal, India
e-mail: prof.sbanerjee@gmail.com

S. Banerjee and J. K. Mandal (eds.), *Advances in Smart Communication Technology and Information Processing*, Lecture Notes in Networks and Systems 165,
https://doi.org/10.1007/978-981-15-9433-5_1

1 Introduction

Wireless communication through which people communicate worldwide very quickly is becoming a part of human life. Also, users can upload videos, play games, can use social media with a speed of real time. All those advancements in wireless communication requires high data rate and increased channel capacity. This can be achieved by increasing transmitted power (for enhancement of SNR) or band width as per channel capacity formulae. These two matrices are very unfavourable to implement as there are regulations on maximum power transmission levels of wireless terminals for avoidance of interference with other devices and assignment of extra bandwidth is very much costly in the crowded environment. MIMO technology where multiple antennas are used in both transmitter and receiver become a novel solution in that scenario. Major advancement in 4G wireless standard led to large increased data rates and throughput in MIMO antenna system using multiple antennas. Hence multiple antennas should be integrated within a compact area and all such antennas should give independent response simultaneously. Design of MIMO antennas with independent response is a challenging task and the design engineer should take precautions on several issues that were not present on single antenna system design such as isolation, correlation coefficient, diversity gain etc.

Much research has been carried out using microstrip antennas to implement MIMO system in wireless communication [1–4]. Planar antennas are very useful candidate in recent years for low profile and easy integration with PCB. However, in high frequency applications, conductor loss intensifies and limits the use of metallic antennas. A ceramic based material with attractive features is introduced in order to solve this problem. This radiating element placed on top of the substrate is called dielectric resonator antenna (DRA). Dielectric resonator antennas (DRAs) have several advantages such as light weight, higher impedance bandwidth, higher gain, no conductor loss, ease of excitation and so forth [5]. They also have shape versatility [6–8]. Despite such features DRAs did not get much attention as MIMO antenna. A limited number of works has been carried out on MIMO DRAs [9–11].

In this paper a two element MIMO DRA having polarization diversity is investigated at 5.8 GHz frequency band which is best suited for intelligent transportation system (ITS). Rectangular shape providing more degrees of freedom in design than hemispherical and cylindrical shape is chosen here. The proposed MIMO antenna elements are placed orthogonally for polarization diversity. With proper excitation two orthogonal modes are generated inside the DRA elements.

2 Antenna Design

The layout view of the designed MIMO DRA is depicted in Fig. 1a and its fabricated prototype is shown in Fig. 1b. The structure has two radiating elements of dimension $A \times B \times H$ with relative permittivity 20 and $\tan\delta = 0.002$. The footprint of the

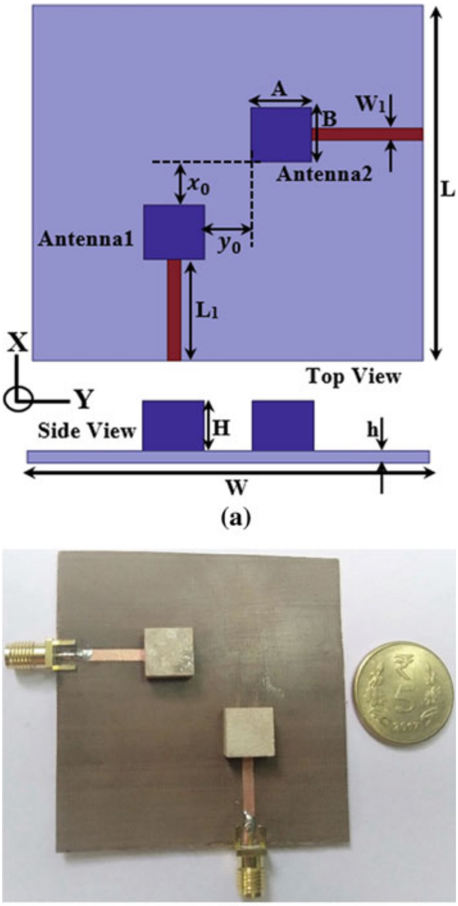

(b)

Fig. 1 **a** Layout view of the MIMO antenna **b** fabricated prototype

antenna is of $W \times L$ square units. The DR is mounted above the substrate having dielectric constant 2.7 and tan$\delta = 0.0023$. The MIMO antenna element is fed by 50 Ω microstripline having width W_1. The antenna element is in offset from each other by x_0 and y_0 for better isolation. The numeric values of the design parameters are given in Table 1.

3 Result and Discussion

The optimized MIMO antenna is fabricated on Arlon AD320 substrate and parameters are measured using vector network analyser. Figure 2a shows the simulated and measured scattering parameters of the proposed MIMO DRA. As the antenna

Table 1 Design parameters

Parameters	Value (mm)	Parameters	Value (mm)
L	62	B	9.525
L_1	15.537	H	6.2
W	62	h	0.79
W_1	2.13	x_0	7.475
A	9.525	y_0	7.475

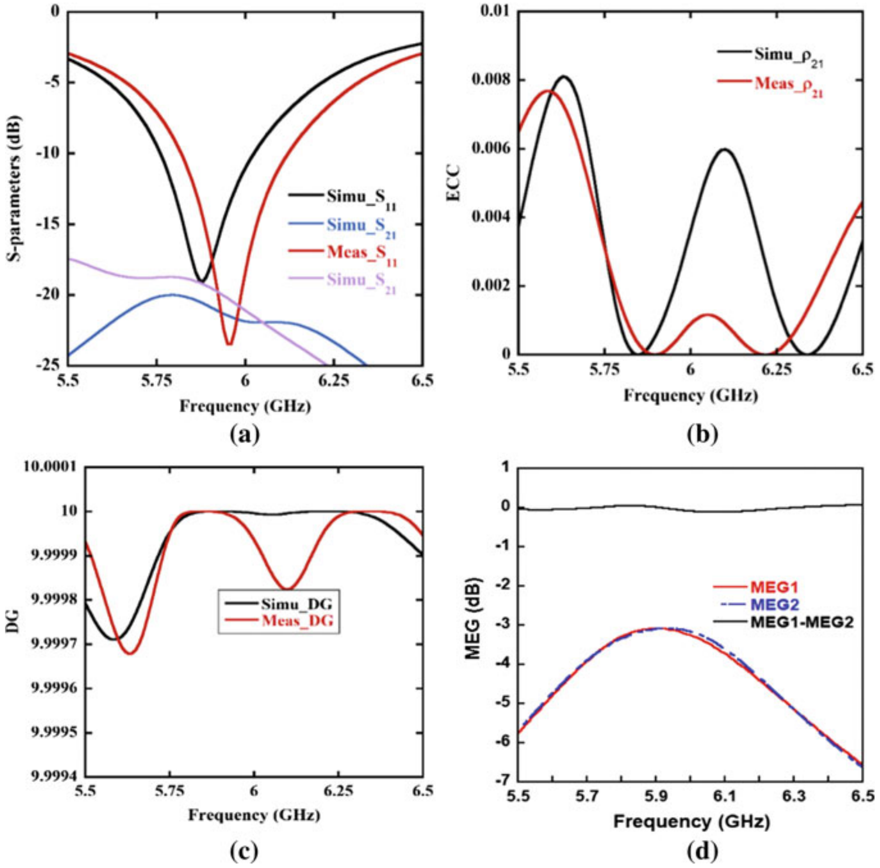

Fig. 2 **a** Scattering parameters of the MIMO DRA **b** ECC plot of the MIMO DRA **c** plot of DG with frequency **d** MEG and its difference with frequency

structure is symmetric, hence only s-parameters of port1 are shown. The level of reference for impedance bandwidth is −10 dB. It should be noted that the measured impedance band width is 5.6%. It is observed that isolation in worst case is 18 dB in the operating band. The envelope correlation coefficient (ECC) is demonstrated in Fig. 2b. It is observed as less than 0.006 over the operating frequency band which shows good diversity performance of the proposed MIMO antenna. The value of ECC for two port antenna system is calculated using Eq. (1) [12],

$$\rho_e = \frac{\left|S_{11}^* S_{12} + S_{21}^* S_{22}\right|^2}{\left(1 - |S_{11}|^2 - |S_{21}|^2\right)\left(1 - |S_{12}|^2 - |S_{22}|^2\right)} \tag{1}$$

where ρ_e is the envelope correlation coefficients and S_{ii} and S_{ij} stands for standard scattering parameters.

Diversity gain is one of the most important parameters to characterize a MIMO system. It should be closer to 10 for good diversity. It is calculated using [13] as,

$$DG = 10\sqrt{1 - |\rho_e|^2} \tag{2}$$

The simulated along with measured DG is demonstrated in Fig. 2c. From the figure DGs are observed nearly to be of value 10.

Other than these two parameters, mean effective gain (MEG) and its difference are also determined for evaluation of MIMO performances of the antenna. The difference of MEG should be nearly 0 dB for a MIMO antenna having good diversity performance. Plot of MEG and its difference are shown in Fig. 2d. From the figure it is clear that the MEG difference is around 0 dB through the operating frequency band. The normalized radiation characteristics of the proposed MIMO antenna for port1 and port2 are shown in Fig. 3. and Fig. 4. respectively. In both E-plane and H-plane radiation patterns are unidirectional and broadside. In addition to that simulated peak gain is observed as 5.7 dBi for both the ports.

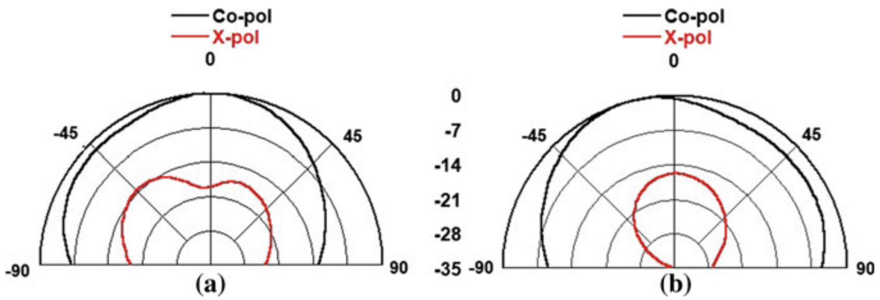

Fig. 3 Simulated 2-D radiation patterns of proposed antenna for port1 **a** E-plane (xz-plane). **b** H-plane (yz-plane)

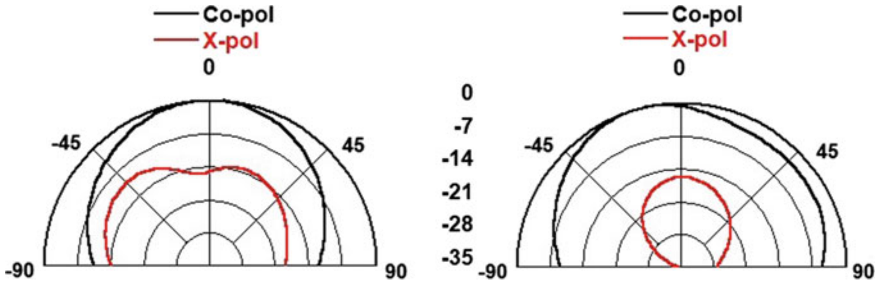

Fig. 4 Simulated 2-D radiation patterns of proposed antenna for port2 **a** E-plane (yz-plane). **b** H-plane (xz-plane)

4 Conclusion

In this paper a MIMO DRA at 5.8 GHz is proposed for application in intelligent transportation system. The proposed antenna gives unidirectional broad side radiation patterns with 5.7 dBi gain for both the ports. The antenna exhibits excellent diversity performance in terms of ECC (<0.006), DG (~10) and MEG (difference of MEG ~ 0 dB) in the entire operating band. Based on the results it can be concluded that the proposed antenna is very much efficient in application in ITS.

References

1. Luo, Y., Chu, Q., Li, J., Wu, Y.: A planar H-shaped directive antenna and its application in compact MIMO antenna. IEEE Trans. Antennas Propag. **61**(9), 4810–4814 (2013)
2. Chang, L.C., Tsai, C.H., Hsu, P., Liu, C.C.: A polarization diversity MIMO antenna design for WiMAX dongle application. In: Proceedings of Asia-Pacific Microwave Conference, pp. 762–765 (2010)
3. Zhu, J., Li, S., Feng, B., Deng, L., Yin, S.: Compact dual polarized UWB quasi-self-complementary MIMO/diversity antenna with band-rejection capability. IEEE Antennas Wirel. Propag. Lett. **15**, 905–908 (2016)
4. Lin, M., Chung S.: A compact MIMO antenna system with three closely spaced multi-band antennas for WLAN application. In: Proceedings of Asia-Pacific Microwave Conference, Bangkok, Thailand, pp. 1–4 (2007)
5. Rao, Q., Wang, D.: A compact dual-port diversity antenna for long term evolution handheld devices. IEEE Trans. Veh. Technol. **59**(3), 1319–1329 (2010)
6. Khalily, M., Rahim, M.K.A., Kishk, A.A., Danesh, S.: Wideband P-shaped dielectric resonator antenna. Radioengineering **22**(1), 281–285 (2013)
7. Feed, W.A.M., Chaudhary, R.K., Member, S., Kumar, R.: Wideband ring dielectric resonator antenna with annular-shaped microstrip feed. IEEE Antennas Wirel. Propag. Lett. **12**, 595–598 (2013)
8. Abedian, M., Rahim, S.K.A., Khalily, M.: Two-segments compact dielectric resonator antenna for UWB application. IEEE Antennas Wirel. Propag. Lett. **11**, 1533–1536 (2012)
9. Ishimiya, K., Langbacka, J., Ying, Z., Takada, J.I.: A compact MIMO DRA antenna. In: Proceedings of the IEEE International Workshop on Antenna Technology: Small Antennas and Novel Metamaterials (IWAT'08), Chiba, Japan, pp. 286–289 (2008)

10. Yan, J.B., Bernhard, J.T.: Design of a MIMO dielectric resonator antenna for LTE femtocell base stations. IEEE Trans. Antennas Propag. **60**(2), 438–444 (2012)
11. Nasir, J., Jamaluddin, M.H., Khalily, M., Kamarudin, M.R., Ullah, I.: Design of an MIMO dielectric resonator antenna for 4G applications. Wirel. Pers. Commun. **88**(3), 525–536 (2016)
12. Blanch, S., Romeu, J., Corbella, I.: Exact representation of antenna system diversity performance from input parameter description. Electron. Lett. **39**(9), 705–707 (2003)
13. Rosengren, K., Kildal, P.: Radiation efficiency, correlation, diversity gain and capacity of a six-monopole antenna array for a MIMO system: theory, simulation and measurement in reverberation chamber. IEE Proc. Microw. Antennas Propag. **152**(1), 7–16 (2005)

Some Studies on Microstrip Patch Antennas for Wearable Applications

Sandipan Mitra, Subhadip Santra, Anuplab Chatterjee, Surjya Prakash Saha, and Aditya Brahmachari

Abstract This paper presents a comparative study of three inset-fed patch antennas of different shapes like rectangular, circular and triangular for body wearable applications. Antenna parameters such as gain, bandwidth and return loss are simulated for best performance and the optimized antenna so obtained is mounted on a triple layered phantom. Simulation studies are being carried out to study and analyse the effects of such antenna-phantom composite structure as wearable antenna. The antennas are designed on FR4-epoxy substrate at the resonating frequency of 2.4 GHz (ISM band).

Keywords Patch antenna · Wearable antenna · Inset feed · Phantom model · ISM band

1 Introduction

In the modern era of wireless communication, wearable devices or more specifically wearable antennas, are gaining huge amount of interest for monitoring different biological signals. There is a rapid growth in the usage of flexible materials as substrate of an antenna. In order to reduce the radiation effects on human body, different structural designs and different feeding techniques have already been proposed in literature [1]. This paper basically focuses on such designs and development of wearable antennas for biomedical applications. One of the dominant research topics in antennas for body-centric communications is wearable, fabric-based antennas. The wearable antennas for all modern applications require light weight, low cost with almost zero maintenance. There are number of specialized occupational segments that require body centric communication systems, such as paramedics, fire fighters, and military. Besides, wearable antennas also can be applied

S. Mitra (✉) · S. Santra · A. Chatterjee · S. P. Saha · A. Brahmachari
Department of Electronics & Communication Engineering, University of Engineering & Management, Kolkata, India
e-mail: sandipanmitra97@gmail.com

S. Banerjee and J. K. Mandal (eds.), *Advances in Smart Communication Technology and Information Processing*, Lecture Notes in Networks and Systems 165,
https://doi.org/10.1007/978-981-15-9433-5_2

for youngsters, the aged and the athletes for the purpose of monitoring different biological responses.

The reasons for the choice of using microstrip patch antennas are its advantages being very low profile, having simple structure and low manufacturing cost. Moreover, they are mechanically robust, when mounted on rigid surfaces [2]. However, their main disadvantage lies in having very low bandwidth. Inset feeding technique is used as it is simple to design, facilitates in planar feeding and offers good input matching [3]. Most of the important wireless applications lie in the band starting from 900 MHz to 5.8 GHz. In this paper, three microstrip inset-fed patch antennas are designed to work at 2.4 GHz ISM band frequency. After comparing the parameters, the antenna with lowest profile and highest gain is to be mounted on the phantom, which is a prototype of the human torso. The human body is an irregularly shaped medium with frequency dependent permittivity and conductivity. The distribution of the electromagnetic field inside the body and the scattered field depends largely on the physiological parameters of the body and its geometry apart from being dependent on frequency and polarization of the incident field. Due to the high permittivity of body tissues, the resonant frequency in the antenna changes and detunes to a lower value.

2 Antenna Design and Analysis

The geometries of the proposed antennas are etched on an FR4-epoxy substrate of thickness 1.58 mm and relative permittivity (ε_r) of 4.4. Initially the antenna geometries were calculated using the basic antenna designing formulae [4] and the antennas were designed accordingly. Later, these antenna parameters were optimized using Ansys make HFSS simulator to obtain the best optimized results. The antenna design equations are as follows:

For rectangular patch, the antenna width (w) is given by

$$\mathrm{w} = \frac{c}{2f_r}\left(\sqrt{\frac{2}{\varepsilon_r + 1}}\right) \tag{1}$$

Antenna length (L) is given by

$$\mathrm{L} = \frac{c}{2f\sqrt{\varepsilon_{reff}}} - 2\Delta\mathrm{L} \tag{2}$$

Extension of antenna length (ΔL) is given by

$$\Delta\mathrm{L} = \frac{(\varepsilon_{reff} + 0.3)(\frac{w}{h} + 0.264)}{(\varepsilon_{reff} - 0.258)(\frac{w}{h} + 0.8)} \tag{3}$$

Effective dielectric constant is given by

$$\varepsilon_{reff} = \frac{\varepsilon_r + 1}{2} + \frac{\varepsilon_r - 1}{2}\left[\frac{1}{\sqrt{1 + 12(\frac{h}{w})}}\right] \tag{4}$$

Length of the feed line is given by

$$\text{Lf} = \frac{6h}{2} \tag{5}$$

Width of the 50 Ω feed line is given by

$$\text{wf} = \frac{60}{\sqrt{\varepsilon_{reff}}}\ln\left(\frac{8h}{w} + \frac{w}{4h}\right) \tag{6}$$

For circular and triangular patch, the radius of the patch is given by

$$\text{a} = \text{F}\{1 + \frac{2h}{\pi F \varepsilon_r}[\ln(\frac{\pi F}{2h}) + 1.7726]\} - 1/2 \tag{7}$$

$$\text{where F} = \frac{8.791 \times 10^9}{f_r\sqrt{\varepsilon_r}} \tag{8}$$

The different inset fed antenna designs which are compared to select the best optimized one to be mounted on the phantom are shown below.

2.1 *Design of Different Shaped Patch Antennas*

Figure 1a shows the schematic diagram of the rectangular patch antenna that had been found out after optimization using optimetrics in HFSS software. Figure 1b shows the return loss of the antenna upon simulation in free space. Figure 2a represents the schematic diagram of the circular patch antenna after optimization in HFSS software and its return loss is depicted in Fig. 2b. Figure 3a shows the schematic diagram of the triangular patch shaped antenna with its return loss plotted in Fig. 3b.

Table 1 enlists a comparative study of different patch shaped antennas and their simulated antenna parameters. A close study of the antenna parameters of the different antennas reveal that the gain of the rectangular inset feed antenna is of highest value (5.32 dBi) and lowest profile and hence is the most suitable one for designing wearable biomedical antennas.

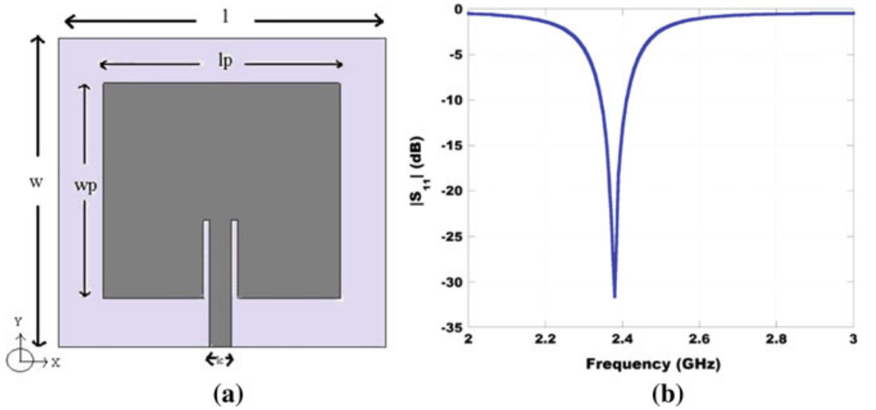

Fig. 1 **a** Top view of the designed rectangular patch antenna (l = 45 mm, w = 45 mm, lp = 30 mm, wp = 30 mm, lc = 3.25 mm), **b** simulated reflection coefficient of the rectangular patch antenna

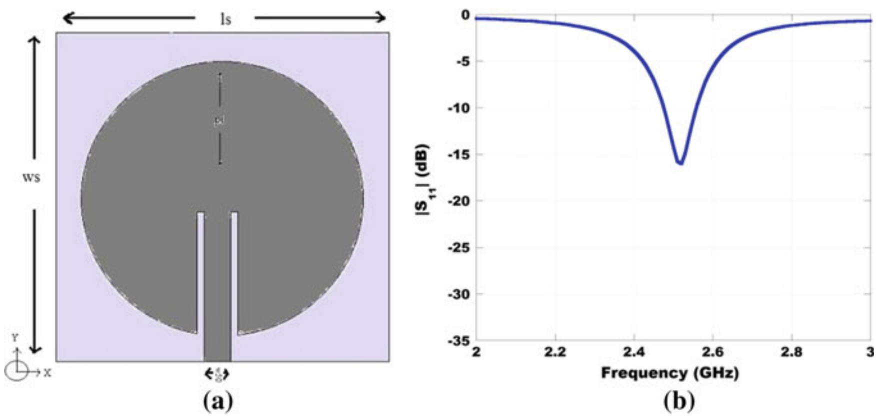

Fig. 2 **a** Top view of the designed circular patch antenna (ls = 40 mm, ws = 40 mm, pl = 17 mm, w50 = 3.02 mm), **b** simulated reflection coefficient of the circular patch antenna

2.2 Design of Phantom Structure

Phantom structures are artificial structures designed to emulate properties of human body in matters such as, including, but not limited to, light scattering and optics, electrical conductivity and sound wave reception. Phantoms have been used experimentally in lieu of, or as supplement to, human subjects to maintain consistency as well as to protect human beings from electromagnetic radiation hazards, to verify reliability of technologies, or reduce experimental expenses. They have also been employed as training material for different processes. For the analysis of wearable and implantable antennas, it is crucial to assess the interaction between human body and the electromagnetic waves. For this, it is required to have an equivalent phantom

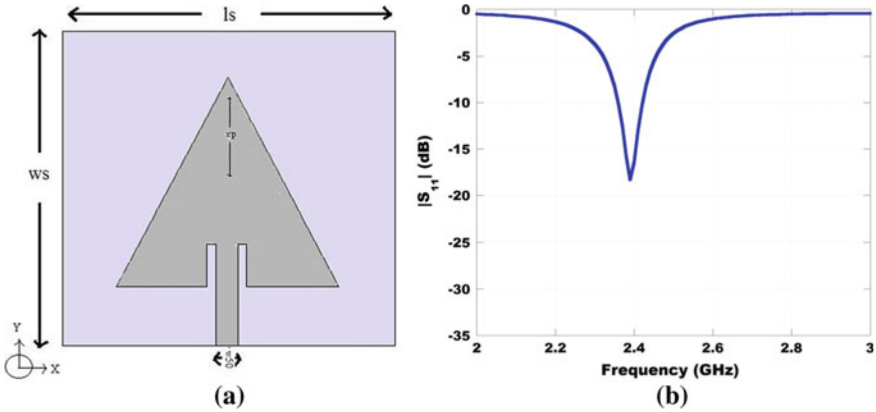

Fig. 3 **a** Top view of the designed triangular patch antenna (ls = 50 mm, ws = 50 mm, xp = 17 mm, w50 = 3.02 mm), **b** simulated reflection coefficient of the triangular patch antenna

Table 1 Comparison of simulated antenna parameters

Antenna parameters	Rectangular patch antenna	Circular patch antenna	Triangular patch antenna
Gain (in dBi)	5.32	4.93	3.77
Bandwidth (in MHz)	70 (2.34–2.41 GHz)	50 (2.47–2.52 GHz)	60 (2.36–2.42 GHz)
S_{11} (in dB)	−31.63	−16.04	−18.32

model emulating the dielectric properties of human tissues. The simplest phantom model includes single layer skin flat model with predefined dielectric properties at a given frequencies [5, 6]. However, to more actuate the tissue model inside the human body, a three layer phantom model is generally used which comprises of skin, fat and muscle layers [7, 8]. A multilayer tissue model is used here to study the antenna performance in on-body scenarios. The proposed antenna is placed 5 mm above a phantom (skin: $\varepsilon_r = 36.41$, $\sigma = 1.43$ S/m, fat: $\varepsilon_r = 8.29$, $\sigma = 0.18$ S/m and muscle: $\varepsilon_r = 53.4$, $\sigma = 2.06$ S/m) [9] with dimensions of 100 mm × 100 mm × 31.8 mm as shown in Fig. 4.

3 Simulated Results and Discussion

As the rectangular patch results in highest simulated gain value of 5.32 dBi, so it is used here and is mounted at a height of 5 mm above the phantom. The rectangular patch results in a simulated return loss of −31.63 dB in free space or air medium. Upon mounting on phantom, it results in a return loss of −24.49 dB. Figure 5 shows these values of simulated return loss of the antenna, in free space as well as on

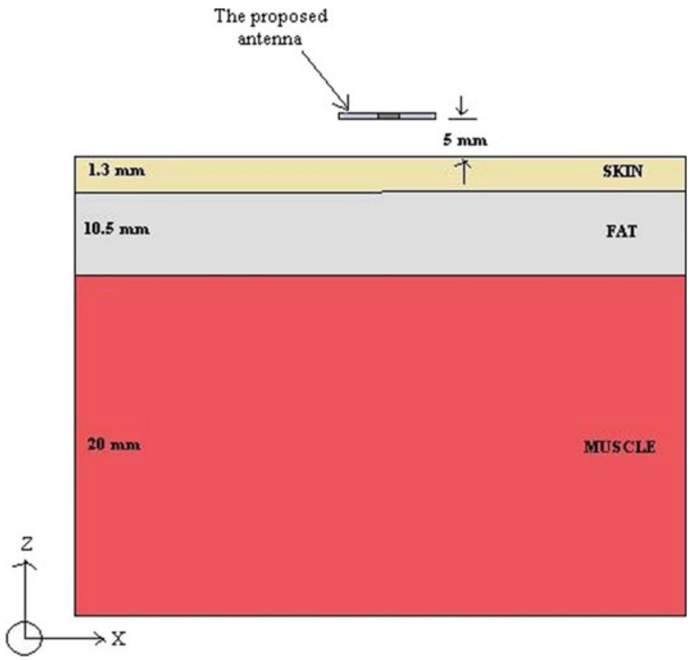

Fig. 4 Side view of the simulated patch antenna on three-layer phantom model

Fig. 5 Simulated reflection coefficient of the rectangular patch antenna in free space and when mounted on phantom

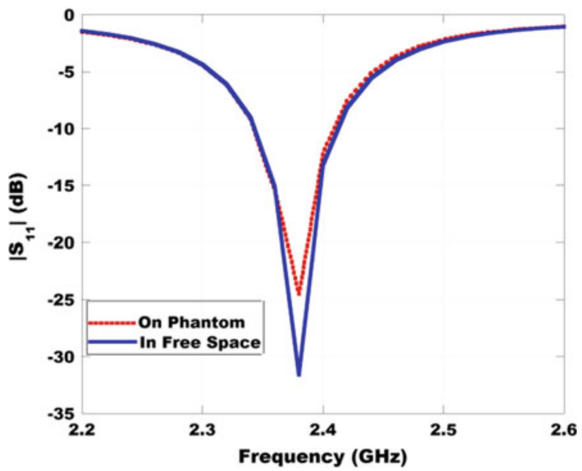

phantom. Figure 6 shows the radiation patterns of the inset-fed rectangular patch antenna when simulated in free space. The E-plane co-pol simulated value is found to be 5.32 dBi while the H-plane co-pol simulated gain is also found to be 5.32 dBi. Here the cross-pol values for both E- and H-plane are at least 40 dBi below their

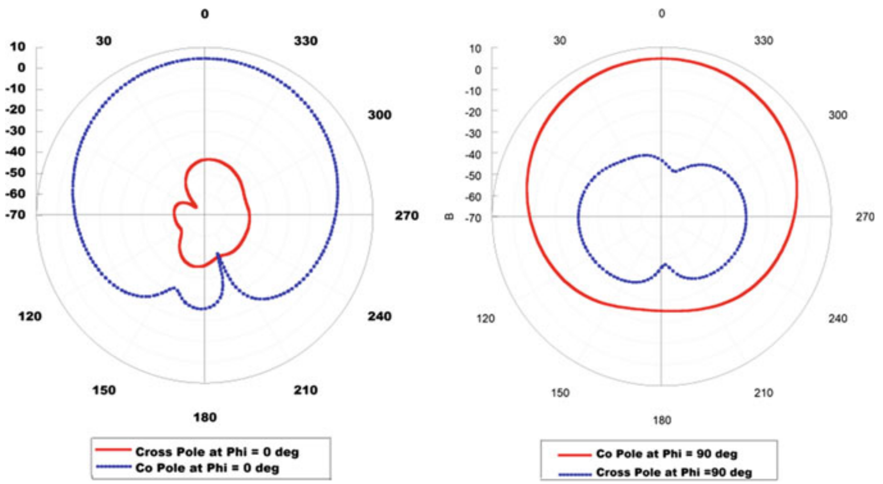

Fig. 6 Radiation pattern of the antenna when simulated in free space

respective co-pol values. Figure 7 shows the radiation patterns of the same antenna mounted on phantom. The E- plane co-pol simulated gain value is found to be 0.5 dBi while the H-plane co-pol simulated gain is found to be 1.7 dBi. Here the cross-pol values for both E- and H-plane are at least 40–50 dBi below their respective co-pol values.

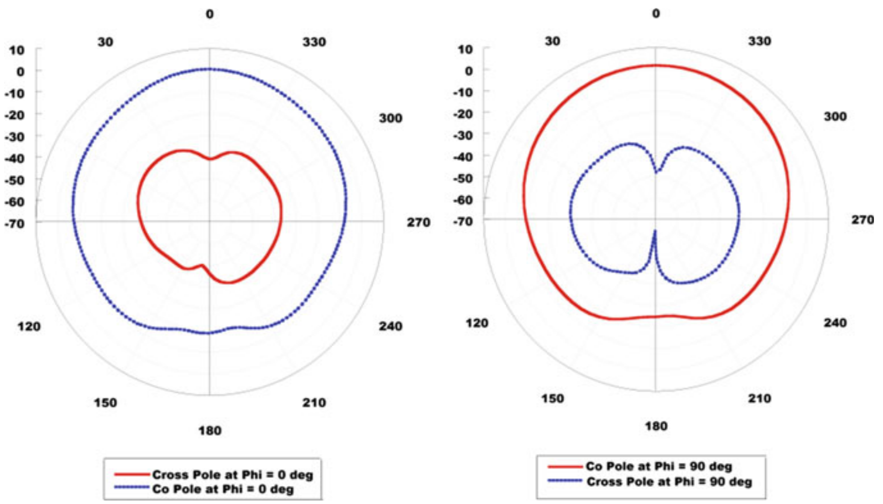

Fig. 7 Radiation pattern of the antenna when simulated on phantom

4 Conclusion

This paper presents three inset-fed patch antennas, amongst which the rectangular patch is chosen for its best performance in terms of simulated E-plane gain (5.32 dBi) and return loss (−31.63 dB). Upon mounting the same on phantom, the return loss of the antenna-phantom composite structure obtained is −24.49 dB with a simulated E-plane gain of 0.5 dBi. So this inset fed antenna can be utilised as a perfect candidate to be used as wearable antenna for biomedical applications.

Acknowledgements The authors express their sincere thanks to the Professors and research workers of Microwave Laboratory at Indian Institute of Engineering Science and Technology, Shibpur for their valuable guidance, help and support to carry out the research work.

References

1. Manna, S., Bose, T., Bera, R.: Wearable antennas for medical application: a review. Advances in Electronics, Communication and Computing, pp. 115–130. Springer, Singapore (2014)
2. Meena, M., Kumar, P.: Analysis of microstrip patch antenna for four different shapes and substrates. ICTACT J. Microelectron. **04**(01) (2018)
3. Varshney, H.K., Kumar, M., Jaiswal, A.K., Saxena, R., Jaiswal, K.: A survey on different feeding techniques of rectangular microstrip patch antenna. Int. J. Curr. Eng. Technol. **4**(3), 1418–1423 (2014)
4. Azlan, A.A., Badrun, M.K.A.B., Ali, M.T., Awang, Z., Saad, Z.B.M., Awang, A.H.B.: A comparative study of material leucaenaleucocephala stem wood plastic composite (WPC) substrate with FR4 substrate throughout single patch antenna design. Prog. Electromagn. Res. **59**, 151–166 (2014)
5. Tak, J., Lee, S., Choi, J.: All-textile higher order mode circular patch antenna for on-body to on-body communications. IET Microw. Antennas Propag. **9**(6), 576–584 (2014)
6. Gabriel, C.: Compilation of the dielectric properties of body tissues at RF and microwave frequencies. King's Coll London (United Kingdom) Dept of Physics (1996)
7. Abdalla, M.A., El Atrash, M., Elhennawy, H.M.: A wearable dual-band low profile high gain low SAR antenna AMC-backed for WBAN applications (2019)
8. Zhu, X.Q., Guo, Y.X., Wu, W.: Miniaturized dual-band and dual-polarized antenna for MBAN applications. IEEE Trans. Antennas Propag. **64**(7), 2805–2814 (2016)
9. vanZyl, F.J., Marais, J., Nieuwoudt, M., Niesler, T.R.: Computer simulation and physical phantom models for estimating the dielectric properties of rhinoceros tissue. PLOS One **14**(5) (2019)

Ultra Wide Band Planar Inverted F Antenna Design

Priyanka Das, S. Navyashri, Diya Chatterjee, Reeju Ray, and Pooja Mukherjee

Abstract By incorporating a suspended metallic patch with two different slots and a shorting post as a support of suspension, an ultra wide band PIFA has been proposed which leads to an achievement of a gain greater than 11 dB in the operating frequency range 7.39–15.98 GHz with a ultra wide bandwidth of 8.53 GHz and over 95% fractional bandwidth. The width of the shorting post and the height of the patch from ground plane are optimised to 4 mm and 2 mm. respectively. The metallic patch is suspended above the ground plane with the help of the shorting pin. To secure a maximized return loss, the lumped port and the shorting post are placed at the edge. The rectangular and circular slot is optimally positioned on the patch for securing a high bandwidth.

Keywords Ultra wide band PIFA · Micro-strip patch · High gain

1 Introduction

In the modern era of miniaturization there is a requirement of designing a low profile antenna which yields optimum characteristics like wide bandwidth and high gain. PIFA is the most promising candidates in this regard. It provides small size, light weight, omni-directional radiation pattern, reasonable gain and acceptable bandwidth. It is a challenging task to acquire high gain and high bandwidth simultaneously for PIFA. In the recent reported works, PIFA operates in 4 bands by inserting U shaped slits on the patch [1] which causes a 55% size reduction. Liu et al. [2] reports size miniaturization of PIFA by employing hook-shaped slots at the edges of the radiating patch. Leelaratne et al. [3] presents compact PIFA antennas operating at mobile telephone bands which exhibits horizontal polarization sensitivity. A flat structured hexaband PIFA for mobile handset applications is proposed in [4] while an UWB PIFA working from 817–11.5 GHz is mentioned in [5] having return loss less

P. Das (✉) · S. Navyashri · D. Chatterjee · R. Ray · P. Mukherjee
University of Engineering and Management, Kolkata, India
e-mail: priyanka.das@uem.edu.in

S. Banerjee and J. K. Mandal (eds.), *Advances in Smart Communication Technology and Information Processing*, Lecture Notes in Networks and Systems 165,
https://doi.org/10.1007/978-981-15-9433-5_3

than −6 dB. Broadband characteristics are achieved with two branchlined meander structured PIFA in [6]. The effect of dielectric constant of the substrate on return loss, impedance bandwidth, resonant frequency and gain are explored for a PIFA having dimensions 15.3 mm × 15.3 mm in [7].

In this paper, a novel design of ultra wide band PIFA that exploits the frequency range of 7.39 GHz to 15.98 GHz with a high bandwidth of 8.53 GHz and a fractional bandwidth of 95.5% has been proposed. The design consists of a metallic patch having two different shaped slots which is suspended above the ground plane with the help of a shorting post of width 4 mm. One slot is rectangular in shape and the other slot is made by integration of a rectangular slot and circular slot which enhances the operating bandwidth of the antenna without perturbing its high gain characteristics in the radiation pattern. The gain of the proposed PIFA is about 5 dB which ensures low power loss and higher directivity in point to point communication systems.

2 Structure of the Proposed PIFA

The PIFA has been designed and analyzed using the following design equations. The length and width of the patch corresponding to the design frequency for high gain has been calculated based on the following equations.

$$\mathrm{l} + \mathrm{w} = \lambda/4 \tag{1}$$

when

$$\mathrm{w/l} = 1,\ \mathrm{l} + \mathrm{h} = \lambda/4 \tag{2}$$

when $\mathrm{w} = 0$,

$$\mathrm{l} + \mathrm{w} + \mathrm{h} = \lambda/4 \tag{3}$$

where

$\varepsilon_r = 4.4$, the relative permittivity of FR4epoxy.

l is the top patch length.

w is the top patch width.

λ is the wavelength corresponding to resonant frequency.

h is the height from the ground patch.

The input impedance of the antenna is controlled by the width ‘w’ of the patch of the antenna (Fig. 1). The gain of the PIFA can be increased by increasing the width. The resonating frequency is inversely proportional to the length l of the patch. The height of the patch from the ground plane has significant impact on the operating bandwidth and it is optimized to 2 mm for achieving a wide bandwidth. PIFA is widely used in wireless communication because of its feature that it exhibits moderate to

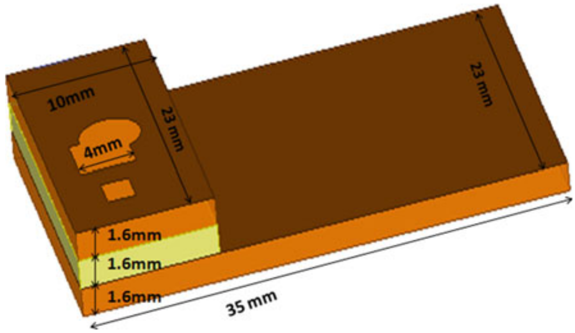

Fig. 1 Structure of the proposed PIFA

high gain values in both horizontal and vertical states of polarization. In. addition to it, it possesses features like high efficiency and wideband characteristics.

The design of the proposed antenna is shown in Fig. 2. The proposed PIFA consists of the ground plane, metallic patch, lumped port and shorting post. The metallic patch is suspended in the air with the assistance of a shorting post. The metallic plate consists of two slots. One slot is the rectangular slot and other slot is made by the merging rectangular and circular slots. The slotted patch is etched on the FR4 substrate. The slots are the important elements in increasing the gain of the antenna as they assist in modifying the current distribution on the patch.The position of the shorting post and lumped port determines the frequency of operation of the antenna. The slots compel the current to flow around the impediments which increases the electrical path length. The slots thus increase the electrical dimensions which excites low frequency modes for enabling the antenna to resonate at lower frequencies. The slots are capacitively coupled for improvement in matching.

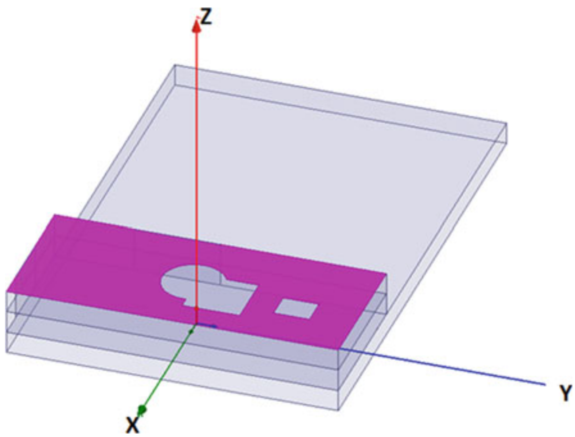

Fig. 2 Structure of the radiating patch

2.1 Analysis and Design

The physical dimensions of the ground plane are 10 mm × 23 mm. The shape and size of the ground plane is the important factor in determining the gain of the antenna. The physical dimension of the patch plane is 10 mm × 15 mm. The patch is formed on FR4 epoxy, a kind of dielectric material having a dielectric constant of 4.4. A dielectric substrate is important because it improves the electrical and mechanical stability. The dielectric material is employed to supply the displacement current which produces time varying Magnetic field (by Ampere's Law). Dielectric materials also are helpful in reducing the dimensions of the antenna due to higher permittivity (Figs. 3 and 4). The length of the substrate below the bottom plane is 35 mm whereas the width of the substrate below the bottom plane is 23 mm. The space between the patch and

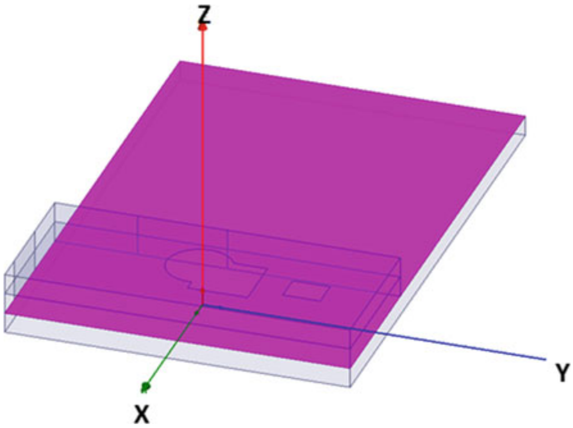

Fig. 3 Structure of the ground

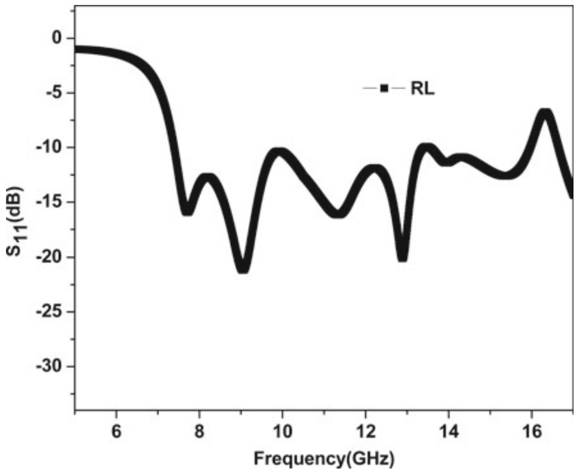

Fig. 4 Reflection Coefficient of the proposed PIFA

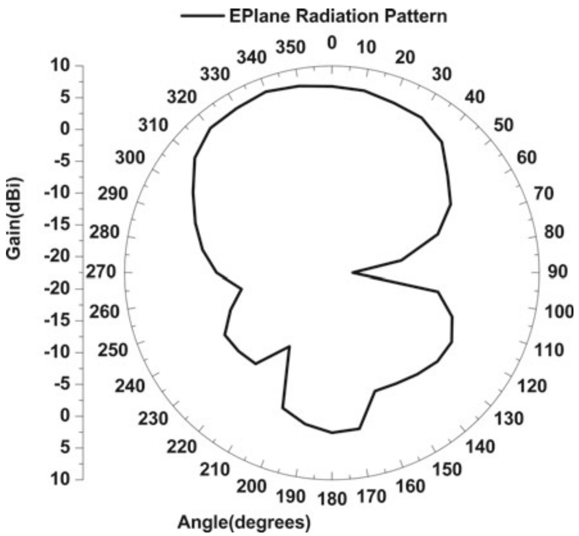

Fig. 5 Radiation Pattern at 9 GHz

the ground plane is 2 mm. The ground plane in this design has the dimension of 15 mm by 23 mm. The lumped port and the shorting post are substituted at the edge so that the return loss is maximized. The metallic patch is suspended in the air with a shorting pin. In the design it is shown by the air box above the ground plane. The dimension of the metallic patch is 10 mm by 23 mm. The bandwidth of the PIFA is affected by the position of the metallic patch and also the slots over it, above the ground plane. In this design a high bandwidth of 8.53 GHz is achieved which is ultra wide band and is ideal for mostly all kind of communication networks. The antenna is functioning in the frequency range of 7.39 GHz to 15.98 GHz. The gain of the antenna is 5 dB. The radiation pattern and gain of the proposed PIFA is analogous to that of a monopole antenna as shown in Fig. 5.

Antenna's feed position is also a necessary parameter as the correct feed—position assists impedance matching. Usually, coaxial feed is used as the feeding port but in our design we have used lumped port of physical dimension 12 mm $\times$ 6 mm. The lumped port helps in finding the response of the antenna in terms of S-parameters which helps to determine its impedance matching and insertion loss. The radiation efficiency of the antenna is 102% in the operating bandwidth (Figs. 6 and 7; Table 1).

The lowest resonant frequency is determined by the altitude of the antenna and location of the closest edge of the short-circuited wall. The upper frequencies are adjusted by the width of the vertical wall. At the resonant frequency 9.4 GHz, maximum current distribution occurs on the patch due to electrical resonance.

Fig. 6 3D Polar plot of the proposed PIFA

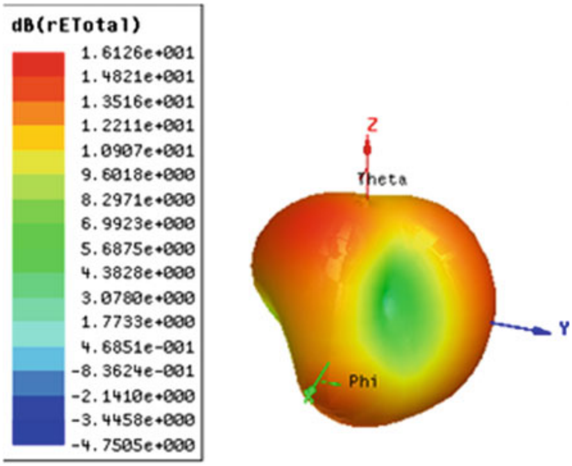

Fig. 7 Surface Current distribution on the patch at 9.4 GHz

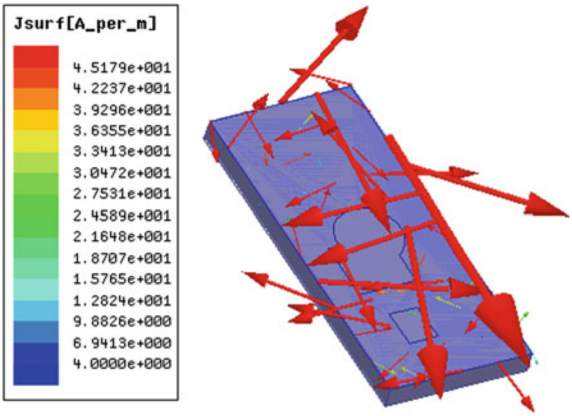

Table 1 Optimised Dimensions Of the PIFA Antenna

Parameters	Values
Patch length (l)	10 mm
Patch width (w)	23 mm
Lumped port position (lp)	12 mm
Lumped port width (lpw)	6 mm
Shorting post position (sp)	−2 mm
Shorting post width (spw)	4 mm
Length of the substrate below ground plane (lg1)	35 mm
Height of the Air box (h1)	1.62 mm

3 Conclusion

In this design two slots are formed on the patch namely a smaller rectangular slot and a slot which is made by uniting the areas of a rectangular slot and circular slot. The novelty of the proposed work lies in the design of the slot which is responsible for enhancing the bandwidth of the antenna by perturbing the electric field distribution on the patch. The proposed antenna exhibits a high gain which makes it suitable for modern communication systems.

References

1. Nashaat, D.M., Elsadek, H.A., Ghali, H.: Single feed compact quad-band PIFA antenna for wireless communication applications. IEEE Trans. Antennas Prop. **53**, 8 (2005)
2. Liu, W.-C., Chen, S.-H., Wu, C.-M.: Bandwidth enhancement and size reduction of an implantable Pifa antenna for biotelemetry devices. Microwave Optical Technol. Lett. **51**(3), (2009)
3. Leelaratne, R., Langley, R.: Multiband PIFA vehicle telematics antennas. IEEE Trans. Vehicular Technol. **54**(2), (2005)
4. Kang, D.-G., Sung, Y.: Compact hexaband PIFA antenna for mobile handset applications. IEEE Antennas Wireless Prop. Lett. **9**, (2010)
5. Gomez-Villanueva, R., Linares-y-Miranda, R., Tirado-Mendez, J.S., Jardon-Aguilar, H.: Ultra-wideband planar inverted-f antenna (pifa) for mobile phone frequencies and ultra-wideband applications. Progress Electromag. Res. **43**, (2013)
6. Choi, D.G., Shin, C.S., Kim, N., Shin, H.S.: Design and SAR analysis of broadband PIFA with triple band. Progress in Electromagnetics Research Symposium 2005, Hangzhou, China, Aug. 22–26 (2005)
7. Dabhi, A.P., Patel, S.K.: Response of planar inverted F antenna over different dielectric substrates. Int. J. Sci. Technol. Res. **3**(5), 2014

A Novel Design of Circularly Polarized Antenna with Asymmetric Slots

Priyanka Das, Shubhadeep Dey, and Saswata Banerjee

Abstract In this paper, a novel design of circularly polarized antenna has been implemented over a wide angular range of 60° at 7.9 GHz. The antenna exhibits a return loss of −19 dB of 7.8 GHz. A L-shaped asymmetric slot has been cut on a truncated cornered rectangular micro-strip patch to create circularly polarized radiation. The simulation is performed in HFSS software and the simulated results of the antenna are presented. The proposed antenna is compact (33.3 mm × 29.6 mm × 1.6 mm) and exhibits a low profile. The simulated return loss, axial ratio and radiation pattern validate the conditions for circular polarization.

Keywords Wide angular range · Axial ratio · Asymmetric slots · Circular polarization

1 Introduction

Polarization [1] refers to the path traced by the tip of the electric field vector as function of time. It is strongly desirable to control the polarization state of electro-magnetic wave to nullify the effect of faraday's rotation caused by the ionosphere for which polarization conversion is required [2]. CP antennas are widely used in WLAN, Wi-Max, GPS and RFID systems since they does not impose any restriction on the orientation of the transmitter and the receiver. Moreover CP antennas are immune to polarization mismatch losses due to wrong alignment of the transmitting and the receiving antenna [3]. depicts a triple-band circularly polarized (CP) antenna with the capability of switching its polarization by employing a monopole loop antenna integrated with a parasitic loop around it. Circularly polarized waves have a major role in mobile and satellite communication [4] since they prevent errors due to multi-path reflections. Circularly polarized waves ameliorate signal propagation in Global Navigation Satellite Systems (GNSS) [5]. Having single or double feeding patches,

P. Das (✉) · S. Dey · S. Banerjee
University of Engineering and Management, Kolkata, India
e-mail: priyanka.das@uem.edu.in

S. Banerjee and J. K. Mandal (eds.), *Advances in Smart Communication Technology and Information Processing*, Lecture Notes in Networks and Systems 165,
https://doi.org/10.1007/978-981-15-9433-5_4

CP antennas are widely used as good radiators in communication system [6]. For this operation micro strip patch antenna is used for its low profile, light weight and low cost of fabrication. The circular polarization can be obtained in the microstrip patch if two orthogonal modes are excited with a 90° time-phase difference between them [7]. In this design a single feed technique (co-axial) is used.

2 Model Analysis and Design

In this paper a circular polarized antenna model is constructed using HFSS 15. The antenna model is designed with substrate Rogers RT/duroid5880(tm) whose relative permittivity is 2.2($\varepsilon_r = 2.2$). The thickness of the substrate (h) = 1.6 mm. This model is employed using a modified square patch and co-axial feeding technique. The substrate dimensions are 29.6 mm × 33.3 mm × 1.6 mm.

To obtain the two orthogonal modes of excitation having 90° phase-shift between them, an asymmetric L-shaped slot, made by two rectangles of different dimensions, has been cut on the patch to perturb the electric field distribution on the patch. In this particular design, each corner of the rectangular patch has been cut to excite orthogonal modes on the patch. These orthogonal fields should be of equal magnitude and 90° out of phase to ensure circular polarization.

The proposed design exhibits a return loss of −18 dB at 7.9 GHz which ensures good matching at the feed point. The radiation pattern of the electric fields in theta direction(E_θ) and in phi direction(E_φ) overlap with each other thus suggesting equal excitation of orthogonal modes which serves as a condition for circular polarization. The peak gain is positive. The axial ratio (E_θ/E_φ) is close to 1 for a wide angular range of 60° at 7.9 GHz. The width of the vertical thin rectangle of the slot is optimised to get proper axial ratio and radiation pattern of E-field, so that orthogonal modes excited are of equal magnitude and 90° out of phase. The horizontal rectangular slot is affects the E field distribution along the horizontal direction. It is optimized to achieve wide angular beamwidth. The rectangular slot creates higher order modes on the patch which interfere with the resonant mode.

A positional change in entire L-shaped slot shows negative gain and angular range get decreased to 30° with an improper return loss. The removal of the cuts at each corner convert the patch from circularly polarized antenna to linearly polarized antenna. Keeping the diagonal cuts of the corner alternatively reduces the gain of the radiation pattern and disrupts the 3 dB axial ratio which is otherwise maintained. The input feed location is achieved by theoritical calculations. If altered, then the power to the antenna is not properly fed to it and thus it reduces the gain of the radiation. The coupling capacitance between the metallic patch and the ground plane affects the CP behaviour of the proposed antenna. The proposed design in this paper is unique and fulfills all the major conditions required to provide circular polarization.

3 Model Analysis and Design

W is the width of the patch

c is the speed of light($c = 3 \times 10^{11}$ mm)

εr = relative permittivity of di-electric

($\varepsilon r = 2.2$)

f = resonating frequency

$\boldsymbol{\varepsilon}_{\mathbf{r\,(eff)}} = (\frac{\varepsilon r+1}{2}) + (\frac{\varepsilon r-1}{2})\sqrt[-2]{(1+\frac{12*h}{W})}$.(i)

Where $\boldsymbol{\varepsilon}_{\mathbf{r\,(eff)}}$ is the effective relative permittivity

h = height of the substrate

εr = relative permittivity of di-electric

Where L_{eff} is the length of the patch and L is the length of the patch

$\mathbf{L_{(eff)}} = \frac{c}{2f\sqrt{\varepsilon r(\text{eff})}}$ (ii)

$\mathbf{x_f} = \frac{L}{2\sqrt{\varepsilon r(\text{eff})}}$ (iii)

$\mathbf{x_f}$ is the location of feed

Lg = L + 6 × h (iv)

Where Lg is the length of the substrate

Wg = W + 6 × h (v)

Where Wg is the width of the substrate

The axial ratio depends on the cross-polarization power.

$\mathbf{AR} = 20log_{10}\frac{1+e}{1-e}$ (vi)

$\mathbf{e} = 10^{-PdB/20}$

PdB = CrossPolar power

The asymmetric T shaped slot excites two orthogonal modes on the patch. The dimensions of the rectangular slot are optimized so that the orthogonal modes have equal amplitude at the resonance frequency in order to realize circular polarization (Table 1).

Table 1 Dimensions of the Proposed Circularly Polarized Antenna

Parameters	Dimensions
Length of the substrate (lg)	29.6 mm
Width of the substrate (wg)	33.3 mm
Length of the patch (l)	20 mm
Width of the patch (w)	23.7 mm
The feed location (x_f)	6.35 mm
Cut at each corner of the patch (v × k)	(1.85 mm × 2 mm)
Cut of the patch (horizontal, x × o) Cut of the patch (vertical, x1 × x2)	(14 mm × 3.9 mm) (8 mm × 0.55 mm)
Height of the substrate (h)	1.6 mm

3.1 Geometry of the Antenna Structure

4 Experimental Results

The s-parameter of the implemented design shows −19 dB return loss at 7.8 GHz as shown in Fig. 1. The axial ratio frequency coincides with the return-loss frequency. Figure 2 shows that axial ratio of less than 3 dB is obtained from 7.85 to 8.10 GHz. In Fig. 3, E_θ and E_φ overlap with each other at the frequency 7.9 GHz showing circular polarization plotted in E plane. The proposed CP antenna exhibits LHCP. In case of circular polarization the axial ratio between (E_θ and E_φ) = 1. Ideally, this model shows

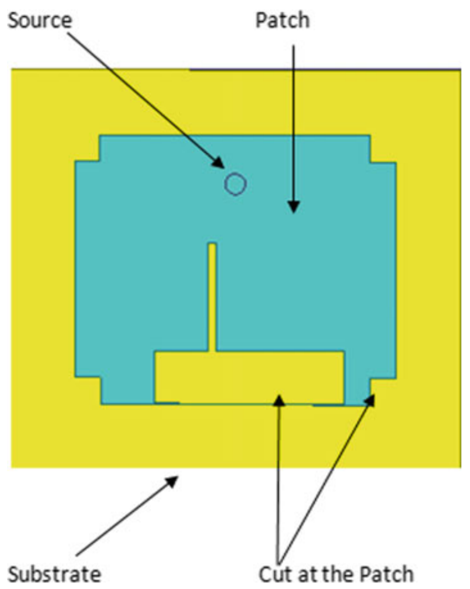

Fig. 1 Antenna geometry

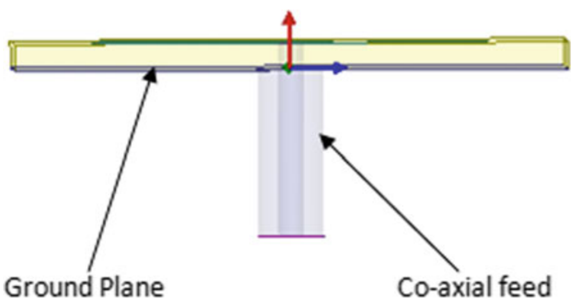

Fig. 2 Co-axial fed CP

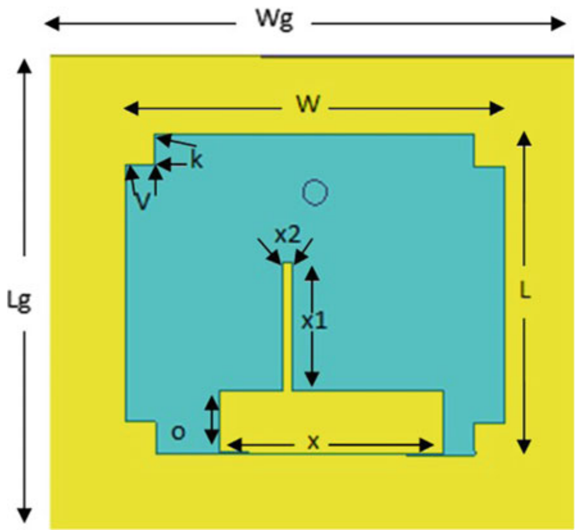

Fig. 3 **a** Dimensions of model **b** reflection coefficient (S_{11} plot)

a wide angular range (40–100°) over which 3 dB axial ratio is maintained as shown in Fig. 7. Impedance plot shows sharp two peaks one is for (E_θ) another one is for ($E\varphi$) excitation as shown in Fig. 8. Finally the 3D plot in Fig. 9 suggests omnidirectional radiation pattern of the proposed circularly polarized microstrip patch antenna.

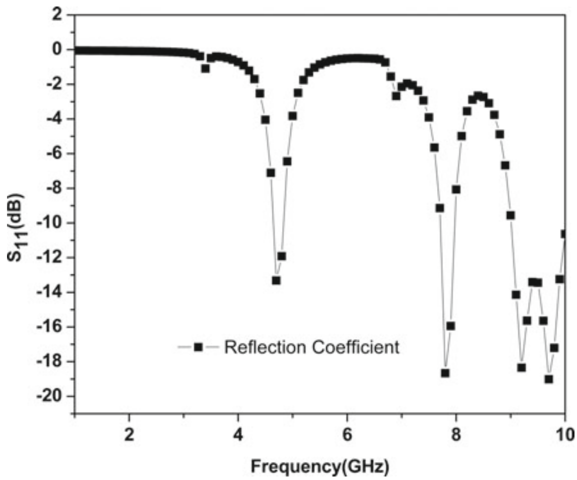

Fig. 4 Reflection Coefficient versus Frequency Plot

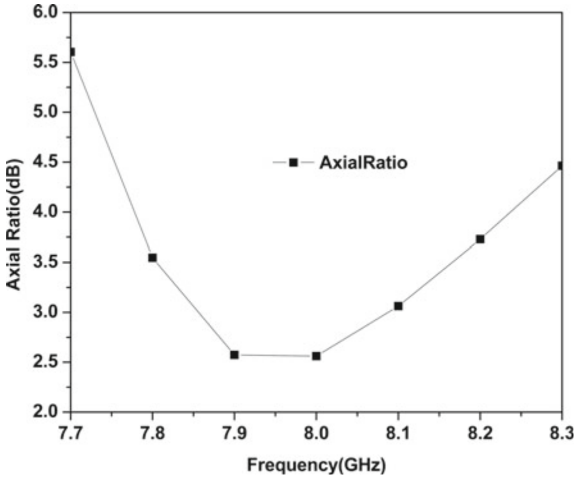

Fig. 5 Axial Ratio versus Frequency Plot

5 Conclusion

A circularly polarized antenna has been designed, implemented and simulated using ansys software 15(HFSS). The resonance frequency of antenna is 7.9 GHz which is suitable for communication purposes. The corresponding value of s parameter shows 19 dB of return loss at 7.8 Ghz frequency. The impedance plot shows two sharp peaks, one for E(θ) and E(φ). The antenna also shows quite good axial ratio which ranges from 1.4 to 2.8 dB over a wide angular range of 30–90° in the frequency range (7.85–8.1 GHz). The proposed antenna is compact in size and simple in design which makes it suitable for modern communication systems.

Fig. 6 LHCP and RHCP radiation pattern

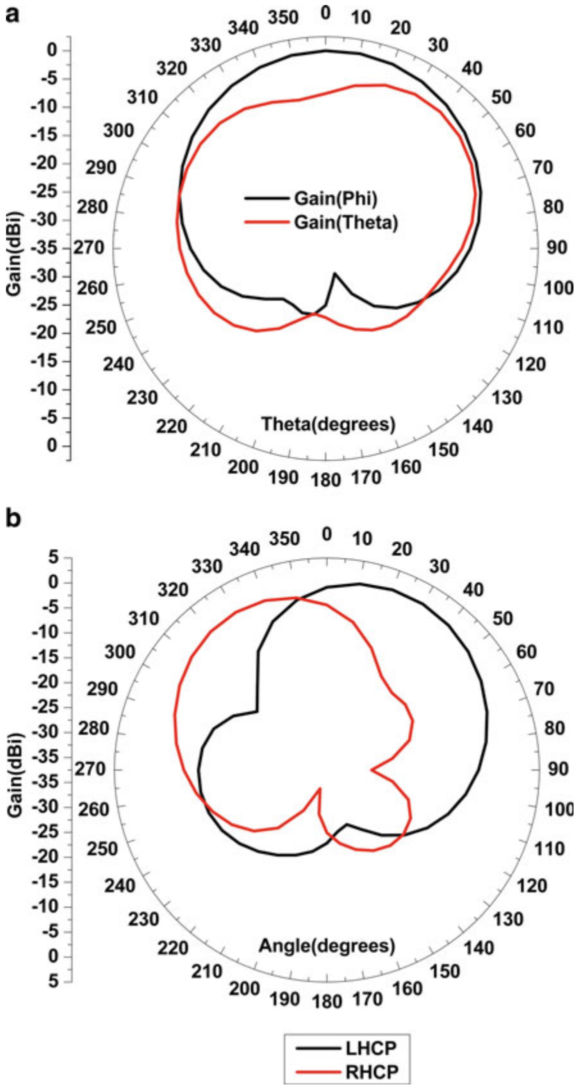

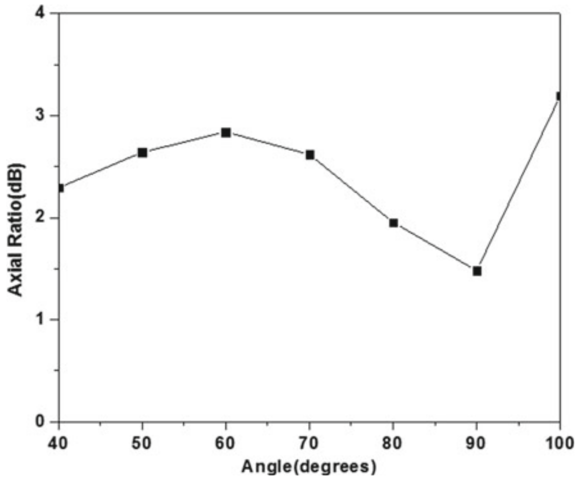

Fig. 7 Axial ratio of CP antenna

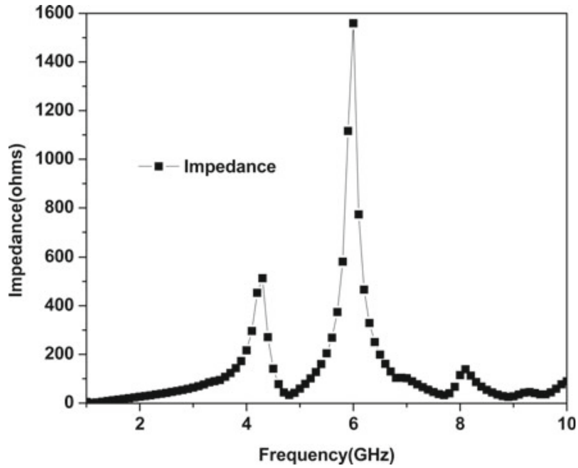

Fig. 8 Impedance plot (freq vs impedance)

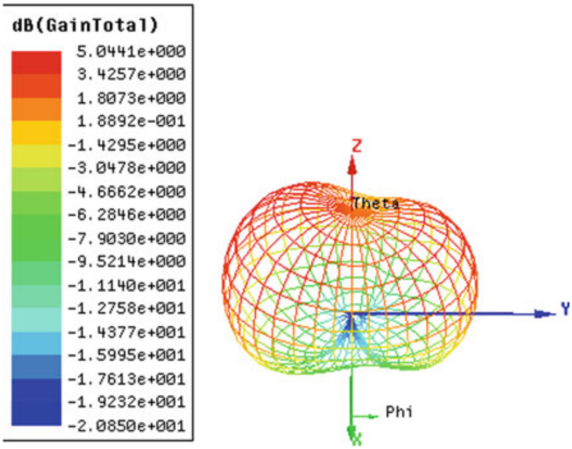

Fig. 9 3D polar plot for circularly polarized antenna

References

1. Li, M., Wang, R., Yao, H., Wang, B.: A low-profile wideband CP end-fire magneto–electric antenna using dual-mode resonances. IEEE Trans. Antenna. Propag. https://doi.org/10.1109/tap.2019.2911399
2. Le Vine, D.M., Jacob, S.D., Dinnat, E.P., de Matthaeis, P., Abraham, S.: The influence of antenna pattern on faraday rotation in remote sensing at L-band. IEEE Trans. Geosci. Remote Sens. **45**(9), 2737–2746 (2007)
3. Le, T.T., Park, H.Y., Yun, T.Y.: Simple reconfigurable circularly polarized antenna at three bands. Sensors (Basel) **19**(10), 2316 (2019)
4. Wu, W.W.: Satellite communications. Proc. IEEE **85**(6) (1997)
5. Nasimuddin, Qing, X., Chen, Z.N.: A compact circularly polarized slotted patch antenna for GNSS applications. IEEE Trans. Antenna. Propag. **62**(12) (2014)
6. Xu, R., Li, J.Y., Liu, J.: A design of Broadband circularly polarized C-shaped slot antenna with sword-shaped radiator and its array for L/S-band applications. IEEE Access, vol. 6, pp. 5891–5896 (2018)
7. Park, D.H.: Design of circularly polarized microstrip patch antenna with wide-band characteristic. Springer (2012)

Novel Design of a Wideband Microstrip Antenna for 5G Applications

Priyanka Das, Mouli Ghosh, Sayani Banik, Subhodeep Mondal, and Sudhanshu Shekhar

Abstract In this paper, a novel ultra wideband microstrip patch antenna array has been designed and analyzed using HFSS software for 5G applications from 24.5–37 GHz. A return loss of 28 dB is observed at resonance frequency, 28 GHz over a fractional bandwidth of 46.43%. The wideband operating frequency range of 13 GHz is accomplished by incorporating arrays of microstrip patches of different shapes. The antenna is compact and has low profile. It is suitable for modern communication systems and upcoming 5G applications.

Keywords Wide band · 28 GHz · 5G antenna · Microstrip patch · Antenna array

1 Introduction

5G is the fifth generation mobile network which plays a major role than previous generations in elevating the mobile network to not only interconnect people, but also interconnect and control machines, objects, and devices. 5G supports significantly faster mobile broadband speeds and lower latencies than previous generations by exploiting the full potential of the Internet of Things. From autonomous vehicles to smart cities and fibre-over-the air, 5G is also quintessential for high data rates. A wideband microstrip patch antenna can improve the quality of communication when designed in millimeter wave bands above 24 GHz. These bands suit macrocells for larger area coverage including fixed wireless access using beam forming. In the millimeter wavelength bands, attenuation and propagation losses are higher. In order to sustain communication at these higher frequencies antennas with high gain are required. In [1], a single band microstrip patch antenna with center frequency 60 GHz has been designed with bandwidth of 30 GHz and the realized gain is 8.82 dB [2] has a proposed antenna which has the center frequency 28 GHz over a narrow band (27–29 GHz). In [3], a 12 port antenna array has been designed which is used

P. Das (✉) · M. Ghosh · S. Banik · S. Mondal · S. Shekhar
University of Engineering and Management, Kolkata, India
e-mail: priyanka.das@uem.edu.in

S. Banerjee and J. K. Mandal (eds.), *Advances in Smart Communication Technology and Information Processing*, Lecture Notes in Networks and Systems 165,
https://doi.org/10.1007/978-981-15-9433-5_5

for MIMO application in mobile handsets. The reflection coefficient is more than −6 dB and the isolation is lower than −12 dB [4] is a scalable 28 GHz beamforming patch antenna which has a gain of 7.5 dB and EIRP of 34.5 dBm with 360° coverage of azimuth angle [5] reports a planar microstrip array antenna having beamforming capability with the resonance frequency of 28 GHz in 4 × 4 configuration for mobile applications. In [6], a hybrid antenna module has been designed which is suitable for cellular devices. This is a combination of a fully optically transparent antenna array and end-fire antenna array which achieved impedance bandwidth of 0.85 and 1.67 GHz at 28 GHz [7] is a substrate integrate wave guide (SIW)-fed linear patch array having two ports for 2 × 2 array. The centre frequency is 28 GHz and the reflection coefficient is 22.5 dB with average gain of 9.2 dBi. Most of the reported works involve complex designs integrated with complicated feeding circuits.

In this paper, a microstrip patch antenna array has been proposed which has the centre frequency of 28 GHz. It is a wideband antenna having a bandwidth of 13 GHz and a return loss of 28 dB. The compact and low profile structure of the antenna makes it suitable for 5G applications in mobile devices. The use of FR4 substrate in the design of the antenna reduces the cost of fabrication. The proposed design uses multi-element antenna arrays for registering a wide bandwidth and high directivity.

2 Evolution of the Array Antenna

2.1 Design of a Single Patch

The first step of the design is to make one single rectangle patch. The length and the width of the patch is 1.4 mm and 6.3 mm respectively. The length, width and height of the FR4 substrate are 10 mm, 15 mm and 1.6 mm respectively. The ground plane has the same length and width as the substrate. Inset feed technique is used here. The length and the width of the feed line is 4.8 mm and 2.65 mm respectively. The observed return loss is 19 dB at the resonant frequency 28 GHz as shown in Fig. 2. A peak gain of 6 dB is registered as observed in Fig. 3. An impedance bandwidth of about 6 GHz is obtained using a single patch antenna (Fig. 1).

The radiation pattern as obtained in Fig. 4 is an omnidirectional pattern with a low gain.

2.2 Design of the 1st Layer with Combination of Different Shaped Patches

In second step of the design 4 extra patches is added with the rectangular patch as shown in Fig. 5. There are 2 circular patches with radius of 1 mm and 2 square shaped patches with length of 1 mm. All these patches are connected to each other using

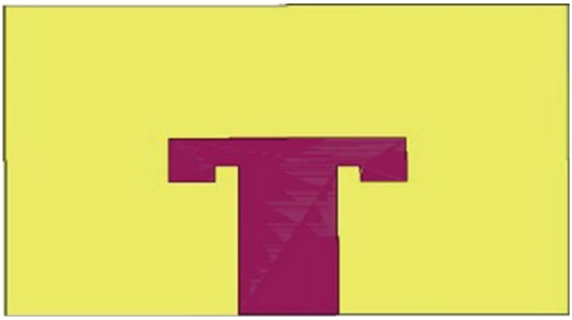

Fig. 1 Design of single rectangular patch

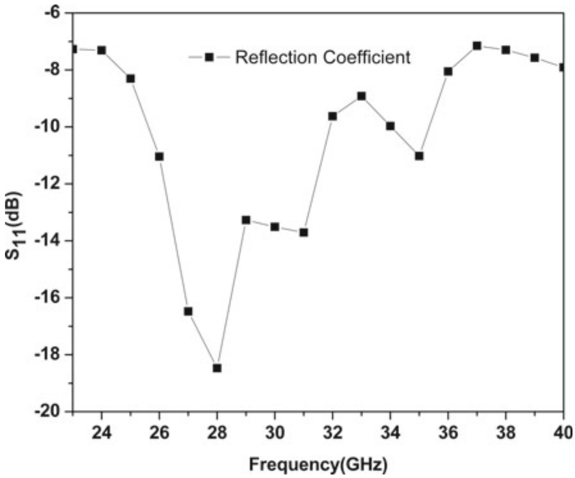

Fig. 2 Reflection coefficient of a single element

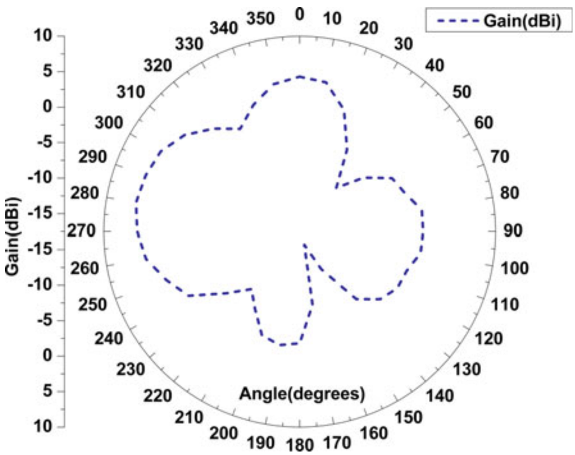

Fig. 3 E plane radiation Pattern of a single element

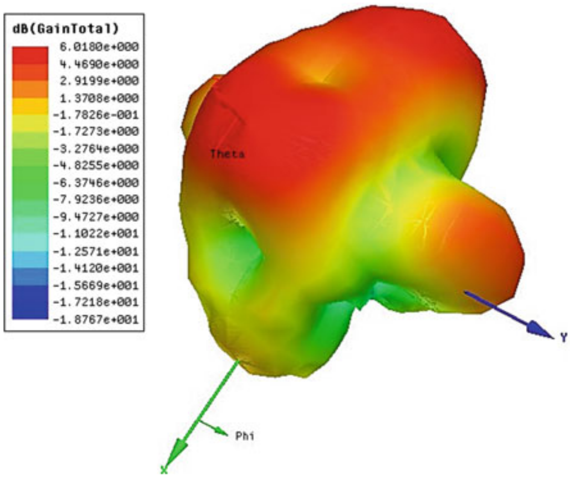

Fig. 4 3D polar plot of single rectangular patch

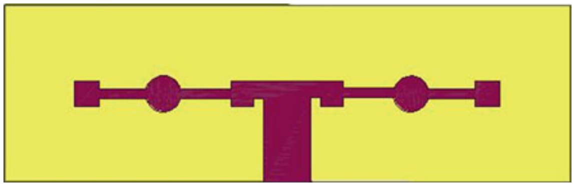

Fig. 5 Design of single layer with 5 patches

a single feed line with length of 4.8 mm and width of 2.65 mm. The length of the substrate is unchanged but the width is increased to 32 mm. The ground plane has the same length and width as that of the substrate. In this step a return loss of 28.39 dB has been observed at the centre frequency of 28 GHz and also a wide bandwidth (25.4–32 GHz) has been observed. In this design the maximum gain is 4.8 dBi as seen from the E plane radiation pattern in Fig. 7 (Fig. 6).

2.3 Design of the Two Layered Array Antenna with the Combination of Rectangular, Circular and Square Shaped Patches

After step 2 now one layer has been increased in step 3 as shown in Fig. 9. In this double layered design there are 5 patches in every layer and the dimensions of those patches are same as step 2. These 2 layers are connected to each other. The width of the substrate is same as previous step but the length has increased to 16 mm. A return loss of 28.8 dB has been observed at the centre frequency 28 GHz and the bandwidth is 11 GHz in this step. The maximum gain is 4.41 dB as observed from the E plane radiation pattern in Fig. 11 (Figs. 8, 10 and 12).

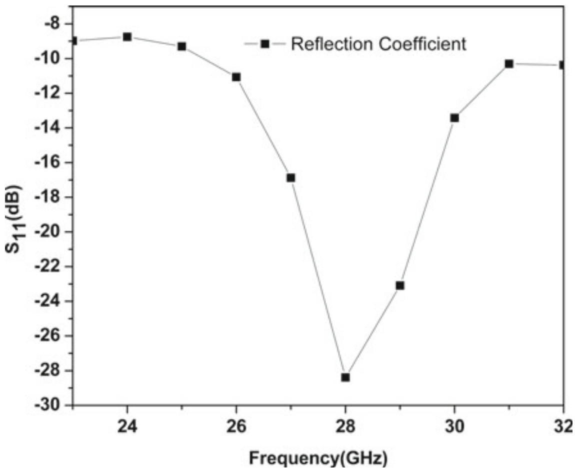

Fig. 6 Reflection coefficient of single layer

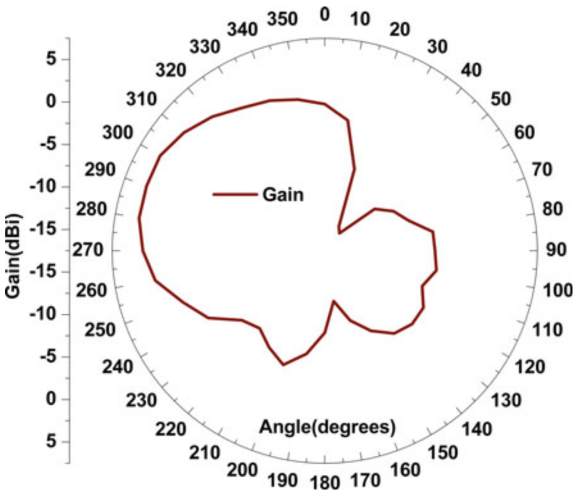

Fig. 7 E plane radiation pattern of single layer

2.4 Design of the Four Layered Array Antenna with the Combination of Rectangular, Circular and Square Shaped Patches

In the 4th and final step there are four layers of the combination of rectangular, circular and square shaped patches. Each layer behaves as an antenna element. The dimensions of the 4 element wideband array antenna are optimized for finding applications in a mobile phone. The antenna performance is investigated, including gain and return loss. The dimensions of these patches remains same as previous. All the layers are interconnected with each other via one feed line in Fig. 13. The length

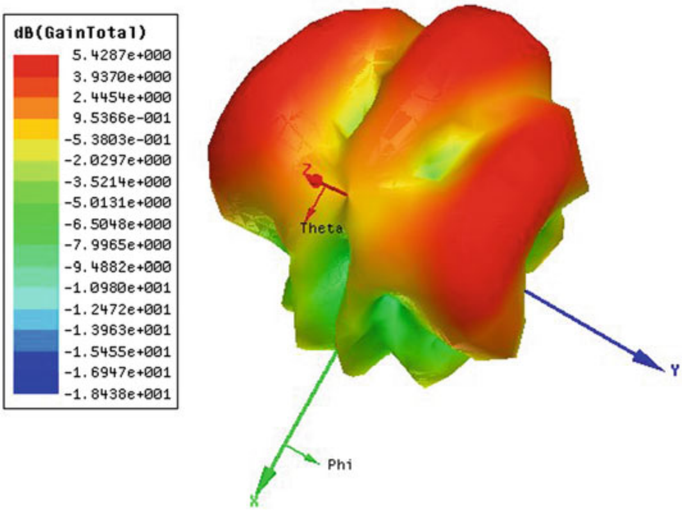

Fig. 8 3D polar plot of single layer

Fig. 9 Design of two layer array antenna

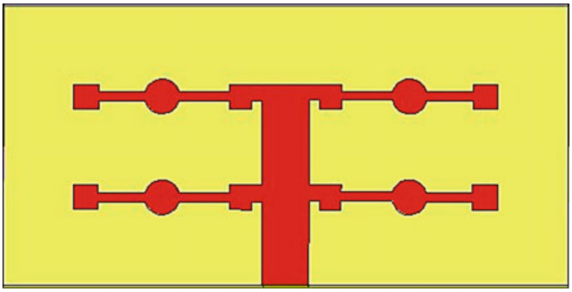

Fig. 10 Return loss of two layer array antenna

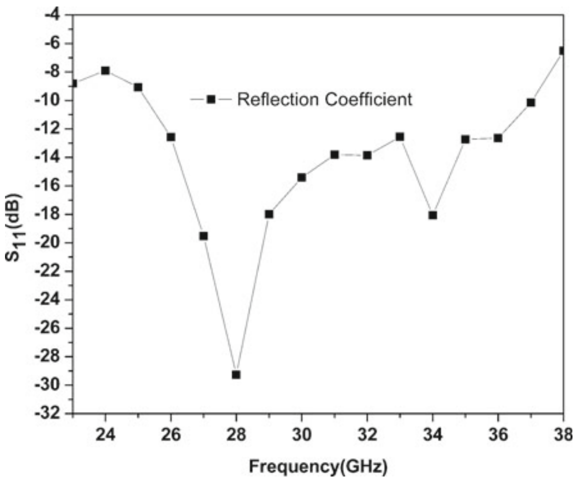

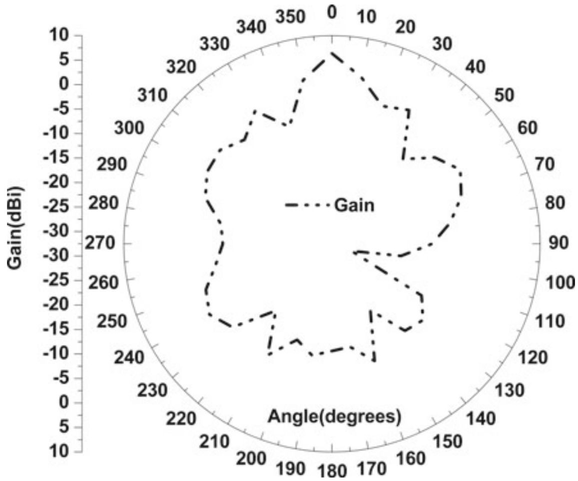

Fig. 11 E plane radiation pattern of two layer array antenna

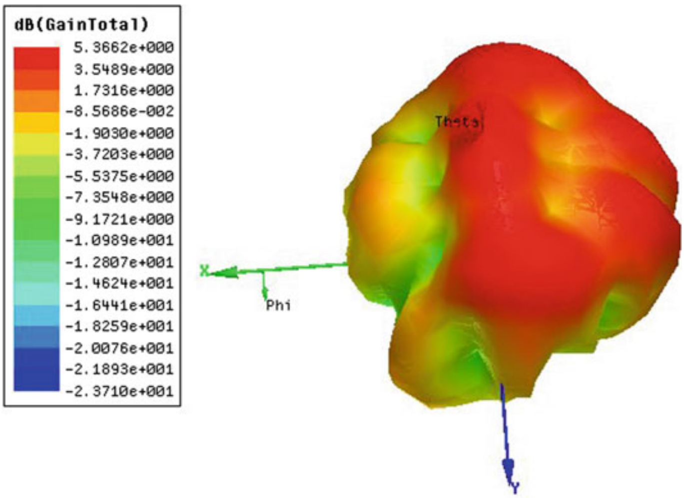

Fig. 12 3D polar plot of two layer array antenna

and the width of the substrate is increased to 26.5 and 34 mm. The ground plane has the same length and width as the substrate. The return loss is 28.18 dB at the centre frequency 28 GHz and the bandwidth is 13 GHz in this final step with the maximum gain of 6.36 dB in the boresight direction. The layers are not increased further in order to maintain the compactness of the antenna so that it can be suitable for mobile applications (Figs. 14, 15 and 16).

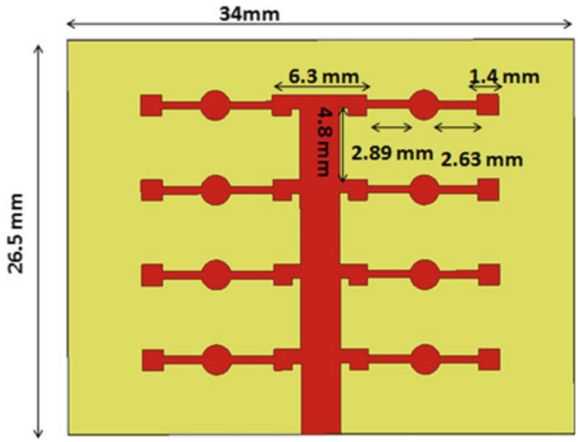

Fig. 13 Design of four layer array antenna

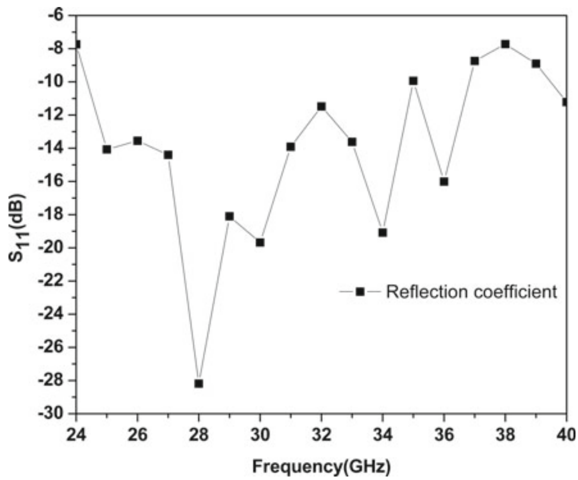

Fig. 14 Reflection coefficient of four layer array antenna

3 Conclusion

A four layered wideband microstrip antenna has been designed with the resonance frequency 28 GHz in 5G millimetre wave bands (24.5–37 GHz). The 26 and 28 GHz bands have a strong impact since they are adjacent and support spectrum harmonisation.It is observed that by increasing the number of layers of microstrip patch elements, the operating bandwidth of the antenna is enhanced. The use of FR4 substrate reduces the fabrication cost.As the size of the antenna is small, it is suitable for mobile applications. The proposed antenna is suited for 5G applications in the frequency band 23–37 GHz.

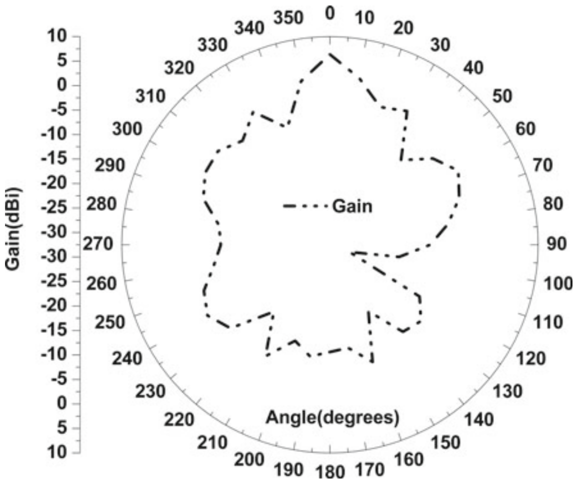

Fig. 15 E plane radiation pattern of four layer array antenna

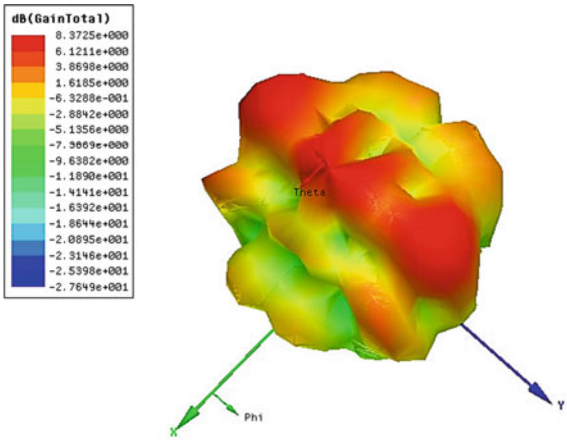

Fig. 16. 3D polar plot of final design (four layered array antenna)

References

1. Muhammad, S., Yaro, A.S., Ya'u, I., Salawudeen, A.T.: Design of 5g mobile millimeter wave antenna. ATBU J. Sci. Technol. Educat. **7**(2) (2019)
2. Ojaroudiparchin, N., Shen, M., Frolund, G.: A 28 GHz FR-4 compatible phased array antenna for 5G mobile phone application. In: 2015 International Symposium on Antennas and Propagation (ISAP), 12 Nov. 2015
3. Li, Y., Sim, C.-Y.-D., luo, Y., Yang, G.: 12-port 5G massive MIMO antenna array in sub-6GHz mobile handset for LTE band 42/43/46 applications. IEEE Access **6** (2017)
4. Aluigi, L., Orecchini, G., Larcher, L.: A 28 GHz scalable beamforming system for 5G automotive connectivity: an integrated patch antenna and power amplifier solution. In: 2018 IEEE MTT-S International Microwave Workshop Series on 5G Hardware and System Technologies (IMWS-5G), 8 October 2018

5. Varum, T., Ramos, A., Mantos, J.N.: Planar microstrip series-fed array for 5G applications with beamforming capabilities. In: 2018 IEEE MTT-S International Microwave Workshop Series on 5G Hardware and System Technologies (MWS-5G), 31 Aug 2018.
6. Park, J., Lee, S.Y., Kim, Y., Lee, J., Hong, W.: Hybrid antenna module concept for 28GHz 5G beamsteering cellular devices. In: 2018 IEEE MTT-S International Microwave Workshop Series on 5G Hardware and System Technologies (MWS-5G), 31 Aug 2018
7. Parthasarathy, R., Chandrasekhar, A., Ramesh, P.G.V.: Design of linear 2x2 array using substrate-integrated-waveguide patch antenna for 28GHz mm-wave applications. In: 2019 TEQIP III Sponsored International Conference on Microwave Integrated Circuits, Photonics and Wireless Networks (IMICPW), 24 May 2019

Performance Analysis of an Electrostatic Doping Assisted Dual Parallel Mach-Zehnder Modulator

Soumi Saha, Rohan Roy, and Subhradeep Pal

Abstract This paper discuss on the performance of a dual-parallel Mach-Zehnder modulator (DP-MZM) using electrostatic doping (ED) assisted optical phase shifters on 220 nm silicon-on-insulator (SOI) platform. Analytical model of the proposed DP-MZM along with nonlinear model is also presented here. The proposed DP-MZM contains two ED-assisted sub-MZMs and an ED-assisted optical phase shifter (PS) in an interferometric structure. Numerical simulations are performed using commercially available tools. Simulation results predict that the proposed DP-MZM with 400 μm long sub-MZMs can offer peak dynamic extinction ratio (ER) of 14 dB with maximum 8.7 dB of insertion loss (IL). Using dual-tone test method, the predicted spurious free dynamic range (SFDR) of the modulator are 62.74 dB $Hz^{1/2}$ and 99.35 dB $Hz^{2/3}$ for second and third harmonic intermodulation distortions (IMD2 and IMD3), respectively. From transient analysis, the estimated maximum operating frequency, and 3-dB EO bandwidth of the modulator are approximately 35.5 GHz, and 32.37 GHz, respectively. Simulation verifies successful transmission of 25 Gb/s OOK modulated PRBS data stream over a 2 km standard single mode fiber (SSMF) link, making it suitable for short reach interconnects.

Keywords Dual parallel Mach-Zehnder modulator · Electrostatic doping · Photonic integrated circuits · Silicon modulator

S. Saha
Department of Electronics and Communication Engineering, University of Engineering & Management (UEM), Newtown, Kolkata 700160, India
e-mail: soumisaha.ece05@gmail.com

R. Roy
School of Electronics Engineering, Kalinga Institute of Industrial Technology (KIIT), Bhubaneswar 751024, Odisha, India
e-mail: 1704289@kiit.ac.in

S. Pal (✉)
Department of EEE, Birla Institute of Technology and Sciece, Pilani (BITS Pilani), Hyderabad 500078, Telangana, India
e-mail: subhradeep@hyderabad.bits-pilani.ac.in

S. Banerjee and J. K. Mandal (eds.), *Advances in Smart Communication Technology and Information Processing*, Lecture Notes in Networks and Systems 165,
https://doi.org/10.1007/978-981-15-9433-5_6

1 Introduction

In the past decade, we have seen a rapid increase in datacenter traffic primarily fuelled by cloud computing and other internet based multimedia applications [1, 2]. This has created a demand for energy efficient, high speed, and compact optical transceivers suitable for datacenter interconnects. The data center traffic is expected to reach approximately 21 zettabytes (ZB) by 2021 among which 70% of the total traffic will be within the datacenter [1]. Current 100 Gb/s transceivers operate on four 25 Gb/s on-off keying (OOK) modulation format while, next generation transceivers will operate at 400 Gb/s. In this aspect, PAM-4 owing to its double spectral efficiency compared to OOK has also been selected as the choice of modulation format. Along with that even stronger forward error correction code (FEC) has been included recently in 400 Gb/s IEEE standard [1]. However, it must be noted that the performance of the transceivers is highly dependent on the modulator(s) which performs the all important electrical-to-optical (E-O) conversion.

In parallel, silicon photonics (SiP) has become a popular solution for the high performance optical interconnects in datacenters. SiP owing to its well understood fabrication methods, low cost, high yield, better integration between electrical and optical components offers compact photonic integrated circuits (PICs) based compact optical transceivers. In those PICs, the choice of modulator limits in between (a) Mach-Zehnder modulator (MZM) (b) microring modulator (MRM) or (c) electro-absorption modulator (EAM). Among these modulators, MRM offers the lowest device footprint and the minimum power consumption but it suffers from the wavelength and temperature dependence. On the other hand, EAM offers high operating bandwidth while suffers from complex device fabrication steps and large device footprint. In this aspect MZM, although free from the limitations of the MRM and complex fabrication steps suffers from large device footprint. To reduce the footprint of MZM, the light- matter interaction in the optical phase shifter (PS) present in the interferometric structure should be improved. One way to achieve is to increase the doping concentration in the active region of PS. Now increasing doping concentration in nano scale regime will lead to problems like random-dopant fluctuations (RDF), undesired and unwanted dopant activation etc. [3]. Dependence of device performance on doping concentration is well discussed in [4–7]. To get rid of these problems, recently electrostatic doping (ED) assisted optical PS has been proposed. Several modulators based on this new variant of optical PS is proposed and their performance have been studied extensively in [8–11]. Such optical PS can also be employed to achieve a dual parallel MZM (DP-MZM).

Among different variants of MZM, DP-MZM finds wide applications in arbitrary waveform generation [12, 13], analog fiber optic link [14, 15], photonic microwave mixer [16], chirp waveform generation [17], IQ modulator [18] etc. In this paper, we propose an ED-assisted optical PS loaded DP-MZM suitable for SiP PICs. The proposed DP-MZM will consist of two sub-MZMs which are connected with an additional ED-assisted optical PS in the form of Mach-Zehnder interferometer (MZI). The ED-assisted optical PS contains three metal-insulator-semiconductor (MIS) junctions and a couple of metal-semiconductor (MS) junctions across a silicon rib waveguide [9]. The optical PS utilized both work-function and bias induced doping [19] to achieve free carrier plasma dispersion effect inside the optical waveguide. The proposed DP-MZM owing to its reduced bias voltage requirement and improved LMI, is expected to offer improvement both in terms of nonlinear performance, and device footprint. The outline for the rest of paper is as follows. In Sect. 2 and Sect. 3, we have described the structure and analytical formulation of the proposed DP-MZM, respectively. In Sect. 4, we present the simulation methodology and results of the proposed modulator obtained from the commercially available tools. Finally in Sect. 5, a conclusion is drawn.

2 Device Description

Figure 1a depicts the complete structure of the proposed ED-assisted DP-MZM. It contains two ED-assisted sub-MZMs (MZM-I and MZM-II) in both upper and lower arms of a MZI. The detailed design and operating principle of sub-MZM are well discussed in [10]. An additional ED-assisted optical PS is included in the lower arm of the MZI. The RF input signal is divided into two parts by a $\gamma_{RF}/(1-\gamma_{RF})$ microwave power splitter and fed to the inputs of both sub-MZMs in conjunction with suitable DC offset voltages (V_{DC1} or V_{DC2}). Figure 1b illustrates the cross-section of the proposed ED-assisted optical PS. The 600 nm wide P-type rib waveguide with doping concentration $N_A = 10^{17}$ cm^{-3} contains tripple MIS junctions vertically, and dual MS junctions laterally. Electrodes E1, E3 are 50 nm wide and made of gold while electrode E2 is 100 nm wide and made of silver. The electrodes of both MS junctions are made of aluminium. The choice of noble metal as electrode material for E1, E2 and E3 is to reduce the modal loss coefficient as discussed in [9, 10]. A 20 nm thick oxide layer is present between the rib waveguide and the electrodes of the MIS junctions. The optimization of electrode dimensions and oxide layer thickness are well documented in [10, 11]. Output from the MZM-II is passed through an additional ED-assisted optical PS to control the phase difference between the sub-MZMs as per our requirement. The additional optical PS operated at V_{DC3} increases both dynamic ER and device footprint, which will be discussed later in the paper.

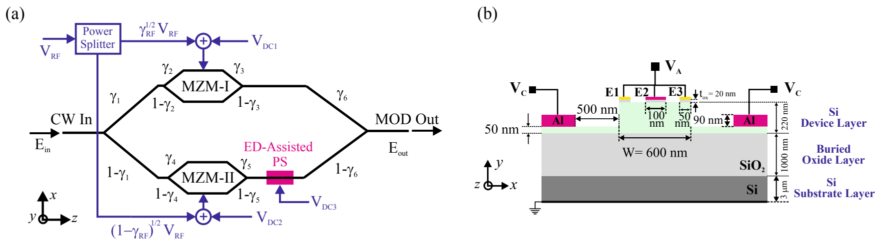

Fig. 1 Schematic of the proposed ED-assisted dual parallel Mach-Zehnder modulator: **a** complete schematic, **b** cross-sectional view of ED-assisted optical PS

3 Analytical Formulation

3.1 Estimation of Device Transfer Function

Refer to Fig. 1a. Assuming the mathematical form of the input continuous wave (CW) signal is $E_{in}e^{j\omega_c t}$, the output electric field (E_{out}) of each sub-MZMs operating at wavelength λ can be represented as,

$$E_{out,i} = \gamma e^{-j\phi_0} e^{-\alpha_0 L_i} \left[1 + e^{-j\Delta\phi(V_i)} e^{-\Delta\alpha(V_i)L_i}\right] E_{in,i}e^{j\omega_c t} \quad \text{for } i = 1, 2 \tag{1}$$

where ϕ_0 and α_0 denotes the phase shift and loss coefficient at unbiased condition; L_i denotes the length of the optical PS present in the sub-MZMs; $\phi(V_i) = 2\pi n(V_i)L_i\lambda^{-1}$ and $\Delta\alpha(V_i)$ denotes the loss coefficient at voltage V_i. In Eq. (1) i, represents the index of the two sub-MZMs. Also for Eq. (1), we have assumed symmetric power splitting at the input and output of each sub-MZMs. Hence, the expression of the electric field for the complete dual-parallel MZM is given by,

$$E_{out} = \left[\sqrt{\gamma_1\gamma_6}E_{out,1} + \sqrt{(1-\gamma_1)(1-\gamma_6)}E_{out,2}e^{-j\phi(V_{DC3})}e^{-\alpha(V_{DC3})L_3}\right] E_{in}e^{j\omega_c t} \tag{2}$$

Assuming symmetric power splitting, the above expression can be rewritten as,

$$E_{out} = \gamma\left[E_{out,1} + E_{out,2}e^{-j\phi(V_{DC3})}e^{-\alpha(V_{DC3})L_3}\right] E_{in}e^{j\omega_c t} \tag{3}$$

3.2 Nonlinear Analysis

In this subsection, an analytical formulation for the nonlinear behaviour of the proposed DP-MZM is presented. Neglecting the voltage induced loss due to plasma dispersion effect, the expression of output electric filed of the proposed DP-MZM is given by [15],

$$E_{out} = \frac{E_{in}}{2}\left[\cos\left(\frac{\phi_1(t)}{2}\right)e^{j\phi_3/2} + \cos\left(\frac{\phi_2(t)}{2}\right)e^{-j\phi_3/2}\right] \tag{4}$$

where $\phi_i = \pi V_i/V_{\pi,i}$ denotes the phase difference the two arms of the i-th sub-MZM controlled by the DC bias V_i, and $V_{\pi,i}$ is the corresponding half-wave voltage of the sub-MZM. Assuming the input RF signal comprises of two RF signals of frequencies ω_1 and ω_2, the photodetected current ($i_{PD}(t)$) can be represented as,

$$i_{PD}(t) = \frac{E_{in}^2}{8}\left[2 + \cos(\phi_2(t)) + \cos(\phi_1(t)) + 4\cos\left(\frac{\phi_1(t)}{2}\right)\cos\left(\frac{\phi_2(t)}{2}\right)\cos(\phi_3)\right] \tag{5}$$

Using similar analysis as described in [15], the coefficients for the fundamental (Υ_f) and third order intermodulation distortion (Υ_{3f}) for the proposed DP-MZM can be represented as,

$$\Upsilon_f = \sin(\phi_1) J_0(m) J_1(m) + 4 \sin\left(\frac{\phi_1}{2}\right) \cos\left(\frac{\phi_2}{2}\right) \cos(\phi_3) J_0\left(\frac{m}{2}\right) J_1\left(\frac{m}{2}\right) \quad (6)$$

$$\Upsilon_{3f} = \sin(\phi_1) J_1(m) J_2(m) + 4 \sin\left(\frac{\phi_1}{2}\right) \cos\left(\frac{\phi_2}{2}\right) \cos(\phi_3) J_1\left(\frac{m}{2}\right) J_2\left(\frac{m}{2}\right) \quad (7)$$

where J_n denotes the nth order Bessel function of first kind. We can adjust the values of ϕ_1, ϕ_2, and ϕ_3 to minimize the effect of IMD3 component in the modulated optical output.

4 Simulation Methodology and Results

4.1 Simulation Methodology

In this section, we describe the simulation methodology for estimating the performance of the proposed DP-MZM. Using Lumerical Device CT [20], a commercial grade device simulator, we have estimated the carrier information across the rib waveguide at different anode voltages (V_A). Then utilizing the estimated carrier information and modified Soref's equations as mentioned in [8], the change in refractive index (Δn) and change in loss coefficient ($\Delta\alpha$) across the rib waveguide is then estimated at different V_A. Lumerical Mode Solutions [21], a commercial grade eigen mode solver, is used to estimate the modal effective refractive index (n_{eff}) and loss coefficient (α_{eff}) for the fundamental guided mode. Lumerical Interconnect [22], a commercial grade circuit simulator for photonic integrated circuits, is then utilized to simulate the dynamic performance of the proposed DP-MZM. For the estimation of nonlinear performance, we have utilized the dual-tone test method in Lumerical Interconnect. Corresponding simulation test setup is depicted in Fig. 2.

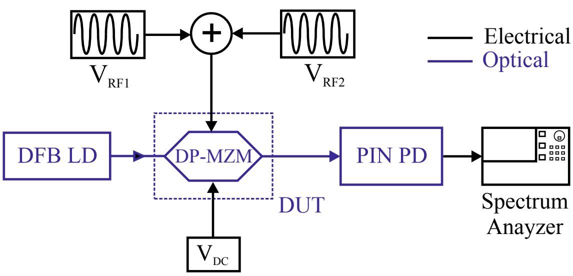

Fig. 2 Simulation test setup used in Lumerical Interconnect for estimation of nonlinear performance of the proposed DP-MZM

4.2 Dynamic Performance

For the estimation of dynamic performance of the proposed DP-MZM, we have varied the coupling coefficient (γ) of the modulator from 0.5 to 0.9 with a step size of 0.1 and the peak-to-peak RF voltage (V_{RF}) is varied from 2 to 8 V with a step size 0.5 V. With these varying parameters, both dynamic extinction ratio (ER) and insertion loss (IL) are measured at 10 Gb/s data rate. We have chosen a lower data rate to ensure that the charge carriers inside the rib waveguide get sufficient amount of time between two successive bit patterns. However, the dynamic ER reduces as the operating speed increases which will be evident from the results later, in this paper. The variation of dynamic ER and IL at $V_{DC3} = 0.5$ and 1.0 V are depicted in Fig. 3. As illustrated, the dynamic ER increases with increasing value of V_{RF} and γ. However, IL also increases in such condition. A trade-off between the required dynamic ER and IL is present in the proposed DP-MZM. At 10 Gb/s data rate, the proposed DP-MZM with $\gamma = 0.62$ and $V_{RF} = 7$ V offers approximately 13.8 dB of dynamic ER with 7.9 dB of IL.

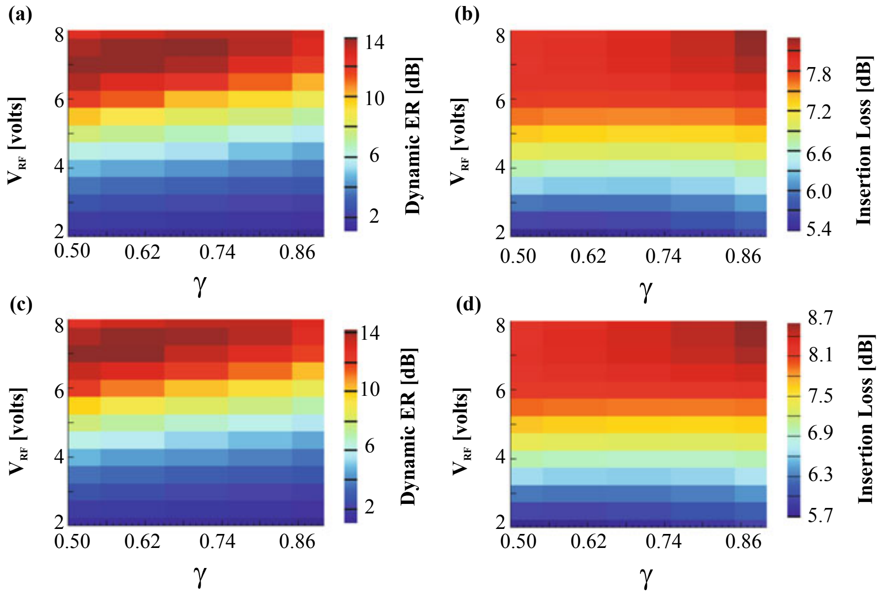

Fig. 3 Variation of dynamic ER and insertion loss at 10 Gb/s data rate with varying γ and V_{RF}: **a**, **b** dynamic ER and IL of proposed DP-MZM with $V_{DC3} = 0.5$ V; **c**, **d** dynamic ER and IL of proposed DP-MZM with $V_{DC3} = 1.0$ V. Other simulation parameters are: $V_{DC1} = V_{DC2} = 3$ V, $P_{in} = 0$ dBm, and $\lambda = 1552.524$ nm

4.3 Nonlinear Performance

Using dual-tone method (refer to Fig. 2), the non-linear performance of the proposed DP-MZM, Fig. 2. In Fig. 4, the nonlinear performance of the modulator for 0 dBm input optical power (P_{in}) is shown. The spurious free dynamic range of the proposed modulator for the IMD2 and IMD3 are calculated using the following relations,

$$SFDR_{IMD2} = \frac{1}{2}\left[OIP_2 - P_{ON} - 10\log_{10}(B)\right] \quad (8)$$

$$SFDR_{IMD3} = \frac{2}{3}\left[OIP_3 - P_{ON} - 10\log_{10}(B)\right] \quad (9)$$

where OIP_2 and OIP_3 are the output optical power at the second and third intermodulation distortion intercept points; P_{ON} refers to the output noise floor and B represents the measurement bandwidth. For the proposed DP-MZM, the estimated value of OIP_2 and OIP_3 are −54.52 dBm and −25.97 dBm. Thus, for measurement bandwidth of 1 Hz and noise floor of −170 dBm, the estimated value of SFDR for IMD2 and IMD3 are 62.74 dB Hz$^{1/2}$ and 99.35 dB Hz$^{2/3}$. Typical state-of-the-art SiP modulators offers approximately 82 dB Hz$^{1/2}$ and 97 dB Hz$^{2/3}$ SFDR for IMD2 and IMD3, respectively [23]. A comparative study of the SFDR of the proposed modulator with some recently reported DP-MZMs is listed in Table 1. From the comparison it is evident that, the proposed DP-MZM offers inferior performance than conventional

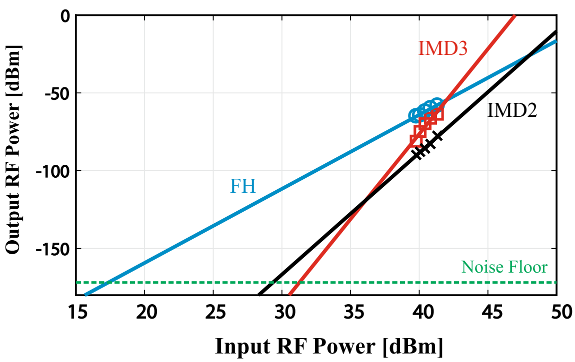

Fig. 4 Simulated nonlinear performance of the proposed DP-MZM using dual-tone test method for $P_{in} = 0$ dBm. Other parameters are: $\lambda = 1552.524$ nm, $V_{DC1} = V_{DC2} = 3$ V and $V_{DC3} = 0.5$ V

Table 1 Modulator linearity comparison

Year	References	Spurious free dynamic range	
		IMD2 (dB Hz$^{1/2}$)	IMD3 (dB Hz$^{2/3}$)
2016	[25]	82	110
2016	[26]	–	96.5
2018	[27]	–	102
2019	[28]	–	102.5
2020	[29]	–	113.5
2020	Present work	62.74	99.35

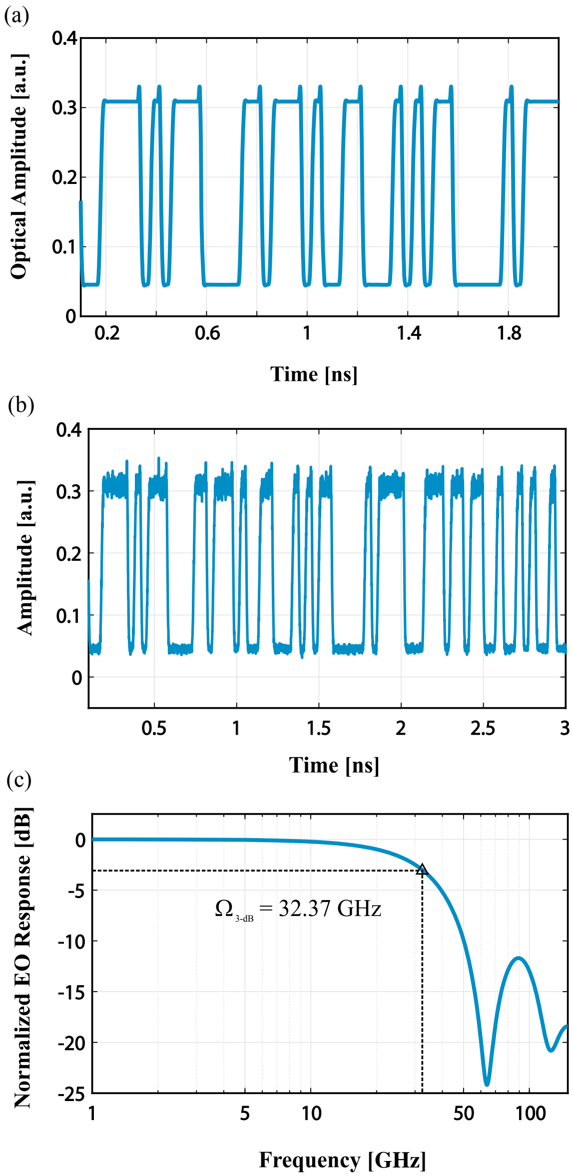

Fig. 5 Transient performance of the proposed DP-MZM: **a** modulated output signal at 25 Gb/s; **b** photodetected signal after 2 km SSMF at 25 Gb/s; **c** simulated electro-optic response

SiP modulator(s) in terms of SFDR for IMD2 and IMD3. One possible explanation is that the proposed DP-MZM contains three nonlinear optical PSs and their combined effect degrades the nonlinear performance. However, the SFDR performance of the proposed DP-MZM can be improved by adjusting the value of V_{DC3} and γ_{RF} which in turn adjust V_{RF} as discussed in [24].

4.4 Transient Performance

As discussed in Sect. 1, current 100 Gb/s transceivers require four 25 Gb/s modulators. Thus, successful operation at 25 Gb/s will ensure the application of the proposed DP-MZM in the 100 Gb/s green field transceivers. For the study of transient performance, a $2^7 - 1$ PRBS signal with 3 V DC offset and 5 V amplitude at 25 Gb/s is applied to drive the proposed DP-MZM. The modulator is connected to a continuous wave (CW) distributed feedback (DFB) laser source with $P_{in} = 0$ dBm at 1552.525 nm. The corresponding modulated optical signal is depicted in Fig. 5a. The optically modulated signal has the dynamic extinction ratio of 7.78 dB which is even higher than required 3.5 dB for short reach interconnects [9]. The estimated values of optical rise time (τ_r) and fall time (τ_f) are 28.20 ps and 22.15 ps, respectively. Hence, the maximum operating speed of the modulator calculated from $f_{max} = 1/\max(\tau_r, \tau_f)$ is approximately 35.5 GHz. Similarly using $BW = 0.35/\max(\tau_r, \tau_f)$, the estimated value of 3-dB optical bandwidth is 12.4 GHz. Figure 5b, depicts the photodetected signal after 2 km of standard single mode fiber (SSMF). For such simulation, we have considered the thermal noise, dark current, and responsivity of PIN PD are −410 dBm/Hz, 5 nA, and 0.83 A/W, respectively. From the result, it is also evident that the received signal after 2 km SSMF will have a distinct threshold level for successful data demodulation. We have also estimated the 3-dB electro-optic bandwidth (Ω_{3-dB}) from the electrical S_{21} response of the proposed DP-MZM. The simulated normalized E-O response of the modulator is illustrated in Fig. 5c. From the normalized response, the estimated value of Ω_{3-dB} is approximately 32.37 GHz. Clearly, the proposed ED assisted DP-MZM offers both high speed operation and wide 3-dB EO bandwidth (>30 GHz).

5 Conclusions

A dual-parallel Mach-Zehnder modulator using electrostatic doping assisted optical phase shifter is proposed and its performance is analyzed in this paper. Theoretical formulation along with analytical nonlinear model of the same is also presented. Numerical simulation predict that the proposed DP-MZM with 400 μm long sub-MZMs offers maximum dynamic ER of 14 dB with peak IL of 8.7 dB at 10 Gb/s. The results also predict that the dynamic performance of the modulator strongly depends on γ and V_{RF}. Dual tone test method predicts SFDR of 62.74 dB Hz$^{1/2}$ and 99.35 dB Hz$^{2/3}$ for IMD2 and IMD3, respectively. From the transient analysis, the estimated value of f_{max}, and Ω_{3-dB} are approximately 35.5 GHz and 32.4 GHz, respectively. Simulation result also predicts the successful transmission of 25 Gb/s OOK modulated PRBS data stream over a 2 km SSMF link which makes the modulator suitable for short reach interconnects.

References

1. Samani, A., El-Fiky, E., Osman, M., Patel, D., Li, R., Jacques, M., Plant, D.: 180 Gb/s single carrier single polarization 16-QAM transmission using an O-band silicon photonic IQM. Opt. Express **27**(10), 14447–14456 (2019)
2. Xu, J., Du, J., Ren, R., Ruan, Z., He, Z.: Optical interferometric synthesis of PAM4 signals based on dual-drive Mach-Zehnder modulation. Opt. Commun. **402**, 73–79 (2017)
3. Shin, C., et al.: Variation-Aware Advanced CMOS Devices and SRAM, vol. 56. Springer
4. Li, X., Yang, F., Zhong, F., Deng, Q., Michel, J., Zhou, Z.: Single-drive high-speed lumped depletion-type modulators toward 10 fJ/bit energy consumption. Photonics Res. **5**(2), 134–142 (2017)
5. Xiao, X., Xu, H., Li, X., Li, Z., Chu, T., Yu, Y., Yu, J.: High-speed, low-loss silicon Mach-Zehnder modulators with doping optimization. Opt. Express **21**(4), 4116–4125 (2013)
6. Shi, W., Xu, Y., Sepehrian, H., LaRochelle, S., Rusch, L.A.: Silicon photonic modulators for PAM transmissions. J. Opt. **20**(8), 083002 (2018)
7. Abraham, A., Anfray, T., Dubray, O., Fowler, D., Olivier, S., Marris-Morini, D., Charbonnier, B.: Optimization of silicon MZM fabrication parameters for high speed short reach interconnects at 1310 nm. Appl. Sci. **6**(12), 395 (2016)
8. Pal, S., Gupta, S.: Performance analysis of an electrostatic doping assisted silicon microring modulator. Opt. Commun. **430**, 131–138 (2019)
9. Pal, S., Tiwari, P.K., Gupta, S.: A proposal for an electrostatic doping-assisted electroabsorption modulator for intrachip communication. IEEE Trans. Electron. Devices **66**(5), 2269–2275 (2019)
10. Pal, S., Gupta, S.: Junction-less optical phase shifter loaded silicon Mach-Zehnder modulator. Opt. Commun. **437**, 110–120 (2019)
11. Pal, S., Gupta, S.: Nonlinear performance and small signal model of junction-less microring modulator. Opt. Commun. **459**, 124984 (2020)
12. Yan, J., Xia, Z., Zhang, S., Bai, M., Zheng, Z.: A flexible waveforms generator based on a single dual-parallel Mach-Zehnder modulator. Opt. Commun. **334**, 31–34 (2015)
13. Zhu, Z., Zhao, S., Zheng, W., Wang, W., Lin, B.: Filterless frequency 12-tupling optical millimeter-wave generation using two cascaded dual-parallel Mach-Zehnder modulators. Appl. Opt. **54**(32), 9432–9440 (2015)
14. Zhu, G., Liu, W., Fetterman, H.R.: A broadband linearized coherent analog fiber-optic link employing dual parallel Mach-Zehnder modulators. IEEE Photonics Technol. Lett. **21**(21), 1627–1629 (2009)
15. Li, S., Zheng, X., Zhang, H., Zhou, B.: Highly linear radio-over-fiber system incorporating a single-drive dual-parallel Mach-Zehnder modulator. IEEE Photonics Technol. Lett. **22**(24), 1775–1777 (2010)
16. Tang, Z., Pan, S.: A filter-free photonic microwave single sideband mixer. IEEE Microw. Wirel. Compon. Lett. **26**(1), 67–69 (2015)
17. Zhu, D., Yao, J.: Dual-chip microwave waveform generation using a dual-parallel Mach-Zehnder modulator. IEEE Photonics Technol. Lett. **27**(13), 1410–1413 (2015)
18. Gao, Y., Wen, A., Jiang, W., Fan, Y., Zhou, D., He, Y.: Wideband photonic microwave SSB up-converter and I/Q modulator. J. Lightwave Technol. **35**(18), 4023–4032 (2017)
19. Gupta, G., Rajasekharan, B., Hueting, R.J.: Electrostatic doping in semiconductor devices. IEEE Trans. Electron. Devices **64**(8), 3044–3055 (2017)
20. Lumerical Device CT R2018a R3. http://www.lumerical.com/tcad-products/device/
21. Lumerical Mode Solutions R2018a R3. http://www.lumerical.com/tcad-products/mode/
22. Lumerical Interconnect R2018a R3. http://www.lumerical.com/tcad-products/interconnect/
23. Zhou, Y., Zhou, L., Su, F., Xie, J., Zhu, H., Li, X., Chen, J.: Linearity measurement of a silicon single-drive push-pull Mach-Zehnder modulator. In: 2015 Conference on Lasers and Electro-optics (CLEO), pp. 1–2. IEEE (2015)

24. Zhang, Q., Yu, H., Jin, H., Qi, T., Li, Y., Yang, J., Jiang, X.: Linearity comparison of silicon carrier-depletion-based single, dual-parallel, and dual-series Mach-Zehnder modulators. J. Lightwave Technol. **36**(16), 3318–3331 (2018)
25. Zhu, D., Chen, J., Pan, S.: Multi-octave linearized analog photonic link based on a polarization-multiplexing dual-parallel Mach-Zehnder modulator. Opt. Express **24**(10), 11009–11016 (2016)
26. Zhou, Y., Zhou, L., Wang, M., Xia, Y., Zhong, Y., Li, X., Chen, J.: Linearity characterization of a dual-parallel silicon Mach-Zehnder modulator. IEEE Photonics J. **8**(6), 1–8 (2016)
27. Liu, W., Ma, J., Zhang, J.: A novel scheme to suppress the third-order intermodulation distortion based on dual-parallel Mach-Zehnder modulator. Photonic Netw. Commun. **36**(1), 140–151 (2018)
28. Zheng, R., Chan, E.H., Wang, X., Feng, X., Guan, B.O.: Linearized fiber-optic link with a high spurious free dynamic range over a wide frequency range. Appl. Opt. **58**(11), 2832–2838 (2019)
29. Yang, H., Zheng, S., Xu, S., Ji, J., Li, F., Zhang, X.: A general analytical method for suppressing the third-order intermodulation in microwave photonic link based on dual-parallel Mach-Zehnder modulator. Opt. Commun. **458**, 124818 (2020)

Semi-hexagonal Half Mode SIW Antennas and Arrays for Vehicular Communication Systems

Soumen Banerjee, Sampoorna Das Mazumdar, Sombuddha Chatterjee, and Susanta Kumar Parui

Abstract In this paper, a semi-hexagonal half-mode SIW antenna is proposed by the authors, generated by splitting the hexagonal SIW cavity along the diametric bisector joining the opposite vertices, which exposes the radiating edge, while the other edges are lined with metallic vias. The proposed antenna, designed on Arlon AD270 substrate, has a gain of 5.8 dBi at 5.9 GHz. The antenna element is further used to design two linear arrays as 1×2 and 1×4 arrays. The resonating frequencies for both 1×2 and 1×4 simulated linear arrays lie at 5.9 GHz, with gains of 8.3 dBi and 11.3 dBi respectively, thereby providing a gain improvement of 2.5 dBi and 5.5 dBi over the single array element. The antennas are of useful application in vehicular communication systems serving as an integral part of Dedicated Short Range Communication devices with frequency of operation lying in the IEEE 802.11p band allocated for such purpose. The antennas also find application in satellite communication in the C-band.

Keywords Antenna gain · Dedicated short range communication (DSRC) · Half-mode SIW (HMSIW) · IEEE 802.11p · Intelligent transportation systems (ITS) · Substrate integrated waveguide (SIW) · Wireless access in vehicular environments (WAVE)

S. Banerjee
University of Engineering and Management, Kolkata, India
e-mail: prof.sbanerjee@gmail.com

S. D. Mazumdar · S. Chatterjee (✉)
Institute of Engineering and Management, Kolkata, India
e-mail: chatterjeesombuddha@gmail.com

S. D. Mazumdar
e-mail: dmsampoorna@gmail.com

S. K. Parui
Indian Institute of Engineering Science and Technology, Shibpur, Howrah, India
e-mail: arkapv@yahoo.com

S. Banerjee and J. K. Mandal (eds.), *Advances in Smart Communication Technology and Information Processing*, Lecture Notes in Networks and Systems 165,
https://doi.org/10.1007/978-981-15-9433-5_7

1 Introduction

Wireless Access in Vehicular Environments (WAVE), a modern vehicular communication system guided by IEEE 802.11p standards, forms the core of Dedicated Short Range Communication (DSRC) in supporting Intelligent Transportation Systems (ITS) applications for short range communication [1]. It provides the basis for establishing inter-communication between vehicles (V2V) or communication between vehicles and roadside information (V2I) in the 5.9 GHz band (5.85–5.925 GHz) [2–5]. The authors present their contribution in extension to the ongoing research pursuits in developing printed antennas and arrays compatible with other devices for short range communication for ITS applications. The choice of Substrate Integrated Waveguide (SIW) is justified by the crucial advantages it offers in design and development of antennas with high quality factor and power handling capabilities, with consistent electrical shielding. In addition to the conventional rectangular and circular waveguide structures, researchers have felt the need for exploring other geometries for development of SIW antennas and filters [6]. The authors have worked on one such structure—the hexagonal SIW, which, although widely popular in use as a filter [7–13], have little been explored in the domain of antennas and arrays. Therefore, the authors, in this paper, have proposed a novel HMSIW antenna, operating at IEEE 802.11p frequency of 5.9 GHz and subsequently developed linear arrays using the former as an array element.

A full-mode SIW (FMSIW) regular hexagonal cavity was designed, operating at the resonant TM_{01} mode at 5.9 GHz, and subsequently bisected along its diagonal to produce the HMSIW antenna while preserving the field configuration of the parent SIW structure. The designed antenna element resonates at a frequency of 5.9 GHz with a gain of 5.8 dBi. The authors further developed linear semi-hexagonal HMSIW antenna arrays resonating in the IEEE 802.11p band. The 1×2 semi-hexagonal HMSIW array operates at a resonating frequency of 5.9 GHz having a gain of 8.3 dBi, while the corresponding 1×4 array resonates at 5.9 GHz providing a gain of 11.3 dBi. The antenna arrays thus designed provide considerable increase in gain without compromising critical properties of the initial element. The antenna and arrays are designed on Arlon AD270 substrate and the necessary full wave simulations are carried out in ANSYS make HFSS v15.0.

2 SIW Hexagonal Antenna

The hexagonal waveguide has been modelled in terms of circular/cylindrical waveguide. The cut-off frequencies for the first twenty-one normal modes are obtained for the E-modes of a regular hexagonal waveguide [14]. The cut-off frequency of the first mode is given as

$$f_{c_{mn}} = \frac{c}{2\pi\sqrt{\varepsilon_r}}\frac{k_{c_{mn}}}{s} \tag{1}$$

where, c is the speed of light in vacuum, $k_{c_{mn}}$ is the cut-off wave number and s is the side length of the regular hexagon. A direct approximation from a circular waveguide leads to the value of $k_{c_{mn}} = 2.75$ [7]. Thus, the formula for the cut-off frequency of a full mode hexagonal SIW cavity, operating in the TM_{01} mode is given by

$$f_r = \frac{2.75c}{2\pi s\sqrt{\varepsilon_r}} \tag{2}$$

Figure 1a depicts the schematics of the full-mode SIW (FMSIW) regular hexagonal cavity with side length s = 15 mm having a centre frequency of 5.9 GHz exciting the fundamental TM_{01} mode. The effective side length of the antenna is reduced to 13.5 mm after the incorporation of metallic vias along its periphery. This antenna is designed on Arlon AD270 substrate (tm). The dimensions are tabulated in Table 1. The fundamental TM_{01} mode at 5.9 GHz and is shown in Fig. 1b.

The hexagonal cavity is symmetrical about two axes. Hence, preserving the TM_{01} mode of the parent hexagonal resonator, we can obtain two types of half mode SIW antennas one by bisecting the cavity along the line joining the opposite edge centres and other along the diagonal of the hexagon as depicted in Fig. 2.

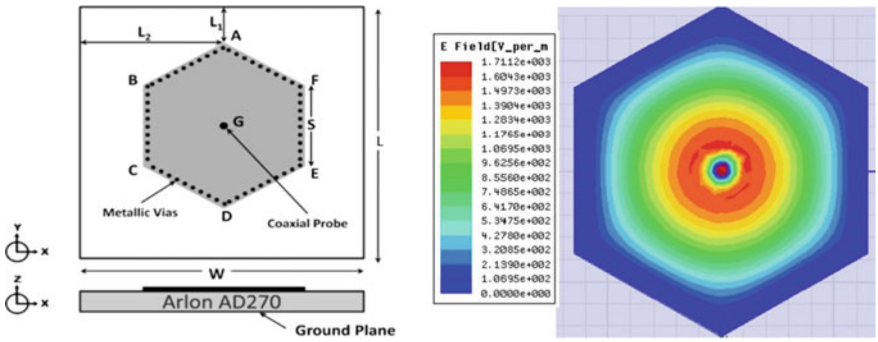

(a) **(b)**

Fig. 1 **a** Geometry of the FMSIW hexagonal, **b** electric field distribution for the principal TM_{01} mode at 5.9 GHz

Table 1 Dimension of hexagonal cavity (in mm)

L	W	h	S	L_1	L_2
60	60	0.79	15	15	30

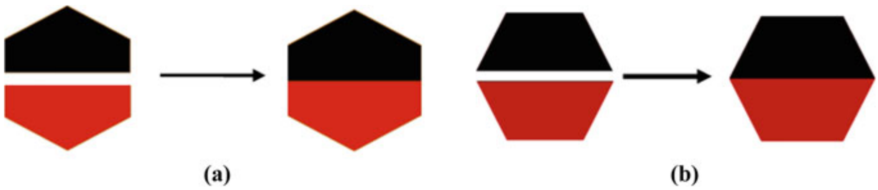

Fig. 2 Design of two HMSIW semi-hexagonal antenna

3 Design of Antenna Array Element

The HMSIW based semi-hexagonal antenna with hexagonal walls lined with metallic vias and the PMC wall along the diagonal of the full mode hexagonal cavity and excited with inset feed is depicted in Fig. 3 with its dimensions tabulated in Table 2. The effective side length is $s = 13.5$ mm and for excitation of the fundamental TM_{01} mode, the inset feed of width $L_7 = 0.58$ mm is inserted at an optimized distance of $L_5 = 7.7$ mm from the base of the semi-hexagonal structure to match with 100 Ω impedance.

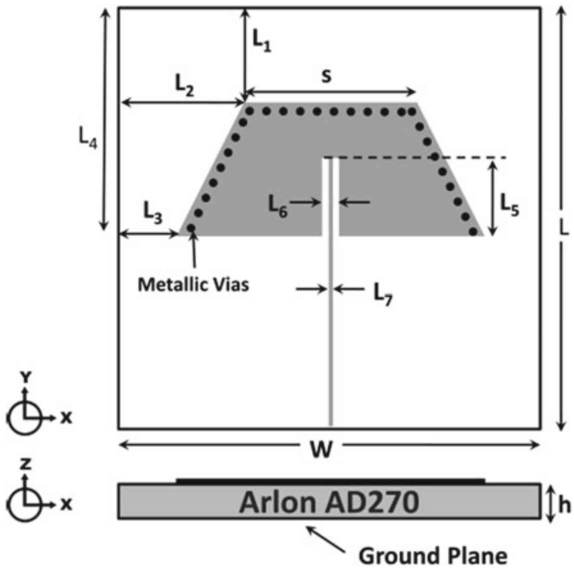

Fig. 3 Geometry of the HMSIW semi-hexagonal antenna

Table 2 Dimension of semi-hexagonal antenna (in mm)

L	W	H	s	L_1	L_2	L_3	L_4	L_5	L_6	L_7
60	60	0.79	15	17	22.5	15	30	7.7	1.74	0.58

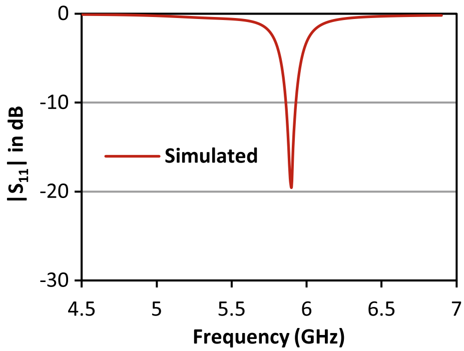

Fig. 4 Simulated return loss value of the HMSIW semi-hexagonal antenna for TM_{01} mode

The optimized return loss for the simulated antenna is −19.48 dB at a fundamental resonating frequency of 5.9 GHz with fractional bandwidth 1.65% as depicted in Fig. 4. The electric field distribution for TM_{01} mode of the antenna is depicted in Fig. 5 and the radiation pattern for E and H planes are presented in Fig. 6. From the

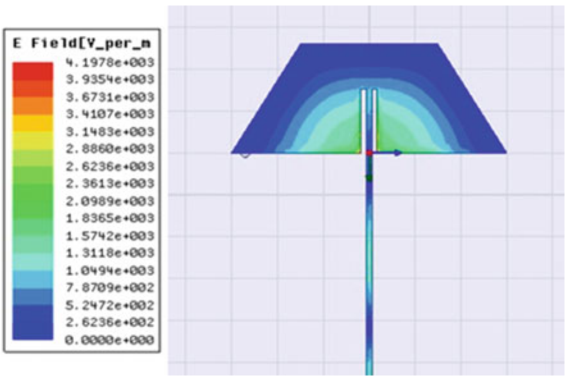

Fig. 5 Electric field distribution at 5.9 GHz for TM_{01} mode

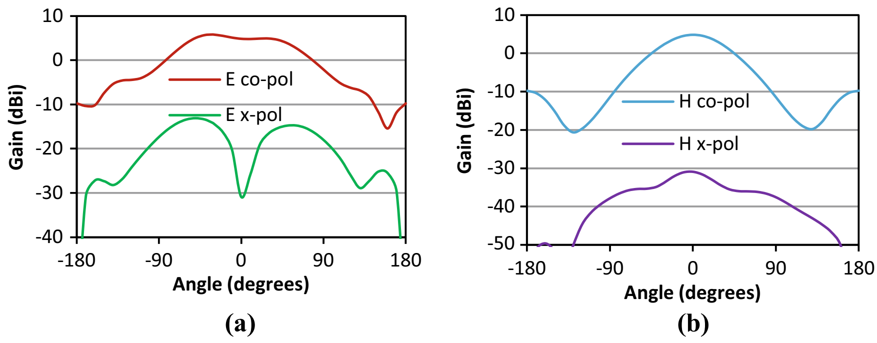

Fig. 6 Simulated **a** E-plane and **b** H-plane radiation pattern of the single element antenna array element at 5.9 GHz

figure, it is evident that the simulated E-plane co-polarized gain is 5.8 dBi and the simulated H-plane gain is 4.8 dBi. However, the cross-polarized values are also well below 20–30 dBi with the antenna depicting 90.14% radiation efficiency.

4 Effect of Mutual Coupling Between Two Similar Array Elements

Table 3 lists the mutual coupling study between two similar HMSIW semi-hexagonal antenna array elements with variations in inter-element spacing (centre-to-centre distance), d. The results are plotted in Fig. 7 and represents variation of S_{11} and S_{21} parameters with frequency (f) for different values of d. The coupled values of S_{21}, for different values of d, are $S_{21} = -27.27$ dB for d = 38.42 mm, $S_{21} = -27.81$ dB for d = 39.42 mm and $S_{21} = -28.77$ dB for d = 40.42 mm. Thus, with change in d, a small shift in the resonating frequency takes place. Owing to the typical design of our antenna array element, the adjacent array elements have non-radiating PEC walls near the proximal regions which results in appreciably low values of mutual coupling between them thereby significantly reducing the total size of the antenna

Table 3 Mutual coupling study between two HMSIW semi-hexagonal antenna elements

d (mm)	f (GHz)	S_{11} (dB)	S_{21} (dB)
38.42	5.89	−35.27	−27.23
39.42	5.88	−39.27	−27.81
40.42	5.89	−36.98	−28.75

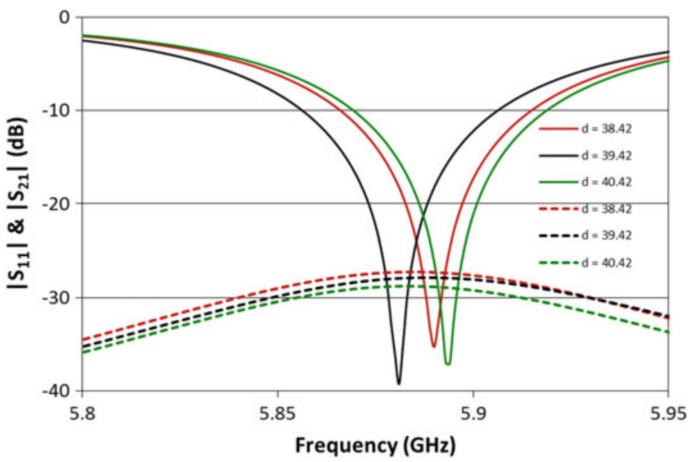

Fig. 7 Variation of S_{11} (solid line) and S_{21} (dashed line) for two antenna array elements with different inter element spacing d

array constituted with such elements as they can be placed significantly close to each other. Here, for designing antenna arrays, the values of d = 39.42 mm ≡ 0.78 λ_0 with corresponding values of $S_{21} = -27.81$ dB and $S_{11} = -39.28$ dB have been chosen.

5 Design of 1 × 2 and 1 × 4 Linear Antenna Arrays

Two types of linear array antennas are constructed using the array element. These antennas viz. Antenna-1 (1 × 2 elements) and Antenna-2 (1 × 4 elements), designed on Arlon AD270 substrate are shown in Fig. 8 and Fig. 9 with their necessary dimensions tabulated in Table 4 and Table 5 respectively.

Each array elements, fed with equal power through power divider network, are spaced at a distance of 0.78 λ_0 from each other. The linear arrays (1 × 2 and 1 × 4) are both found to operate at 5.9 GHz with simulated return loss for Antenna-1

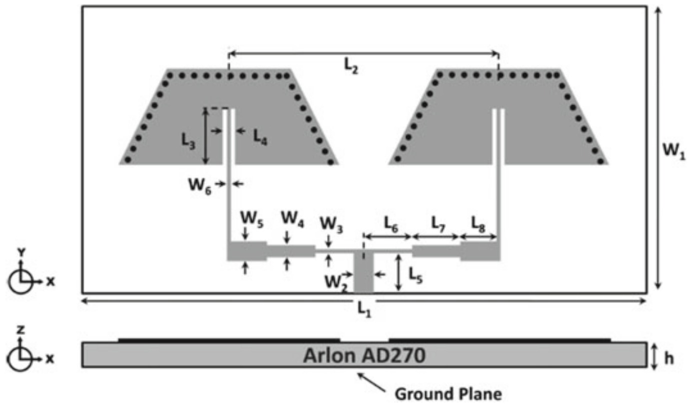

Fig. 8 Geometry of antenna-1 (1 × 2 linear array antenna)

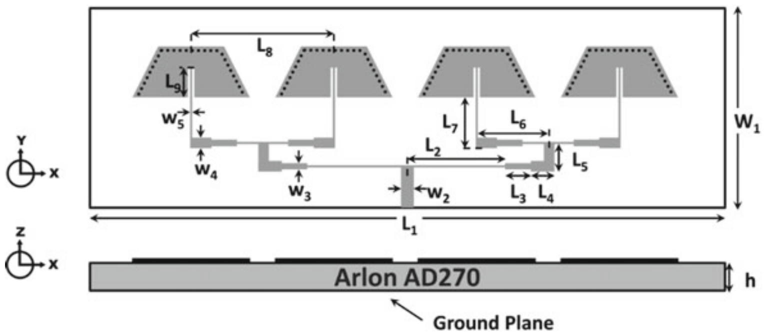

Fig. 9 Geometry of antenna-2 (1 × 4 linear array antenna)

Table 4 Dimension of semi-hexagonal 1 × 2 antenna (in mm)

L_1	L_2	L_3	L_4	L_5	L_6	L_7	L_8	W_1	W_2	W_3	W_4	W_5	W_6
80	39.42	8.75	1.74	6	9.33	6.67	3.42	45	2.1	0.58	1.2	2.1	0.58

Table 5 Dimension of semi-hexagonal 1 × 4 antenna (in mm)

L_1	L_2	L_3	L_4	L_5	L_6	L_7	L_8	L_9	W_1	W_2	W_3	W_4	W_5
175	29.8	6.67	4	6	19.42	12.42	39.42	8.5	45	2.1	1.2	2.1	0.58

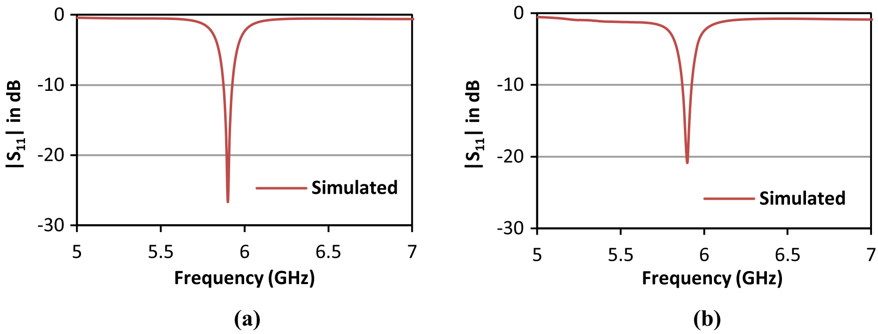

Fig. 10 Simulated return loss (S_{11}) parameters of **a** antenna-1 (1 × 2 array) and **b** antenna-2 (1 × 4 array)

and Antenna-2 being −26.27 dB and −20.8 dB respectively as shown in Fig. 10. The impedance bandwidth obtained at 5.9 GHz for Antenna-1 is 165.4 MHz and Antenna-2 is 179.2 MHz. The variation of electric field for the TM_{01} mode for the two linear arrays is depicted in Fig. 11a and b respectively.

Figures 12 and 13 show the radiation pattern plots of the two linear antenna arrays. For Antenna-1, the simulated E-plane and H-plane co-pol gains are 8.27 dBi and 8.31 dBi respectively. Thus, a gain improvement of 2.47 dBi is achieved with 1 × 2 array compared to the single element antenna. Similarly, for Antenna-2, the simulated E-plane and H-plane co-polarized gains are 11.3 dBi and 11.24 dBi respectively, thereby indicating an enhancement of gain of 5.5 dBi and 3 dBi in comparison to the single element and 1 × 2 array. The cross-polarization gains are found to be far below their corresponding co-pol gain values for both the linear arrays. The first side lobe in case of 1 × 2 linear array is found to be 16 dB lower than the main lobe while it is 12.5 dB lower in case of 1 × 4 linear array. Table 6 depicts the comparative study of the performance characteristics of the linear antenna arrays.

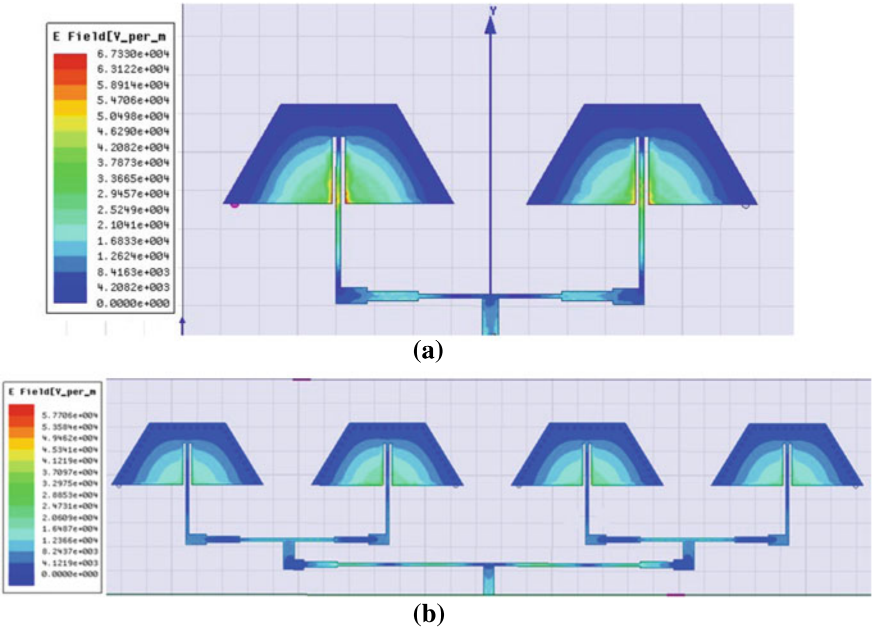

Fig. 11 **a** Electric field distribution of antenna-1 (1 × 2 elements) and **b** antenna-2 (1 × 4 elements) for TM_{01} mode

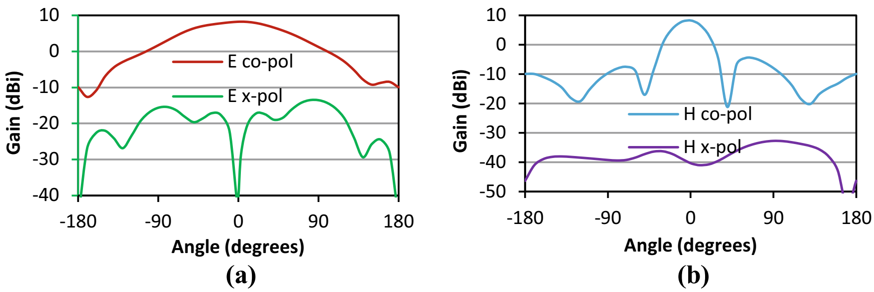

Fig. 12 Simulated **a** E-plane and **b** H-plane radiation pattern of antenna-1 (1 × 2 antenna array) at 5.9 GHz

6 Conclusion

HMSIW based semi-hexagonal antenna is proposed at IEEE 802.11p frequency of 5.9 GHz producing a gain of 5.8 dBi. The semi-hexagonal antenna is used as an array element for designing linear antennas arrays at 5.9 GHz band and their various parameters are studied extensively. The presence of PEC walls along the proximal regions of the array element reduces mutual coupling between the two elements

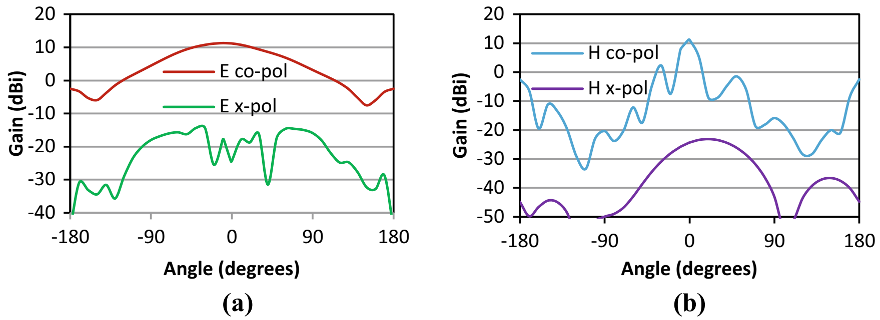

Fig. 13 Simulated **a** E-plane and **b** H-plane radiation pattern of antenna-2 (1 × 4 antenna array) at 5.9 GHz

Table 6 Antenna performance characteristics of the designed array antennas

Antenna	Frequency, GHz	S_{11}, dB	E-plane gain, dBi	H-plane gain, dBi	Increase in gain, dBi	Side lobe reduction, dB
Single element	5.9	−19.48	5.8	4.8	–	–
1 × 2 array	5.9	−26.27	8.3	8.3	2.5	16
1 × 4 array	5.9	−20.8	11.3	11.2	5.5	12.5

thereby facilitating the design of compact arrays with reduced sizes. The primary objective of gain enhancement using arrays has been successfully achieved. The corresponding gain for 1 × 2 and 1 × 4 antenna arrays are 8.27 dBi and 11.3 dBi respectively indicating thereby enhancement of gain by 2.47 and 5.5 dBi over the parent antenna. The designed antenna arrays in the 5.9 GHz unlicensed band will be highly beneficial and find suitable application in Vehicular Communication Systems, developed as a part of ITS, providing necessary backbone in better accident prevention, signalling, speed control, positioning systems and data monitoring and control.

References

1. Jiang, D., Delgrossi, L.: IEEE 802.11p: towards an international standard for wireless access in vehicular environments. In: Proceedings of the IEEE Vehicular Technology Conference (VTC-2008), Calgary, AB, Canada, pp. 2036–2040 (2008)
2. Eichler, S.: Performance evaluation of the IEEE 802.11p WAVE communication standard. In: Proceedings of the IEEE Vehicular Technology Conference (VTC-2007), Baltimore, MD, USA, pp. 2199–2203 (2007)

3. Task Group p: IEEE Standard for Wireless Access in Vehicular Environments (WAVE)—Networking Services. IEEE Std 1609.3–2016 (Revision of IEEE Std 1609.3–2010), pp. 1–160 (2016)
4. Bai, F., Krishnan, H.: Reliability analysis of DSRC wireless communication for vehicle safety applications. In: Proceedings of the IEEE Intelligent Transportation Systems Conference (ITSC-2006), Toronto, pp. 17–20 (2006)
5. Vinel, A.: 3GPP LTE versus IEEE 802.11p/WAVE: which technology is able to support cooperative vehicular safety applications? IEEE Wirel. Commun. Lett. **1**(2), 125–128 (2012)
6. Reddy, J.C., Deshpande, M.D., Cockrell, C.R., Beck, F.B.: Finite element method for eigenvalue problems in electromagnetics. NASA Technical Paper: 3485 (1994)
7. Xu, Z.Q., Shi, Y., Wang, P., Liao, J.X., Wei, X.B.: Substrate integrated waveguide (SIW) filter with hexagonal resonator. J. Electromagn. Waves Appl. **26**(11–12), 1521–1527 (2012) Taylor & Francis
8. Zhang, G., Xu, Z.: Development of circularly polarised antennas based on dual-mode hexagonal cavity. In: Proceedings of the IEEE International Conference on Electronic Packaging Technology (ICEPT-2014), China, pp. 1283–1286 (2014)
9. Chen, J., Wu, B., Wei, L., Jiang, L.W., Liang, C.H.: A compact hexagonal dual-band substrate integrated waveguide filter based on extracted-pole technique. Microw. Opt. Technol. Lett. **53**(3), 562–565 (2011)
10. Chongdar, P., Mukherjee, S., Biswas, A., Srivastava, K.V.: Asymmetric dual mode band-pass filter design using substrate integrated hexagonal cavity (SIHC). In: Proceedings of the IEEE Applied Electromagnetics Conference (AEMC), Bhubaneswar, India, pp. 1–2 (2013)
11. Chongdar, P., Mukherjee, S., Srivastava, K.V., Biswas, A.: Design of dual mode substrate integrated hexagonal cavity (SIHC) filter for X-band application. In: Proceedings of the Asia-Pacific Microwave Conference (APMC), Seoul, Korea, pp. 942–944 (2013)
12. Chongdar, P., Srivastava, K.V., Biswas, A.: Realisation of controllable transmission zeroes by the perturbation technique for designing dual-mode filter using substrate integrated hexagonal cavity. IET Microw. Antennas Propag. **8**(6), 451–457 (2014)
13. Xu, M.J., Chen, K., Xu, Z.Q.: Multilayer dual-mode filter based on substrate integrated hexagonal cavity (SIHC). In: Proceedings of the IEEE International Conference on Electronic Packaging Technology (ICEPT), China, pp. 1400–1403 (2014)
14. Bauer, L., Reiss, E.L.: Cutoff wavenumbers and modes of hexagonal waveguides. Soc. Ind. Appl. Math. J. Appl. Math. **35**(3), 508–514 (1978)

Designing a Framework for Real-Time WiFi-Based Indoor Positioning

Ayan Kumar Panja, Chandreyee Chowdhury, Priya Roy, Sakil Mallick, Sukanto Mondal, Soumik Paul, and Sarmistha Neogy

Abstract Localization in indoor environment is one of the major area of research in the present era. With advancement of technology and extensive use of smartphone applications the requirement for development of fast reliable location based service is needed. RSSI fingerprinting from WiFi sources is a popular procedure for localization in indoor environment although a reliable, ubiquitous end-to-end solution based on machine learning is still at bay. In this work, such a real-time framework for indoor positioning is developed and the design of the implemented prototype is also discussed. The pre-trained models are stored at a local server where the test

A. K. Panja (✉) · C. Chowdhury · P. Roy · S. Mallick · S. Mondal · S. Paul · S. Neogy
Jadavpur University, Kolkata, India
e-mail: ayanpanja1992@gmail.com

C. Chowdhury
e-mail: chandreyee.chowdhury@gmail.com

P. Roy
e-mail: priyaroycse@gmail.com

S. Mallick
e-mail: sakilmallick094@gmail.com

S. Mondal
e-mail: sukantawb1996@gmail.com

S. Paul
e-mail: soumikpaulonly@gmail.com

S. Neogy
e-mail: sarmisthaneogy@gmail.com

A. K. Panja
Institute of Engineering & Management, Kolkata, India

S. Banerjee and J. K. Mandal (eds.), *Advances in Smart Communication Technology and Information Processing*, Lecture Notes in Networks and Systems 165,
https://doi.org/10.1007/978-981-15-9433-5_8

data collected by the smartphones are analyzed in real-time for location prediction. The work has also addressed the class imbalance problem, where a pre-processing procedure is applied before the positioning. An in depth analysis of the accuracy parameter is estimated. Around 1.5 m precision could be observed which is sufficient for indoor positioning of users.

Keywords Indoor localization · RSS fingerprinting · Machine learning · Android application · Pre-processing · Class imbalance · SMOTE

1 Introduction

With the advancement of technology, the need for reliable indoor based location estimation is one of the major sought out domains of research in both the academia as well as in the industry [1]. Some of the popular localization based schemes are mainly implemented using common technologies like Bluetooth low energy (BLE), Wireless Fidelity(WiFi) [2], Ultra wide Band (UWB), Long Range (LoRa) etc., on which methods such as Received Signal Strength (RSS), Time of Arrival (ToA) based approaches are carried out for localization [3]. The indoor localization paradigm using smartphone can be broadly classified into:

- **Device based**: A relative location is estimated by considering some reference points [4].
- **External Sensor based**: The positioning is estimated by capturing passive information with the help of externally deployed sensor nodes [3].
- **Distance based**: A distance from a point of interest in a selected floor plan is estimated to calculate the position [5].

Our society is going through a paradigm shift as more and more devices are getting connected over the Internet. WiFi based approaches are ubiquitously available and found almost everywhere. The Received Signal Strength Indicator (RSSI) measures how well a client device receives signal from access points. Thus, the procedure involves two phases- a collection phase and a prediction phase. During the collection phase, the RSS from the WiFi access points are recorded into a radio map database against each of the location points. The RSS values are then processed and calibration is performed to improve the quality of the radio-map and remove ambiguity.

Developing an end-to-end ubiquitous framework for real time indoor positioning is an important challenge as WiFi signals are not that stable and may not be sufficient for detecting all location points. In this work, we have presented a real-time indoor localization framework based on WiFi RSS which works on the pretext of smartphone application which is used both for data collection as well as to make individual location query. We have also looked into one of the important problem that arises in a radio map database, which is the class imbalance problem. Oversampling procedure is applied to handle this. An end-to-end reliable real-time framework is designed and implemented to form a workable prototype. The solution is tested in one floor of our departmental building at the university. However, it can be easily extended through extending the fingerprint database for providing positioning service at public places. Results are presented both with and without oversampling approach and inferences are drawn accordingly.

The next section summarizes related works in the field while our proposed framework is detailed in Sect. 3. Experimental results are summarized in Sect. 4. Section 5 concludes with a note on future research directions.

2 Related Work

From the last two decades, extensive research works have been proposed in this domain. Still, any commercial and ubiquitous solution of indoor localization and navigation is beyond of our reach. WiFi-based indoor localization is very popular as it depends upon the existing WiFi network infrastructure of a building. However, this approach has various challenges as the RSS of WiFi varies with ambient factors, such as, different times of a day, indoor ambiences, and so on. Hossain et al. [3] have highlighted various challenges associated with WiFi-based fingerprinting approaches, such as, time and labour cost of fingerprint collection, unforeseen circumstances, addition and elimination of APs, device heterogeneity etc. Ghosh et al. [2] have designed an ensemble of classifiers to mitigate the ambient and temporal heterogeneity of RSS. Roy et al. [6, 7] have proposed an indoor localization approach considering minimum number of stable APs that are less susceptible to indoor ambiences. Most of these works follow server-client architecture where smartphones are the client devices. The following supervised classifiers are generally used for location prediction.

K-nearest Neighbour Simplest of the non parametric approaches, K-Nearest Neighbour Algorithm is a very popular procedure where the distance to K adjacent neighbours are estimated to calculate the class label. The distance estimation is done usually using the Euclidean Distance but other distance estimation procedure such as the Chi square, Minkowsky distance can also be considered. Li-Yu et al. in [5] have discussed the effects of the varying distance function in KNN.

Decision Tree During the offline prediction phase, a decision tree can be modelled. The decision tree model works through a bottom up approach where decisions are taken on the attributes or the features, in this case, the RSS Fingerprint data. The leaf nodes are the classes or the reference point coordinate. Training decision forests [8] for a given number of epochs, demonstrates improved classification result.

Naive Bayes Bayesian networks falls under the category of Probabilistic Modelling. The function is modelled in a way of causality where a fingerprint vector X having a respective RSS value from selected multiple APs should fall under Y reference point.

These works generally did not consider real-time location prediction. Another important challenge is insufficient training data. These are addressed through the proposed framework detailed in the next section.

3 Proposed Framework

The variables involved in a WiFi RSS Fingerprinting approach can be generalized for a particular floor F. The physical Floor F is mapped to a reference floor F' where each location is divided into a reference coordinate system (x_k, y_k). Let a particular floor contains P Access Points $\{A_1, \ldots, A_P\}$.R is a 2D Radio Map(RM) vector, where R_{ij}=f_{ij} denotes the RSS fingerprint from the jth AP ($j >= 1$ and $j <= P$) for the reference point at i, N $(1 \geq i \leq N)$ denotes the total recorded fingerprint tuples for the Floor F'.

$$R = \begin{bmatrix} f_{11} & .. & f_{1P} \\ .. & .. & .. \\ f_{N1} & .. & f_{NP} \end{bmatrix} \quad (1)$$

Every row R_i pertains to a fingerprint vector which is recorded and mapped to its respected virtual reference point (x_k, y_k).

The whole localization scheme is built on the pretext of smartphone based approach. The workflow is broken up into two phases:

- **Data collection phase**: It is the offline phase where the fingerprint database is created by collecting the RSS values from the selected APs and assigned a reference point label.
- **Positioning phase**: The positioning is estimated by capturing RSS fingerprint from an unknown location whose label is predicted using a classification model residing in the server in real-time.

In the data collection phase, the RSS database is formed from the site survey using an android application. The fingerprint information was collected for a stipulated number of days so that the classification algorithm can work on. A walk through of the collection process is depicted in Algorithm 1(Radio Map generation).

Algorithm 1 Radio Map Generation

Result: 2D Radio Map Vector R
(q, r) are the virtual x, y coordinate for the floor plan, i is the index of the last recorded fingerprint

Initialization
Perform Scan for a particular Floor F to select the APs.
Form the BSSID[ ] vector containing MAC ID of the valid APs

$X \leftarrow$ Scanned Fingerprint from the available APs for the reference point q, r
for *all* $f \in X$ **do**
  if *MAC ID of* $f \notin BSSID$ **then**
    Remove the f from X
  end
end
/* Pad the reference label $L_k - q - r$ to the fingerprint tuple */
$i \leftarrow i + 1$
$R_i \leftarrow [X|L_k - q - r]$

3.1 Data Collection

A floor plan for the physical floor is constructed where the entire floor plan is divided into virtual grid points which is mapped to reference points (x, y) for position mapping.The size of grid may vary accordingly accordingly with the floor area. In our work, 1×1 m grids are considered which are denoted in the format labelled $L_n - x_i - y_i$; where n denotes the floor number of building L and x_i, y_i denotes the reference point. Figure 1 depicts a visual representation of a constructed floor plan layout with the reference points.

The reference points can be thought of as the class to a prediction problem (Eq. 2).

$$Y' = f(X) \tag{2}$$

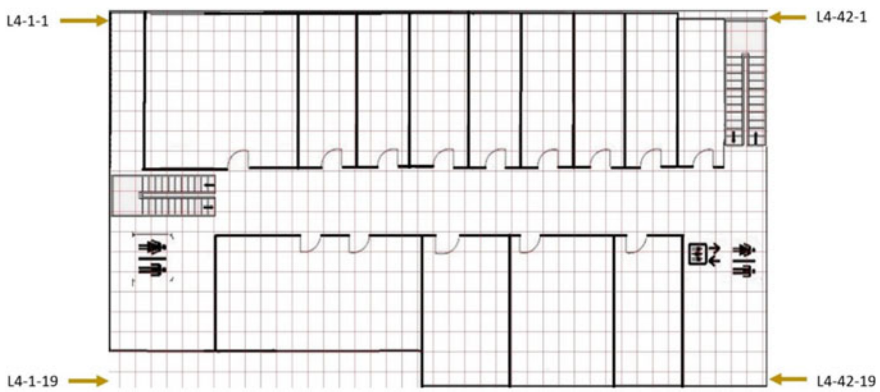

Fig. 1 Floor plan of the experimental region

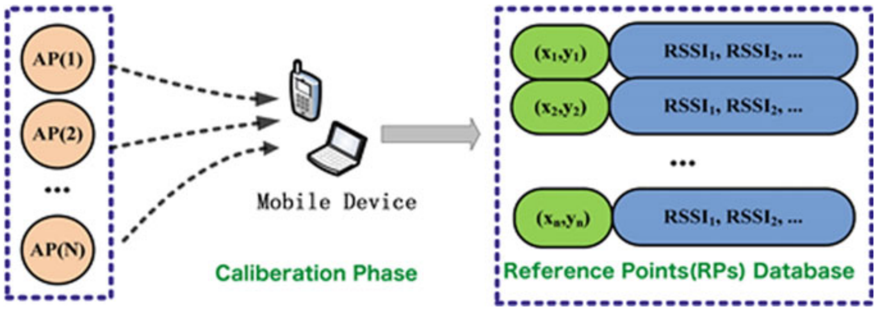

Fig. 2 Reference database construction

The RSS data are collected from every AP for a particular floor to construct the Fingerprint database (Fig. 2). The feature set for the classification process is the RSS values from all selected WiFi APs in a particular floor. Strong RSS values are considered only as the strongest APs provide the highest probability [4] of coverage.

The application for data collection and localization query are both done using a smartphone application (Figure 3a) that we have devised. The collected fingerprint vector from all available APs are sent to the server in a JSON file format. The volley library in android is used to send a JSON request. One of the major features of the volley library is request queuing and automatic scheduling of network request which makes both the collection and query process dynamic.

3.2 Data Pre-processing

Before proceeding with any classification approach, a major computation time investment lies in the pre-processing of the data which involves cleaning the data, filling missing entries, removing unimportant features. The users are subjected to dynamic access points that includes not just WiFi access points but also hotspots. Identifying the hotspots is performed over a course of time where all the APs are monitored and their BSSID are recorded through continuous scanning. A total of 166 APs were recorded. After the removal of hotspots, the AP count stood at 105. The preprocessing process fills the RSS values which are empty or represented as NaN to fixed constant of –110 db indicating negligible signals from them.

During the data collection, one of the major problems is the class imbalance problem. That is, there are a disproportionate ratio of observations in each class (location point). To fix the issue before the predication phase, Synthetic Minority Oversampling Technique (SMOTE) [9, 10] is applied. The SMOTE procedure generates synthetic samples as explained in Algorithm 2. The procedure iterates through all samples in the radio map database to select the minority class. In order to generate the new synthetic sample, a K nearest neighbour to all the sample in minority class is calculated. The over sampled training records are generated by randomly selecting one or more of the nearest neighbors for each samples in the minority class. After the sample reconstruction procedure is done, test samples are classified using state-of-the art classifiers to evaluate its accuracy.

Algorithm 2 SMOTE(R, k, P)

Result: Synthetic sample f'
P - no of sample,k is nearest neighbour, R_{ij} - Radio Map Database(As given in Equation 1)
From R_{ij} determine the Minority class vector Min
for *each* $m \in Min$ **do**
  $T \leftarrow$ no of fingerprint samples in m
  $index \leftarrow$ contains the row number of the fingerprint vectors pertaining to m

  for *i=1 to T* **do**
    $t \leftarrow index_i$
    for *j=1 to P* **do**
      Estimate k nearest neighbour of $R_{t,j}$ and store it in vector $temp_{k,j}$
    end
    Select a random number S between 1 to k.
    /* Choosing one of the nearest neighbour of k. */
    for *l=1 to P* **do**
      $f_i' = R_{t,l} + rand(0, 1) * |R_{t,l} - temp_{S,l}|$
      /* New Synthetic sample generated */
    end
    Include the new synthetic sample f_i' pertaining
    to the minority class m ; $R \leftarrow [f_i'|m]$
  end
end

3.3 Training Model Generation

The training set is pre-processed and a model is created for prediction analysis using a selected classifier. In our work, KNN, Gaussian Naive Bayes and Decision Tree classifiers are used. The integral part of any classification procedure is the knowledge base containing the input features and the output class label. In our approach the radio map database R_{ij} generated in Algorithm 1 contains the recorded RSS for every virtual grid on the floor. The pre-processed fingerprint records act as the X value or the feature values for the model creation. The model is trained in a local server and the implementation is done using python. An Android application is developed for the purpose of real-time localization. The application communicates with the local server where the model is trained by sending a test fingerprint vector from all APs at a position in a floor. The server performs test data preprocessing and prediction. Then it sends back the predicted position to the android application.

3.4 Experimental Setup

The smartphone devices we have considered are Moto G4, Redmi Note 4, Galaxy Tab, Pixel. A total of 116 APs has been detected out of which 105 are valid APs which are registered for fingerprinting. In a particular scan at the clients end (Fig. 3), data is sent as a JSON object. The server side application is implemented using Python which consists of both training and positioning part. The sklearn module of Python is used for the model creation. As the whole process (Fig. 4) happens in real-time, communication with the mobile nodes is established using the Flask module. SMOTE is applied on the training dataset while the test dataset is kept separately for testing. The received test data from the client side application is in JSON format which is taken in a vector. The Prediction of the unknown labelled test data containing the reference point (x, y) is sent back to the client from the server along with the accuracy parameter. The response received from the server is displayed using a Toast object. Figure 3b displays a Predicted location as $L4 - 12 - 40$ which means that the Y or the label for the input RSS is (12, 40).

4 Experimental Results

The real-time localization system has been tested for localization accuracy (Eq. 3) in our university building.

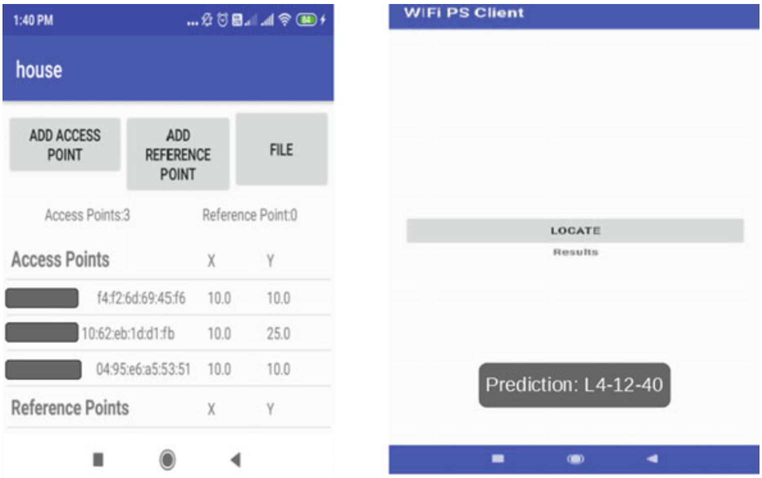

(A) **(B)**

Fig. 3 **a** Android application for data collection **b** Client side location query application showing the predicted location

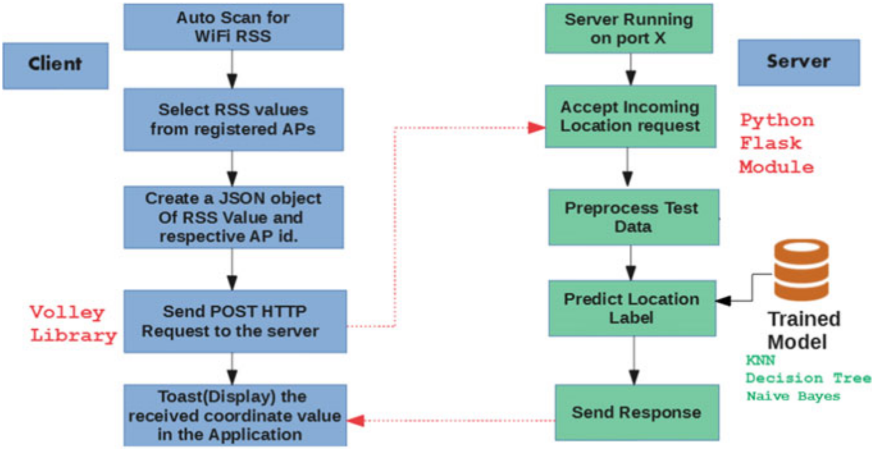

Fig. 4 Working methodology of our approach

$$Accuracy = \frac{\text{Correctly Classified Instances}}{\text{Total Test Instances}} \tag{3}$$

In case of KNN based approach, the selection of K has considerable effect in the positioning process. We have performed exhaustive search to tune the k parameter of KNN and figured out that when k is 4 it is giving the best accuracy result. We have also tuned the depth of the decision tree based approach using Grid Search to optimize the depth of the tree. The average deviation from the actual position varied from 1.5 to 2.5 m. The KNN and decision tree both are found to perform better when oversampling is performed with the SMOTE technique. The improvement occurs because the procedure in SMOTE is based on finding the K nearest samples of the minority class while generating the synthetic records. We have also observed that the deviation from actual position in KNN based approach was consistent (1.5 m) for the test records that were failed to be classified. While Decision Tree and Naive Bayes produced a deviation of more than 2.5 m which slowly converged to 1.5 m as the number of training samples increased.

An overview of prediction plotting on the floor map is shown in Fig. 5. We have plotted some of the wrongly predicted position on the Floor Plan using green and red circles with the deviation from the actual position in meters.

The accuracy is estimated for every classifier taking into consideration the respective virtual grid points on the floor. We have executed the classifier on the training set with and without SMOTE approach. A device wise accuracy is shown in the Fig. 6. The Radio Map database $D1$ and $D2$ dataset corresponding to devices Moto G and Galaxy Tab is significantly unbalanced with only 2 samples in the minority class label. It has been observed that on applying SMOTE there is a sufficient rise in the accuracy in both KNN and Decision Tree based approach. In case of Naive Bayes approach, as it is probabilistic classifier the accuracy depends very much on the distribution of the fingerprint samples. In Naive Bayes approach, the inherent inter

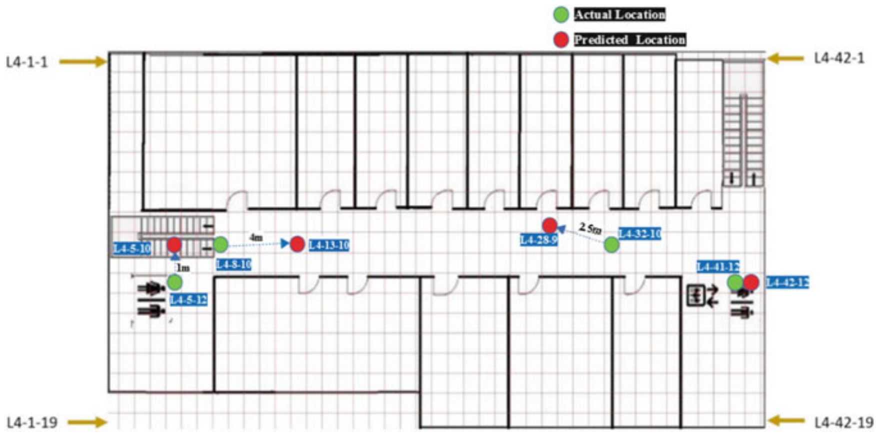

Fig. 5 Localization prediction plotting on the floor map

plays in Bayes rule considers the distribution to be Gaussian. On applying SMOTE approach, distribution of samples in the training set gets a bit perturbed due to which the rise in accuracy is not that significant.

5 Conclusion

Positioning and tracking is of great importance in various applications ranging from robotics to healthcare. The framework that we developed collected the RSS Fingerprints with the help of an Android Application, this phase is the offline phase and was a part of radio map generation. The testing was done in a particular floor of our university building. The approach we have developed and discussed in this paper is a standalone approach. The classifier and the communication mechanism performed perfectly providing a reliable way of positioning in an indoor environment. The system does not require any specialized device but only smartphones and WiFi APs which are widely available thus making the system ubiquitous.

The proposed framework works perfectly for static environment. We hope to modify the existing framework and develop a dynamic auto scalable framework for localization that can be readily adapted for any environment. Furthermore, we wish to work with not just recorded RSS data but we also hope to fuse multiple sensor data like inertial data for the purpose of localization which will also aid in tracking a person's activity during positioning.

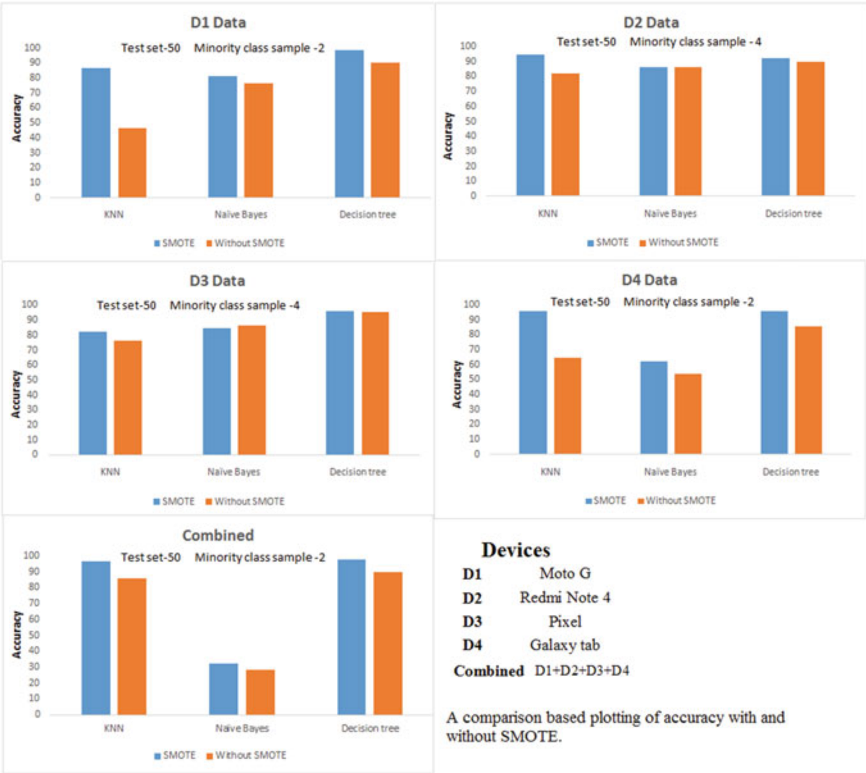

Fig. 6 Device wise localization accuracy

References

1. Winter, S., Tomko, M., Vasardani, M., Richter, K.F., Khoshelham, K., Kalantari, M.: Infrastructure-independent indoor localization and navigation. ACM Comput. Surv. **52**(3) (2019)
2. Ghosh, D., Roy, P., Chowdhury, C., Bandyopadhyay, S.: An ensemble of condition based classifiers for indoor localization. In: 2016 IEEE International Conference on Advanced Networks and Telecommunications Systems (ANTS), pp. 1–6 (2016)
3. Hossain, A.K.M., Soh, W.S.: A survey of calibration-free indoor positioning systems. Comput. Commun. **66**, 1–13 (2015)
4. Rezgui, Y., Pei, L., Chen, X., Wen, F. and Han, C.Rezgui, Y., Pei, L., Chen, X., Wen, F., Han, C.: An efficient normalized rank based SVM for room level indoor WiFi localization with diverse devices. Mob. Inf. Syst. **2017** (2017)
5. Li-Yu, H., Huang, M.-W., Ke, S.-W., Tsai, C.-F.: The distance function effect on k-nearest neighbor classification for medical datasets. SpringerPlus **5**(1), 1304 (2016)
6. Roy, P., Chowdhury, C.: Smartphone based indoor localization using stable access points. In: Proceedings of the Workshop Program of the 19th International Conference on Distributed Computing and Networking, pp. 1–6 (2018)

7. Roy, P., Chowdhury, C.: Indoor localization for smart-handhelds with stable set of wireless access points. In: 2018 Fifth International Conference on Emerging Applications of Information Technology (EAIT), pp. 1–4 (2018)
8. Salamah, A.H., Tamazin, M., Sharkas, M.A., Khedr, M.: An enhanced WiFi indoor localization system based on machine learning. In: 2016 International Conference on Indoor Positioning and Indoor Navigation (IPIN), pp. 1–8. IEEE (2016)
9. Han, H., Wang, W.Y., Mao, B.H.: Borderline-smote: a new over-sampling method in imbalanced data sets learning. In: International Conference on Intelligent Computing, pp 878–887. Springer, Berlin (2005)
10. Nitesh, N.V., Bowyer, K.W., Hall, L.O., Kegelmeyer, W.P.: Smote synthetic minority oversampling technique. J. Artif. Intell. Res. **16**, 321–357 (2002)

CPW Wide-Band Bandpass Filter Using Combination of Series Open and Folded Shunt Short Stubs

P. Mondal, R. Bera, B. Mandal, Soumen Banerjee, A. Ghosh, and Susanta Kumar Parui

Abstract This paper presents a realization of a 3rd order coplanar waveguide (CPW) wide-band bandpass filter (BPF) using the combination of series open stubs and folded shunt short stubs. Four such stubs are placed in close proximity to increase the coupling level and provide the bandpass response of FBW 82.15% at 2.97 GHz, covering the entire S-band frequency regime. Folded shunt stubs minimizes the overall circuit area. A new type of metallic bridge with vias is used to persist the ground planes at the same potential. This type of backside ground metallic bridge is found very simple and cheap compared with formal sophisticated air-bridges. The design mechanism is advantageous in terms of complete planar in nature, easy to integrate with other MMICs, low loss, high roll-off rate and cost effectiveness.

Keywords Bandpass filter · CPW · Folded shunt short stubs · Series open end stubs · Via integrates strip bridge

P. Mondal (✉) · R. Bera
Department of Electronics and Communication Engineering, Gayatri Vidya Parishad College of Engineering, Visakhapatnam 530 048, India
e-mail: pratikmondal@gvpce.ac.in; pratik665@gmail.com

B. Mandal
Division of Solid State Electronics, Department of Engineering Sciences, Angstrom Laboratory, Uppsala University, Uppsala, Sweden

S. Banerjee
Department of Electronics and Communication Engineering, University of Engineering and Management, Kolkata, West Bengal, India

A. Ghosh · S. K. Parui
Department of Electronics and Telecommunication Engineering, Indian Institute of Engineering Science and Technology, Shibpur, Howrah 711103, India

S. Banerjee and J. K. Mandal (eds.), *Advances in Smart Communication Technology and Information Processing*, Lecture Notes in Networks and Systems 165,
https://doi.org/10.1007/978-981-15-9433-5_9

1 Introduction

Coplanar Waveguide (CPW), that place both the signal and ground on the same layer, is an alternative to other planar technologies like; Microstrip and Stripline. In 1969, while working at the RCA's Sarnoff Laboratories, C. P. Wen invented the coplanar waveguide technology [1]. The conductors composed of a center strip separated by narrow gap/space from the two ground planes on either side. The gap is typically very narrow and maintains the electric fields concentrated in the dielectrics. Due to the presence of little/very less fringing field in the air space, CPW exhibits low dispersions. Both of the two ground planes of a CPW must be at the equal potential to diminish unwanted modes from propagation. Sharma et al. [2] reported experimental/practical models of series and shunt elements of CPW in the year 1992. The equivalent lumped circuit models are derived in terms of geometrical parameters of the discontinuity to facilitate their easy utilization in designing coplanar MMICs. A series capacitor and a series inductor in grounded CPW, is generated using interdigital shaped structure with simultaneously an open circuited stub and short circuited stub. Similarly, a shunt capacitor and a shunt inductor is formed by open circuited stubs and short circuited stub to ground. Ponchak et al. [3] in the year 1997, presented an experimental characterization of short and open-circuit series stubs in finite-width coplanar waveguide (FCPW). Hettak et al. [4] presented CPW as uniplanar series resonator circuit and also realized them in pratical applications. To demonstrate the features of series resonators, two distinct miniaturize CPW filters (lowpass and bandpass) are designed. The combined utilization of both parallel and series resonators decrease the dimensions of lowpass and bandpass filters, resulting in compactness of the filter. A CPW BPF using quarter-wavelength resonators based cross-coupling is illustrated by Chen and Cheng [5]. The reported BPF is made of four such proposed resonators, which exhibits improved performances including low IL in passband and high out-of-band rejection in both lower and upper rejection bands. A high selective wideband BPF by using both CPW and microstrip structure is reported [6]. In 2016, a CPW bandpass filter has been demonstrated by Mondal et al. [7] using series combination of four open ended resonators. The resonators are placed in close proximity to increase the bandwidth. Further defected ground structures are used to improve out of band performance.

In this manuscript, a BPF has been realized using the combination of series open end stubs and shunt short end stubs. Both the series open and shunt short stubs provides band accepted response. Using total four such stubs the proposed third order BPF has been realized. Shunt short stubs are folded in shape for overall circuit size minimization. All the stubs are placed very close to each other in order to increase the coupling level, thus wide bandwidth has been achieved. A via integrated strip bridge (new type of bridge) used in the design provides quite good output response and maintain both the top ground planes at the same potential.

2 Characteristics of CPW Short End and Open End Series Stub

Filters are essential blocks in microwave circuits and are among the first few circuit elements studied in any new technology. Microstrip or stripline filters have been studied and very accurate design techniques have been presented by researchers around the globe. However, CPW filter elements have been investigated only experimentally and there is lack of accurate equivalent circuits. Two such filter elements investigated by Dib et al. [8] in the year 1991, are the short-end and open-end series stubs, which are shown in Fig. 1a and b respectively. In this figure PP' refers to the reference planes, which are coincident with the input and output ports of the discontinuity. Figure 1a shows the schematic of the short-end CPW stub. It is also reported that the proposed short end stub provides stop-band characteristics and thus a band-stop filter may be realized by cascading several of these short stubs in series. Figure 1b shows the schematic view for the open-end CPW stub. Owing to its performance, such structures can be used to build band-accepted response. It is quite possible to design CPW stub discontinuities with very low radiation losses.

The short-end CPW stub is modeled by Houdart as a series inductor [9]. This model is unable to predict the resonating nature of the stub as it approaches $\lambda_g/4$ or the asymmetry of the discontinuity, when stub length is very short. The model developed by Ponchak and Simons, an ideal short-ended series stub, anticipated the typical resonant nature of stub but not the asymmetry. The open-end CPW stub modeled by Houdart as a series capacitor, which is also very simple to predict the resonant nature of the stub and is credible only for stubs with very small lengths. Williams elaborated the model to a capacitive π-network and chosen a reference plane which removed the element asymmetry [10]. In the presented literature [8], from scattering parameters lumped equivalent circuit models have been derived. The inductors and capacitors have been represented by closed-form equations, which have possible applications in the design of CPW circuits.

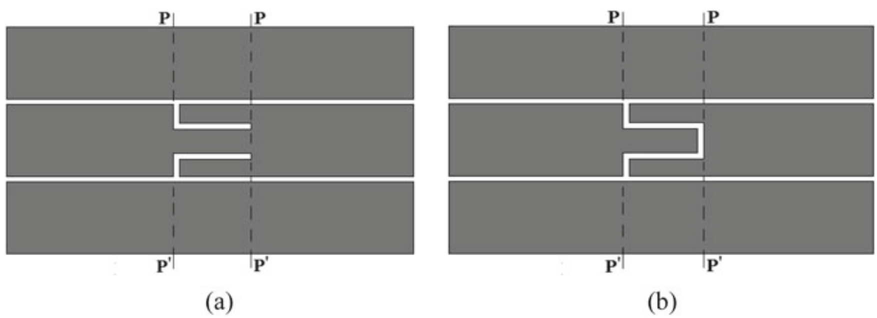

Fig. 1 CPW filter elements **a** short-end CPW series stub and **b** open-end CPW series stub

3 Shunt Short Stubs for Designing Bandpass Filter

The conventional CPW shunt short end stub as sketched in Fig. 2a, also known as a microwave resonator, is often used for designing BPF and impedance matching networks. The air bridge marked with a gray rectangle is employed to suppress the propagation of the parasitic odd mode (slot-line mode).

To reduce the vertical dimension of the stub configuration depicted in Fig. 2a, the stub is folded in a T-shape fashion as portrayed in Fig. 2b. It is clearly stated in the literature [11], both type of structures have a same fundamental resonant frequency. At the lower frequencies of the band, both structures are of similar, however, at the higher frequency of the band there is a deep drop of the return loss for the folded shaped stub. It is also mentioned in the literature that this drop is attributed to enhancement of the radiation loss from the folded section of the stub. Indeed, the folded section essentially functions like a slot antenna at the higher frequency of the band. Figure 3 depicts the corresponding lumped equivalent circuit of the folded shunt short stub. The inductor (L_1) is used to describe the characteristics of this short stub in the lower frequency regime. Hence, the lower cut-off frequency of this structure is mainly controlled by L_1. In the higher frequency regime, a resonant circuit composed of L_2 and C_1 is used to describe its characteristics. It is worth mentioning that the higher cut-off frequency of this structure is determined by the resonant frequency of this resonant circuit.

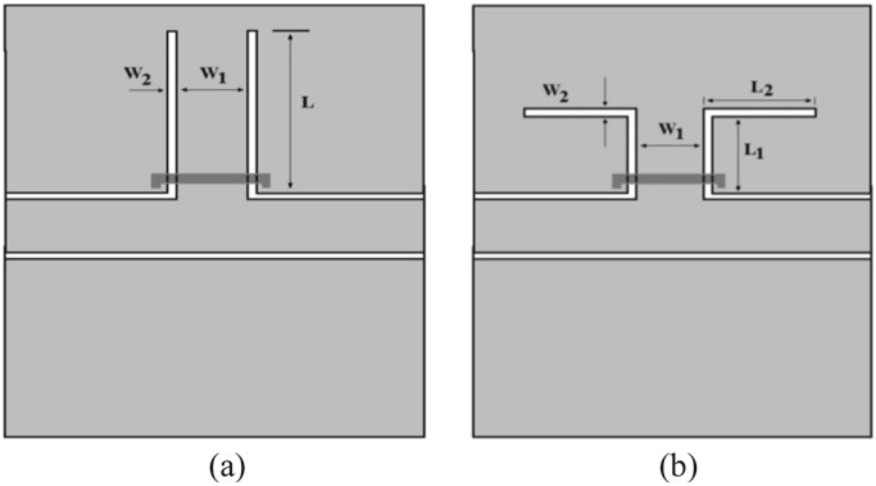

Fig. 2 Schematic diagram of **a** conventional shunt short stub and **b** folded shunt short stub

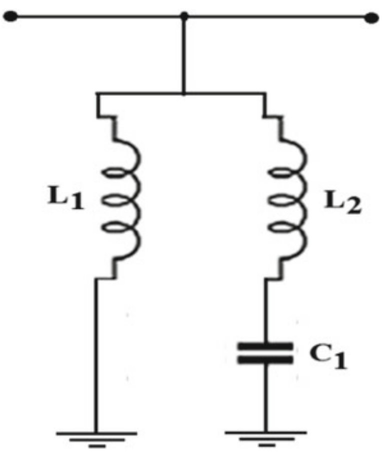

Fig. 3 The lumped equivalent circuit model of the CPW folded shunt short stub

4 3rd Order CPW BPF in Combination with Series Open End Stubs and Folded Shunt Short End Stubs

The proposed bandpass filter is designed using series open end stubs connected in series with folded shunt short end stubs. Total four such resonating stubs (two series open end stubs and two shunt short end stubs) are used for designing the 3rd order bandpass filter. The BPF is designed at a centre frequency of 3 GHz. It is observed that using shunt stubs acquires a considerable amount of space. Thus the block dimension no more remains small as the shunt stub extends vertically in the ground. Now in order to reduce the circuit size, such folding mechanism is applied to the shunt short stub by extending it horizontally such that overall length of the shunt short still remains the same as it would have been while it was straight. Thus obtain a distinguishable miniaturized dimension (around 43% metallic area) as depicted in Fig. 4a. The stubs are placed close enough in order to get wideband frequency response.

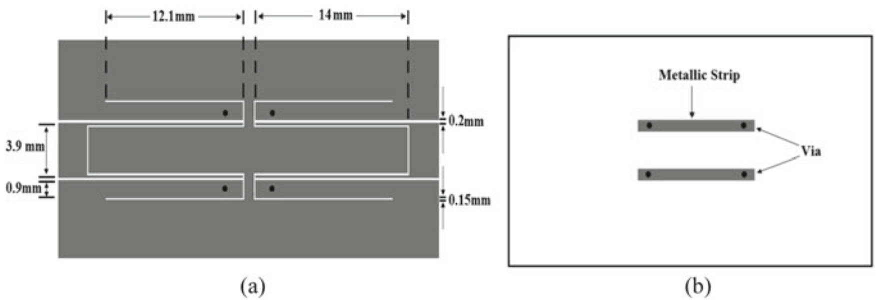

Fig. 4 Geometric Layout of **a** front view and **b** bottom view of proposed 3rd order CPW BPF using folded shunt-short and series-open stubs

Here introduces a new technique for utilizing the bridge concept using via integrated into the circuit where the bridging is required. Now these pairs of vias are connected by a strip at the back side of the circuit i.e. at the bottom. The front view and the bottom view of the proposed filter are sketched in the Fig. 4a and b respectively.

This circuit is simulated using CST EM-simulator software and the result is obtained as depicted in Fig. 5. The result describes a centre frequency of 2.98 GHz, insertion loss of 0.158 dB, bandwidth of 85.42% with rising edge Selectivity of 33.33 dB/GHz and falling edge Selectivity of 39.53 dB/GHz. The ground plane extension also matters to the output response; excess of ground plane makes the circuit vulnerable to degrade output and the circuit results as lossy. Hence using the folded structure circuit loss also minimized. It is also observed that the new type of via integrated strip bridge used in the design, provides a good response or output of the circuit other than using the conventional air bridge which is very costly and sophisticated to design as sub-micron technology is needed. It is verified by the CST simulation software and found it as an efficient way to avoid air bridges.

Finally, the proposed bandpass filter in combination with series open-ended and shorted shunt stubs has been fabricated on a FR4 substrate having relative permittivity of 4.4, height of 1.59 mm. and loss of 0.02 as shown in Fig. 6a and b.

The fabricated structure is then measured and obtained results are compared with the simulated responses. It is observed that the measured results have near agreement with the simulated response as shown in Fig. 6c.

The measured result depicts a centre frequency of 2.97 GHz, IL of 0.21 dB, FBW of 82.15% with rising edge selectivity of 29.82 dB/GHz and falling edge selectivity of 34.01 dB/GHz in comparison with the simulated value of centre frequency

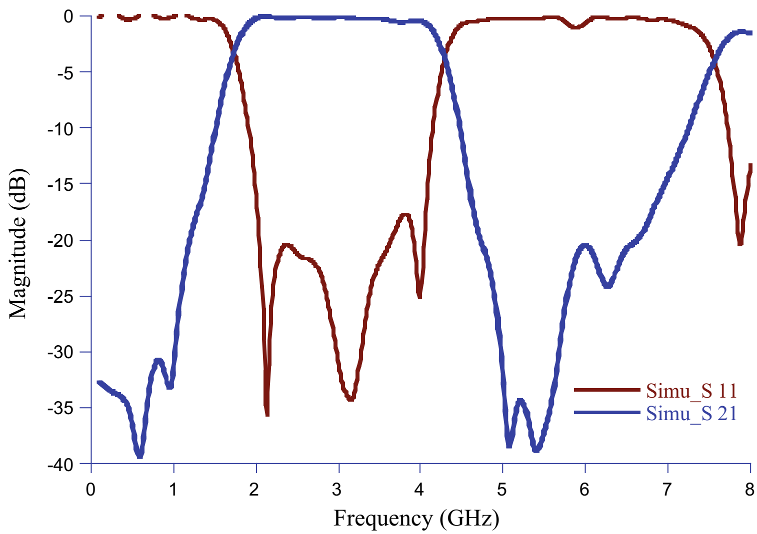

Fig. 5 Simulation result of BPF with series open stubs and folded shunt shorted stub

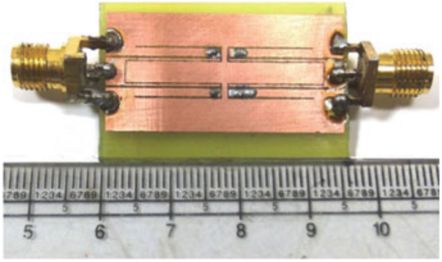

(a)

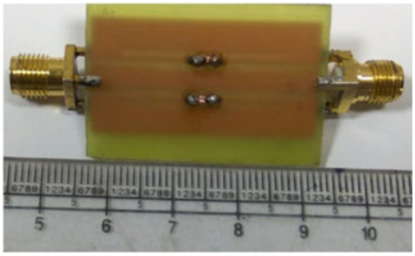

(b)

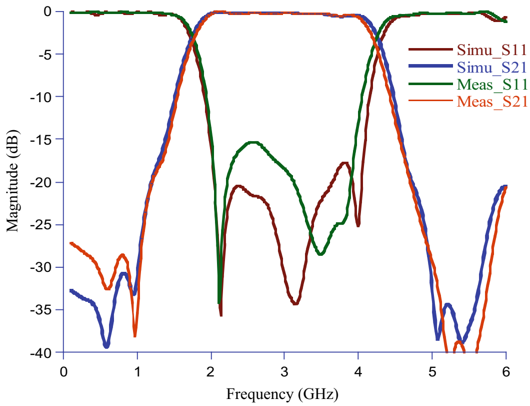

(c)

Fig. 6 Fabricated prototype of proposed CPW BPF and it's **a** front view **b** bottom view **c** comparative study between measured and simulated S-parameter responses

2.985 GHz, IL of 0.158 dB, FBW of 85.42% with rising edge and falling edge selectivity of 33.33 dB/GHz and 39.53 dB/GHz, respectively. Small deviations in the measured results are obtained due to manual fabrication inaccuracy and instrumental non-idealities.

5 Conclusion

A CPW wideband bandpass filter is designed and discussed in the manuscript using two series open and two folded shunt short stubs for S-band application. For circuit size miniaturization, folding of shunt stubs are good approach and after verifying through simulation, it is found that closer the horizontal bend of shunt stubs to the centre of the circuit, the better is the response. Thus again it helps in miniaturization but a considerable amount of space must be kept for bridging the ground around the shunt stubs. It is also observed that a new type of bridge used, provides a good output response which is an alternative to the traditional air bridges made of sub-micron technology. The design technique has advantage of adequate size reduction around 43%. The design also found to be simple, low loss, high roll-off and low cost. Thus the design technique might be useful for designing different broadband miniaturized planar circuits.

References

1. Wen, C.P.: Coplanar waveguide: a surface strip transmission line suitable for nonreciprocal gyromagnetic device applications. IEEE Trans. Microw. Theory Tech. **17**(12), 1087–1090 (1969)
2. Sharma, A.K., Wang, H.: Experimental models of series and shunt elements in coplanar MMICs. In: IEEE MTT-S International Microwave Symposium Digest, pp. 1349–1352, IEEE, USA (1992)
3. Ponchak, G.E., Katehi, L.P.B.: Open-and short-circuit terminated series stubs in finite-width coplanar waveguide on silicon. IEEE Trans. Microw. Theory Tech. **45**(6), 970–976 (1997)
4. Khelifa, H., Dib, N., Sheta, A.F., Toutain, S.: A class of novel uniplanar series resonators and their implementation in original applications. IEEE Trans. Microw. Theory Tech. **46**(9), 1270–1276 (1998)
5. Chen, D., Cheng, C.H.: Coplanar waveguide bandpass filter using quarter-wavelength resonators. Electron. Lett. **43**(9), 526–527 (2007)
6. Gholipour, V., Moshiri, S.M.M., Alighanbari, A., Yahaghi, A.: Highly selective wideband bandpass filter using combined microstrip/coplanar waveguide structure. Electron. Lett. **52**(13), 1145–1147 (2016)
7. Mondal, P., Sahoo, M., Parui, S.K.: Improvement of stop-band performance of a CPW bandpass filter using DGS. Microw. Opt. Technol. Lett. **58**(3), 593–597 (2016)
8. Dib, N.I., Katehi, L.P.B., Ponchak, G.E., Simons, R.N.: Theoretical and experimental characterization of coplanar waveguide discontinuities for filter applications. IEEE Trans. Microw. Theory Tech. **39**(5), 873–882 (1991)
9. Houdart, M.: Coplanar lines: application to broadband microwave integrated circuits. In: 6th European Microwave Conference (EuMC), pp. 49–53, IEEE, Rome (1976)
10. Williams, D.F., Schwarz, S.E.: Design and performance of coplanar waveguide bandpass filters. IEEE Trans. Microw. Theory Tech. **31**(7), 558–566 (1983)
11. Wang, S.N., Chen, N.W.: Compact, ultra-broadband coplanar-waveguide bandpass filter with excellent stopband rejection. Prog Electromagn. Res. B **17**, 15–28 (2009)

Design of Circularly Polarized On-Chip Slot Antenna with Enhanced Gain Using Micromachining

Harshavardhan Singh, Sachin Kumar, Biki Raj Hazarika, and Sujit Kumar Mandal

Abstract In this chapter, a circularly polarized on-chip antenna (OCA) is designed on a low resistivity silicon (Si) wafer by considering standard CMOS technology. The lossy electrical properties of Si are not suitable for the design of OCA and responsible for its gain reduction. The proposed OCA achieved the significant gain enhancement of +22.15 dB by using micromachining technique. The OCA resonates at 1.26 GHz and covers complete L-band. The size of OCA is miniaturized up to $\lambda_0/15.8 \times \lambda_0/23.8\,\text{mm}^2$ by using two double diamond shaped symmetrical slots on the patch. These slots not only miniaturized the antenna size but also provided the circular polarization for the OCA. The OCA shows a bandwidth (BW) of 1.7 GHz (BW < 10 dB) and axial ratio (AR) bandwidth of 4.3% (AR < 3 dB) from 1.23–1.30 GHz range. All the simulated results and corresponding figures have been thoroughly explained in various sections of this chapter.

Keywords On-chip antenna · Gain enhancement · Micromachining · Antenna miniaturization · Circular polarization

H. Singh (✉) · S. Kumar · B. R. Hazarika · S. K. Mandal
Department of Electronics and Communication engineering, National Institute of Technology Durgapur, Durgapur, India
e-mail: harshvardhan8289@gmail.com

S. Kumar
e-mail: sachin.ishwar97@gmail.com

B. R. Hazarika
e-mail: hazarika.bikiraj@gmail.com

S. K. Mandal
e-mail: skmandal2006@gmail.com

S. Banerjee and J. K. Mandal (eds.), *Advances in Smart Communication Technology and Information Processing*, Lecture Notes in Networks and Systems 165,
https://doi.org/10.1007/978-981-15-9433-5_10

1 Introduction

Gain enhancement and miniaturization of the on-chip antenna (OCA) are some of the prime challenges among the wireless system on chip (SoC) researchers nowadays [1, 2]. As CMOS technology is generally preferred Si as a substrate to fabricate the SoC based devices due to its favourable properties and abundant availability, it becomes an obvious choice to design and integrate the OCA on same chip with other circuitries [2]. Si substrate has a high dielectric constant (ε_r = 11.9) and low resistivity (ρ = 10 Ω cm) due to which most of the radiated waves propagate towards the substrate instead of going outside and create substrate waves which subsequently produce a substrate loss [2, 3]. This substrate loss is one of the reasons for low gain of OCA. Many research works have been reported for gain enhancement of the on-chip antenna like Si lens [4], electronics band gap (EBG) structure [5], dielectric resonators [6, 7], artificial magnetic conductors (AMCs) [8] partially shield layer (PSL) [9] high impedance layers [10] and un-doped Si [11], micromachining [12–14] and obtain enhanced gain successfully. On the other hand, miniaturization of antenna size becomes compulsory for lower microwave frequencies (1–10 GHz) as the wavelengths at these frequencies are in centimetre range which does not help to provide suitable size of OCAs for the chip applications. Many techniques namely loading of reactive elements [15, 16], stacking [17], fractals [18, 19], slotting [20], meandering [21, 22], looping [23], shorting pins [24] of antenna miniaturization have been successfully reported in various literature. Also, circular polarization (CP) is very popular in the current trends of antenna designs as it removes the barrier of orientation of the transmitter or/and receiver antennas. In the linear polarized antenna, signal loss chances increases due to multipath rejection which is not in the case of circularly polarized antennas. To achieve CP for a patch antenna, many techniques are mentioned in [25–27]. In the proposed design, a circularly polarized OCA is designed for L-band applications with enhanced gain using the micromachining technique. To reduce the size of the antenna, slotting miniaturization technique is adopted for the OCA design. The arrangement of the chapter is as follow: The design steps and consideration of proposed OCA are discussed in the next section. All the important results with brief explanation are demonstrated in section third and the conclusion has been drawn in the final section.

2 Circular Polarized On-Chip Antenna (CPOCA)

2.1 Standard CMOS Layout for OCA

Si based standard CMOS technology has been considered for the design of OCA. A standard CMOS layout contains six to nine metal layers sandwiched between the silicon dioxide (SiO_2) [9]. In the proposed OCA, only the top layer of CMOS layout is used for antenna design. The layout diagram of the proposed antenna is shown in

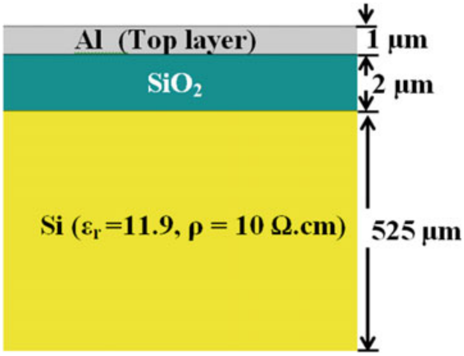

Fig. 1 Layered view of proposed on-chip antenna

Fig. 1. A Si wafer with a thickness of 525 μm is considered as a substrate for OCA. The low resistivity Si (ρ = 10 Ω cm) is taken with a grown SiO_2 layer of 1.5 µm thickness on it. The aluminium (Al) metal layer is deposited on the SiO_2 layer for the antenna design. The Co-planar waveguide (CPW) feed is generally considered for the OCA and contact made through the GSG (ground-signal-ground) probes. This is because the size of the OCA doesn't allow to find suitable size co-axial cables for the feeding. However, as the pitch (gap between feed and pads) of the proposed OCA is larger for GSG probes, the antenna will be feed by the connectors.

2.2 On-Chip Antenna Design

In the initial step, a simple patch having dimension 15 × 10 × 0.525 mm^3 is designed, which is resonating at 1.4 GHz covering the complete L band [28, 29]. The top view of the simple patch OCA with all the dimensions is depicted in Fig. 2a. In the next step, the two double diamond shaped symmetrical slots are introduced on patch. The reason for cutting two slots on patch is to achieve the CP for the antenna. Fig. 2b shows the top view of the slotted OCA with necessary dimensions. As discussed in [26, 27], the properly positioned and shaped slot is responsible to achieve CP antenna, an extensive parametric optimization with slot dimensions is performed to achieve CP for OCA. These slots also provide miniaturization in patch antenna as after implementation of the slots the electrical length of the antenna increased which causes an increment in wavelength. Hence, the resonating frequency shifted towards the lower frequency and thus, the miniaturization occurs. In the third step, for the enhancement of gain, micromachining of the OCA is done by etching of the substrate from the bottom side below the slots. The depth of the micromachining of wafer is parametrically optimized for the enhanced gain. The dimensions of the micromachined etched section from Si below both the slots are 6 × 4 × 0.4 mm^3. Cross sectional layered view, bottom view and the cross sectional side view of the

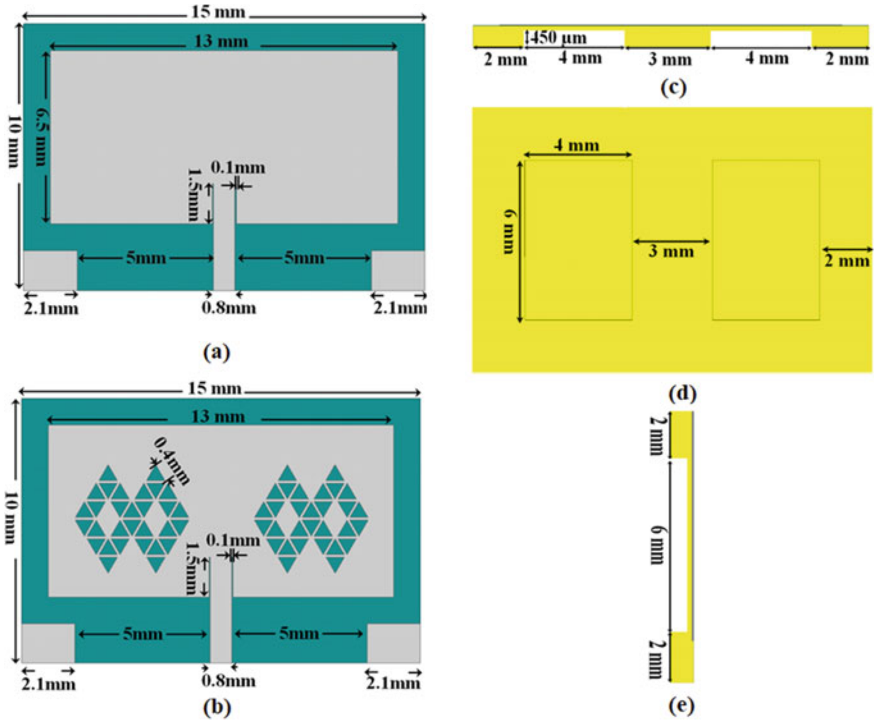

Fig. 2 Step wise view of the proposed antenna. Top view of; **a** simple patch; **b** slotted antenna. **c** Cross sectional layered view; **d** bottom view; **e** Cross sectional side view; of micromachined antenna

micromachined OCA are shown in Fig. 2c–e respectively. All the simulations are performed on Ansys-HFSS platform.

3 Results and Discussion

3.1 Return Loss and Impedance

The return loss characteristics for the OCA are shown in Fig. 3. The simple patch, slotted patch and micromachined patch resonance occurred in L-band of microwave with the center frequencies 1.35 GHz, 1.265 GHz and 1.261 GHz respectively. The small frequency shift can be observed due to slot in the slotted patch when compared to the simple patch. There is not any significant shift observed in frequency by the micromachining of substrate but a slight effect on the matching of 50 Ω impedance can be observed from the figure. However, all the three designs are well below the

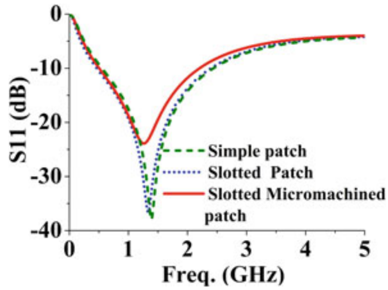

Fig. 3 Return loss comparison of simple, slotted and micromachined OCA

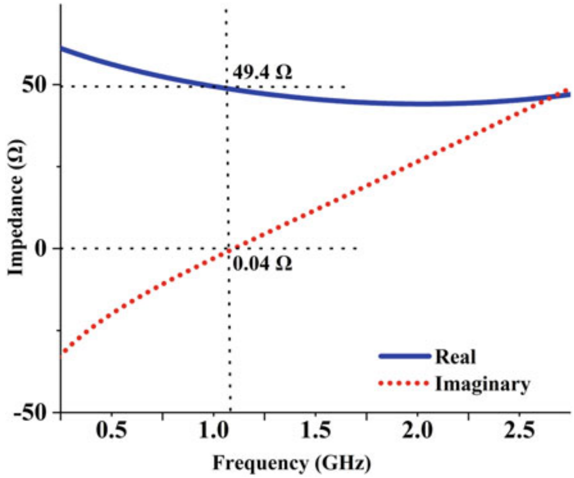

Fig. 4 Impedance versus frequency plot for the OCA

−10 dB and shows excellent return loss characteristics. The reason of the good impedance matching is selection of optimized feed width and inset length of the feed [28, 29]. The impedance versus frequency curve for the micromachined OCA is shown in the Fig. 4. The real part of the impedance is 49.4 Ω while the imaginary part is 0.04 Ω at resonance frequency.

3.2 Gain Enhancement

The micromachined OCA shows excellent gain enhancement when it compared to simple OCA. Here, Si is used as a substrate in simple patch and the obtained gain is −42.85 dB. The gain is very less because Si has very low resistivity and high permittivity which allows the larger part of radiation from antenna towards inside the substrate. This radiation produces substrate wave inside Si and produces substrate loss and reduce the gain of OCA. After introduction of micromachining, the etching of Si from bottom significantly changes the effective di-electric constant of

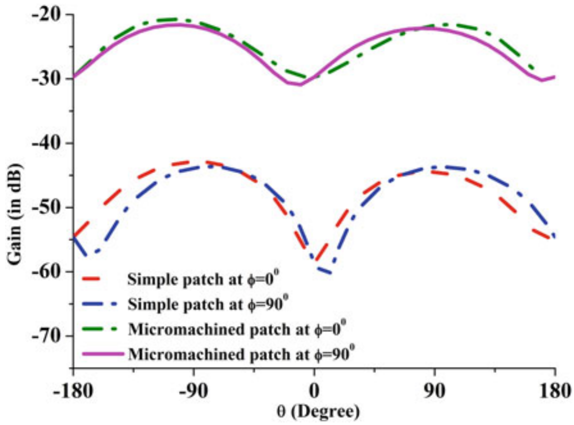

Fig. 5 Gain comparison plot between simple and micromachined OCA

the substrate and it is one of the primary reasons for enhancing the gain of OCA. Also, the effective resistivity of the bottom substrate becomes comparatively higher than Si, which doesn't allow the EM wave to travel towards the substrate in the manner when they travels in to pure Si substrate. Thus, the appearance of the micromachining provide the +22.15 dB gain enhancement and provide the gain value of −20.70 dB. The gain enhancement from simple OCA to micromachined OCA is shown in Fig. 5. There is not any significant change noticed in gain of the slotted OCA when compare to that of the simple patch and hence it is ignored in the plot.

3.3 Circular Polarization

A circular polarized antenna is not restricted for any particular orientation as in linearly polarized antenna. There is not any phase component loss of the signal in the CP antenna. Also the linear polarized antenna signals suffers from signal

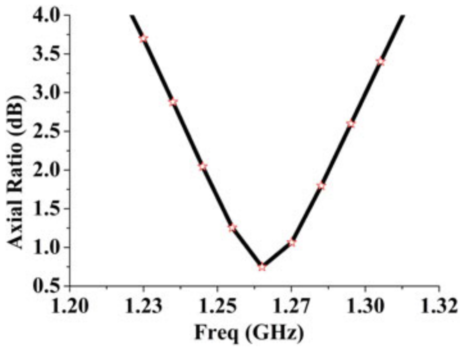

Fig. 6 Axial ratio plot of micromachined OCA

interference due to multipath rejection, which is not the case in CP antenna. In the proposed OCA, to obtain CP, simple patch cut by two double diamond shaped symmetrical slots. The slot position and its shape are optimized to obtain CP. The axial ratio plot in Fig. 6 shows the CP of the proposed antenna. Generally, the AR value below 3 dB is considered for an antenna to be circularly polarized. The valley AR value is 0.73 dB at 1.265 GHz with 4.3% AR bandwidth from 1.22–1.29 GHz as shown in Fig. 6.

4 Conclusion

This work successfully presented the design of a circularly polarized on-chip slot antenna (OCA) with the gain enhancement. As Si electrical properties degrade the gain of the OCA, proposed antenna achieved the significant gain enhancement of +22.15 dB using micromachining technique in the same low resistive Si substrate. The proposed antenna resonated at 1.26 GHz while covering complete L-band. Antenna size is miniaturized up to $\lambda_0/15.8 \times \lambda_0/23.8\,\text{mm}^2$ by using two double diamond shaped symmetric slots on the patch. These slots provided the circular polarization for the OCA. The L-band OCA shows the bandwidth of 1.7 GHz and good axial ratio (AR) bandwidth of 4.3% from 1.22–1.29 GHz range. All these characteristics make the proposed on-chip antenna suitable and ideal candidate for L-band SoC applications.

Acknowledgements This work is supported by Visvesvaraya Ph.D. scheme, Ministry of Electronics and Information Technology, Govt. of India, Grant No. Ph.D.-MLA/4(29)/2015-16/01.

References

1. Kim, K, et al.: On-chip antennas in silicon ICs and their application. IEEE Trans. Electron Dev. **52**(7), 1312–1323 (2005)
2. Cheema, H.M., Shamim, A.: The last barrier: on-chip antennas. IEEE Microwave Mag. **14**(1), 79–91 (2013)
3. Kim, J.-I., Peroulis, D.: 30 GHz self-assembled highly-efficient on-chip monopole antennas. Electron. Lett. **44**25, 1437–1439 (2008)
4. Mosallaei, H., Sarabandi, K.: Antenna miniaturization and bandwidth enhancement using a reactive impedance substrate. IEEE Trans. Antennas Propag. 52(9) (2004)
5. Payandehjoo, K., Abhari, R.: On-chip implementation of compact electromagnetic bandgap structures for 60 GHz applications. In: IEEE International Symposium on Antennas and Propagation (APSURSI), pp. 1816–1819. Spokane, WA (2011)
6. Hou, D., Xiong, Y., Goh, W., Hu, S., Hong, W., Madihian, M.: 130-GHz On-chip meander slot antennas with stacked dielectric resonators in standard CMOS technology. IEEE Trans. Antennas Propag. **60**(9), 4102–4109 (2012)
7. Bijumon, P.V., Antar, Y.M.M., Freundorfer, A.P., Sayer, M.: Dielectric resonator antenna on silicon substrate for system on-chip applications. IEEE Trans. Antennas Propag. **56**(11), 3404–3410 (2008)

8. Nafe, M., Syed, A., Shamim, A.: Gain-enhanced on-chip folded dipole antenna utilizing artificial magnetic conductor at 94 GHz. IEEE Antennas Wirel. Propag. Lett. **16**, 2844–2847 (2017)
9. Singh, H., Mandal, S., Mandal, S.K., Karmakar, A.: Design of miniaturised meandered loop on-chip antenna with enhanced gain using shorted partially shield layer for communication at 9.45 GHz'. IET Microw. Antennas Propag. (2019). https://doi.org/10.1049/iet-map.2018.5974
10. Pan, S., Wang, D., Guclu, C., Capolino, F.: High impedance layer for CMOS on-chip antenna at millimeter waves. IEEE Antennas Propag. Symp. 903–907 (2011)
11. Liu, L., Pano, V., Patron, D., Dandekar, K., Taskin, B.: Innovative propagation mechanism for inter-chip and intra-chip communication. In: IEEE 16th Annual Wireless and Microwave Technology Conference (WAMICON), pp. 1–6, Cocoa Beach, FL (2015)
12. Liu, P., Chang, L., Li, Y., Zhang, Z., Wang, S., Feng, Z.: A millimeter-wave micromachined air-filled slot antenna fed by patch. IEEE Trans. Compon. Packag. Manuf. Technol. **7**(10), 1683–1690 (2017)
13. Dey, D., Kshetrimayum, R.S.: high gain and efficient patch antenna on micromachined GaAs EBGs with increased bandwidth. Annu. IEEE India Conf. New Delhi **2006**, 1–5 (2006)
14. Khan, W.T., et al.: A D-band micromachined end-fire antenna in 130-nm SiGe BiCMOS technology. IEEE Trans. Antennas Propag. **63**(6), 2449–2459 (2015)
15. Xu, L.J., Guo, Y.X., Wu, W.: Miniaturized dual-band antenna for implantable wireless communications. IEEE Antennas Wirel. Propag. Lett. **13**, 1160–1163 (2014)
16. Lee, C.-M., Yo, T.-C., Luo, C.-H., Tu, C.-H., Juang, Y.-Z.: Compact broadband stacked implantable antenna for biotelemetry with medical devices. Electron. Lett **43**(12) (2007)
17. Gianvittorio, J.P., Rahmat-Samii, Y.: Fractal antennas: a novel antenna miniaturization technique, and applications. IEEE Antennas Propag. Mag. **44**(1), 20–36 (2002)
18. Alibakhshi-Kenari, M., Naser-Moghadasi, M., Ali Sadeghzadeh, R., Virdee, B.S., Limiti, E.: Dual-band RFID tag antenna based on the Hilbert-curve fractal for HF and UHF applications. IET Circuits, Dev. Syst. **10**(2), 140–146 (2016)
19. Haque, S.M., Parvez, K.M.: Slot antenna miniaturization using slit, strip, and loop loading techniques. IEEE Trans. Antennas Propag. **65**(5), 2215–2221 (2017)
20. Wong, K.L., Tang, C.L., Chen, H.T.: A compact meandered circular microstrip antenna with a shorting pin. Microw. Opt. Technol. Lett. **15**(3), 147–149 (1997)
21. Alibakhshi-Kenari, M., Naser-Moghadasi, M., Sadeghzadeh, R.A., Virdee, B.S., Limiti, E.: A new planar broadband antenna based on meandered line loops for portable wireless communication devices. Radio Sci. **51**(7), 1109–1117 (2016)
22. Liu, H., Cheng, Y., Yan, M.: Electrically small loop antenna standing on compact ground in wireless sensor package. IEEE Antennas Wirel. Propag. Lett. **15**, 76–79 (2016)
23. Wu, D., Chen, X., Yang, L., Fu, G., Shi, X.: Compact and low-profile omnidirectional circularly polarized antenna with four coupling arcs for UAV Applications. IEEE Antennas Wirel. Propag. Lett. **16**, 2919–2922 (2017)
24. Babakhani, A., Guan, X., Komijani, A., Natarajan, A., Hajimiri, A.: A 77-GHz phased-array transceiver with on-chip antennas in silicon: receiver and antennas. IEEE J. Solid-State Circuits **41**(12), 2795–2806 (2006)
25. Toh, B.Y., Cahill, R., Fusco, V.F.: Understanding and measuring circular polarization. IEEE Transactions on Education **46**(3), 313–318 (2003)
26. Chen, J., Row, J.: Wideband circularly polarized slotted-patch antenna with a reflector. IEEE Antennas Wirel. Propag. Lett. **14**, 575–578 (2015)
27. Row, J., Liu, W., Chen, T.: Circular polarization and polarization reconfigurable designs for annular slot antennas. IEEE Trans. Antennas Propag. **60**(12), 5998–6002 (2012)
28. Constantine, A.: Balanis, microstrip antennas: analysis, design, and application. In: Modern Antenna Handbook. Wiley (2008)
29. Pozar, D.M., Schaubert, D.H.: Microstrip Antennas: The Analysis and Design of Microstrip Antennas and Arrays, edn 1, Wiley-IEEE Press (1995)

Synthesis of Unequally Spaced Time-Modulated Linear Arrays Through Optimized Position and On-Time Using Differential Evolution

S. Patra, Sujit Kumar Mandal, G. K. Mahanti, and N. Pathak

Abstract In this paper, a novel method for designing unequally spaced time-modulated arrays (UESTMAs) with fewer optimization parameters in two steps has been investigated. Different cases of synthesis method such as position-only (PO), on-time only (OTO), on-time then position (OTTP) and position then on-time (PTOT) have been considered to design the array. For each case under consideration, the global search stochastic algorithm based on differential evolution (DE) has been employed to achieve the array pattern with significantly suppressed sidelobe levels (SLLs) and sideband levels (SBLs) by separately considering the element position and switch on-time of the array elements as the optimization parameters. Through detail comparative results, it is shown that the performance of PTOT synthesis method with fewer optimization parameters in two steps provides better or equivalent performance as compared with the reported approach where both position and on-time are considered simultaneously. The representative numerical results for a 32 element linear array have been presented to show the effectiveness of the proposed approach.

Keywords Time-modulation · Position-only · Position on-time · Sidelobe level · Sideband level · Differential evolution

S. Patra (✉)
Department of ECE, SMIT-TIG, Guptipara, Hooghly, WB, India
e-mail: somnath.tech@gmail.com

S. Patra · S. K. Mandal · G. K. Mahanti
Department of ECE, NIT Durgapur, Durgapur, WB, India
e-mail: skmandal2006@gmail.com

G. K. Mahanti
e-mail: gautammahanti@yahoo.com

N. Pathak
Department of ECE, Dr. B.C. Roy Engineering College, Durgapur, WB, India

S. Banerjee and J. K. Mandal (eds.), *Advances in Smart Communication Technology and Information Processing*, Lecture Notes in Networks and Systems 165,
https://doi.org/10.1007/978-981-15-9433-5_11

1 Introduction

Over the past years, there are various numerical and analytical techniques such as Dolph-Chebyshev and Taylor distribution method [1] which are used to synthesize low sidelobe antenna array patterns. These numerical methods are applicable for equally spaced antenna elements where non-uniform amplitude excitation is required to reduce sidelobe level (SLL). The non-uniform amplitude excitation as required in equally spaced antenna arrays increases the complexity and cost of the feed network [2, 3]. However, in contrast to equally spaced antenna arrays, in the recent past years, unequally spaced antenna array has been found to be effective to realize low sidelobe patterns with uniform amplitude excitation. The additional advantage of using unequally spaced antenna array is that the low sidelobe pattern can be obtained with less number of antenna elements for a given aperture size [4].

On the other hand, in 1959, Shanks [5] first proposed time-modulation to synthesize power pattern in antenna arrays by controlling ON-OFF switching sequence of the radiating elements using high-speed RF switches. As a result of periodical commutation of the antenna elements with some predetermined timing sequence, 'time' is additionally introduced as 'fourth dimension' for synthesizing antenna arrays to reduce the sidelobe level (SLL) significantly to low and ultra-low values [6]. In [7], simple ON-OFF switching devices in the feeding network of uniformly excited linear array helps to suppress the SLL of the power pattern by optimizing the time pulse value at certain RF frequency. Time modulated antenna arrays with uniform amplitude excitations have been realized to be efficient for generating low/ultra-low sidelobe pattern for radar and communication system in [8]. The time-modulation principle is also proved to be effective in antenna array synthesis problems which include the synthesis of sum and difference pattern [9], and flat-top shaped beam pattern in linear array [10]. Since, the power pattern in time-modulated arrays (TMAs) is controlled using set of switch-on time sequence of the array elements. Further, in contrast to the traditional method, the switching sequence can be accurately maintained instantly with the help of software. However, the sideband radiation due to the periodical commutation of the antenna elements is the major problem in TMAs. In this regards, many nature inspired global optimization algorithms such as, differential evolution (DE) [11–13], simulated annealing (SA) [9], genetic algorithm (GA) [14] and artificial bee colony (ABC) [15] are used to obtain desired power patterns by minimizing sideband level simultaneously to sufficiently low values. Also, in some application it is shown that the sideband radiation of TMA are useful to generate simultaneous multiple beam patterns [16, 17].

However, it is mentioned in the beginning of this section that the effectiveness of unequally spaced antenna arrays is to realize low sidelobe patterns with uniform static amplitude excitation. In, [12], a method based on differential evolution is proposed for synthesis of uniform amplitude unequally spaced time-modulated arrays. In the reported approach, DE as detailed in [18] is adopted to optimize simultaneously the element positions and switch-on times of the elements of UESTMA. Simultaneous consideration of the positions and switch-on-time of the elements as the optimization parameter vector, increases the number of unknown parameters to be determined by the algorithm. The performance of the optimization algorithm is not well approved for large number of optimization parameters. Therefore, for large UESTMAs, simultaneous consideration of both position and on-time durations leads to increase the number of unknown parameters greatly and synthesis of such arrays with optimization algorithms may not provide the desired power pattern by finding large unknown parameters. In this paper, our objective is to synthesize UESTMAs with less number of optimizing parameters. In this regards, position and on-time of the elements are separately considered as the optimization parameters for synthesizing the arrays. As a consequence, different cases of synthesis methods such as position-only (PO), on-time only (OTO), on-time then position (OTTP) and position then on-time (PTOT) have been considered. For a 32 element UESTMA, it is observed that the performance of PTOT is better or comparable to that of simultaneous consideration of both position and on-time. The rest of the paper is arranged as follows. In Sect. 2, theoretical analysis and problem formulation has been discussed. Numerical result for the different synthesis method is presented in Sect. 3. Finally, some conclusion about the superiority of the proposed approached has been made in Sect. 4.

2 Theory and Problem Formulation

2.1 Theory

Let us consider a linear array with N isotropic elements, placed along the x-axis as shown in Fig. 1. If the elements are located at x_1, x_2, …x_n, the corresponding array factor expression of such unequally spaced conventional antenna array (CAA) is

Fig. 1 An unequally spaced N-element linear array geometry

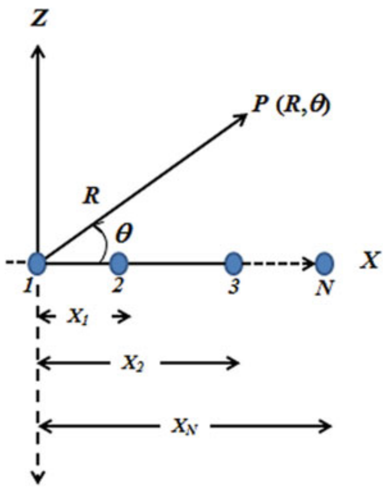

written as

$$AF^{C}(\theta, t) = \sum_{n=1}^{N} A_n e^{j\alpha_n}.e^{j\beta x_n \cos\theta} \tag{1}$$

where A_n and α_n are the static excitation amplitude and phase; x_n is the position of the nth element from the reference position say origin of the coordinate system; $\beta = 2\pi/\lambda$, λ is the wavelength; θ is the observation angle measured from the array axis.

If each element in the array is connected with high-speed RF switches and the elements are periodically commutating in pre-specified on-time duration, the array factor expression in (1) is modified as [5],

$$AF^{T}(\theta, t) = \sum_{n=1}^{N} A_n e^{j\alpha_n} U_n(t).e^{j\beta x_n \cos\theta} \tag{2}$$

In (2), $U_n(t)$ is the periodical time switching function with time modulation period, T and is expressed as,

$$U_n(t) = \begin{cases} 1, & 0 \le t \le \tau_n \ \forall n \in [1, N] \\ 0, & Otherwise \end{cases} \tag{3}$$

where, τ_n is the on-time duration of the nth element. As $U_n(t)$ is a periodical function of time, it can be decomposed in Fourier series to obtain the array factor at different harmonic components as follows

$$AF_k^{T}(\theta, t) = e^{j\{2\pi(f_0 + kf_m)t\}}.\sum_{n=1}^{N} (A_n e^{j\alpha_n}).C_{nk}.e^{j\beta x_n \cos\theta} \tag{4}$$

where, f_0 is the carrier signal frequency, f_m = 1/T is the modulation frequency and C_{nk} is the Fourier coefficient of the nth element at kth harmonic and is obtained as [10, 11],

$$C_{nk} = \frac{A_n \tau_n}{T} \cdot \frac{\sin(\pi n f_m \tau_n)}{(\pi n f_m \tau_n)}.e^{-j\pi n f_m \tau_n} \tag{5}$$

As uniform static excitation amplitude is considered so, $A_n = 1$, and phase, $\alpha_n = 0$; $\forall n = 1, 2, \ldots N$. For such an array, the array factor at center frequency f_0 is obtained from (4) as

$$AF_0^T(\theta, t) = e^{j2\pi f_0 t}.\sum_{n=1}^{N} \frac{\tau_n}{T}.e^{j\beta x_n \cos\theta} \tag{6}$$

Hence, by proper selection of element positions (x_n) and on-time durations (τ_n), the optimized power pattern with reduced SLL and SBL can be achieved.

2.2 Problem Formulation

For the case of PO synthesis, the optimization aim is to suppress the sidelobe level (SLL) by finding the optimum element position whereas for OTO synthesis, only on-time of the antenna elements is optimized to realize power pattern with reduced SLL and SBL. For OTTP, first on-time is considered as the optimization parameter and then by setting the on-time of the respective antenna elements to this optimum on-time sequence, the element positions are optimized. Finally, for PTOT synthesis, first the element position is optimized and then by setting the element positions to this optimum values, on-time is taken as the optimization parameter vector. Let us symbolize 'b' to denote array synthesis method and 'a' as the desired design parameters of the antenna arrays. Thus, PO synthesis, the array becomes a conventional antenna arrays and the array factor as defined in (1) is used for the design problem by the minimization of the following cost functions as introduced in (7).

$$\psi = \sum_{a=1}^{3} W_a^b \delta_a^b H_a\left(\delta_a^b\right) \tag{7}$$

where, δ_a^b with $a = 1, 2$ represents the difference between desired and obtained values of the design parameters of the respective beam as considered in the 'b = PO' synthesis method and is given as $\delta_1^b = \left|SLL_d^b - SLL_{\max}^b\right|$, $\delta_2^b = \left|FNBW_d^b - FNBW^b\right|$.

For OTO, OTTP, PTOT synthesis the following cost function of (8) is introduced,

$$\psi = \sum_{a=1}^{2} W_a^b \delta_a^b H_a\left(\delta_a^b\right) + W^b SBL_{\max}^b \tag{8}$$

In (8), 'b' represents OTO, OTTP and PTOT synthesis. δ_a^b with $a = 1, 2$ and 3 represents the difference between the desired and obtained values of proper design specifications of the respective beam and is given as $\delta_1^b = \left|SLL_d^b - SLL_{\max}^b\right|$, and $\delta_3^b = \left|FNBW_d^b - FNBW^b\right|$; where, $SLL_{\max}$ represents the maximum values of SLL; *FNBW* is the obtained beam-width between first null of the main beam. SLL_d, and $FNBW_d$ are their respective desired values; $SBL_{\max}^b$ is the obtained maximum value of SBL in the different synthesis method; W_a be the weighting factors of the related design parameters and $H_a$is Heaviside step function.

3 Results and Discussion

The DE algorithm is applied to synthesis 32 element linear arrays. It is assumed that the array is symmetrical about the origin of the co-ordinate axis. The DE parameters are selected as—number of optimization parameters (N_{PAR}) = 32, mutation intensity (η) = 0.5, crossover probability (P_{cross}) = 0.85 and the population size (N_{POP}) = 3*N_{PAR}. As considered in [12], the search range of the optimization parameter vectors are taken as—element position (0.55, 1) and on-time (0.01, 1). At center frequency, desired value of SLL and FNBW are set as $SLL_d = -30$ dB and $\mathrm{FNBW_d} = 10^0$ respectively and the aim to suppress SBL as low as possible. For each case, DE runs for 1000 iterations and the corresponding selected results of different cases are presented as follows.

3.1 Case 1: Position Only (PO) Synthesis

As mentioned in Sect. 2.2, for PO synthesis only element position (x_n) is considered as optimization parameter. The DE optimized normalized power pattern is shown in Fig. 2 and the normalized on-time duration of the antenna elements is shown in Fig. 3. The returned value of SLL in this case is obtained as −21.2 dB, with FNBW 6^0.

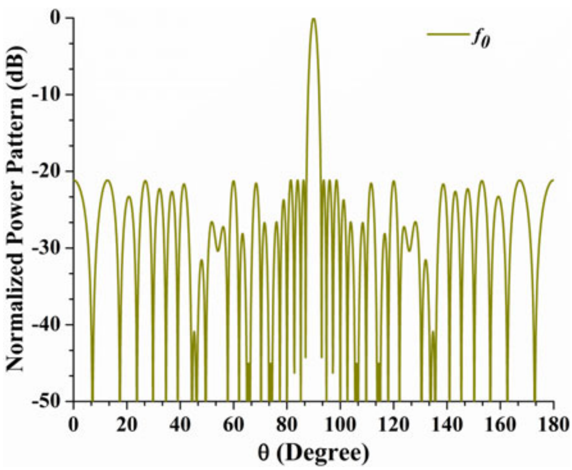

Fig. 2 DE Optimized PO synthesis pattern with obtained values of SLL = −21.2 dB, FNBW = 6^0

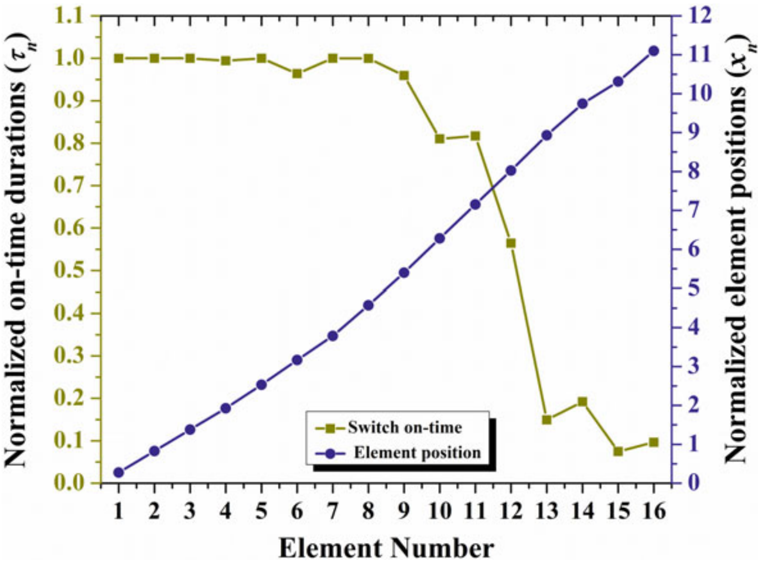

Fig. 3 For a 32 element linear array, the DE optimized element position as obtained in case 1 and with same element position the corresponding on-time durations in case 4

3.2 Case 2: On-Time Only (OTO) Synthesis

For OTO synthesis, only on-time with equal element spacing is optimized using DE. The inter-element spacing of the array is taken as 0.7λ. The corresponding normalized far-field pattern and on-time durations of the elements are shown in Figs. 4 and 5 respectively. The obtained values of SLL, SBL and FNBW in this case

Fig. 4 DE optimized OTO synthesis pattern with obtained values of SLL = 19.88 dB, FNBW = 10.4^0 and SBL = −28.90 dB

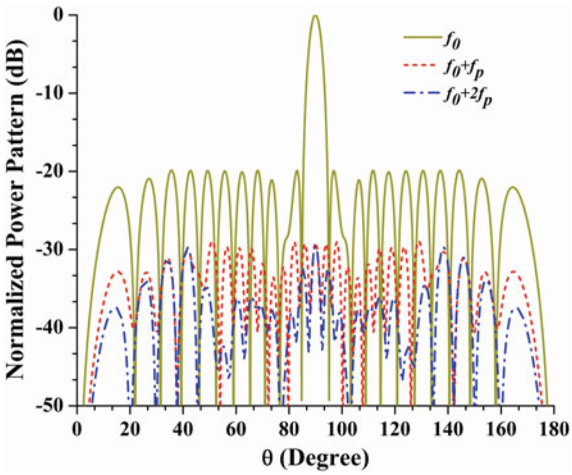

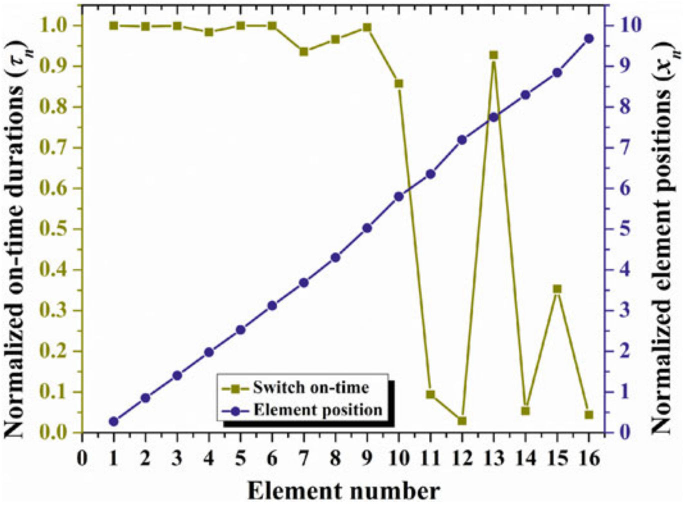

Fig. 5 For a 32 element linear array, the DE optimized on-time as obtained case 2 and with same on-time the corresponding element position in case 3

are −19.88 dB, −28.90 dB and 10.4^0 respectively.

3.3 Case 3: On-Time then Position (OTTP) Synthesis

For OTTP synthesis, first the on-time is considered as optimization parameter then with the optimized on-time, the element position is optimized. Thus with the optimized on-time as obtained in case 2, DE is employed to determine the element positions. The radiation obtained pattern is shown in Fig. 6 and the element positions are shown in Fig. 5. The values of SLL, SBL and FNBW are obtained in this case as −20.72 dB, −29.09 dB and 9.6^0 respectively. Therefore, in this case improvement in SLL as compared to case 2 is only 0.88 dB.

3.4 Case 4: Position then On-Time (PTOT)synthesis

For PTOT synthesis, first the element position is considered as optimization parameter and then with the optimized element positions, on-time durations is optimized. Figure 7 shows the obtained pattern which is synthesized at center frequency, f_0 by suppressing SBL_{max} as low as possible. The corresponding switch on-time sequence of the elements is shown in Fig. 3. The values of SLL, SBL and FNBW obtained in this case are −30 dB, −24.13 dB and 8.8^0 respectively. Thus it is clearly observed

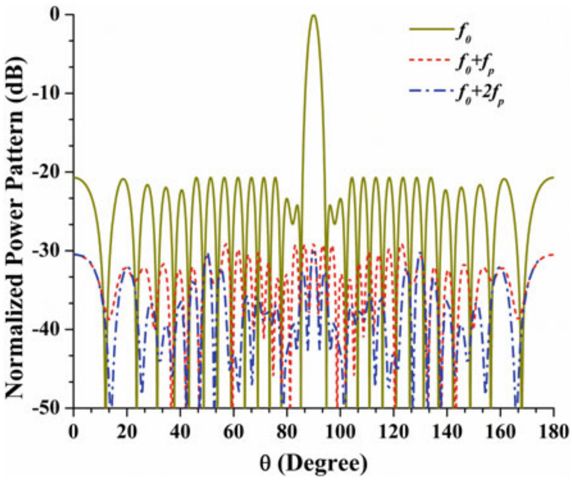

Fig. 6 DE optimized OTTP synthesis pattern with obtained values of SLL = −20.72 dB, FNBW = 9.6^0 and SBL = −29.09 dB

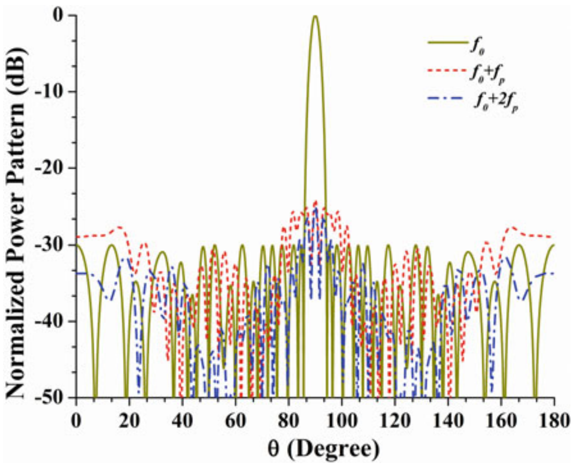

Fig. 7 DE optimized PTOT synthesis pattern with obtained values of SLL = −30 dB, FNBW = 8.8^0 and SBL = −24.13 dB

that remarkable improvement in SLL of 8.8 dB is obtained with respect to the pattern that realized in Case 1.

Table 1 compares the parameters of the patterns obtained under different cases and other related reported results. With respect to [2, 3], the improvement in SLL is observed as 7.35 dB and 7.47 dB respectively. In [12] the pattern is obtained by considering both element position and on-time simultaneously. It can be seen that, the PTOT synthesis method provides almost same result as compared to [12]. Thus

Table 1 Comparison of different optimization cases obtained using DEA

Optimization Cases	SLL (dB)	SBL (dB)	FNBW (Deg.)	HPBW (Deg.)
PO	−21.2	–	6	2.6
OTO	−19.88	−28.90	10.4	4.2
OTTP	−20.72	−29.09	9.6	3.8
PTOT	−30	−24.13	8.8	3.4
Ref. [3]	−22.53	–	–	–
Ref. [12]	−30	−22.7	–	2.7
Ref. [2]	−22.65	–	–	–

for large UESTMAs, the PTOT synthesis method can be suitable as compared to simultaneous consideration of both element position and on-time.

4 Conclusion

In this paper, DE algorithm is utilized to optimize element position and switch on-time for synthesizing unequally space time-modulated arrays. With the study of different synthesis method such as PO, OTO, OTTP and PTOT, it is observed that PTOT synthesis method provides equivalent results as compared to the reported method where both the optimization parameters of the problem are considered simultaneously. Though the performances of the methods are based on 32 elements array, however for large UESTMAs, this is to be verified. Thus, this work can be extended for large arrays to verify the suitability of the PTOT synthesis method.

References

1. Elliot, R.S.: Antenna Theory and Design. Prentice-Hall, Englewood Cliffs, NJ (1981)
2. Lin, C., Qing, A., Feng, Q.: Synthesis of unequally spaced antenna arrays by using differential evolution. IEEE Trans. Antennas Propag. **58**(8), 2553–2561 (2010)
3. Kurup, D. G., Himdi, M., Rydberg, A.: Synthesis of uniform amplitude unequally spaced antenna arrays using the differential evolution algorithm. IEEE Trans. Antennas Propag. **51**(9), 2210–2217 (2003)
4. You, P., Liu, Y., Chen, S.L., Xu, K.D., Li, W., Liu, Q.H.: Synthesis of unequally spaced linear antenna arrays with minimum element spacing constraint by alternating convex optimization. IEEE Antennas Wirel. Prop. Lett. **16**, 3126–3130 (2017)
5. Shanks, H.E., Bickmore, R.W.: Four-dimensional electromagnetic radiators. J. Canad, J. Phys. **37**, 263–275 (1959)
6. He, C., Wang, L., Chen, J., Jin, R.: Time-modulated arrays: a four-dimensional antenna array controlled by switches. J. Commun. Inf. Netw. **3**(1), 1–14 (2018)
7. Fondevila, J., Bregains, J.C., Ares, F., Moreno, E.: Optimizing uniformly excited linear arrays through time modulation. IEEE Antennas Wirel. Prop. Lett. **3**, 298–301 (2004)

8. Kummer, W.H., Villeneuve, A.T., Fong, T.S., Terrio, F.G.: Ultra-low sidelobes from time-modulated arrays. IEEE Trans. Antennas Propagat. **11**(5), 633–639 (1963)
9. Fondevila, J., Brégains, J.C., Ares, F., Moreno, E.: Application of time modulation in the synthesis of sum and difference patterns by using linear arrays. Microw. Opt. Technol. Lett. **48**(5), 829–832 (2006)
10. Yang, S., Gan, Y.B., Tan, P.K.: A new technique for power pattern synthesis in time modulated linear arrays. IEEE Antennas Wirel. Propagat. Lett. **2**, 285–287 (2003)
11. Mandal, S.K., Mahanti, G.K., Ghatak, R.: Differential evolution algorithm for optimizing the conflicting parameters in time-modulated linear array antennas. Prog. Electromagn. Res., PIER B, **51**, 101–118 (2013)
12. Li, G., Yang, S., Huang, M., Nie, Z.: Sidelobe suppression in time modulated linear arrays with unequal element spacing. *J. Electromagn. Waves Appl.*, vol. 24, pp. 775–783(2012).
13. Mandal, S.K., Mahanti, G.K., Ghatak, R.: A single objective approach for suppressing sideband radiations of ultra-low side lobe patterns in time-modulated antenna arrays. J. Electromagn. Waves Appl., **27**(14), 1767–1775 (2013)
14. Yang, S., Gan, Y.B., Qing, A., Tan, P.K.: Design of a uniform amplitude time modulated linear array with optimized time sequences. IEEE Trans. Antennas Propag. **53**(7), 2337–2339 (2005)
15. Mandal, S.K., Mahanti, G.K., Ghatak, R.: Design of digitally-controlled multiple-pattern time-modulated antenna arrays with phase-only difference. Ann. Telecommun. **70**, 29–35 (2014a). https://doi.org/10.1007/s12243-014-0426-7https://doi.org/10.1007/s12243-014-0426-7
16. Poli, L., Rocca, P., Oliveri, G., Massa, A.: Harmonic beamforming in time modulated linear arrays. IEEE Trans. Antennas Propag. **59**(7), 2538–2545 (2011)
17. Mandal, S.K., Mahanti, G.K., Ghatak, R.: Synthesis of simultaneous multiple-harmonic-patterns in time modulated linear antenna arrays. Prog. Electromagn. Res. M **34**, 135–142 (2014b)
18. Storn, R., Price, K.: Differential evolution—a simple and efficient adaptive scheme for global optimization over continuous spaces. J. Glob. Optim., Kluwer Acad. Publ. **11**(4), 341–359 (1995)

Meta Sensing Ovarian Cancer Cells at THz from C Band Radiation Biophysics

Abhirupa Saha, Sanjib Sil, Srikanta Pal, Bhaskar Gupta, and Piyali Basak

Abstract A resonating plasmon like behavior obtained in a metasurface composite to acquire the real-time teratocarcinoma biophysical information is proposed, miniaturization has been done with respect to frequency in order to combat the skin depth challenges of THz communication in bio sensing from C band data. Metamaterial units are programmed to induce a non radiative energy loss resulting in an absorbance property utilized for raising the temperature of the cells that serves for targeted ablation therapy. While resonant frequency shifts illustrate the sensitivity, threshold level of power density for the minimal energy that the cells can receive without dielectric property changes is determined experimentally in the far field region. With label free detection from THz illumination, metamaterial trapped bound state continuum amplifies the malignant cell's thermal energy and this is further applied for explicitly dissipating enough heat to initiate a smart cell death. This gives a mechanism of proliferative apoptosis stimulated with near photonic manipulation via the spectroscopic response of cell dielectric on a metasurface based sensor to calibrate power density for identifying the cell signature at 4 GHz.

Keywords Cancer · Metasurfaces · Plasmonic metamaterials · Terahertz · Dielectric measurement · Split ring resonator · Apoptosis · Radiation therapy

A. Saha (✉) · B. Gupta · P. Basak
Jadavpur University, Kolkata, India
e-mail: abhirupa_21@rediffmail.com

S. Sil
Calcutta Institute of Engineering and Management, Calcutta, India

S. Pal
Birla Institute of Technology, Ranchi, India

S. Banerjee and J. K. Mandal (eds.), *Advances in Smart Communication Technology and Information Processing*, Lecture Notes in Networks and Systems 165,
https://doi.org/10.1007/978-981-15-9433-5_12

1 Introduction

A microwave sensor resistant to temperature changes is an interesting problem to solve when working with biological cells from an in vitro as well as in vivo perspective. This becomes intriguing when a scaled version of a new metamaterial (MM) Split Ring Resonator (SRR) topology is inculcated as the biosensing platform. The chapter describes THz prognostics of ovarian cancer towards a single cell resolution that is still shallow explored in the high frequency community, diverse carcinoma phenotype of every patients sequence is different and this research aims to identify each of the cell signatures by bridging shift in resonant frequency. This is to find out the cell type that is seeded as the analyte and interacts non-invasively with the radiation. By introducing asymmetry in the design of the SRRs loaded patch, the coupling of eigen modes induced by wave matter interaction between the metal and the radiation will be affected as shown in Sect. 1.5, hence the name electromagnetically induced transparency (EIT) like resonance. We are not new to the harmful effects of radiation therapy on cells after ablation, apart from its therapeutic beauty it calls for undesired radioactive decays throughout the body. The research presented detects the effect of varying power levels of incident 4 GHz band radiation on the cells at far field by a C band horn. Instead of tissues, consider the ovarian germ line cancer cells to study their response under external RF source that is connected to the horn antenna radiating the C band power to the cells. Temperature was checked simultaneously to understand the thermal changes of the incident low-power microwave energy to back track the power density that could induce a resultant heating. Opto-electromagnetic properties of a normal and mutated cell create dynamic features and contribute to the formation of polaritons at the interface of cell metal dielectric interface when the high frequency incident signal is focused on a metal surface at considerable high frequency till 2THz (Figs. 1, 2, 3 and 4).

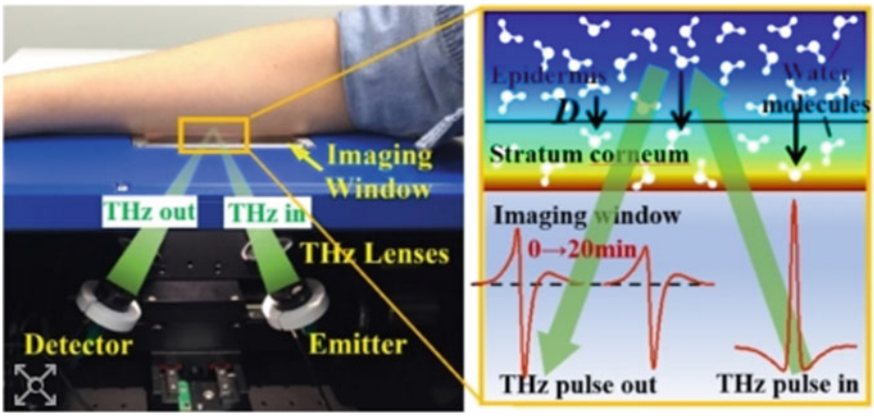

Fig. 1 THz set up to check water content in stratum corneum. [1]

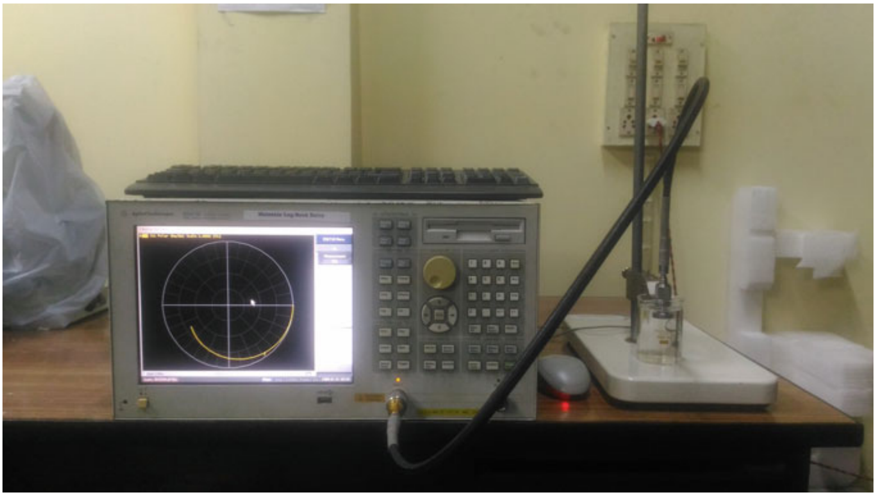

Fig. 2 Open ended Coax Probe Measurement set up

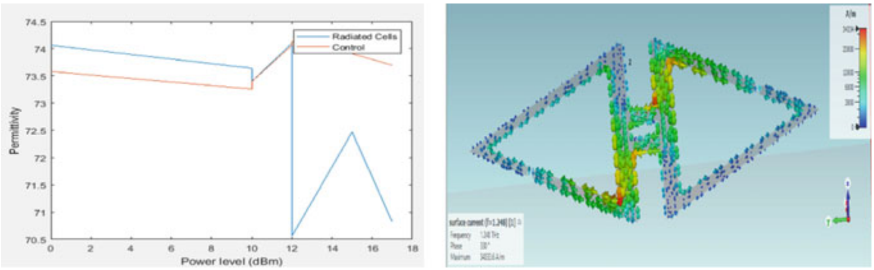

Fig. 3 Plot of permittivity versus power level, and the corresponding surface current

Fig. 4 Novel unit cell structure

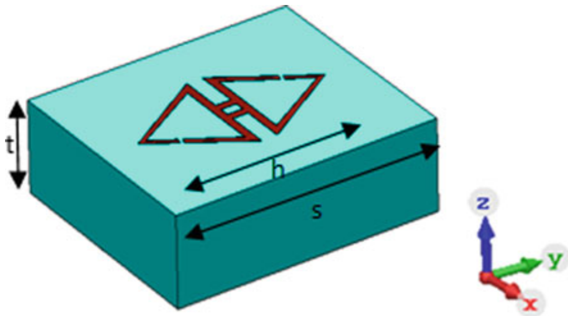

Table 1 Measured permittivity and loss tangent of cell lines and media

Cell line or media	Temperature (°C)	Frequency (GHz)	Permittivity	Loss tangent
PBMC (RPMI)	24–27	4	62	0.3513
MDAMB 231 (DMEM)	24–27	4	63.6	0.3714
PBS	24–27	4	67.3602	0.238
MEM alpha	25–27	4	71.1167	0.2425
Ovarian cancer	24–27	4	73.5793	0.2643

THz regime optimizes skin depth and ionization further letting the electric field confinement to be brought about using metasurface at those places where the cells can interact. Interesting factors determining bio-molecular properties required to dielectric study [2] have to start with the effect of external stimulants to the cell membrane and to have the insight about the electromagnetic changes taking place in time and frequency domain. It is seen that damping of oscillating dipoles can be used to represent the cell membrane and cytoplasmic material along with the nucleus inside. With the help of dielectric behavior, changes with radiation at a given voltage applied for a long duration is judged to understand whether the after process is reversible. This is done by keeping the control sample untreated and the same sample after exposure inside the incubator for a few hours, and then tripan blue can be used to stain and check the viable cells present or absent as a result of radiation. After certain time duration, even feeble power microwave C band exposure impacts the orientation of the dipoles and thus dielectric material is then incapable of reaching a state of equilibrium. Surface Plasmon resonance (SPR) band peaks get shifted [3] with the interaction of cancer cells with the nanoparticles if coated on the metal layer. Generally for Silver nanoparticle (AgNp) the SPR is observed at 400 nm, with the cell layer adhered on the surface, the manner in which the light will interact with the electron gas of the complex AgNp on the initial metal structure is to be observed, if this can be tuned to get notable shifts in the malignant and normal tissues the selectivity will improve (Table 1).

2 Radiation Changes on Cell Viability

The mystery of what happens when the biological cells are exposed to the microwave radiation towards photonic range can be resolved by taking a look deep into the biochemical reactions. The associated energy can be just as less as required to call for an ionization process to start over, where the electrons are forced to be pulled out of their orbits. The high energy of the ions make them unstable for which the amount of time to revert back is coined as reversible that will be illustrated with the help of dielectric permeability changes in the following section. The threshold level of energy that can let the cell chromosome molecules not affected can be mapped by modeling a radiation window that can let non malignant cells be unaffected, and thus preventing the damage to the chromosomal DNA sequence, that further requires gene sequencing to recover back. When excited and displaced from their energy levels, ionization causes electrons to scatter the energy to local areas where non malignant cells are present. The interaction of cells with microwave has to be matched with the spectral signature of biological cells which is possible in frequency domain that is available in CST. The thermal analysis in CST lets us analyze the amount of trapped energy needed to effectively start ablation. Non radiative decay is caused with the combined model of cells on the metasurface that is designed in a way to confine the fields so that it can only target the cancerous site. The average number of radiation induced yields and the number of particle entering a nucleus [4] can be expressed by DNA double-strand breaks (DSBs) through a linear energy transfer model:

$$N = YXD \tag{1}$$

$$n = \frac{\pi R^2 \text{x D x } \rho}{\text{LET x } 1.602\text{x } 10^{-19}} \text{x } 10^{-18} \tag{2}$$

where Y is the yield for DSB, D is the radiation dosage, R is the radius of the nucleus, ρ is the density of cells per unit volume, n being the number of primary particle passing through the nucleus. The premature disturbance in DNA that can be caused due to extended period of exposure may not be exactly creating apoptosis, whereas the DNA damage caused by significant radiation with unavoidable ionization can be analyzed using Monte Carlo damage simulation. The reversible changes that take place implicitly is witnessed using trypan blue, the resultant density of viable cells are counted, and some unusual behavior of the cell was witnessed as the time of radiation was increased cumulatively. Live-cell condition is hardly noticed generally, where the cells condition is captured at a particular time only. Near field is chosen to irradiate the cells with so that the propagation loss is minimal. Ablation and apoptosis are the two therapeutic techniques of treating the cancerous cells to damage their DNA, hence stop them from dividing.

3 Dielectric Analysis

Dielectric measurement is unique perspective to segregate the different types of cancer cells and the corresponding stages with the water content changes. There are numerous ways to find out the dielectric properties of tissues with frequency in both botanical and zoological contexts. In our present study we are concerned with the carcinoma cells to find out their electric field trapping capabilities by a metasensor, and this has been hardly unexplored.

3.1 Open Ended Coaxial Probe Measurement

This is a very well known method that is available in our laboratory at Jadavpur University it uses a truncated portion of a transmission line that is dipped inside the media to be tested to calculate the reflected power for finding the scattering parameters that is used to measure the complex permittivity of the media under test. Thus we avoid the use of antennas or other hardware to measure the permittivity directly.

Keysight technologies have a plethora of rectangular and coaxial probes [5] some are flange free for small tissue specimens: some have flanged aperture and adaptable software with the suitable algorithm that extracts the complex permittivity of cells using Gaussian impulse as the testing signal. Slim form types are the best suited for firm grip as well as better access to falcon pellets.

3.2 Dielectric Modeling

Complex scattering parameters were reported for a wide spectrum up to 1.1 THz including DNA solutions [6], as well as physical compounds [7]. The change in frequency can be used as an input variable to calculate the dielectric property of the sample under test. Biomaterials are broadly determined on the basis of electrostatic charge storing capability that is defined by the mechanical stress between adjacent charges when a voltage is applied that is enough to cause a breakdown or discharge. The permittivity can be a complex value being a function of frequency; imaginary part gives the loss tangent from where conductivity is measured.

$$\varepsilon(\omega)^* = \varepsilon'(\omega) - j\varepsilon''(\omega) = \varepsilon'(\omega) - j\frac{\sigma(\omega)}{\omega\varepsilon_0} \tag{3}$$

Out of various dielectric modeling techniques, a consolidated model can be plotted with the Havriliak–Negami relaxation [5], which is an empirical modification of the Debye relaxation model, accounting for the asymmetry and broadness of the dielectric dispersion curve:

$$\varepsilon(\omega)^* = \varepsilon_\infty + \frac{\varepsilon_s - \varepsilon_\infty}{\left[1 + (j\omega\tau)^{1-\alpha}\right]^\beta} + \frac{\sigma_s}{j\omega\varepsilon_0} \tag{4}$$

The polar materials are classified with various models each having exponential terms for relaxation time τ, permittivity at an extrapolated point $\varepsilon(\omega)$ while Cole Cole models need constant phase elements, ω is the frequency, ε_∞ the permittivity at infinite frequencies due to electronic polarizability, ε_s is the static (low frequency) permittivity, σ_s stands for conductivity at static charge condition, α, and β are the variables for distribution in relaxation and symmetry deviation.

4 Microwave Propagation Through Cells

A cell can be considered as a medium that changes its refractive index under varied spectral conditions that excite surface plasmon polaritons (SPP) upon the incidence of near field radiation to obtain a matrix of refractive index at each point [8]. The various factors that affect the orientation of the cell change the orientation of the oscillating dipoles. With high intensities such as the ones used from radio isotopes in hospitals the tissues get burnt, explaining the irreversible changes in the biological cell's dielectric that could only get ablated. The following factors define the health of cells under test.

4.1 Power Density

At first, we will examine the effects of power level of the incident far field radiation that will penetrate the cells. The reason we are considering the power level effect is that, even when constructing the sensor, that will be used to ablate, we only want to segregate the type of cell first, if that is cancerous we will steer the power level so that the field strength is high enough to penetrate the cell membrane to create pores such that the threshold power level up to which the cells maintain their malignancy is determined, considering the footprint of the horn at radiating far field, while keeping an effective amount of received power for the cells by Friis transmission equation.

Temperature changes are measured to be nominal that proves the non ionizing capabilities of this region of the microwave spectrum that we used to detect. **An unusual phenomenon of decreasing permittivity of these germ line ovarian cancerous cells is experimentally observed to occur sharply at 12dBm** is observed after a 15 min interval, with the increase in power to 15dBm the real permittivity again raised to 72.5.

4.2 Time of Exposure and Material

The metal dielectric (cell) interface should have enough electron gas so that the incident energy can irradiate the sensor to test its Time Domain Spectroscopy (TDS). For in vitro clinical purpose, instead of wave ports excitation, C band horn is used to radiate power to the cells in the glass dish according to a designed protocol to be explained in Sect. 6, have a real time analysis of the cell to capture each time frame, a common solution has been taken and the radiation is progressively aided by an RF source, for 10 min, and 15 min at each power density. Silicon Carbide becomes a common choice as implantable sensor antennas [9] whereas Graphene [10] can be used for fabricating since it has sufficient conductivity at THz range of frequencies, easily available Copper FR4 composite was tested to have appreciable sensitivity. If we coat AgNp, at times, metallic thin films are prone to micro-cracks and require self-healing techniques such as electro pulsing [11]. One has to optimize between the proper media in which the cells can be compatible since tissues are not used, the cells must be kept alive till the duration of the experiment, dispersed inside the proper cell culture media housed in a falcon.

5 Metasurface for Biosensing from THz to GHz

The area of illumination to detect a sample can be approximated on a 10 microns scale which is the single cell resolution, our sensor has a strip width of 3microns. At first a micro version of the metasensor was simulated, the entire meta surface is similar to that of the unit cell that consists of two asymmetrically placed slots from either sides of the y axis, thus introducing symmetry breaking double splits, at equal and unequal distances from the ends for each cell, the structure is made on the xy plane, it is to be excited by a y-polarized plane wave hence while designing in CST microwave studio, we chose the magnetic boundary condition in the x direction, electric boundary condition for y direction, and left the z direction open, for the energy vector to get impinged on the surface of the entire array normally. Floquet port analysis can be done to create the excitation beam for the entire surface of the array instead of one unit cell. Instead of creating tissue phantoms [12], our in vitro MS sensor has the uniqueness to work in Terahertz while being compatible to be implanted as an in vivo, offset due to orientation of the substrate does not affect much as the entire operation is taking place in sub wavelength range.

5.1 The Sensor Design

The sensor has to receive irradiated power and the scattering parameters have to be such that both the S_{11} and S_{21} have to be simultaneously negative. The frequency shift in fetching and trapping the energy is found for calculating the sensitivity per ml. Inset fed microstrip patch antennas on FR4 are designed to transmit the power to the sensor surface at 4.1 GHz to direct the radiation to the cells. With the nano particles dispersed on the metal, the microwave radiation activates the ablation only when the sensor decides the analyte is carcinoma, hence the ablation is catalyzed only if the cell has to be destroyed. Practically it has been observed that when cells are dispersed on metal surfaces, the layer of the cells forms a dielectric superstrate that resides on top of the metal layer that excite changes in the metal dielectric interface propagation surface, a dielectric relaxation due to Maxwell Wagner effect that can be relatable to muscles tissue protein [13], while similar principles can be studied in cell glucose albumin content [14]. Plasmon polariton waves, this plasmonic behavior of the cells create transparency windows that match with the spectral signature of the cancer cells.

5.1.1 The Asymmetric Metasurface

The resonator is designed to work as a sensor and a medium for ablation after the acceptable threshold is determined by subjecting the cells separately under radiation. Each unit component that repeats itself periodically in xy plane is the meta-atom. An atom implies a split ring resonating (SRR) structure with two asymmetrically placed gaps [8] diagonally opposite to each other; this design was used as a single component in the previous work. This work mainly focuses on using the unit cell to make the miniaturized pattern so that it is used as a layer on a system on chip with in vitro placement of carcinoma cells on the chip. This time bolch-wave irradiation of one MM cell is simulated, and the effect of one cell on adjacent neighbor cells is used as a source to act as a resonator d. Periodicity of each unit SRR is maintained to be less than λ/4 to induce sub wavelength effect on the structure that is 5λ to get properly irradiated by the transmitting patch. Previously a spiral structure was constructed whose radius controlled the inductance and capacitance created by the metal pattern, but the sensitivity and resonating capability was not appreciable but here, singularities are encountered by the impinging wave matter interaction. The metallic sub unit cell array in Fig. 5 comprises the equivalent of nanosensor should resonate at C band.

The scaled up dimensions of sub unit cell is a by b: 72 mm by 44 mm, the metal with a depth of 0.1 mm such that miniaturization was accomplished with respect to resonating frequency. Floquet boundaries were simulated for periodic array response from a unit cell. As y polarized excitation was normally incident, x direction had a magnetic boundary condition, $H_t = 0$, while the y direction had electric boundary condition, $E_t = 0$, thus PMC, PEC walls and the z direction consisted of the pointing vector, hence open boundary was set. The THz simulation was carried out in the frequency domain solver of CST for the range of 0.5 THz to 2THz, with field monitors set to plot the 2D or 3D results. To excite the metasurface, the wave port dimensions along the yz plane coincide with the length of the substrate and the width is more than five times the thickness of the substrate. The sensor was fabricated,

Fig. 5 Fabricated meta atom

the illuminating patch was designed at 4.10 GHz, and experimentally resonated at 4.16 GHz, simulations have been done in CST microwave studio, frequency solver domain, and miniaturization has been conducted from 0.5–2 THz to a 3 GHz–6 GHz frequency sweep range.

5.2 Ablation and Sensing

When upon terahertz excitation that is aligned along the axis of the array structure the metasurface acts like plasma. Plasmonics deal with the interaction of light (a few THz towards optical region) with the free electrons in metals. The SPPs dispersive relation can be dealt with proper boundary conditions dielectric constant of the metal and the dielectric material as respectively, the dispersion relation of surface plasmons; if ε_m, ε_d are the permittivity of the metal and dielectric respectively, the wave vector of the SPPs k_z is given by (6).

$$k_z = \frac{\omega}{c}\sqrt{\left(\frac{\varepsilon_m \varepsilon_d}{\varepsilon_m + \varepsilon_d}\right)} \tag{6}$$

The Drude model describes mobile charge carrier oscillations which is a frequency dependent dielectric constant of materials:

$$\varepsilon_m(\omega) = 1 - \frac{\omega_p^2}{\omega(\omega + i\gamma)} \tag{7}$$

where ω_p is the bulk plasmon frequency and γ is the damping frequency. Changing the wave port orientation and the width of the slots and their distance from the edges is also a way of modifying the Plasmon resonance frequency. Equation (6) shows that the wave vector normal to the surface is imaginary, and the SPPs become lossy when the threshold plasma frequency is exceeded. The optical phenomena of plasmonic resonance result due to the patterning of nanostructures. We control optical surface waves, such as SPPs, in the near-field regime, exploiting the negative electric and magnetic response of MMs. Seeding the cancerous and non cancerous cells on the surface causes a resonance shift that determines sensitivity that is evident from s parameters in Fig. 6, along with some higher order modes for multiple resonances. Overall, we enhance the skin depth [15] by narrowing to the 4 GHz neighborhood so that the injected radiation can reach the cells on the sensor if implanted. With this we can claim that THz can be useful not only due to the multiple of the value of frequency, but also as a short wavelength signal, and can be an indicative of the scaled version of its lower frequency counterpart with sufficient optimization (Fig. 7), each of the sub unit cells have been individually analysed to provide unique results as well [16].

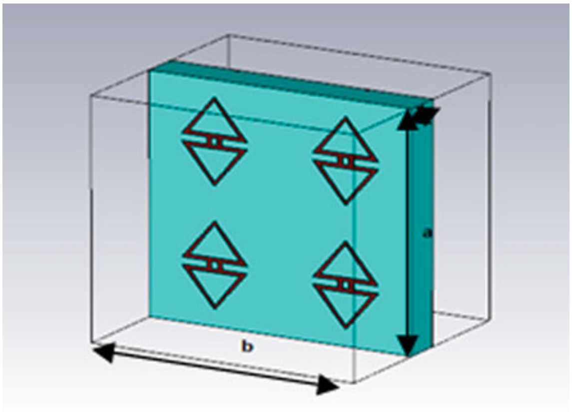

Fig. 6 Nanoparticle embedded metasurface for biosensing

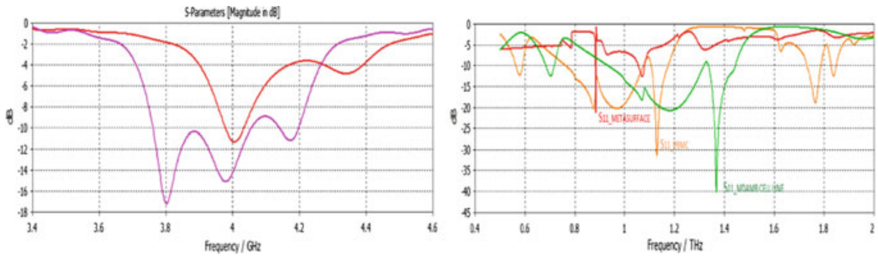

Fig. 7 Transition from C band towards the THz band showing S_{11} response

6 Conclusion

A cumulative study of the effect of C band radiation exposure on a metasensor with changing power intensity levels has been taken into account. A sensor that can differentiate and ablate is novel and has been miniaturized to the lower THz band. The type of cells to be determined might change, but the biosensor should be able to distinguish between different types of cells the deciding factor being the permittivity of the cell under test. The positive part of this research is the utilizable threshold of C band (4–8 GHz) for study of thermal dielectric changes of cells under radiation. The challenge is to identify the type and the stage of the cancer from the available information. While checking the threshold power density that for the sensor test signal, the project deals with the design of metamaterials loaded with SRR unit cells to bring in a deviation in the permeability of the overall composite so that the shift in the refractive index is comparable to that of the normal cells and the type of cancer can be determined from that henceforth. Thus the metasurface can safely sense the cells before a threshold 15dBm that is capable of inducing ablation by trapping thermal energy. A contrast in coupling is seen under carcinoma and normal cells, as EIT like transparency window gets simulated more prominently under THz, but as we miniaturize the dielectric contrast becomes more significant. The PA 1 epithelial teratocarcinoma cells suspended in MEM alpha media were subjected to radiation and studied using open ended coaxial probe technique in the microwave laboratory, department of electronics and telecommunication engineering (ETCE), Jadavpur University, the authors acknowledge Dr. Sib Sankar Ray and Priti Chatterjee, Indian Institute of Chemical Biology (IICB) CSIR Kolkata for contributing to the ovarian cancer cell culture procedure.

References

1. Hatcher, H., Cebrian, J., Hardwicke, J., Pickwell-MacPherson, E.: Evaluation of in vivo THz Sensing for Assessing Human Skin Hydration. J. Phy.: Photonics (2020)
2. La Gioia, A., Porter, E., Merunka, I., Shahzad, A., Salahuddin, S., Jones, M., O'Halloran, M.: Open-ended coaxial probe technique for dielectric measurement of biological tissues: challenges and common practices. Diagnostics **8**(2), 40 (2018)
3. Smith, D.R., Padilla, W.J., Vier, D.C., Nemat-Nasser, S.C., Schultz, S.: Phys. Rev. Lett. **84**, 4184–4187 (2000)
4. Wang, W., Li, C., Qiu, R., et al.: Modelling of cellular survival following radiation-induced DNA double-strand breaks. Sci Rep **8**, 16202 (2018)
5. Alekseev, S.I., Ziskin, M.C.: Human skin permittivity determined by millimeter wave reflection measurements. Bioelectromagn. J Bioelectromagn. Soc. Soc. Phys. Regul. Biol. Med. Eur. Bioelectromagn. Assoc. **28**(5), 331–9 (2007)
6. Ermilova, E., Bier, F.F., Hölzel, R.: Dielectric measurements of aqueous DNA solutions up to 110 GHz. Phys. Chem. Chem. Phys. **16**(23), 11256–11264 (2014)
7. Gulich, R., Köhler, M., Lunkenheimer, P., Loidl, A.: Dielectric spectroscopy on aqueous electrolytic solutions. Radiat. Environ. Biophys. **48**, 107–114 (2009)
8. Yan, X., Yang, M., Zhang, Z., Liang, L., Wei, D., Wang, M., Zhang, M., Wang, T., Liu, L., Xie, J., et al.: The terahertz electromagnetically induced transparency-like metamaterials for sensitive biosensors in the detection of cancer cells. Biosens. Bioelectron. **126**, 485–492 (2019)
9. Afroz, S., Thomas, S.W., Mumcu, G., Saddow, S.E.: Implantable SiC based RF antenna biosensor for continuous glucose monitoring. SENSORS, IEEE, pp. 1–4 (2013)
10. Gupta, S., Upadhayay, M.D., Pal, S.: Graphene based monopole terahertz antennas on polyimide substrate. In: 2018 International Conference On Advances in Communication and Computing Technology (ICACCT) Amrutvahini College of Engineering, Sangamner, Ahmednagar, India, 8–9 Feb 2018
11. Sun, S., et al.: Gradient-index meta-surfaces as a bridge linking propagating waves and surface waves. Nat. Mater. **11**, 426–431 (2012)
12. Truong, B.C.Q., Fitzgerald, A.J., Fan, S., Wallace, V.P.: Concentration analysis of breast tissue phantoms with terahertz spectroscopy. Biomed. Opt. Express **9**, 1334–1349 (2018)
13. Foster, K.R., Schepps, J.L., Schwan, H.P.: Microwave dielectric relaxation in muscle—a second look. Biophys J. **29**, 271–281 (1980)
14. Nazarov, M.M., Cherkasova, O.P., Shkurinov, A.P.: Study of the dielectric function of aqueous solutions of glucose and albumin by THz time-domain spectroscopy. Quantum Electron. **46**(6), 488 (2016)
15. David, M.: Microwave Engineering. Wiley, Inc. (1998)
16. Saha, A., Basak, P., Gupta B., Pal, S.: A Biodegradable THz metasensor for malignancy apoptosis, 2019 Int. Conf. Electr. Electron. Comput. Eng. (UPCON), ALIGARH, India, pp. 1–5 (2019)

Intelligent Systems and Information Processing

A Metaheuristic Approach for Image Segmentation Using Genetic Algorithm

Joy Bhattacharjee, Soumen Santra, and Arpan Deyasi

Abstract Euclidian distance between any two observations in M $\times$ N matrix is computed using genetic algorithm. RGB image is classified using K-means clustering, and Euclidian distance matrix is calculated involving fitness function. Higher limit for terminating the program are assigned for both normal (500) as well as for higher accuracy values (2000). Clusters are assigned in such a way that closest distance can be obtained from the distance matrix, which is optimum. When image element becomes equals to cluster number, it is replaced. PSNR value is much higher for segmented image compared to the data obtained from thresholding, which clearly speaks in favor of genetic algorithm. Cluster value and image matrix can be changed with the objective to reduce the fitness function.

Keywords Segmentation · K-means clustering · Euclidian distance · Fitness function · Genetic algorithm

1 Introduction

Genetic Algorithm (GA) is a search based Meta-heuristic approach that is inspired by Charles Darwin's theory of natural evolution [1]. It gives the clear indication how the process of natural selection where only selected individuals are assigned to the task for reproduction. Actually it resolves the problems like chromosome structure

J. Bhattacharjee (✉)
Department of Electronic Science, A.P.C College, Barasat 700131, India
e-mail: joybhatta1000@gmail.com

S. Santra
Department of Computer Application, Techno International Newtown, Rajarhat 700156, India
e-mail: soumen70@gmail.com

A. Deyasi
Department of Electronics and Communication Engineering, RCC Institute of Information Technology, Kolkata 700015, India
e-mail: deyasi_arpan@yahoo.co.in

S. Banerjee and J. K. Mandal (eds.), *Advances in Smart Communication Technology and Information Processing*, Lecture Notes in Networks and Systems 165,
https://doi.org/10.1007/978-981-15-9433-5_13

using various operators like selection, crossover, mutation etc. [2, 3]. This method as optimizers in the field of segmentation of medical images is already utilized by researchers [4, 5] which leads to detection of cancerous cell from various MRI, CT scan, and mammogram images. There is a possibility to presence of various noisy multimodal hidden regions in sectional image portions [6] due to carcinogenic portion.

Medical image segmentation based on genetic algorithm works on the basis of difference in between pixel values, brightness, active contour and some other parameters [7, 8]. Cancerous cell presents in the medical images has some discontinuities within the whole image. Mutation and crossover in between various generations helps us to detect those cancerous cell positions [9] and segment that portion very properly based on their fittest values among others.

As the image is tricoloured it has three colour segments red, blue and green. In the present work, we consider the red, blue and green plane as three different matrices individually. Then, we construct another three different matrices based on the formulation. These new matrices are coupled with fitness functions where dimension of the function will be the product of all elements of decision variable matrix. To control the genetic algorithm structure we define an structure with level of display contains iteration and time limit, which is a scalar quantity controls the generation numbers (higher for better operations). Then, we calculate the distance matrix and assigns cluster and find closest distance based on that distance matrix. Here we introduce the canonical approach of GA based on selection and recombination features which gives a search space. This search space contains all the possible fittest regions those are presently carcinogenic and may be in future will be possessed as one.

2 Process Description

Genetic algorithm is based on Charles Darwin's Survival of Fittest theory. Out target is to produce new generations consisting offspring's with better fitness than parents. In terms of mathematics we have to find the global maxima or global minima of the given function, this process will generate some generations with some global value either maximum or minimum and will terminated as the convergence condition satisfied [10]. As the genetic algorithm is centred with biological system, the global value, functions are termed as fitness and chromosomes respectively.

The whole process is simulated by flowchart above, and the description is given below:

I. ***Initializing a number of populations***: In the first stage we have to initialize a number of populations of individuals, which can label as parent. We can treat the parent as the chromosome consisting of a fixed number of cells. Each chromosome in population has a certain fitness value, i.e. for a different environment how they survive and that survival score is replicated as fitness score.

II. ***Selection of parents***: Based on the fitness score, we select a finite number of parents. This is based on the fact that the individuals, chromosome or parent is more fit than others they can pass their genes to the next generation or to the offspring. This fitness score is not mandatory to be the maximum always, it may be the chromosome having minimum fitness score will selected for reproduction, this selection with respect to fitness score is purely dependent on the way we calculate the fitness value, i.e. the fitness function. There is some ways to selection of parent with respect to the fitness score:

i. *Tournament Selection*: In this selection method a tournament is conducted between all the chromosomes present in the population. For selection of each parent we have to conduct a tournament. These tournaments results are based on the fitness of chromosome. By this method every chromosome is getting a fair chance to become a parent for producing new generation, i.e. probability of selection of every chromosome is nearly same. After the number of tournament we got a number of winners, those are become parent for new generations.

ii. *Roulette Wheel Selection*: It is a fitness proportionate selection, i.e. in this case the probability of selection is proportional to the fitness score of each individual. We made a pie chart for each chromosome with respect to their fitness value. This pie chart is rotated and a portion is selected randomly. The chromosome occupied a larger area having highest probability to be selected as parent. As the process is similar to the famous casino game Roulette named after the French word meaning little wheel, this process is termed as Roulette Wheel Selection.

iii. *Rank Based Selection*: This selection process is quite similar to the Roulette Wheel Selection technique. Here a ranking is generated for each chromosome with respect to their fitness score, unlikely in Roulette Wheel Selection here the ranking is generated in ascend order, i.e. the chromosome having least fitness score will get the highest ranking. Then the percentage of ranking is made by the ranking score and the total number of individuals and these percentages are fed into the Roulette Wheel. This technique indicates that each chromosome is nearly equal probable to get selected as parent.

III. ***Crossover***: It is the first step to generate the new generation from parents. Crossover can be termed as the exchange or swapping of genetic material of parents to produce the new generation. Crossover can be operated with some techniques, discussed below:

i. *Single Point Crossover*: In this crossover technique a single point is chosen for crossover. With respect to that point the genes are swapped and generate new offspring with combination of parent's genetic material. As the crossover is operated with respect to a single point, this type of crossover is termed as single point crossover. If the number of point of crossover is two or more, then those techniques termed as double point crossover or multipoint crossover respectively.

ii. *Uniform Crossover*: This Crossover technique is based on third party crossover masking or coin tossing crossover. In crossover masking a masking array is generated of same size as parent and the crossover is operated with respect to that masking array, on the other hand coin tossing is a similar technique but unlikely in crossover masking, the masking array is generated randomly.

These crossover techniques are operated to generate the offspring. As per our target all offspring must have better fitness than parent, to satisfy this criterion these crossover techniques operated as per requirement.

IV. *Mutation*: This is the last stage of the reproduction phase in the genetic algorithm. The generations generated from crossover must have an enormous change in fitness with respect to parents or previous generation. Mutation helps us to alter the genetic information of offspring to change in the fitness value. As per biological mutation, here mutation is also performed by flipping the genetic information between the chromosomes. These operations can be done using a mutation probability factor or swapping some random genes between chromosomes to modify the fitness of new generation (Fig. 1).

The process of genetic algorithm is briefly discussed in the above paragraph. As per the process there should be an initial population and their fitness scores. In this paper we consider the k-means clustering as the fitness score evaluation function. As the input image is a RGB image, it has three color plane Red, Green and Blue. Three feature matrix is generated and concated, we will use this concated matrix as the input matrix in cluster algorithm. Further we assign 4 clusters, i.e. the cluster algorithm will have 4 cluster centers. Then we find the minimum Euclidian distance between

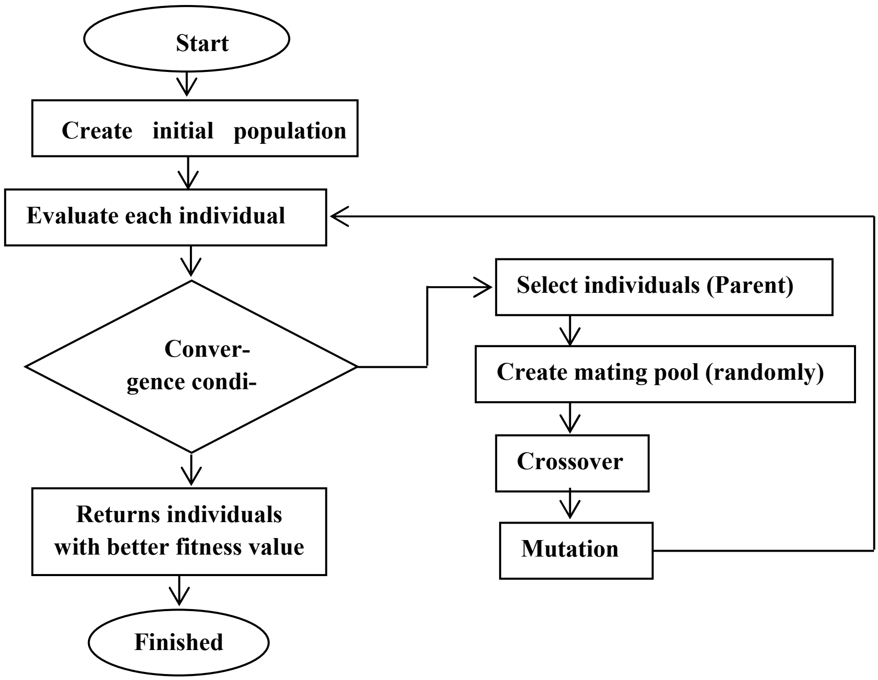

Fig. 1 Flow diagram of the process

the centered values which is actually global minimum and return the summation of all distances as the fitness score of the individuals. In this paper we consider the minimum fitness scores is the better fitness indications. Then, we setting up the crossover and mutation operation with some parameters like number of variables we going to use or implement in the crossover, which is 12 in this case, the range of global minimum solution and so on. We use the a time limit as convergence condition and set it as 50, better the time limit better the results. We use multipoint crossover and tournament selection, described in the previous field to operate the process. This process returns the global minimum or the solution, which also known as centered value is a row matrix of size we define before. We calculate the fitness score of the global minimum which is actually the new generation generated from the color matrices. At the final stage of segmentation from the fitness calculation of the indices of minimum Euclidian distances is taken into account. This is a column matrix which is reshaped with respect to the row and column number of the input image. This reshaped column matrices' data points has been altered for obtain the segmented image. Mutation is performed by this altering of data points, where our goal to achieve a segmented image which is more fit than the input image. For data point's value 1, 2, 3 and 4 mutation probability factor is chosen as 0, 85, 170, and 255 respectively. Finally we got the segmented image of the sensitive medical images after this mutation process (Fig. 2).

3 Results and Discussions

Here we use the genetic algorithm for image segmentation with k-means clustering as the fitness function. Genetic algorithm is biologically inspired optimization process which is used here as search algorithm for searching of discontinuities present in the image. The segmentation process is based on operation of fitness function. Segmented image may contains many other portions which are not the parts of cancerous cell due to presence of in the image or any other kind of discontinuity present due to error in capturing process, this errors can be minimized or corrected using geometrical transformation like affine transformation [11].

Three feature matrices are created by separation of three color plane and calculated by the approximated formulation given below:

$$\frac{\text{Colour plane matrix} - \text{minimum of colour plane matrix}}{\text{maximum of colour matrix} - \text{minimum of colour matrix}}$$

This is basically the ratio of two-color plane matrices. In this particular segmentation process fitness function is the k-means clustering, which actually helps to segment the sensitive medical images more accurately and minimizes the error. In this research work we set the time limit to 50, which is basically the parameter for termination of segmentation process. This termination parameter is applied when genetic algorithm method sets up. At the end of segmentation process is done by

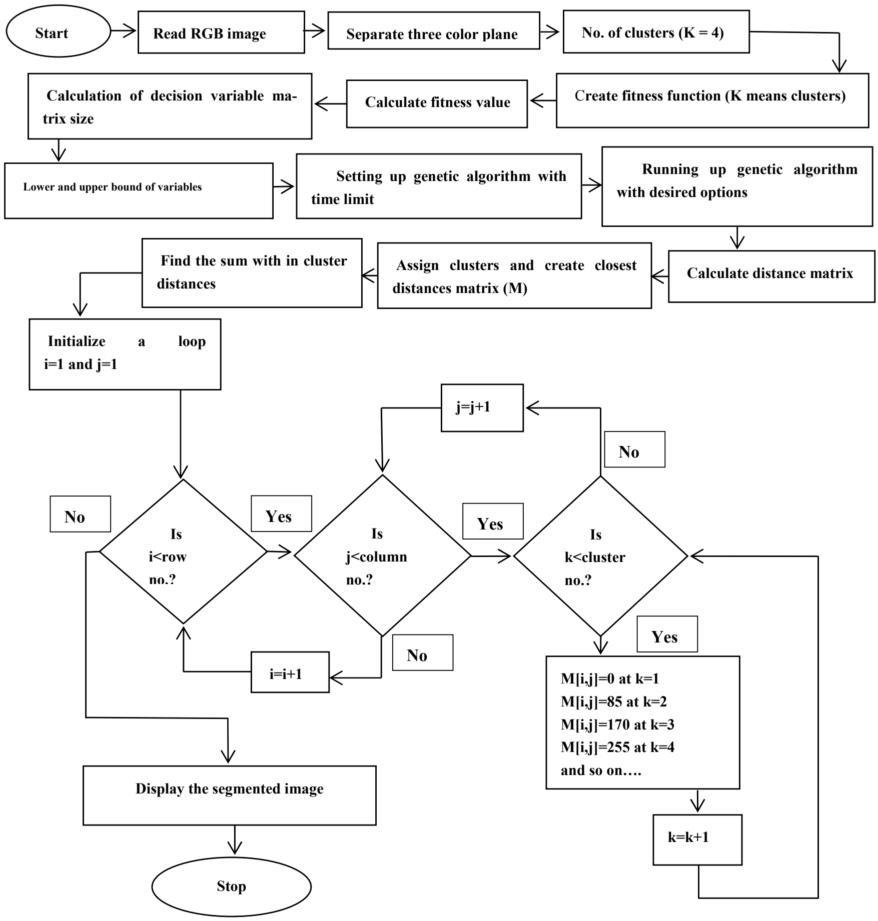

Fig. 2 Algorithm of the process

substituting the image matrix elements contains 1, 2, 3, 4 by 0, 85, 170, 255. In this paper the number of clusters is taken 4 for k-means clustering.

In the Table 1 we show the original image, segmented image by genetic algorithm.

This work is different from others for:

K-means clustering is used as the fitness function in the operation of genetic algorithm.

A new segmentation method of cancerous cell from sensitive medical image (like brain tumour MRI, breast cancer mammogram etc.) with the help of genetic algorithm. Results are given in Table 1.

Image [12] is the MRI of brain tumour and its corresponding segmented image is shown in the Table 1. The segmentation of cancerous portion from the original image is nearly perfect. Image [13], Image [14], Image [16], Image [17], Image [18],

Table 1 Original image and corresponding segmented Image after application of Genetic algorithm

Original image	Segmented image
Brain tumour MRI [12] 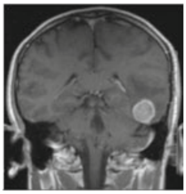	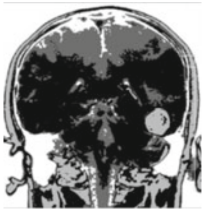
Brain tumour MRI [13] 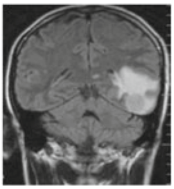	
Brain tumour MRI [14] 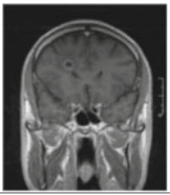	
Breast cancer mammogram [15] 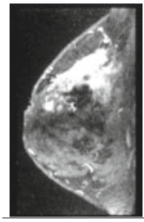	
Brain tumour MRI [16] 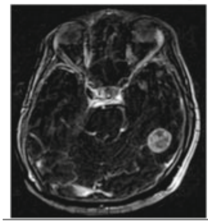	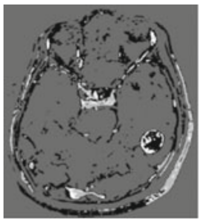

(continued)

Table 1 (continued)

Original image	Segmented image
Brain tumour MRI [17] 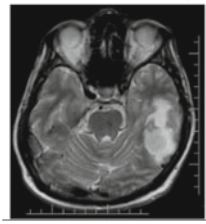	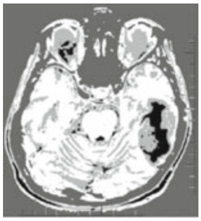
Brain tumour MRI [18] 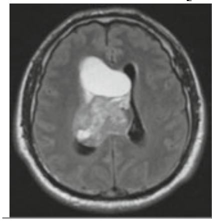	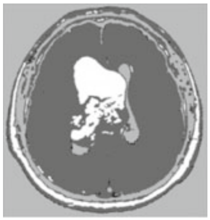
Brain tumour MRI [19] 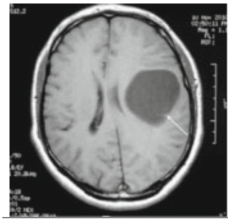	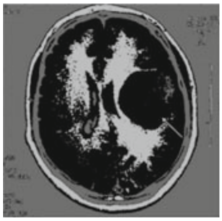
Breast cancer mammogram [20] 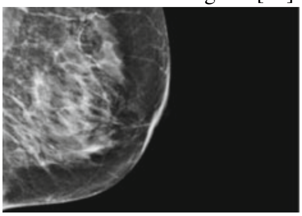	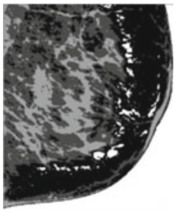
Breast cancer mammogram [21] 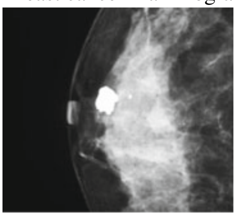	

Table 2 PSNR value for segmentation and thresholding

Image number	PSNR between original and threshold image	PSNR between original and segmented image
Image 1 [12]	5.0483	11.4556
Image 2 [13]	2.7829	11.0111
Image 3 [14]	3.1166	12.0802
Image 4 [15]	3.8227	11.2975
Image 5 [16]	1.1549	16.7702
Image 6 [17]	1.4575	12.4729
Image 7 [18]	3.8838	11.6974
Image 8 [19]	2.7746	10.8519
Image 9 [20]	8.2664	13.4754
Image 10 [21]	2.0217	13.5788

Image [19] are the MRI of brain tumour. Image [15], Image [20], Image [21] are the mammogram images of breast cancer.

Table 2 gives the PSNR value for the segmented image w.r.t original image, and comparative study is also made if the original one is thresholded.

In the above table the PSNR value are shown. In column 1, 2, the PSNR value in between original and threshold image and PSNR value between original image and segmented image have been shown respectively. As we know the PSNR value determines the image reconstruction and better PSNR value indicates the better performance, then all the values in the above table clearly shows the segmented image by genetic algorithm with k-means clustering as fitness function is better than the threshold image.

4 Conclusion

Comparative study between segmented image and threshold image reveals the superiority of the proposed genetic algorithm as observed from PSNR. For mammogram images of breast cancer as well as brain tumour images, the analysis si carried out, and for each case, our study has shown better performance. Henceforth, form reconstruction point of view, the algorithm will work fine, and can be applied in medical sectors.

References

1. McCall, J.: Genetic algorithms for modelling and optimisation. J. Comput. Appl. Math. **184**(1), 205–222 (2020)
2. Al-Hajri, M.T., Abido, M.A.: Assessment of genetic algorithm selection, crossover and mutation techniques in reactive power optimization. In: IEEE Congress on Evolutionary Computation (2009)
3. Shrestha, A., Mahmood, A.: Improving genetic algorithm with fine-tuned crossover and scaled architecture. J. Math. **2016**, 4015845 (2016)
4. Maulik, U.: Medical image segmentation using genetic algorithms. IEEE Trans. Inf Technol. Biomed. **13**(2), 166–173 (2009)
5. Jedlicka, P., Ryba, T.: Genetic algorithm application in image segmentation. Pattern Recognit. Image Anal. **26**, 497–501 (2016)
6. Dandolo, C.L.K., Lopez, M., Fukunaga, K., Ueno, Y., Pillay, R., Giovannacci, D., Du, Y.L., Bai, X., Menu, M., Detalle, V.: Toward a multimodal fusion of layered cultural object images: complementarity of optical coherence tomography and terahertz time-domain imaging in the heritage field. Appl. Opt. **58**, 1281–1290 (2019)
7. Angelina, S., Suresh, L.P., Veni, S.H.K.: Image segmentation based on genetic algorithm for region growth and region mergin. In: IEEE International Conference on Computing, Electronics and Electrical Technologies (2012)
8. Tan, C., Sun, Y., Li, G., Tao, B., Xu, S., Zeng, F.: Image segmentation technology based on genetic algorithm. In: Proceedings of the 3rd International Conference on Digital Signal Processing, pp. 27–31 (2019)
9. Hesamian, M.H., Jia, W., He, X., Kennedy, P.: Deep learning techniques for medical image segmentation: achievements and challenges. J. Digit. Imaging **32**, 582–596 (2019)
10. Man, K.F., Tang, K.S., Kwong, S.: Genetic algorithms: concepts and applications [in engineering design]. IEEE Trans. Industr. Electron. **43**(5), 519–534 (1996)
11. Santra, S., Bhattacherjee, J., Deyasi, A.: Cancerous cell detection using affine transformation with higher accuracy and sensitivity, accepted in book series: advances in intelligent systems and computing. Intelligent Computing: Image Processing based Applications. Springer (2020)
12. Dilmen, N.: CC BY-SA 3.0 https://commons.wikimedia.org/w/index.php?curid=18633693
13. Dilmen, N.: CC BY-SA 3.0. https://commons.wikimedia.org/w/index.php?curid=18633668
14. Dilmen, N.: CC BY-SA 3.0. https://commons.wikimedia.org/w/index.php?curid=18747783
15. Unknown photographer: This image was released by the National Cancer Institute, an agency part of the National Institutes of Health, with the ID 2703 (image) (next)., Public Domain. https://commons.wikimedia.org/w/index.php?curid=24052431
16. Dilmen, N.: CC BY-SA 3.0. https://commons.wikimedia.org/w/index.php?curid=18633656
17. Dilmen, N.: CC BY-SA 3.0. https://commons.wikimedia.org/w/index.php?curid=18633651
18. Dawes, L.: Radiopaedia, CC BY 3.0. https://commons.wikimedia.org/w/index.php?curid=3615309
19. Rocka, S., Neverauskiene, L., Nelson, E.L, et al.: Papillary Glioneuronal Tumour: a case report. Cureus 11(3): e4215 (2019).
20. Imperial College London. Research collaboration aims to improve breast cancer diagnosis using AIby RyanO'Hare
21. SCiardullo,2014

Improved Twitter Sarcasm Detection by Addressing Imbalanced Class Problem

Kushankur Ghosh, Arghasree Banerjee, Mayukh Bhattacharjee, and Sankhadeep Chatterjee

Abstract Sarcasm detection is one of the challenging tasks in the domain of text mining. With the advancements in machine learning reasonable accuracy have been achieved in sarcasm detection. Studies have revealed that highly imbalanced classes affect the performance of the classifiers in sarcasm detection. The current study addresses the class imbalance problem in the sarcasm detection in tweets. Synthetic Minority Oversampling Technique (SMOTE) has been used to mitigate the imbalanced class problem present in the data collected from tweeter. Two well-known classifiers have been trained and tested with varying degrees of balance ratio of SMOTE. Results have indicated that the SMOTE is highly successful in addressing the imbalanced class problem in sarcasm detection by improving the classifier performance to a greater extent.

Keywords SMOTE · Naïve Bayes · Logistic regression · Sarcasm detection

1 Introduction

The study regarding machine intelligence has spread its roots into many domains. Various studies regarding machine learning has been performed by eminent researchers over the years [1–8]. In the recent years the field of text mining [9–12]

K. Ghosh · A. Banerjee · M. Bhattacharjee · S. Chatterjee (✉)
Department of Computer Science & Engineering, University of Engineering & Management, Kolkata, India
e-mail: chatterjeesankhadeep.cu@gmail.com

K. Ghosh
e-mail: kush1999.kg@gmail.com

A. Banerjee
e-mail: banerjeearghasree@gmail.com

M. Bhattacharjee
e-mail: mayukhofficial12@gmail.com

S. Banerjee and J. K. Mandal (eds.), *Advances in Smart Communication Technology and Information Processing*, Lecture Notes in Networks and Systems 165,
https://doi.org/10.1007/978-981-15-9433-5_14

has evolved into an incredible platform of research. Their works on the extraction of knowledge from text data is very neat and useful to make the computers understand the human nature. One of the most critical sectors in text mining is detecting sarcasm. Dynel [13] stated sarcasm as aggressive humor or the humor overlying a negative reality. Twitter incorporates a total count of more than 34 million Indian users and 330 million overall users in 2019 [14] which was 326 million in 2018 [15]. Twitter is the greatest source of public opinion and can be very useful to understand the pubic nature. Sarcastic tweets are very much prominent in twitter for any random topic.

India is a country with diversity with every aspect and has accomplished various milestones in the fields of science [16], technology [17], sports [18]. The mass appreciation of the country is widely available in social platforms [19] for each of its accomplishments. Among all the positive tweets about the country there exists many sarcastic statements relating to it. Our paper focusses on those sarcastic tweets which are imposed by any individual related to the country. Classifying a tweet to be sarcastic or non-sarcastic can turn into a challenging situation. Various researchers have contributed with various solutions [20–25]. A remarkable application of sarcasm detection was presented in [26], where the researchers constructed a model to identify sarcastic texts from student feedback. Joshi et al. presented another stately application of sarcasm detection in [27]. Their approach focused on classifying sarcastic dialogues from a popular TV series 'Friends' and received a highest precision score of 84.4%.

In recent years the Sarcasm detection techniques were identified to be prone to the Class-Imbalance problem [28–30]. In [31–33] the authors classified the problem to be one of the most critical issues affecting a classifier's performance by making it prone to conclude decisions in favor of the majority class. The issue of imbalanced distribution of classes was dealt by various researchers over the years [34–38] among which, the SMOTE [34] was one of the most remarkable approaches to impose synthetic data in the minority class. Motivated by this, in the current study, the class imbalance problem associated with sarcasm detection of tweets has been addressed. The imbalanced classes have been balanced using SMOTE [34] and two well-known classifiers in the domain of sentiment analysis have been used to establish the improvement in classification.

2 Proposed Method

2.1 Data Extraction

The tweets are extracted in such a way that they are mainly focused on the topic "India". Our main goal is to classify the tweets which are representing a sarcastic towards the country. Each tweet is manually classified as sarcastic as well as non-sarcastic based on some specific keywords such as, #sarcastic, #sarcasm, #lol, #proud, #success (Table 1). In order to make a concrete corpus, the tweets related to India are

Table 1 Sample sarcastic tweets in the dataset used

Tweets
As markets are up now, you will see lot of Warren Buffet, Peter Lynch, Charlie Munger, Rakesh Jhunjhunwala Am I missing someone? #Sarcasm
Reading ANARCHY! Is this a preparation to get out of the anarchy? Or is he making sure whether there is really anarchy in my country or not? 😂 #imrankhanPTI #sarcasm

extracted based on keywords specifying India or Indians. A total count of 786 tweets are extracted among which, 661 belong to the class non-sarcastic and 125 belong to the class sarcastic. The extracted tweets are refined by removing the irregular expressions and symbols such as punctuation marks and emojis. The stopwords are removed and stemming and lemmatization is performed.

2.2 Feature Extraction

For our experiment we have considered the Unigram, Bigram and Trigram features to tokenize the words. An n-gram is a contiguous sequence of n term from a given text or speech. A n-gram of size 1 is called a unigram, that of size 2 is called a bigram and of size 3 is called a trigram. In the performed experiment we have dissected our model by combining the n-gram feature. The combined features considered:

- Unigram
- Unigram+ bigram+ trigram

2.3 SMOTE

There is a difference of 536 tweets between the sarcastic and non-sarcastic tweets in our constructed dataset. Hence it is clearly evident, that there is a major imbalance between the two classes, that is, sarcastic and non-sarcastic. Due to this imbalance between classes, there is a high probability that the performance of any classifier on our dataset will be less. In order to deal with this imbalance problem, we take help of the algorithm called SMOTE [34]. Here we increase the minority class data samples by the injection of artificially created data in order to create a balance between the two classes.

2.4 Classification Algorithm

Bernoulli Naive Bayes

Bernoulli Naïve Bayes (BNB) classification model [39] is very popular for its document classification tasks. It has been widely experimented in the domain of opinion mining [40–42]. We use it also because of its binary features which can be useful in a two-class classification problem. Here the text can be either sarcastic or non-sarcastic. The likelihood of a text being in a class Ck is given by Eq. 1. In this scenario there are only two classes, i.e., C = {sarcastic, non-sarcastic}.

$$\Delta(\alpha|C_k) = \prod_{l=1}^{y} S_l{}^{(1-\alpha_l)} \tag{1}$$

$$S = \Delta_{Zl}^{\alpha_l}(1 - \Delta_{Zl}) \tag{2}$$

Δ_{Zl} is the probability of the class C_k generating the term α_l.

Logistic Regression

The Logistic Regression Classifier (LRC) has also been utilized in various domains on text mining [43–45]. It is used to model a binary dependent variable. It takes the help of the Logistic function, the Logistic function being,

$$\rho(y) = \frac{1}{1 + e^{-y}} \tag{3}$$

where the dependent variable $y = A + \sum_{j=1} B_j X_j$ such that all the X represents the independent variables. A and B represents the constant terms. The range of the function is between 0 and 1 thus detecting whether a text is sarcastic or non-sarcastic.

3 Experimental Analysis

In current study we have used SMOTE (Synthetic Minority Oversampling Technique), a technique to oversample the minority data points. In the Original Dataset the total number of Majority data points were 661 while the total number of Minority data points were 125. For this Data Imbalance we have applied SMOTE.c

Table 2 shows a tabular comparison between the Majority Data Points and Minority Data Points in case of the Original Dataset and the Training Dataset. We can clearly see that the dataset is highly imbalanced and hence we apply the aforementioned process called SMOTE to oversample our minority data.

Figure 1 represents the Majority Data Points and the gradual increase in the Minority Data Points in our training dataset after imposing the SMOTE. In this

Table 2 Count of data instances in the dataset used

Dataset	Majority data points	Minority data points	Imbalance ratio
Original dataset	661	125	5.28
Training dataset	598	109	5.48

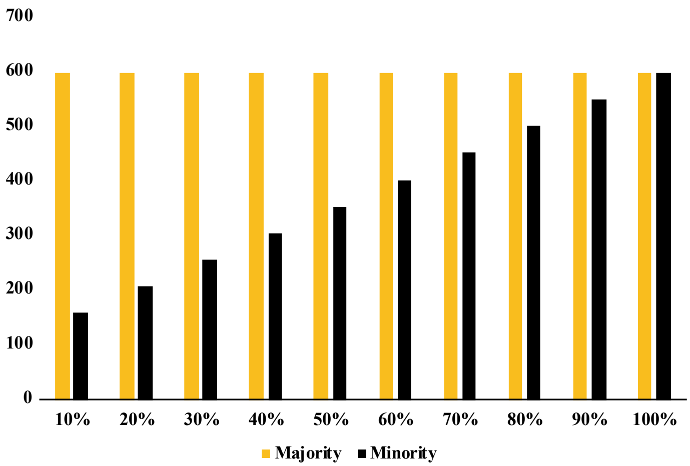

Fig. 1 Pictorial representation of over-sampling the minority classes in our training dataset

paper, we have used two features on our dataset namely Unigram and the other one is Unigram+ Bigram+ Trigram. We use two classifiers namely BNB and LRC and calculated the performance of both the classifiers. Table 3 shows that before oversampling the performance of BNB is greater than LRC with minor differences.

Tables 4 and 5 documents the change in the performance of both the classifiers with the increase of minority class samples at an interval of 20% focusing on Unigram.

Table 6 reports the performance of classifiers while using Unigram+Bigram+Trigram features before oversampling. Tables 7 and 8 shows the variation in the performance of both the classifiers with the increase of minority class samples at an interval of 20% focusing on Unigram+ Bigram+ Trigram.

In Fig. 2a we compare Accuracy between BNB and LRC, applying the feature Unigram. At 20% oversampling, BNB acquires around 0.95 accuracy count while LRC acquires 0.9 accuracy count. After 60% oversampling, BNB reaches a steady

Table 3 Performance of classifiers before oversampling for Unigram

Classifying algorithms	Acc	Pre	Rec
BNB	0.88	0.88	0.89
LRC	0.87	0.89	0.87

Table 4 Deflection in performance of BNB at different percentage of over-sampling for Unigram

Synthetic data generated (%)	Acc	Prec	Rec
20	0.95	0.95	0.95
40	0.95	0.95	0.95
60	0.92	0.92	0.92
80	0.92	0.92	0.92
100	0.92	0.92	0.92

Table 5 Deflection in performance of LRC at different percentage of over-sampling for Unigram

Synthetic data generated (%)	Acc	Prec	Rec
20	0.9	0.91	0.9
40	0.92	0.92	0.92
60	0.93	0.92	0.92
80	0.94	0.94	0.94
100	0.94	0.94	0.94

Table 6 Performance of classifiers before oversampling for Unigram+ Bigram+ Trigram

Classifying algorithms	Acc	Pre	Rec
BNB	0.87	0.87	0.87
LRC	0.86	0.86	0.86

Table 7 Deflection in performance of BNB at different percentage of over-sampling for Unigram+ Bigram+ Trigram

Synthetic data generated (%)	Acc	Pre	Rec
20	0.89	0.91	0.9
40	0.9	0.92	0.9
60	0.92	0.92	0.92
80	0.92	0.92	0.92
100	0.95	0.95	0.95

state condition (no increase or decrease) while in case of LRC there is a steep increase and then it also reaches a same condition. Hence we conclude that BNB reaches the maximum accuracy (95%) at a low oversampling rate. In Fig. 2b we compare the

Table 8 Deflection in performance of LRC at different percentage of over-sampling for Unigram+ Bigram+ Trigram

Synthetic data generated (%)	Acc	Pre	Rec
20	0.9	0.91	0.9
40	0.9	0.91	0.9
60	0.94	0.94	0.94
80	0.92	0.92	0.92
100	0.95	0.95	0.95

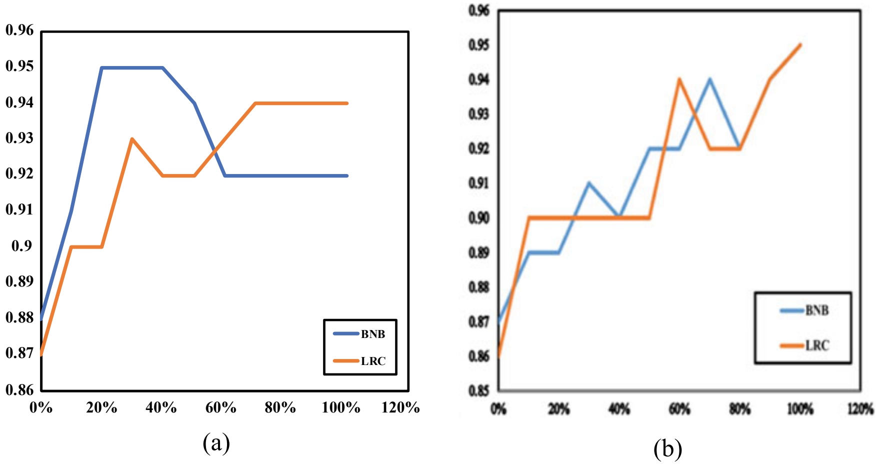

Fig. 2 Pictorial representation of accuracy development of BNB and LRC with the increase in minority samples for Unigram and Unigram+ Bigram+ Trigram feature

Accuracy between BNB and LRC, applying the feature Unigram+ Bigram+ Trigram. At 20% oversampling, BNB acquires around 0.89 Accuracy count. LRC acquires 0.90 Precision count at 10% and it continues at the same count upto 50% oversampling. At 80% oversampling, the Accuracy count of BNB decreases to 0.92 and then increase to 0.94 at 90% oversampling and 0.95 at 100% oversampling. In case of LRC too, the same thing is seen as that in BNB.

In Fig. 3a we compare Recall between BNB and LRC, applying the feature Unigram. At 20% oversampling, BNB acquires around 0.95 Recall count while LRC

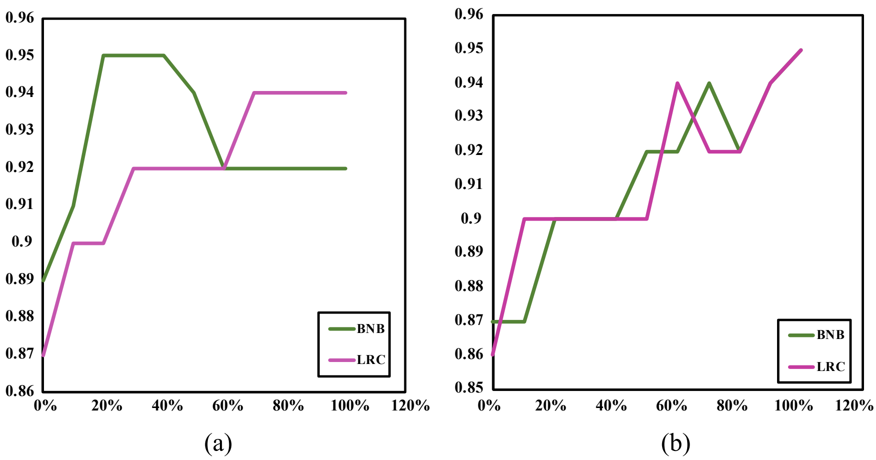

Fig. 3 Pictorial representation of Recall development of BNB and LRC with the increase in minority samples for Unigram and Unigram+ Bigram+ Trigram feature

acquires 0.90 accuracy count. After 60% oversampling, BNB acquires a Recall count of 0.92 and reaches a steady state condition while in case of LRC there is a steep increase till 80% and then it also reaches a same condition. Hence we conclude that BNB reaches the maximum Recall (95%) at a low oversampling rate. In Fig. 3b we compare the Recall count between BNB and LRC, applying the feature Unigram+ Bigram+ Trigram. At 20% oversampling, BNB acquires around 0.90 Recall count. LRC acquires 0.90 Recall count at 10% and it continues at the same count upto 50% oversampling. At 80% oversampling, the Recall count of BNB decreases to 0.92 and then increase to 0.94 at 90% oversampling and 0.95 at 100% oversampling. In case of LRC the same thing is seen as that in BNB.

In Fig. 4a we compare the Precision between BNB and LRC, applying the feature Unigram. At 20% oversampling, BNB acquires around 0.95 Precision count while LRC acquires 0.91 Precision count. After 60% oversampling, the Precision count of BNB decreases to 0.92 and reaches a steady state condition while in case of LRC there is a steep increase of Precision count to 0.94 till 70% and then it also reaches a same steady state condition. Hence we conclude that BNB reaches the maximum Precision (95%) at a low oversampling rate. In Fig. 4b we compare the Precision between BNB and LRC, applying the feature Unigram+ Bigram+ Trigram. At 20% oversampling, BNB acquires around 0.91 Precision count. LRC acquires 0.91 Precision count at 10% and it continues at the same count upto 50% oversampling. At 80% oversampling, the Precision count of BNB decreases to 0.92 and then increase to 0.94 at 90% oversampling and 0.95 at 100% oversampling. In case of LRC the same thing is seen as that in BNB.

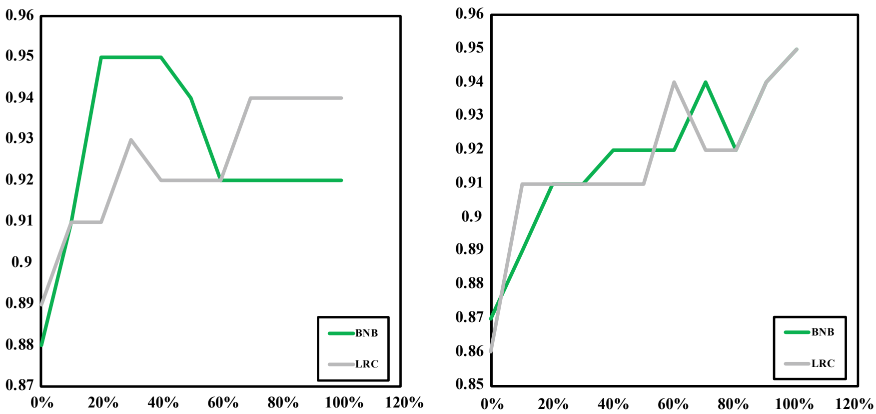

(a) (b)

Fig. 4 Pictorial representation of Precision development of BNB and LRC with the increase in minority samples for Unigram feature

4 Conclusion

The current study proposed a synthetic minority oversampling technique method to address the issue of imbalanced class problem observed in sarcasm detection. Unigram, Bigram and Trigram features were extracted from Tweets collected on different topics after manually classifying them into sarcastic and non-sarcastic. Results revealed that after applying SMOTE the performance of both classifiers used in the current study have improved. Performance of the classifiers for varying degrees of oversampling was reported. Both Unigram and combination of unigram, bigram and trigram features have shown significant improvement. Combination of all three features, when oversampled 100%, achieved best performance for both classifiers. Future studies can be conducted to analyze the effects of other variations of synthetic oversampling techniques in detecting satirical tweets.

References

1. Eidelberg, A., Jacob, C., Denzinger, J.: Using active probing by a game management AI to faster classify players. In: 2019 IEEE Conference on Games (CoG), pp. 1–8. IEEE (2019)
2. Sailunaz, K., Alhajj, R.: Emotion and sentiment analysis from twitter text. J. Computat. Sci. **36**, 101003 (2019)
3. Bari, A.S.M.H., Gavrilova, M.L.: Artificial neural network based gait recognition using kinect sensor. IEEE Access **7**, 162708–162722 (2019)
4. Yi, X., Eramian, M., Wang, R., Neufeld, E.: Identification of morphologically similar seeds using multi-kernel learning. In: 2014 Canadian Conference on Computer and Robot Vision, pp. 143–150. IEEE (2014)
5. Oyibo, K., Adaji, I., Vassileva, J.: Social cognitive determinants of exercise behavior in the context of behavior modeling: a mixed method approach. Digital Health **4**, 2055207618811555 (2018)
6. Teyhouee, A., Osgood, N.D.: Cough detection using hidden markov models. In: International Conference on Social Computing, Behavioral-Cultural Modeling and Prediction and Behavior Representation in Modeling and Simulation, pp. 266–276. Springer, Cham (2019)
7. Dey, S., Singh, A.K., Prasad, D.K., Mcdonald-Maier, K.D.: SoCodeCNN: program source code for visual CNN classification using computer vision methodology. IEEE Access **7**, 157158–157172
8. Nasoz, F., Lisetti, C.L., Vasilakos, T.: Affectively intelligent and adaptive car interfaces. J. Inf. Sci. Intell. Syst. Appl. Int. J. **180**(20), 3817–3836 (2010)
9. Kim, D.Y., Li, X., Wang, S., Zhuo, Y., Lee, R.K.-W.: Topic enhanced word embedding for toxic content detection in Q&A sites. In: Proceedings of the 2019 IEEE/ACM International Conference on Advances in Social Networks Analysis and Mining, pp. 1064–1071 (2019)
10. Ghosh, K., Banerjee, A., Chatterjee, S., Sen, S.: Imbalanced twitter sentiment analysis using minority oversampling. In: 2019 IEEE 10th International Conference on Awareness Science and Technology (iCAST), pp. 1–5. IEEE (2019)
11. Jin, W., Wu, X.: HCAMiner: mining concept associations for knowledge discovery through concept chain queries. In: Proceedings of the 23rd International Conference on Computational Linguistics (COLING 2010), Beijing, China, August 23–27th, 2010, pp. 29–32
12. Narouei, M., Takabi, H., Nielsen, R.: Automatic extraction of access control policies from natural language documents. In: IEEE Trans. Depend. Secure Comput. https://doi.org/10.1109/TDSC.2018.2818708

13. Dynel, M.: Beyond a joke: types of conversational humour. Lang. Ling. Compass **3**(5), 1284–1299 (2009)
14. https://www.statista.com/statistics/282087/number-of-monthly-active-twitter-users/
15. Singh, A., Blanco, E., Jin, W.: Incorporating emoji descriptions improves tweet classification. In: Proceedings of the 2019 Conference of the North American Chapter of the Association for Computational Linguistics: Human Language Technologies, vol. 1 (Long and Short Papers), pp. 2096–2101 (2019)
16. Prakash, G.: Another reason: science and the imagination of modern India. Princeton University Press (1999)
17. Shastry, G.K.: Human capital response to globalization education and information technology in India. J. Human Res. **47**(2), 287–330 (2012)
18. Ghosh, A.K., Ahuja, A., Khanna, G.L.: Pulmonary capacities of different groups of sportsmen in India. Br. J. Sports Med. **19**(4), 232–234 (1985)
19. Arun, K., Srinagesh, A., Ramesh, M.: Twitter sentiment analysis on demonetization tweets in India using R language. Int. J. Comput. Eng. Inf. Technol. **9**(6), 119 (2017)
20. Filatova, E.: Sarcasm detection using sentiment flow shifts. In: Proceedings of the Thirtieth International Florida Artificial Intelligence Research Society Conference, pp. 264–269 (2017)
21. Rajadesingan, A., Zafarani, R., Liu, H.: Sarcasm detection on twitter: a behavioral modeling approach. In: WSDM '15 Proceedings of the Eighth ACM International Conference on Web Search and Data Mining, ACM, pp. 97–106. China (2015)
22. Khattri, A., Joshi, A., Bhattacharyya, P., Carman, M.J.: Your sentiment precedes you: using an author's historical tweets to predict sarcasm. In: Proceedings of the 6th Workshop on Computational Approaches to Subjectivity, Sentiment and Social Media Analysis, pp. 25–30. Portugal (2015)
23. Bouazizi, M., Ohtsuki, T.O.: A pattern-based approach for sarcasm detection on twitter. IEEE Access **4**, 5477–5488 (2016)
24. del Pilar Salas-Zárate, M., Paredes-Valverde, M.A., Rodriguez-García, M.Á., Valencia-García, R., Alor-Hernández, G.: Automatic detection of satire in twitter: a psycholinguistic-based approach. Know.-Based Syst. **128**, 20–33, Elsevier (2017)
25. Parde, N., Nielsen, R.: Detecting sarcasm is extremely easy ;-). In: Proceedings of the Workshop on Computational Semantics beyond Events and Roles, pp. 21–26. Louisiana (2018)
26. Altrabsheh, N., Cocea, M., Fallahkhair, S. Detecting sarcasm from students' feedback in twitter. In: Conole, G., Klobučar, T., Rensing, C., Konert, J., Lavoué, E. (eds.) Design for Teaching and Learning in a Networked World. Lecture Notes in Computer Science, vol. 9307. Springer, Cham (2015)
27. Joshi, A., Tripathi, V., Bhattacharyya, P., Carman, M.J.: Harnessing sequence labeling for sarcasm detection in dialogue from TV series 'friends'. In: Proceedings of The 20th SIGNLL Conference on Computational Natural Language Learning, pp. 146–155. Germany (2016)
28. Liu, P., Chen, W., Ou, G., Wang, T., Yang, D., Lei, K.: Sarcasm detection in social media based on imbalanced classification. In: International Conference on Web-Age Information Management, pp. 459–471. Springer, Cham (2014)
29. Abercrombie, G., Hovy, D.: Putting sarcasm detection into context: the effects of class imbalance and manual labelling on supervised machine classification of twitter conversations. In: Proceedings of the ACL 2016 student research workshop, pp. 107–113 (2016)
30. Hazarika, D., Poria, S., Gorantla, S., Cambria, E., Zimmermann, R., Mihalcea, R.: CASCADE: Contextual sarcasm detection in online discussion forums. arXiv:1805.06413 (2018)
31. Japkowicz, N., Stephen, S.: The class imbalance problem: a systematic study. Intell. Data Anal. **6**(5), 429–449 (2002)
32. Galar, M., Fernandez, A., Barrenechea, E., Bustince, H., Herrera, F.: A review on ensembles for the class imbalance problem: bagging-, boosting-, and hybrid-based approaches. IEEE Trans. Syst. Man Cyber. Part C (Appl. Rev.) **42**(4), 463–484 (2012)
33. García, V., Sánchez, J.S., Mollineda, R.A.: On the effectiveness of preprocessing methods when dealing with different levels of class imbalance. Know.-Based Syst. **25**(1), 13–21 (2012)

34. Chawla, N.V., Bowyer, K.W., Hall, L.O., Kegelmeyer, W.P.: SMOTE: synthetic minority over-sampling technique. J. Arti. Intell. Res. **16**, 321–357. AI Access Foundation and Morgan Kaufmann Publishers (2002)
35. Han, H., Wang, W.-Y., Mao, B.-H.: Borderline-SMOTE: a new over-sampling method in imbalanced data sets learning. In: International Conference on Intelligent Computing, pp. 878–887. Springer (2005)
36. Bunkhumpornpat, C., Sinapiromsaran, K., Lursinsap, C.: Safe-level-SMOTE: safe-level-synthetic minority over-sampling technique for handling the class imbalanced problem. In: Pacific-Asia Conference on Knowledge Discovery and Data Mining, pp. 475–482. Springer (2009)
37. Maciejewski, T., Stefanowski, J.: Local neighbourhood extension of SMOTE for mining imbalanced data. In: 2011 IEEE Symposium on Computational Intelligence and Data Mining (CIDM), pp. 104–111. IEEE (2011)
38. Ramentol, E., Caballero, Y., Bello, R., Herrera, F.: SMOTE-RSB*: a hybrid preprocessing approach based on oversampling and under sampling for high imbalanced data-sets using SMOTE and rough sets theory. Know. Inf. Syst. **33**(2), 245–265, Springer (2011)
39. Sayfullina, L., Eirola, E., Komashinsky, D., Palumbo, P., Miche, Y., Lendasse, A., Karhunen, J.: Efficient detection of zero-day android malware using normalized bernoulli naive bayes. In: 2015 IEEE Trustcom/BigDataSE/ISPA, vol. 1, pp. 198–205. IEEE (2015)
40. Aggarwal, C.C., Zhai, C.X. (eds.): Mining text data. Springer Science & Business Media (2012)
41. Wang, S., Jiang, L., Li, C.: Adapting naive Bayes tree for text classification. Knowl. Inf. Syst. **44**(1), 77–89 (2015)
42. Pronoza, E., Yagunova, E., Volskaya, S.: Corpus-based information extraction and opinion mining for the restaurant recommendation system. In: International Conference on Statistical Language and Speech Processing, pp. 272–284. Springer, Cham (2014)
43. Barnaghi, P., Ghaffari, P., Breslin, J.G.: Opinion mining and sentiment polarity on twitter and correlation between events and sentiment. In: 2016 IEEE Second International Conference on Big Data Computing Service and Applications (BigDataService), pp. 52–57. IEEE (2016)
44. Ramadhan, W.P., Novianty, A., Setianingsih, C.: Sentiment analysis using multinomial logistic regression. In: 2017 International Conference on Control, Electronics, Renewable Energy and Communications (ICCREC), pp. 46–49. IEEE (2017)
45. Kalaivani, P., Shunmuganathan, K.L.: Feature reduction based on genetic algorithm and hybrid model for opinion mining. Scientific Programming 2015 (2015)

Classification of Citrus Fruits and Prediction of Their Largest Producer Based on Deep Learning Architectures

Kyamelia Roy, Sheli Sinha Chaudhuri, Soumi Bhattacharjee, and Srijita Manna

Abstract Classification of the various kinds of citrus fruits based on their skin colour is a laborious task and consumes a lot of time. A robotic system if trained to classify citrus fruits based on their outer skin colour, it would be of great help for the industries that perform sorting and grading of the agricultural products. This research paper aims at providing a perspective for the categorization of six different kinds of citrus fruits by a trained automated system. The system is so trained that it would predict the largest producer of the concerned citrus fruit in the world and will also convey a message comprising of the nutrient value or health benefits of the specific citrus fruit. The pretrained convolution neural network models such as AlexNet, GoogleNet and Resnet50 when retrained with a dataset of 626 images gave us feasible results with an accuracy of 98.50%, 92.50% and 97.50% respectively. The experimental results in the form of accuracy and loss percentage shown in the graphs validates the effectiveness of the suggested techniques.

Keywords AlexNet · GoogleNet · ResNet-50 · Classification

K. Roy (✉) · S. S. Chaudhuri
Jadavpur University, Kolkata 700032, India
e-mail: kyamelia2015@gmail.com

S. S. Chaudhuri
e-mail: shelisinhachaudhuri@gmail.com

S. Bhattacharjee · S. Manna
University of Engineering and Management, Kolkata 700160, India
e-mail: sbhattacharjee2020@gmail.com

S. Manna
e-mail: sm311256@gmail.com

S. Banerjee and J. K. Mandal (eds.), *Advances in Smart Communication Technology and Information Processing*, Lecture Notes in Networks and Systems 165,
https://doi.org/10.1007/978-981-15-9433-5_15

1 Introduction

Citrus fruits cannot be stored for a longer period of time. They perish in quality as well as quantity if there is a long time difference between harvesting and consumption. Besides being used in juice production, citrus fruits have also found its involvement in the development of hard liquor by fermentation. Many investigations have been undertaken to explore the potentials of citrus fruits for the production of wine Wines from various citrus fruits were compared for their different physicochemical properties. Citrus fruits are the main source of peel oil, citric acid and cosmetics which have international market value. After mango and banana, citrus fruit industry is the third largest fruit industry in India. In this research paper [1] the authors have utilised the neural network models such as LeNet and Network in Network (NiN) to detect and classify burn wounds in pediatric cases and facial databases were also used for facial keypoints detection. The performance and computational efficiency of both methods has been compared. They have got a highest performance accuracy of 75.9% in the burn database, a highest accuracy of 26.5% in the painting database and a highest accuracy of 100% in the facial database. So, the architectures such as LeNet and NiN gave promising results for low complexity classification but they are not sufficient for problems of higher complexity.

The authors [2] proposed spatially-adaptive normalization, a simple but effective layer for synthesizing photorealistic images given an input semantic layout. In the previous methods, the semantic layout has been fed directly as input to the deep learning network, which then undergoes a sequence of convolution, normalization and non-linearity layer. This is insignificant as the normalization layers filter out the semantic information. To overcome this the authors have proposed a method of using the input layer t modulate the activations in normalization layers via a spatially-adaptive, learnt transformation. This approach is advantageous over existing methods in case of visual fidelity and alignment with input layouts.In this prospectus [3], the authors have considered a standard dataset of flowers for the experiment. The input images undergoes preprocessing such as noise removal and segmentation using threshold for the elimination of background details. The segmented images have been used for the extraction of texture feature using GLCM (Gray Level Co-occurrence Matrix) method and for the extraction of the colour feature using Color Moment. Neural Network Classifier has been used for the classification and the gross accuracy of the system is 95.0%. The accuracy of the system can be further improved by considering other features such as edge and shape.

There are varieties of plant species all over the world and humans lack the ability to classify them, specially the visually small classes. So, Rzanny et al. [4] made an attempt for plant species classification using three different datasets consisting of the Oxford Flower 17, the Oxford Flower 102 and Jena Flower 30. They made a comparative study of local feature representations. The entire process includes resizing, colour space conversion, detection of positions of local features as computed by mathematical definitions, extraction or quantification of the local features using an extractor. Then the local descriptors are aggregated into a global image representation in the encoding step for training and testing the classifier with the corresponding image class level. The local features of the flower has been used for higher classification accuracies as compared to analyzing the entire flower image equally. The Jena Flower 30 dataset had the higher amount of classes and gave classification accuracy of 94% with a well designed classification pipeline based on local features. In this paper [5], the authors have employed Probabilistic Neural Network (PNN) with image processing as well as data processing techniques to implement an automated leaf recognition algorithm for plant classification. They have extracted 12 leaf features and orthogonalized those features into 5 principal parameters consisting of the input vector of the PNN. A dataset of 1800 leaves has been used to train the network for the classification of 32 kinds of plants that results in an accuracy of more than 90% This approach is fast in execution and easy in implementation as compared to all algorithms. In [6], the authors have used three different datasets namely Oxford 102, Oxford 17 and Zou-Nagy for their two step flower classification problem using Deep Convolutional Neural Networks. At first, segmentation is utilised for localisation of the concerned flower region. This flower segmentation technique is modelled as a binary classifier in a fully convolutional neural network. Secondly, they built a convolutional neural network based classifier to distinguish between different flower types. There classification results exceeded 97% on all the three datasets. Ayesha Gurnani and Viraj Mavani [7] have used the Visual Geometry Group's 102 category flower dataset having 8189 images of 102 categories of flowers for the categorization of flowers using Deep Convolutional Neural Networks. They have used two different CNN architectures GoogleNet and AlexNet for classification and compared the corresponding results. By keeping the same hyper parameters for both the architectures, they found that the Top 1 and Top 5 accuracies of GoogleNet are 47.15% and 69.17% respectively, whereas 43.39 and 68.68% are the Top 1 and Top 5 accuracies of AlexNetarchitecture respectively. In Flower Species Recognition System using CNN and Transfer Learning [8], a Deep Learning approach using CNN has been used to identify flower species with higher accuracy. Images of plant species are captured using the built in camera module of a mobile phone. Transfer Learning has been used for the feature extraction purpose. On top of it, Logistic Regression or Random Forest Classifier is used to obtain a higher rate of accuracy. The hardware requirement to train a CNN intensively is minimized by this technique. Transfer Learning approach when combined with CNN produces noble Rank-1 accuracies of 73.05, 93.41 and 90.60% using OverFeat, Inception-v3 and Xception architectures, respectively as Feature Extractors.

This research paper [9] aims at introducing a new technique for classifying fruits based on quality applicable to small scale farmers using Deep Learning. Authors have used Google's open source library interface "Tesorflow" to classify a single fruit grade, and the accuracy of the constructed model was 0.73%. The authors have stated that, though the percentage of accuracy of the proposed work is less but in future, producers will be able to create higher accuracy value and the model will be more reliable compared to imported classification products, and the consumers will be able to choose quality fruits at appropriate price. Identification of various kinds of fruits is one of the most difficult task in fruit shops and supermarkets. So, in automatic fruit recognition based on DCNN for Commercial Source Trace

System [10], the authors have portrayed an automated fruit recognition system. Due to the examinations and evaluations under limited dataset the previous approaches had some limitations, more over the external environmental changes were not taken into considerations. They have entrenched a fruit image dataset having 15 different categories consisting of 44406 images which were gathered within a period of six months keeping in mind the limitations of training and identification without feature extraction. DCNN has a unique feature of learning the optimal features from images through adaptation process. The experimental results display that the proposed work is efficient and has an accuracy of 99%.

2 Method Overview

Here in the proposed method we have made a training dataset of 626 images of citrus fruits comprising of six different kinds of citrus fruits namely sweet lemon, oranges, grapefruit, tangerine, lime and lemon. The training dataset helps us to train the model and make the model learn to give the desired output according to the user problem. A test dataset is made for testing the efficiency of the machine in classifying by randomly selecting few images from each type of fruit. We have tried to display the largest producer of each type of citrus fruit and the nutrients contained in them. The classification has been done based on skin colour of the citrus fruit.

The different Architectures used in the present work are described as under-

- **AlexNet Architecture**: AlexNet is an incredibly powerful convolutional neural network model capable of achieving high accuracies on very challenging datasets. The network is 8 layers deep and has an image input size of 227-by-227. In our work we have used 25 layers deep AlexNet Architecture
- **GoogleNet**: GoogleNet is a pretrained convolutional neural network that is 22 layers deep. In our proposed work we have used 144 layers deep GoogleNet Architechture. It takes input in the form of images of size 224-by-224 and classifies them into their respective classes. GoogleNet trains faster than VGG.
- **ResNet-50**: ResNet is a powerful backbone model that is used very frequently in many computer vision tasks. This helps it mitigate the vanishing gradient problem. The network is 53 layers deep and can classify images into 1000 object categories. In our proposed work we have used 177 layers deep ResNet-50 Architechture.224-by-224 is the image input layer.

DATASET: Our training dataset comprises of 626 images of 6 different types citrus fruits namely Lemon, Sweet Lemon, Lime, Orange, Grapefruit, Tangerine.

We have tested our machine with the testing dataset comprising of 100 images which constituting 16% of our training dataset for each class of citrus fruit. Our validation dataset includes 18 images, 2 from each class constituting 2% of the training dataset (Fig. 1 and Tables 1 and 2).

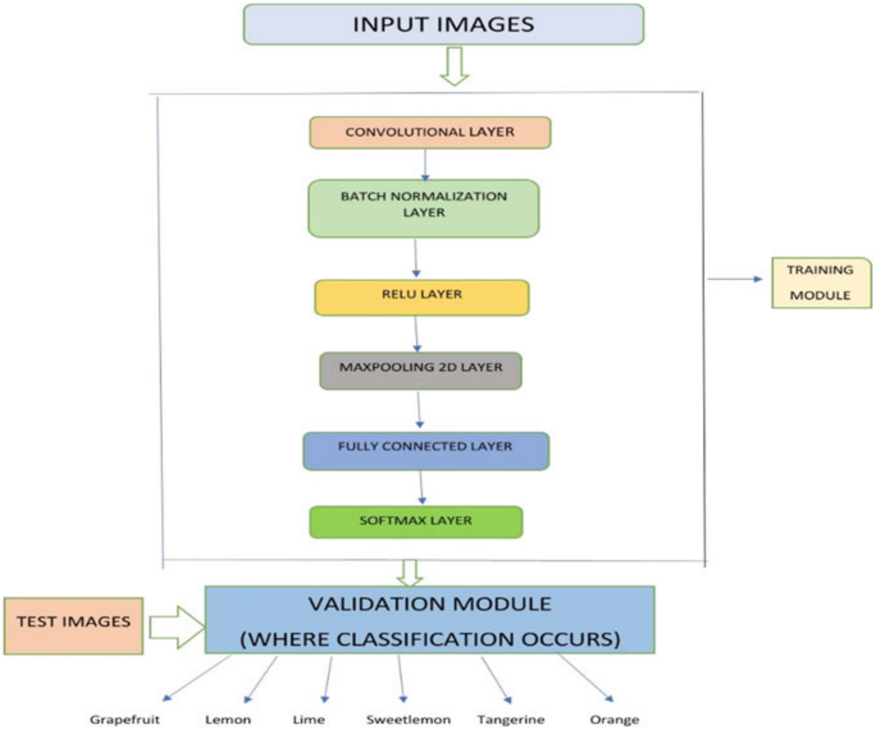

Fig. 1 Generalised Flow Diagram of the proposed work

Table 1 Accuracy of 3 different architectures used

Name of the architecture	Accuracy (%)	Preceision	F-measure	Recall
AlexNet architecture	98.50	0.34	0.33	0.38
GoogleNet architecture	92.50	0.62	0.65	0.67
ResNet-50 architecture	97.50	0.54	0.56	0.59

Table 2 Comparison table

Architecture	Salient feature	Accuracy (%)	Total parametres	Floating point operations
AlexNet	Deeper network	98.50	62 million	1.5B
GoogleNet	Wider parallel kernel	92.50	6.4 million	2B
ResNet-50	Shortcut connections	97.50	60.3 million	11B

Architectures Description:

The architectures that has been used possess different layers consisting as under-

Name of the architecture	Layers
AlexNet architecture	Total number of layers = 25 Image Input layer = 1 Convolution layers = 5 ReLU layers = 7 Cross normalization layers = 2 Maxpool layers = 3 Dropout layers = 2 Softmax layer = 1 Fully connected layers = 3 Classification output layer = 1
GoogleNet architecture	Total number of layers = 144 Image input layer = 1 Convolution layers = 57 ReLU layers = 59 Cross normalization layers = 2 Maxpool layers = 13 Average pooling layer = 1 Dropout layer = 1 Softmax layer = 1 Fully connected layer = 1 Classification output layer = 1
ResNet-50 architecture	Total Number of Layers = 177 Image Input Layer = 1 Convolution layers = 53 ReLU layers = 48 Batch normalization layers = 53 Maxpool Layer = 1 Average pooling layer = 1 Addition layers = 14 Softmax layer = 1 Fully connected layer = 1 Classification output layer = 1

2.1 A. Methodology

See Fig. 1

3 Experimental Results

The following Output Images are the resultant images of the 3 Architectures used. The output images are obtained in the command window of MATLAB2019b. The classified citrus fruit according to each class is shown in part (a) and part (b) shows the predicted largest producer of the citrus fruit and the nutrient content. The accuracy and loss graphs are shown in part (c) and (d) respectively (Fig. 2).

4 Conclusion

Image classification helps us to categorize images into their respective classes logically. Using the AlexNet Architecture we have successfully classified the six classes of citrus fruits with the highest accuracy of 98.50% followed by ResNet-50 Architecture having an accuracy of 97.50% and the least accuracy of 92.50% is given by the GoogleNet Architecture. The various methods used in the classification of citrus fruits have given us promising results.

This classification of citrus fruits and prediction of their largest producer in the globe and their nutrient contents has a greater future scope in countries like India where the classification promises us to give a clean cut differentiation among fruits thereby helping the future food technology to provide unbiased products and easy importation of fruits from the places they are abundantly produced in. The instant display of the nutrients contained in the concerned fruit will help the printing and packaging unit and ultimately will help attract more customers.

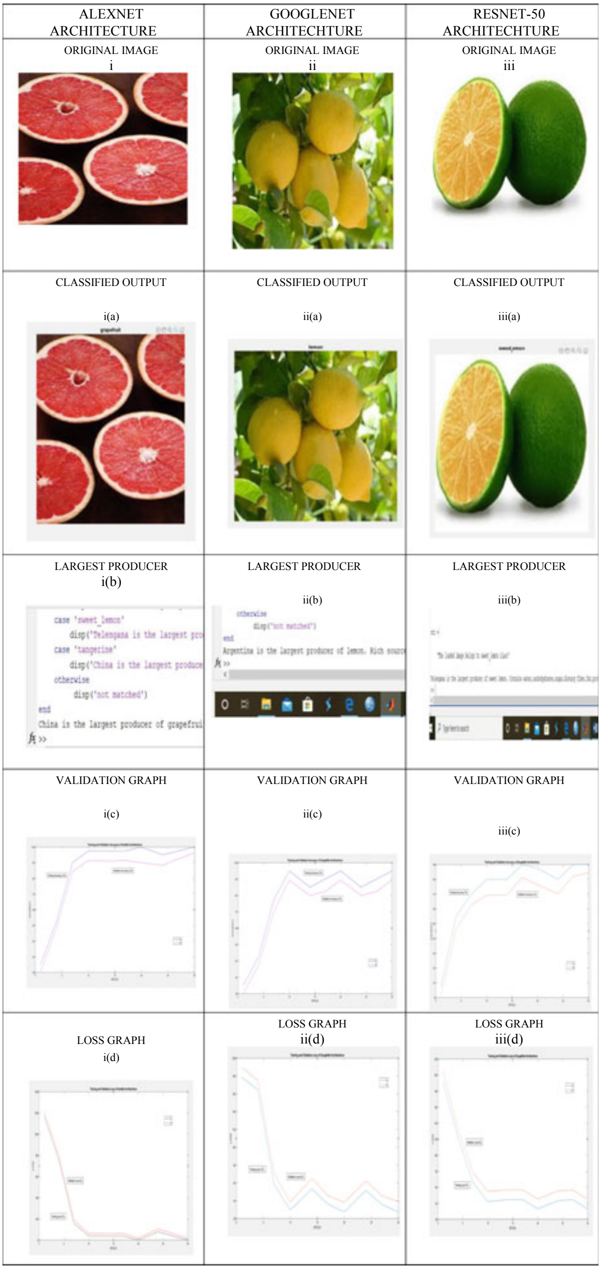

(a)-Classified Output Image

(b)-Predicted Largest Producing country Global

Fig. 2 i, ii, iii-Original image **a** classified output image **b** predicted largest producing country global **c** training and validation accuracy graph **d** training and validation loss graph

References

1. Badea, M.S., Felea, I.I., Florea, L.M., Vertan, C.: The use of deep learning in image segmentation, classification and detection. arXiv preprint (2016). arXiv:1605.09612
2. Park, T., Liu, M. Y., Wang, T. C., Zhu, J.Y.: Semantic image synthesis with spatially-adaptive normalization. In: Proceedings of the IEEE Conference on Computer Vision and Pattern Recognition, pp. 2337–2346 (2019)
3. Shaparia, R., Patel, N., Shah, Z.: Flower classification using texture and color features. Kalpa Publications Comput. **2**, 113–118 (2017)
4. Seeland, M., Rzanny, M., Alaqraa, N., Wäldchen, J., Mäder, P.: Plant species classification using flower images—a comparative study of local feature representations. PloS one **12**(2) (2017)
5. Wu, S.G., Bao, F.S., Xu, E.Y., Wang, Y.X., Chang, Y.F., Xiang, Q.L.: A leaf recognition algorithm for plant classification using probabilistic neural network. In: 2007 IEEE International Symposium On Signal Processing And Information Technology, pp. 11–16 (2007). IEEE
6. Specht, D.F.: A general regression neural network. IEEE Trans. Neural Netw. **2**(6), 568–576 (1991)
7. Hiary, H., Saadeh, H., Saadeh, M., Yaqub, M.: Flower classification using deep convolutional neural networks. IET Comput. Vis. **12**(6), 855–862 (2018)
8. Gurnani, A., Mavani, V., Gajjar, V., Khandhediya, Y.: Flower categorization using deep convolutional neural networks. arXiv preprint (2017). arXiv:1708.03763
9. Gogul, I., Kumar, V.S.: Flower species recognition system using convolution neural networks and transfer learning. In: 2017 Fourth International Conference on Signal Processing, Communication and Networking (ICSCN), pp. 1–6 (2017). IEEE
10. Jeong, S., Yoe, H: Design of deep learning based fruit classification system platform. In: Proceedings of the International Conference on Wireless Networks (ICWN), pp. 64–67 (2018), The Steering Committee of The World Congress in Computer Science, Computer Engineering

Unsupervised Machine Learning Algorithm Based Rotten Fruit Segmentation

Kyamelia Roy, Sayan Pramanik, and Sheli Sinha Chaudhuri

Abstract The process of segmentation is very effective in digital images for different types of machine learning application. Segmentation of the rotten part in fruit is such an application. This paper deals with different types of segmentation techniques to detect a rotten fruit. Fruits get rotten due to unsuitable temperature and weather and also due to lack of right preservation techniques. Segmentation or rotten area identification comes very useful in solution to those problems. This paper represents some approach to segment the rotten areas of fruits like apple and banana. In this paper segmentation using image processing algorithms like random walker algorithm-based segmentation, entropy-based segmentation, Histogram based segmentation and unsupervised machine learning algorithm like Gaussian mixture model-based segmentation are used among these algorithms Gaussian mixer model or GMM has shown the best and promising results.

Keywords Segmentation · Histogram · Gaussian mixture model · Gradient · Unsupervised · Machine-learning

1 Introduction

Global fruit production report in 2018 portrays around 800 million metric tons of fruit is produced every year. Fruit processing sectors uses 60–65% of this amount of produced fruit. The entire process from fruit production to transportation is a time-consuming phenomenon and is one of the main reasons for fruits get rotten. In fruit processing industry to maintain the quality of production, sorting of fruit correctly is very much necessary. Proper segmentation is very much needed to sort them correctly.

K. Roy · S. S. Chaudhuri
Jadavpur University, Kolkata 700032, West Bengal, India
e-mail: kyamelia2015@gmail.com

S. Pramanik (✉)
University of Engineering & Management, Kolkata 700156, West Bengal, India
e-mail: sayan.pramanik8175@gmail.com

S. Banerjee and J. K. Mandal (eds.), *Advances in Smart Communication Technology and Information Processing*, Lecture Notes in Networks and Systems 165,
https://doi.org/10.1007/978-981-15-9433-5_16

Color, gradient, texture, are the most important identifier for segmentation. In this paper, a segmentation-based approach has been adopted to sort out the fruits as rotten and healthy. The idea is to build an intelligent system capable of distinguishing between the fresh and rotten fruit, thereby improving the quality of the products manufactured in the industries. This type of systems can help and assist the sorting process with less time and less workforce. As there is not much pre-labeled dataset on fruit segmentation is available, so supervised machine learning algorithm cannot be used. Therefore, unsupervised machine learning algorithm and image processing algorithms are most efficient for the task. An exhaustive study has been done on the fruit segmentation techniques and quality gradation and accordingly the work has seen framed out. Authors [1] used k-means clustering for defect segmentation in fruit disease based on some parameters like textural cue and color spaces, color coherence vector and global color histogram. Authors [2] used some machine learning algorithms like local binary pattern, support vector machine and feature extraction like global color histogram (GCH), Completed local binary pattern to locate and thereby identify the rotten area in the fruit's image. Roy et al. in [3] discussed about different segmentation technique viz. marker-based segmentation, color based and filtering-thresholding technique for rotten part identification. This paper also focuses some of the image segmentation using some image processing techniques which also generalizes some parameter like histogram, color, gray level intensity. In Random-Walker [4] Image Segmentation when CLHE (Contrast Limited Adapted Histogram Equalization) is applied over images, then the differences or the contrast in the gray level intensity of local pixels is enhanced. Low level gray levels of histogram are equalized and relatively high intensity pixels are equalized. Then various different areas of different intensity levels are marked. Another segmentation technique based on gradient detection over image pixel which is mostly identifies the change in the pixels while transiting one pixel to another side pixel, based on where high difference is detected. Those areas are highlighted and marked, in this way border areas of rotten part are identified. In [5, 6] author proposed some automatic classification based on segmentation like histogram features, gray level, co-occurrence matrix which determines the distinct pixel of varying gray level in many iterations and it also highlights on the use of CNN (Convolutional Neural Network) and use of HOG (Histogram of Oriented Gradient) & BOF (bag of features). In [7] Agarwal et al. discussed about apple's disease detection and classification based on some supervised machine learning algorithm and Otsu segmentation techniques, K-means clustering for area of disease identification and SVM (Support Vector Machine) to classify the diseases. As mentioned earlier lack of labeled dataset for segmentation is a big obstacle for supervised learning. So unsupervised algorithm like Gaussian Mixture models [9, 10] is very much useful. The paper is organized as following Sect. 2, represents the methodology, Sect. 3 highlights the experimental results and discussion. Section 4 states the conclusions and 5 shows the references.

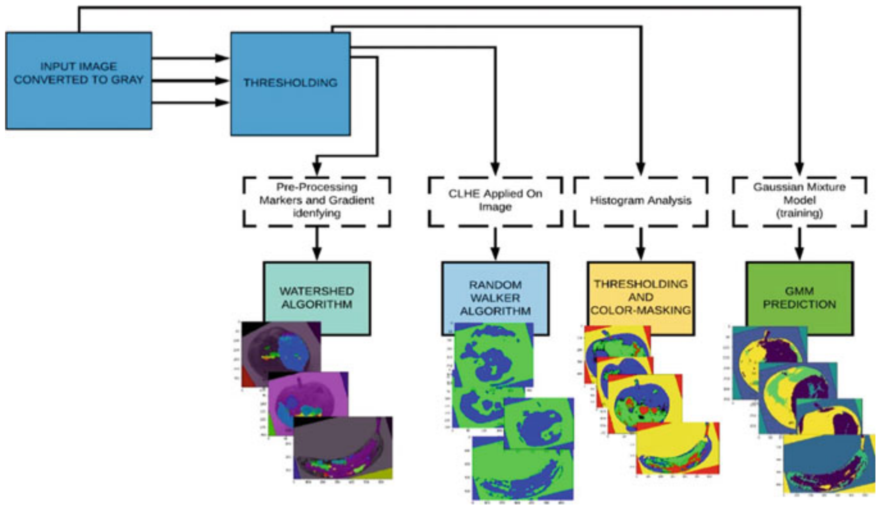

Fig. 1 Workflow diagram of the proposed methodology

2 Methodology

In the proposed method for identification and segmentation of rotten areas of a fruit, all images have been pre-processed through some basic image processing steps before they are undergone through segmentation task. Using the 'OPEN-CV' image processing library the 3-layer (RGB) images are converted to one layer black & white gray images. Most of the algorithms presented in this paper uses some kind of probability distribution function to identify the rotten areas and fresh areas, then those identified areas are masked and segmented in the image. But for the gradient-based watershed algorithm, identification of gradient using binary-inversion and identifying the high occurrence pixels in the image. Next steps are different for different segmentation algorithm they are discussed below in details. II. (a), II (b), II (c), II (d) describes Random walker segmentation, Histogram based segmentation, Gradient-based watershed segmentation, Gaussian mixer model segmentation respectively (Fig. 1).

2.1 Random-Walker Image Segmentation

The random walker segmentation [4] algorithm is a specific type of algorithm which segments an image based on markers labelled in more than 2 iterations. Random walker works by solving anisotropic diffusion equation. The diffusivity co-efficient goes higher when neighboring pixels have nearly same value. In this diffusion process each unknown or unlabeled pixel gets the label of the marker which have the highest

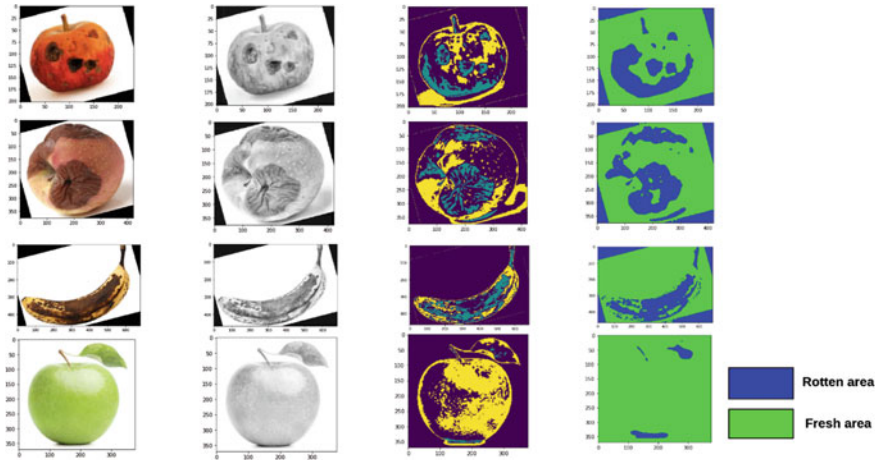

(a) (b) (c) (d)

Fig. 2 Results obtained using random walker based segmentation. **a** shows original fruit images **b** shows CLHE applied gray images **c** shows images labeled by random walker d Segmented images

probability. First the input image (Fig. 2a) is converted to gray label images. Next, the images data is normalized. Then CLHE (Contrast Limited Adapted Histogram Equalization) is applied on the image data. It is an algorithm which enhance the local contrast based on histogram of the images computed over different tile of image (Fig. 2b). CLHE works on very tiny regions of images known as tiles, instead of entire image it first measures the contrast for each image tiles. After that it transform the contrast of those tiles to make an artificial border and makes low intensity area low and high intensity areas high which means it redistribute the values in the image. Many images may not need CLHE but for a generalized process for every image it is very much helpful and do not decrease the efficiency of the proposed method. Using thresholding the dark and contrasting part are marked in a new image (Fig. 2c). Next that image array is applied into Random walker algorithm by which labels are generated. Then labels and images are imposed (Fig. 2d).

Used image processing library: Sci-kit image, Open-cv.

2.2 *Histogram Based Image Segmentation*

Histogram of an image is graphical representation plotted based on values observed from various features of an image viz. color, intensity of gray level etc. The process of segmentation is discussed below. At first histogram of gray images are obtained. The low intensity regions are identified using Histogram. For rotten part it is typically <60 In histogram plotting. For most fruit, color intensity in three color channels (R,

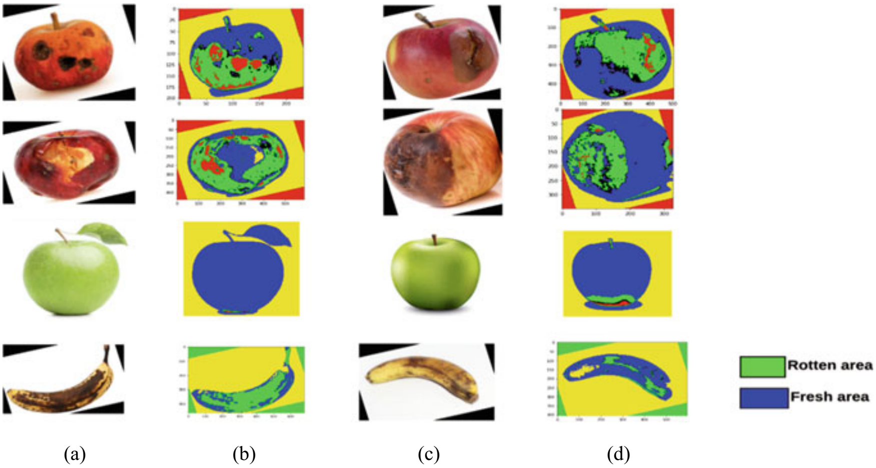

Fig. 3 Output images obtained using histogram based image segmentation. **a** and **c** shows images of fruits and **b** and **d** shows rotten area segmented image using histogram-based segmentation

G, B) for rotten area is relatively dark and it is experimental that using threshold as 60 identifies the rotten area most accurately. Then thresholding is applied based on gray level intensity and based on this thresholding different areas of the fruit is segmented. In Fig. 3a, d the segmented areas have been marked as green.

2.3 Gradient-Based Watershed Segmentation

Image gradient is the measure of change in image function, F(x, y) in x (across columns) and y (across rows) and in watershed algorithm [8] for segmentation of images, the images are assumed to be landscape of valley, ridges. The values are typically represented by gray level values of the pixel. Illustration with mathematical representation: Image Gradient (∇F).

Figure 4a, b, c shows change in gradient in x-axis, in y-axis and in (x-y)-axis respectively.

Fig. 4 Visual representation of change in gradient in different axis

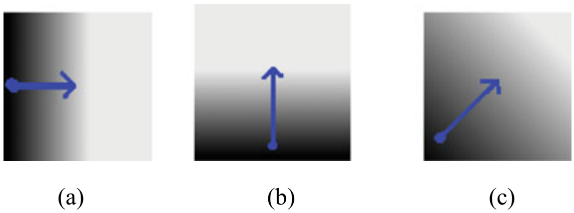

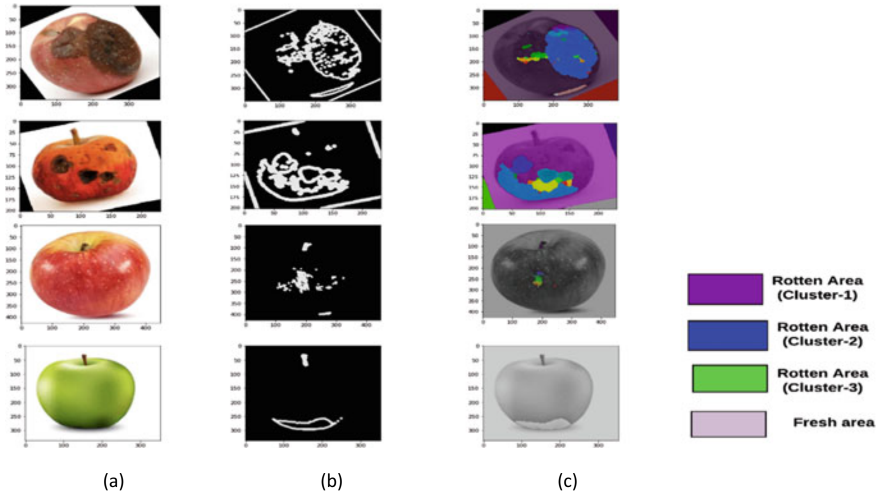

Fig. 5 Results obtained from gradient-based watershed segmentation. **a** Shows the RGB fruit images, **b** Gradient identified images and c shows the watershed labeled segmented images

$$\nabla F = \left[\frac{\delta F}{\delta x}, 0\right] \tag{1}$$

$$\nabla F = \left[0, \frac{\delta F}{\delta y}\right] \tag{2}$$

$$\nabla F = \left[\frac{\delta F}{\delta x}, \frac{\delta F}{\delta y}\right] \tag{3}$$

Direction of gradient is represented by

$$\Theta = \tan^{-1}\left[\frac{\delta F}{\delta y} / \frac{\delta F}{\delta x}\right] \tag{4}$$

Binary thresholding is done on gray images. Markers are found out using gradient calculating over the image pixels. Markers are converted to labels using watershed algorithm. Labels and image are super-imposed.

2.4 Gaussian Mixture Model

This paper also depicts and describes how unsupervised learning can help in segmenting out the rotten part of the fruit, because there is no pre-labeled data. Even K-means clustering [1] is a data point clustering technique with limitation in the algorithm that is it does not use any measure of uncertainty or probability. Gaussian mixture model [9, 10] or GMM is useful when data points of different class are in an overlapped manner. Using probability distribution function, it finds outs the maximum probability of each gaussian and identify the area of particular gaussians with maximum probability. Because of this, it is very effective to correctly classify the area than K-means clustering techniques (Fig. 7).

A Gaussian Mixture Model is special type of function which contains many Gaussians. Every Gaussian is identified by M ∈ {1, 2, …, M}.

So, no. of maximum gaussians is M, which denotes different types of data points in our image dataset. The areas which are fresh and the areas which are rotten in fruit image has different gray level intensity, texture etc. Then gaussian of fresh area is different than gaussian of rotten areas in a fruit. Gaussians are identified then probability distributions are used to identify which areas has high probability of rotten. In above diagram Fig. 7. GMM using M = 3. And it shows 3 different type of data point and its probability density.

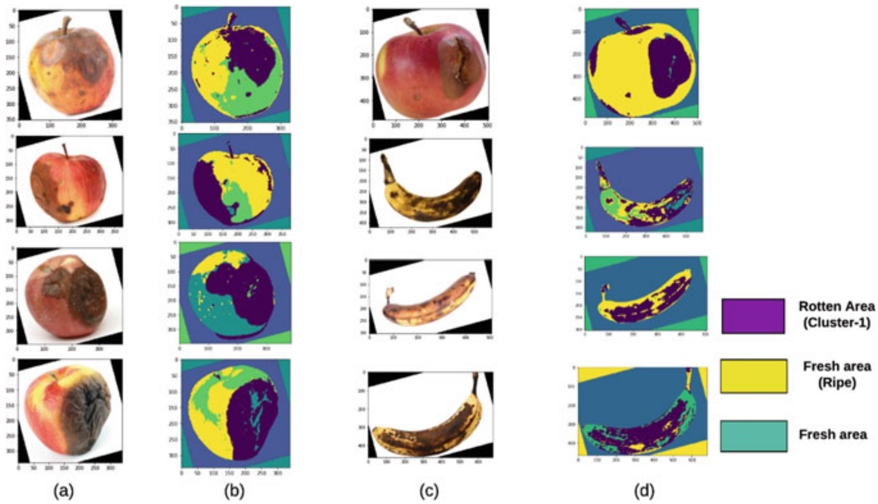

Fig. 6 Results obtained from gaussian mixer model. **a** and **c** shows images of fruits & **b** and **d** shows GMM segmented fruits

Fig. 7 Gaussian mixture model distribution example (For M = 3)

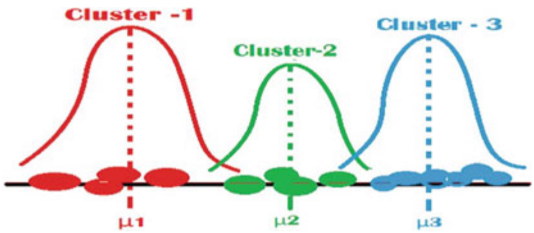

$$\sum_{M=1}^{M=3} \varphi_M = 1 \tag{5}$$

In Eq. (5), mean (μ) that defines center of probability distribution. Mixing Probability (φ) which determines how big or small is the gaussian. So, GMM is represented by this equation

$$f(x) = \sum_{m=1}^{M} \alpha_m \varphi\left(x; \mu_m, \quad \sum m\right) \tag{6}$$

where, $\left(x; \mu_m, \quad \sum m\right)$ is a gaussian with mean (μ_m) and co-variance matrix is $\sum m$ in Eq. (6).

Dataset: The dataset has been derived from Kaggle "Fruit fresh and rotten for classification". The dataset consists of four classes of fruits' image apple, banana and orange. All classes have fresh and rotten subclasses. This paper only uses two classes of fruits apple and banana class with subclasses rotten and fresh [9].

3 Experimental Results & Discussion:

In this paper 4 types of techniques to segment rotten part of fruit from image, has been discussed. The results of the process in each technique is detailed below.

For random walker segmentation. Figure 8a Refers to original fruit image. Figure 8b shows the converted gray image. Figure 8c shows the different datapoint identified by random walker. Figure 8d shows the segmented image rotten part identified by blue region.

In Fig. 9a, b, c, d, e fruit segmentation using K-means clustering represented by Dubey and Jalal [2].

Figure 10a Refers to original fruit image. Figure 10b shows the converted gray

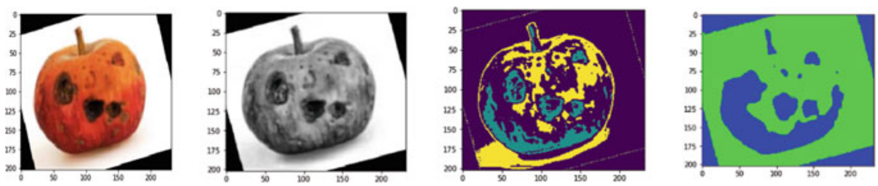

(a) (b) (c) (d)

Fig. 8 For random walker segmentation. (**a**) Refers to original fruit image. (**b**) shows the converted gray image. (**c**) shows the different data point identified by random walker. (**d**) shows the segmented image rotten part identified by blue region

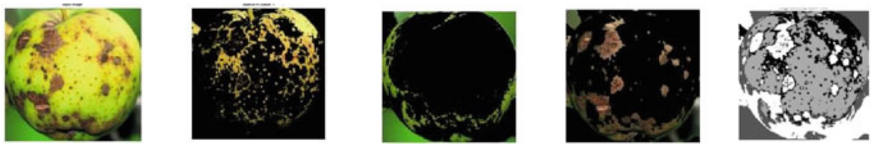

(a) (b) (c) (d) (e)

Fig. 9 (**a**–**e**) fruit segmentation using K-means clustering represented by Dubey and Jalal [2]

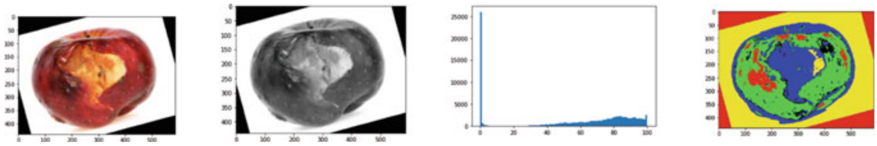

(a) (b) (c) (d)

Fig. 10 (**a**) Refers to original fruit image. (**b**) shows the converted gray image. (**c**) shows the histogram representation of the image. (**d**) shows the segmented image based on histogram representation and thresholding

image. Figure 10c shows the histogram representation of the image. Figure 10d shows the segmented image based on histogram representation and thresholding.

Figure 11a Refers to original fruit image. Figure 11b shows the converted gray image with gradient calculated over the image. Figure 11c shows the segmented using gradient watershed algorithm.

Figure 12a, b Refers to the output of GMM (Gaussian Mixer model), in which GMM algorithm randomly picked up Violet color for the rotten area based on probability distribution.

Among these all segmentation algorithms presented in the paper Gaussian Mixer Model (GMM) has given best result which can be visually observed. This paper uses Silhouette clustering metric to analysis the segmentation cluster for every method quantitatively. Silhouette analysis is used to observe and measure between the separating clusters. Silhouette Coefficient measures the mean of intra-cluster distances. The value of the measurement lies between (-1) and $(+1)$. High positive value

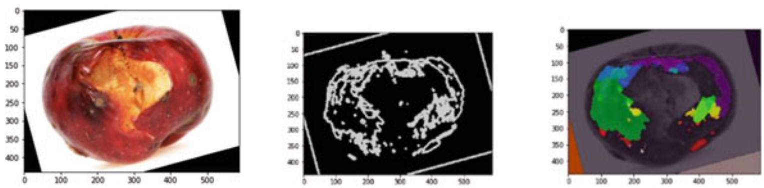

(a) (b) (c)

Fig. 11 (**a**) Refers to original fruit image. (**b**) shows the converted gray image with gradient calculated over the image. (**c**) shows the segmented using gradient watershed algorithm

Fig. 12 (**a**–**b**) Refers to the output of GMM (Gaussian Mixer model), in which GMM algorithm randomly picked up Violet color for the rotten area based on probability distribution

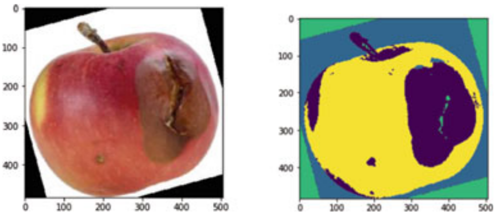

(a) (b)

describes the masking or labels are well matched. And negative value shows, the labels assigned to wrong cluster which is not well matched. See (Fig. 13). The watershed segmentation method uses one specific type of masking method which returns

Segmentation Method	Original image	Segmented image	Silhouette scores
Random-Walker Segmentation	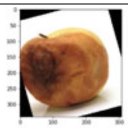	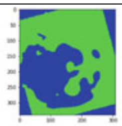	-0.06451
	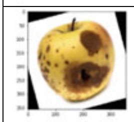	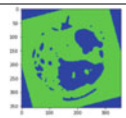	0.133709
	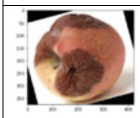	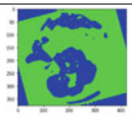	-0.012847
Histogram-based Segmentation	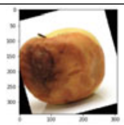		0.38444
	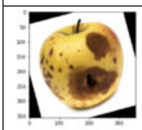	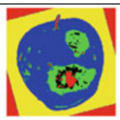	0.45462899
	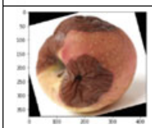	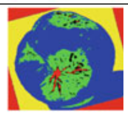	0.3460768

Fig. 13 Output of segmentation techniques and corresponding Silhouette scores

Gaussian Mixer Model Segmentation	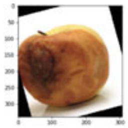	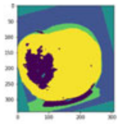	0.55560
	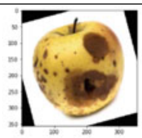	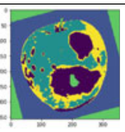	0.6347680
Gaussian Mixer Model Segmentation	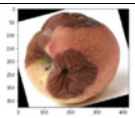	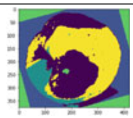	0. 4649733

Fig. 13 (continued)

array of different cluster individually and those are super-imposed to segment the image so it is not possible to compare the different array of different shape using silhouette clustering metric. However, the output of the Gaussian mixer model is better than the output of watershed algorithm, which can be visually observed. Hence, it is the most suited segmentation technique for rotten fruit identification among all other algorithms used in the present paper. In all the algorithms except random walker segmentation and Gaussian mixer model do not uses probability distribution functions. All other algorithms only use generalized image processing techniques like gradient calculating, thresholding depending upon gray level histogram representation, binary inversion etc. In contradiction Gaussian Mixture Model (GMM) uses probability distribution function which identifies the areas based on maximum probability of same class label.

Figure 13 shows the output of each method and corresponding Silhouette scores for each image. From the scores it can be observed that Gaussian Mixer Model or (GMM) has highest positive score Fig. 14).

4 Conclusion

Sorting of fruit based on the segmentation of images and if fruits are partially rotten then classifying them into usable or not-usable and taking them using a multi-stage process to use into production will be very much helpful. In this paper the technique and the method proposed is unique and efficient way to segmenting-out and identifying rotten part of fruit like apple and banana. As discussed previously, in a market many kinds of apple or other fruit can be available but there cannot be a greater number of algorithms to identify rotten part in various types of fruits. There must be only one general technique to identify the part, hence unsupervised algorithm like

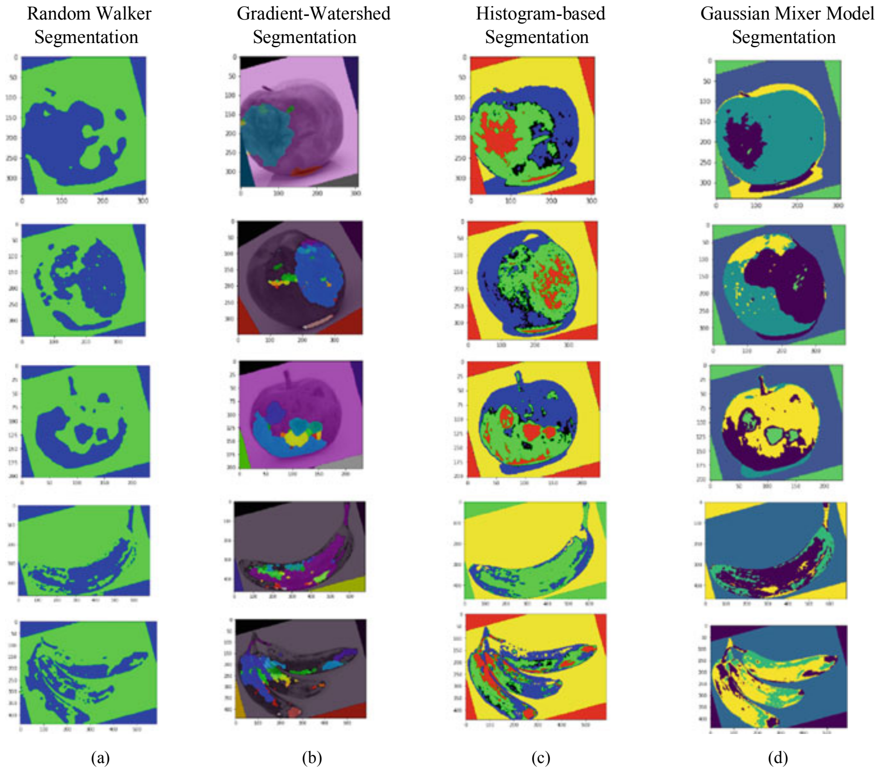

Fig. 14 Experimental results of used algorithms. **a** shows outputs of Random Walker segmentation, column –**b** represents output of gradient-based watershed algorithm, **c** shows the outputs of histogram-based segmentation and **d** shows output images of gaussian mixer model-based segmentation techniques

Gaussian mixer model, Random walker segmentation technique comes into picture. As there is no specific performance metric to determine the quality of an unsupervised algorithm. The process has only to rely upon probability distribution function, is giving promising results, which can be observed.

References

1. Dubey, S.R., Jalal, A.S.: Fusing color and texture cues to categorize the fruit diseases from images (2014). arXiv:1412.7277
2. Dubey, S.R., Jalal, A.S.: Adapted approach for fruit disease identification using images. Int. J. Comput. Vis. Image Process. (IJCVIP) **2**(3), 44–58 (2012)
3. Roy, K., Chaudhuri, S.S., Bhattacharjee, S., Manna, S., Chakraborty, T.: Segmentation techniques for rotten fruit detection. In: 2019 International Conference on Opto-Electronics and Applied Optics (Optronix), pp. 1–4. IEEE (2019)

4. Grady, L.: Random walks for image segmentation. IEEE Trans. Pattern Anal. Mach. Intell. **28**(11), 1768–1783 (2006)
5. Karakaya, D., Ulucan, O., Turkan, M.: A comparative analysis on fruit freshness classification. In: 2019 Innovations in Intelligent Systems and Applications Conference (ASYU), pp. 1–4. IEEE
6. Yang, C.: Colorful fruit image segmentation based on texture feature. In: Advances in Intelligent Information Hiding and Multimedia Signal Processing, pp. 305–311. Springer, Singapore (2020)
7. Agarwal, A., Sarkar, A., Dubey, A.K.: Computer vision-based fruit disease detection and classification. In: Smart Innovations in Communication and Computational Sciences, pp. 105–115. Springer, Singapore (2019)
8. Singh, N.P., Dixit, S., Akshaya, A.S., Khodanpur, B.I.: Gradient magnitude based watershed segmentation for brain tumor segmentation and classification. In: Proceedings of the 5th International Conference on Frontiers in Intelligent Computing: Theory and Applications, pp. 611–619. Springer, Singapore (2017)
9. Xie, X., Huang, W., Wang, H.H., Liu, Z.: Image de-noising algorithm based on Gaussian mixture model and adaptive threshold modeling. In: 2017 International Conference on Inventive Computing and Informatics (ICICI), pp. 226–229. IEEE (2017)
10. Reynolds, D.: Gaussian mixture models. In: Li, S.Z., Jain, A.K. (eds.) Encyclopedia of Biometrics. Springer, Boston, MA (2015)
11. Fruit fresh and rotten for classification.https://www.kaggle.com/sriramr/fruits-fresh-and-rotten-for-classification. Last accessed 23 March 2020

Capsule Neural Network Architecture Based Multi-class Fruit Image Classification

Kyamelia Roy, Probhakar Roy, and Sheli Sinha Chaudhuri

Abstract This paper aims to provide a study on the performance of a variation of Hinton's CapsNet Architecture on Fruits-360 Dataset with a moderate number of data points for use in Multi-Class Fruit Classification Tasks with 118 different classes. The proposed model is observed to outperform the Convolutional Neural Network-based Architecture for the same objective task on Fruits-360 Dataset with a state-of-the-art validation accuracy of 99.95% whereas the Convolutional Neural Network-based Architectures were able to achieve a maximum validation accuracy of 97.04%. The proposed model was also able to achieve greater than 99.9% score for each F1 Score, Precision, and Recall performance parameters.

Keywords CapsNet architecture · Convolutional neural network · Robotic Process Automation (RPA)

1 Introduction

Artificial Intelligence-based Classification Frameworks has taken over the industrial automation sector. A reliable and accurate object classification system has become an essential and fundamental part of the field of Robotic Process Automation (RPA). A fruit classification system with the ability to classify a large variety of fruits with low as well as a high correlation factor i.e. the ability to classify a type of fruit as well as it's sub-varieties with state-of-the-art performance and accuracy is an integral deciding factor for large scale industrial deployment of the system. This paper proposes the use of a variant of Hinton's CapsNet Architectures as described in [1] instead of Convolutional Neural Network Architectures for Multi-Class Fruit Classification.

K. Roy (✉) · S. S. Chaudhuri
Jadavpur University, Jadavpur, Kolkata 700032, India
e-mail: kyamelia.2017@gmail.com

P. Roy
University of Engineering and Management, Kolkata 700160, India

S. Banerjee and J. K. Mandal (eds.), *Advances in Smart Communication Technology and Information Processing*, Lecture Notes in Networks and Systems 165,
https://doi.org/10.1007/978-981-15-9433-5_17

The earlier works done on this objective task includes the work done by Bargoti et al. as described in [2] was mostly focused on building a Faster Region-based Convolutional Neural Network (Faster R-CNN) object detection framework for classification or detection in orchards that included mangoes, almonds and apples. Kapach et al. discussed the need and practical success of Machine Learning Algorithms in harvesting robots with a review on some classical as well as state-of-the-art computer vision solutions employed by such systems in their work as described in [3]. Whereas Payne et al. [4] extends on their previously conducted study on mango crop yield estimation with night time imaging and computer vision algorithms. Sa et al. [5] presented the approach of using Deep Convolutional Neural Networks to construct fruit detection systems and adapt in their work the Faster R-CNN model using transfer learning technique to train the model. Rahnemoonfar et al. [6] also proposed a simulated Deep Convolutional Neural Network for yield estimation for deployment in agriculture or food industry. Ren et al. [7] proposed a Region Proposal Network (RPN) which shares convolutional feature-maps with the detection network for object detection tasks. Roy et al. [8] proposed a segmentation based approach to fruit quality detection. An overview of the different contributions for achieving the current state in the field of Deep Learning is accurately covered by Schmidhuber [9].

The earlier works as mentioned above on this subject varied in aspects of the deep learning architecture only for faster performance of their proposed systems. But as suggested in [10], It is essential to have varied dataset like the Fruits-360 Dataset to train classifier on such Multi-Class Fruit Classification problems with large number of classes to test and validate the performance restrict the correlation between similar classes leading an increase in loss parameter of the proposed model. As there are 118 numbers of classes in Fruits-360 Dataset with 80,550 data points, it's actually perfect for testing and validation of our proposed model in perspective of deployment of the model to RPA systems or automated harvesting system in agriculture or food industry.

Among the different advantages of Hinton's CapsNet Architectures as described in [1] over previously used Convolutional Neural Networks is that it address the "Picasso problem" in image recognition: images that have all the proper elements however that aren't within the correct spatial relationship (e.g., if in a "face", the positions of the mouth and one eye are switched) whereas Convolutional Neural Networks fails to address this problem. For image recognition, Capsule Networks exploit the fact that while viewpoint changes have nonlinear effects at the pixel level, they have linear effects at the part or object level. This can be compared to inverting the rendering of an object of multiple parts.

This paper also showcases the performance of the proposed model on the Fruit-360 dataset used in the paper [1] that shows best test/validation accuracy of 97.05% with convolutional neural network based architectures whereas with our proposed capsule neural network architecture we were able to get a test/validation accuracy of 99.95%.

2 Methodology

The proposed methodology of our present work is presented in the workflow diagram shown in Fig. 1. The workflow diagram represents all the steps involved in the training and testing of the proposed model using TensorFlow Framework on Google Colaboratory with Nvidia Tesla T4 GPU acceleration.

The Fruits-360 dataset [10] is extracted, transformed and loaded using TensorFlow's high-level data API's for the creation of an effective input data pipeline for effective prefetching of training and testing data to the network resulting in reduced data loading time before training a batch.

The input data pipeline also maps the images to function for resizing as well as normalization of the images. The image labels are also mapped to a function for converting them to one-hot encodings i.e. binary vectors for the representation of categorical variables. Then the pipeline splits the dataset containing 80,550 data points i.e. tuples of image and its corresponding labels into a training dataset containing 60,412 data points and a testing/validation dataset containing 20,137 data points. The pipeline divides each dataset into batches of 16 data points.

The Training Module mentioned in Fig. 1 was developed using TensorFlow's high-level keras API's for building the layers as covered in the Sect. 3.2. The accuracy and loss logs were exported to csv files for generation of the results. The actual capsule layer in the proposed architecture was build using inherited Tensorflow keras layer class for creating a custom layer with associated initialized weights, input shape initialization method, output shape initialization method and operation for computing the layer output according to Hinton's CapsNet Architecture [1].

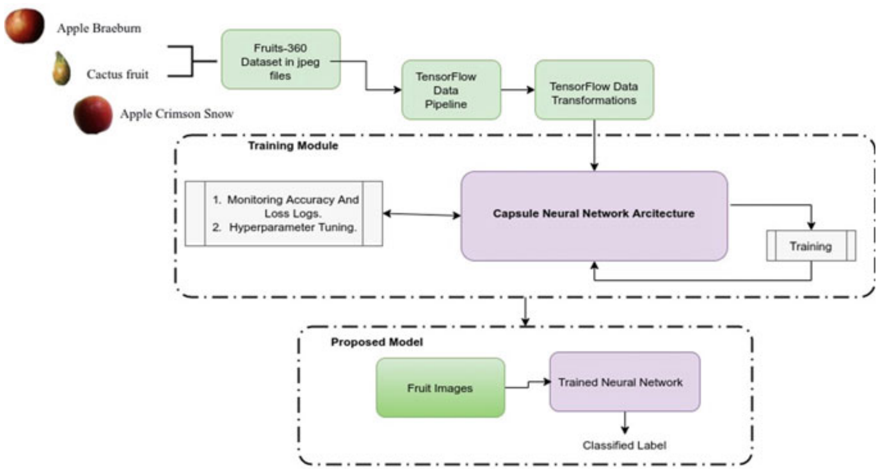

Fig. 1 Workflow diagram of the proposed methodology

The proposed model is initialized with Xavier's weight initialization and optimized using Adam Optimization Algorithm with Margin Loss functions as the objective function.

2.1 Dataset

The Fruit-360 Dataset contains 118 different classes of fruits with 80,550 images of size 100 pixel $\times$ 100 pixel and its corresponding class or labels. Some of the fruits-360 classes and it' corresponding images are shown in Table 1.

CLASSES: Apple [Braeburn, Crimson Snow, Golden 1, Golden 2, Golden 3, Granny Smith, Pink Lady, Red 1, Red 2, Red 3, Red Delicious, Red Yellow 1, Red Yellow 2], Apricot, Avocado, Avocado ripe, Banana, Banana Lady Finger, Banana Red, Beetroot, Blueberry, Cactus fruit, Cantaloupe 1, Cantaloupe 2, Carambula, Cherry 1, Cherry 2, Cherry Rainier, Cherry Wax Black, Cherry Wax Red, Cherry Wax Yellow, Chestnut, Clementine, Cocos, Dates, Ginger Root, Granadilla, Grape Blue, Grape Pink, Grape White, Grape White 2, Grape White 3, Grape White 4, Grapefruit Pink, Grapefruit White, Guava, Hazelnut, Huckleberry, Kaki, Kiwi, Kohlrabi, Kumquats, Lemon, Lemon Meyer, Limes, Lychee, Mandarine, Mango, Mango Red, Mangostan, Maracuja, Melon Piel de Sapo, Mulberry, Nectarine, Nectarine Flat, Nut Forest, Nut Pecan, Onion Red, Onion Red Peeled, Onion White, Orange, Papaya, Passion Fruit, Peach, Peach 2, Peach Flat, Pear, Pear Abate, Pear Forelle, Pear Kaiser, Pear Monster, Pear Red, Pear Williams, Pepino, Pepper Green, Pepper Red, Pepper Yellow, Physalis, Physalis with Husk, Pineapple, Pineapple Mini, Pitahaya Red, Plum, Plum 2, Plum 3, Pomegranate, Pomelo Sweetie, Potato Red, Potato Red Washed, Potato Sweet, Potato White, Quince, Rambutan, Raspberry, Redcurrant,

Table 1 Sample dataset images

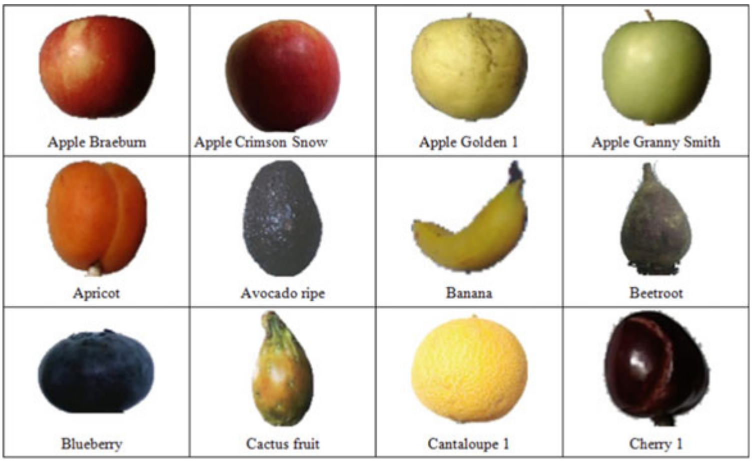

Salak, Strawberry, Strawberry Wedge, Tamarillo, Tangelo, Tomato 1, Tomato 2, Tomato 3, Tomato 4, Tomato Cherry Red, Tomato Maroon, Tomato Yellow, Walnut.

3 Experimental Results and Discussions

The proposed model was trained on Google Colaboratory with Nvidia Tesla T4 GPU acceleration taking approximately 45 min training time per epoch resulting in a training accuracy of 99.7% and a test/validation accuracy of 99.95% after the 8th epoch. The performance of the proposed model as compared to best performing convolutional neural network-based architecture from [10] is given in the Table 2. As can be clearly observed our proposed model out-performs the convolutional neural network-based architecture resulting in a state-of-the-art model performance on Fruits-360 Dataset [10]. Another key factor to consider is that the convolutional neural network-based architecture from [10] shows signs of overfitting at the mentioned test accuracies.

3.1 Model Architecture

The proposed model as described through the TensorFlow Keras computed model plot shown in Fig. 2, consists of two 2D Convolutional layers of 3×3 kernel size with 64 and 128 numbers of kernels on the first layer and second layer respectively. The computed output is feeded to a 2D Average Pooling layer for reducing the

Table 2 Model performance comparison

Sl. no.	Model configuration			Train accuracy (%)	Test accuracy (%)
1	Our proposed model			99.7	99.95
2	Convolutional	5×5	16	99.86	97.04
	Convolutional	5×5	32		
	Convolutional	5×5	64		
	Convolutional	5×5	128		
	Fully connected	–	1024		
	Fully connected	–	256		
3	Convolutional	5×5	16	99.93	97.00
	Convolutional	5×5	32		
	Convolutional	5×5	64		
	Convolutional	5×5	128		
	Fully connected	–	512		
	Fully connected	–	256		

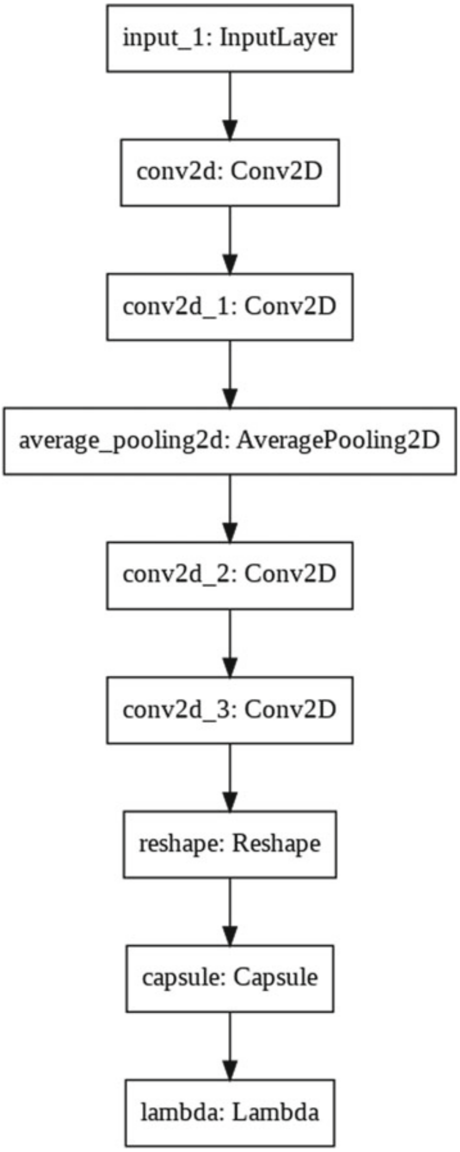

Fig. 2 Tensorflow Keras model plot

computational cost after convolutional layers. Then the computed output follows two 2D Convolutional layers of 3×3 kernel size with 128 numbers of kernels each before getting reshaped and feeded to the Capsule Layer followed by a Lambda layer that computes L2 norm on the vector outputs of the capsule layer i.e. the square root of the sum of the squared vector values. to transform the vector into a probability distribution similar to softmax activation function.

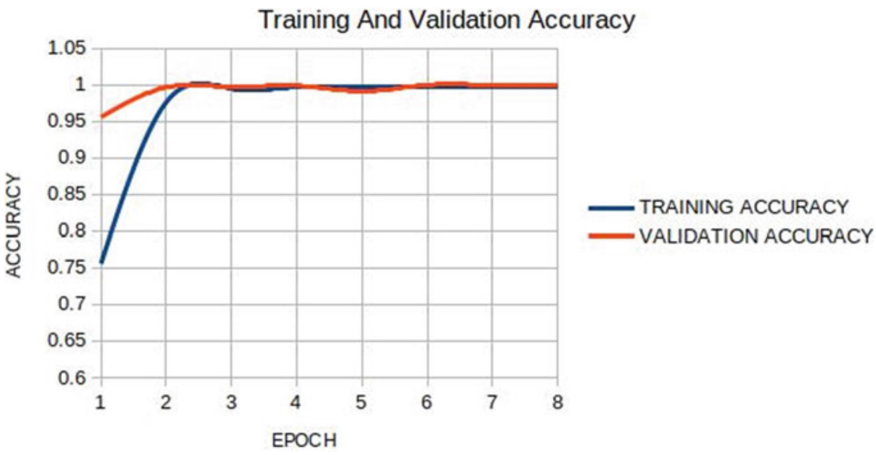

Fig. 3 The proposed model training and validation accuracy

Some of the important model features and parameters to reproduce our experimental results are as follows:-

- **Input Layer**: The image with Input Shape [None, 100, 100, 3] was feeded to the network.
- **Hidden Layer Activation Functions**: Squash Activation Functions was used in the Capsule layers [1] and RELU activation function for Convolution layers.
- **Weight Initialization**: Xavier's Weight Initialization.
- **Optimization Algorithm**: Adam Optimization Algorithm with initial hyper parameters details:-
  - learning rate = 0.001
  - beta1 = 0.9
  - beta2 = 0.999
  - epsilon = 1e–07.

Figure 3 shows the proposed models training and validation accuracy per epoch. As can be observed the validation accuracy for the proposed model is quite high from the 1st epoch but the thing to considered here is the ability of the proposed model to achieve the state-of-the-art validation accuracy without overfitting as can also be confirmed from Fig. 4 that show the training and validation losses per epoch.

3.2 *Performance Parameters*

To validate the performance of our model, some statistical measures has been taken into consideration viz. Precision, Recall, F1 Score, etc. These statistical parameters are calculated in terms of True Positive (TP) i.e. correctly identified labels, True

Fig. 4 The proposed model training and validation loss

Negative (TN) i.e. correctly rejected labels, False Positive (FP) i.e. incorrectly identified labels, and False Negative (FN) i.e. incorrectly rejected labels for each 118 different classes according to the below mentioned relations (1–3).

$$\text{Precision} = \frac{\text{TP}}{(\text{TP} + \text{FP})} \tag{1}$$

$$\text{Recall} = \frac{\text{TP}}{(\text{TP} + \text{FN})} \tag{2}$$

$$\text{F1 Score} = \frac{2 \times (\text{Precision} \times \text{Recall})}{(\text{Precision} \times \text{Recall})} \tag{3}$$

Table 3 shows the Precision, Recall, and F1 score values for our proposed models computed using Tensor Flow's scikit-learn wrapper API that yields the metrics values using three different built-in averaging method viz. Macro (calculates metrics for each class and finds their unweighted mean), Micro (calculates metrics globally by counting the total TP, FN, and FP), Weighted (calculates metrics for each class and

Table 3 Performance metrics

Performance parameters	Averaging method		
	Macro (%)	Micro (%)	Weighted (%)
Precision	99.909	99.910	99.913
Recall	99.91	99.91	99.91
F1 Score	99.90	99.91	99.91

finds their average weighted by the number of occurrences of each true class label i.e. TP + FN) methods for averaging over the computed metrics values of the 118 different classes.

Some other performance parameters are mentioned in Table 4 computed using PyCM module [11]. Definition of the mentioned parameters and their relevance and interpretation can be referred to from [11].

Table 4 Some other performance parameters

Performance parameters		Performance parameters		Performance parameters	
95% CI	(0.99869, 0.99952)	Cross Entropy	6.85506	Overall CEN	0.00074
ACC Macro	0.99998	Gwet AC1	0.9991	Overall J	(117.78794, 0.9982)
AUNP	0.99955	Hamming Loss	0.00089	Overall MCC	0.9991
AUNU	0.99955	Joint Entropy	6.86128	Overall MCEN	0.00127
Bennett S	0.9991	KL Divergence	4e-05	Overall RACC	0.00883
CBA	0.99824	Kappa	0.9991	Overall RACCU	0.00883
Chi-Squared	2350781.72318	Kappa 95% CI	(0.99868, 0.99951)	Zero-one Loss	18
Chi-Squared DF	13689	Kappa No Prevalence	0.99821	PPV Macro	0.9991
Conditional Entropy	0.00626	Kappa Standard Error	0.00021	PPV Micro	0.99911
Kappa Unbiased	0.9991	Mutual Information	6.84877	Pearson C	0.99575
Lambda A	0.99909	NIR	0.01555	Overall CEN	0.00074
Lambda B	0.99909	Overall ACC	0.99911	Overall J	(117.78794, 0.9982)
Phi-Squared	116.79162	SOA1 (Landis & Koch)	Almost Perfect	SOA5 (Cramer)	Very Strong
RCI	0.99909	SOA2 (Fleiss)	Excellent	SOA6 (Matthews)	Very Strong
RR	170.57627	SOA3 (Altman)	Very Good	Scott PI	0.9991
Reference Entropy	6.85502	SOA4 (Cicchetti)	Excellent	Standard Error	0.00021
Response Entropy	6.85504	SOA1 (Landis & Koch)	Almost Perfect	TPR Macro	0.9991
TPR Micro	0.99911	–	–	–	–

4 Conclusion

The Proposed work has been fully implemented and tested producing a state-of-the-art model performance on fruits-360 dataset that can be deployed for Robotic Process Automation (RPA) in agriculture or food industry for reliable and accurate classification results. The proposed model with a state-of-the-art validation accuracy of 99.95% on the on Fruits-360 Dataset whereas the Convolutional Neural Network-based Architectures were able to achieve a maximum validation accuracy of 97.04%. The proposed model was also able to achieve greater than 99.9% score for each F1 Score, Precision, and Recall parameter with faster training time and much smaller number of epochs to reach the state-of-the-art validation accuracy. Our work also shows the superiority of Hinton's CapsNet Architecture for classification task on moderate-sized datasets with the further benefits of negligible effects of overfitting as well as ability to address the "Picasso problem".

References

1. Sabour, S., Frosst, N., Hinton, G.E.: Dynamic routing between capsules. In: Advances in Neural Information Processing Systems, pp. 3856–3866 (2017)
2. Bargoti, S., Underwood, J.: Deep fruit detection in orchards. In: 2017 IEEE International Conference on Robotics and Automation (ICRA), pp. 3626–3633. IEEE (2017)
3. Kapach, K., Barnea, E., Mairon, R., Edan, Y., Ben-Shahar, O.: Computer vision for fruit harvesting robots–state of the art and challenges ahead. Int. J. Comput. Vis. Robot. **3**(1/2), 4–34 (2012)
4. Payne, A., Walsh, K., Subedi, P., Jarvis, D.: Estimating mango crop yield using image analysis using fruit at 'stone hardening' stage and night time imaging. Comput. Electron. Agric. **100**, 160–167 (2014)
5. Sa, I., Ge, Z., Dayoub, F., Upcroft, B., Perez, T., McCool, C.: Deepfruits: a fruit detection system using deep neural networks. Sensors **16**(8), 1222 (2016)
6. Rahnemoonfar, M., Sheppard, C.: Deep count: fruit counting based on deep simulated learning. Sensors **17**(4), 905 (2017)
7. Ren, S., He, K., Girshick, R., Sun, J.: Faster r-cnn: towards real-time object detection with region proposal networks. In Advances in neural information processing systems, pp. 91–99 (2015)
8. Roy, K., Chaudhuri, S.S., Bhattacharjee, S., Manna, S., Chakraborty, T.: Segmentation techniques for rotten fruit detection. In: 2019 International Conference on Opto-Electronics and Applied Optics (Optronix), pp. 1–4. IEEE (2019)
9. Schmidhuber, J.: Deep learning in neural networks: an overview. Neural Netw. **61**, 85–117 (2015)
10. Mureşan, H., Oltean, M.: Fruit recognition from images using deep learning. Acta Univ. Sapientiae, Inform. **10**(1), 26–42 (2018)
11. Haghighi, S., Jasemi, M., Hessabi, S., Zolanvari, A.: PyCM: multiclass confusion matrix library in Python. J. Open Source Softw. **3**(25), 729 (2018)

Effects of Class Imbalance Problem in Convolutional Neural Network Based Image Classification

Arghasree Banerjee, Kushankur Ghosh, Arya Sarkar, Mayukh Bhattacharjee, and Sankhadeep Chatterjee

Abstract Convolutional Neural Networks (CNNs) have revolutionized the image classification tasks to a greater extent. Various research works reported the high accuracy of CNNs in image classification problems related to science and engineering. It has been found that many image classification problems carry an additional challenge of imbalanced classes in the dataset. In absence of a suitable analysis of the effect of imbalanced image data on the performance of CNNs, the current study thoroughly analyzed the same. CNN models are evaluated in terms of Sensitivity, Specificity, G-Mean and Bookmaker Informedness with varying degrees of imbalance ratio. The experimental results have revealed that the performance of CNN is severely affected by increased imbalance ratio.

Keywords CNN · Imbalance · Image classification

1 Introduction

Almost every modern individual utilizes the facilities of the current technologies for the creation and sharing of images of any kind. This sharing of images has eased the mode of visual communication over the years. However, the quality of this communication mostly depends on the processing [1] than the quality of image. An image can be of any type starting from biomedical images [2, 3], document images [4], satellite images [1] and PolSAR images [5]. An intelligent system is very much necessary to identify the category of an image from a thick chunk of wide variety of images. The application of machine learning in real life issues has been studied and experimented over a wide range of time [6–11]. With the expansion of the field, the application of Neural Networks (NN) is gradually suppressing the implementations of other machine learning algorithms [12]. A NN based image classification [13] model can

A. Banerjee · K. Ghosh · A. Sarkar · M. Bhattacharjee · S. Chatterjee (✉)
Department of Computer Science & Engineering, University of Engineering & Management, Kolkata, India
e-mail: chatterjeesankhadeep.cu@gmail.com

S. Banerjee and J. K. Mandal (eds.), *Advances in Smart Communication Technology and Information Processing*, Lecture Notes in Networks and Systems 165,
https://doi.org/10.1007/978-981-15-9433-5_18

generate better results compared to any other traditional image classification technique due to the robustness of the prior model. A popular way of classifying an image is by using Convolutional Neural Networks (CNN) [14]. Over the years CNN based models have gained a wide popularity and has been implemented to resolve various real-life issues starting from face detection [15] to language matching [16]. However, in the recent years CNN has become a very concrete tool for image classification and segmentation. The classification of images incorporates the task of putting any selected image of a kind to its relative category based on intelligent computations. Various studies over the years successfully developed concrete models delivering effective classifications on chunks of images both offline and online. However, in the recent years the techniques of image classifications using CNN are documented to suffer from the imbalanced classification problem. The Class-Imbalanced problem was coined in the early 1990s and have been studied for more than two decades. A imbalanced dataset is mostly a common situation and can be very much prominent in any day to day practical scenarios. Apart from image classification, the problem has also become very popular in sentiment analysis [10], sarcasm detection [17], botnet detection [18] and twitter-spam detection [19]. In this paper a detailed documentation of class-imbalance problem in CNN based image classification is presented. The classification challenges and the future research scope are also discussed.

2 Image Classification Using CNN

A Convolutional Neural Network (Conv-Net/CNN) is a Deep Learning Based algorithm which is basically applied to analyse image data. A CNN consists of an input layer, an output layer and multiple hidden layers. Input is a visual imagery tensor with shape (number of images) * (image width) * (image height) * (image depth). After passing through the convolutions, the image gets absorbed to a feature map. In [20], the authors make an account for the early applications of CNN in speech recognition, text recognition, handwriting recognition and later in natural image recognition. In [21] the authors documented the behaviour of CNN on a set of 1.2 million high resolution images consisting of 1000 different variety of classes in ILSVRC-2010 competition. The authors found that CNN gives us a remarkable performance but can undergo some complications if a layer is removed. In the ILSVRC-2012 competition, the authors averaged the predictions of two CNNs that were pre-trained on the entire Fall 2011 release with the five CNNs which gave an error rate of 15.3%. The application of CNNs to multi-categorical classifications applied in the earlier paper, attracted a lot of attention in the computer vision research community. In [22] a pre-trained CNN model generated at the full-connected layers extracts features better than conventional hand-crafted features on all datasets in image retrieval application. In a comparative study done by Yi Hou et al. in [23], we get to know how CNN-based image descriptors are better than the state-of-the-art hand-crafted image descriptors in the visual loop closure detection application. In [24], the authors introduced 3D CNN models for action recognition. From adjacent input frames the authors generate multiple channels of information. Convolution and subsampling is performed separately in each channel after that. The CNN based image classification is thus now used in many medical examinations as it significantly improved the best performance for many image databases [25]. CNN based image classification is still an interesting topic among researchers. In [26] a recently published paper presents a method to optimize input for CNN-based HSI classification. Liu et al. [27] proposed a detailed study by investigating the middle layers of the CNN and conducted experiments on different image datasets. Their approach fused the latent features extracted in the middle layers of the CNN which effectively improves the classifier's performance. Another remarkable application of CNN was demonstrated by Peng et al. [28] to detect fruit flies by using the FB-CNN technique. In [29], the authors utilized the texture filters to classify between histopathological images.

3 Class-Imbalance Problem in Image Classification

The imbalanced classification problem can occur in both binary or multi-class dataset. The problem occurs when the count of a particular class in a dataset becomes more dominant compared to the other classes. At this scenario, the classifying algorithm will have a tendency to generate decisions in favour of the class with the majority count. This mostly results in a wide deflection in performance of a machine learning model. The most common approaches to mitigate the issue are oversampling of minority instances or the under-sampling of majority instances. However, the most popular way to handle this problem is by making the minority class denser as under-sampling can result in a loss of valuable information from the dataset. Some of the popular techniques developed for oversampling over the years are SMOTE [30], Borderline-SMOTE [31], ADASYN [32] and Safe-Level-SMOTE [33] and. However, in [34, 35] the authors described the consequences of oversampling and also presented a remarkable majority focussed approach to overcome that. The earliest reference of the effects of class imbalance in image classification is found in [36]. However, in the recent years it has become a significant problem in the domain of image classification [37–41]. The problem mostly arise when the model is made to classify images in any practical domain. Classification with CNNs also undergo the same problem, like any other techniques of image classification. In [42] Lee et al. encountered with the class imbalance problem in Plankton image classifications. The authors proposed a novel approach based on CNN and avoided the problem by training the CNN with normalized data. The principle idea behind their approach depends on the value of threshold μ which is selected to construct the normalized data by sampling the original data. The normalized data is constructed in a way such that no class is larger than μ. The primary problem behind this approach is the loss of data. In the following year Wang et al. [43] developed a Generative Adversarial Network (GAN) based Plankton classification model. The primary concern of their technique was to perform an effective image classification by resolving the class imbalance problem. The proposed architecture CGAN-Plankton generates the minority class data using the Generative model which is discriminated using the Discriminative model. The approach widely outperforms other CNN based models. Mahmood et al. [44] also faced the class imbalance problem while proposing a technique to classify corals. Their proposed approach was also based on CNN and used the MLC dataset for the experiment which is prone to the class imbalance problem. A simple down-sampling of data was done to mitigate the problem which also resulted in the loss of valuable data. Rahman and Wang [45] used a Fully-Convolutional Neural Network (FCNN) for an augmentation in the IoU score. The main objective of the paper is to mitigate the object category segmentation problem and in their series of experiments they encountered the class-imbalance problem. In [46] the authors developed an efficient model by hybridizing CNN with uneven-margin based SVM to conduct an effective performance on imbalanced visual problems. Uneven margins were introduced to SVM to handle imbalanced data and was constructed by implying a margin parameter to the standard SVM model which is a ratio of the positive margin to the negative margin. In the proposed model of [46], the rearmost layer of the CNN is replaced by the uneven SVM which produced better performance than the standard model of SVM. In 2017 [47] Yue discussed the effects of imbalanced classification on CNN based malware image classification and also introduced the weighted softmax loss approach to mitigate the issue. The weight ω_k is calculated by,

$$\omega_k = (\Delta - \emptyset/C \times \Delta) + 1$$

where Δ is the dimension of the majority class, Ø is dimension the selected class and C is the constant controlling the scaling of the weighted loss. Sahu et al. [48] performed a CNN based multi-label classification to detect a surgical tool. Their approach also faced a class-imbalance problem while training the CNN. The authors performed their experiments on M2CAI tool detection dataset by considering the co-occurrences of the tools. In [49] Li et al. proposed an imbalanced-aware CNN to mitigate the problem in vehicle classifications from aerial images. The authors extended the CNN model with a cost-effective imbalance aware feature map. In [50] the authors presented a very novel technique detect lithographic hotspots in electronic circuits based on CNN. The authors encountered a the imbalanced classification problem while performing the experiments and applied mirror-flipping and up-sampling to mitigate the issue, which resulted a significant improvement in the performance. Pouyanfar et al. in [51] performs a dynamic on the samples of each class of a dataset based on the F1-score to mitigate the imbalance data. A data augmentation module is present in the model is used to generate real time image data. In recent years some of the best improvements of CNN in imbalanced datasets can be found in mammal detection from UAV dataset [52], Marine image classification [53], sewer damage detection from CCTV images [54] and automatic bird detection [55].

4 Experimental Analysis

The most commonly known metric to evaluate a model's performance is Accuracy. However, highly imbalanced training or testing data provides a biasness to the accuracy [56] and deflects its values. This problem has been coined in various experiments [57, 58] suggesting it to be a very inferior metric to test on imbalanced data. However, some of the most commonly used metrics to evaluated these datasets are Area Under Curve (AUC) and Receiver Operating Characteristic curve (ROC). In [58] the authors suggested that Sensitivity (S_s) and Specificity $\left(S_p\right)$ are undoubtedly an improvement over the Accuracy metric to evaluate the performance classes individually. The metrices can be defined as,

$$S_s = \frac{\epsilon_1}{\epsilon_1 + \epsilon_3} \tag{1}$$

$$S_p = \frac{\epsilon_4}{\epsilon_4 + \epsilon_2} \tag{2}$$

where, ϵ_1 represents True Positive values, ϵ_2 represents False Positive values, ϵ_3 represents False Negative values and ϵ_4 represents True Negative values. However, the authors constructed the G-Mean metric G, for their experiments. The metric can be written as,

$$G = \sqrt[2]{S_p \times S_s} \tag{3}$$

Johnson and Khoshgoftaar [59] also mentioned the accuracy-based evaluation anomalies in their comprehensive study. The authors mentioned that Precision values alone is critically affected by imbalanced distribution. However, Sensitivity values always remains unaffected as it only deals with the positive class. Luque et al. [60] stated the G-Mean metric and the Bookmaker Informedness B_{If}, as the best metrics which provides unbiased performance values. The B_{If} values can be calculated as,

$$B_{If} = S_p + S_s - 1 \tag{4}$$

We are going to concern ourselves with the particular case of Imbalanced Image Classification and compare these metrics that are a good fit for the problem while using CNN as a solution to our classification problem [47]. To document the performance of CNN, in our experiment we concentrated on using CIFAR-10 [61] and Fashion-MNIST [62] datasets. We eliminated data from 4 individual classes in Cifar-10 and 5 individual classes in Fashion-MNIST at similar rates to deliberately achieve imbalance and document the performance deflection. The CNN is trained at 100 epochs.

From Fig. 1a we see that the sensitivity deflection of the CNN for Cifar-10 indicates a downward trend in the metric score hence suggesting an overall reduction of the score with increase in Imbalanced data. However, initially the curve followed a

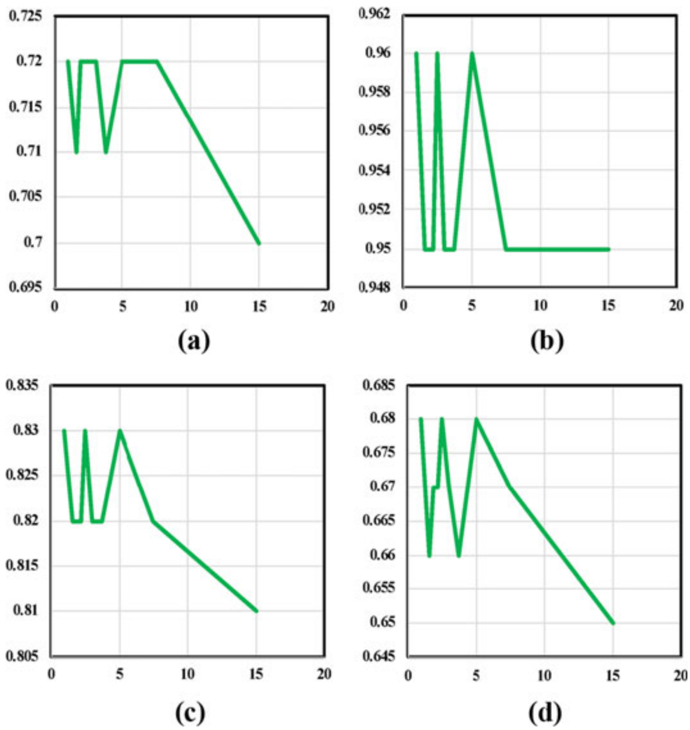

Fig. 1 Performance deflection of CNN for Cifar-10 dataset with the increase in imbalance ratio: **a** sensitivity, **b** specificity, **c** G-Mean and, **d** bookmaker informedness

zigzag trajectory but eventually ended up with a score of 0.7 from an initial recorded score of 0.72 during balanced state. A sharp downward curve of specificity from a score of 0.96–0.95 is also visible from Fig. 1b after crossing an IR value of 5 and an immediate stabilization of deflection indicates a unique characteristic of the data in the prediction of negative cases. From Fig. 1c we see the gradual drop in the G-mean score on crossing an IR value of 5 and eventually recording a deflection in score from 0.83 to 0.81. The deflection curve of the Bookmarker Informedness in Fig. 1d exhibits a trajectory similar to that of the G-Mean. A similar sharp drop in scores are visible after crossing an IR value of 5 recording a deflection from 0.68 to 0.65.

In Fig. 2a the Sensitivity value has a highest count of 0.92 when imbalance ratio is lowest. When the IR is at approximately 2.5, the sensitivity value decreases to 0.91. When the ratio is around 6 it further decreases to 0.89. Finally, when the ratio is approximately 12.5 the count reduces to 0.86. From here we can conclude that the overall sensitivity value decreases in a very rapid pace. Figure 2b suggests that the Specificity value has a highest count of 0.99 when IR is lowest. The specificity count drastically decreases when the IR count increases very little. After this decrease, the specificity count remains constant throughout the increase in imbalance. The G-Mean values exhibits abrupt rise and fall in Fig. 2c. During initial state, the G-Mean

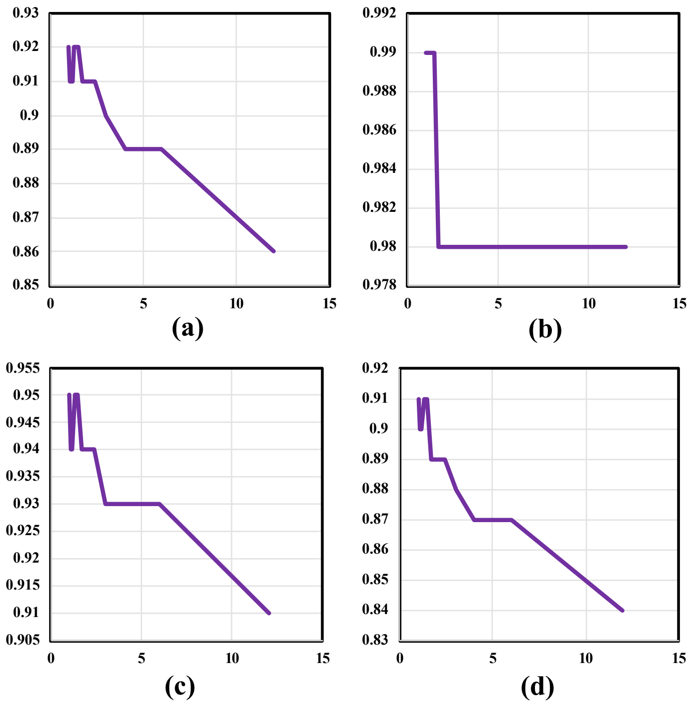

Fig. 2 Performance deflection of CNN for fashion MNIST dataset with the increase in imbalance ratio: **a** sensitivity, **b** specificity, **c** G-Mean and, **d** bookmaker informedness

count is highest, that is 0.95. With the gradual increase in the IR value, the G-Mean value decreases and then again rises. When the IR count is near to 6, the value is constant at 0.93. Finally, the G-Mean count decreases to 0.91 when the IR value is extreme. From Fig. 2d we see that the Bookmaker Informedness value is 0.91 during the balanced condition. It reduces and again increases within a very short interval. Till the imbalance ratio count is near to 6 the value keeps on decreasing after which we can see the value decreasing in a steep way. For the extreme value of IR, the Bookmaker Informedness value is as low as 0.84.

5 Conclusion

The current study evaluated CNNs in presence of imbalance classes. The study involved two artificially modified well known dataset CIFAR-10 and Fashion-MNIST. Multiple classes are perturbed by gradually removing samples and thereby making the dataset more imbalanced every time. The CNN is trained and tested in terms of well known performance metrics namely Sensitivity, Specificity, G-Mean and Bookmaker Informedness which are specifically used to measure classifier performance in presence of imbalanced classes. The results revealed that the performance of CNN is severely affected when the imbalance ratio is increased. In case of CIFAR-10 the performance monotonically decreased after imbalance ratio is increased above 5 and a similar trend is observed for fashion-MNIST above 2.5. Future studies can be focused on developing algorithms to mitigate the performance issue of CNNs in presence of imbalanced classes.

References

1. Längkvist, M., Kiselev, A., Alirezaie, M., Loutfi, A.: Classification and segmentation of satellite orthoimagery using convolutional neural networks. Remote Sens. **8**(4), 329 (2016)
2. Roy, M., Chakraborty, S., Mali, K., Swarnakar, R., Ghosh, K., Banerjee, A., Chatterjee, S.: Data security techniques based on DNA encryption. In: International Ethical Hacking Conference, pp. 239–249. Springer, Singapore (2019)
3. Xu, H., Murphy, B., Fyshe, A.: Brainbench: a brain-image test suite for distributional semantic models. In: Proceedings of the 2016 Conference on Empirical Methods in Natural Language Processing, pp. 2017–2021 (2016)
4. Kang, L., Kumar, J., Ye, P., Li, Y., Doermann, D.: Convolutional neural networks for document image classification. In: 2014 22nd International Conference on Pattern Recognition, pp. 3168–3172. IEEE (2014)
5. Yang, C., Hou, B., Ren, B., Hu, Y., Jiao, L.: CNN-based polarimetric decomposition feature selection for PolSAR image classification. IEEE Trans. Geosci. Remote Sens. **57**(11), 8796–8812 (2019)
6. Choi, J., Hwang, S.J., Sigal, L., Davis, L.S.: Knowledge transfer with interactive learning of semantic relationships. In: Thirtieth AAAI Conference on Artificial Intelligence (2016)
7. Ahmed, M.O., Vaswani, S., Schmidt, M.: Combining bayesian optimization and lipschitz optimization. Mach. Learn. 1–24 (2019)
8. Joty, S., Carenini, G., Ng, R., Murray, G.: Discourse processing and its applications in text mining. In: 2018 IEEE International Conference on Data Mining (ICDM), pp. 7–7. IEEE (2018)
9. Fatemi, B., Kazemi, S.M., Poole, D.: Record Linkage to Match Customer Names: A Probabilistic Approach. arXiv preprint arXiv:1806.10928 (2018).
10. Ghosh, K., Banerjee, A., Chatterjee, S., Sen, S.: Imbalanced twitter sentiment analysis using minority oversampling. In: 2019 IEEE 10th International Conference on Awareness Science and Technology (iCAST), pp. 1–5. IEEE (2019)
11. Liu, X., Mou, L., Cui, H., Zhengdong, Lu., Song, S.: Finding decision jumps in text classification. Neurocomputing **371**, 177–187 (2020)
12. Chatterjee, S., Sarkar, S., Hore, S., Dey, N., Ashour, A.S., Balas, V.E.: Particle swarm optimization trained neural network for structural failure prediction of multistoried RC buildings. Neural Comput. Appl. **28**(8), 2005–2016 (2017)
13. Zhu, F., Ma, Z., Li, X., Chen, G., Chien, J.T., Xue, J.H., Guo, J.: Image-text dual neural network with decision strategy for small-sample image classification. Neurocomputing **328**, 182–188 (2019)
14. Dey, S., Singh, A.K., Prasad, D.K., Mcdonald-Maier, K.D.: SoCodeCNN: program source code for visual CNN classification using computer vision methodology. IEEE Access **7**, 157158–157172 (2019)

15. Li, H., Lin, Z., Shen, X., Brandt, J., Hua, G.: A convolutional neural network cascade for face detection. In: Proceedings of the IEEE Conference on Computer Vision and Pattern Recognition, pp. 5325–5334 (2015)
16. Hu, B., Lu, Z., Li, H., Chen, Q.: Convolutional neural network architectures for matching natural language sentences. In: Advances in Neural Information Processing Systems, pp. 2042–2050 (2014)
17. Liu, P., Chen, W., Ou, G., Wang, T., Yang, D., Lei, K.: Sarcasm detection in social media based on imbalanced classification. In: International Conference on Web-Age Information Management, pp. 459–471. Springer, Cham (2014)
18. Khanchi, S., Vahdat, A., Heywood, M.I., Nur Zincir- Heywood, A.: On botnet detection with genetic programming under streaming data label budgets and class imbalance. Swarm Evol Comput **39**, 123–140 (2018).
19. Li, C., Liu, S.: A comparative study of the class imbalance problem in Twitter spam detection. Concur. Comput.: Pract. Exp. **30**(5), e4281 (2018)
20. Liang, Z., Powell, A., Ersoy, I., Poostchi, M., Silamut, K., Palaniappan, K., Huang, J.X.: CNN-based image analysis for malaria diagnosis. In: 2016 IEEE International Conference on Bioinformatics and Biomedicine (BIBM), pp. 493–496. IEEE (2016)
21. Krizhevsky, A., Sutskever, I., Hinton, G.E.: Imagenet classification with deep convolutional neural networks. In: Advances in Neural Information Processing Systems, pp. 1097–1105 (2012)
22. Wan, J., Wang, D., Hoi, S.C.H., Wu, P., Zhu, J., Zhang, Y., Li, J.: Deep learning for content-based image retrieval: a comprehensive study. In: Proceedings of the 22nd ACM International Conference on Multimedia, pp. 157–166. ACM (2014)
23. Hou, Y., Zhang, H., Zhou, S.: Convolutional neural network-based image representation for visual loop closure detection. In: 2015 IEEE International Conference on Information and Automation, pp. 2238–2245. IEEE (2015)
24. Ji, S., Xu, W., Yang, M., Yu, K.: 3D convolutional neural networks for human action recognition. IEEE Trans. Pattern Anal. Mach. Intell. **35**(1), 221–231 (2013)
25. Li, Q., Cai, W., Wang, X., Zhou, Y., Feng, D.D., Chen, M.: Medical image classification with convolutional neural network. In: 2014 13th International Conference on Control Automation Robotics & Vision (ICARCV), pp. 844–848. IEEE (2014)
26. He, X., Chen, Y.: Optimized input for CNN-based hyperspectral image classification using spatial transformer network. IEEE Geosci. Remote Sens. Lett. (2019)
27. Liu, X., Zhang, R., Meng, Z., Hong, R., Liu, G.: On fusing the latent deep CNN feature for image classification. World Wide Web **22**(2), 423–436 (2019)
28. Peng, Y.Q., Liao, M.X., Song, Y.X., Liu, Z.C., He, H.J., Deng, H., Wang, Y.L.: FB-CNN: feature fusion based bilinear CNN for classification of fruit fly image. IEEE Access (2019)
29. de Matos, J., de Souza Britto, A., de Oliveira, L.E.S., Koerich, A.L.: Texture CNN for Histopathological Image Classification. arXiv preprint arXiv:1905.12005 (2019).
30. Chawla, N.V., Bowyer, K.W., Hall, L.O., Philip Kegelmeyer, W.: SMOTE: synthetic minority over-sampling technique. J. Artif. Intell. Res. **16**: 321–357 (2002)
31. Han, H., Wang, W.-Y., Mao, B.- H.: Borderline-SMOTE: a new over-sampling method in imbalanced data sets learning. In: International Conference on Intelligent Computing, pp. 878–887. Springer, Berlin, Heidelberg (2005)
32. He, H., Bai, Y., Garcia, E.A., Li, S.: ADASYN: adaptive synthetic sampling approach for imbalanced learning. In: 2008 IEEE International Joint Conference on Neural Networks (IEEE World Congress on Computational Intelligence), pp. 1322–1328. IEEE (2008)
33. Bunkhumpornpat, C., Sinapiromsaran, K., Lursinsap, C.: Safe-level-smote: Safe-level-synthetic minority over-sampling technique for handling the class imbalanced problem. In: Pacific-Asia Conference on Knowledge Discovery and Data Mining, pp. 475–482. Springer, Berlin, Heidelberg (2009)
34. Sharma, S., Bellinger, C., Krawczyk, B., Zaiane, O., Japkowicz, N.: Synthetic oversampling with the majority class: a new perspective on handling extreme imbalance. In: 2018 IEEE International Conference on Data Mining (ICDM), Singapore, pp. 447–456 (2018)

35. Bellinger, C., Sharma, S., Japkowicz, N., Zaıane, O.: Framework for Extreme Imbalance Classification SWIM: Sampling With the Majority Class
36. Mari Antonie, M.-L., Zaiane, O.R., Coman, A.: Application of data mining techniques for medical image classification. In: Proceedings of the Second International Conference on Multimedia Data Mining, pp. 94–101. Springer (2001)
37. Ryan, C., Fitzgerald, J., Krawiec, K., Medernach, D.: Image classification with genetic programming: building a stage 1 computer aided detector for breast cancer. In: Handbook of Genetic Programming Applications, pp. 245–287. Springer, Cham (2015)
38. Su, F., Xue, L.: Graph learning on K nearest neighbours for automatic image annotation. In: Proceedings of the 5th ACM on International Conference on Multimedia Retrieval–ICMR '15 (2015)
39. Schaefer, G., Nakashima, T.: Strategies for addressing class imbalance in ensemble classification of thermography breast cancer features. In: 2015 IEEE Congress on Evolutionary Computation (CEC), pp. 2362–2367. IEEE (2015)
40. Pérez-Ortiz, M., Sáez, A., Sánchez-Monedero, J., Gutiérrez, P.A., Hervás-Martínez, C.: Tackling the ordinal and imbalance nature of a melanoma image classification problem. In: 2016 International Joint Conference on Neural Networks (IJCNN), pp. 2156–2163. IEEE (2016)
41. Dai, B., Xiangqian, Wu., Wei, Bu.: Retinal microaneurysms detection using gradient vector analysis and class imbalance classification. PLoS ONE **11**(8), e0161556 (2016)
42. Lee, H., Park, M., Kim, J.: Plankton classification on imbalanced large scale database via convolutional neural networks with transfer learning. In: 2016 IEEE International Conference on Image Processing (ICIP) (2016)
43. Wang, C., Yu, Z., Zheng, H., Wang, N., Zheng, B.: CGAN-plankton: towards large-scale imbalanced class generation and fine-grained classification. In: 2017 IEEE International Conference on Image Processing (ICIP), pp. 855–859. IEEE (2017)
44. Mahmood, A., Bennamoun, M., An, S., Sohel, F., Boussaid, F., Hovey, R., Kendrick, G., Fisher, R.B.: Coral classification with hybrid feature representations. In: 2016 IEEE International Conference on Image Processing (ICIP), pp. 519–523. IEEE (2016)
45. Rahman, Md.A., Wang, Y.: Optimizing intersection-over-union in deep neural networks for image segmentation. In: International Symposium on Visual Computing, pp. 234–244. Springer, Cham (2016)
46. Geng, M., Wang, Y., Tian, Y., Huang, T.: CNUSVM: hybrid CNN-uneven SVM model for imbalanced visual learning. In: 2016 IEEE Second International Conference on Multimedia Big Data (BigMM), pp. 186–193. IEEE (2016)
47. Yue, S.: Imbalanced malware images classification: a CNN based approach. arXiv preprint arXiv:1708.08042 (2017).
48. Sahu, M., Mukhopadhyay, A., Szengel, A., Zachow, S.: Addressing multi-label imbalance problem of surgical tool detection using CNN. Int. J. Comput. Assist. Radiol. Surg. **12**(6), 1013–1020 (2017)
49. Li, F., Li, S., Zhu, C., Lan, X., Chang, H.: Cost-effective class-imbalance aware CNN for vehicle localization and categorization in high resolution aerial images. Remote Sens. **9**(5), 494 (2017)
50. Yang, H., Luo, L., Jing, Su., Lin, C., Bei, Yu.: Imbalance aware lithography hotspot detection: a deep learning approach. J. Micro/Nanolith. MEMS MOEMS **16**(3), 033504 (2017). https://doi.org/10.1117/1.JMM.16.3.033504https://doi.org/10.1117/1.JMM.16.3.033504
51. Pouyanfar, S., Tao, Y., Mohan, A., Tian, H., Kaseb, A.S., Gauen, K., Dailey, R. et al.: Dynamic sampling in convolutional neural networks for imbalanced data classification. In: 2018 IEEE Conference on Multimedia Information Processing and Retrieval (MIPR), pp. 112–117. IEEE (2018)
52. Kellenberger, B., Marcos, D., Tuia, D.: Detecting mammals in UAV images: best practices to address a substantially imbalanced dataset with deep learning. Remote Sens. Environ. **216**, 139–153 (2018)
53. Langenkämper, D., van Kevelaer, R., Nattkemper, T.W.: Strategies for tackling the class imbalance problem in marine image classification. In: International Conference on Pattern Recognition, pp. 26–36. Springer, Cham (2018)

54. Li, D., Cong, A., Guo, S.: Sewer damage detection from imbalanced CCTV inspection data using deep convolutional neural networks with hierarchical classification. Autom. Constr. **101**, 199–208 (2019)
55. Niemi, J., Tanttu, J.T.: Deep learning case study on imbalanced training data for automatic bird identification. In: Deep Learning: Algorithms and Applications, pp. 231–262. Springer, Cham (2020)
56. Buda, M., Maki, A., Mazurowski, M.A.: A systematic study of the class imbalance problem in convolutional neural networks. Neural Netw **106**, 249–259 (2018)
57. Sarkar, S., Khatedi, N., Pramanik, A., Maiti, J.: An ensemble learning-based undersampling technique for handling class-imbalance problem. In: Proceedings of ICETIT, pp. 586–595. Springer, Cham (2020)
58. Tang, Y., Zhang, Y.-Q., Chawla, N.V., Krasser, S.: SVMs modeling for highly imbalanced classification. IEEE Trans. Syst. Man, Cybern. Part B (Cybernetics) **39**(1): 281–288 (2008)
59. Johnson, J.M., Khoshgoftaar, T.M.: Survey on deep learning with class imbalance. J. Big Data **6**(1), 27 (2019)
60. Luque, A., Carrasco, A., Martín, A., de las Heras, A.: The impact of class imbalance in classification performance metrics based on the binary confusion matrix. Pattern Recognit. **91**, 216–231 (2019)
61. Yang, L., Bankman, D., Moons, B., Verhelst, M., Murmann, B.: Bit error tolerance of a CIFAR-10 binarized convolutional neural network processor. In: 2018 IEEE International Symposium on Circuits and Systems (ISCAS), pp. 1–5. IEEE (2018)
62. Xiao, H., Rasul, K., Vollgraf, R.: Fashion-mnist: a novel image dataset for benchmarking machine learning algorithms. arXiv preprint arXiv:1708.07747 (2017)

Smart Plant Monitoring System Using BLYNK Application

Abhinandan Mohanty and Sreyashi Roy

Abstract Plant monitoring is seen as one of the most important tasks in any farming or agriculture based environment. This paper automates plant monitoring and smart gardening using IoT in the NodeMCU system platform. The main purpose of this paper is to provide comfort to the farmer by reducing the manual work by improving the overall performance of the system without the user's direct interaction. The important parameters for the quality and productivity of plant growth are soil and air temperature, humidity, sunlight and soil moisture. The plant health and growth information has to be provided to the user continuously by monitoring and recording these garden parameters. All the sensors used in this project are interfaced with the NodeMCU. And this information about the plant can be directly monitored and controlled by the farmer through their smart phone using IoT. This smart gardening system will provide convenience and comfort to the user by sensing and controlling the parameters of the plants without their physical presence. Any android supported device can be used to install the smart gardening application. The softwares used are Arduino IDE & Blynk IoT platform. Ardunio IDE is used for compling and uploading the programe to NodeMCU and Blynk IoT platform is used for displaying of temperature, humidity, atmospheric pressure & soil moisture and can be accessed from any distance. This will help the farmer to understand the relation between the plant growth and mentioned plant parameters.

Keywords Blynk app · BPM180 · DHT11 · ESP8266 · Home gardening · Humidity detector · Internet of things (IoT) · Soil wetness detector · Temperature detector · Weather monitoring system · Wireless sensor network

A. Mohanty · S. Roy (✉)
School of Electronics Engineering, (Deemed To Be University), Kalinga Institute of Industrial Technology, Bhubaneswar, Odisha, India
e-mail: sreyashi.royfet@kiit.ac.in

A. Mohanty
e-mail: abhinandanmohanty28@gmail.com

S. Banerjee and J. K. Mandal (eds.), *Advances in Smart Communication Technology and Information Processing*, Lecture Notes in Networks and Systems 165,
https://doi.org/10.1007/978-981-15-9433-5_19

1 Introduction

Nowadays everything can be controlled and worked automatically. But there are yet a couple of significant parts in our nation where mechanization has not been received or on the other hand has not been put to an undeniable use, maybe in light of a few reasons one such explanation is cost. One of such field is agriculture. Agribusiness has been one of the basic occupations of the man since early improvements and even today manual intercessions in developing are unavoidable. Plant checking structure a critical bit of the agribusiness and development zones in our country as they can be used to create plants under controlled climatic conditions for perfect production. Robotizing a plant means watching and controlling of the climatic parameters which authentically or by suggestion direct the plant improvement and thus their produce. Robotization is a process control of present day device and methodology, right now human directors. In this paper plant monitoring system technology is provided by the feedback to the user through smart phone. The automated system will reduce the need of man power hence reducing the error. For a large scale area, it is possible for a farmer to monitor the efficiency of the system by implementing this technology by using their smart phones.

2 Literature Review

The most important factors for the quality and productivity of plant growth are temperature, humidity, light and the level of the carbon dioxide. Continuous monitoring of these environmental variables gives information to the grower to better understand, how each factor affects growth and how to manage maximal growth of plants. Climate control and monitoring of the plant is one of important aspects in agriculture [1, 2, 3]. The aspects we are presenting resembles the concept of precision agriculture, this is the trend of farming presented in recent years for commercial and research agriculture. In the precision agriculture framework the main focus is on understanding the environment through the interpretation of a wide variety of data coming from GPS systems, satellite imaging, and in-field sensors. Cypress is one of top semiconductor company in the world. Currently they have envisioned the scope by moving towards Internet of Things, with the major focus on "Internet of plants" [4]. The main motivation of the project is for the user to monitor the plants or cultivation to get enough resources such as light and water without the user need to be present at the plants or cultivation area, and also could manipulate the resources provided to the plants depending on the climate of the plant's location (Example: if there is enough rain or moisture for the day, the sensor in the soil would detect accordingly for the operation to begin and intimate the user). This could help user not only to give the resources to the plants everyday without much manual effort also helps the constant and healthy growth of a plant [5–10].

3 Basic Concepts

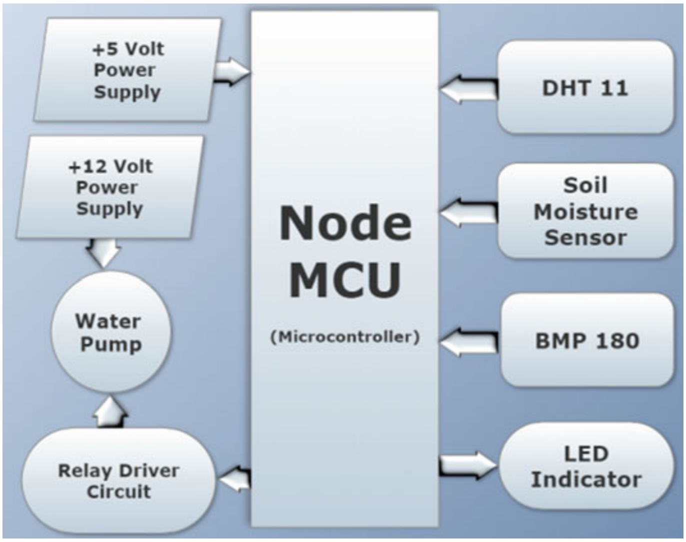

Fig. 1 Technical block diagram

The block diagram for the project is shown in Fig. 1. It consists of a power circuit which gives +5 V and +12 V for various components operations. Node MCU is the micro-controller to which +5 V power is supplied. Other sensors and components like DHT11 (Temperature and Humidity sensor), soil moisture sensor, BMP180 (Barometric Pressure/Temperature/Altitude Sensor), LED indicator, relay driver circuit and water pump (connected to +12 V power supply) are also connected to Node MCU.

The DHT11 and BMP180 sensor senses various environmental parameters and send signal to the micro-controller. The soil moisture sensor will sense the moisture of the soil and sends the signal to the micro-controller whenever the moisture level goes up or down.

LEDs give outputs in different conditions of the moisture content in soil and there is a relay drive circuit which act as switch to control the pump for supplying water from the water source. Whenever the pump get signal that there is low moisture present in the soil it will automatically start. When the moisture level will maintain in the soil automatically the pump will stop. Here the pump is connected to +12 V power supply (connected only to the pump and to the Relay driver system).

A. Node MCU

Node MCU is an open source IoT platform [11]. It has been selected as the controller for this system due to its compact size, compatibility, easy interfacing over several other types of controller including, (PCI) Programmable Integrated Circuit and others. It built on top of the chip manufacturer's proprietary SDK. The firmware provides a simple programming environment [12], which is a very simple and fast scripting language on a standard circuit board. The board has a built-in USB port that is already wired up with the chip; a hardware reset button, Wi-Fi antenna, LED lights, and standard-sized GPIO (General Purpose Input Output) pins that can plug into a bread board. Figure 2 shows the diagram of NODEMCU (ESP8266). It has Processor called L106 32bit RISC microprocessor core based on the Tensilica Xtensa Diamond Standard 106 Micro running at 80 MHz and has a memory of 32 KB instruction RAM, 32 KB instruction cache RAM, 80 KB user data RAM &16 KB system data RAM. It has inbuilt Wi-Fi module of IEEE 802.11 b/g/n Wi-Fi [13].

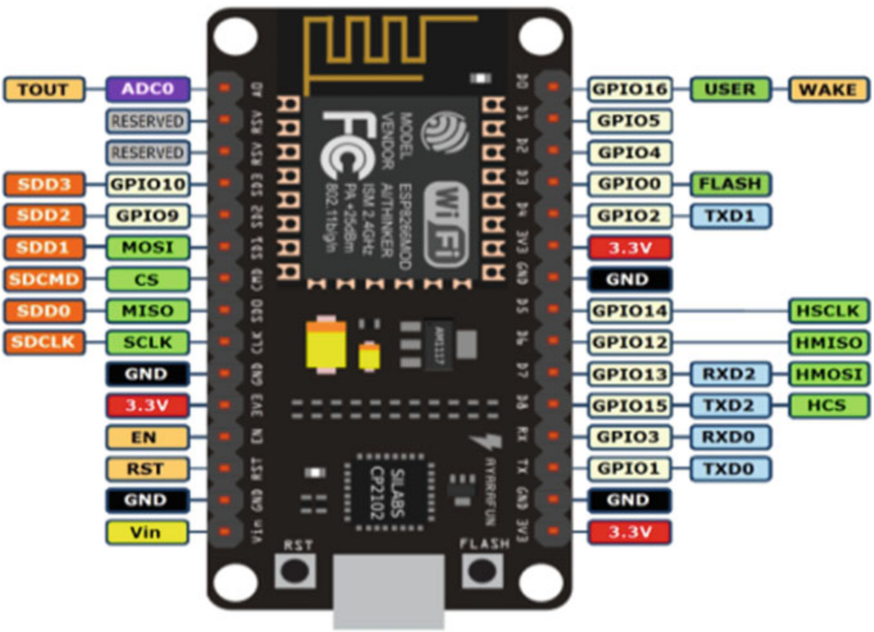

Fig. 2 Node MCU pin configuration

B. Relay Driver Circuit

The relay is an electrically controlled device which performs the actions of a switch. Relays can be broadly classified into two type's namely electro-mechanical relays (EMR) and solid state relays (SSR) here we have used the former one. Contacts in EMR are opened and closed with the help of magnetic force whereas in SSR switching is completely electronic and no contacts are present [14]. The principle behind its working is that of an Electromagnet operating as a switch mechanically. Generally, we use relays where it is important to control another circuit using a different low power signal or where multiple circuits are to be controlled using one signal. Here we are using a single pole double throw relay. Because of its internal configuration, SPDT has quite many applications, it has two different configuration terminals and a common terminal: one of which is normally closed while the other being normally open. Therefore SPDT is capable of performing the action of switching between two circuits i.e. when no voltage is being applied to the coil, current is received by one of the circuits whereas the other doesn't and vice versa when the coil is energized. In general, control circuit handling smaller currents are switched by relays. In addition, with the help of amplification even larger voltage and amperes can be controlled by it.

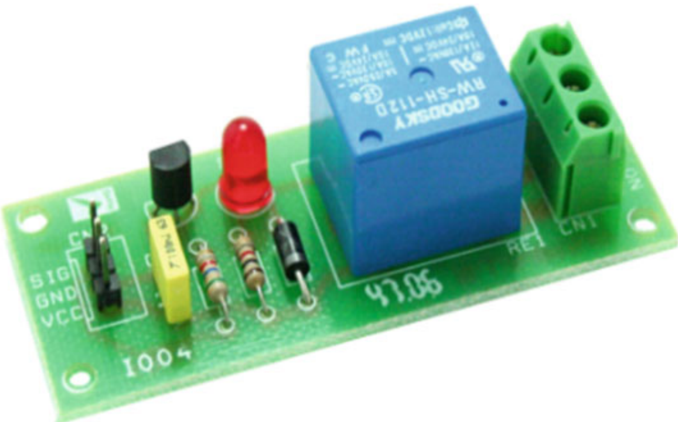

Fig. 3 Relay driver circuit

C. DHT11 (Temperature and Humidity) sensor

It has a humidity measuring module, a thermistor and an integrated circuit on the back of the sensor unit. The humidity measurement module consists of two electrodes. Sandwiched between the two electrodes is a substrate that is capable of holding moisture. Change in humidity alters the conductivity of the moisture holding substrate which at the same time changes the resistance. The integrated circuit then processes the change in the resistance and humidity value is measured [15].

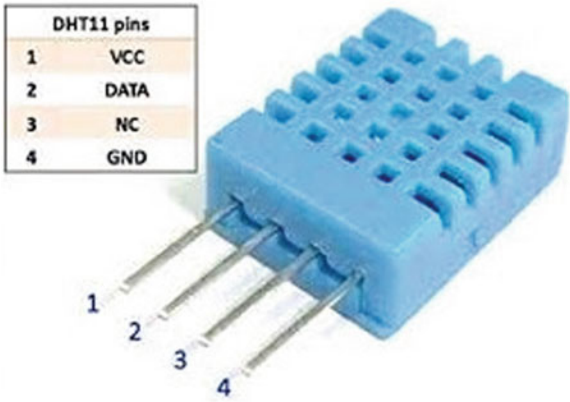

Fig. 4 DHT11 (Temperature and Humidity) sensor

On the other hand, change in temperature changes the resistance of the thermistor which is processed by the integrated circuit and the calibration results into a value of the temperature.

D. FC-28 Soil Moisture Hygrometer Sensor

Two probes estimate the volumetric content of water in the soil. Current passes through the soil and then through the probes, after which the moisture value is calculated based on the resistance offered. In more water, soil becomes more conductive and which means resistance decreases [16]. Therefore moisture value displayed is higher. Dry soil is a poor electricity conductor, so, less moisture means less conduction of electricity. Therefore, the moisture level is lessened [17].

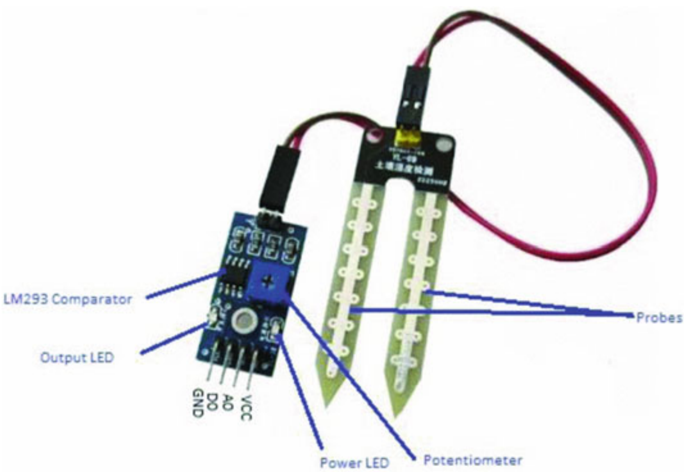

Fig. 5 Soil moisture sensor

E. Pump

A pump is basically a device which uses mechanical action to transfer fluid (liquids). The mechanism used in a pump is mainly reciprocating or rotary and in order to do this mechanical work, they also consume some energy. Pumps are available in varying sizes ranging from smaller pumps used for medical purposes to larger ones used in industries. Figure 6 depicts the Pump which has been used. Here we have used a mini dc pump which runs on 12 V dc supply. Pumps can be operated manually or using electricity. Some are also operated using engines and power generated from the wind [18].

Fig. 6 Water pump

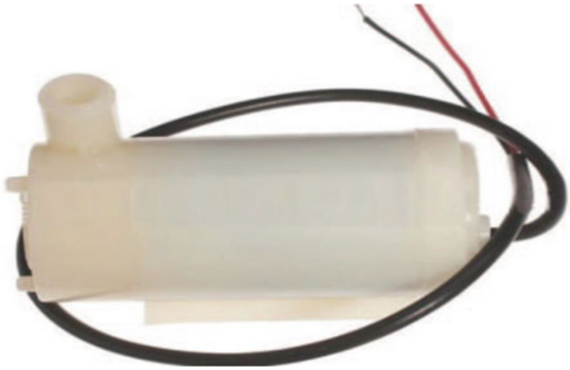

F. Barometric Pressure Module Sensor

Barometric Pressure Module Sensor is an important component for creating a weather station system. The main function of the barometric pressure module sensor is to calculate the atmospheric pressure. The unit for atmospheric pressure is in hPa. This sensor can detect the altitude from the sea level. For the distances, the unit for measurement is in the meter. Lastly, this barometric pressure can detect the temperature surrounding. For this project, BMP180 will be used as it is the most stable version. To test the temperature, it needs to be compared with DHT11 as the testing will be conducted at the room temperature. Table 1 shows the barometric pressure value with the types of environment. Figure 7 shows the image of a sample of barometric pressure sensor.

Table 1 Barometric pressure and environment

Environment	Value (MB)	Online database (MB)
Cloudy day	1011	1009
Light rain	1010	1009
Rainy	1010	1008
Night	1014	1012

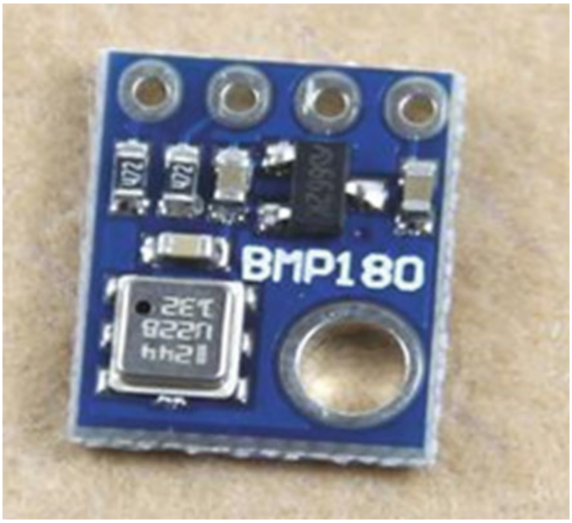

Fig. 7 Barometric pressure sensor

4 Methodology

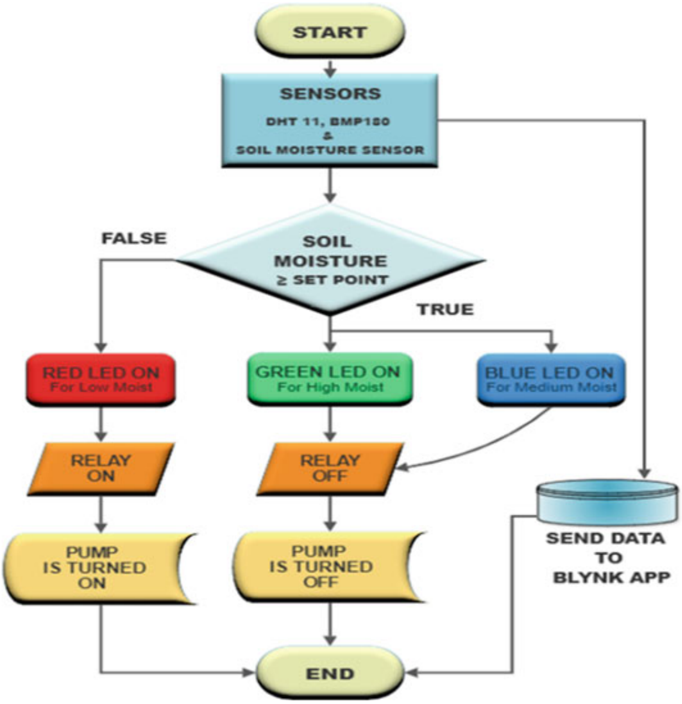

Fig. 8 Algorithm depicting the working principle

According to the given algorithm, DHT11 (Temperature and Humidity), BMP180 (Barometric Pressure/ Temperature/ Altitude Sensor) And Soil Moisture Sensor set first and send the various environmental measured parameters to Blynk App. In order to control the soil moisture level water pump is used. When the moisture level is less than the moist set point, Red LED glows. A Relay module is interfaced to NodeMCU at the receiver end while on the transmitter end, a set point on the soil moisture sensor is considered. If the moisture of the soil falls below the set-point, the relay switches on and allows the Water pump to conduct and supply water to the crop fields. When the moist level get close to the medium set point a blue LED continues to glow. Once the required moisture level is reached, the soil moisture sends the signal to the relay module via NodeMCU. The relay switches off and thus switching off the water pump and green LED get glow to indicate the moisture is at maximum level.

It shows how the control shifts from the soil moisture sensor to the pump depending upon whether the soil moisture is the same as required by the crop.

5 Implementation and Results

A. Implementation

Implementation of smart plant monitoring system using BLYNK Application is done using NodeMCU micro-controller chip via Wi-Fi [19, 20]. For the user interface, we are using Android version BLYNK Application through which user can monitor the gardens or farms easily from anywhere in the world (Fig. 9).

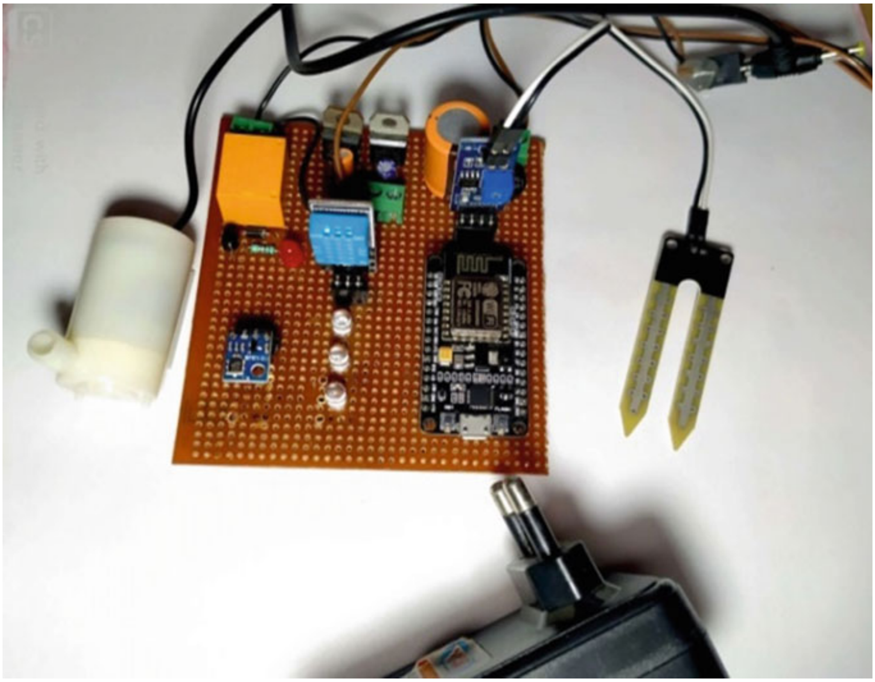

Fig. 9 Hardware implementation

B. Results

Results have been obtained after the successful implementation of the circuitry. Figure 10 shows the design view of the android application. In this Gardening Automation, soil moisture, temperature and humidity are measured by using DHT11 sensor and BMP180 and the live results are clearly viewed in the Blynk Application. Soil Threshold value can be manually adjusted by analyzing the soil.

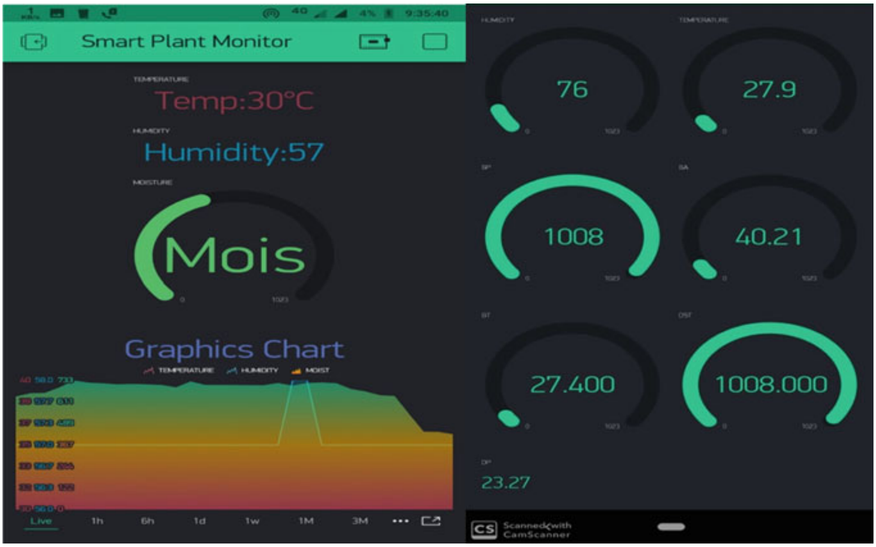

Fig. 10 Measured parameters on blynk app

Table 2 Comparison among the projects

Project name	Soil moisture sensor	Temperature sensor	Barometric pressure sensor	Led Indicators for soil moisture	Humidity sensor
Smart Gardening Automation using IoT With BLYNK App	Yes	Yes	No	No	Yes
An IoT-based Smart Garden with Weather Station System	Yes	Yes	Yes	No	Yes
Smart Plant Monitoring System Using BLYNK Application (Proposed work)	Yes	Yes	Yes	Yes	Yes

6 Conclusion

The capable automation on watching and control of the plants require new and dynamic game plans. Remote sensor frameworks can respond to essential by offering an exact and viably configurable watching structure. In this work, the DHT11, BMP180 and Soil moisture sensor are used. This is the prototype for monitoring and control system for plants. Unlike other automated system which relies on automated data, this model is more intelligent to utilize the resources according to the changes in weather conditions. This proposed model has the capability to integrate with any mobile platform.

This proposed model is made to help the farmers and make their gather moderate by helping them in security reason traveling side, school and for each body, etc. By this work, the wastage of water and the use of power by motor can be diminished with the objective that they are proportioned for the future use. This structure gives all out watching action of sensors in fields that are definitely not hard to control the field. It moreover gives epic security to the plants.

7 Future Scope

The performance of the system can be improved by increasing operating speed, memory capacity of the micro-controller by using other high end controllers. The quantity of channels can be expanded to interface progressively number of sensors.

References

1. Binti Sulaiman, N.A., Bin Sadli, N.D.D.: An IoT-based smart garden with weather station system (2019)
2. Susmitha, P., Bala, G.S.: Design and implementation of weather monitoring and controlling system. Int. J. Comput. Appl. **97**, 19–22 (2014)
3. Naik, P., et al.: Arduino based automatic irrigation system using IoT. Int. J. Sci. Res. Comput. Sci. Eng. Inf. Technol. (IJSRCSEIT) **2**(3), 881–886 (2017)
4. Cypress. https://www.cypress.com/blog/corporate/futureiotarchitectures-cypress-based-hands-graduate-class
5. Kumar, R., Gautam, H.R.: Climate change and its impact on agricultural productivity in India. J. Climatol. Weather. Forecast. **2**(1), 2–4 (2014)
6. Gainwar, S.D., Rojatkar, D.V.: Soil parameter monitoring with auto-matic irrigation system. Int. J. Sci., Eng. Technol. Res. **IV**(11) 2015
7. Fisher, D.K., Kebede, H.: A low-cost microcontroller-based system to monitor crop temperature and water status. Comput. Electron. Agric. **74**(1), 168–173 (2010). https://doi.org/10.1016/j.compag.2010.07.006[CitationTime(s):1]https://doi.org/10.1016/j.compag.2010.07.006[CitationTime(s):1]
8. Vellidis, G., Tucker, M., Perry, C., Kvien, C., Bednarz, C.: A real-time wireless smart sensor array for scheduling irrigation. Comput. Electron. Agric. **61**(1), 44–50 (2008). https://doi.org/10.1016/j.compag.2007.05.009https://doi.org/10.1016/j.compag.2007.05.009
9. Sinha, B.S.K., Singh, B., Gupta, A.K.:IOT based smart garden monitoring system. Int. J. Sci. Eng. Res. (2017)
10. TongKe, F.: Smart Agriculture Based on Cloud Computing and IOT. J. Converg. Inf. Technol. **8**(2) (2013)
11. https://en.wikipedia.org/wiki/NodeMCU
12. Arduino.: AnOpen-Source Electronics Prototyping Platform (2012). https://www.arduino.cc. [Citation Time(s):2]
13. Srivastava, P., Bajaj, M., Rana, A.S.: Overview of ESP8266 Wi-Fi module based smart irrigation system using IOT,In: IEEE (AEEICB-18) (2018)
14. https://circuitdigest.com/article/relay-working-types-operationapplications
15. https://www.instructables.com/id/Interface-DHT11-Humidity-Sensor-Using-NodeMCU/
16. Vagulabranan, R., Karthikeyan, M., Sasikala, V.: Automatic irrigation system on sensing soil moisture content. Int. Res. J. Eng. Technol. **3**(1), 2012–2019 (2015)
17. https://www.instrumentchoice.com.au/emails/Monthly%20Newsletter/10-5-16/soilmoisture-sensors-and-how-they-work
18. https://www.globalspec.com/learnmore/flow_control_flow_transfer/pumps/dc_pumps
19. Sheth, M., Rupani, P.: Smart gardening automation using IoT with BLYNK app. In: Third International Conference on Trends in Electronics and Informatics (2019)
20. Blynk (2017). https://www.blynk.cc/

Performance Improvement of Convolutional Neural Network Using Random Under Sampling

Kushankur Ghosh, Arya Sarkar, Arghasree Banerjee, and Sankhadeep Chatterjee

Abstract With the advent of Convolutional Neural Networks, the image classification tasks have become easier to tackle. Numerous applications have been reported that successfully utilized image classification techniques based on CNNs. Recent studies reported that the presence of imbalanced classes in the training data might affect the performance of the CNN to a greater extent. Motivated by this, the current study proposes a Random Under Sampling (RUS) based method to overcome the problem of imbalanced classes. The existing RUS based method has been modified accordingly to make it suitable for the current application. To analyze the performance of the CNN, two modified well-known datasets have been used for training and testing. Further, different degrees of under sampling have been used to better understand the appropriate under sampling ratio required to achieve acceptable improvement. Results have indicated that the RUS based method has been able to significantly improve CNNs performance in terms of sensitivity, G-mean.

Keywords CNN · Under sampling · Image classification

K. Ghosh · A. Sarkar · A. Banerjee · S. Chatterjee (✉)
Department of Computer Science & Engineering, University of Engineering & Management, Kolkata, India
e-mail: chatterjeesankhadeep.cu@gmail.com

K. Ghosh
e-mail: kush1999.kg@gmail.com

A. Sarkar
e-mail: aryasarkarwork@gmail.com

A. Banerjee
e-mail: banerjeearghasree@gmail.com

S. Banerjee and J. K. Mandal (eds.), *Advances in Smart Communication Technology and Information Processing*, Lecture Notes in Networks and Systems 165,
https://doi.org/10.1007/978-981-15-9433-5_20

1 Introduction

Images have become a common entity in the day-to-day lives of any person linked to the internet. These images help to galvanize the course of any possible work. Intelligent socially-aware systems can also play a very vital role to manage and ease these works. Recently, various examples of socially-aware systems have been created, studied and modified by various researchers [1–4]. Systems that learn from images are very prominent examples of socially-aware systems. Image-based learning is implied mostly on social problems occurring in real life [5–8]. In recent years efficient models for image segmentations have been thoroughly studied and experimented [9–15] and have become one of the most widely implemented models of the past decade and it is being actively integrated by most organizations with different sectors of our lives to make human life easier [9, 16–18].

The class imbalance problem has been a subject of much research since the beginning of the twenty-first century [19]. However, the age-old class imbalance problem is more so a severe problem in these image-based, training approaches due to the adverse effects of negatively skewed data on the predictions involving the minority class, and even more so this problem needs to be dealt with to get more accurate predictions [20, 21]. Now to deal with the imbalance problem, in both text and image-based data there exists many use case-specific as well as general metrics and techniques that have been developed to deal with these kinds of data [22–27]. Under-sampling and Oversampling methods are two of the textbook approved approaches to dealing with an imbalanced dataset and among the two although less used compared to its counterpart, under-sampling is an effective way to tackle missing data.

In simple terms, Random Under-sampling [28] is one such method used to optimize the training data of our model by selecting a set of data from the majority class to create a subset that is equal to the minority class in terms of frequency [29, 30]. An equal magnitude of class data is very important to train accurate image classification models and to tackle that problem, under-sampling provides a solution [31]. The approach has been proved to be effective to tackle various imbalanced datasets and has been studied thoroughly over many decades [32–34].

2 Proposed Approach

Dealing with real-world datasets be it image or text leads to the encounter of some challenges that need to be overcome to avoid discrepancies in our predictive models. The Class Imbalance Problem [35] occurs when some classes have a much higher or lower magnitude of data than the other classes. In simpler terms, it is a machine learning problem caused due to uneven magnitudes of data that greatly affect the credibility of our predictive models by negatively or positively skewing our data towards a particular result that may not be as dominant in real-world scenarios.

From Fig. 1 the disparity in the data can be visualized, which indicates that the

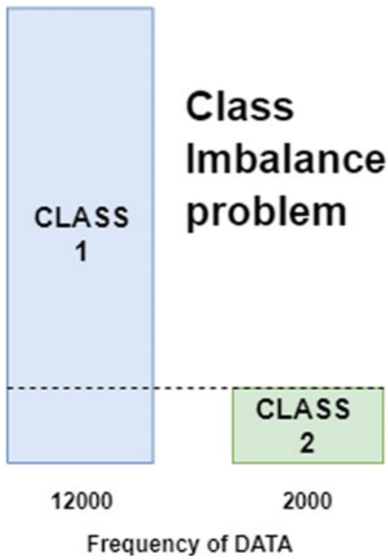

Fig. 1 Representation of an imbalanced dataset having a majority and a minority class

predictive model will be greatly inclined towards the majority class which does not do justice to our requirements. The imbalance in the magnitudes of data between the classes needs to be optimized to have a better prediction. An imbalanced dataset can cause many problems while training a model [36]. If a model is trained using an imbalanced class the predictions have a higher chance of being skewed towards the majority class. This problem needs to be addressed before training the model to avoid a prediction which is largely biased towards the majority class [37]. Image Classification suffers even more so from imbalanced data due to the sensitive nature of image-based classification models [38]. Small errors in many image classification models can greatly harm human lives as many of these models are greatly used in the medical sector, so dealing with the imbalance problem is even more so of utmost importance [39–41]. In our model, we handle the class imbalance which takes place in images due to the presence of a majority class and a minority class. We have taken binary classes for our experiment and in order to have a balance between the two classes we under-sample the majority class. This approach can be explained by three steps as shown with the help of the diagram Fig. 2. The first step being the data preparation, the imbalance is created between the two classes. In the next step, we tackle the imbalance problem by concentrating on the majority class and the resultant data is fed to the Convolutional Neural Networks algorithm.

Fig. 2 Flow-diagram of our model

2.1 Data Preparation

For our model, we concentrated on using the Cifar-10 [42] dataset and the cats and dogs [43] dataset. We deliberately made both the dataset imbalanced to show the effectiveness of our model. Cifar-10 is a widely used dataset containing 10 separate classes each having 5000 images of that class. However, for our model we merged the 10 existing classes into 2 separate classes in a way so that one class represents the non-living beings and another represents the living beings. To obtain an imbalanced class distribution we further removed the images of 2 non-living classes from the training dataset, which initially were in the class represented by truck and ship. The majority class or the living class ended up with a count of 30,000 samples whereas the non-living class which is the minority class ended up with 10,000. We also make use of the cats and dogs dataset which is another famous dataset comprising image samples of dogs and cats. We skew the pre-balanced dataset towards dogs by reducing the number of samples from the cat class and hence, creating a class imbalance problem like in the previous dataset to test our model.

2.2 Random Under Sampling (RUS)

Under-sampling techniques are one of the most widely used methods to deal with the class imbalance problem that occurs due to the difference in the magnitude of data in different classes [44]. A disparity between the magnitude of the majority and minority class can be amended with ease using one of the many methods [44–46] available. Random Under Sampling (RUS) is one such method that can be used to deal with the class imbalance problem. As the name suggests, it's an under-sampling technique that randomly selects instances from the majority class by resizing the total number of elements in it to roughly match the minority class thereby reaching an equilibrium state between the classes which is our ideal condition to get rid of the class imbalance problem and train our models to have the most accurate prediction. It has been widely tested and implemented in several instances both text and image-based and great results have been obtained from various sources [47, 48] indicating its viability as a good boosting algorithm to improve the predictive model by overcoming the class imbalance problem.

2.3 Convolutional Neural Network (CNN)

Convolutional Neural Network, popularly called CovNETs, is one of the hottest research topics for over a few decades ever since it was coined by LeCun et al. back in 1989 [49] hence solidifying a major foothold into image recognition and deep learning domain. A neural network cannot be directly implemented on image-based data and language processing due to its limitations to make assumptions regarding the data. This problem is overcome with the use of Convolutional Neural Networks or CovNETs which simplifies complex images and then understands it using the unique Convolutional, Pooling and Fully Connected layers. It's a form of a feed-forward network system where the output of the previous layer is fed to the next and finally to the fully connected layer for the classification of the image data from where the output is identified using the image data. It deals with the management of spatial data and is used today in a variety of areas [50–53] in image classification, big data analysis among many other cases. The extra convolutional layer in a CovNET vastly reduces the training time for the model and reduces the minimum number of samples we require among many other benefits, hence making it very useful in most cases.

Figure 3 represents a schematic diagram of the internal architecture of a convolutional neural network. It consists of several layers that break down the input image and transforms a 3-D input volume to a 3-D output volume. Firstly, the raw pixel value of the image is fed into the convolutional layer where the main computation to calculate the output of the neurons occurs. It then goes through a RELU layer which is responsible for the implementation of element-specific activation functions to keep the volume intact. Next the image is fed into the Pooling layer which performs a downsizing operation on the height and width of the image keeping the depth intact. This sequence is repeated as many times as required and, in the end, the output volume is passed to the Fully Connected Layer, which calculates the class-specific

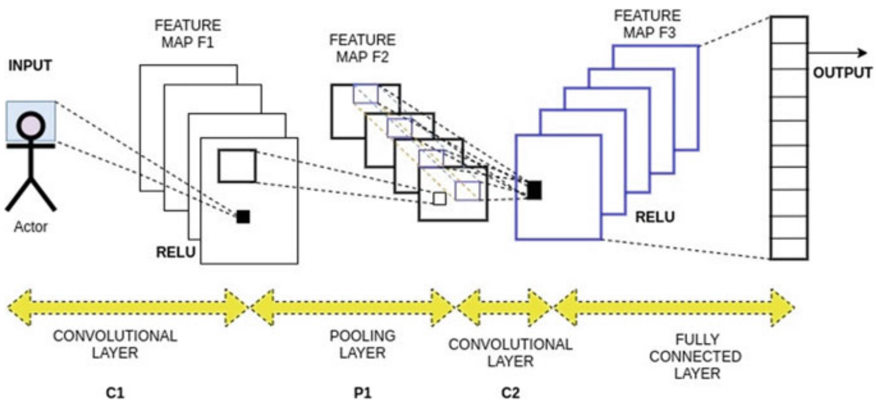

Fig. 3 Schematic diagram of convolutional neural network

scores to determine what the input object actually was based on the dataset we are using.

3 Experimental Analysis

Accuracy is one of the most common metrics used to rate the credibility of machine learning models. Loosely, it can be defined as the total number of successful predictions with respect to the absolute number of predictions made by the model. Let's assume some symbols to define the mathematical formulas of the metrics in a more efficient way. Let, True Positive $= \nabla$, True Negative $= \partial$, False Positive $= \mu$, False Negative $= \omega$ then accuracy, Aq can be defined as,

$$Aq = \frac{\nabla + \partial}{\nabla + \partial + \mu + \omega}$$

Sensitivity is a useful metric when dealing with imbalanced data [54]. The increase in Sensitivity directly influences the prediction by making it more inclined towards the ∇ predictions and decreasing the occurrence of ω. It can be calculated as,

$$Sensitivity = \frac{\nabla}{\nabla + \omega}$$

In simplest terms, Sensitivity can be stated as the correctness of the positive cases and specificity as that of all the negative cases of prediction and has a lot of uses over traditional accuracy metric [55]. The G-mean score, ꝺis another famous metric that overcomes the one-dimensional nature of existing sensitivity and specificity metrices which is the nature of either considering the positive class or the negative class. Mathematically ꝺcan be calculated as,

$$\text{ꝺ} = \sqrt{\frac{\partial}{\partial + \mu} \times \frac{\nabla}{\nabla + \omega}}$$

As stated via multiple sources [56, 57], ꝺis one of the well-studied possible metrics to evaluate a predictive model due to the unchanging nature of sensitivity irrespective of imbalance due to its affiliation with only the positive class whose one-dimensionality is overcome using the ꝺ.

In our experiment we trained our CNN with 100 epochs each time. The cifar-10 and Cats and Dogs datasets in both exhibit an accuracy deflection in Fig. 4a, b over a range with the increase in the percentage of under-sampled data in Fig. 4. The score exhibits a stabilizing trend with the increase of under-sampling quantity and peaks at 50% in Fig. 4a, and 40% in Fig. 4b respectively. However, a 50% under-sampling

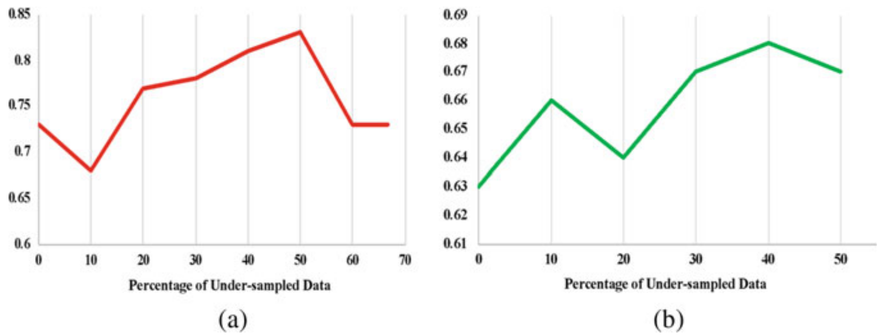

Fig. 4 Accuracy deflection of CNN with the increase in Under-sampling quantity on **a** cifar-10 dataset and, **b** cats and dogs dataset

for the cifar-10 dataset is not always feasible. An improved score is visible for the cats and dogs dataset for 30% under-sampling of the majority class.

From Fig. 5 it is visible that the sensitivity deflection over the range of Fig. 5a, b indicates the nature of the metric which deals with positive classes only. With the increase in the percentage of under-sampled data, the graph seems to stabilize from 60% in Fig. 5a and 40% in Fig. 5b respectively indicating the less occurrence of positive classes in Fig. 5a compared to Fig. 5b. Improved scores are visible after 10% under-sampling for the cifar-10 however, cats and dogs resulted in minimal positive deflection for sensitivity.

From Fig. 6 the deflection of ɔobserved with the gradual increase in the percentage of undersampled data and stabilization after 60% in Fig. 6a and 40% in Fig. 6b indicates a possible correlation with the sensitivity curve in Fig. 2. The highest scores are obtained at 50% under-sampling of the cifar-10 data and 10% under-sample of the cats and dogs dataset. However, 50% reduction of data is not feasible but a 30% under-sampling also yielded an improvement over the imbalanced condition. All the trajectories representing different metrices mostly followed an upward deflection. It is also visible that the deflection of the metrices over the range of under-sampled

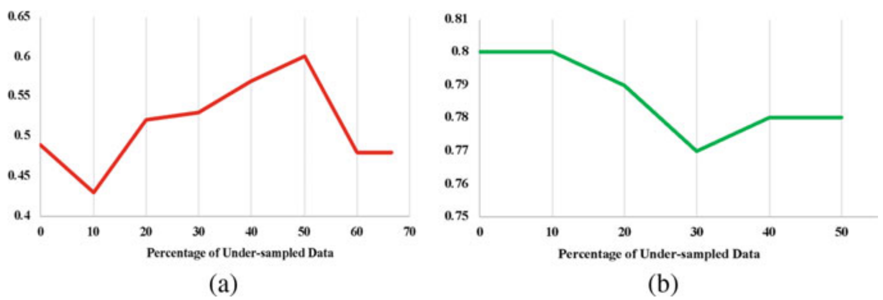

Fig. 5 Sensitivity deflection of CNN with the increase in under-sampling quantity on **a** cifar-10 dataset and, **b** cats and dogs dataset

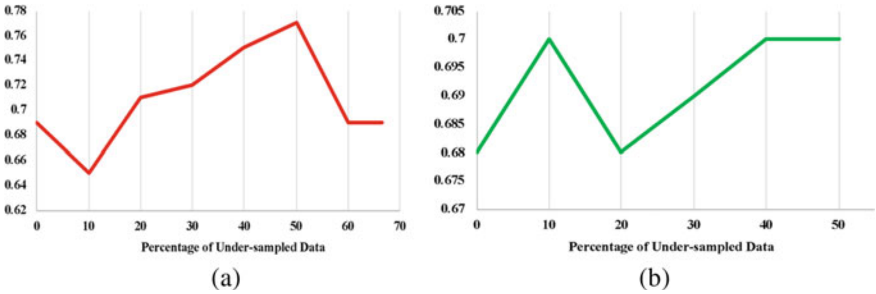

Fig. 6 G-Mean scores deflection of CNN with the increase in under-sampling quantity on **a** cifar-10 dataset and, **b** cats and dogs dataset

data observed indicates that Figs. 1 and 3 gradually become closer with increase in under-sampling quantity in comparison to Figs. 2 and 3, indicating the closeness of Aq deflection with the Ↄdeflection compared to the sensitivity curve deflection hence, highlighting the problem of one-dimensionality of sensitivity.

4 Conclusion

To mitigate the effect of imbalanced classes in image classification using CNNs, a Random Under Sampling based method is proposed. Two artificially perturbed well-known datasets have been used to establish the ingenuity of the proposed RUS based method. Experimental results revealed that the RUS based method improves the performance of the classifier. However, the degree of under sampling is an important issue and found to be affecting the CNN performance. Future research can be focused towards developing more accurate algorithms to combat the issue of imbalanced class problem in image classification by exploring other existing strategies as well as generalizing the already existing method over a broader variety of datasets to establish it as a generic approach to tackle the problem of class imbalance in diverse use cases.

References

1. Chatterjee, S., Sarkar, S., Hore, S., Dey, N., Ashour, A.S., Balas, V.E.: Particle swarm optimization trained neural network for structural failure prediction of multistoried RC buildings. Neural Comput. Appl. **28**(8), 2005–2016 (2017)
2. Ghosh, K., Banerjee, A., Chatterjee, S., Sen, S.: Imbalanced Twitter sentiment analysis using minority oversampling. In: 2019 IEEE 10th International Conference on Awareness Science and Technology (iCAST), pp. 1–5. IEEE (2019)
3. Kundu, S., Maulik, U.: Vehicle pollution detection from images using deep learning. Intelligence Enabled Research, pp. 1–5. Springer, Singapore (2020)

4. Bharadwaj, A., Mehta, D., Kumar, V., Karar, V., Poddar, S.: Neural network-based modeling of radial distortion through synthetic images. Recent Trends in Communication and Intelligent Systems, pp. 175–183. Springer, Singapore (2020)
5. MacLeod, H., Bennett, C.L., Morris, M.R., Cutrell, E.: Understanding blind people's experiences with computer-generated captions of social media images. In: Proceedings of the 2017 CHI Conference on Human Factors in Computing Systems, pp. 5988–5999 (2017)
6. Kadam, S., Rathod, V.: Fractal coding for texture, satellite, and gray scale images to reduce searching time and complexity. Intelligent Engineering Informatics, pp. 253–262. Springer, Singapore (2018)
7. Liu, J., Singh, G., Al'Aref, S., Lee, B., Oleru, O., Min, J.K., Dunham, S., Sabuncu, M.R., Mosadegh, B.: Image registration in medical robotics and intelligent systems: fundamentals and applications. Adv. Intell. Syst. **1**(6), 1900048 (2019)
8. Khadanga, G., Jain, K.: Agriculture parcel boundary detection from remotely sensed images. In: Proceedings of 3rd International Conference on Computer Vision and Image Processing, pp. 307–312. Springer, Singapore (2020)
9. Oktay, O., et al.: Anatomically constrained neural networks (ACNNs): application to cardiac image enhancement and segmentation. IEEE Trans. Med. Imaging **37**(2), 384–395 (2018). https://doi.org/10.1109/TMI.2017.2743464https://doi.org/10.1109/TMI.2017.2743464
10. Lee, M.C.H., Petersen, K., Pawlowski, N., Glocker, B., Schaap, M.: TeTrIS: template transformer networks for image segmentation with shape priors. IEEE Trans. Med. Imaging **38**(11), 2596–2606 (2019). https://doi.org/10.1109/TMI.2019.2905990https://doi.org/10.1109/TMI.2019.2905990
11. Nan, A., Tennant, M., Rubin, U., Ray, N.: DRMIME: differentiable mutual information and matrix exponential for multi-resolution image registration (2020). arXiv:2001.09865
12. Singh, A., Kalke, H., Loewen, M., Ray, N.: River ice segmentation with deep learning (2019). arXiv:1901.04412
13. Pei, Z., Huang, L., Zhang, Y., Ma, M., Yang, Y.H.: Focus measure for synthetic aperture imaging using deep network. IEEE Access **7**, 19762–19774 (2019)
14. Mai, X., Zhang, H., Jia, X., Meng, M.Q-H.: Faster R-CNN with classifier fusion for automatic detection of small fruits. IEEE Trans. Autom. Sci. Eng. (2020)
15. Dey, S., Singh, A.K., Prasad, D.K., Mcdonald-Maier, K.D.: SoCodeCNN: program source code for visual CNN classification using computer vision methodology. IEEE Access **7**, 157158–157172 (2019)
16. Eamthanakul, B., Ketcham, M., Chumuang, N.: The traffic congestion investigating system by image processing from CCTV camera. In: 2017 International Conference on Digital Arts, Media and Technology (ICDAMT), Chiang Mai, 2017, pp. 240–245. https://doi.org/10.1109/ICDAMT.2017.7904969
17. Pathak, B., Pondkule, D., Shaha, R., Surve, A.: Visual cryptography and image processing based approach for bank security applications. In: Smys, S., Senjyu, T., Lafata, P. (eds) Second International Conference on Computer Networks and Communication Technologies. ICCNCT 2019. Lecture Notes on Data Engineering and Communications Technologies, vol. 44. Springer, Cham (2020)
18. Singh, V., Misra, A.K.: Detection of plant leaf diseases using image segmentation and soft computing techniques. Inf. Process. Agric. **4**(1), 41–49 (2017). ISSN 2214-3173
19. Japkowicz, N.: The class imbalance problem: significance and strategies. In: Proceedings of the International Conference on Artificial Intelligence (2000)
20. Zhang, C., Tavanapong, W., Kijkul, G., Wong, J., de Groen, P.C., Oh, J.: Similarity-based active learning for image classification under class imbalance. In: 2018 IEEE International Conference on Data Mining (ICDM), Singapore, pp. 1422–1427 (2018)
21. Chan, R., et al.: Application of decision rules for handling class imbalance in semantic segmentation (2019). arXiv:1901.08394
22. Boughorbel, S., Jarray, F., El-Anbari, M.: Optimal classifier for imbalanced data using Matthews correlation coefficient metric. PLoS One **12**(6), e0177678 (2017). https://doi.org/10.1371/journal.pone.0177678

23. Guo Haixiang, L.Y., Shang, J., Mingyun, G., Yuanyue, H., Bing, G.: Learning from class-imbalanced data: review of methods and applications. Expert Syst. Appl. **73**, 220–239 (2017). ISSN 0957-4174
24. Zeng, M., Zou, B., Wei, F., Liu, X., Wang, L.: Effective prediction of three common diseases by combining SMOTE with Tomek links technique for imbalanced medical data. In: 2016 IEEE International Conference of Online Analysis and Computing Science (ICOACS), Chongqing, 2016, pp. 225–228
25. Hashemi, S.R., Mohseni Salehi, S.S., Erdogmus, D., Prabhu, S.P., Warfield, S.K., Gholipour, A.: Asymmetric loss functions and deep densely-connected networks for highly-imbalanced medical image segmentation: application to multiple sclerosis lesion detection. IEEE Access **7**, 1721–1735 (2019)
26. Wardhani, N.W.S., Rochayani, M.Y., Iriany, A., Sulistyono, A.D., Lestantyo, P.: Cross-validation metrics for evaluating classification performance on imbalanced data. In: 2019 International Conference on Computer, Control, Informatics and its Applications (IC3INA), Tangerang, Indonesia, pp. 14–18 (2019)
27. Xie, Y., Peng, L., Chen, Z., Yang, B., Zhang, H., Zhang, H.: Generative learning for imbalanced data using the Gaussian mixed model. Appl. Soft Comput. **79**, 439–451 (2019). ISSN 1568-4946
28. Yen, S.J., Lee, Y.S.: Under-sampling approaches for improving prediction of the minority class in an imbalanced dataset. In: Huang, D.S., Li, K., Irwin, G.W. (eds.) Intelligent Control and Automation. Lecture Notes in Control and Information Sciences, vol. 344. Springer, Berlin, Heidelberg (2006)
29. Tong, T., Ledig, C., Guerrero, R., Schuh, A., Koikkalainen, J., Tolonen, A., Rhodius, H., Barkhof, F., Tijms, B., Lemstra, A.W., Soininen, H., Remes, A.M., Waldemar, G., Hasselbalch, S., Mecocci, P., Baroni, M., Lötjönen, J., van der Flier, W., Rueckert, D.: Five-class differential diagnostics of neurodegenerative diseases using random undersampling boosting (2017)
30. Liu, B., Tsoumakas, G.: Dealing with class imbalance in classifier chains via random undersampling. Knowl. Based Syst. 105292 (2019). ISSN 0950-7051
31. Sun, Z., Song, Q., Zhu, X., Sun, H., Xu, B., Zhou, Y.: A novel ensemble method for classifying imbalanced data. Pattern Recogn. **48**(5), 1623–1637 (2015). ISSN 0031-3203
32. Liu, X.-Y., Wu, J., Zhou, Z.-H.: Exploratory undersampling for class-imbalance learning. IEEE Trans. Syst. Man Cybern. Part B (Cybernetics) **39**(2), 539–550 (2008)
33. Galar, M., Fernández, A., Barrenechea, E., Herrera, F.: EUSBoost: enhancing ensembles for highly imbalanced data-sets by evolutionary undersampling. Pattern Recogn. **46**(12), 3460–3471 (2013)
34. Wang, Z., Cao, C., Zhu, Y.: Entropy and confidence-based undersampling boosting random forests for imbalanced problems. IEEE Trans. Neural Netw. Learn. Syst. (2020)
35. Amin, A., Anwar, S., Adnan, A., Nawaz, M., Howard, N., Qadir, J., Hussain, A., et al.: Comparing oversampling techniques to handle the class imbalance problem: a customer churn prediction case study. IEEE Access **4**, 7940–7957 (2016). https://doi.org/10.1109/access.2016.2619719
36. Buda, M., Maki, A., Mazurowski, M.A.: A systematic study of the class imbalance problem in convolutional neural networks. Neural Netw. **106**, 249–259 (2018). ISSN 0893-6080
37. Munkhdalai, L., Munkhdalai, T., Ryu, K.H.: GEV-NN: a deep neural network architecture for class imbalance problem in binary classification. Knowl. Based Syst. 105534 (2020)
38. Krawczyk, B., Galar, M., Jeleń, Ł., Herrera, F.: Evolutionary undersampling boosting for imbalanced classification of breast cancer malignancy. Appl. Soft Comput. **38**, 714–726 (2016). ISSN 1568-4946
39. Ding, H., et al.: Plankton image classification via multi-class imbalanced learning. In: 2018 OCEANS—MTS/IEEE Kobe Techno-Oceans (OTO), Kobe, pp. 1–6 (2018)
40. Zhang, Y., et al.: (2019) From Whole Slide Imaging to Microscopy: Deep Microscopy Adaptation Network for Histopathology Cancer Image Classification. In: Shen D. et al. (eds) Medical Image Computing and Computer-Assisted Intervention – MICCAI 2019. MICCAI 2019. Lecture Notes in Computer Science, vol 11764. Springer, Cham

41. Faes, L., Wagner, S.K., Fu, D.J., Liu, X., Korot, E., Ledsam, J.R., Back, T., Chopra, R., Pontikos, N., Kern, C., Moraes, G., Schmid, M.K., Sim, D., Balaskas, K., Bachmann, L.M., Denniston, A.K., Keane, P.A.: Automated deep learning design for medical image classification by healthcare professionals with no coding experience: a feasibility study. The Lancet Digit. Health **1**(5), e232–e242 (2019). ISSN 2589-7500
42. Çalik, R.C., Fatih Demirci, M.: Cifar-10 image classification with convolutional neural networks for embedded systems. In: 2018 IEEE/ACS 15th International Conference on Computer Systems and Applications (AICCSA). IEEE (2018)
43. Gangwar, K., et al.: Classification of image dataset using convolutional neural network. (2019). SSRN 3349594
44. Shelke, M.S., Deshmukh, P.R., Shandilya, V.K.: A review on imbalanced data handling using undersampling and oversampling technique. IJRTER **3**(4) (2017)
45. Bader-El-Den, M., Teitei, E., Perry, T.: Biased random forest for dealing with the class imbalance problem. IEEE Trans. Neural Netw. Learn. Syst. **30**(7), 2163–2172 (2018)
46. Feng, W., Huang, W., Ren, J.: Class imbalance ensemble learning based on the margin theory. Appl. Sci. **8**(5), 815 (2018)
47. Liu, B., Tsoumakas, G.: Dealing with class imbalance in classifier chains via random undersampling. Knowl. Based Syst. 105292 (2019)
48. Hassan, A.R., Haque, Md.A.: An expert system for automated identification of obstructive sleep apnea from single-lead ECG using random under sampling boosting. Neurocomputing **235**, 122–130 (2017)
49. Le Cun, Y., et al.: Handwritten digit recognition: applications of neural network chips and automatic learning. IEEE Commun. Mag. **27**(11), 41–46 (1989)
50. Sung, M., Joe, H., Kim, J., Yu, S.: Convolutional neural network based resolution enhancement of underwater sonar image without losing working range of sonar sensors. In: 2018 OCEANS—MTS/IEEE Kobe Techno-Oceans (OTO), Kobe, pp. 1–6 (2018)
51. Jin, K.H., et al.: Deep convolutional neural network for inverse problems in imaging. IEEE Trans. Image Process. **26**(9), 4509–4522 (2017)
52. Raghavendra, U., et al.: Deep convolution neural network for accurate diagnosis of glaucoma using digital fundus images. Inf. Sci. **441**, 41–49 (2018)
53. Li, G., et al.: Hand gesture recognition based on convolution neural network. Clust. Comput. **22**(2), 2719–2729 (2019)
54. Tang, Y., Zhang, Y.-Q., Chawla, N.V, Krasser, S.: SVMs modeling for highly imbalanced classification. IEEE Trans. Syst. Man Cybern. Part B (Cybern.) **39**(1), 281–288 (2008)
55. Akosa, J.: Predictive accuracy: a misleading performance measure for highly imbalanced data. In: Proceedings of the SAS Global Forum (2017)
56. Luque, A., Carrasco, A., Martín, A., de las Heras, A.: The impact of class imbalance in classification performance metrics based on the binary confusion matrix. Pattern Recogn. **91**, 216–231 (2019). ISSN 0031-3203
57. Kuncheva, L.I., Arnaiz-González, Á., Díez-Pastor, J.-F., Gunn, I.A.D.: Instance selection improves geometric mean accuracy: a study on imbalanced data classification. Prog. Artif. Intell. (2019)

Robust and Atomic Technique for Edge Detection to Identify Edges Present in Digital Image Using DSCTHS Method

Debkumar Chowdhury, Sanjukta Mishra, Sujoy Paul, Sreejit Bagchi, Hazim Ahmed, Trisha Das, and Chinmoy Mandal

Abstract The goal of this research paper is to examine the process and effects of Edge Detection and to propose an effective and standard algorithm for the same Edges are a suburb of honed discontinuity of pixel worth and Edge detection is about discerning those edges. Edge detection is used to extricate the intelligence an image i.e., in both image inspection and managing. To discern edges in an image there are assorted expertise or methodologies unearthed by distinct scientists. Among them some are Robert cross edge detector, Sobel Edge detector, Canny edge detection, Prewitt Edge detection, Palladian of Gaussian, Zero cross edge detection. Each methodology has different Shortcomings like for Robert Edge Detection technique the main drawback is it is much vulnerable to noise, like this, we scrutinized all the edge detection techniques and tried to vanquish the drawbacks in the algorithm that is Executed in this paper. In this paper, we have implemented a newly cultivated edge detection technique and filtration blueprint for detecting edges present in the digital image and removal of noise.

D. Chowdhury · S. Paul (✉) · S. Bagchi · H. Ahmed · T. Das · C. Mandal
University of Engineering and Management, Kolkata, India
e-mail: psujoy09@gmail.com

D. Chowdhury
e-mail: debkumar.cse@gmail.com

S. Bagchi
e-mail: sreejitbagchi@gmail.com

H. Ahmed
e-mail: hazimahmed088@gmail.com

T. Das
e-mail: trisha.uemkcse@gmail.com

C. Mandal
e-mail: chinmoy7365@gmail.com

S. Mishra
Brainware University, Kolkata, India
e-mail: sanjuktamish@gmail.com

S. Banerjee and J. K. Mandal (eds.), *Advances in Smart Communication Technology and Information Processing*, Lecture Notes in Networks and Systems 165,
https://doi.org/10.1007/978-981-15-9433-5_21

Keywords Edge detection · Robert operator · Prewitt operator · Sobel operator · Canny operator · Laplacian operator

1 Introduction

A digital image is an image or delineation constituted digitally i.e., in Category of amalgamation bits (0 or 1) called pixels. Digital image processing is the technology of orchestrating these melding of bits (or pixels) to aggrandize the idiosyncrasy of the image or fabricate contrasting panorama from the image digitally, with the help of computer algorithms. Edge detection is an image processing technique for perceiving the peripheries of objects within images. It works by espying discontinuities in brightness. Edge detection is used for image segmentation and data unsheathing in the area such as image processing, computer vision, and machine vision. Edges are curtly changes in pixel data or can be commutated as consequential local changes of intensity in an image. Edge detection is the process of distinguishing those local discontinuities. A edge detection techniques performs on the actual data content and succor in processing a gargantuan image file. Edges can be classified into different types. They are 1. Step edge 2. Roof edge 3. Line edge. Prewitt Operator—The cardinal advantage of Prewitt operators it's lucidity and ability to apprehend edges and their orientation. Very much is intuitive to noise. Sobel Operator—It gives an imprecise value to the gradient immensity which helps to detect the edges and their orientations. The major disadvantage of the Sobel operator was the signal to noise ratio. With the ameliorate in noise the gradient magnitude of the edges also demeans which breed erroneous results. Robert Operator—It is very meteoric to enumerate the results where only subtraction and addition are applied which regulate the output of each pixel. Its main drawbacks are that since it uses such a small kernel, it is very compassionate to noise. It also engenders very weak Feedback to hypocritical edges unless they are very sharp. Canny Operator—It helps to eliminate the noise in an image with the use of a Gaussian filter. It uses the threshold methods to descry the edges in the noisy state. It proffers superior localization and response. It gives immune to noisy environments. The main drawback of the Canny edge detector is that it is time-consuming, due to its complex computation. Zero-Crossing Operator—It helps to discern the edges and their orientations and it has fixed idiosyncrasy in every direction. It fixed mannerisms in all directions. Laplacian Operator—It is also called as a derivative operator. It helps in deemphasizing images with slowly varying grey levels with the help of grey level discontinuities in an image. Very much sensitive to noise and get debased of edges are not sharp.

Table 1 Chronological table of previous works

Serial no.	Year	Author	Method
1	2010	Liu et al. [1]	Richer convolutional features for edge detection
2	2011	Xiang et al. [2]	An edge detection algorithm based-on Sobel operator for images captured by the binocular microscope
3	2012	Muthukrishnan et al. [3]	Interpretation of image contents is one of the objectives in computer vision specifically in image processing
4	2013	El-Zaart et al. [4]	Edge detection in radar images using Weibull distribution
5	2014	Krishnaswamy et al. [5]	Enhancing template security of face biometrics by using edge detection and hashing
6	2015	Melo et al. [6]	A fingerprint-based Access control using principal component analysis and edge detection
7	2016	Chen et al. [7]	Semantic image segmentation with task-specific edge detection using CNNs and a discriminatively trained domain transform
8	2017	Zhang et al. [8]	A digital fuzzy edge detector for color images
9	2018	Al-Jarrah et al. [9]	A novel edge detection algorithm for mobile robot path planning
10	2019	Anas et al. [10]	Impact of edge detection algorithm in medical image processing

2 Literature Survey

In this section, we have performed a literature survey on some existing works performed in the last few years. We have examined the different methodology proposed. Based on this analysis we have designed a chronological table that indicates method name and main methodology (Table 1).

3 Proposed Methodology

In our proposed method we have developed a unique edge detection technique along with a filtration technique known as SNPRNOB filter (Salt and Pepper Noise Reduction with Original and Noisy Images Using Bilateral Filter). It is simple and easy to implement. The first step is to calculate the value of the original images and to perform edge detection using a composite method. The second step is to add both original and noisy images. The third step resultant of both the first and second steps gets subtracted. Fourth step it calculates the pixel value and gets subtracted with original images. At last resultant of the third step gets divided by the resultant of the fourth step. The mathematical formula in this proposed filter is:

$$f1 = (2 * x1), f2 = (x1 + y1), \ f3 = (f1 - f2), \ f4 = (2 * 255) - x1, \ f5 = f3/f4 \tag{1}$$

where x1 is an original image denoted by img and y1 is a noisy image denoted by noise_img.

4 Algorithm

Step1: Start
Step2: Import image and image filter from the library
Step3: Store image in image object and image.
Step4: Enhance the image by image enhancement filter
Step5: Store the enhance image in img
Step6: Import library
Step7: Store the original image in im and im1
Step8: Add Gaussian blur to the image.
Step9: Use Canny, Prewitt, and Sobel operator to the image separately
Step10: Display the original image, enhancement image, along with all other operators
Step11: Stop.

Algorithm before filtration

Step1: Start
Step2: Insert img as an original image and noise_img as a noisy image
Step3: Convert original image into a grayscale image and insert salt and paper noise into a grayscale image with respective percentage of noise and display original, grayscale, and Noisy image respectively.
Step4: Calculate MSE, RMSE, PSNR, and SNR each one by one using the original image (img) and noisy image (noise_img) respectively.

Algorithm after filtration

Step1: Now we have to take a value of a pixel from (0-255)
Step2: Calculate the filtered image using the original image, noisy image, and the maximum value of the pixel. With the help of these techniques which is SNPRONB, we get our filter image as follows.

$$\text{Filter} = (2 * \text{img}) - (((\text{img} + \text{noise\_img})//(2 * 255)) - \text{img}) \tag{2}$$

Step3: Store the filtered image in filter
Step4: Calculate MSE, RMSE, PSNR, and SNR each one by one on using filter image and noise image respectively.

Fig. 1 Block diagram of the proposed method

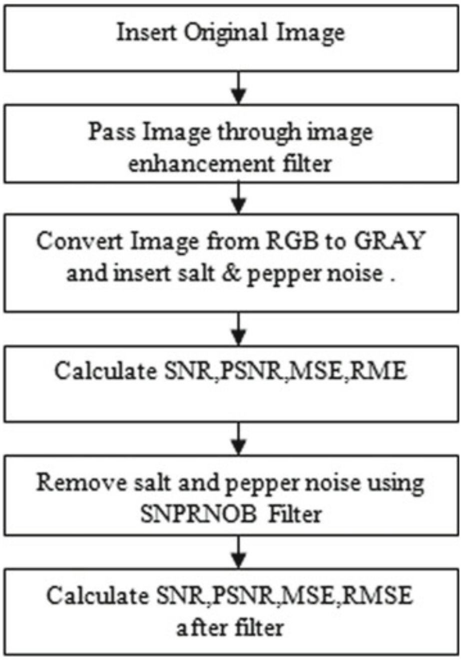

Step5: Display the original image, grayscale image, noisy image, and filter image respectively

Step6: Stop.

4.1 Block Diagram

See Fig. 1.

4.2 Flow Chart

See Fig. 2.

5 Experimental Results and Analysis

In this section, we have highlighted multiple tables, figures, and graphs that display the SNR, PSNR, MSE, and RMSE values for before filtration and after filtration with different noise intensity values (Figs. 3, 4, 5, 6, 7 and 8) and Tables (2, 3 and 4).

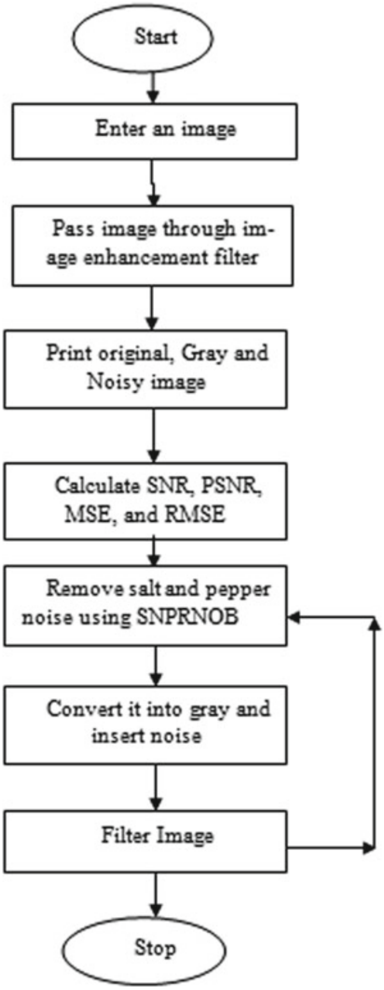

Fig. 2 Flow chart of the proposed method

Fig. 3 Edge detection steps for 30% noise intensity

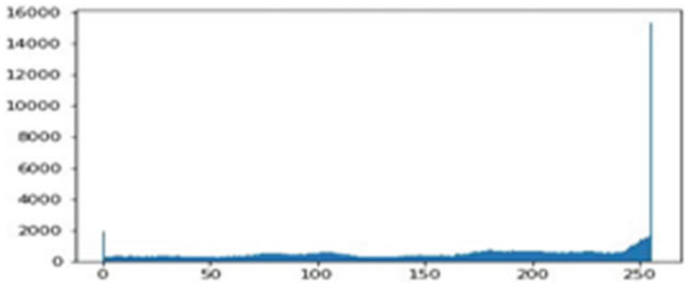

Fig. 4 A graph with 30% noise intensity eradication after filtration

Fig. 5 Edge detection steps for 60% noise intensity

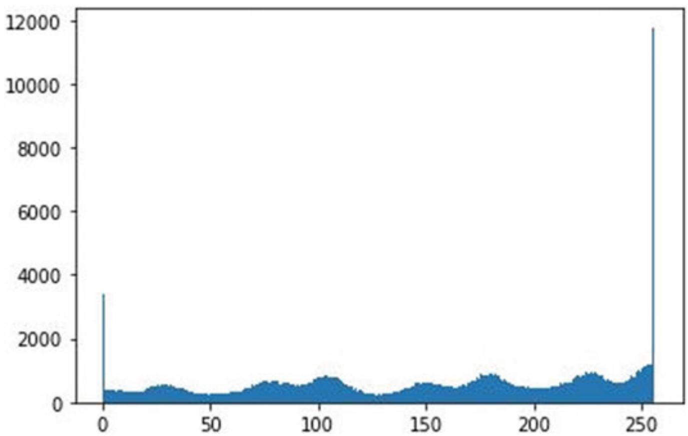

Fig. 6 A graph with 60% noise intensity eradication after filtration

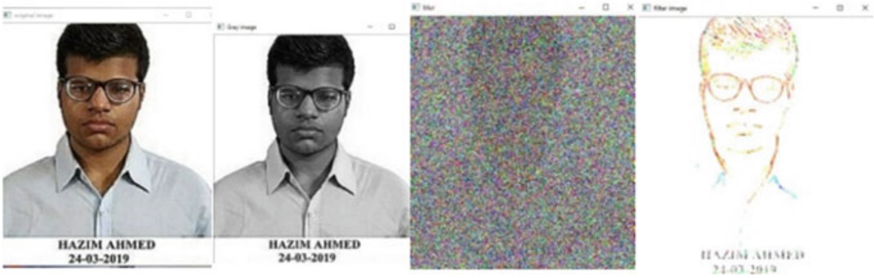

Fig. 7 Edge detection steps for 90% noise intensity

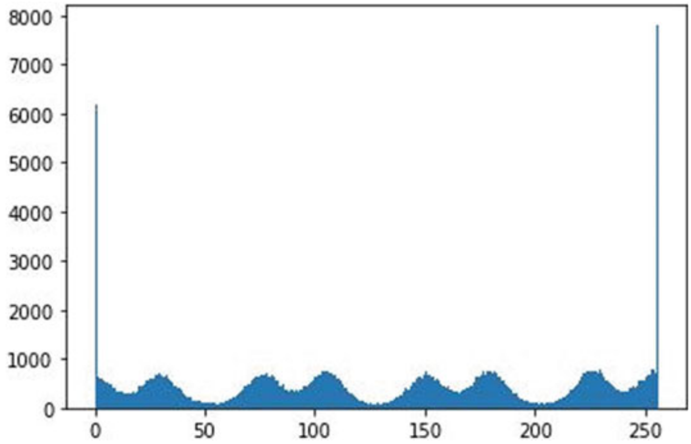

Fig. 8 A graph with 90% noise intensity eradication after filtration

Table 2 Noise intensity 30% removals using before and after filter

Types of filter	SNR	PSNR	MSE	RMSE
Before filter	0.67	−89.232	544.0	738.213
After filter	0.23	−119.1127	5.3009	230.432

Table 3 Noise intensity 60% removals using before and after filter

Types of filter	SNR	PSNR	MSE	RMSE
Before filter	0.89	−89.252	547.0	739.125
After filter	0.20	−119.158	5.357	231.777

Table 4 Noise intensity 90% removals using before and after filter

Types of filter	SNR	PSNR	MSE	RMSE
Before filter	0.91	−89.272	55002.0	7416.140
After filter	0.18	−119.072	5.252	229.843

6 Conclusion

In this paper, we have implemented a newly cultivated edge detection technique and filtration blueprint for detecting edges present in the digital image and removal of noise. In the future we would like to enhance the performance of this filter, so that accuracy, efficiency, and capability of this filter can be improved.

References

1. Liu, Y., Cheg, M.M., Hu, X., Wang, K., Bai, X.: Richer convolutional features for edge detection. IEEE, Jan 2010
2. Xiang, X., Yan, B., Cai, Q., Zou, G.: An edge detection algorithm based on Sobel operator for images captured by binocular microscope. IEEE 12376274, Sep 2011
3. Muthuskrishnan, R., Radha, M.: Edge detection techniques for image segmentation. IEEE (2012)
4. El-Zoart, A., Al-Jibory, W.K.: Edge detection in radar images using Weibull distribution. IEEE (2013)
5. Krishnaswamy, M., Kumar, G.H.: Enhancing template security of face biometrics by using edge detection and hashing. IEEE (2014)
6. Melo, E.F., de Oliveria, H.M.: A fingerprint-based access control using principal component analysis and edge detection. IEEE (2015)
7. Chen, L.C., Barron, J.Y., Papandreon, G., Murphy, K., Yuille, A.L.: Semantic image segmentation with task-specific edge detection using CNNs and a discriminatively trained domain transform. IEEE, May 2016
8. Zhang, Y.H., Li, X., Xiao, J.Y.: A digital fuzzy edge detector for color images. IEEE (2017)
9. Al-Jarrah, R., Al-Jarrah, M., Roth, H.: A novel edge detection algorithm for mobile robot path planning. IEEE 1969834, 1 Jan 2018
10. Anas, R., Elhadi, H.A., Ali, E.S.: Impact of edge detection algorithms in medical image processing. IEEE WSN **118**, 129–148 (2019)

Performance Improvement of Artificial Neural Networks by Addressing Class Overlapping Problem

Sankhadeep Chatterjee, Asit Kumar Das, Kushankur Ghosh, Arghasree Banerjee, Mayukh Bhattacharjee, and Soumen Banerjee

Abstract The class overlapping problem is one of the most prominent challenges of Machine Learning in recent years. In spite of the rapid development of well performing machine learning models for classification tasks, majority of them suffers from overlapped classes. Artificial Neural Network (ANN), being an extremely successful machine learning model suffers from these issues. Studies have found the effect of imbalanced classes in ANNs. However, the effect of overlapped classes is still not well studied. Motivated by this, the present article proposes a soft membership based overlapping removal technique (SMORET) to improve the performance of ANNs in presence of overlapped classes. The proposed method is capable of detecting the data points in the overlapped region and removing them from the training phase dataset. The proposed method is tested using real and artificial datasets, specially

S. Chatterjee (✉)
Indian Institute of Engineering Science & Technology, Shibpur, India
e-mail: chatterjeesankhadeep.cu@gmail.com

K. Ghosh · A. Banerjee · M. Bhattacharjee
Department of Computer Science & Engineering, University of Engineering & Management, Kolkata, India
e-mail: kush1999.kg@gmail.com

A. Banerjee
e-mail: banerjeearghasree@gmail.com

M. Bhattacharjee
e-mail: mayukhofficial12@gmail.com

A. K. Das
Department of Computer Science & Technology, Indian Institute of Engineering Science and Technology, Shibpur, India
e-mail: akdas@cs.iiests.ac.in

S. Banerjee
Department of Electronics & Communication Engineering, University of Engineering & Management, Kolkata, India
e-mail: prof.sbanerjee@gmail.com

S. Banerjee and J. K. Mandal (eds.), *Advances in Smart Communication Technology and Information Processing*, Lecture Notes in Networks and Systems 165,
https://doi.org/10.1007/978-981-15-9433-5_22

designed to understand the effect of overlapped classes, in terms of various performance measuring metrics. The results have indicated that SMORET is capable of detecting the most significant and hardest-to-learn data points in the overlapping region. Further, it improves the performance of ANNs in classification tasks to a greater extent.

Keywords Class overlapping · Artificial neural networks · Soft membership · Imbalanced class

1 Introduction

Machine Learning (ML) is one of the most emerging branches that uses different type of algorithms which are capable of imitating human intelligence by learning from the environment and has become a core area of research [1–8]. The process of learning begins with observations or data, such as examples, direct instructions and experiments, in order to look for patterns in data and make better future predictions depending on the data we provide. The primary aim is to allow the computers learn automatically without any human assistance and adjust actions accordingly. The main five porotypes for Machine Learning have been described [9] and they are: Neural networks, Instance based learning algorithms, Genetic algorithms that is represented by binary features, Decision trees and finally Analytic learning. Machine Learning exists in major problem domains. Some remarkable fields are bioinformatics [10], Data mining [11], Big Data Processing [12], Computer Vision [13] and from engineering sciences to social networking [14, 15]. Supervised machine learning algorithms performs on labelled data to predict future events [16]. Starting from the analysis of a training dataset, the algorithm produces an inferred function to make predictions based on the values poured into it and also consists of various types of methods described in [17] whereas, unsupervised machine learning algorithms are used when the information used to train is neither classified nor labelled [18]. However, despite its numerous advantages, there are still risks and challenges. One of the drawbacks of machine learning is its affinity to errors. Depending on the data fitted for training, it is able to make predictions keeping unintentional and hidden biases. Among all the other problems, the Class-Imbalance [19, 20] and the Class-Overlapping [21] issues has become one of the most critical among them in the field of Data Mining [22] and ML [23]. The problem of class overlapping was previously coined in many papers [24, 25] and was identified as a factor providing a major hindrance in achieving a reliable accuracy. Over the past years, researchers have dealt with this problem, that exists in various real-life domains such as credit card fraud detection [26], detection of oil spillage [27]. The problem of class overlapping in the domain of Machine Learning has proved to be a matter of concern for various machine learning classifiers where the data samples seem to belong to one or more class [28, 29]. As explained by domain experts there still exists minute differences in the instances of two different classes which are difficult to capture using only attributes of it. In [21], the authors documented the behaviour of overlapped animal sound signal data and also proposed a remarkable classification strategy for overlapped data. Gupta et al. [30] mentioned that one of the most important factors that causes class overlapping is noise and 6–80% of overlapped instances are recognized as noise with the help of noise filters. To handle the problem of class overlapping and class imbalance together, Alejo et al. [31] proposed a unified use of editing techniques and a modified MSE (Mean Square Error) cost function for MLP (Multilayer Perceptron) which provided reliable outputs.

Further study revealed that there is no concrete research solely addressing the overlapped classification problem in machine learning. Motivated by this, in this paper we proposed Soft Membership based Overlapping Removal Technique (SMORET) by solely addressing the class overlapping problem.

2 Proposed Method

2.1 Soft Membership Based Overlapping Removal Technique (SMORET)

The class overlapping problem has been addressed in earlier literature in domain specific applications. One of the earliest mentions can be found in [32], where the class overlapping problem is observed in the context of face recognition. Initially, Fisher's Linear Discriminant is used to overcome the effect of imbalanced classes. Due to its inability in alleviating the problem, a new Euclidean distance-based method was proposed. The study also pointed out the challenges in learning overlapped classes by ANNs. Visa et al. [33] proposed a fuzzy rule-based method to learn imbalanced and overlapped classes. The proposed method only relies upon the fuzzy membership values of data points and partitioning data points in to fuzzy sets. However, no distance-based criterion is utilized as used in [32]. Batista et al. [34] indicated that class imbalance problem could be affected by the presence of overlapped classes, especially in minority classes. More studies have reported the same along with the effects of class imbalance in presence of different degrees of overlapping [35, 36]. Considering a two-class classification problem where, point p and q both belongs to class '1' and point q is in the overlapping region of the clusters corresponding to two classes. Whereas, point p is not in the overlapping region. The distance of point p from cluster centers '1' and '2' are $d_{p,1}$ and $d_{p,2}$ respectively and the same for point q are $d_{q,1}$ and $d_{q,2}$. The soft membership for point p can be calculated as;

$$\mu_p = [\mu_{p,1}, \mu_{p,2}]$$

where,

$$\mu_{p,1} = 1 - \frac{d_{p,1}}{d_{p,1} + d_{p,2}} \text{and}\ \mu_{p,2} = 1 - \frac{d_{p,2}}{d_{p,1} + d_{p,2}}$$

and the same for point q are as follows;

$$\mu_q = [\mu_{q,1}, \mu_{q,2}]$$

where,

$$\mu_{q,1} = 1 - \frac{d_{q,1}}{d_{q,1} + d_{q,2}}$$

and $\mu_{q,2} = 1 - \frac{d_{q,2}}{d_{q,1}+d_{q,2}}$

To determine the data points in the overlapping region of the clusters, the α metric for both data points have been defined;

$$\alpha_1 = \mu_{p,1} * d_{p,1} + \mu_{p,2} * d_{p,2} \tag{1}$$

$$\alpha_2 = \mu_{q,1} * d_{q,1} + \mu_{q,2} * d_{q,2} \tag{2}$$

The α metric value reveals whether a data point is actually close to overlapping region or not. The α metric value of a point in the overlapping region is always less than a point which is not in overlapping region. The following algorithm uses the α metric to pick up points less likely to be in overlapping region.

Algorithm: Soft Membership based Overlapping Removal Technique (SMORET)

Input: Dataset $D = \{p_1, p_2, \ldots, p_n\}$ where p_i is a m-dimensional column vector ($p_i = [x_1, x_2, \ldots, x_m]^T$), Cluster centres $C_1, C_2, \ldots, C_c$
Output: Set of data points for training ($Train$)
T is a $1 \times n$ array. $T_{p_i,i}$ denotes the sum of the distances of p_i from all cluster centers.
μ is a $n \times c$ array. $\mu_{p_i,j}$ denotes the soft membership value of p_i for cluster C_j where $j = 1,2, \ldots, c$
d is a $n \times c$ array. $d_{p_i,j}$ denotes the Euclidean distance between p_i and cluster C_j where $j = 1,2, \ldots, c$
α is a $1 \times n$ array. α_t denotes the threshold value

1: for p_i in D:
2:   for each C_j:
3: $d_{p_i,j} = \|p_i - C_j\|$
4: $T_{p_i} = T_{p_i} + d_{p_i,j}$
5: for p_i in D:
6:   for d_i in d:
7: $\mu_{p_i,i} = d_{p_i,i}/T_{p_i}$
8: for p_i in D:
9: $\alpha_i = 0$
10:   for μ_j in μ:
11: $\alpha_i = \alpha_i + \mu_{p_i,j} * d_{p_i,j}$
12: for α_i in α:
13:   if $\alpha_i > \alpha_t$:
14: $Train = Train \cup p_i$

Steps 1–4 calculate distance of every point (p_i) from all the cluster centres (C_j) and also stores the sum of all distances in T. Next, steps 5–7 calculate the soft membership of every point and stores in μ. Thereafter, in steps 8–11, the α metric for every data point is calculated. Finally, in steps 12–14, the data points whose α metric value is more than the α-threshold (α_t). We try to pick up data points with the α metric value greater than a predetermined value (α_t).

3 Experimental Analysis

SMORET has been applied on two artificially generated datasets containing overlapped distribution of balanced instances. The synthetic datasets are two-dimensional in nature holding a count of 600 data with 2 classes each.

Figure 1a, b depicts the synthetic datasets used in the experiment representing a circular trajectory of data. From Fig. 1a we can see that the data instances are spread over a smaller area whereas, 1b portraits a comparatively wider data spreading. ANN is applied on each of the dataset for their individual α_t values. The performance of the classifier is evaluated based on the values of precision, Þ$_{pr}$and the recall, Þ$_{re}$values, which can be mathematically written as.

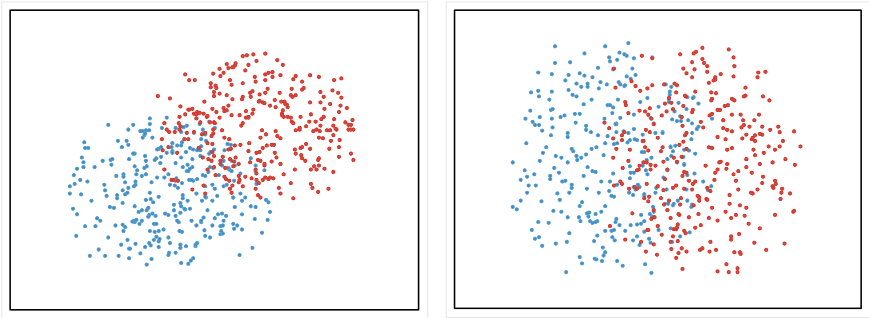

(a) (b)

Fig. 1 Scatter Plots of our datasets affected with Class-Overlapping: **a** Dataset 1, and **b** Dataset 2

$$Þ_{pr} = \frac{\varphi_{PS}}{\varphi_{PS}+\omega_{PS}} \tag{3}$$

$$Þ_{re} = \frac{\varphi_{PS}}{\varphi_{PS}+\omega_{NG}} \tag{4}$$

It can be clearly analyzed that each of the curves plotted in the Fig. 2 follows a similar trajectory with minor differences. In each of the figures we can see that curve of Data Remaining cuts the curve of Precision or Recall for some α_t value between 1.057 and 1.157. It can be further observed that after crossing the intersecting point, as the α_t value increases the performance of the classifier also increases but with the increasing cost of data loss.

Figure 3b gives us a detailed graphical overview of the recall value deflection for Dataset 2 for a constant increase of α_t value. We can see that both the curves follow a similar trajectory for a constant data degradation represented by the red line. Figure 3a the precision trajectory can be analysed thoroughly. It can be seen

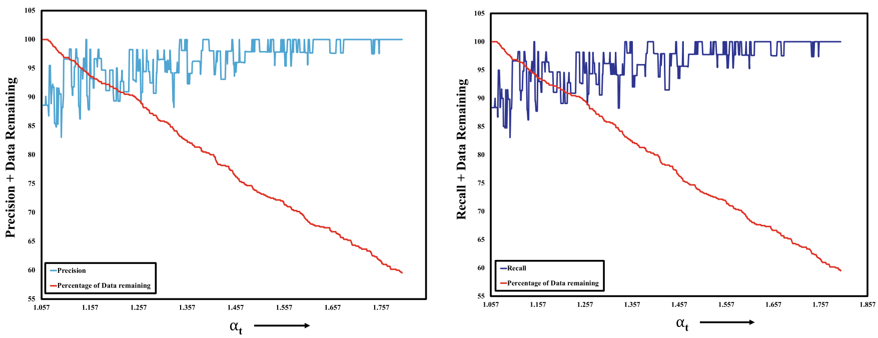

(a) (b)

Fig. 2 Performance evaluation of ANN after applying SMORET on Dataset 1 with the cost of Data for a constant increase in α_t: **a** Precision, **b** Recall

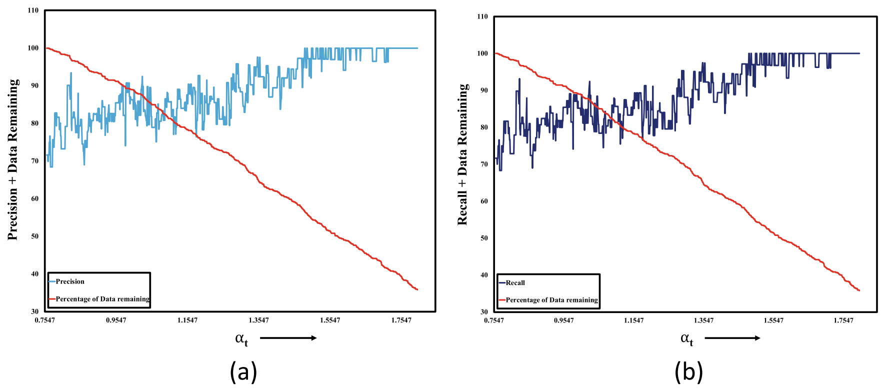

Fig. 3 Performance evaluation of ANN after applying SMORET on Dataset 2 with the cost of Data for a constant increase in α_t: **a** Precision, **b** Recall

that the precision curve intersects the data curve represented in red negligibly earlier compared to the recall trajectory represented in the figure. However, it is clearly visible from the figure that the intersecting points for each performance metrices lies between an α_t value of 0.9547 and 1.1547 with a data loss less than 15%.

4 Conclusion

The current article proposes a soft membership based overlapping removal technique (SMORET) in order to address the class overlapping problem encountered in classification tasks using ANNs. The algorithm is capable of estimating how far a data point is from the overlapped region. Experimental results have revealed that the overlapping region detection is highly accurate. Further, SMORET is capable of selecting most confident data points based on how far they are to the overlapping region. Five artificial datasets, specially designed to understand the effect of overlapping only, are used in the current study to test SMORET. As, the data ratio is kept equal in all the classes of the artificial datasets, it provided the opportunity to study the effect of overlapping in absence of imbalanced classes. It is concluded that overlapped classes have significantly reduced the classification accuracy of ANNs. It has been found that the performance of ANN in classification has been significantly improved by employing SMORET. Moreover, real datasets with overlapped classes have been used as well to test the same. Future studies can be directed towards understanding the effectiveness of SMORET with other machine learning models. Studies can be conducted on how to optimize the selection of data points based on the soft membership based metric devised in SMORET.

References

1. Eidelberg, A., Jacob, C., Denzinger, J.: Using active probing by a game management AI to faster classify players. In: 2019 IEEE Conference on Games (CoG), pp. 1–8. IEEE (2019)
2. Barral, O., Sébastien, L., Conati, C.: Understanding the effectiveness of adaptive guidance for narrative visualization: a gaze-based analysis. In: Proceedings of the 25th International Conference on Intelligent User Interfaces, pp. 1–9 (2020)
3. Berseth, G., Kyriazis, A., Zinin, I., Choi, W., van de Panne, M.: Model-based action exploration for learning dynamic motion skills. In: 2018 IEEE/RSJ International Conference on Intelligent Robots and Systems (IROS), pp. 1540–1546. IEEE (2018)
4. Kalash, M., Rochan, M., Mohammed, N., Bruce, N., Wang, Y., Iqbal, F.: A deep learning framework for malware classification. Int. J. Digital Crime Forensics (IJDCF) **12**(1), 90–108 (2020)
5. Bianchi, F.M., Livi, L., Mikalsen, K.Ø., Kampffmeyer, M., Jenssen, R.: Learning representations of multivariate time series with missing data. Pattern Recognit. **96**, 106973 (2019).
6. Ghosh, K., Banerjee, A., Chatterjee, S., Sen, S.: Imbalanced twitter sentiment analysis using minority oversampling. In 2019 IEEE 10th International Conference on Awareness Science and Technology (iCAST), pp. 1–5. IEEE (2019)
7. Singh, A., Pietrasik, M., Natha, G., Ghouaiel, N., Brizel, K., Ray, N.: Animal detection in man-made environments. In: The IEEE Winter Conference on Applications of Computer Vision, pp. 1438–1449 (2020)
8. Chatterjee, S., Sarkar, S., Hore, S., Dey, N., Ashour, A.S., Balas, V.E.: Particle swarm optimization trained neural network for structural failure prediction of multistoried RC buildings. Neural Comput. Appl. **28**(8), 2005–2016 (2017)
9. Langley, P., Simon, H.A.: Applications of machine learning and rule induction. Publ. Mag. Commun. ACM **38**(11), 54–64 (1995)
10. Larrañaga, P., Calvo, B., Santana, R., Bielza, C., Galdiano, J., Inza, I., Lozano, J.A., Armañanzas, R., Santafé, G., Pérez, A., Robles, V.: Machine learning in bioinformatics. Brief. Bioinform. **7**(1), 86–112 (2006)
11. Witten, I.H., Frank, E., Hall, M.A., Pal, C.J.: DATA MINING: Practical Machine Learning Tools and Techniques. A volume in the Morgan Kaufmann Series in Data Management Systems, 3rd edn (2011)
12. Qiu, J., Wu, Q., Ding, G., Xu, Y., Feng, S.: A survey of machine learning for big data processing. EURASIP J. Adv. Sig. Process. **67** (2016)
13. Dey, S., Singh, A.K., Prasad, D.K., Mcdonald-Maier, K.D.: SoCodeCNN: Program source code for visual cnn classification using computer vision methodology. IEEE Access **7**, 157158–157172 (2019)
14. Wang, A.H.: Detecting spam bots in online social networking sites: a machine learning approach. In: Foresti, S., Jajodia, S. (eds.) Data and Applications Security and Privacy XXIV. DBSec 2010. Lecture Notes in Computer Science, vol. 6166. Springe (2010)
15. Pennacchiotti, M., Popescu, A.M.: A machine learning approach to twitter user classification. In: Proceedings of the Fifth International Conference on Weblogs and Social Media, Barcelona, Catalonia, Spain (2011)
16. Kotsiantis, S.B.: Supervised machine learning: a review of classification techniques. In: Proceedings of the 2007 Conference on Emerging Artificial Intelligence Applications in Computer Engineering: Real Word AI Systems with Applications in eHealth, HCI, Information Retrieval and Pervasive Technologies, pp. 3–24 (2007)
17. Caruana, R., Niculescu-Mizil, A.: An empirical comparison of supervised learning algorithms. In: Published in ICML 06 Proceedings of the 23rd International Conference on Machine Learning, pp. 161–168 (2006)
18. Barlow, H.B.: Unsupervised learning. Neural Comput. **1**(3), 295–311 (1989)
19. Guo, X, Yin, Y., Dong, C., Yang, G., Zhou, G.: On the class imbalance problem,. In: 2008 Fourth International Conference on Natural Computation, Jinan, 2008, pp. 192–201

20. Bellinger, C., Sharma, S., Japkowicz, N., Zaïane, O.R.: Framework for extreme imbalance classification: SWIM—sampling with the majority class. Knowl. Inf. Syst. **26**
21. Lin, N., Sun, H., Zhang, X.: Overlapping animal sound classification using sparse representation. In: 2018 IEEE International Conference on Acoustics, Speech and Signal Processing (ICASSP), Calgary, AB, pp. 2156–2160 (2018)
22. Chawla, N.V.: Data mining for imbalanced datasets: an overview. In: Maimon, O., Rokach, L. (eds.) Data Mining and Knowledge Discovery Handbook (2005)
23. Prati, R.C., Batista, G.E.A.P.A., Monard, M.C.: Class imbalances versus class overlapping: an analysis of a learning system behavior. In: Monroy, R., Arroyo-Figueroa, G., Sucar, L.E., Sossa H. (eds.) MICAI 2004: Advances in Artificial Intelligence. MICAI 2004. Lecture Notes in Computer Science, vol. 2972, pp. 312–321 (2004)
24. KOC, H.A.G.H.G.: Concept representation with overlapping feature intervals. Publ. J. Cybern. Syst. Int. J. **29**(3), 263–282 (2010)
25. Bradley, A.P.: The use of the area under the ROC curve in the evaluation of machine learning algorithms. J. Pattern Recognit. **30**(7), 1145–1159 (1997)
26. Brause, R., Langsdorf, T., Hepp, M.: Neural data mining for credit card fraud detection. In: Proceedings 11th International Conference on Tools with Artificial Intelligence, pp. 103–106. IEEE (1999)
27. Salem, F., Kafatos, M., El-Ghazawi, T., Gomez, R., Yang, R.: Hyperspectral image assessment of oil-contaminated wetland. Int. J. Remote Sens. **26**(4), 811–821 (2005)
28. Luengo, J., Herrera, F.: Shared domains of competence of approximate learning models using measures of separability of classes. Inf. Sci. **185**(1), 43–65 (2012)
29. Kretzschmar, R., Karayiannis, N.B., Eggimann, F.: Handling class overlap with variance-controlled neural networks. In Proceedings of the International Joint Conference on Neural Networks, pp. 517–522. IEEE (2003)
30. Gupta, S., Gupta, A.: Handling Class Overlapping to detect noisy instances in classification. Knowl. Eng. Rev. **33**, E8 (2018)
31. Alejo R., Sotoca J.M., García V., Valdovinos R.M.: Back propagation with balanced MSE cost function and nearest neighbor editing for handling class overlap and class imbalance. In: Cabestany, J., Rojas, I., Joya, G. (eds) Advances in Computational Intelligence. IWANN 2011. Lecture Notes in Computer Science, vol. 6691 (2011)
32. Er, M.J., Wu, S., Lu, J., Toh, H.L.: Face recognition with radial basis function (RBF) neural networks. IEEE Trans. Neural Netw. **13**(3), 697–710 (2002)
33. Visa, S., Ralescu, A.: Learning imbalanced and overlapping classes using fuzzy sets. In Proceedings of the ICML, vol. 3, pp. 97–104 (2003)
34. Batista, G.E., Prati, R.C., Monard, M.C.: A study of the behavior of several methods for balancing machine learning training data. ACM SIGKDD Explor. Newsl **6**(1), 20–29 (2004)
35. Prati, R.C., Batista, G.E., Monard, M.C.: Class imbalances versus class overlapping: an analysis of a learning system behavior. In Mexican International Conference on Artificial Intelligence, pp. 312–321. Springer, Berlin, Heidelberg (2004).
36. Batista, G.E., Prati, R.C., Monard, M.C.: Balancing strategies and class overlapping. In: International Symposium on Intelligent Data Analysis, pp. 24–35. Springer, Berlin, Heidelberg (2005)

Multilabel Sentiment Prediction by Addressing Imbalanced Class Problem Using Oversampling

Mayukh Bhattacharjee, Kushankur Ghosh, Arghasree Banerjee, and Sankhadeep Chatterjee

Abstract Sentiment analysis has become an essential tool for Social Network data analysis. With the application of machine learning sentiment analysis has become even more accurate. It has been possible to classify text sentiments into multiple labels. The performance of such machine learning models highly depends on the data being used to train model. However, studies have indicated that data collected from Social networks may highly imbalanced. Motivated by this, the current study proposed a minority class oversampling method to address the class imbalance problem in multi label sentiment analysis using Imbalanced Ratio per Label and the Mean Imbalanced Ratio. Two well known classifiers have been engaged to establish the ingenuity of the proposed method. Experimental results revealed that the proposed method can significantly improve the performance of classifiers in multilabel sentiment analysis.

Keywords Multilabel classification · Sentiment analysis · Oversampling

1 Introduction

Over the recent years, there have been numerous works on various emerging domains [1–5] while on the other hand some have not been introduced. Sentiment Analysis

M. Bhattacharjee · K. Ghosh · A. Banerjee · S. Chatterjee (✉)
Department of Computer Science & Engineering, University of Engineering & Management, Kolkata, India
e-mail: chatterjeesankhadeep.cu@gmail.com

M. Bhattacharjee
e-mail: mayukhofficial12@gmail.com

K. Ghosh
e-mail: kush1999.kg@gmail.com

A. Banerjee
e-mail: banerjeearghasree@gmail.com

S. Banerjee and J. K. Mandal (eds.), *Advances in Smart Communication Technology and Information Processing*, Lecture Notes in Networks and Systems 165,
https://doi.org/10.1007/978-981-15-9433-5_23

is the process of computational evaluation of a piece of text, in order to determine whether the writer's frame of mind regarding a particular product or topic is Positive, Negative or Neutral. There are various techniques to carry out sentiment analysis. *Hatzivassiloglou* and *McKeown* extracted adjectives that had a count of more than 20 times in the Wall Street journal [6]. *Bieneke* et al. [7] introduced a model that fit Naïve Bayes classifier. Total 10 words (five positive and five negative) were selected and the respective list was expanded using Wordnet. Classifier was trained using a tagged corpus and model was cleaned and applied on test data. *Nakov* et al. [8] introduced two new different techniques for Sentiment Analysis. Single Label classification deals with a single label from a set of disjoint labels. Multi-label classification is concerned with differentiating instances into multiple classes. But there exist problems belonging to multilabel classification and are required by present-day use such as protein function classification [9] and semantic classification [10]. The two main categories for dealing with the Multi-label classification *Tsoumakas* and *Katakis* [11] are problem transformation and algorithm adaptation method. Multi-label and Multi-task are two main features of Sentiment and Topic-analysis, however they are treated independently. *Huang* et al. [12] proposed a method to render solution to Multi-label and Multi-task problem in a unified way. Social media is one of the ultimate platforms to express emotions online and classifying the user emotion automatically help us understand general public review. In [13] the authors have introduced a new technique for classification of user emotion over tweets and news headlines. Sentiment analysis is not only confined to English language but also on other languages. In [14] the authors have discussed a technique to identify sentiment and extraction of emotions from Bangla texts.

The class imbalance problem is a real menace which hinders the performance of the classifier [15]. In [16] the authors provide a systematic study based on simple strategies related to Class Imbalance problem. The most common way to tackle the problem of class imbalance is over-sampling the minority class or under-sampling the majority. In [17] the authors proved that over-sampling the minority and under-sampling the majority can provide better results than only under-sampling the majority class. Class imbalance problem also exists in real life, in [18] the authors investigate to handle class imbalance in customer churn prediction. The class imbalance problem is also prevalent in Sentiment analysis. If such a problem arises, the classifier becomes biased towards the majority class which leads to poor prediction [19]. One among many approaches to multi label learning is AID *Montañés* et al. [20] whose main property is to sum up independent and dependent labels under the supposition that, for a given example, models can be predicted using only the description of the object, but others require to consider their dependences with respect to other labels. In sentiment analysis, the problem has been tackled by many researchers over the years. Prusa et al. [21] demonstrated a way to tackle imbalanced sentiment analysis by using the Random Undersampling algorithm. In [22] the authors proposed a unique technique to generate synthetic texts by utilizing word embeddings. In [23] the authors proposed the one-vs-one decomposition to tackle multi-class imbalance in sentiment analysis. *Ghosh* et al. [24] has proposed a technique based on the effect of class imbalance in sentiment-analysis by hybridizing it with Synthetic Minority

Oversampling Technique (SMOTE). Further study revealed that there is no concrete research addressing the problem in multi-label sentiment analysis and no effective algorithm is designed yet to tackle it. Motivated by this, in our paper we proposed an effective technique to handle the Class Imbalance problem in Multi-Label Sentiment analysis.

2 Proposed Method

In our experiment, we handle the bias that results due to the formation of imbalanced classes in Multi-Label sentiment classification which arises due to small number of samples belonging to single or multiple classes. Our proposed approach can be best explained in mainly four steps described in the diagram in Fig. 1. In our approach, before identifying the minority labeled Tweets, the first two steps are maintained. In the first step, the Tweets are extracted from Twitter. Once they have been extracted, the tweets are cleaned and are get ridded of unwanted expressions. In the second step the tweets are vectorized into numerical format by calculating the frequency of each term in a particular tweet. The Minority Labels are then identified and are sent to the next process of steps, where oversampling takes place. Other minority samples are synthetically generated, thus increasing the population of the minority tweets.

2.1 Tweets Extraction and Feature Extraction

Millions of tweets get posted daily focusing on topics ranging from sensitive country-politics to a trivial Thanksgiving shopping. However, mining valuable and impactful tweets is the primary step of constructing the model. The focal criteria of tweet extraction for the model is to select tweets focusing on a topic which is socially sensitive but can also produce mixed emotions and sentiments for certain communities. For our model, we have mined tweets focusing on various aspects of United States. A

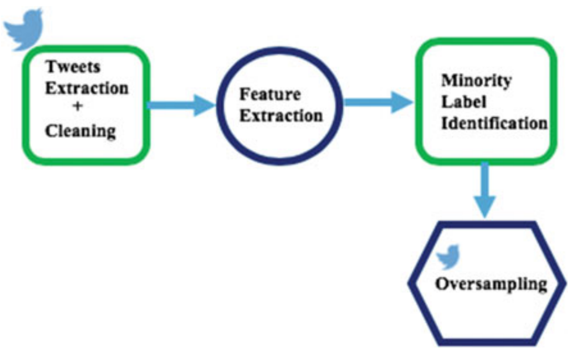

Fig. 1 Pictorial representation of proposed method

total count of 9294 live tweets are extracted and are split into two frames containing a count of 7149 training data and 2145 test data. Each tweet is manually examined and cleaned by removing the URLs, retweets, irregular expressions, symbols, annotations. The tweets are then transformed into numerical format. For our model we have used the Term Frequency-Inverse Document Frequency vectorizer q, [25] considering the unigram feature which results in a sparse matrix. The expression can be mathematically defined as,

$$q_d(k, \in) = tf(\in, d) \times \emptyset(k, \in) \tag{1}$$

where,

$$\emptyset(k, \in) = \log(k/\Delta(\in)) \tag{2}$$

where, Δ returns the count of the twitter texts which holds the term $\in$ from a total k number of tweets in a document d and, tf returns the total count of any term in the complete document.

2.2 Multi-label Sentiment Classification

A real-world data can be termed as a multilabel data, if more than one label is associated with it. Unlike single-labeled datasets, Multi-Labeled datasets (MLD) comprise of a multi-dimensional output attribute. Multi-label data are commonly visible in the fields of images [26], audio classification [27], facial action detection [28] and emotion classification [29]. In single-labeled datasets, the count of the labels equals to the size of the dataset whereas, in multi-labeled datasets, the sum of the counts of each label is always greater than the size of the total dataset as each label holds an overlapped region with other labels. However, twitter-based sentiment analysis encounters with a large number of tweets exhibiting multiple sentiments [30]. A text data which encompasses a negative tone of sentiment can also represent a toxic insult or a state of intense fear or both at the same time. In the same way, a satirical or ironical tweet can also represent a positive sentiment. The sentiment of each tweet is determined by Vader subjectivity scores [31] and Textblob polarity score [32]. The tweets are distinguished based on *Highly-Emotional, Moderately-Emotional, Unemotional, Constructive, Toxic* and *Non-Supportive* where each tweet holds more than one label in their label set.

2.3 Imbalanced Label Identification and Oversampling

The Class Imbalance problem occurs when a particular class in a dataset holds insufficient data compared to that of the other class or classes present in it. This results in an inaccurate classification by making the classifier to take decisions in favor of the class with the majority count. This behavior of the classifier cannot be termed as the biasness of the classifier. Biasness occurs through a natural phenomenon where an individual works to favor someone to fulfill their personal intentions [33] and not because of data distribution anomalies. Various recent studies identified the problem and also proposed novel approaches to tackle it in multi-labeled datasets [34–37]. However, the foremost important task while handling the problem is the identification of the imbalanced label. Figure 2 describes the class distribution in our extracted tweets used for training our model. It is clearly visible from the Figure that the constructive class holds the least count of tweets in our training data. However, in this scenario of Class-Imbalance for MLDs a proper mathematical approach is necessary to determine the minority class as, it is not always feasible to determine visually. The task appears to be trivial while dealing with single-labeled datasets where the minimum count label represents the minority class, but however, tends to be more complex while dealing with overlapped labels. In [38] Charte et al. proposed a very unique way to identify a minority label in an MLD. They calculated the Imbalanced Ratio per Label ∂, and the Mean Imbalanced Ratio μ, to determine whether a particular label is imbalanced or not. Both the measures can be mathematically formulated as,

$$\partial(y) = {}_{k=q_1}^{q_L} argmax\left(\sum_{x=1}^{N} \beta(k, \Delta_x)\right)/\tau(y) \tag{3}$$

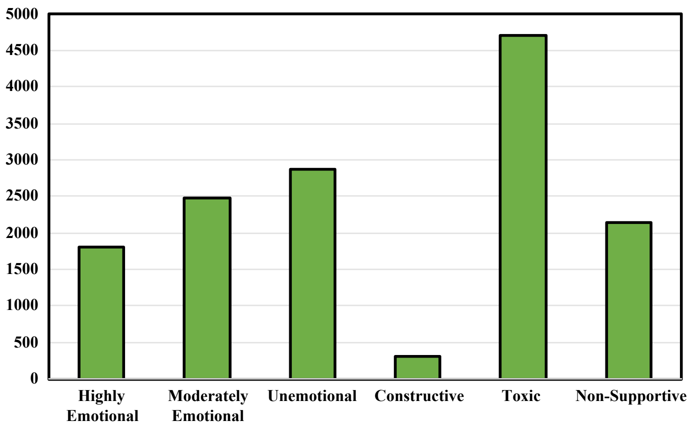

Fig. 2 Class Distribution of the extracted tweets in our Corpus

$$\tau(y) = \sum_{x=1}^{N} \beta(y, \Delta_x) \tag{4}$$

$$\mu = \frac{\sum_{j=q_1}^{q_L} (\partial(j))}{L} \tag{5}$$

where, y is the label that is to be checked, L is the size of the label set where the ith label is represented as q_i, N is the size of the MLD and Δ_x is the label set associated to a particular tweet. Considering y as any label of the dataset then, the function β is defined as,

$$\beta(y, \Delta_x) = \begin{cases} 1, \; y \in \Delta_x \\ 0, \; y \in \Delta_x \end{cases} \tag{6}$$

The label y is considered as minority if the value of $\partial(y)$ is greater than that of the μ. In our approach, we performed a random injection of synthetic data in the minority class following the random oversampling algorithm. The minority label is identified using ∂ and μ and synthetic data are added to the training set. However, the value of both the parameters are subject to change with each set of addition of synthetic data. In some cases, these changes may also imbalance a label which was initially balanced due to the over addition of synthetic data belonging to any other label. The value of ∂ for all the labels and μ has to be checked every time after the injection of the artificial instances. The oversampling is terminated once a particular class reaches a balanced state and then a next set of oversampling is performed if any other class is found having a ∂ value greater than the μ.

3 Experimental Analysis

Evaluating the machine learning algorithm is the most important part of any work. There are various types of metrics namely Log-Loss, Accuracy, Precision, AUC (Area Under Curve) etc. It has been found that Highly Imbalanced data has an affinity towards Accuracy [39] and tampers its value. This problem has been discussed widely in various experiments [40, 41] proving Accuracy to provide biased result for Imbalanced Data. In [41] it has been stated by the authors that Sensitivity (S_s) and Specificity $\left(S_p\right)$ are a major boost up over Accuracy to evaluate the performance of Imbalanced Data. The aforementioned metrices can be described as,

$$(S_s) = \frac{\theta_1}{\theta_1 + \theta_3} \tag{7}$$

$$\left(S_p\right) = \frac{\theta_4}{\theta_4 + \theta_2} \tag{8}$$

where, θ_1 represents True Positive value, θ_2 represents False Positive value, θ_3 represents False Negative value and θ_4 represents True Negative value. The authors also mentioned another metric named G-Mean, G which can be represented as,

$$G = \sqrt[2]{S_s \times S_p} \tag{9}$$

It has also been stated by *Johnson* and *Khoshgoftaar* [42], that Precision value is highly affected in case of Imbalanced Data. So, there exist anomalies in accuracy-based evaluation techniques. However, *Luque* et al. [43] mentioned that G-Mean metric (G) is one of the best metrices as they provide unbiased result even while dealing with Imbalanced Data. We have documented the performance of our model based on all these metrices until the value of *IRLBL* (for any particular class) becomes less than *MeanIR*. We have used two classifiers for our experiment. One of them is *Multinomial Naïve-Bayes (MNB)* which is very reputed for its accurate performance in Text Categorization [44]. The other classifier used is *Multilayer Perceptron (MLP)*, which is a class of feed-forward artificial neural network (ANN) which is also proved to be a remarkable classifier for text-based classifications [45]. To tackle the anomaly of Class Imbalance in Multilabel Sentiment there are no previous baseline works to compare our study with it.

In Fig. 3 we compare the Sensitivity values between MNB and MLP classifiers. At 0% oversampling, MLP has a sensitivity count of 0.65 and MNB has a count of 0.66. When synthetic data count rises to 4000, the count of MLP rises to 0.6556 (approx.) and MNB has a count of 0.66. When the synthetic data count is highest, that is 8000 (approx.), MLP has a count of 0.66 and MNB has a count of 0.67. Hence, we can conclude that MNB provides a better Sensitivity count than MLP.

In Fig. 4 we compare the Specificity values between MNB and MLP classifiers. During Imbalanced condition, MLP has a count of 0.31 and MNB has a count of 0.30. When synthetic data count is 4000 the count of MLP decreases to 0.3002 (approx.) and MNB has a count of 0.317 (approx.). When the synthetic data count is highest, that is 8000 (approx.), MLP has a count of 0.31 and MNB has a count of 0.32. Hence, we can conclude that MNB provides a better overall Specificity count than MLP. The

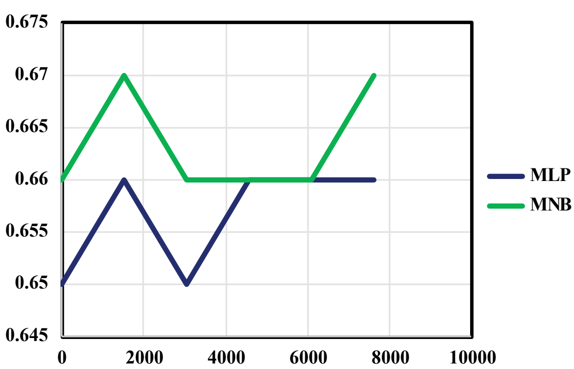

Fig. 3 Sensitivity deflection of the model with the augmentation of synthetic data

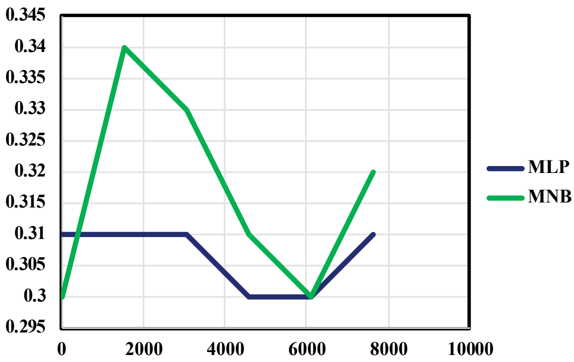

Fig. 4 Specificity deflection of the model with the augmentation of synthetic data

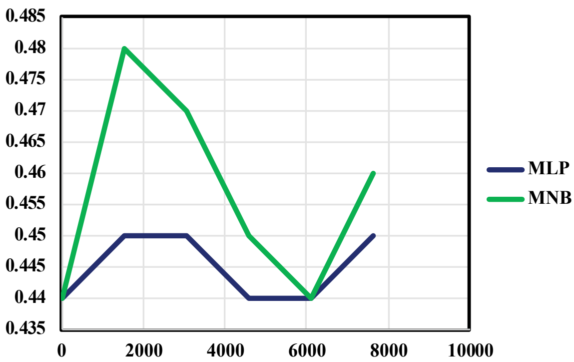

Fig. 5 G-Mean deflection of the model with the augmentation of synthetic data

highest count is reached by MNB that is 0.34 when the synthetic data count is slightly less than 2000.

In Fig. 5 we compare the G-Mean values between MNB and MLP classifiers. During Imbalanced condition both MLP and MNB has a G-Mean count of 0.44. In case of MLP, when the synthetic data count is between 2000 and 4000, the count is stable at 0.45. In case of MNB, when the data count is slightly less than 2000, it reaches the highest count that is 0.48. When the synthetic data count is 6000 both MNB and MLP has a decreased count of 0.44. Finally, when the data count increases to its maximum, both MNB and MLP has an increased data count of 0.46 and 0.45 respectively. Hence, we can conclude that MNB shows an overall better result than MLP.

4 Conclusion

The current study proposed a minority class oversampling method to address the class imbalance problem associated with multilabel sentiment analysis. Two well-known classifiers namely *Multinomial Naïve-Bayes* and Multilayer Perceptron have been trained and tested with varying degrees of oversampling in terms of specificity, sensitivity and G-mean. Experimental results have indicated that the proposed minority class oversampling can significantly improve the classifier performance in multilabel sentiment prediction. Future studies may be conducted to develop an algorithm solely focusing to mitigate the Class Imbalance problem in Multilabel Sentiment Analysis.

References

1. Dey, S., Singh, A.K., Prasad, D.K., McDonald-Maier, K.D.: SoCodeCNN: program source code for visual cnn classification using computer vision methodology. IEEE Access **7**, 157158–157172 (2019)
2. Chatterjee, S., Sarkar, S., Hore, S., dey, N., Ashour, A.S., Balas, V.E.: Particle swarm optimization trained neural network for structural failure prediction of multistoried RC buildings. Neural Comput. Appl. **28**(8), 2005–2016 (201)
3. Soltaninejad, S., Basu, A., Cheng, I.: Automatic classification and monitoring of denovo parkinson's disease by learning demographic and clinical features. In: 2019 41st Annual International Conference of the IEEE Engineering in Medicine and Biology Society (EMBC), pp. 3968–3971. IEEE (2019)
4. Schlegel, M., Chung, W., Graves, D., Qian, J., White, M.: Importance resampling for off-policy prediction. In: Advances in Neural Information Processing Systems, pp. 1797–1807 (2019)
5. Ahmed, F., Bari, A.S.M.H., Gavrilova, M.L.: Emotion recognition from body movement. IEEE Access **8**, 11761–11781 (2019)
6. Hatzivassiloglou, V., McKeown, K.R.: Predicting the semantic orientation of adjectives. In: Proceedings of the 35th Annual Meeting of the Association for Computational Linguistics and Eighth Conference of the European Chapter of the Association for Computational Linguistics, pp. 174–181 (1997)
7. Beineke, P., Hastie, T., Vaithyanathan, S.: The sentimental factor: improving review classification via human-provided information. In: Proceedings of the 42nd Annual Meeting on Association for Computational Linguistics, Article No. 263 (2004)
8. Nakov, P., Ritter, A., Rosenthal, S., Sebastiani, F., Stoyanov, V.: SemEval-2016 task 4: Sentiment analysis in Twitter. arXiv preprint arXiv:1912.01973 (2019)
9. Zhang, M.-L., Zhou, Z.-H.: A k-nearest neighbor based algorithm for multi-label classification. In: Paper Presented to Proceedings of the 1st IEEE International Conference on Granular Computing (2005)
10. Boutell, M.R., Luo, J., Shen, X., Brown, C.M.: Learning multi-label scene classification. Pattern Recogn. **37**(9), 1757–1771 (2004)
11. Tsoumakas, G., Katakis, I.: Multi-label classification: an overview. Int. J. Data Warehouse. Mining (IJDWM) **3**(3), 1–13 (2007)
12. Huang, S., Peng, W., Li, J., Lee, D.: Sentiment and topic analysis on social media: a multi-task multi-label classification approach. In: Proceedings of the 5th Annual ACM Web Science Conference, pp. 172–181 (2013)
13. Li, J., Rao, Y., Jin, F., Chen, H., Xiang, X.: Multi-label maximum entropy model for social emotion classification over short text. Neurocomputing **210**, 247–256 (2016)

14. Tripto, N.I., Ali, M.E.: Detecting multilabel sentiment and emotions from bangla youtube comments. In: 2018 International Conference on Bangla Speech and Language Processing (ICBSLP), pp. 1–6. IEEE (2018)
15. Japkowicz, N.: The class imbalance problem: significance and strategies. In: Proceedings of the International Conference on Artificial Intelligence (2000)
16. Japkowicz, N., Stephen, S.: The class imbalance problem: a systematic study. Intell. Data Anal. **6**(5), 429–449 (2002)
17. Chawla, N.V., Bowyer, K.W., Hall, L.O., Philip Kegelmeyer, W.: SMOTE: synthetic minority over-sampling technique. J. Artif. Intell. Res. **16**, 321–357 (2002)
18. Burez, J., Van den Poel, D.: Handling class imbalance in customer churn prediction. Expert Syst. Appl. **36**(3), 4626–4636 (2009)
19. Desai, M., Mehta, M.A.: Techniques for sentiment analysis of Twitter data: a comprehensive survey. In: 2016 InternationalConference on Computing, Communication and Automation (ICCCA), pp. 149–154. IEEE (2016)
20. Montañés, E., Quevedo, J.R., del Coz, J.J.: Aggregating independent and dependent models to learn multi-label classifiers. In: Machine learning and knowledge discovery in databases, pp. 484–500. Springer (2011)
21. Prusa, J., Khoshgoftaar, T.M., Dittman, D.J., Napolitano, A.: Using random undersampling to alleviate class imbalance on tweet sentiment data. In: 2015 IEEE International Conference on Information Reuse and Integration, pp. 197–202. IEEE (2015)
22. Xu, R., Chen, T., Xia, Y., Qin, L., Liu, B., Wang, X.: Word embedding composition for data imbalances in sentiment and emotion classification. Cognitive Comput. **7**(2), 226–240 (2015)
23. Krawczyk, B., McInnes, B.T., Cano, A.: Sentiment classification from multi-class imbalanced twitter data using binarization. In: International Conference on Hybrid Artificial Intelligence Systems, pp. 26–37. Springer, Cham (2017)
24. Ghosh, K., Banerjee, A., Chatterjee, S., Sen, S.: Imbalanced twitter sentiment analysis using minority oversampling. In: 2019 IEEE 10th International Conference on Awareness Science and Technology (iCAST), pp. 1–5. IEEE (2019)
25. Ohba, M., Gondow, K.: Toward mining 'concept keywords' from identifiers in large software projects. In: MSR '05 Proceedings of the 2005 International Workshop on Mining Software Repositories, pp. 1–5, ACM New York, NY, USA (2005)
26. Wang, J., Yang, Y., Mao, J., Huang, Z., Huang, C., Xu, W.: Cnn-rnn: a unified framework for multi-label image classification. In: Proceedings of the IEEE Conference on Computer Vision and Pattern Recognition, pp. 2285–2294 (2016)
27. Oramas, S., Nieto, O., Barbieri, F., Serra, X.: Multi-label music genre classification from audio, text, and images using deep features. arXiv preprint arXiv:1707.04916 (2017)
28. Ji, X., Ding, Y., Li, L., Chen, Y., Fan, C.: To-sequence: Multi-label Relation Modeling in Facial Action Units Detection. arXiv preprint arXiv:2002.01105 (2020)
29. Jabreel, M., Moreno, A.: A deep learning-based approach for multi-label emotion classification in tweets. Appl. Sci. **9**(6), 1123 (2019)
30. Hutto, C.J., Gilbert, E.: Vader: a parsimonious rule-based model for sentiment analysis of social media text. In: Eighth International AAAI Conference on Weblogs and Social Media (2014)
31. Loria, S.: textblob Documentation. Release 0.15 2 (2018)
32. Tahir, M.A., Kittler, J., Yan, F.: Inverse random under sampling for class imbalance problem and its application to multi-label classification. Pattern Recognit. **45**(10), 3738–3750 (2012)
33. Wolke, D., Waylen, A., Samara, M., Steer, C., Goodman, R., Ford, T., Lamberts, K.: Selective drop-out in longitudinal studies and non-biased prediction of behaviour disorders. Br. J. Psychiatry **195**(3), 249–256 (2009)
34. Charte, F., Rivera, A.J., del Jesus, M.J., Herrera, F.: REMEDIAL-HwR: tackling multilabel imbalance through label decoupling and data resampling hybridization. Neurocomputing **326**, 110–122 (2019)
35. Braytee, A., Liu, W., Anaissi, A., Kennedy, P.J.: Correlated multi-label classification with incomplete label space and class imbalance. ACM Trans. Intell. Syst. Technol. (TIST) **10**(5), 1–26 (2019)

36. Charte, F., Rivera, A.J., el Jesus, M.J., Herrera, F.: Dealing with difficult minority labels in imbalanced mutilabel data sets. Neurocomputing **326**(2019): 39–53.
37. Charte, F., Rivera, A.J., del Jesus, M.J., Herrera, F.: MLSMOTE: approaching imbalanced multilabel learning through synthetic instance generation. Knowl.-Based Syst. **89**, 385–397 (2015)
38. Charte, F., Rivera, A., José del Jesus, M., Herrera, F.: A first approach to deal with imbalance in multi-label datasets. In: International Conference on Hybrid Artificial Intelligence Systems, pp. 150–160. Springer, Berlin, Heidelberg (2013)
39. Buda, M., Maki, A., Mazurowski, M.A.: A systematic study of the class imbalance problem in convolutional neural networks. Neural Netw. **106**, 249–259 (2018)
40. Sarkar, S., Khatedi, N., Pramanik, A., Maiti, J.: An ensemble learning-based undersampling technique for handling class-imbalance problem. In: Proceedings of ICETIT 2019, pp. 586–595. Springer, Cham (2020)
41. Tang, Y., Zhang, Y.-Q., Chawla, N.V., Krasser, S.: SVMs modeling for highly imbalanced classification. IEEE Trans. Syst. Man Cybern. Part B (Cybernetics) **39**(1), 281–288 (2008)
42. Johnson, J.M., Khoshgoftaar, T.M.: Survey on deep learning with class imbalance. J. Big Data **6**(1), 27 (2019)
43. Luque, A., Carrasco, A., Martín, A.,de las Heras, A.: The impact of class imbalance in classification performance metrics based on the binary confusion matrix. Pattern Recognit. **91**, 216–231 (2019)
44. Kibriya, A.M., Frank, E., Pfahringer, B., Holmes, G.: Multinomial naive bayes for text categorization revisited. In: Australasian Joint Conference on Artificial Intelligence, pp. 488–499. Springer, Berlin, Heidelberg (2004)
45. Das, N., Das, B., Sarkar, R., Basu, S., Kundu, M., Nasipuri, M.: Handwritten Bangla basic and compound character recognition using MLP and SVM classifier. arXiv preprint arXiv:1002.4040 (2010)

Image Segmentation Based on Galactic Swarm Optimization

Shouvik Chakraborty, Kalyani Mali, Arghasree Banerjee, Mayukh Bhattacharjee, and Sankhadeep Chatterjee

Abstract Image segmentation is one of the most challenging and interesting research topics and draws the attention of the many researchers. Different methods have been proposed but a single method is not sufficient enough to segment a wide variety of images. Due to this reason, continuous research need to be carried out to improve the efficiency and the real life acceptability. In this work, a new image segmentation method is proposed which is based on galactic swarm optimization. Galactic swarm optimization is new metaheuristic method which is based on the movement of stars, galaxies and other objects of space. The proposed method use thresholding with the galactic swarm optimization where, the value of the threshold is to be determined by the metaheuristic algorithm. The optimal threshold value can efficiently segment an image. Experiments shows the efficiency and drawbacks of the proposed method. The advantages and problems of this method is discussed along with the future research directions.

Keywords Image segmentation · Galactic swarm optimization · Thresholding · Optimization

S. Chakraborty (✉) · K. Mali
University of Kalyani, Kalyani, West Bengal, India
e-mail: shouvikchakraborty51@gmail.com

K. Mali
e-mail: kalyanimali1992@gmail.com

A. Banerjee · M. Bhattacharjee · S. Chatterjee
Department of Computer Science & Engineering, University of Engineering & Management, Kolkata, India
e-mail: banerjeearghasree@gmail.com

M. Bhattacharjee
e-mail: mayukhofficial12@gmail.com

S. Chatterjee
e-mail: chatterjeesankhadeep.cu@gmail.com

S. Banerjee and J. K. Mandal (eds.), *Advances in Smart Communication Technology and Information Processing*, Lecture Notes in Networks and Systems 165,
https://doi.org/10.1007/978-981-15-9433-5_24

1 Introduction

Computers become an inevitable part of our daily life. Various problems are solved using computers in various fields [1, 3, 5, 9, 10, 23]. Digital image processing is an active field of research that has various application in our daily life [13, 15, 16, 22]. Image segmentation is one of the most frequently used job in digital image processing. It is necessary in various automated tasks in computer vision and object recognition. Image segmentation methods generally divide an image and identify individual sections of an image. For example, if an image consists of a river, house and a tree then it is desirable that the automated image segmentation algorithm can identify all these three segments separately. Image segmentation has different applications to solve various types of problems. Each pixel should belong to some class. Image is divided into various regions and contours are extracted to get the separated regions of the image [2, 6]. Image segmentation has several applications including automated object recognition, computer aided diagnostics, authentication, scene understanding, intelligent devices etc. With the advancement in technology, various algorithms are proposed by many scientists to solve this problem. A single method may not be sufficient enough to segment different types of images [8, 19]. Therefore, it is necessary to put continuous effort in this particular field. Specially, subject specific segmentation is quite popular and frequently used in various applications. Researchers are working on designing segmentation algorithm which are specifically works well for a certain class of images. In general images under consideration can be contaminated with noise [7, 18]. Images can be corrupted with some foreign artifacts, blur and out-of-focus related issues [20, 21] which may cause various problems in automated segmentation [15]. Sophisticated algorithms are required to handle these problems and generate good quality segmented output. In this work, a new image segmentation method is proposed which is based on galactic swarm optimization and thresholding. Galactic swarm optimization is a metaheuristic algorithm which is inspired from the movements and the attraction forces of the stars and galaxies [15]. This algorithm is applied to compute the optimal value of the threshold so that precise segmentation output can be achieved. The proposed method is tested on some standard images and obtained outcome is very promising. As discussed earlier, the image segmentation is a very interesting topic and there is a lot of scope to pursue research, future directions with a roadmap is given in this article.

2 Background

2.1 The Galactic Swarm Optimization (GSO)

The GSO algorithm is one of the new metaheuristic algorithms [4] which is inspired from the motion of stars, galaxies and superclusters. In general, galaxies are not distributed uniformly in the cosmos. Galaxies hold the stars i.e. stars form clusters inside a galaxy. But stars also have a non-uniform distribution inside the cosmos. The attraction force of the stars to the large bodies inside a galaxy and the attraction force of the galaxies to the large objects are mimicked. Here, one solution gets attracted by the better solutions. A superswarm is formed by assuming that a subpopulation contains only the best solutions found up to a certain time. In general, a cluster of stars i.e. a galaxy is represented as a subswarm and a cluster of galaxies is represented as the superswarm. So, the global best solution of a subswarm is a representative of that particular subswarm in a superswarm. Steller masses in the galaxy experience an force towards the largest amount of decrease in the gravitational energy. The attraction force which is exercised by the large objects like sun on the smaller objects is implemented by the stochastic shift of a solution towards a better solution. One galaxy is represented by the center of mass. In general, there are two types motions should be considered in this context. First on is the motion of the objects inside the galaxies and the second one the is the motion of the center of masses of the galaxies. These two motions are implemented in the galactic swarm optimization by updating the individual subswarms in the first stage and then updating the superswarms accordingly in the second stage. The detailed illustration of this algorithm can be found in [17].

2.2 Thresholding

Thresholding is a method that separates the foreground and the background objects of an image. If an image consists of N intensity levels then 0 to $(N-1)$ will be the range of the pixel values. To separate an image into foreground and background, one single value is required to compute [12, 14]. Let us assume that the value is t then the image can be divided in to two classes using the Eqs. 1 and 2 [11].

$$C_0 = \{\operatorname{Im} g(i, j) \in X \mid 0 \le \operatorname{Im} g(i, j) \le t - 1\} \tag{1}$$

$$C1 = \{\operatorname{Im} g(i, j) \in X \mid t \le \operatorname{Im} g(i, j) \le N - 1\} \tag{2}$$

Here, C_0 and C_1 are the two classes and X is the image under consideration. $\operatorname{Im} g(i, j)$ is a pixel of X.

3 Proposed Method

In this work, the galactic swarm optimization is used with the thresholding to segment an image. Calculation of the optimal threshold value is a difficult job and therefore the galactic swarm optimization method is allowed to perform the same. The main job of the galactic swarm optimization is to find the optimal threshold value by considering the threshold value as particles and evolve accordingly. The objective function which is considered for this job is the Otsu's interclass variance and the equation for the same is given in Eq. 3.

$$\sigma_k^2 = \psi_k\left(\mu_k - \mu_g^2\right) \tag{3}$$

Here, $\mu_0,\ \mu_{1,\ldots,}\ \mu_k$ is the mean of the intensity values of the corresponding classes and μ_g is the global mean. μ_k is defined in Eq. 4.

$$\mu_k = \frac{\sum_{i=t_k}^{N-1} i \times prob_i}{\psi_1} \tag{4}$$

Here, $prob_i$ is the probability of the intensity of a pixel and the value of i can starts from 0 and ranges up to 255. The ψ_k is defined in Eq. 5.

$$\psi_k = \sum_{i=t_k}^{N-1} prob_i \tag{5}$$

The galactic swarm optimization maximizes the Otsu's interclass variance and the optimal threshold value is returned. The proposed method is also applicable for the color images also.

4 Experimental Results and Analysis

The proposed method is tested using some standard images Cameraman, Baboon, airplane, coins and hestain. The segmented output can be observed in Fig. 1.

The algorithm is numerically tested using two parameters Mean Squared Error (MSE) and Peak Signal to Noise Ratio (PSNR). MSE is defined in Eq. 6 and PSNR is defined in Eq. 7.

$$MSE = \frac{1}{M \times N} \sum_{j=1}^{M} \sum_{i=1}^{N} \left(IMG_{j,i} - IMG'_{j,i}\right) \tag{6}$$

Here, $[M \times N]$ is the size of the image, IMG and IMG' are the original and segmented image respectively.

$$PSNR = 10 \log_{10}\left(\frac{255^2}{MSE}\right) \tag{7}$$

The obtained MSE and PSNR values are reported in Table 1.

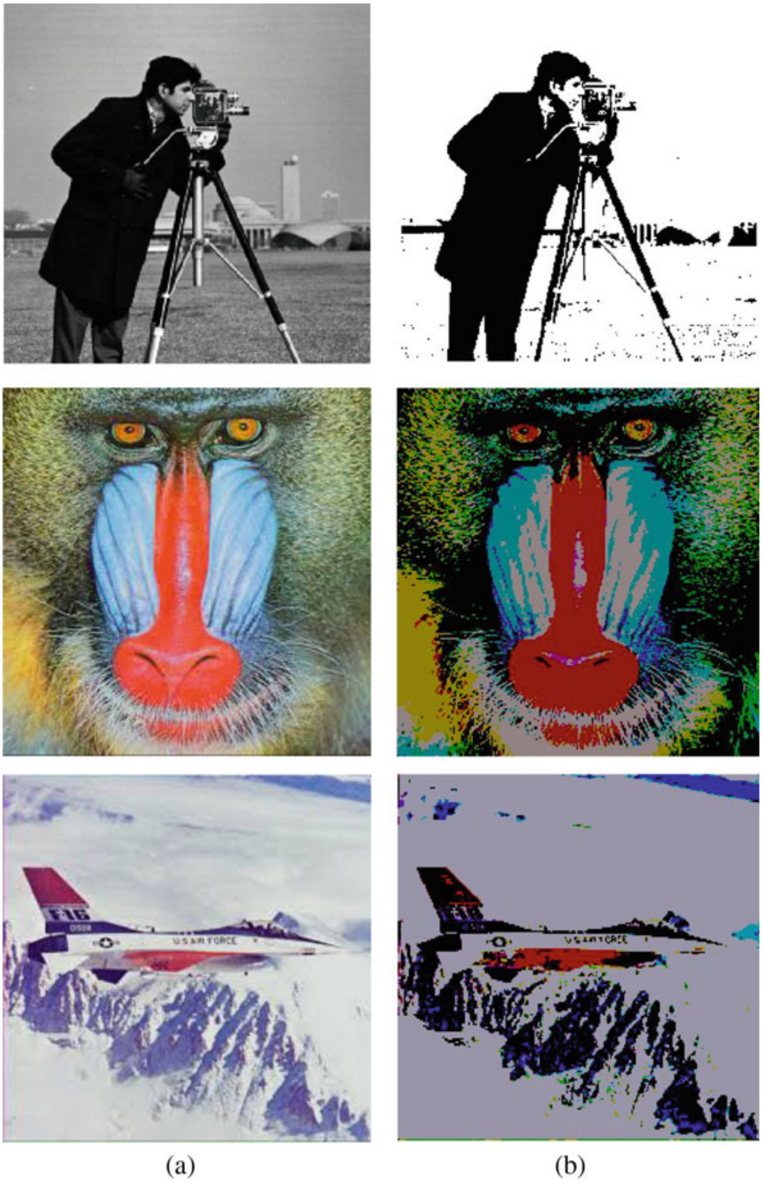

Fig. 1 Result of the segmentation using galactic search optimization **a** original image, **b** Segmented output. From top to bottom: Cameraman, Baboon, Airplane, Coins and Hestain images can be observed

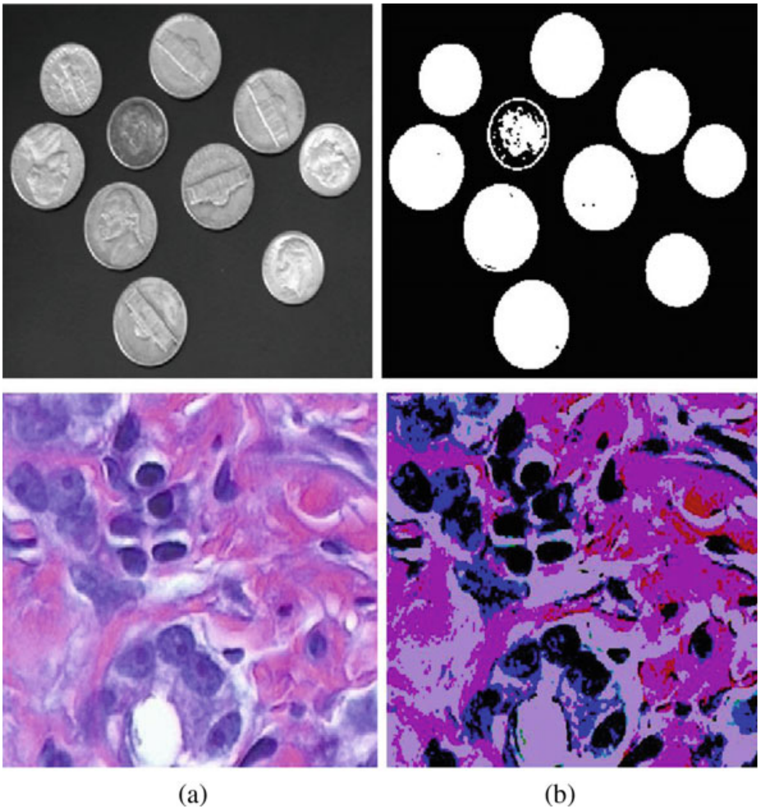

Fig. 1 (continued)

Table 1 Obtained MSE and PSNR values

Image	MSE	PSNR
Cameraman	724.3365	19.5313
Baboon	668.3621	19.8807
Airplane	698.2506	19.6907
Coins	706.3663	19.6405
Hestain	669.3369	19.8744

5 Conclusion and Future Scopes

This article presents a new method of image segmentation which is based on the galactic swarm optimization and thresholding. In this work, only binary segmentation is considered i.e. only threshold value is computed by the propose method and on the basis of the computed values the image is segmented. The segmentation output is quite satisfactory. This work can be further extended and the galactic swarm optimization can be employed to find the multiple threshold values so that an image can be segmented into various regions. In this work only one objective fgunstion is considered which is nothing but the Otsu's interclass variance. This method can also be tested using some other standard objective function or some new objective functions can also be contributed.

References

1. Burlina, P., et al.: Detection of age-related macular degeneration via deep learning. In: Proceedings—International Symposium on Biomedical Imaging, pp. 184–188. IEEE Computer Society (2016). https://doi.org/10.1109/ISBI.2016.7493240
2. Chakraborty, S., et al.: A novel lossless image encryption method using DNA substitution and chaotic logistic map. Int. J. Secur. Appl. **10**(2), 205–216 (2016). https://doi.org/10.14257/ijsia.2016.10.2.19
3. Chakraborty, S.: An advanced approach to detect edges of digital images for image segmentation. In: Chakraborty, S., Mali, K. (eds.) Applications of Advanced Machine Intelligence in Computer Vision and Object Recognition: Emerging Research and Opportunities. IGI GLobal (2020). https://doi.org/10.4018/978-1-7998-2736-8.ch004
4. Chakraborty, S., et al.: An elitist model for obtaining alignment of multiple sequences using genetic algorithm. In: 2nd National Conference NCETAS 2015, pp. 61–67. International Journal of Innovative Research in Science, Engineering and Technology (2015)
5. Chakraborty, S., et al.: An integrated method for automated biomedical image segmentation. In: 2017 4th International Conference on Opto-Electronics and Applied Optics (Optronix), pp. 1–5. IEEE (2017). https://doi.org/10.1109/OPTRONIX.2017.8349978
6. Chakraborty, S., et al.: An integrated method for automated biomedical image segmentation. In: 2017 4th International Conference on Opto-Electronics and Applied Optics, Optronix 2017 (2018). https://doi.org/10.1109/OPTRONIX.2017.8349978
7. Chakraborty, S., et al.: Automated breast cancer identification by analyzing histology slides using metaheuristic supported supervised classification coupled with bag-of-features. In: 2018 Fourth International Conference on Research in Computational Intelligence and Communication Networks (ICRCICN), pp. 81–86. IEEE (2018). https://doi.org/10.1109/ICRCICN.2018.8718736
8. Chakraborty, S., et al.: Contrast optimization using elitist metaheuristic optimization and gradient approximation for biomedical image enhancement. In: 2019 Amity International Conference on Artificial Intelligence (AICAI), pp. 712–717. IEEE (2019). https://doi.org/10.1109/AICAI.2019.8701367
9. Chakraborty, S., et al.: Dermatological effect of UV rays owing to ozone layer depletion. In: 2017 4th International Conference on Opto-Electronics and Applied Optics (Optronix), pp. 1–6. IEEE (2017). https://doi.org/10.1109/OPTRONIX.2017.8349975
10. Chakraborty, S., et al.: Detection of skin disease using metaheuristic supported artificial neural networks. In: 2017 8th Annual Industrial Automation and Electromechanical Engineering Conference (IEMECON), pp. 224–229. IEEE (2017). https://doi.org/10.1109/IEMECON.2017.8079594
11. Chakraborty, S., et al.: Modified cuckoo search algorithm in microscopic image segmentation of hippocampus. Microsc. Res. Tech. May, 1–22 (2017). https://doi.org/10.1002/jemt.22900
12. Chakraborty, S., et al.: Penalized fuzzy C-means enabled hybrid region growing in segmenting medical images. Presented at the (2020). https://doi.org/10.1007/978-981-13-8930-6_3
13. Chakraborty, S., Mali, K.: An overview of biomedical image analysis from the deep learning perspective. In: Chakraborty, S., Mali, K. (eds.) Applications of Advanced Machine Intelligence in Computer Vision and Object Recognition: Emerging Research and Opportunities. IGI Global (2020). https://doi.org/10.4018/978-1-7998-2736-8.ch008

14. Chakraborty, S., Mali, K.: Applications of advanced machine intelligence in computer vision and object recognition: emerging research and opportunities
15. Hore, S., et al.: An integrated interactive technique for image segmentation using stack based seeded region growing and thresholding. Int. J. Electr. Comput. Eng. **6**(6), 2773–2780 (2016). https://doi.org/10.11591/ijece.v6i6.11801
16. Mali, K., et al.: A study on statistical analysis and security evaluation parameters in image encryption. IJSRD-Int. J. Sci. Res. Dev. **3**, 2321–2613 (2015)
17. Muthiah-Nakarajan, V., Noel, M.M.: Galactic swarm optimization: a new global optimization metaheuristic inspired by galactic motion. Appl. Soft Comput. J. **38**, 771–787 (2016). https://doi.org/10.1016/j.asoc.2015.10.034
18. Roy, M., et al.: A dual layer image encryption using polymerase chain reaction amplification and dna encryption. In: 2019 International Conference on Opto-Electronics and Applied Optics, Optronix 2019. Institute of Electrical and Electronics Engineers Inc. (2019). https://doi.org/10.1109/OPTRONIX.2019.8862350
19. Roy, M., et al.: A study on the applications of the biomedical image encryption methods for secured computer aided diagnostics. In: 2019 Amity International Conference on Artificial Intelligence (AICAI), pp. 881–886 IEEE (2019). https://doi.org/10.1109/AICAI.2019.8701382
20. Roy, M., et al.: Biomedical image security using matrix manipulation and DNA encryption. In: Advances in Intelligent Systems and Computing, pp. 49–60 Springer (2020). https://doi.org/10.1007/978-981-15-0361-0_4
21. Roy, M., et al.: Data security techniques based on DNA encryption. In: Advances in Intelligent Systems and Computing, pp. 239–249. Springer (2020). https://doi.org/10.1007/978-981-15-0361-0_19
22. Sarddar, D., et al.: An efficient approach to calculate dynamic time quantum in round Robin algorithm for efficient load balancing. Int. J. Comput. Appl. **123**(14), 48–52 (2015). https://doi.org/10.5120/ijca2015905701
23. Seal, A., et al.: A new and resilient image encryption technique based on pixel manipulation, value transformation and visual transformation utilizing single–level Haar wavelet transform. In: Proceedings of the First International Conference on Intelligent Computing and Communication, pp. 603–611. Springer, Singapore (2017). https://doi.org/10.1007/978-981-10-2035-3_61

A Biomedical Image Segmentation Approach Using Darwinian Particle Swarm Optimization and Thresholding

Shouvik Chakraborty, Kalyani Mali, Kushankur Ghosh, Arya Sarkar, and Sankhadeep Chatterjee

Abstract Automated image segmentation has several application in real life. Biomedical image segmentation is one of them that has great impact on the automated computer aided diagnostics process. Automated identification of different parts of an image reduces the headache of the human experts. Moreover, precise detection and identification of a region of interest is possible. Inherent human errors can be reduced and faster results can be achieved with the help of automated and intelligent system. In this work, a biomedical image segmentation method is proposed which is based on Darwinian Particle Swarm Optimization (DPSO) and thresholding. The proposed method is tested both visually and numerically and the obtained results are quite promising.

Keywords Biomedical image segmentation · Metaheuristic algorithms · PSO · Thresholding · Computer aided diagnostics

---

S. Chakraborty (✉) · K. Mali
University of Kalyani, Kalyani, West Bengal, India
e-mail: shouvikchakraborty51@gmail.com

K. Mali
e-mail: kalyanimali1992@gmail.com

K. Ghosh · A. Sarkar · S. Chatterjee
Department of Computer Science & Engineering, University of Engineering & Management, Kolkata, India
e-mail: kush1999.kg@gmail.com

A. Sarkar
e-mail: aryasarkarwork@gmail.com

S. Chatterjee
e-mail: chatterjeesankhadeep.cu@gmail.com

S. Banerjee and J. K. Mandal (eds.), *Advances in Smart Communication Technology and Information Processing*, Lecture Notes in Networks and Systems 165,
https://doi.org/10.1007/978-981-15-9433-5_25

1 Introduction

Application of automated and computer based systems can be observed in different areas of science and technology [11, 12, 26]. Various difficult problems becomes easier with the blessings of the advanced technology [13, 23]. Digital image processing is no exception and using the it to solve various complex problems [3, 24]. Image segmentation is one of them and is a major concern of the researchers for a long time. Different solution are proposed to solve the problems of the image segmentation but a single solution may not be a good fit for various types of images. Therefore, continuous research is necessary in this domain because the foundation of the solutions of several problems is the automated image segmentation [5]. In computer aided diagnostics, image segmentation is often required for many purposes [6]. Precise and fast analysis is often required to save many precious lives by providing correct and timely treatment to the patient [4, 25]. In this article a new approach is proposed to segment biomedical images. It is based on the Darwinian Particle Swarm Optimization (DPSO) and thresholding where the DPSO algorithm is used to find the optimal threshold value. The proposed method is tested on some of the biomedical images of different modalities. Visual and quantitative investigation found that the proposed method is quite impressive can be used for the real life biomedical image segmentation problems. Moreover, a future roadmap is given to improve the efficiency of the proposed work.

2 Proposed Method

As discussed earlier, PSO suffers from one major problem i.e. it can get stuck in the local optima. Therefore, the conventional PSO algorithm works for some problems but may not work for some other problems. In [27], one modification to the conventional PSO is proposed which is known as the Darwinian Particle Swarm Optimization (DPSO). The main difference between the conventional PSO and the DPSO method is that in DPSO, more than one swarm can exists. The evolution of the individual swarms in similar like the conventional PSO [7, 17, 22]. The rules in PSO for the selection is also similar in the individual swarms of the DPSO. In general, PSO does not use genetic operators like mutation, crossover etc. DPSO enhances the concept of the PSO algorithm and includes the theory of the Darwin i.e. survival of the fittest. Here some parallel PSO algorithms are concurrently executed with different swarms i.e. different populations of the same problem. If a particular search instance is likely to be confined in the local optima then that one is completely discarded and the focus is shifted towards an another instance. Better swarms are rewarded by various method like extending the life of a particle. If a particle failed to reach a desired goal within a pre-specified number of steps then, the particle is deleted. A swarm can be deleted if the number of particles reaches a lower bound. A new swarm can also be generated from an existing swarm if any of the particle has not

Table 1 Parameters and their values for the DPSO algorithm

Parameters	Value
Iteration count	50
Size of the population	50
Minimum population	20
Maximum population	50
Swarm count	5
Minimum swarms	5
Maximum swarms	8

been deleted earlier. One constraint is that the number of maximum swarms should not be exceeded. There the probability of the new swarm creation $prob_{sc}$ is given in Eq. 1.

$$prob_{sc} = \frac{r}{\max_{scount}} \tag{1}$$

Here, r is a random number in [0, 1] and $\max_{scount}$ is the maximum number of possible swarms. Equation 1 restrict the new swarm creation if there is a large number of swarms are already present. In a new swarm, half of the particles are randomly chosen from the parent swarm and another half is selected from the other swarms. To get effective results, some parameters of the DPSO is also needs to be tuned appropriately. The parameters and their corresponding values are given in Table 1.

Co-efficient values in DPSO algorithm is selected as 1.5.

The DPSO algorithm is used with the thresholding [2, 16]. Thresholding is nothing but an image segmentation approach in which a value is to be determined which is used to segment an image. The threshold value can divide the total number of pixels into two classes. It can be done with the help of Eqs. 2 and 3 [8, 18, 20].

$$Cl_0 = \{\mathrm{Im}\,(i, j) \in IMG \,|\, 0 \le \mathrm{Im}\,(i, j) \le th - 1\} \tag{2}$$

$$Cl_1 = \{\mathrm{Im}\,(i, j) \in IMG \,|\, th \le \mathrm{Im}\,(i, j) \le N - 1\} \tag{3}$$

Here, $\mathrm{Im}\,(i, j)$ is a pixel of an image IMG. th is the compute threshold value and N is the number of intensity levels. So the range of the pixel value can from 0 to $N - 1$ [10, 19].

The chosen objective function is the Otsu's interclass variance and the equation for this objective function is given in Eq. 4 [9, 14, 15].

$$\sigma_k^2 = \psi_k\big(\mu_k - \mu_g^2\big) \tag{4}$$

Here, $\mu_0,\ \mu_{1,\ldots,}\mu_k$ is the mean of the intensity values of the corresponding classes and μ_g is the global mean. μ_k is defined in Eq. 5.

$$\mu_k = \frac{\sum_{i=t_k}^{N-1} i \times prob_i}{\psi_1} \tag{5}$$

Here, $prob_i$ is the probability of the intensity of a pixel and the value of i can starts from 0 and ranges up to 255. The ψ_k is defined in Eq. 6

$$\psi_k = \sum_{i=t_k}^{N-1} prob_i \tag{6}$$

The propose method tries to maximize the Otsu's interclass variance and the optimal threshold value is returned. The proposed method can also be applied on the color images.

3 Experimental Results

The experiment is performed using some biomedical images with different modalities such as Axial view of brain with T2 weighted MRI [28], Axial view of brain with CT Scan [29], Chest X-Ray [30], Transvaginal USG of ovary [1] and Microscopic image of a tissue [21]. The experiments are performed in Matlab R2014a with 4 GB of RAM and Intel Core i3 processor with 18 GHz speed. The experimental results are given in Fig. 1. The execution speed and the computed optimal threshold value is reported in Table 2.

The proposed method is quantitatively investigated using two well-known parameters. These are the Mean Squared Error (MSE) and the Peak Signal to Noise Ratio (PSNR). MSE is defined in Eq. 7 and PSNR is defined in Eq. 8.

$$MSE = \frac{1}{R \times C} \sum_{j=1}^{R} \sum_{i=1}^{C} \left(IMG_{j,i} - IMG'_{j,i} \right) \tag{7}$$

Here, $[R \times C]$ is the size of the image, IMG and IMG' are the original and segmented image respectively.

$$PSNR = 10 \log_{10} \left(\frac{255^2}{MSE} \right) \tag{8}$$

The obtained MSE and PSNR values are reported in Table 3.

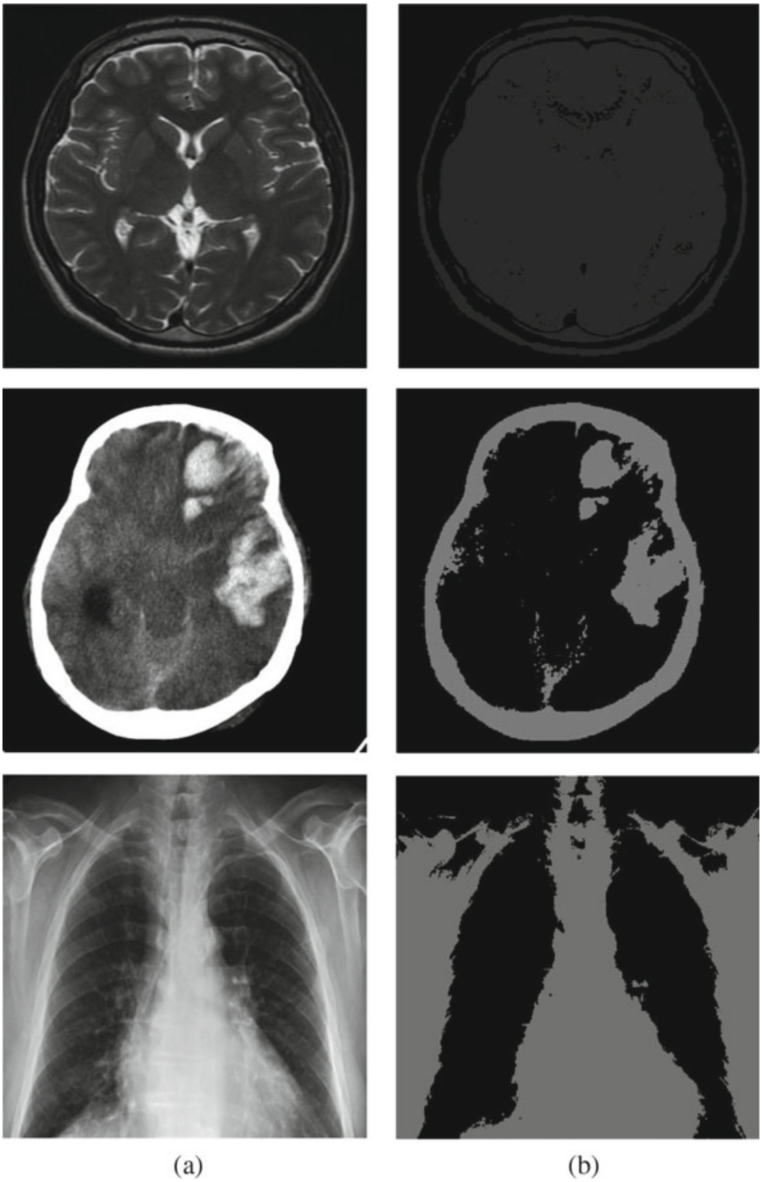

Fig. 1 The result of the segmented output **a** original image, **b** segmented output. From top to bottom: MRI, CT Scan, X-Ray, USG and Microscopic images can be observed

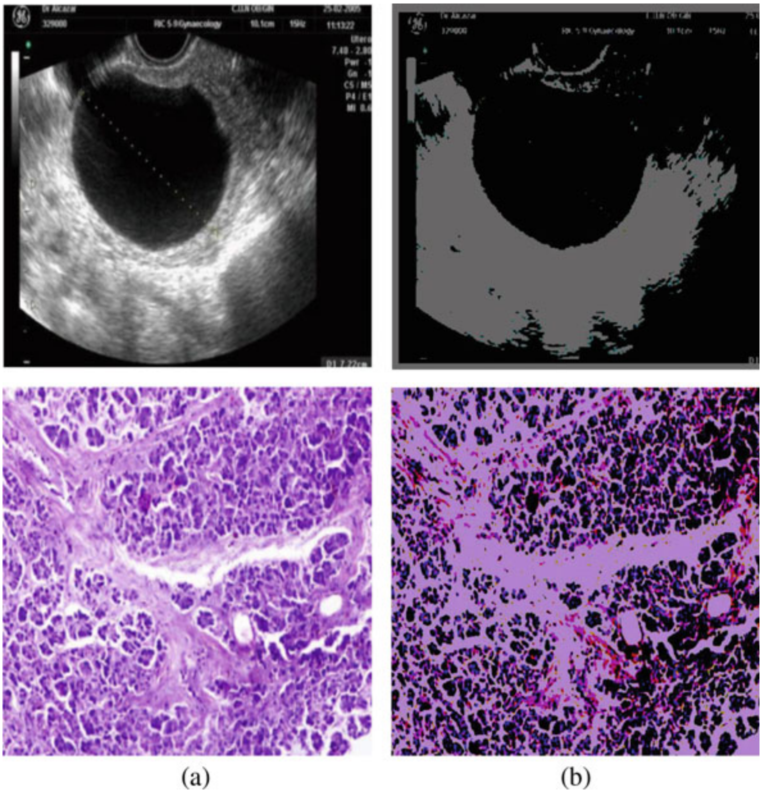

Fig. 1 (continued)

Table 2 CPU execution time and the optimal threshold values for various images

Image	CPU execution time	Optimal threshold value
MRI	5.2064	40
CT Scan	6.1286	131
X-Ray	5.5044	122
USG	5.5562	104
Microscopic	5.7496	171

Table 3 Obtained MSE and PSNR values

Image	MSE	PSNR
MRI	597.3625	20.3684
CT Scan	529.7003	20.8905
X-Ray	619.3369	20.2115
USG	607.1003	20.2982
Microscopic	697.9741	19.6924

4 Conclusion and Future Scope

A new biomedical image segmentation method is presented in this article which is based on the DPSO and thresholding. In this article, only bi-level thresholding is considered i.e. the proposed method is computing is only single threshold value. The proposed work can be enhanced to obtain multiple threshold values because for many images, binary thresholding is not acceptable. Moreover, the objective function can also be replaced with some other functions to test the efficiency of the proposed method.

References

1. Alcazar, J.L.: Ovarian simple cysts in asymptomatic postmenopausal women detected at transvaginal ultrasound: a review of literature. World J. Obstet. Gynecol. **4**(4), 108 (2015). https://doi.org/10.5317/wjog.v4.i4.108
2. Chakraborty, S., et al.: A novel lossless image encryption method using DNA substitution and chaotic logistic map. Int. J. Secur. Appl. **10**(2), 205–216 (2016). https://doi.org/10.14257/ijsia.2016.10.2.19
3. Chakraborty, S.: An advanced approach to detect edges of digital images for image segmentation. In: Chakraborty, S., Mali, K. (eds.) Applications of Advanced Machine Intelligence in Computer Vision and Object Recognition: Emerging Research and Opportunities. IGI GLobal (2020). https://doi.org/10.4018/978-1-7998-2736-8.ch004
4. Chakraborty, S., et al.: An elitist model for obtaining alignment of multiple sequences using genetic algorithm. In: 2nd National Conference NCETAS 2015, pp. 61–67. International Journal of Innovative Research in Science, Engineering and Technology (2015)
5. Chakraborty, S., et al.: An integrated method for automated biomedical image segmentation. In: 2017 4th International Conference on Opto-Electronics and Applied Optics, Optronix 2017 (2018). https://doi.org/10.1109/OPTRONIX.2017.8349978
6. Chakraborty, S., et al.: Contrast optimization using elitist metaheuristic optimization and gradient approximation for biomedical image enhancement. In: 2019 Amity International Conference on Artificial Intelligence (AICAI), pp. 712–717. IEEE (2019). https://doi.org/10.1109/AICAI.2019.8701367
7. Chakraborty, S., et al.: Intelligent computing in medical imaging: a study. In: Dey, N. (ed.) Advancements in Applied Metaheuristic Computing, pp. 143–163. IGI Global (2017). https://doi.org/10.4018/978-1-5225-4151-6.ch006
8. Chakraborty, S., et al.: Modified cuckoo search algorithm in microscopic image segmentation of hippocampus. Microsc. Res. Tech. May, 1–22 (2017). https://doi.org/10.1002/jemt.22900
9. Chakraborty, S., et al.: Penalized fuzzy C-means enabled hybrid region growing in segmenting medical images. Presented at the (2020). https://doi.org/10.1007/978-981-13-8930-6_3
10. Chakraborty, S., Bhowmik, S.: An efficient approach to job shop scheduling problem using simulated annealing. Int. J. Hybrid Inf. Technol. **8**(11), 273–284 (2015). https://doi.org/10.14257/ijhit.2015.8.11.23
11. Chakraborty, S., Bhowmik, S.: Blending roulette wheel selection with simulated annealing for job shop scheduling problem. In: IET Conference Publications (2015). https://doi.org/10.1049/cp.2015.1696
12. Chakraborty, S., Bhowmik, S.: Job shop scheduling using simulated annealing. In: First International Conference on Computation and Communication Advancement, pp. 69–73. McGrawHill Publication (2013)

13. Chakraborty, S., Mali, K.: An overview of biomedical image analysis from the deep learning perspective. In: Chakraborty, S., Mali, K. (eds.) Applications of Advanced Machine Intelligence in Computer Vision and Object Recognition: Emerging Research and Opportunities. IGI Global (2020). https://doi.org/10.4018/978-1-7998-2736-8.ch008
14. Chakraborty, S., Mali, K.: Application of multiobjective optimization techniques in biomedical image segmentation—a study. In: Multi-Objective Optimization, pp. 181–194. Springer Singapore, Singapore (2018). https://doi.org/10.1007/978-981-13-1471-1_8
15. Chakraborty, S., Mali, K.: Applications of advanced machine intelligence in computer vision and object recognition: emerging research and opportunities
16. Hore, S., et al.: An integrated interactive technique for image segmentation using stack based seeded region growing and thresholding. Int. J. Electr. Comput. Eng. **6**(6) (2016). https://doi.org/10.11591/ijece.v6i6.11801
17. Hore, S., et al.: Analysis of different feature description algorithm in object recognition (2016). https://doi.org/10.4018/978-1-5225-1025-3.ch004
18. Hore, S., et al.: Finding contours of hippocampus brain cell using microscopic image analysis. J. Adv. Microsc. Res. **10**(2), 93–103 (2015). https://doi.org/10.1166/jamr.2015.1245
19. Mali, K., et al.: A study on statistical analysis and security evaluation parameters in image encryption. IJSRD-Int. J. Sci. Res. Dev. **3**, 613–2321 (2015)
20. Mali, K., et al.: An efficient image cryptographic algorithm based on frequency domain using Haar Wavelet transform. Int. J. Secur. Appl. **9**(12), 279–288 (2015). https://doi.org/10.14257/ijsia.2015.9.12.26
21. Nayak, B.S., et al.: Half annular pancreas—a cadaveric case report. El Mednifico J. **2**(4), 411 (2015). https://doi.org/10.18035/emj.v2i4.346
22. Roy, M., et al.: A robust image encryption method using Chaotic Skew-Tent map. In: Chakraborty, S., Mali, K. (eds.) Applications of Advanced Machine Intelligence in Computer Vision and Object Recognition: Emerging Research and Opportunities (2020). https://doi.org/10.4018/978-1-7998-2736-8.ch001
23. Roy, M., et al.: Biomedical image enhancement based on modified Cuckoo Search and morphology. In: 2017 8th Annual Industrial Automation and Electromechanical Engineering Conference (IEMECON), pp. 230–235. IEEE (2017). https://doi.org/10.1109/IEMECON.2017.8079595
24. Roy, M., et al.: Cellular image processing using morphological analysis. In: 2017 IEEE 8th Annual Ubiquitous Computing, Electronics and Mobile Communication Conference (UEMCON), pp. 237–241. IEEE (2017). https://doi.org/10.1109/UEMCON.2017.8249037
25. Roy, M., et al.: Data security techniques based on DNA encryption. In: Advances in Intelligent Systems and Computing, pp. 239–249. Springer (2020). https://doi.org/10.1007/978-981-15-0361-0_19
26. Seal, A., et al.: A new and resilient image encryption technique based on pixel manipulation, value transformation and visual transformation utilizing single–level Haar wavelet transform (2017). https://doi.org/10.1007/978-981-10-2035-3_61
27. Tillett, J., et al.: Darwinian particle swarm optimization
28. File:Normal axial T2-weighted MR image of the brain.jpg—Wikimedia Commons. https://commons.wikimedia.org/wiki/File:Normal_axial_T2-weighted_MR_image_of_the_brain.jpg. Last accessed 25 March 2020
29. Head Computed tomography scanning: background, indications, contraindications. https://emedicine.medscape.com/article/2110836-overview. Last accessed 25 March 2020
30. MIMIC Chest X-Ray database to provide researchers access to over 350,000 patient radiographs. MIT News. https://news.mit.edu/2019/mimic-chest-x-ray-database-0201. Last accessed 25 March 2020

An Image Security Method Based on Low Dimensional Chaotic Environment and DNA Encoding

Mousomi Roy, Shouvik Chakraborty, Kalyani Mali, Deepayan Roy, and Sankhadeep Chatterjee

Abstract Transmission of digital images (or any other types of data) incurs a risk factor associated with it. Intruders always try to get access of the transmitted data. Therefore, it is necessary to protect the precious data before transmission, so that the threats, which are associated with the data transmission can be avoided and data communication becomes stress free. In this article, a new image encryption method is proposed which is based on chaos theory and DNA computing. Experiments show some promising results both visually and numerically. Various statistical analysis proves the power of the proposed image encryption method against various types of attacks. The method is simple to implement and strong enough to resist various types of attacks.

Keywords Image encryption · Chaos theory · DNA encryption

M. Roy · S. Chakraborty (✉) · K. Mali · D. Roy
University of Kalyani, West Bengal Kalyani, India
e-mail: shouvikchakraborty51@gmail.com

M. Roy
e-mail: iammouroy@gmail.com

K. Mali
e-mail: kalyanimali1992@gmail.com

D. Roy
e-mail: deepayan.per@gmail.com

S. Chatterjee
Department of Computer Science & Engineering, University of Engineering & Management, Kolkata, India
e-mail: chatterjeesankhadeep.cu@gmail.com

S. Banerjee and J. K. Mandal (eds.), *Advances in Smart Communication Technology and Information Processing*, Lecture Notes in Networks and Systems 165,
https://doi.org/10.1007/978-981-15-9433-5_26

1 Introduction

With the increasing use of internet and the significant advancements in the field of communication, digital image transmission is an inevitable part of our daily lives. With the advanced technology intelligent systems has some wide spread application in different domains [2, 13, 14, 16, 23, 25, 30, 33, 40, 42]. Different images are transmitted to various regions of the world over various communication media. It is observed that the security techniques or the data encryption methods which are applied on the text data, are not work well for the image data. Some characteristics of image data is different from the text data. The conventional data encryption methods are not very suitable for the image data. That is why, continuous effort is required to develop some sophisticated image encryption techniques for secured and hassle free digital image transmission. Various strategies are used to solve different problems of computer science [6, 7, 10–12, 17, 18, 20, 24, 26, 27, 36, 38]. Some of them are inspired from the nature or various other real life phenomena [4, 5, 8, 9, 15, 22, 31, 34, 35, 37, 39]. Chaos theory is one of the important topics from the perspective of the image encryption. Many researchers are working on the chaos based cryptographic systems. Certain properties of the chaos theory make it attractive to be used in the cryptographic applications. Chaotic systems possesses some properties like sensitivity to the initial values along with the values of the system parameters, pseudo-randomness, ergodicity etc. which makes it suitable for applications in the cryptography. Chaos based encryption methods are frequently used in the image encryption due to its performance and efficiency.

DNA encryption is one of the modern methods of securing digital data. DNA computing is very trending now a days due to its high storage capacity and efficiency of data representation. Image pixels can be encoded into DNA sequences in different ways. DNA encoding methods have direct impact on the quality of the encryption. Some points needs to be remembered while designing a secured image encryption method. The encrypted image must be highly sensitive to the initial image as well as the choice of the key i.e. a small change in the original image or in the key controlling parameters should produce a significant difference in the encrypted image [21, 32]. Keys are the most important part of any encryption method. If someone can find the keys then the encryption method does not make sense. Therefore, any encryption method must be efficient enough so that it can protect the keys from being predicted. Moreover, sometimes the encrypted data can be decrypted totally or partially using some other keys except the actual keys. It can be happened when the encryption method is structurally weak. Complexity of the underlying algorithm is also an important factor from the perspective of the image encryption.

2 Background

2.1 DNA and DNA Computing

DNA computing it inspired from the DNA structures of the living organisms. DNAs are constructed using a long strands of nucleotides. The nucleotides are constructed using nitrogen base, sugar with five carbons and a phosphate group. Nucleotide is given on the basis of the consisting nitrogen base. Nitrogen bases can be classified in four ways as follows: Adenine (A), Thymine (T), Guanine (G) and Cytosine (C). The DNA strands are formed in such a way in which Adenine is paired with Thymine and Guanine is combined with Cytosine. DNA strands generally forms a double helix structure. Variations in the long nucleotide chains make different species and variations in the properties among different species and also within the same species.

DNA computing exploits the combination of different properties of the DNA strands. Cryptography is one of the most important applications of the DNA computing methods. Data can be encoded in different ways using DNA computing. DNA computing based method has some significant properties like huge storage capacity and massive parallelism. DNA computing based methods to encode binary data in different ways. Binary number system consider zero and one as complementary [43]. The complementary base pairs are often used encode binary data in DNA format. In this work, DNA encoding is used along with the chaotic systems to secure digital images.

2.2 Chaos Theory and Their Application in Data Security

The chaos theory is basically based on some chaotic maps. The chaotic systems have some interesting properties which makes it suitable to be used for data security purposes. One of the most important properties of the chaotic systems is sensitivity to the initial conditions i.e. A very small change in the system can cause a huge change in the behavior of the system. Therefore if you can change the initial parameters of a chaotic map then large variation in output can be observed. Moreover the chaotic systems are deterministic in nature. The non-linearity of the system makes it suitable to generate complex encryption mechanism which is difficult to break. The chaos theory can effectively represent a dynamical system with mathematics. The main interest of the chaos theory is nonlinear dynamics. The advantages of nonlinear dynamics with non-periodicity, deterministic behavior and DNA computing is exploited in this work to get a secured and better image Encryption Algorithm [1, 3, 19, 29]. Both discrete and continuous chaotic systems can be used to encrypt digital data. Different types of chaotic maps are used to generate the chaotic sequences which are in turn used to generate the pseudo-random bit sequences. The output of the chaotic maps can be varied significantly with a small change in the controlling parameters. This feature increases the security of the encryption algorithm and allows us to choose the values of the controlling parameters as an additional set of keys along with the actual keys. It introduces an additional layer of security.

3 Proposed Method

The proposed system is based on the DNA encryption and chaotic system. In this work, two chaotic maps are used to increase the security. The chaotic logistic map and the chaotic tent map is used to produce the secret key. The chaotic logistic map is given in Eq. 1 and the chaotic skew-tent map is given in Eq. 2. The encryption process is given in algorithm 1. Decryption can also be performed by performing the exactly opposite method of algorithm 1.

$$x_{i+1} = f(x_i) = r * x_i * (1 - x_i) \tag{1}$$

Here x_i is the state parameter and the initial value is denoted by x_0. x_i can belongs to the [0, 1] range. r is the system parameter and can have any value between 1 and 4.

$$y_{i+1} = f(\alpha, y_i) = \begin{cases} \frac{y_i}{\alpha} & y_i \in [0, \alpha) \\ \frac{1-y_i}{1-\alpha} & y_i \in (\alpha, 1] \end{cases} \tag{2}$$

Here y_i is the state parameter and the initial value is denoted by y_0. y_i can belongs to the [0, 1] range. α is the system parameter.

Algorithm 1: Encryption algorithm

1. Select a 64 bit key randomly
2. Generate a pseudorandom bit sequence of length 64 bits using Eqs. 4a, 4b and 5.
3. Perform XOR operation between the 64 bits of step 1 and step 2.
4. Divide 64 bits which are obtained in step 3 into 8 groups of 8 bits each.
5. Divide the obtained bit sequence into three parts considering the bit sequence from MSB i.e. from left to right. So, we should get a division like 3, 3, 2. The last segment can be padded with a trailing 0. This procedure can be easily understood from Fig. 1. B0-b7 are bits of a group of 8 bits. Three groups are formed as follows: $\langle B7, B6, B5\rangle$, $\langle B4, B3, B2\rangle$, $\langle B1, B0, P\rangle$. Here, P is padding bit. In this work we are considering it as 0. But, it can be also be taken as 1.
6. Now perform XOR operation between these groups as given in Eq. 3.

$$\langle b2, b1, b0\rangle = \langle B7, B6, B5\rangle \oplus \langle B4, B3, B2\rangle \oplus \langle B1, B0, P\rangle \tag{3}$$

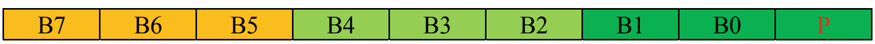

Fig. 1 Grouping method

Table 1 DNA encoding possible combinations

0		1		2		3		4		5		6		7	
A	00	A	00	C	00	C	00	G	00	G	00	T	00	T	00
C	01	G	01	A	01	T	01	A	01	T	01	C	01	G	01
G	10	C	10	T	10	A	10	T	10	A	10	G	10	C	10
T	11	T	11	G	11	G	11	C	11	C	11	A	11	A	11

7. Now convert the binary group $\langle b2, b1, b0 \rangle$ into decimal. This decimal number will be used as the selector of one of the DNA encoding rules from the eight possible combinations from Table 1.
8. Now, convert every pixel into binary form and divide it into 4 groups. Replace each group with its corresponding pair. Remember A can be replaced with T and G can be replaced with C.
9. Now perform the XOR operation between the replaced 8 bit sequence which is obtained from step 8 and the group of 8 bits obtained in step 4.
10. Convert the obtained binary bit sequence from step 9 into decimal and place it as an encrypted pixel. If the set of 64 bits which is obtained in step 2 gets exhausted (this set will get exhausted after each 8 bits) then obtain an another set of 64 bits using Eqs. 6a, 6b and 7 and continue it alternatively until all the pixels are processed.

$$x_{i+1} = f(x_i) = r * x_i(1 - x_i) \tag{4a}$$

$$y_{i+1} = f(y_i) = r * y_i(1 - y_i) \tag{4b}$$

$$prbs_i = PRBG(x_i, y_i) = \begin{cases} 0 & if\ x_i \le y_i \\ 1 & if\ x_i > y_i \end{cases} \tag{5}$$

$$p_{i+1} = f(\alpha, p_i) = \begin{cases} \frac{p_i}{\alpha} & p_i \in [0, \alpha) \\ \frac{1-p_i}{1-\alpha} & p_i \in (\alpha, 1] \end{cases} \tag{6a}$$

$$q_{i+1} = f(\alpha, q_i) = \begin{cases} \frac{q_i}{\alpha} & q_i \in [0, \alpha) \\ \frac{1-q_i}{1-\alpha} & q_i \in (\alpha, 1] \end{cases} \tag{6b}$$

$$prbs_i = PRBG(p_i, q_i) = \begin{cases} 0 & if\ p_i \le q_i \\ 1 & if\ p_i > q_i \end{cases} \tag{7}$$

4 Experimental Results

The experiments are performed using Matlab R2014a in a computer with 4 GB ram and Intel i3 processor. Experiments are performed on some standard images called Cameraman, Peeper and Aeroplane. The result of the encryption and decryption using the proposed method is given in Fig. 2. Some evaluation parameters are discussed below [28, 37, 39, 41].

4.1 Correlation Coefficient

In general, images possesses high correlation among pixels. A good encryption algorithm must break this correlation in order to resist cryptanalysis. Figure 3 gives an example of the correlation coefficients of the cameraman image.

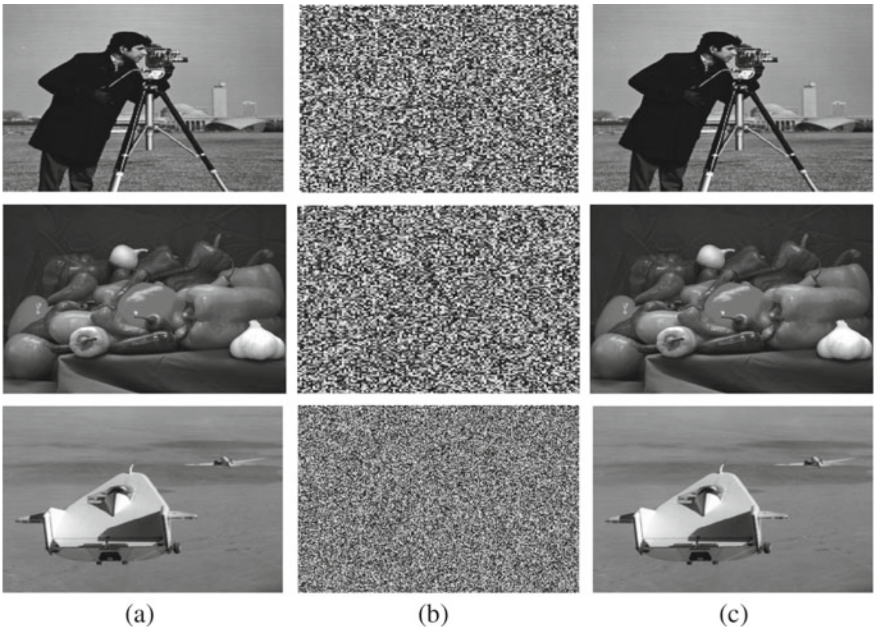

Fig. 2 Results of the encryption and decryption **a** original image, **b** encrypted image, **c** decrypted image. From top to bottom: Cameraman, Peeper and Airplane image

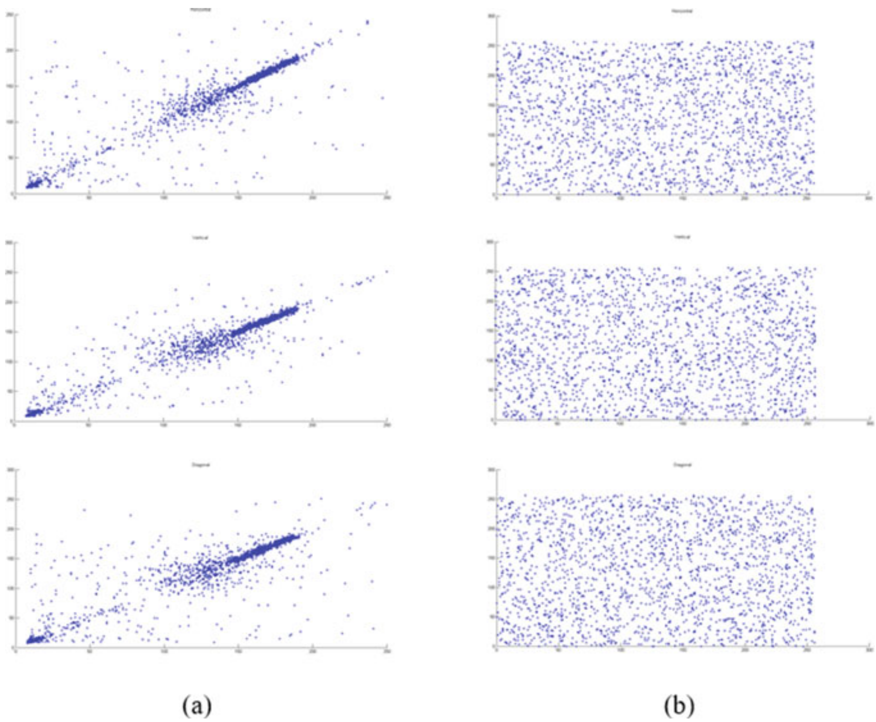

Fig. 3 Results of the correlation coefficients of the cameraman image **a** correlation coefficients of the original image **b** correlation coefficients of the encrypted images. From top to bottom: horizontal, diagonal and vertical correlation coefficients

4.2 Histogram

Histogram is one of the most important parameters to evaluate an image encryption scheme. A good encryption algorithm must distribute the pixels of an image equally or near equally in almost every gray levels. Figure 4. show the histogram of the original, encrypted and decrypted Aeroplane image.

4.3 Key Space

Key space is very important point to be analyzed from the perspective of the brute force attacks. Small key space makes the algorithm vulnerable against the brute force attacks. In this algorithm initially 64 bits are used as the key. These 64 bits are completely decided by the user and does not have any dependency on the algorithm. So for this, the key space will be 2^{64}. Now the set of initial values of the parameters i.e. $\langle x_i, y_i, p_i, q_i, r, \alpha \rangle$ of the chaotic logistic map and the skew-tent map can be used

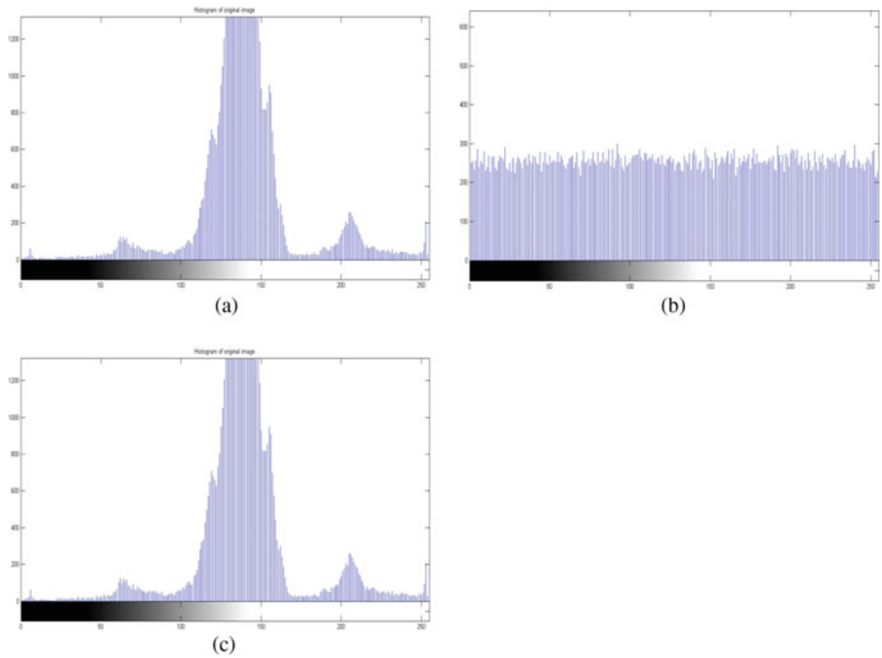

Fig. 4 Histograms of the cameraman image **a** original, **b** encrypted and **c** decrypted

as a set of keys. Theoretically these parameters can take infinite values. But for the sake of analysis, if we consider that these parameters can take precise values up to two decimal points then also the possible combinations will be the multiplication of all the possible numbers.

5 Conclusion

From the above discussion it is clear that the proposed encryption method is efficient enough and simple to implement. The security of this method makes it suitable to be applied for various real life applications. High dimensional chaotic systems are preferred over low dimensional chaotic systems because of the high complexity involved in the higher dimensional chaotic systems. Longer periods are highly desirable for secured encryption systems. Low dimensional chaotic maps suffers from the low key space which makes the system vulnerable to attacks but these type of chaotic systems are easy to implement. Proposed system proves that the efficient design can also achieve good quality security using low dimensional chaotic maps. The key and other security parameters must be sufficient enough to resist the various types of attacks.

References

1. Chakraborty, S. et al.: A novel lossless image encryption method using DNA substitution and chaotic logistic map. Int. J. Secur. Appl. **10**(2), (2016). https://doi.org/10.14257/ijsia.2016.10.2.19
2. Chakraborty, S., et al.: A study on different edge detection techniques in digital image processing (2016). https://doi.org/10.4018/978-1-5225-1025-3.ch005
3. Chakraborty, S.: An advanced approach to detect edges of digital images for image segmentation. In: Chakraborty, S., Mali, K. (eds.) Applications of Advanced Machine Intelligence in Computer Vision and Object Recognition: Emerging Research and Opportunities. IGI GLobal (2020). https://doi.org/10.4018/978-1-7998-2736-8.ch004
4. Chakraborty, S. et al.: An integrated method for automated biomedical image segmentation. In: 2017 4th International Conference on Opto-Electronics and Applied Optics, Optronix 2017 (2018). https://doi.org/10.1109/OPTRONIX.2017.8349978.
5. Chakraborty, S. et al.: Automated breast cancer identification by analyzing histology slides using metaheuristic supported supervised classification coupled with bag-of-features. In: 2018 Fourth International Conference on Research in Computational Intelligence and Communication Networks (ICRCICN), pp. 81–86. IEEE (2018). https://doi.org/10.1109/ICRCICN.2018.8718736
6. Chakraborty, S. et al.: Bag-of-features based classification of dermoscopic images. In: 2017 4th International Conference on Opto-Electronics and Applied Optics (Optronix), pp. 1–6. IEEE (2017). https://doi.org/10.1109/OPTRONIX.2017.8349977
7. Chakraborty, S. et al.: Bio-medical image enhancement using hybrid metaheuristic coupled soft computing tools. In: 2017 IEEE 8th Annual Ubiquitous Computing, Electronics and Mobile Communication Conference, UEMCON 2017 (2018). https://doi.org/10.1109/UEMCON.2017.8249036
8. Chakraborty, S. et al.: Contrast optimization using elitist metaheuristic optimization and gradient approximation for biomedical image enhancement. In: 2019 Amity International Conference on Artificial Intelligence (AICAI), pp. 712–717. IEEE (2019). https://doi.org/10.1109/AICAI.2019.8701367
9. Chakraborty, S. et al.: Dermatological effect of UV rays owing to ozone layer depletion. In: 2017 4th International Conference on Opto-Electronics and Applied Optics, Optronix 2017 (2018). https://doi.org/10.1109/OPTRONIX.2017.8349975
10. Chakraborty, S. et al.: Detection of skin disease using metaheuristic supported artificial neural networks. In: 2017 8th Annual Industrial Automation and Electromechanical Engineering Conference (IEMECON), pp. 224–229. IEEE (2017). https://doi.org/10.1109/IEMECON.2017.8079594.
11. Chakraborty, S. et al.: Gradient approximation in retinal blood vessel segmentation. In: 2017 4th IEEE Uttar Pradesh Section International Conference on Electrical, Computer and Electronics (UPCON), pp. 618–623. IEEE (2017). https://doi.org/10.1109/UPCON.2017.8251120
12. Chakraborty, S. et al.: Image based skin disease detection using hybrid neural network coupled bag-of-features. In: 2017 IEEE 8th Annual Ubiquitous Computing, Electronics and Mobile Communication Conference (UEMCON), pp. 242–246. IEEE (2017). https://doi.org/10.1109/UEMCON.2017.8249038
13. Chakraborty, S. et al.: Intelligent computing in medical imaging: a study. In: Dey, N. (ed.) Advancements in Applied Metaheuristic Computing, pp. 143–163. IGI Global (2017). https://doi.org/10.4018/978-1-5225-4151-6.ch006
14. Chakraborty, S. et al.: Modified cuckoo search algorithm in microscopic image segmentation of hippocampus. Microsc. Res. Tech. 1–22 (2017). https://doi.org/10.1002/jemt.22900
15. Chakraborty, S., et al.: Penalized fuzzy c-means enabled hybrid region growing in segmenting medical images. Presented (2020). https://doi.org/10.1007/978-981-13-8930-6_3
16. Chakraborty, S., Bhowmik, S.: An efficient approach to job shop scheduling problem using simulated annealing. Int. J. Hybrid Inf. Technol. **8**(11), 273–284 (2015). https://doi.org/10.14257/ijhit.2015.8.11.23

17. Chakraborty, S., Bhowmik, S.: Blending roulette wheel selection with simulated annealing for job shop scheduling problem. In: Michael Faraday IET International Summit 2015, pp. 100 (7). Institution of Engineering and Technology (2015). https://doi.org/10.1049/cp.2015.1696.
18. Chakraborty, S., Bhowmik, S.: Job shop scheduling using simulated annealing. In: First International Conference on Computation and Communication Advancement. pp. 69–73 McGrawHill Publication (2013)
19. Chakraborty, S., Mali, K.: An overview of biomedical image analysis from the deep learning perspective. In: Chakraborty, S., Mali, K. (eds.) Applications of Advanced Machine Intelligence in Computer Vision and Object Recognition: Emerging Research and Opportunities. IGI Global (2020). https://doi.org/10.4018/978-1-7998-2736-8.ch008
20. Chakraborty, S., Mali, K.: Application of multiobjective optimization techniques in biomedical image segmentation—a study. In: Multi-Objective Optimization, pp. 181–194. Springer Singapore, Singapore (2018). https://doi.org/10.1007/978-981-13-1471-1_8
21. Chakraborty, S., Mali, K.: Applications of advanced machine intelligence in computer vision and object recognition : emerging research and opportunities
22. Datta, S. et al.: Optimal usage of pessimistic association rules in cost effective decision making. In: 2017 4th International Conference on Opto-Electronics and Applied Optics (Optronix), pp. 1–5. IEEE (2017). https://doi.org/10.1109/OPTRONIX.2017.8349976
23. Hore, S. et al.: An integrated interactive technique for image segmentation using stack based seeded region growing and thresholding. Int. J. Electr. Comput. Eng. **6**(6), 2773–2780 (2016). https://doi.org/10.11591/ijece.v6i6.11801
24. Hore, S., et al.: Analysis of different feature description algorithm in object recognition (2016). https://doi.org/10.4018/978-1-5225-1025-3.ch004
25. Hore, S., et al.: Finding contours of hippocampus brain cell using microscopic image analysis. J. Adv. Microsc. Res. **10**(2), 93–103 (2015). https://doi.org/10.1166/jamr.2015.1245
26. Huo, Y., et al.: Towards portable large-scale image processing with high-performance. Computing (2018). https://doi.org/10.1007/s10278-018-0080-0
27. Libbrecht, M.W., Noble, W.S.: Machine learning applications in genetics and genomics. Nat. Rev. Genet. **16**(6), 321–332 (2015). https://doi.org/10.1038/nrg3920
28. Mali, K., et al.: A study on statistical analysis and security evaluation parameters in image encryption. IJSRD-Int. J. Sci. Res. Dev. **3**, 2321–2613 (2015)
29. Mali, K. et al.: An efficient image cryptographic algorithm based on frequency domain using haar wavelet transform. Int. J. Secur. Appl. **9**(12), 279–288 (2015).https://doi.org/10.14257/ijsia.2015.9.12.26
30. Mayo, R.C., Leung, J.: Artificial intelligence and deep learning–radiology's next frontier? (2018). https://doi.org/10.1016/j.clinimag.2017.11.007
31. Nguyen, G.N., et al.: A survey of the state-of-the-arts on neutrosophic sets in biomedical diagnoses. Int. J. Mach. Learn. Cybern. **10**, 1 (2019). https://doi.org/10.1007/s13042-017-0691-7
32. Patro, K.A.K., et al.: A secure multi-stage one-round bit-plane permutation operation based chaotic image encryption. Microsyst. Technol. **25**(6), 2331–2338 (2019). https://doi.org/10.1007/s00542-018-4121-x
33. Greenes, R.A.: Computer-aided diagnostic strategy selection. Radiol. Clin. North Am. **24**(1), 105–120 (1986)
34. Roy, M. et al.: A dual layer image encryption using polymerase chain reaction amplification and DNA encryption. In: 2019 International Conference on Opto-Electronics and Applied Optics, Optronix 2019. Institute of Electrical and Electronics Engineers Inc. (2019). /https://doi.org/10.1109/OPTRONIX.2019.8862350
35. Roy, M. et al.: A study on the applications of the biomedical image encryption methods for secured computer aided diagnostics. In: 2019 Amity International Conference on Artificial Intelligence (AICAI), pp. 881–886. IEEE (2019). https://doi.org/10.1109/AICAI.2019.8701382

36. Roy, M. et al.: Biomedical image enhancement based on modified cuckoo search and morphology. In: 2017 8th Annual Industrial Automation and Electromechanical Engineering Conference (IEMECON), pp. 230–235. IEEE (2017). https://doi.org/10.1109/IEMECON.2017.8079595
37. Roy, M. et al.: Biomedical image security using matrix manipulation and DNA encryption. In: Advances in Intelligent Systems and Computing, pp. 49–60. Springer (2020). https://doi.org/10.1007/978-981-15-0361-0_4
38. Roy, M. et al.: Cellular image processing using morphological analysis. In: 2017 IEEE 8th Annual Ubiquitous Computing, Electronics and Mobile Communication Conference, UEMCON 2017 (2018). https://doi.org/10.1109/UEMCON.2017.8249037
39. Roy, M. et al.: Data security techniques based on DNA encryption. In: Advances in Intelligent Systems and Computing, pp. 239–249. Springer, Berlin (2020). https://doi.org/10.1007/978-981-15-0361-0_19
40. Sarddar, D., et al.: An efficient approach to calculate dynamic time quantum in round robin algorithm for efficient load balancing. Int. J. Comput. Appl. **123**(14), 48–52 (2015). https://doi.org/10.5120/ijca2015905701
41. Seal, A. et al.: A new and resilient image encryption technique based on pixel manipulation, value transformation and visual transformation utilizing single–level haar wavelet transform (2017). https://doi.org/10.1007/978-981-10-2035-3_61
42. Tedmori, S., Al-Najdawi, N.: Image cryptographic algorithm based on the Haar wavelet transform. Inf. Sci. (Ny) **269**, 21–34 (2014). https://doi.org/10.1016/j.ins.2014.02.004
43. Zhang, Y.: A DNA-based encryption method based on DNA chip and PCR amplification techniques. https://works.bepress.com.pdf

Penalized Fuzzy C-Means Coupled Level Set Based Biomedical Image Segmentation

Shouvik Chakraborty, Kalyani Mali, Kushankur Ghosh, and Arya Sarkar

Abstract The biomedical image segmentation is one of the challenging task and an interesting topic of research since a long time. In the field of biomedical image based disease analysis, automated segmentation methods plays a crucial role in fast and accurate disease analysis. It is also helpful to treat the at the early stage of a disease which often saves many lives. In this work, a new biomedical image segmentation method is proposed based on penalized fuzzy c-means coupled with level set method. The proposed method is tested on different types of biomedical images and some inspiring results are observed. Experimental results makes it suitable for the real life deployment in the diagnostic field to save some precious time for diagnostics.

Keywords Fuzzy C-means · Level set segmentation · Biomedical image segmentation · Automated diagnosis

1 Introduction

In the field of computer vision and digital image analysis, image segmentation is always a challenging task and various approaches are proposed to solve this problem. A single approach may not be always suitable for all images under consideration. One image may suffer from various issues like poor contrast [1], noise, presence of foreign

S. Chakraborty (✉) · K. Mali
University of Kalyani, Kalyani, West Bengal, India
e-mail: shouvikchakraborty51@gmail.com

K. Mali
e-mail: kalyanimali1992@gmail.com

K. Ghosh · A. Sarkar
Department of Computer Science & Engineering, University of Engineering & Management, Kolkata, India
e-mail: kush1999.kg@gmail.com

A. Sarkar
e-mail: aryasarkarwork@gmail.com

S. Banerjee and J. K. Mandal (eds.), *Advances in Smart Communication Technology and Information Processing*, Lecture Notes in Networks and Systems 165,
https://doi.org/10.1007/978-981-15-9433-5_27

artifacts, poor illumination etc. [2]. A single method may not always handle all of these problems simultaneously and therefore continuous improvement in this domain is necessary [3–5]. With the advancement of technology, computer aided solutions are frequently used in various domains [6–11]. With the increasing use of the artificial intelligence and machine learning based solutions makes the life easier and different problems can be solved very efficiently [6, 12–14]. Biomedical image segmentation is no exception and frequently use various machine learning, artificial intelligence and soft computing tools [15–18]. Automated biomedical image analysis methods have widespread application in diagnostic field. It helps in timely diagnosis and also reduce the chances of the inherent human error. Accurate and timely diagnosis of a disease increases the chance of timely recovery because precise diagnostic results play a vital role in early treatment and prevention from successive effects [3, 19–21]. Level set method is one of the frequently used methods for image segmentation. It starts from an initial contour and evolve further to segment an image. In this work, level set method is hybridized with the penalized fuzzy c-means. The energy function is developed from the equation of the penalized fuzzy c-means [22, 23]. Experiments are performed on different types of biomedical images and the experimental results proves the efficiency of the proposed method.

2 Background

2.1 Penalized Fuzzy C-Means

In the context of image segmentation Fuzzy C-Means is a well-known method that uses fuzzy method to assign a particular pixel to some class. In short, it is nothing but an optimization method that iteratively optimize an objective function which is given in Eq. 1.

$$
\begin{aligned}
&K = \sum_{p=1}^{N} \sum_{q=1}^{c} \mu_{qp}^{m} \left\| x_p - v_q \right\|^2 \\
&such\ that \sum_{q=1}^{c} \mu_{qp} = 1 \quad \forall\, p \quad and\, 0 \le \mu_{qp} \le 1 \quad \forall q, p
\end{aligned}
\tag{1}
$$

Here, the basic assumption is that the N number of pixels are to be partitioned into c clusters. μ_{qp} is the membership function of a pixel x_p in a cluster p and it is given in Eq. 2. v_q is the center of the qth cluster and it is updated using Eq. 3. $\|.\|$ is norm metric and it represents the general Euclidean distance. The value of the parameter m does not change and in this work, this value is considered as 2. This parameter decides the amount of fuzziness.

$$\mu_{qp} = \frac{1}{\sum_{i=1}^{c} \left(\frac{\|x_p - v_q\|}{\|x_p - v_i\|} \right)^{2/m - 1}} \tag{2}$$

$$v_q = \frac{\sum_{p=1}^{N} \mu_{qp}^m x_p}{\sum_{p=1}^{N} \mu_{qp}^m} \tag{3}$$

One of the major problem which is associated with the conventional fuzzy c-means method is that it is highly sensitive to noise due to the lacking of information about the spatial context. The penalized fuzzy c-means method is inspired from the neighborhood expectation maximization method [24] and used to solve this problem. The modified objective function is given in Eq. 4. The penalty term is used to track the spatial dependence of the objects.

$$\begin{aligned} K_{PFCM} &= \sum_{p=1}^{N} \sum_{q=1}^{c} \mu_{qp}^m \|x_p - v_q\|^2 + \sigma \sum_{p=1}^{N} \sum_{r=1}^{N} \sum_{q=1}^{c} \mu_{qp}^m (1 - \mu_{qr})^m \omega_{pr} \\ such\ that &\sum_{q=1}^{c} \mu_{qp} = 1 \quad \forall\, p\ and\, 0 \le \mu_{qp} \le 1 \quad \forall q, p \end{aligned} \tag{4}$$

σ is a controlling parameter that controls the effect of the penalty term. ω_{pr} is defined in Eq. 5. μ_{qp} is the membership function and for the penalized version, it is given in Eq. 6. v_q is the center of the qth cluster and it is updated using Eq. 7.

$$\omega_{pr} = \begin{cases} 0\ if\ x_p\ and\ x_r\ are\ neighbours\ and\ p \neq r \\ \quad 1\ otherwise \end{cases} \tag{5}$$

$$\mu_{qp} = \frac{1}{\sum_{i=1}^{c} \left(\frac{d^2(x_p, q_q) + \sigma \sum_{r=1}^{N} (1 - \mu_{qr})^m \omega_{pr}}{d^2(x_p, q_i) + \sigma \sum_{r=1}^{N} (1 - \mu_{ir})^m \omega_{pr}} \right)^{\frac{1}{m-1}}} \tag{6}$$

$$v_q = \frac{\sum_{r=1}^{N} (\mu_{qr})^m x_r}{\sum_{r=1}^{N} (\mu_{qr})^m} x + y = z \tag{7}$$

2.2 Level Set Method

Level set method is a part of the active contour based segmentation methods. It can efficiently handle the shapes and contours of an object. In the context of two dimensional image segmentation, the level set function is used to represent a closed curve. This represented closed curve is the zero level set of the distance function

ϕ. This closed curve begins from a randomly selected contour, the evolution of this curve depends on the level set equation which is given in Eq. 8 [25].

$$\frac{\partial \theta}{\partial t} + \vec{V}.\nabla\phi = b.\Delta\phi \tag{8}$$

Here, $\nabla\phi$ represents the gradient of ϕ and $\Delta\phi$ represents the laplacian of ϕ. $b.\Delta\phi$ represents the artificial viscosity. As per the proposal found in [26], $b.\Delta\phi$ term can be replaced with $b.k.|\Delta\phi|$ for better evolution, where k represents the curvature of the ϕ. So the Eq. 8 can be rewritten as the modified level set equation which is given in 9.

$$\frac{\partial \theta}{\partial t} + \vec{V}.\nabla\phi = b.k.|\Delta\phi| \tag{9}$$

3 Proposed Approach

In this work, a penalized fuzzy c-means based level set method is proposed which is applied on the biomedical image segmentation. As discussed earlier, penalized fuzzy c-means method has better capability than the normal fuzzy c-means method. This property is highly desirable and useful from the context of biomedical image analysis.

3.1 Energy Function and Level Set Equation

Equation 4 is the equation which is to be optimized for the penalized fuzzy c-means method. K_{PFCM} can be written as the function of the three terms $K_{PFCM}(M, X, V)$ where M is the partition matrix. It contains the value of the membership μ_{qp} i.e. membership of the pth pixel to the qth class. X is the collection of pixels i.e. $X = \{x_p\}_{p=1}^{N}$. V is an array or vector that contains the centroid of the qth class v_q. As per [27], one bias field can be introduced. To do so, first the relationship among the actual intensity X_p, observed intensity X'_p and gain G_p for the pth pixel for total N number of pixels can be established using Eq. 10.

$$X'_p = X_p G_p \quad \forall p \in \{1, 2, 3, \ldots, N\} \tag{10}$$

After taking the log transform both sides of Eqs. 10 and 11 can be written.

$$x'_p = x_p + \psi_p \quad \forall p \in \{1, 2, 3, \ldots, N\} \tag{11}$$

Here x'_p and x_p are the log transformed observed intensity and actual intensity of the pth pixel respectively. ψ_p is the bias for the pth pixel. Now, by substituting Eq. 11 in Eqs. 4, 12 can be derived.

$$K(M, X', \Psi, V)_{PFCM} = \sum_{p=1}^{N}\sum_{q=1}^{c} \mu_{qp}^{m}\left\|x'_P - \psi_P - v_q\right\|^2 + \sigma \sum_{p=1}^{N}\sum_{r=1}^{N}\sum_{q=1}^{c} \mu_{qp}^{m}\left(1-\mu_{qr}\right)^m \omega_{pr} \tag{12}$$

$$such\ that \sum_{q=1}^{c} \mu_{qp} = 1 \quad \forall p \quad and\, 0 \le \mu_{qp} \le 1 \quad \forall q, p$$

Here, $X' = \left\{x'_p\right\}_{p=1}^{N}$ is the collection of the observed intensities which is nothing but the observed image. $\Psi = \left\{\psi_p\right\}_{p=1}^{N}$ is the bias image. In continuous domain, Eq. 12 can be rewritten as Eq. 13 where Ω is used for the penalty term.

$$\begin{aligned} &K(M, X', \Psi, V)_{PFCM} \\ &\quad = \sum_{q=1}^{c} \int_{\pi_q} M_q^m\left(x, x'\right)\left\|X'\left(x, x'\right) - \Psi\left(x, x'\right) - v_q\right\|^2 dxdy + \Omega_q \\ &such\ that \sum_{q=1}^{c} M_q\left(x, x'\right) = 1 \quad \forall x,\ x' \quad 0 \le M_q\left(x, x'\right) \le 1 \quad \forall q,\ x,\ x' \end{aligned} \tag{13}$$

Assume $c = 2$ for the sake of discussion then, a level set function can be added to Eq. 13 and, can be rewritten as Eq. 14.

$$\begin{aligned} &K(M, X', \Psi, V, \phi)_{PFCM} \\ &\quad = \int_{\pi} M_1^m\left(x, x'\right)\left\|X'\left(x, x'\right) - \Psi\left(x, x'\right) - v_1\right\|^2 \mathrm{Z}(\phi) dxdy + \Omega_1 \\ &\quad + \int_{\pi} M_2^m\left(x, x'\right)\left\|X'\left(x, x'\right) - \Psi\left(x, x'\right) - v_2\right\|^2 (1 - \mathrm{Z}(\phi)) dxdy + \Omega_2 \\ &s.t.\ M_1\left(x, x'\right) + M_2\left(x, x'\right) = 1 \ \forall x,\ x'\ and\ 0 \le M_q\left(x, x'\right) \le 1 \ \forall q,\ x,\ x' \end{aligned} \tag{14}$$

The energy function $EF\left(M, X', \Psi, V, \phi\right)$ which is given in Eq. 15, can be derived from Eq. 14 where λ is a constant parameter with $\lambda > 0$, C represents the curve at the zero level of ϕ and $|C|$ is the length of C which can be computed using Eq. 16 [28].

$$EF\left(M, X', \Psi, V, \phi\right) = K(M, X', \Psi, V, \phi)_{PFCM} + \lambda|C| \tag{15}$$

$$|C| = \int_{\pi} |\nabla Z(\phi)| dxdy \tag{16}$$

Now, the level set equation can be obtained by minimizing the energy function [29] which is given in Eq. 15.

4 Experimental Results

The proposed method is tested on some biomedical images with different modalities. The experiments are performed using Matlab R2014a with an Intel core i3 processor with clock speed of 1.8 GHz and 4 GB RAM. The selected images are T2 weighted MRI of brain (axial view) [30], CT Scan of brain (axial view) [31], Chest X-Ray [32], Transvaginal USG of ovary [33] and Microscopic images of pancreas tissue [34]. The results are given in Fig. 1. The initial contour is selected manually. The segmented images produce smooth and thin contour which makes it suitable for real life applications. The proposed method is also applicable for color images.

5 Conclusion

The proposed method can deal with different types of biomedical images with various modalities. This hybrid method can also handle noisy images efficiently and the generated output consist of smooth and thin segmenting lines which makes the proposed method suitable for precise application. The segmented regions are prominent and near accurate and there helpful in automated diagnosis and further analysis. The proposed method can be improved in several ways. The design of the optimization function can be modified accordingly so that it can model the spatial context more efficiently. Research can improve the evolution and can make the whole process faster.

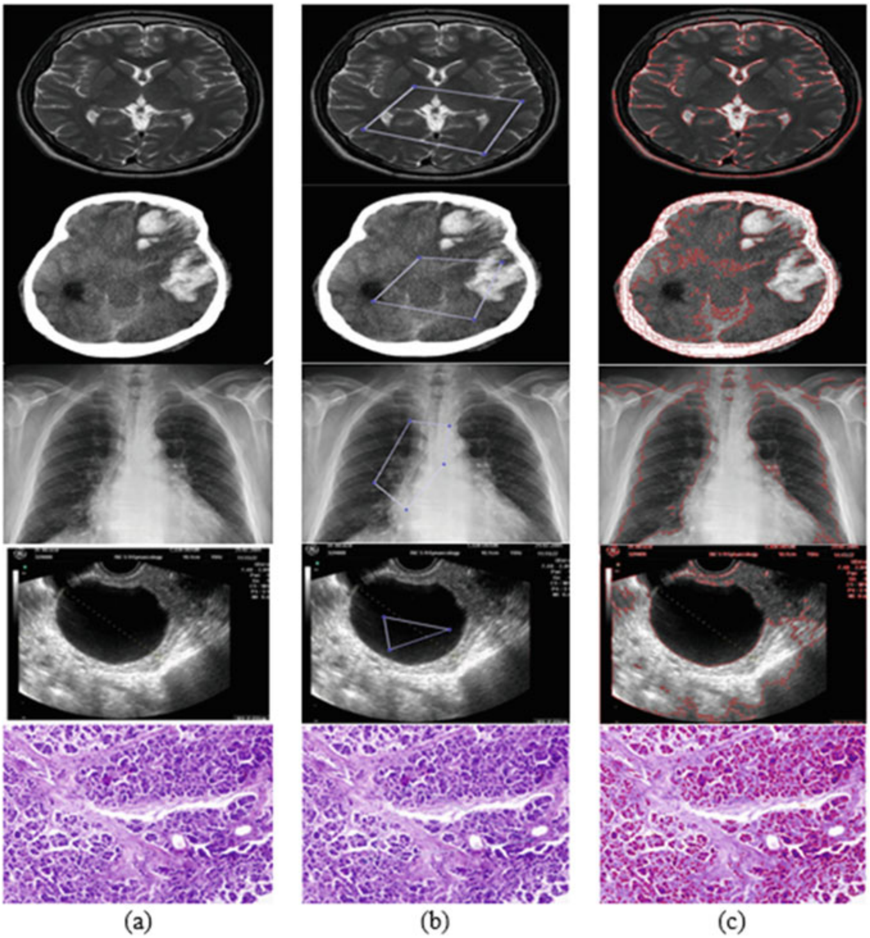

Fig. 1 Results obtained by applying the proposed method on the biomedical images of different modalities **a** the original image, **b** initial contour which is selected interactively, **c** final segmented output. From top to bottom: Images of MRI, CT Scan, X-Ray, USG and Microscopic image

References

1. Chakraborty, S., et al.: Contrast optimization using elitist metaheuristic optimization and gradient approximation for biomedical image enhancement. In: 2019 Amity International Conference on Artificial Intelligence (AICAI), pp. 712–717. IEEE (2019). https://doi.org/10.1109/AICAI.2019.8701367
2. Chakraborty, S., et al.: Automated breast cancer identification by analyzing histology slides using metaheuristic supported supervised classification coupled with bag-of-features. In: 2018 Fourth International Conference on Research in Computational Intelligence and Communication Networks (ICRCICN), pp. 81–86. IEEE (2018). https://doi.org/10.1109/ICRCICN.2018.8718736

3. Chakraborty, S., et al.: An integrated method for automated biomedical image segmentation. In: 2017 4th International Conference on Opto-Electronics and Applied Optics (Optronix), pp. 1–5. IEEE (2017). https://doi.org/10.1109/OPTRONIX.2017.8349978
4. Nguyen, G.N., et al.: A survey of the state-of-the-arts on neutrosophic sets in biomedical diagnoses. Int. J. Mach. Learn. Cybern. **10**, 1 (2019). https://doi.org/10.1007/s13042-017-0691-7
5. Roy, M., et al.: A robust image encryption method using chaotic skew-tent map. In: Chakraborty, S., Mali, K. (eds.) Applications of Advanced Machine Intelligence in Computer Vision and Object Recognition: Emerging Research and Opportunities (2020). https://doi.org/10.4018/978-1-7998-2736-8.ch001
6. Chakraborty, S.: An advanced approach to detect edges of digital images for image segmentation. In: Chakraborty, S., Mali, K. (eds.) Applications of Advanced Machine Intelligence in Computer Vision and Object Recognition: Emerging Research and Opportunities. IGI GLobal (2020). https://doi.org/10.4018/978-1-7998-2736-8.ch004
7. Chakraborty, S., Bhowmik, S.: Blending roulette wheel selection with simulated annealing for job shop scheduling problem. In: Michael Faraday IET International Summit 2015, p. 100. Institution of Engineering and Technology (2015). https://doi.org/10.1049/cp.2015.1696
8. Chakraborty, S., Bhowmik, S.: Job shop scheduling using simulated annealing. In: First International Conference on Computation and Communication Advancement, pp. 69–73. McGrawHill Publication (2013)
9. Greenes, R.A.: Computer-aided diagnostic strategy selection. Radiol. Clin. North Am. **24**(1), 105–120 (1986)
10. Sarddar, D., et al.: An efficient approach to calculate dynamic time quantum in round robin algorithm for efficient load balancing. Int. J. Comput. Appl. **123**(14), 48–52 (2015). https://doi.org/10.5120/ijca2015905701
11. Seal, A., et al.: A new and resilient image encryption technique based on pixel manipulation, value transformation and visual transformation utilizing single–level haar wavelet transform. In: Proceedings of the First International Conference on Intelligent Computing and Communication, pp. 603–611. Springer, Singapore (2017). https://doi.org/10.1007/978-981-10-2035-3_61
12. Chakraborty, S. et al.: An elitist model for obtaining alignment of multiple sequences using genetic algorithm. In: 2nd National Conference NCETAS 2015, pp. 61–67 Int. J. Innov. Res. Sci. Eng. Technol. (2015)
13. Chakraborty, S., et al.: Modified cuckoo search algorithm in microscopic image segmentation of hippocampus. Microsc. Res. Tech. **80**(10), 1051–1072 (2017). https://doi.org/10.1002/jemt.22900
14. Hore, S., et al.: Finding contours of hippocampus brain cell using microscopic image analysis. J. Adv. Microsc. Res. **10**(2), 93–103 (2015). https://doi.org/10.1166/jamr.2015.1245
15. Chakraborty, S., Bhowmik, S.: An efficient approach to job shop scheduling problem using simulated annealing. Int. J. Hybrid Inf. Technol. **8**(11), 273–284 (2015). https://doi.org/10.14257/ijhit.2015.8.11.23
16. Mali, K., et al.: A study on statistical analysis and security evaluation parameters in image encryption. IJSRD Int. J. Sci. Res. Dev. **3**, 2321–2613 (2015)
17. Mali, K., et al.: An efficient image cryptographic algorithm based on frequency domain using haar wavelet transform. Int. J. Secur. Appl. **9**(12), 279–288 (2015). https://doi.org/10.14257/ijsia.2015.9.12.26
18. Peterson, L.E., Coleman, M.A.: Machine learning-based receiver operating characteristic (ROC) curves for crisp and fuzzy classification of DNA microarrays in cancer research. Int. J. Approx. Reason. **47**(1), 17–36 (2008). https://doi.org/10.1016/j.ijar.2007.03.006
19. Chakraborty, S., et al.: A study on different edge detection techniques in digital image processing (2016). https://doi.org/10.4018/978-1-5225-1025-3.ch005
20. Chakraborty, S., Mali, K.: An overview of biomedical image analysis from the deep learning perspective. In: Chakraborty, S., Mali, K. (eds.) Applications of Advanced Machine Intelligence in Computer Vision and Object Recognition: Emerging Research and Opportunities. IGI Global (2020). https://doi.org/10.4018/978-1-7998-2736-8.ch008

21. Hore, S., et al.: Analysis of different feature description algorithm in object recognition. (2018). https://doi.org/10.4018/978-1-5225-5204-8.ch023
22. Chakraborty, S., et al.: Penalized fuzzy C-means enabled hybrid region growing in segmenting medical images (2020). https://doi.org/10.1007/978-981-13-8930-6_3
23. Chakraborty, S., Mali, K.: Applications of advanced machine intelligence in computer vision and object recognition: emerging research and opportunities
24. Hu, T., et al.: Initialization of the neighborhood EM algorithm for spatial clustering. In: Lecture Notes in Computer Science (including subseries Lecture Notes in Artificial Intelligence and Lecture Notes in Bioinformatics), pp. 487–495. Springer, Berlin, Heidelberg (2009). https://doi.org/10.1007/978-3-642-03348-3_48
25. Balla-Arabé, S., et al.: A fast and robust level set method for image segmentation using fuzzy clustering and lattice Boltzmann method. IEEE Trans. Cybern. **43**(3), 910–920 (2013). https://doi.org/10.1109/TSMCB.2012.2218233
26. Chen, Y., et al.: Cellular automata based level set method for image segmentation. In: 2007 IEEE/ICME International Conference on Complex Medical Engineering, CME 2007, pp. 171–174 (2007). https://doi.org/10.1109/ICCME.2007.4381715
27. Chen, W., Giger, M.L.: A fuzzy c-means (FCM) based algorithm for intensity inhomogeneity correction and segmentation of MR images. In: 2004 2nd IEEE International Symposium on Biomedical Imaging: Macro to Nano, pp. 1307–1310 (2004). https://doi.org/10.1109/isbi.2004.1398786
28. Evans, L.C., Gariepy, R.F.: Measure Theory and fine Properties of Functions
29. Li, C., et al.: Distance regularized level set evolution and its application to image segmentation. IEEE Trans. Image Process. **19**(12), 3243–3254 (2010). https://doi.org/10.1109/TIP.2010.2069690https://doi.org/10.1109/TIP.2010.2069690
30. File: Normal axial T2-weighted MR image of the brain.jpg—Wikimedia Commons. https://commons.wikimedia.org/wiki/File:Normal_axial_T2-weighted_MR_image_of_the_brain.jpg. Accessed 25 Mar 2020
31. Head computed tomography scanning: background, indications, contraindications. https://emedicine.medscape.com/article/2110836-overview. Accessed 25 Mar 2020
32. MIMIC chest X-ray database to provide researchers access to over 350,000 patient radiographs. MIT News. https://news.mit.edu/2019/mimic-chest-x-ray-database-0201. Accessed 25 Mar 2020
33. Alcazar, J.L.: Ovarian simple cysts in asymptomatic postmenopausal women detected at transvaginal ultrasound: a review of literature. World J. Obstet. Gynecol. **4**(4), 108 (2015). https://doi.org/10.5317/wjog.v4.i4.108
34. Nayak, B.S., et al.: Half annular pancreas—a cadaveric case report. El Mednifico J. **2**(4), 411 (2015). https://doi.org/10.18035/emj.v2i4.346

Utilization of Hyperchaotic Environment and DNA Sequences for Digital Image Security

Mousomi Roy, Shouvik Chakraborty, Kalyani Mali, and Deepayan Roy

Abstract Propagation of digital images (or any other types of digital data) is always susceptible to intrusion and a risk factor is always associated with it. Various persons or organizations always try to get access of the transmitted data. Therefore, it is essential to design a mechanism to secure the precious data during transmission. It will be helpful in reducing various associated threats during data transmission and the total transmission process will be protected. In this article, a new image encryption method is proposed which is based on the hyperchatic environment and DNA computing. Obtained results are inspiring and proves the efficiency of the proposed method. Various statistical Experiments are performed to prove the power of the proposed image encryption method and the tolerance of the proposed method against various types of attacks can also be established. The method is strong enough and easy to implement.

Keywords Image encryption · Chaos theory · DNA encryption · Hyper chaotic environment

M. Roy · S. Chakraborty (✉) · K. Mali
University of Kalyani, Kalyani, West Bengal, India
e-mail: shouvikchakraborty51@gmail.com

M. Roy
e-mail: iammouroy@gmail.com

K. Mali
e-mail: kalyanimali1992@gmail.com

D. Roy
Department of Computer Science & Engineering, University of Engineering & Management, Kolkata, India
e-mail: deepayan.per@gmail.com

S. Banerjee and J. K. Mandal (eds.), *Advances in Smart Communication Technology and Information Processing*, Lecture Notes in Networks and Systems 165,
https://doi.org/10.1007/978-981-15-9433-5_28

1 Introduction

Transmission of digital images is very frequent nowadays because of the drastic development in network technology. Application of advanced science & technology can be observed in different domains [3, 8, 9, 14, 16, 21, 24, 27, 29]. Various types of images are transmitted to many parts of the globe using different communication media. Encryption techniques for the text data may not be suitable always for all kind of image data due to some inherent properties of image data. Therefore, dedicated image encryption methods are required to protect the digital images. Different methods and procedures are developed for different problems of computer science [3, 5–7, 10–12, 15, 17, 18]. Many solutions of different problems of the computer science are inspired partially or totally from the natural phenomena [4, 22, 25, 26]. Chaos and DNA computing based encryption methods are very popular and frequently used nowadays. Many researchers throughout the world are working on the chaos based cryptographic solutions. Some inherent features of the chaotic systems makes it attractive for the cryptographic applications. For example, chaotic systems are highly sensitive to the initial conditions, ergodicity, pseudo-randomness etc. These properties are exploited to design the encryption system.

DNA encryption is one of the advanced methods to secured digital data and very trending in recent days. Pixel values can be encoded into DNA sequences. A small change in the actual image or in the initial parameters should generate a huge deviation in the encrypted image [23]. Keys are the prime component of any encryption method. Therefore, security of the keys are the prime concern.

2 Background

2.1 DNA Encryption

DNA encryption uses the concept of DNA structures. There are four types Nitrogen bases found in DNA sequences as follows: Adenine (A), Thymine (T), Guanine (G) and Cytosine (C). The Adenine is paired with Thymine and Guanine is combined with Cytosine. DNA computing has some interesting features like huge storage capacity and massive parallelism. Binary number system consider zero and one as complementary [31]. The complementary base pairs are often used encode binary data in DNA format. In this work, DNA encoding is used along with the hyperchaotic system to encrypt images.

2.2 Chaos Theory and Their Application in Data Security

The chaos theory is adapted in the field of cryptography from the perspective of some chaotic maps. As discussed earlier, one of the prime properties of the chaotic systems is sensitivity to the initial conditions. Therefore, a small change in the initial values of the controlling parameters of a chaotic map can generate huge deviation in the output. DNA computing is employed in this work to get a strong and resilient image Encryption Algorithm [1, 20]. The values of the parameters that controls a chaotic map can be used as an additional set of keys along with the actual keys that incorporates an additional layer of security.

3 Proposed Method

The proposed system is based on the DNA encryption and hyper chaotic system. Hyperchaos is generated from the chaos and it has more than one positive Lyapunov exponents. Hyperchaotic systems have a higher complexity than the conventional chaotic systems. The underlying hyperchaotic systems generates higher key space. In this work, the adapted hyperchaotic system is given in Eq. 1 [13].

$$\begin{cases} \dot{x}_1 = -\alpha_1 x_1 + \alpha_2 x_2 \\ \dot{x}_2 = \alpha_3 x_1 - x_1 x_3 - x_2 + x_4 \\ \dot{x}_3 = x_1^2 - \alpha_4 (x_1 + x_3) \\ \dot{x}_4 = -\alpha_5 x_1 \end{cases} \tag{1}$$

Here, $(x_1, x_2, x_3, x_4)^T \in R^4$ is a vector that represents the state and $\alpha_i (i = 1, 2, 3, 4, 5)$ are the controlling parameters of this hyper chaotic system. The values of these controlling parameters are as follows: $\alpha_1 = 25$, $\alpha_2 = 60$, $\alpha_3 = 40$, $\alpha_4 = 4$, $\alpha_5 = 5$. The proposed encryption algorithm is given below.

Algorithm 1: Encryption algorithm

1. Select a 128 bit key randomly
2. Generate a pseudorandom bit sequence of length 128 bits using the hyperchaotic system as given in Eq. 1 and by following the method as described in [30].
3. Perform XOR operation between the 128 bits of step 1 and step 2 after reversing every alternate octets of the pseudorandom bit sequence as shown in Fig. 1 where K_i and P_i is the ith bit of the key and the pseudorandom sequence respectively.
4. Divide the obtained 128 bits into 16 groups each having 8 bits.
5. For each groups, reverse the bit sequence and convert it into decimal and find the remainder from this number by dividing with 8. This decimal number will be used as the selector of one of the DNA encoding rules from the eight possible combinations from Table 1.

K_1	K_2	K_3	K_4	K_5	K_6	K_7	K_8	K_9	K_{10}	…………………	K_{127}	K_{128}
								$\oplus$				
P_8	P_7	P_6	P_5	P_4	P_3	P_2	P_1	P_9	P_{10}	…………………	P_{127}	P_{128}

Fig. 1 Grouping method

Table 1 DNA encoding possible combinations

0		1		2		3		4		5		6		7	
A	00	A	00	C	00	C	00	G	00	G	00	T	00	T	00
C	01	G	01	A	01	T	01	A	01	T	01	C	01	G	01
G	10	C	10	T	10	A	10	T	10	A	10	G	10	C	10
T	11	T	11	G	11	G	11	C	11	C	11	A	11	A	11

6. Now, convert every pixel into binary form and divide it into 4 groups. Replace each group with its corresponding pair. Remember A can be replaced with T and G can be replaced with C.
7. Now perform the XOR operation between the replaced 8 bit sequence which is obtained from step 6 and the group of 8 bits obtained in step 4.
8. Convert the obtained binary bit sequence from step 7 into decimal and place it as an encrypted pixel. If the set of 128 bits which is obtained in step 2 gets exhausted (this set will get exhausted after each 16 pixels) then obtain an another set of 128 bits using the hyperchaotic system and continue it alternatively until all the pixels are processed.

4 Experimental Results

The experiments are performed using Matlab R2014a in a computer with 4 GB RAM and Intel i3 processor. Experiments are performed on some standard images called Cameraman, Barbara, Peeper and Aeroplane. The result of the encryption and decryption using the proposed method is given in Fig. 2. Some of the standard evaluation parameters and their values for various images is given below [2, 19, 28].

4.1 Correlation Coefficient

Meaningful digital images generally contains high correlation among pixels. A suitable and strong image encryption algorithm must consider this property in order to protect an image. Figure 3 gives an example of the correlation coefficients of the cameraman image.

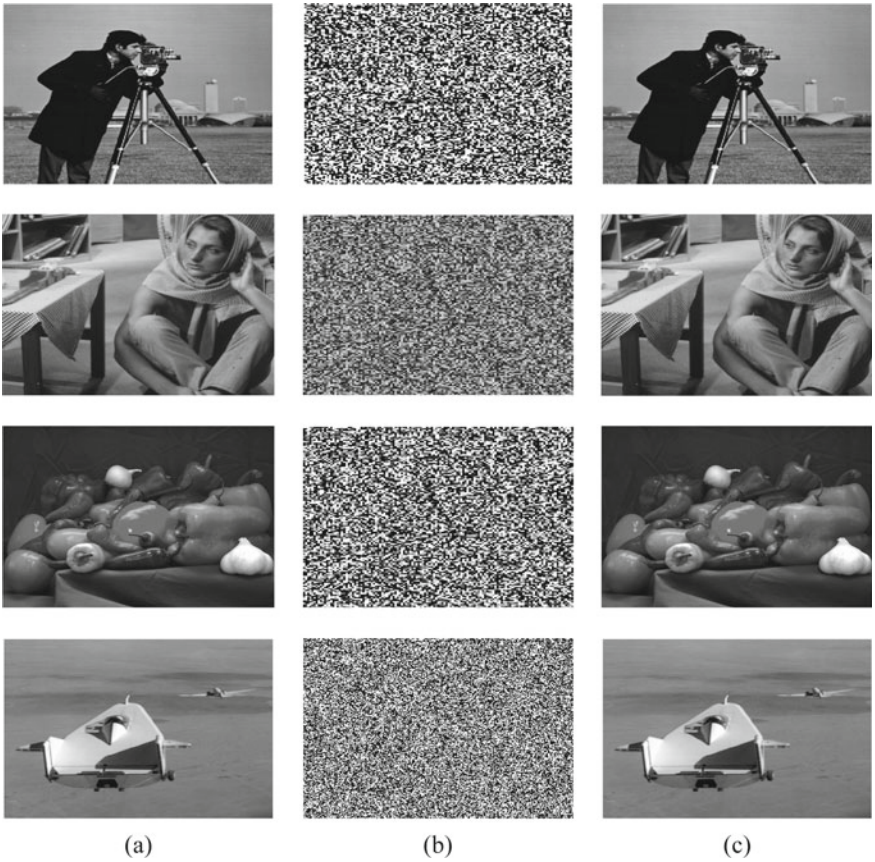

Fig. 2 Results of the encryption and decryption **a** original image, **b** encrypted image, **c** decrypted image. From top to bottom: Cameraman, Peeper, Barbara and Airplane image

4.2 Histogram

Histogram is one of the most important parameters to evaluate an image encryption scheme. A good encryption algorithm must distribute the pixels of an image equally or near equally in almost every gray levels. Figure 4 show the histogram of the original, encrypted and decrypted Aeroplane image.

4.3 Key Space

Key space is very important point to be analyzed from the perspective of the brute force attacks. Small key space makes the algorithm vulnerable against the brute

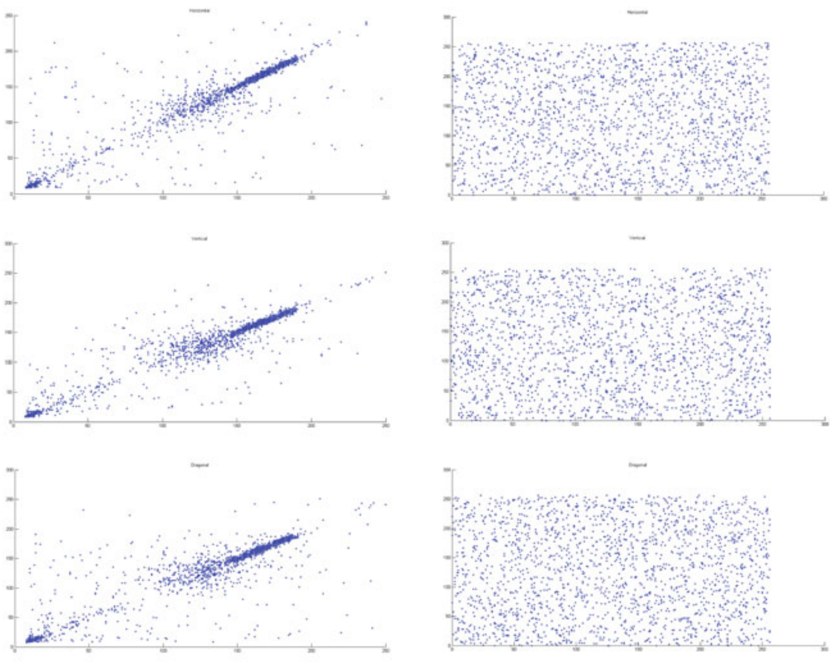

(a) (b)

Fig. 3 Results of the correlation coefficients of the cameraman image **a** correlation coefficients of the original image **b** correlation coefficients of the encrypted images. From top to bottom: horizontal, diagonal and vertical correlation coefficients

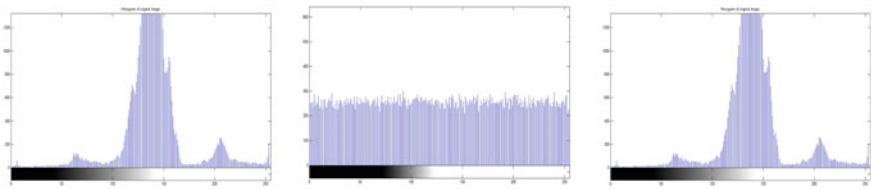

(a) (b) (c)

Fig. 4 Histograms of the cameraman image **a** original, **b** encrypted and **c** decrypted

force attacks. In this algorithm initially 64 bits are used as the key. These 64 bits are completely decided by the user and does not have any dependency on the algorithm. So for this, the key space will be 2^{128}. Now the set of initial values of the different controlling parameters of the hyperchaotic systems i.e. $\langle \alpha_1, \alpha_2, \alpha_3, \alpha_4, \alpha_5 \rangle$ can be considered as a set of keys.

5 Conclusion

The proposed image encryption system is designed with the help of the hyper chaotic systems and DNA encoding. The proposed method is simple to implement and resilient against different types of attacks. Large key space makes the proposed method strong enough against brute-force attacks and it is very difficult to predict the key. The higher dimensional chaotic system makes the complexity of the method significantly. It contributes significantly to the security measures of the algorithm. Conventional chaotic systems often suffers from the low key space which can be removed in the proposed method.

References

1. Chakraborty, S. et al.: A novel lossless image encryption method using DNA substitution and chaotic logistic map. Int. J. Secur. Appl. **10**(2) (2016). https://doi.org/10.14257/ijsia.2016.10.2.19
2. Chakraborty, S.: An advanced approach to detect edges of digital images for image segmentation. In: Chakraborty, S., Mali, K. (eds.) Applications of Advanced Machine Intelligence in Computer Vision and Object Recognition: Emerging Research and Opportunities. IGI GLobal (2020). https://doi.org/10.4018/978-1-7998-2736-8.ch004.
3. Chakraborty, S., et al.: An integrated method for automated biomedical image segmentation. In: 2017 4th International Conference on Opto-Electronics and Applied Optics (Optronix), pp. 1–5. IEEE (2017). https://doi.org/10.1109/OPTRONIX.2017.8349978
4. Chakraborty, S., et al.: Dermatological effect of UV rays owing to ozone layer depletion. In: 2017 4th International Conference on Opto-Electronics and Applied Optics, Optronix 2017 (2018). https://doi.org/10.1109/OPTRONIX.2017.8349975
5. Chakraborty, S., et al.: Detection of skin disease using metaheuristic supported artificial neural networks. In: 2017 8th Annual Industrial Automation and Electromechanical Engineering Conference (IEMECON), pp. 224–229. IEEE (2017). https://doi.org/10.1109/IEMECON.2017.8079594
6. Chakraborty, S., et al.: Gradient approximation in retinal blood vessel segmentation. In: 2017 4th IEEE Uttar Pradesh Section International Conference on Electrical, Computer and Electronics (UPCON), pp. 618–623. IEEE (2017). https://doi.org/10.1109/UPCON.2017.8251120
7. Chakraborty, S., et al.: Image based skin disease detection using hybrid neural network coupled bag-of-features. In: 2017 IEEE 8th Annual Ubiquitous Computing, Electronics and Mobile Communication Conference (UEMCON), pp. 242–246. IEEE (2017). https://doi.org/10.1109/UEMCON.2017.8249038
8. Chakraborty, S., et al.: Modified cuckoo search algorithm in microscopic image segmentation of hippocampus. Microsc. Res. Tech. (2017). https://doi.org/10.1002/jemt.22900
9. Chakraborty, S., Bhowmik, S.: An efficient approach to job shop scheduling problem using simulated annealing. Int. J. Hybrid Inf. Technol. **8**(11), 273–284 (2015). https://doi.org/10.14257/ijhit.2015.8.11.23
10. Chakraborty, S., Bhowmik, S.: Blending roulette wheel selection with simulated annealing for job shop scheduling problem. In: Michael Faraday IET International Summit 2015, p. 100. Institution of Engineering and Technology (2015). https://doi.org/10.1049/cp.2015.1696
11. Chakraborty, S., Bhowmik, S.: Job shop scheduling using simulated annealing. In: First International Conference on Computation and Communication Advancement, pp. 69–73. McGrawHill Publication (2013)

12. Chakraborty, S., Mali, K.: An overview of biomedical image analysis from the deep learning perspective. In: Chakraborty, S., Mali, K. (eds.) Applications of Advanced Machine Intelligence in Computer Vision and Object Recognition: Emerging Research and Opportunities. IGI Global (2020). https://doi.org/10.4018/978-1-7998-2736-8.ch008
13. Gao, Y., Liang, C.: A new 4D hyperchaotic system and its generalized function projective synchronization. Math. Probl. Eng. **2013**, 13 (2013). https://doi.org/10.1155/2013/701756https://doi.org/10.1155/2013/701756
14. Hore, S., et al.: An integrated interactive technique for image segmentation using stack based seeded region growing and thresholding. Int. J. Electr. Comput. Eng. **6**(6), 2773–2780 (2016). https://doi.org/10.11591/ijece.v6i6.11801
15. Hore, S., et al.: Analysis of different feature description algorithm in object recognition. (2016). https://doi.org/10.4018/978-1-5225-1025-3.ch004
16. Hore, S., et al.: Finding contours of hippocampus brain cell using microscopic image analysis. J. Adv. Microsc. Res. **10**(2), 93–103 (2015). https://doi.org/10.1166/jamr.2015.1245https://doi.org/10.1166/jamr.2015.1245
17. Huo, Y., et al.: Towards portable large-scale image processing with high-performance computing (2018). https://doi.org/10.1007/s10278-018-0080-0
18. Libbrecht, M.W., Noble, W.S.: Machine learning applications in genetics and genomics. Nat. Rev. Genet. **16**(6), 321–332 (2015). https://doi.org/10.1038/nrg3920https://doi.org/10.1038/nrg3920
19. Mali, K., et al.: A study on statistical analysis and security evaluation parameters in image encryption. IJSRD Int. J. Sci. Res. Dev. **3**, 2321–2613 (2015)
20. Mali, K., et al.: An efficient image cryptographic algorithm based on frequency domain using Haar wavelet transform. Int. J. Secur. Appl. **9**(12), 279–288 (2015). https://doi.org/10.14257/ijsia.2015.9.12.26
21. Mayo, R.C., Leung, J.: Artificial intelligence and deep learning—radiology's next frontier? (2018). https://doi.org/10.1016/j.clinimag.2017.11.007
22. Nguyen, G.N., et al.: A survey of the state-of-the-arts on neutrosophic sets in biomedical diagnoses. Int. J. Mach. Learn. Cybern. **10**, 1 (2019). https://doi.org/10.1007/s13042-017-0691-7https://doi.org/10.1007/s13042-017-0691-7
23. Patro, K.A.K., et al.: A secure multi-stage one-round bit-plane permutation operation based chaotic image encryption. Microsyst. Technol. **25**(6), 2331–2338 (2019). https://doi.org/10.1007/s00542-018-4121-xhttps://doi.org/10.1007/s00542-018-4121-x
24. Greenes, R.A.: Computer-aided diagnostic strategy selection. Radiol. Clin. North Am. **24**(1), 105–120 (1986)
25. Roy, M., et al.: A robust image encryption method using chaotic skew-tent map. In: Chakraborty, S., Mali, K. (eds.) Applications of Advanced Machine Intelligence in Computer Vision and Object Recognition: Emerging Research and Opportunities (2020). https://doi.org/10.4018/978-1-7998-2736-8.ch001
26. Roy, M., et al.: Data security techniques based on DNA encryption. In: Advances in Intelligent Systems and Computing, pp. 239–249. Springer (2020). https://doi.org/10.1007/978-981-15-0361-0_19
27. Sarddar, D., et al.: An efficient approach to calculate dynamic time quantum in round robin algorithm for efficient load balancing. Int. J. Comput. Appl. **123**(14), 48–52 (2015). https://doi.org/10.5120/ijca2015905701https://doi.org/10.5120/ijca2015905701
28. Seal, A., et al.: A new and resilient image encryption technique based on pixel manipulation, value transformation and visual transformation utilizing single–Level haar wavelet transform (2017). https://doi.org/10.1007/978-981-10-2035-3_61
29. Tedmori, S., Al-Najdawi, N.: Image cryptographic algorithm based on the Haar wavelet transform. Inf. Sci. (Ny) **269**, 21–34 (2014). https://doi.org/10.1016/j.ins.2014.02.004https://doi.org/10.1016/j.ins.2014.02.004

30. Zhan, K., et al.: Cross-utilizing hyperchaotic and DNA sequences for image encryption. J. Electron. Imaging. **26**(1), 013021 (2017). https://doi.org/10.1117/1.jei.26.1.013021.
31. Zhang, Y.: A DNA-based encryption method based on DNA chip and PCR amplification techniques. works.bepress.com

A Biomedical Image Segmentation Approach Using Fractional Order Darwinian Particle Swarm Optimization and Thresholding

Shouvik Chakraborty, Kalyani Mali, Arghasree Banerjee, and Mayukh Bhattacharjee

Abstract Image segmentation is one of the inevitable parts of the digital image processing and very useful to solve different real life problems. Biomedical image segmentation is a prime domain of application of digital image processing. and automated computer aided diagnostics process has high dependency on it. Automated identification of different regions of an image are often required by the human experts. Moreover, accurate detection and identification of a region of interest is possible using the automated methods. Errors are common for the human experts and can be reduced and faster results can be achieved with the help of automated and intelligent systems. This work proposes a biomedical image segmentation process using Fractional Order Darwinian Particle Swarm Optimization (FODPSO) and thresholding. The efficiency of the proposed method is tested both visually and quantitatively and the results speaks itself about the efficiency of the proposed work.

Keywords Biomedical image segmentation · Metaheuristic algorithms · PSO · Thresholding · Computer aided diagnostics · Fractional calculus · FODPSO

S. Chakraborty (✉) · K. Mali
University of Kalyani, Kalyani, West Bengal, India
e-mail: shouvikchakraborty51@gmail.com

K. Mali
e-mail: kalyanimali1992@gmail.com

A. Banerjee · M. Bhattacharjee
Department of Computer Science & Engineering, University of Engineering & Management, Kolkata, India
e-mail: Banerjeearghasree@gmail.com

M. Bhattacharjee
e-mail: mayukhofficial12@gmail.com

S. Banerjee and J. K. Mandal (eds.), *Advances in Smart Communication Technology and Information Processing*, Lecture Notes in Networks and Systems 165,
https://doi.org/10.1007/978-981-15-9433-5_29

1 Introduction

Use of intelligent automated with computer aided systems can be traced in various domains of science and technology [10, 14, 15, 29]. Many complex problems becomes simpler with the blessings of the modern technology [16, 25]. Digital image processing is an important and frequently used domain, it is used to solve various complex problems of computer vision [5, 7, 9]. Image segmentation is one of the prime application of the digital image processing and is a major topic of the researchers for a long time. Various solutions are developed to solve different types of problems of the image segmentation. A particular solution may not be a good fit for different types of images. Therefore, research and investigation is required in this domain because the solutions of several problems is the automated image segmentation [8]. In computer aided diagnostics investigations, image segmentation is frequently required for many purposes [24]. Accurate and quick analysis is often required to get the results of the investigations save many lives by providing precise and timely treatment to the patient [6, 26, 27]. Time is extremely important in the medical field. In this article a new method is proposed for biomedical image segmentation. It is based on the FODPSO and thresholding. The FODPSO algorithm is used to determine the optimal threshold value. The experiments are performed on some of the biomedical images of different modalities. Visual and quantitative results proves the efficiency of the proposed method. Moreover, a future plan is provided to improve the efficiency of the proposed work.

2 Proposed Method

In general, PSO has a major drawback i.e. it can stuck in the local optima and may not always reach the global optima always. So, the actual PSO algorithm may be suitable for some problems but may not be applicable for some problems which have various local optima. In [30], one enhancement to the actual PSO is proposed which is known as the Darwinian Particle Swarm Optimization (DPSO). The prime difference between the actual PSO and the DPSO method is that in DPSO, more than one swarm is possible and can execute simultaneously. The evolution of the each swarms in similar like the actual PSO [4, 11, 19]. The selection rules in PSO is also similar for each swarms of the DPSO. In general, PSO does not have genetic operators like mutation, crossover etc. DPSO improves the basic idea of the PSO algorithm and incorporates the Darwinian theory survival of the fittest. Here different populations of the same problem can execute in parallel. If a particular instance tends to be restricted by the local optima then that instance can be completely discarded and an another instance can be considered. Better swarms are rewarded using various strategies like extending the life of a particle. If a particle is unsuccessful to achieve a desired state within a pre-specified number of steps then, the particle is removed from the swarm. A swarm can also be removed if the number of particles reaches a certain threshold.

A new swarm can also be introduced by deriving from an existing swarm if any of the particle has not been deleted earlier. One major constraint is that the count of the maximum swarms should not be exceeded. Here the probability of the introduction of a new swarm $prob_{sc}$ is given in Eq. 1.

$$prob_{sc} = \frac{n}{\max_{scount}} \tag{1}$$

Here, n is a random number in [0, 1] and $\max_{scount}$ is the maximum number of possible swarms. Equation 1 restricts the new swarm creation depending on the number of swarms which are already available. For a newly generated swarm, half of the total particles are selected randomly from the parent swarm and rest of the half is selected from the other swarms. An another modification of DPSO is explained in [32] which is known as fractional order DPSO (FODPSO). Fractional calculus has a wide range of applications in various fields of science and technology. Introducing fractional calculus in DPSO makes it more diverge. The value of the fractional coefficient should be carefully chosen. The required time for the FODPSO is sometimes higher than the DPSO method. To get effective results, some parameters of the FODPSO is also needs to be tuned appropriately. The parameters and their corresponding values are given in Table 1.

The FODPSO algorithm is used with the thresholding [3, 18, 28]. Thresholding is a frequently used image segmentation method in which a value which is known as threshold value is to be determined which is used to segment an image. The threshold value is used divide the total set of pixels into two classes. It can be done with the help of Eqs. 2 and 3 [12, 20, 22].

$$Cls_0 = \{\mathrm{I}(i, j) \in IMG | 0 \leq \mathrm{I}(i, j) \leq thrs - 1\} \tag{2}$$

$$Cls_1 = \{\mathrm{I}(i, j) \in IMG | thrs \leq \mathrm{I}(i, j) \leq N - 1\} \tag{3}$$

Table 1 Parameters and their values for the FODPSO algorithm

Parameters	Value
Iteration count	50
Size of the population	50
Minimum population	20
Maximum population	50
Swarm count	5
Minimum swarms	5
Maximum swarms	8
Fractional coefficient	0.7

Here, $\mathrm{I}(i, j)$ is a pixel of an image *IMG*. *thrs* is the compute threshold value and N is the total count of intensity levels. Therefore, the pixel values can ranges from 0 to $N-1$ [13, 21].

The Otsu's interclass variance is used as the objective function and the equation for this is given in Eq. 4 [17].

$$\sigma_k^2 = \psi_k\left(\mu_k - \mu_g^2\right) \tag{4}$$

Here, $\mu_0, \mu_1, \ldots, \mu_k$ is the mean of the intensity values of the corresponding classes and μ_g is the global mean. μ_k is defined in Eq. 5.

$$\mu_k = \frac{\sum_{i=t_k}^{N-1} i \times prob_i}{\psi_1} \tag{5}$$

Here, $prob_i$ is the probability of the intensity of a pixel and the value of i can starts from 0 and ranges up to 255. The ψ_k is defined in Eq. 6

$$\psi_k = \sum_{i=t_k}^{N-1} prob_i \tag{6}$$

The propose method tries to maximize the Otsu's interclass variance and the optimal threshold value is returned. The proposed method can also be applied on the color images.

3 Experimental Results

The proposed method is tested on some of the biomedical images. These images are selected from different modalities such as Axial view of brain with T2 weighted MRI [31], PET MRI [2], Axial view of brain with CT Scan [33], Chest X-Ray [34], Transvaginal USG of ovary [1] and Microscopic image of a tissue [23]. The experiments are performed in Matlab R2014a with 4 GB of RAM and Intel Core i3 processor with 18 GHz speed. The experimental results are reported in Fig. 1. The execution speed and the computed optimal threshold value is reported in Table 2.

The proposed method of biomedical image segmentation is quantitatively investigated using two well-known parameters. These are the Mean Squared Error (MSE) and the Peak Signal to Noise Ratio (PSNR). MSE is defined in Eq. 7 and PSNR is defined in Eq. 8.

$$MSE = \frac{1}{S_1 \times S_2} \sum_{j=1}^{S_1} \sum_{i=1}^{S_2} \left(IM_{j,i} - IM_{j,i}^{'}\right) \tag{7}$$

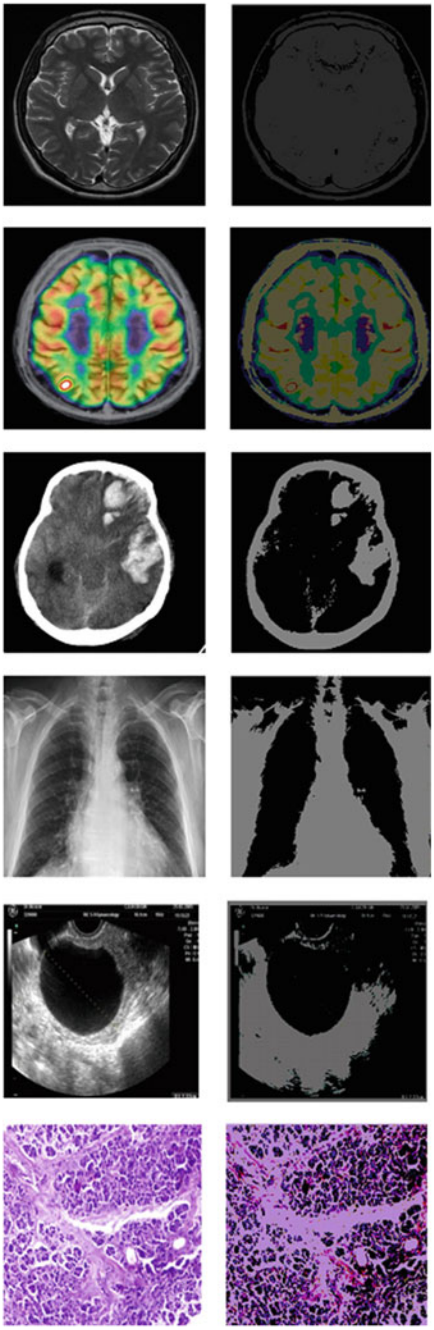

Fig. 1 The result of the segmented output **a** original image, **b** segmented output. From top to bottom: MRI, PET MRI, CT Scan, X-Ray, USG and Microscopic images can be observed

Table 2 CPU execution time and the optimal threshold values for various images

Image	CPU execution time	Optimal threshold value
MRI	8.7714	40
PET MRI	6.4818	85
CT scan	7.5132	133
X-Ray	7.8448	122
USG	6.1060	102
Microscopic	6.4932	179

Table 3 Obtained MSE and PSNR values

Image	MSE	PSNR
MRI	547.3196	20.7484
PET MRI	598.3327	20.3614
CT scan	543.7193	20.7771
X-Ray	639.1103	20.0750
USG	597.3717	20.3684
Microscopic	657.7913	19.9499

Here, $[S_1 \times S_2]$ is the size of the image, IM and $IM^{'}$ are the original and segmented image respectively.

$$PSNR = 10\log_{10}\left(\frac{255^2}{MSE}\right) \tag{8}$$

The obtained MSE and PSNR values are reported in Table 3.

4 Conclusion and Future Scope

A new biomedical image segmentation method is presented in this work which is based on the FODPSO and thresholding. In this article, only two levels of thresholding is considered. The proposed method is finding only single threshold value. The proposed work can be extended to generate multiple thresholds. It is necessary because for many images, only one value of the threshold is not acceptable for many images. Moreover, the objective function can be changed and some other objective functions cane be used to test the efficiency of the proposed method.

References

1. Alcazar, J.L.: Ovarian simple cysts in asymptomatic postmenopausal women detected at transvaginal ultrasound: a review of literature. World J. Obstet. Gynecol. **4**(4), 108 (2015). https://doi.org/10.5317/wjog.v4.i4.108
2. Borrazzo, C., et al.: PET and MRI-guided focused ultrasound surgery for neurological applications. In: 2016 IEEE Nuclear Science Symposium, Medical Imaging Conference and Room-Temperature Semiconductor Detector Workshop, NSS/MIC/RTSD 2016. Institute of Electrical and Electronics Engineers Inc. (2017). https://doi.org/10.1109/NSSMIC.2016.8069530
3. Chakraborty, S., et al.: A novel lossless image encryption method using DNA substitution and chaotic logistic map. Int. J. Secur. Appl. **10**(2), 205–216 (2016). https://doi.org/10.14257/ijsia.2016.10.2.19
4. Chakraborty, S., et al.: A study on different edge detection techniques in digital image processing. (2016). https://doi.org/10.4018/978-1-5225-1025-3.ch005
5. Chakraborty, S.: An advanced approach to detect edges of digital images for image segmentation. In: Chakraborty, S. and Mali, K. (eds.) Applications of Advanced Machine Intelligence in Computer Vision and Object Recognition: Emerging Research and Opportunities. IGI GLobal (2020). https://doi.org/10.4018/978-1-7998-2736-8.ch004
6. Chakraborty, S., et al.: An elitist model for obtaining alignment of multiple sequences using genetic algorithm. In: 2nd National Conference NCETAS 2015, pp. 61–67 Int. J. Innov. Res. Sci. Eng. Technol. (2015)
7. Chakraborty, S., et al.: An integrated method for automated biomedical image segmentation. In: 2017 4th International Conference on Opto-Electronics and Applied Optics (Optronix). pp. 1–5. IEEE (2017). https://doi.org/10.1109/OPTRONIX.2017.8349978
8. Chakraborty, S., et al.: An integrated method for automated biomedical image segmentation. In: 2017 4th International Conference on Opto-Electronics and Applied Optics, Optronix 2017 (2018). https://doi.org/10.1109/OPTRONIX.2017.8349978
9. Chakraborty, S., et al.: Dermatological effect of UV rays owing to ozone layer depletion. In: 2017 4th International Conference on Opto-Electronics and Applied Optics (Optronix), pp. 1–6. IEEE (2017). https://doi.org/10.1109/OPTRONIX.2017.8349975
10. Chakraborty, S., et al.: Detection of skin disease using metaheuristic supported artificial neural networks. In: 2017 8th Annual Industrial Automation and Electromechanical Engineering Conference (IEMECON), pp. 224–229. IEEE (2017). https://doi.org/10.1109/IEMECON.2017.8079594
11. Chakraborty, S., et al.: Intelligent computing in medical imaging: a study. In: Dey, N. (ed.) Advancements in Applied Metaheuristic Computing, pp. 143–163. IGI Global (2017). https://doi.org/10.4018/978-1-5225-4151-6.ch006
12. Chakraborty, S., et al.: Modified cuckoo search algorithm in microscopic image segmentation of hippocampus. Microsc. Res. Tech. 1–22 (2017). https://doi.org/10.1002/jemt.22900
13. Chakraborty, S., Bhowmik, S.: An efficient approach to job shop scheduling problem using simulated annealing. Int. J. Hybrid Inf. Technol. **8**(11), 273–284 (2015). https://doi.org/10.14257/ijhit.2015.8.11.23
14. Chakraborty, S., Bhowmik, S.: Blending roulette wheel selection with simulated annealing for job shop scheduling problem. In: IET Conference Publications (2015). https://doi.org/10.1049/cp.2015.1696
15. Chakraborty, S., Bhowmik, S.: Job shop scheduling using simulated annealing. In: First International Conference on Computation and Communication Advancement, pp. 69–73 McGrawHill Publication (2013)
16. Chakraborty, S., Mali, K.: An overview of biomedical image analysis from the deep learning perspective. In: Chakraborty, S. and Mali, K. (eds.) Applications of Advanced Machine Intelligence in Computer Vision and Object Recognition: Emerging Research and Opportunities. IGI Global (2020). https://doi.org/10.4018/978-1-7998-2736-8.ch008

17. Chakraborty, S., Mali, K.: Application of multiobjective optimization techniques in biomedical image segmentation—a study. In: Multi-Objective Optimization, pp. 181–194. Springer Singapore, Singapore (2018). https://doi.org/10.1007/978-981-13-1471-1_8
18. Hore, S., et al.: An integrated interactive technique for image segmentation using stack based seeded region growing and thresholding. Int. J. Electr. Comput. Eng. **6**, 6 (2016). https://doi.org/10.11591/ijece.v6i6.11801
19. Hore, S., et al.: Analysis of different feature description algorithm in object recognition. (2016). https://doi.org/10.4018/978-1-5225-1025-3.ch004
20. Hore, S., et al.: Finding contours of hippocampus brain cell using microscopic image analysis. J. Adv. Microsc. Res. **10**(2), 93–103 (2015). https://doi.org/10.1166/jamr.2015.1245
21. Mali, K., et al.: A study on statistical analysis and security evaluation parameters in image encryption. IJSRD-Int. J. Sci. Res. Dev. **3**, 2321–0613 (2015)
22. Mali, K., et al.: An efficient image cryptographic algorithm based on frequency domain using haar wavelet transform. Int. J. Secur.Appl. **9**(12), 279–288 (2015). https://doi.org/10.14257/ijsia.2015.9.12.26
23. Nayak, B.S., et al.: Half annular pancreas—a cadaveric case report. El Mednifico J. **2**(4), 411 (2015). https://doi.org/10.18035/emj.v2i4.346
24. Roy, M., et al.: A robust image encryption method using chaotic skew-tent map. In: Chakraborty, S. and Mali, K. (eds.) Applications of Advanced Machine Intelligence in Computer Vision and Object Recognition: Emerging Research and Opportunities (2020). https://doi.org/10.4018/978-1-7998-2736-8.ch001
25. Roy, M., et al.: Biomedical image enhancement based on modified Cuckoo Search and morphology. In: 2017 8th Annual Industrial Automation and Electromechanical Engineering Conference (IEMECON), pp. 230–235. IEEE (2017). https://doi.org/10.1109/IEMECON.2017.8079595
26. Roy, M., et al.: Biomedical image security using matrix manipulation and DNA encryption. In: Advances in Intelligent Systems and Computing, pp. 49–60. Springer (2020). https://doi.org/10.1007/978-981-15-0361-0_4
27. Roy, M., et al.: Data security techniques based on DNA encryption. In: Advances in Intelligent Systems and Computing, pp. 239–249. Springer (2020). https://doi.org/10.1007/978-981-15-0361-0_19
28. Sarddar, D., et al.: An efficient approach to calculate dynamic time quantum in round robin algorithm for efficient load balancing. Int. J. Comput. Appl. **123**(14), 48–52 (2015). https://doi.org/10.5120/ijca2015905701
29. Seal, A., et al.: A new and resilient image encryption technique based on pixel manipulation, value transformation and visual transformation utilizing single-level Haar wavelet transform (2017). https://doi.org/10.1007/978-981-10-2035-3_61
30. Tillett, J., et al.: Darwinian particle swarm optimization
31. File:Normal axial T2-weighted MR image of the brain.jpg—Wikimedia Commons. https://commons.wikimedia.org/wiki/File:Normal_axial_T2-weighted_MR_image_of_the_brain.jpg. Accessed 25 March 2020
32. Fractional-order darwinian PSO. SpringerBriefs Appl. Sci. Technol. **182**, 11–20 (2016). https://doi.org/10.1007/978-3-319-19635-0_2
33. Head computed tomography scanning: background, indications, contraindications. https://emedicine.medscape.com/article/2110836-overview. Accessed 25 March 2020
34. MIMIC Chest X-Ray database to provide researchers access to over 350,000 patient radiographs | MIT News. http://news.mit.edu/2019/mimic-chest-x-ray-database-0201. Accessed 25 March 2020

An Intelligent and Smart Belt for the Blind People

Souvik Chakraborty, Avishek Bhadra, Samrat Mondal, Suraj Prasad, and Shouvik Chakraborty

Abstract In this article, a basic idea about how a person who is blind can walk freely and do everything without any help from others or any assistance. The name of the proposed device is Intelligent Smart Belt and it is used for the blind people so that they can walk like a normal people. It is a belt in which any people can wear around there waist and does not need to hold anything in their hands. Many sensors are attached with the belt to sense any type of obstacles that appears in front of the blind people. The sensor data are in turn connected by an arduino, 1sheeld to understand the obstacles and what they are and it helps to communicate with the blind person using a mobile application.

Keywords Intelligent devices · Automated road trackers · Smart devices

1 Introduction

Healthier, Safer and Smarter lifestyle with ease of living is an inevitable part of the living organisms. It is necessary and essential to uplift the quality of the life with affordable technology [12–14, 19, 20, 34, 39]. Technology is a blessings for the

S. Chakraborty · A. Bhadra · S. Mondal · S. Prasad
M.B.C. Institute of Engineering & Technology, Bardhaman, West Bengal, India
e-mail: souvikchakraborty472@gmail.com

A. Bhadra
e-mail: avishekbhadra2014@gmail.com

S. Mondal
e-mail: msamrat111@gmail.com

S. Prasad
e-mail: surajprasad457@gmail.com

S. Chakraborty (✉)
University of Kalyani, Kalyani, West Bengal, India
e-mail: shouvikchakraborty51@gmail.com

S. Banerjee and J. K. Mandal (eds.), *Advances in Smart Communication Technology and Information Processing*, Lecture Notes in Networks and Systems 165,
https://doi.org/10.1007/978-981-15-9433-5_30

modern generation using which various problems can be solved very easily [6–11, 24, 32, 33, 35, 36]. That is why use of latest technology can be observed almost in every places [2, 5, 16, 25, 27–29, 37, 38]. Computers and other smart devices are inevitable part of our daily life [18]. Various application of intelligent and smart systems can be found in the literature. According to Times Of India out of 37 million people in the world who are blind, 15 million are from India and there is a shortage of optometrists (eye physicians) and donated eyes for the treatment of blindness [41]. Every year India needs 2.5 lakhs donated eyes but it manages to collect only 25000 eyes. There have been many electronic devices and non-electronic devices to guide blind people but still they find their mobility difficult for not identifying the obstacles [3, 15, 17, 22, 23, 26]. Many electronic devices are there for blind people to detect obstacles but their drawback is, they response only when the obstacle is in contact with it [30]. So, this device is used which is of low cost, easy to use, low power consumption and can detect obstacles within the range of three or four metres [31]. It can detect the surface of ground and also moving obstacles too, stopping the blind person to hit any vehicles. This technology is created with some factors keeping in mind: detecting the obstacles and guiding them, localization system of navigation, and for any help or emergency the device will send a message [4, 21, 22]. To work outdoor, blind people face a lot of difficulties and they cannot lead a normal life. Their autonomous navigation with detecting obstacles becomes the major task of their life. A robot uses sensors to avoid obstacles so the same technology is used for a blind person to walk safely by using many sensors attached to the belt that the blind person will be wearing. The sensors that are used doesn't scan the area but instead it sends a signal and receives the signal back through which it understands how far and what type of obstacle it is. Many technologies like laser cane, talking sings, smart shoe, guide cane have been made but either they have many drawbacks or they are not easy to use which means only trained peoples can only use them. So overcoming all these drawbacks the technology-Intelligent Smart Belt is made which is been discussed in this article. It can identify holes, stairs, vehicles etc. and give mobility to a blind man.

2 Device Requirements

The devices used to develop the proposed technology are: Arduino, Ultrsonic Sensor, 1sheeld, Infrared Sensor, Camera (optional), Battery, Vibration Motor. The description of each component is given below.

Arduino: Arduino is a low cost programmable open-source microcontroller board used for building electronics projects. It is based on the Microchip ATmega328P microcontroller. It is the combination of hardware and software or IDE (Integrated Development Environment) that runs on the computer. Arduino was mainly designed for students or for those who have interests in creating interactive objects and artists, designers, electronics engineer used the Arduino. It can interlude with Buttons, LEDs, Speakers, GPS units, Cameras, Motors, the Internet, even the Smart Phone or the TV.

It has many types like Arduino UNO, LilyPad Arduino, Red Board, Arduino Mega, Arduino Leonardo, Arduino Due etc. It is used in electronics, Security, Robotics, Home Automation, Automobile platforms, Industries, and also IoT and many other places. We can use Arduino UNO for this project also. The pointed diagram for arduino uno board is given in Fig. 1 [1].

Infrared or IR Sensor: It has two main parts IR Transmitter and IR Receiver which Transmits and Receives the Infrared waves. IR Transmitter transmits Infrared waves which gets reflected back by the object and receives by the IR Receiver. If there is no object in front of the sensor, then no infrared waves will be received by the IR Receiver. Mainly, it is used to detect the object and measure the distance. It is controlled by the Arduino board. There is a potentiometer which is used to control the output of the sensor. The pointed diagram of the IR Sensor is given in Fig. 2.

Ultrasonic Sensor: It is mainly used for calculating the distance based on the time required to receive the transmitted signal. It has two human-like eyes. One is the transmitter which transmits the signal and other is receiver which receives the transmitted signal that has been reflected back by the object. It transmits high frequency (Ultrasonic waves) and also sound waves which is of low frequency. The speed of sound is 343 m/s (1125 feet/second) and it depends on the variation of temperature and humidity. Ultrasonic sensor can also be used underwater. The speed of sound is 4.3 times faster in water as air. It is basically used in Robotics projects. The pointed diagram is given in Fig. 3.

1Sheeld: It is a new component which can be easily configured. It is connected to a mobile app (1Sheeld: The Arduino Shield) through an Android Smart Phone or iso device which allows to control all the features such as voice recognition, Gyroscope,

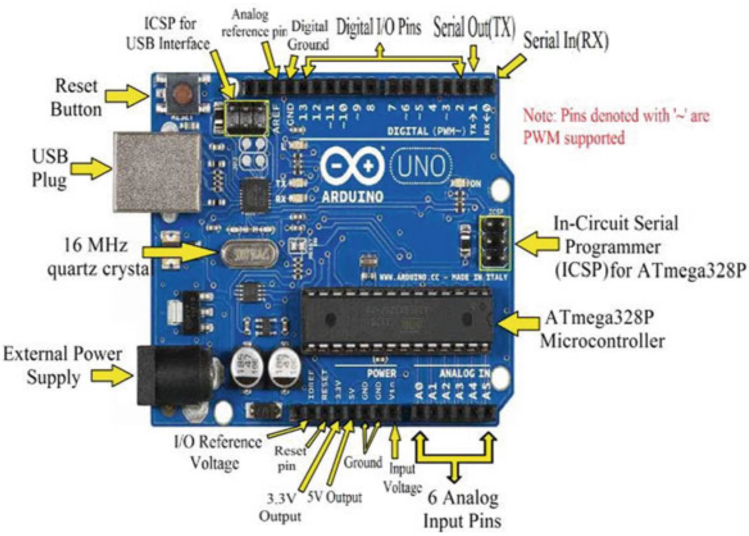

Fig. 1 Pointed diagram of Arduino Uno Board

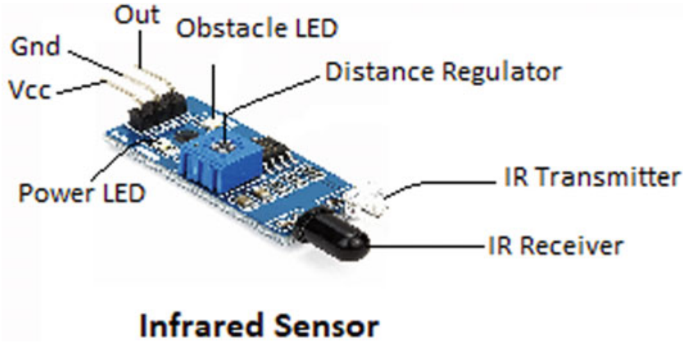

Fig. 2 Pointed diagram of IR sensor

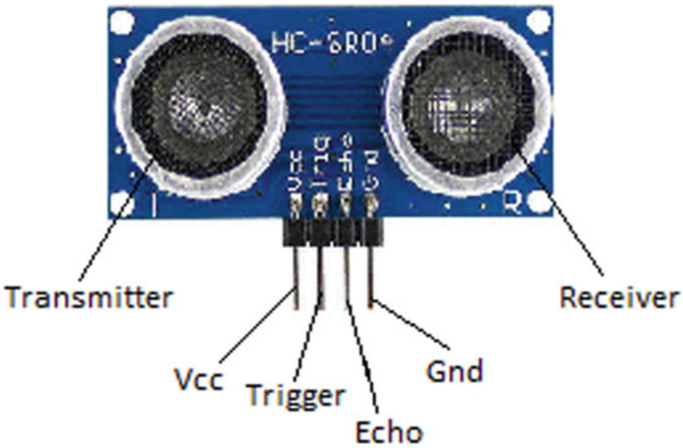

Fig. 3 Pointed diagram of ultrasonic sensor

Switches, camera, Face detection, Internet, Mic, Text to speech, Accelerometer, Magnetometer, GSM, Wi-Fi and GPS etc. It consists of two parts—first one which is physically connected with the Arduino board and any Smart Phones via Bluetooth and second one is the Software part. It mainly works as a middle-man between Arduino and Android Smart Phone via Bluetooth. By doing that it can be use 1sheeld as a input or output from Arduino and make use all of the sensors available in your circuit. The image of the 1sheeld board and mobile app is given in Fig. 4 [40].

Technical specification of 1Sheeld

- It uses a standard HC-06 Bluetooth adapter (Bluetooth 2.1) for communication
- Its range up to 30 feet
- It runes at Atmel ATMega162
- 16 MHz operating frequency

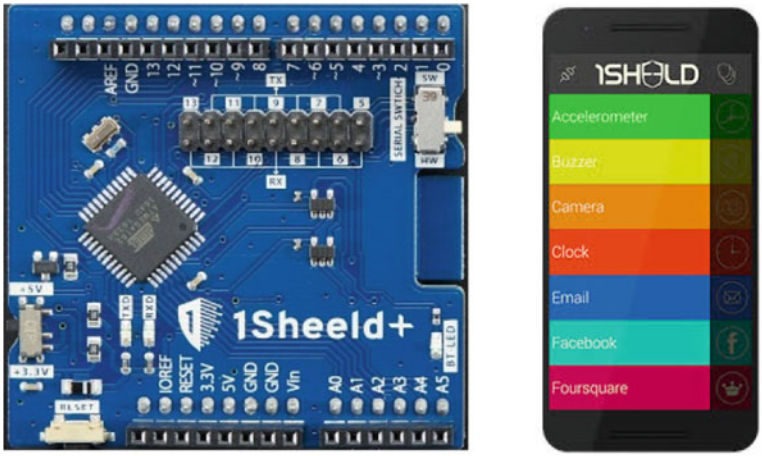

(a) (b)

Fig. 4 1sheeld **a** Board, **b** Android application

- Communicate with Arduino using UART.

3 Proposed Approach

This technology guides the blind to its destination and alerting him about stairs or anything within the height of 15 cm above the head of the blind person using it and also about the obstacles of the ground level. All the features of GSM module, speech module, voice recognition, GPS comes under the 1Sheeld which allows the user to locate its current location and to find places and to know how far it is. The 1Sheeld gives the feature to send a message to given number in case of emergency. The belt is selected as the user will not feel that he or she is carrying some extra things. The ultrasonic sensors that are being used must be placed in such a way that there is not too much movement. So, the belt is used as it will remain in the waist of body which does not have so much movement while walking. A single ultrasonic sensor may give wrong data of the object for which five ultrasonic sensors are being used to detect obstacles like staircases, trees, vehicles, holes. An IR sensor is also used to detect overhead obstacles.

The next thing is the placement of the ultrasonic sensors to the belt. The input is given to the sensor by the arduino. It detects objects by sending a sound wave around 40 kHz and then listens to the echo which strikes the obstacle and comes back. It gives the output pulse to the arduino after getting the echo according to which the distance is measured. The five sensors are placed in the belt at different angles to detect obstacles of every side. Some of which detects obstacles from the belt to the ground while the others detect from the belt to 15 cm above the user's head. The distance between the sensors have to be also kept in mind to determine which sensor is detecting an object as the ultrasonic waves will overlap. One IR sensor is used to detect overhead obstacles and it works same as the ultrasonic sensor and gets input from the arduino. The sensors are kept at an angle so the distance that they are showing is the hypotenuse of a triangle (if we consider it). Applying Pythagoras theorem, the horizontal distance from the user to the obstacle is calculated and thus the user gets to know about it. The height of the object can also be determined. As the hypotenuse and the horizontal distance are known we can find the angle that the object makes with the sensor. Then finding the virtual projection of the hypotenuse by the angle we find the vertical distance between the sensor and the obstacle. Thus subtracting it from the distance between the sensor and the ground we get the height of the obstacle.

The sensors will also detect the stairs and holes as in case of stairs when the ultrasonic wave strikes the beginning of the first stair and then strikes the edge of second one, either the distance measured by the sensor will slowly decrease in case of upstairs or the distance will increase slowly in case of downstairs. The distance measured according to the five sensors will either increase or decrease according to moving vehicles also. So whenever, an obstacle is detected the vibration motor vibrates and the user gets to know about it. Now to make the user clear about the distance as well as the location of the user itself and some landmarks 1Sheeld is used which connects everything with the android smart phone through an app. Just by audible words the app will give the whole details of the obstacle to the user as well as it helps to navigate from one place to another detecting landmarks, restaurants etc. and telling it to the user in audible words through earphones. In case of emergency or help the app will send the location of the user to the specific number that will be given. A cover box have to be made for the arduino and the 1Sheeld as safety of these two devices is important. A battery is used to give power supply to each devices used in this technology.

We may also use a digital camera (optional) to take images of the obstacles. And through image processing we can detect the obstacles and find out what type of object it is. It have disadvantages also as during night time the image processing won't be so clear to find out what type of object it is for which it may or may not be implemented. The schematic diagram of the proposed approach is given in Fig. 5.

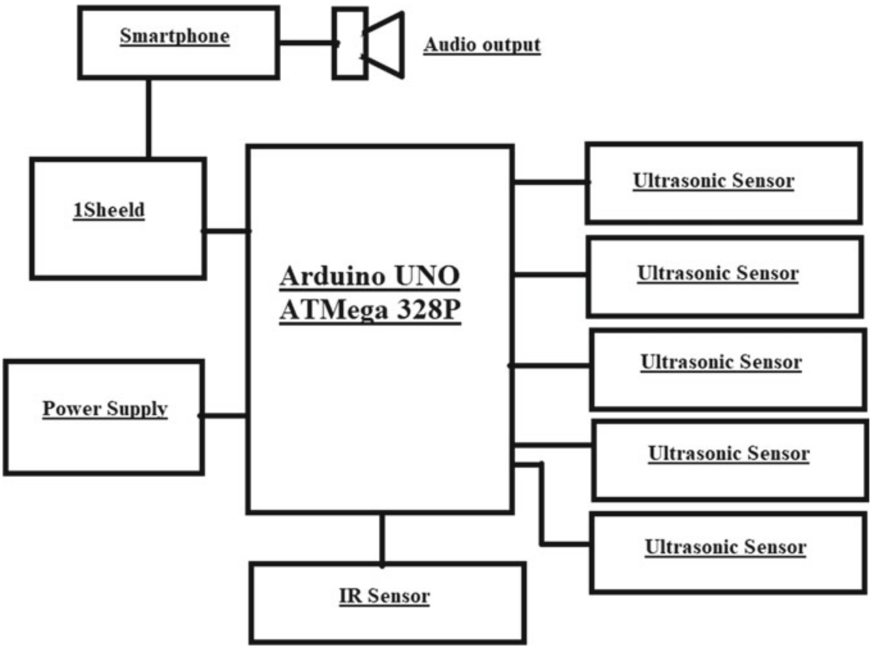

Fig. 5 The schematic diagram of the proposed approach

4 Conclusion

The proposed technology i.e. Intelligent Smart Belt which is been developed will give blind people the power to navigate smoother everywhere and a self-confidence that they are like normal people. This technology also fulfills all the drawbacks that other supporting devices had and it completes all the objectives for which this technology has been made. This technology cannot differentiate between living obstacles and non-living obstacles. So in future, more works will be done on this technology to solve this issue.

References

1. Alhebshi, F., et al.: Monitoring the operation of transmission line in a smart grid system through IoT. In: 2018 15th Learning and Technology Conference, L and T 2018, pp. 139–146. Institute of Electrical and Electronics Engineers Inc. (2018). https://doi.org/10.1109/LT.2018.8368498
2. Chakraborty, S., et al.: A novel lossless image encryption method using DNA substitution and chaotic logistic map. Int. J. Secur. Appl. **10**, 2 (2016). https://doi.org/10.14257/ijsia.2016.10.2.19
3. Chakraborty, S., et al.: A study on different edge detection techniques in digital image processing. (2016). https://doi.org/10.4018/978-1-5225-1025-3.ch005

4. Chakraborty, S.: An advanced approach to detect edges of digital images for image segmentation. In: Chakraborty, S. and Mali, K. (eds.) Applications of Advanced Machine Intelligence in Computer Vision and Object Recognition: Emerging Research and Opportunities. IGI GLobal (2020). https://doi.org/10.4018/978-1-7998-2736-8.ch004
5. Chakraborty, S., et al.: An Elitist model for obtaining alignment of multiple sequences using genetic algorithm. In: 2nd National Conference NCETAS 2015, pp. 61–67. Int. J. Innov. Res. Sci. Eng. Technol. (2015)
6. Chakraborty, S., et al.: An integrated method for automated biomedical image segmentation. In: 2017 4th International Conference on Opto-Electronics and Applied Optics (Optronix), pp. 1–5. IEEE (2017). https://doi.org/10.1109/OPTRONIX.2017.8349978
7. Chakraborty, S., et al.: Automated breast cancer identification by analyzing histology slides using metaheuristic supported supervised classification coupled with bag-of-features. In: 2018 Fourth International Conference on Research in Computational Intelligence and Communication Networks (ICRCICN), pp. 81–86. IEEE (2018). https://doi.org/10.1109/ICRCICN.2018.8718736
8. Chakraborty, S., et al.: Bag-of-features based classification of dermoscopic images. In: 2017 4th International Conference on Opto-Electronics and Applied Optics, Optronix 2017 (2018). https://doi.org/10.1109/OPTRONIX.2017.8349977
9. Chakraborty, S., et al.: Bio-medical image enhancement using hybrid metaheuristic coupled soft computing tools. In: 2017 IEEE 8th Annual Ubiquitous Computing, Electronics and Mobile Communication Conference, UEMCON 2017 (2018). https://doi.org/10.1109/UEMCON.2017.8249036
10. Chakraborty, S., et al.: Contrast optimization using elitist metaheuristic optimization and gradient approximation for biomedical image enhancement. In: 2019 Amity International Conference on Artificial Intelligence (AICAI), pp. 712–717. IEEE (2019). https://doi.org/10.1109/AICAI.2019.8701367
11. Chakraborty, S., et al.: Dermatological effect of UV rays owing to ozone layer depletion. In: 2017 4th International Conference on Opto-Electronics and Applied Optics (Optronix), pp. 1–6. IEEE (2017). https://doi.org/10.1109/OPTRONIX.2017.8349975
12. Chakraborty, S., et al.: Detection of skin disease using metaheuristic supported artificial neural networks. In: 2017 8th Industrial Automation and Electromechanical Engineering Conference, IEMECON 2017. (2017). https://doi.org/10.1109/IEMECON.2017.8079594
13. Chakraborty, S., et al.: Gradient approximation in retinal blood vessel segmentation. In: 2017 4th IEEE Uttar Pradesh Section International Conference on Electrical, Computer and Electronics (UPCON), pp. 618–623. IEEE (2017). https://doi.org/10.1109/UPCON.2017.8251120
14. Chakraborty, S., et al.: Image based skin disease detection using hybrid neural network coupled bag-of-features. In: 2017 IEEE 8th Annual Ubiquitous Computing, Electronics and Mobile Communication Conference (UEMCON), pp. 242–246. IEEE (2017). https://doi.org/10.1109/UEMCON.2017.8249038
15. Chakraborty, S., et al.: Intelligent computing in medical imaging: a study. In: Dey, N. (ed.) Advancements in Applied Metaheuristic Computing, pp. 143–163. IGI Global (2017). https://doi.org/10.4018/978-1-5225-4151-6.ch006
16. Chakraborty, S., et al.: Modified cuckoo search algorithm in microscopic image segmentation of hippocampus. Microsc. Res. Tech. **80**, 10 (2017). https://doi.org/10.1002/jemt.22900
17. Chakraborty, S., et al.: Penalized fuzzy C-means enabled hybrid region growing in segmenting medical images (2020). https://doi.org/10.1007/978-981-13-8930-6_3
18. Chakraborty, S., Bhowmik, S.: An efficient approach to job shop scheduling problem using simulated annealing. Int. J. Hybrid Inf. Technol. **8**(11), 273–284 (2015). https://doi.org/10.14257/ijhit.2015.8.11.23
19. Chakraborty, S., Bhowmik, S.: Blending roulette wheel selection with simulated annealing for job shop scheduling problem. In: IET Conference Publications (2015). https://doi.org/10.1049/cp.2015.1696

20. Chakraborty, S., Bhowmik, S.: Job shop scheduling using simulated annealing. In: First International Conference on Computation and Communication Advancement, pp. 69–73. McGrawHill Publication (2013)
21. Chakraborty, S., Mali, K.: An overview of biomedical image analysis from the deep learning perspective. In: Chakraborty, S., Mali, K. (eds.) Applications of Advanced Machine Intelligence in Computer Vision and Object Recognition: Emerging Research and Opportunities. IGI Global (2020). https://doi.org/10.4018/978-1-7998-2736-8.ch008
22. Chakraborty, S., Mali, K.: Application of multiobjective optimization techniques in biomedical image segmentation—a study. In: Multi-Objective Optimization, pp. 181–194. Springer Singapore, Singapore (2018). https://doi.org/10.1007/978-981-13-1471-1_8
23. Chakraborty, S., Mali, K.: Applications of advanced machine intelligence in computer vision and object recognition: emerging research and opportunities
24. Datta, S., et al.: Optimal usage of pessimistic association rules in cost effective decision making. In: 2017 4th International Conference on Opto-Electronics and Applied Optics (Optronix), pp. 1–5. IEEE (2017). https://doi.org/10.1109/OPTRONIX.2017.8349976
25. Hore, S., et al.: An integrated interactive technique for image segmentation using stack based seeded region growing and thresholding. Int. J. Electr. Comput. Eng. **6**, 6 (2016). https://doi.org/10.11591/ijece.v6i6.11801
26. Hore, S., et al.: Analysis of different feature description algorithm in object recognition. https://doi.org/10.4018/978-1-5225-1025-3.ch004
27. Hore, S., et al.: Finding contours of hippocampus brain cell using microscopic image analysis. J. Adv. Microsc. Res. **10**(2), 93–103 (2015). https://doi.org/10.1166/jamr.2015.1245
28. Mali, K., et al.: A study on statistical analysis and security evaluation parameters in image encryption. IJSRD-Int. J. Sci. Res. Dev. **3**, 2321–0613 (2015)
29. Mali, K., et al.: An efficient image cryptographic algorithm based on frequency domain using Haar wavelet transform. Int. J. Secur. Appl. **9**(12), 279–288 (2015). https://doi.org/10.14257/ijsia.2015.9.12.26
30. Misbahuddin, S., et al.: IoT based dynamic road traffic management for smart cities. In: 2015 12th International Conference on High-Capacity Optical Networks and Enabling/Emerging Technologies, HONET-ICT 2015. Institute of Electrical and Electronics Engineers Inc. (2016). https://doi.org/10.1109/HONET.2015.7395434
31. Prince, N., et al.: Implementation of IoT Based Attendance System on a Dedicated Web-Server (2016)
32. Roy, M., et al.: A dual layer image encryption using polymerase chain reaction amplification and dna encryption. In: 2019 International Conference on Opto-Electronics and Applied Optics, Optronix 2019. Institute of Electrical and Electronics Engineers Inc. (2019). https://doi.org/10.1109/OPTRONIX.2019.8862350
33. Roy, M., et al.: A study on the applications of the biomedical image encryption methods for secured computer aided diagnostics. In: 2019 Amity International Conference on Artificial Intelligence (AICAI), pp. 881–886. IEEE (2019). https://doi.org/10.1109/AICAI.2019.8701382
34. Roy, M., et al.: Biomedical image enhancement based on modified Cuckoo Search and morphology. In: 2017 8th Annual Industrial Automation and Electromechanical Engineering Conference (IEMECON), pp. 230–235. IEEE (2017). https://doi.org/10.1109/IEMECON.2017.8079595
35. Roy, M., et al.: Biomedical image security using matrix manipulation and DNA encryption. In: Advances in Intelligent Systems and Computing, pp. 49–60. Springer (2020). https://doi.org/10.1007/978-981-15-0361-0_4
36. Roy, M., et al.: Cellular image processing using morphological analysis. In: 2017 IEEE 8th Annual Ubiquitous Computing, Electronics and Mobile Communication Conference (UEMCON), pp. 237–241. IEEE (2017). https://doi.org/10.1109/UEMCON.2017.8249037
37. Roy, M., et al.: Data security techniques based on DNA encryption. In: Advances in Intelligent Systems and Computing, pp. 239–249. Springer (2020). https://doi.org/10.1007/978-981-15-0361-0_19

38. Sarddar, D., et al.: An efficient approach to calculate dynamic time quantum in round robin algorithm for efficient load balancing. Int. J. Comput. Appl. **123**(14), 48–52 (2015). https://doi.org/10.5120/ijca2015905701
39. Seal, A., et al.: A new and resilient image encryption technique based on pixel manipulation, value transformation and visual transformation utilizing single-level Haar wavelet transform. In: Proceedings of the First International Conference on Intelligent Computing and Communication, pp. 603–611. Springer, Singapore (2017). https://doi.org/10.1007/978-981-10-2035-3_61
40. 1Sheeld—All Arduino shields on your Smartphone. https://1sheeld.com/. Accessed 31 March 2020
41. India has largest blind population | India News—Times of India. https://timesofindia.indiatimes.com/india/India-has-largest-blind-population/articleshow/2447603.cms. Accessed 31 March 2020

Spam Detection Using Threshold Method on Whatsapp Image Data

Arunabha Tarafdar, Hrittika Paul, Shubhojit Gupta, Labani Acharjee, Akash Sah, and Soham Ganguly

Abstract We receive many wishing images during the festive season which actually spam our devices or fill up the necessary space of storage. In this paper, we are discussing a method to find out those redundant images using a threshold method. The proposed algorithm discuss in this paper will remove the redundant images in a targeted folder and keep them aside.

Keywords Threshold · Redundant · Hamming distance · Spam messages

1 Introduction

Image processing is been extensively use for many purposes may be it in the medical field or general development field. Image processing along with pattern recognition becomes a strong methodology which can counter many recent industry-based problem or challenges we face. Spam [1] detection remains one of the challenges we come across many a time through many software or applications but we can't take or consider one methodology to detect the spam.

Spam can be anything like a message asking your information telling you that you have won a lottery or informing about a sale of carpet. For a particular person, spam is completely different from respect to others. Although there are few spam messages that are the same for everyone irrespective of their choices.

It is the first of January and you want to send a very important message to your colleague which is definitely not wishing him a happy new year what your colleague does is he completely ignores the message or just replies to you the same to you. Now, you might be thinking your colleague is rude no that is absolutely not the case your colleague, on the other hand, has received so many spam messages as due to festivities he just ignored it because he considers your message also to be one those unwanted wishing images.

A. Tarafdar (✉) · H. Paul · S. Gupta · L. Acharjee · A. Sah · S. Ganguly
Computer Science & Engineering, University of Engineering and Management, Kolkata, India
e-mail: 10arunabha82@gmail.com

S. Banerjee and J. K. Mandal (eds.), *Advances in Smart Communication Technology and Information Processing*, Lecture Notes in Networks and Systems 165,
https://doi.org/10.1007/978-981-15-9433-5_31

This could have been avoided if all the festive message was considered as spam and marked and kept aside and the important messages could be displayed as it is. Our proposed algorithm is actually trying to find those redundant [2] messages and remove them keeping the important messages untouched.

In short we are call those messages to be spam if a single message is being circulated on a particular festival day over WhatsApp as forwarded messages.

2 Related Works

Spam filtering method includes generating a query histogram representation of an image forming at least part of an electronic communication, determining a histogram distance between the query histogram representation and a reference histogram representation, and making a determination whether the electronic communication is spam or non-spam according to the histogram [3] distance. In some embodiments, determining the histogram distance includes comparing a first bin of the query histogram representation to a range of second bins of the reference histogram representation (or comparing a first bin of the reference histogram representation to a range of second bins of the query histogram representation) to determine a similarity between the first bin and the range of second bins, and employing the similarity between the first bin and the range of second bins to determine the histogram distance between the query histogram and the reference histogram.

Prashant Kumar, Mantosh Biswas (2017) proposed an approach that involves detecting spam images from emails using SVM and Gaussian Kernel method [4]. The detailed explanation of the spam image classification steps includes preprocessing, vocabulary list, feature extraction, training, and prediction. Every data item is plotted as a point in p-dimensional space (where p is a number of features) and each feature's value is denoted by that particular coordinate's value. Classification is carried on by ascertaining the hyper plane which distinguishes the two classes. Support Vectors are the coordinates of individual observation, separate the two classes properly (hyper-plane/line). Gaussian kernel in SVM has been used for finding non-linear decision boundaries. It is parameterized by a bandwidth parameter, μ which determine how quickly similarity metric decrease. Experiments were conducted on ISH, TREC07, Dredze and personal images datasets considering parameters such as accuracy, recall, precision, and F-measure. Results indicated that the approach performed comparatively better than the other spam detection methods based on performance parameters.

Fatemeh Naiemi, Vahid Ghods, Hassan Khalesi (2019) in '*An efficient character recognition method using enhanced HOG for spam image detection*' provided a method to recognize the spam image using the optical character recognition based on HOG [5]. The character in the spam image was separated from the background, is carried out in the pre-processing stage and then normalized to a pre-defined size. Two other heuristic modifications of thickening of the thin characters and non-discrimination in recognition of the uppercase and lowercase letters with the same shapes have been presented. Optimizing cutoff point (threshold) in ROC curve has a significant outcome on the performance. This method was examined on Char74K and ICDAR2003 databases and the results have ensured an improvement for the spam image detection.

3 Proposed Method

Hamming distance [6] refers to the difference of number of corresponding bits that differ from two binary data. While using the technique of hamming distance on the top of the 'Dhash'—which is a python library that generates a 'difference hash' for a given image, we are able to detect the similar images. In hashing we need the difference of the gradient intensities of two images to be exactly similar or else there will be two different hashes, where in hamming technique, even if the intensities are slightly, there are high possibilities of the two images to be similar to each other.

Example—Here representing two images as a form of arrays consisting if binary data [1, 0, 0, 0, 0] and another one as [0, 0, 0, 0, 0]. In [1, 0, 0, 0, 0] and [0, 0, 0, 0, 0] there is only one difference while the others are equal, so the hamming distance here will be 1 (out of 5 elements) = 0.20.

Hamming distance is obtained by performing X or calculation between two binary data. In this case if we allow hamming distance of 0.12 we will be getting the similar image for that of the original one. The images are needed to be one dimensional arrays. Hamming distance refers by what percentage one image is different from another, so the lower the difference is, the lower will be the percentage and similarly the higher the difference is, the higher will be the percentage. In this case, we will always require a lower hamming distance.

Firstly, we will create a dictionary and we will store the long gradient intensities as the values and the image names as keys. The values will then turn as the difference score. We need to compare all the gradient values of each other. Here we import itertools [7]—a module in python which works on iterators, so it will prevent us from repetitive checks by taking combinations of 2.

We will then select an arbitrary value and then compare the hamming distances of two images at an iteration with that value and when the result of the comparison comes less than the selected value then we will append it as a similar image of the original image. We obtain the count of the similar images and the similar images in the output despite the change of the parameters such as size, brightness, intensities etc. from that of the original images (Fig. 1).

3.1 Algorithm

STEP 1: Starting with converting the images into gray scale images, assuring that the images contain three channels.

Fig. 1 Hamming distance calculation

1.1 Multiply the values with the 3 channels [8] and then average it.

STEP 2: Resizing the images using interpolation and then the images are flattened.

2.1 Calculating the gradient value based on intensity to see whether it is increasing or decreasing which helps in obtaining the fingertips of the images accurately.
2.2 Boolean indexing comparison between the row values and column values.

STEP 3: Combining all the necessary functions in one function in order to generate the custom hash value.

3.1 Except the gray images, all the other images are filtered, due to which we receive a null value as an output because here we cannot detect duplicate images.

STEP 4. Comparing all the gradient values with each other and the python module used here saves from multiple checks by taking combinations of 2. Then hamming distances of the images are compared with an arbitrarily selected value, if the difference is less than the arbitrary value, we append it as a similar image of an original image.

4.1 Gives the count of similar images after running all the functions.
4.2 The desired detection of the similar images from the original ones is obtained.

3.2 Threshold Calculation

The threshold [9] which is set for the algorithm is manually interpreted. We started with a very low threshold value and started to increase the value gradually to reach at a certain point where we find that our proposed algorithm is providing the best results. With our observation we find that we can actually set a particular or a very slice range of values which will provided us the optimal or best results. Further has been discussed in future scope section.

4 Experiment Results

Images coming on Whatsapp [10] have a specific threshold value. Now user selects one image and adds it's to the spam. We have taken a general threshold value as. Now based upon the threshold value of that image all the similar images who have a threshold less than or equal to that threshold value will be automatically added to the spam from the next time.

All images used to deduce the results are Whatsapp forward in a particular Whatsapp Group with admin privilege.

4.1 Sub-text "Good Morning"

For the subtext "Good Morning" we have taken 50 images and have taken the threshold value as 0.525. We have taken a range for the threshold value as 0.545–0.65 to get the similar image which will get added to the spam. Here by giving this range of threshold values we have got all the 50 images which are added to the spam. We have taken a small range to get optimal number of images within that range as if the range is large then other images may also get added to the spam.

After providing all the 50 images the algorithm is selecting this images as a reference images.

With respect to the above images the similar images are marked as the following.

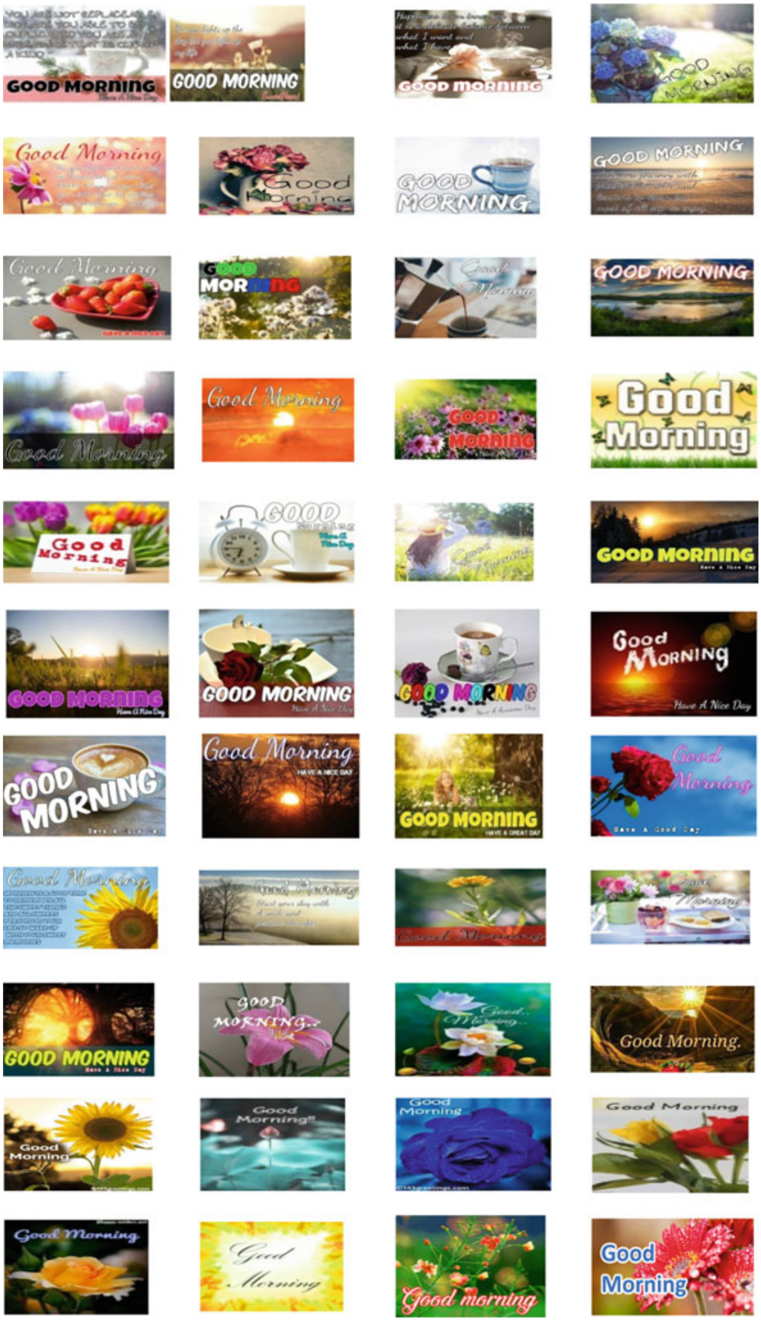

All of the images provided are treated as spam images and can be very easily treated as ignorable messages. For the above case we achieved a 100% accuracy.

Table 1 Image redundancy threshold values for English spam images

Sl no	Type of image	Number of images taken (20 min)	Number of similar images (obtained)	Threshold	Accuracy (%)
1	Good morning wishes	50	50	0.525	100
2	Good night wishes	50	50	0.520	100
3	Happy new year	20	19	0.545	95
4	Happy birthday	20	19	0.570	95
5	Happy durga puja	20	19	0.545	95
6	Happy dussehra	20	19	0.525	95
7	Merry christmas	20	19	0.530	95
8	Happy holi	20	19	0.565	95
9	Happy diwali	20	19	0.680	95
10	Happy anniversary	20	20	0.510	100

Keeping every parameter to be same as it is we achieved accuracy for various text the given below table will provide us with a clear picture (Table 1).

4.2 Bengali Sub-text

For the subtext "Happy Durga Puja" we have taken 20 images and have taken the threshold value as 0.545. We have taken a range for the threshold value as 0.545 to 0.65 to get the similar image which will get added to the spam. Here by giving this range of threshold values we have got 19 images which are added to the spam. We have taken a small range to get optimal number of images within that range as if the range is large then other images may also get added to the spam.

Selected Image.

Similar Image detected by the algorithm as follows.

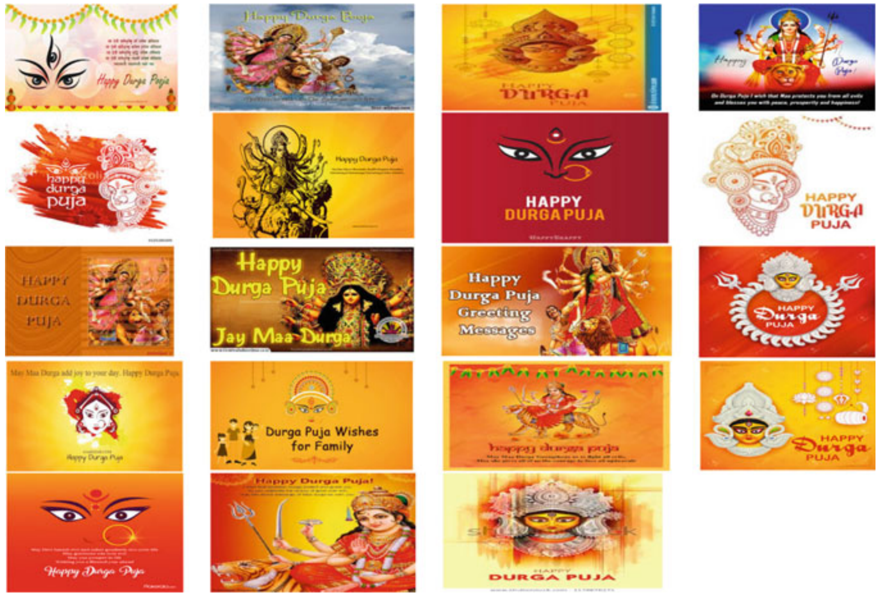

Accuracy achieved is 95%.

5 Future Scope

There is two avenue where the study can be more precisely focused. Firstly, the model should calculate the threshold point with help of machine learning, as we have mentioned that the threshold calculation is total human intervened so there is a good amount of scope to design a machine learning algorithm which can determine the threshold value and feed it to the algorithm so that the threshold value not has to tune for every new dataset.

Another point is that that the whole algorithm is right now working on a targeted folder we can uploaded or work the whole model in a clod base service so that we get a better and hassle free result.

6 Conclusion

In this paper, we have stated a new technique for the detection of spam images from Whatsapp data. We have used the hamming distance algorithm to find the similar images and then by taking a threshold value of the similar images we are adding the images in the spam folder directly. Spam detection remains one of the challenges we come across many a time through many software or applications but we can't take or consider one methodology to detect the spam.

So, spam detection is important as a large number of spam images comes through the Whatsapp and it fills our mobile storage quickly. The technique reduces the chance of storage filling to a great extent. We are able to classify the images as spam or non-spam. With high number of images it will be difficult to handle, but our algorithm can deals with many of them.

References

1. Aslam, U., Jayabalan, M., Aziz, H.I., Sohail, A.: A survey on opinion spam detection methods. Int. J. Sci. Technol. Res. **8**, 1355–1363 (2019)
2. Su, C.-Y., Shen, D.-F., Lin, G.-S.: An image spam detection method 71–72. https://doi.org/10.1109/ICCE-China.2017.7991000 (2017)
3. Pang, Y., Teoh, A., Ooi, S.Y., Low, C.-Y.: Enhanced independent spectral histogram representations in face recognition. Multimedia Tools Appl **77**. https://doi.org/10.1007/s11042-017-5028-8 (2017)
4. Kumar, P., Biswas, M.: SVM with Gaussian kernel-based image spam detection on textual features 1–6. https://doi.org/10.1109/CIACT.2017.7977283 (2017)
5. Ghods, V., Khalesi, H.: An efficient character recognition method using enhanced HOG for spam image detection. Soft Computing. **23**. https://doi.org/10.1007/s00500-018-03728-z (2019)
6. Bookstein, A., Kulyukin, V.A., Raita, T.: Generalized hamming distance. Inf. Retrieval **5**, 353–375 (2002). https://doi.org/10.1023/A:1020499411651
7. Hunt, J.: Collection related modules. In: A Beginners Guide to Python 3 Programming. Undergraduate Topics in Computer Science. Springer, Cham (2019)
8. Melo, P., Messias, J., Resende, G., Garimella, K., Almeida, J., Benevenuto, F.: WhatsApp monitor: a fact-checking system for whatsapp
9. Tarafdar, A., Roy, S., Mondal, A., Sen, R., Adhikari, A.: Image segmentation using background subtraction on colored images. In: 2019 International Conference on Opto-Electronics and Applied Optics (Optronix), pp. 1–4. IEEE (2019)
10. Zhang, W., Lu, J., Lin, X., Wen, Z., Gong, J.: Design of multi-channel image processing acquisition card **36**, 486–490 (2015)

Skin Lesion Classification Using Deep Convolutional Neural Network and Transfer Learning Approach

Pravin Kumar Samanta and Nirmal Kumar Rout

Abstract For biomedical image processing and prediction of skin diseases, deep learning methods are playing a very significant role in better decision making. This paper has proposed an automatic classification system of images containing a skin lesion as malignant or benign. In this method the transfer learning and a pre-trained deep learning network are implemented. In this proposed work transfer learning is applied to VGGNet architecture by replacing the last layer by a softmax layer for the classification of two different lesions (malignant and benign). Fine-tuning, data augmentations, and cross-validations are also added to the method. After evaluating the performances of the proposed method on the testing set of the ISIC dataset the method has achieved a significantly higher classification accuracy rate of 98.02%, the sensitivity of 98.10%, and Specificity of 97.05%.

Keywords Skin lesion · Biomedical image processing · Convolutional neural network · DCNN · Transfer learning

1 Introduction

Among various deadly human diseases skin cancer is one of them which causes death [1]. Most well-known skin cancer types are mainly melanoma and nonmelanoma. Because of melanoma lesions in the last few years the death rate has raised highly. Early-stage detection of this skin lesion is very essential. The curing rate can be possible over 90% if these lesions are detected at a very early stage by the physicians [2]. Visual examination of skin cancer is very hard and inefficient because many more similarities are there among different types of skin lesions [3]. For manually skin disease detection needs intensive human efforts and time. Highly magnifying

P. K. Samanta (✉) · N. K. Rout
School of Electronics Engineering, KIIT Deemed to be University, Bhubaneswar, India
e-mail: pravin.samanta95@gmail.com

N. K. Rout
e-mail: nkrout@kiit.ac.in

S. Banerjee and J. K. Mandal (eds.), *Advances in Smart Communication Technology and Information Processing*, Lecture Notes in Networks and Systems 165,
https://doi.org/10.1007/978-981-15-9433-5_32

and illuminated images are required for the improvement of the clarity of the spots [4]. Even for trained medical experts, by only visual investigation it is very difficult to distinguish between melanoma and nonmelanoma. In this aspect, the computer-aided classification system for skin lesion images is an alternative solution [5]. Using digital image processing techniques and artificial intelligence technologies for this automatic system time, endeavor, and human life are saved. Recently, for detection, classification, segmentation, and diagnosis of many skins disease deep learning is providing many computerized automated systems [6]. In this proposed research work, two type classification problems are represented, determining the skin lesions whether it is malignant or benign lesions. Here deep learning methods are used, mainly deep convolutional neural network (DCNN) with transfer learning for two type classification and pre-trained VGG-16 architecture is chosen for implementation. This paper is organized as follows: Sect. 2 describes related work; the method for classification of color skin images is described in Sects. 3 and 4 describes the results and discussion along with some comparative study with other methods; finally, Sect. 5 offers concluding part of the proposed work.

2 Related Work

In early days computer-aided systems used to face some difficulties for classification of dermatological images. The first problem was the data crisis or insufficiency of data [7] and the second challenge was image processing of skin images. For skin images simple dermoscopy devices are mainly used but for other biomedical images microscopy and biopsy are used [8]. The previous approaches [9, 10] used to require extensive preprocessing, segmentation, and feature extraction processes for the classification of the skin images. Current time the researchers are utilizing deep learning in visual tasks [11]. In [12] Codella et al. designed a hybrid model to classify melanoma using a combinational Artificial Neural Network (ANN) model of Support Vector Machine (SVM), deep learning, and sparse coding and accrued high accuracy. Barata et al. [13] had utilized two different models for the melanoma in skin images with the help of global and local features and concluded that better performances of color features than texture features. After applying different machine learning classification methods into melanoma for normal and abnormal cases Ozkan and Koklu et al. [14] achieved the highest accuracy of 92.5% from the ANN model. In [15] Litjens et al. suggested that the convolutional networks are very suitable to learn from features hierarchically and very much applicable for the analysis of biomedical images. For large datasets applications the accuracy for medical image classification is raised by applying deep convolution neural network and Transfer Learning [16]. By combined use of supervised learning and deep learning Premaladha and Ravichandran et al. [17] developed a diagnosis system for skin cancer classification. After applying the median filter and normalized Otsu's segmentation for normal skin separation an accuracy rate of 92.89% is achieved. Adria Romero et al. [18] proposed a system for classifying a dermoscopy image containing a skin lesion as malignant or benign built around the CNN model and used the transfer learning methods. In [19] Yu et al. proposed a Mask R-CNN and U-net for segmentation analysis of skin specially applied for the ISIC 2017 dataset.

3 Proposed Model of Transfer Learning

Several layers of neural networks are used to form a Deep Convolution Neural Network (DCNN). This model is very useful for extraction features from different images and classification of images [20]. There are many architectures of DCNN which are LeNet, VGGNet, AlexNet, ZFNet, GoogLeNet, ResNet, Efficient Net, Dense Net, etc. [21]. These architectures are applied for image classification, object detection, image segmentation, and many other complex tasks. VGGNet is one of the well-known and widely used model for DCNN [22]. For this proposed model the DCNN pre-trained VGG-16 architecture is used. In VGG-16 the number 16 means 16 layers that have weights. In Fig. 1 the process flow model of the architecture is described and an illustration of the proposed VGG-16 architecture is displayed in Fig. 2.

3.1 Image Augmentation

For better performance of the neural network, a large training dataset is required which gives a good learning experience to the network. Image augmentation techniques are applied to increase virtually the size of training data for good performance of neural network classifiers. Different data augmentation techniques are also applied using multiple ways of combination like rotating the images, flipping the images, and shearing the image.

3.2 Description of the Architecture

For classification of image dataset efficiently Deep Convolutional Neural Network (DCNN) is a most useful model. The proposed architecture of VGG-16 (described in Fig. 2) is used here for the classification of lesions. In the convolution layer for obtaining of feature matrix, a kernel matrix is multiplied with the image matrix. The input size of the RGB image which is provided in the convolution layer is $224 \times 224 \times 3$. In this architecture there are a total of 13 convolution layers. The model contains two convolution layers of size $224 \times 224 \times 64$, then another two layers of size $112 \times 112 \times 128$ also three layers of size $56 \times 56 \times 256$, along with another three layers having size $28 \times 28 \times 512$. Rectified Linear Unit (ReLU) activation function is added to each layer followed by Max Pooling so that all the negative values are

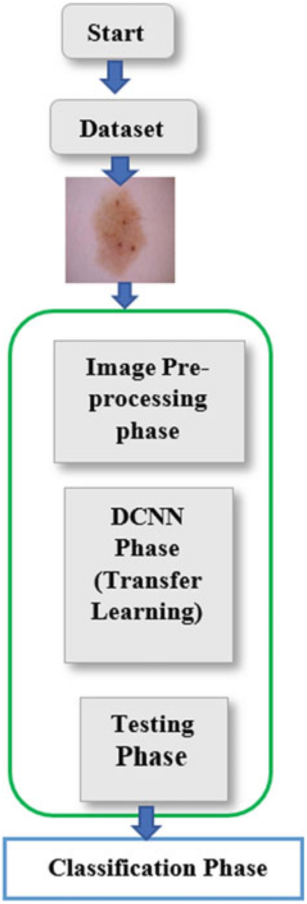

Fig. 1 Process flow model

not passed to the next layer. A matrix is produced as an output by the pooling layer in the proposed network that is working as the input for a fully connected layer. The last layer is a dense layer followed by another dense layer with Softmax activation which has given the output classes of the images. By the use of flatten() function one matrix is connected to a long vector and linear operations are performed in the dense() layer. Relu() and Softmax are used as an activation function. The dense layers are consists of two dense layer of 4096 units each and one dense layer of Softmax layer of 4 units. ReLU function is used for both the dense layer of 4096 units to stop forwarding negative values through the network.

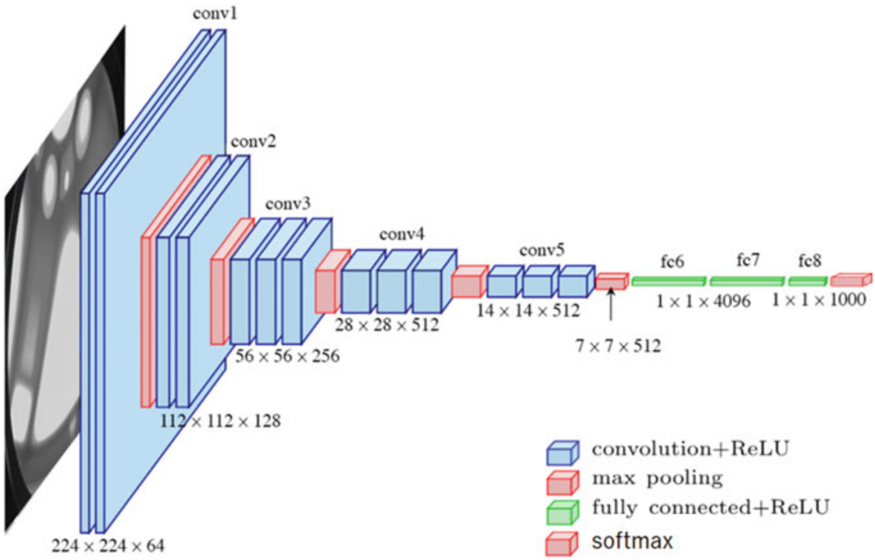

Fig. 2 Description of proposed VGG-16 model

4 Results and Discussion

In this paper ISIC image dataset of Skin cancer is used to train the model [23]. It contains a binary label that is benign and malignant. 1800 images of benign skin cancer images and 1497 images of malignant images are used. Among these 1440 images for training and 360 for testing of benign are used for this model. Among the malignant images 1197 are used for training and 300 images for testing. After testing the cross-validation is also done using 20% of the total images. Since there are a lot of images, so a lot of processing power is also required for the model. Since the PC where the model is coded has low processing power, therefore Google's cloud platform is used to execute the model. It is not only providing a virtual RAM but also providing a high-end virtual GPU to run the proposed model. For the implementation of the deep learning network the well-known Keras framework of Python is used for this model. For the evaluation of the performance measure of the proposed methods, three-evaluation measures such as accuracy, sensitivity and specificity are used by the help of the confusion matrix. Some common terminologies are used such as (i) True Positive (TP): Number of images for Malignant correctly classified as Malignant, (ii) True Negative (TN): Number of images of Benign correctly predicted as Benign, (iii) False Positive (FP): Number of images predicted as Benign but it is Malignant, (iv) False Negative (FN): Number of images classified as Malignant but it is Benign. The equations are defined as:

$$\text{Accuracy} = \frac{(TP + TN)}{(TP + FP + TN + FN)} \tag{1}$$

Table 1 Comparative study of the proposed model with other models

	Image type	Classification model	Accuracy (%)	Sensitivity (%)	Specificity (%)
Esteva et al. [24]	RGB	SVM	72.1	–	–
Pham et al. [25]	RGB	SVM	89	55.6	97.1
Hosny et al. [26]	RGB	DCNN	95.91	88.47	93.00
Adria Romero Lopez et al. [27]	RGB	DCNN and transfer learning	95.95	96.21	95.60
Proposed method	RGB	DCNN and transfer learning	98.02	98.10	97.05

$$\text{Sensitivity} = \frac{TP}{(TP + FN)} \tag{2}$$

$$\text{Specificity} = \frac{TN}{(FP + TN)} \tag{3}$$

In this paper, the proposed model is achieved with very good results, with an accuracy of 98.02%, a Sensitivity of 98.10% and also Specificity of 97.05% which are significantly better than the others methods of Esteva et al. [24], Pham et al. [25], Hosny et al. [26], Adria Romero Lopez et al. [27], which are mentioned in Table 1. In Fig. 3 some sample images of Malignant and Benign are shown which are collected from the ISIC image data set. Figure 4a depicts the accuracy for both training and validation accuracy of the model for epoch values and Fig. 4b represents the loss for both training and validation.

5 Conclusion

In this paper the deep convolutional model is implemented for two type classification applications, more specifically for Malignant and Benign skin lesion prediction. The image augmentations are applied to overcome the challenges of a crisis of labeled more images for the training of the model. The proposed method is able to classify more than two type lesions only by replacing the last layer to the softmax layer for more than two classifications. The weights of the proposed model are also fine-tuned. With the computation of three performance measures i.e., accuracy, sensitivity, and specificity, and comparing with other existing models, the obtained results of this model are significantly better than others. Along with the accuracy that the loss of

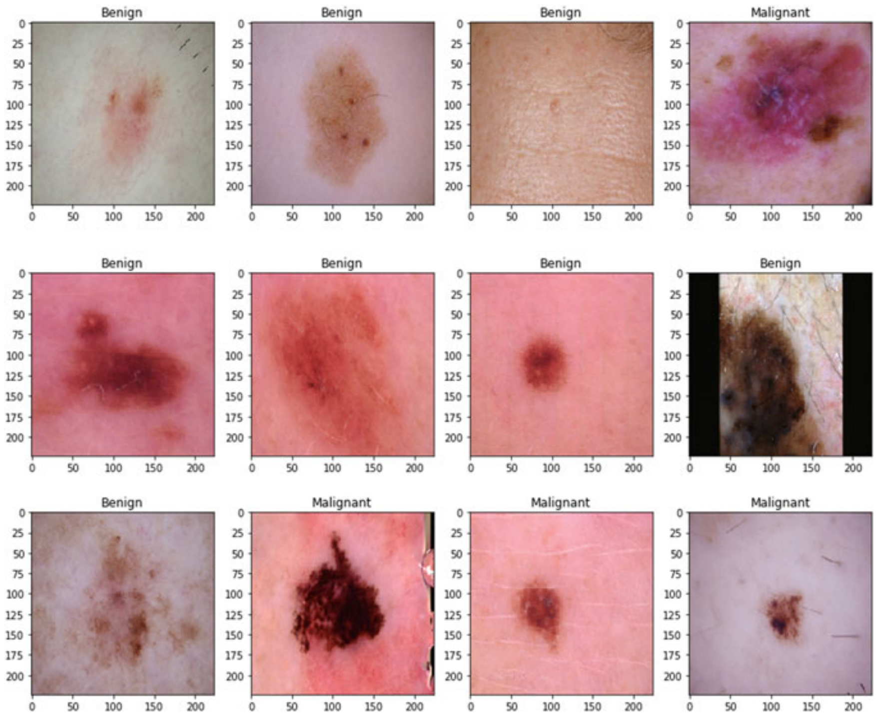

Fig. 3 Sample images of Malignant and Benign skin lesions from the ISIC dataset

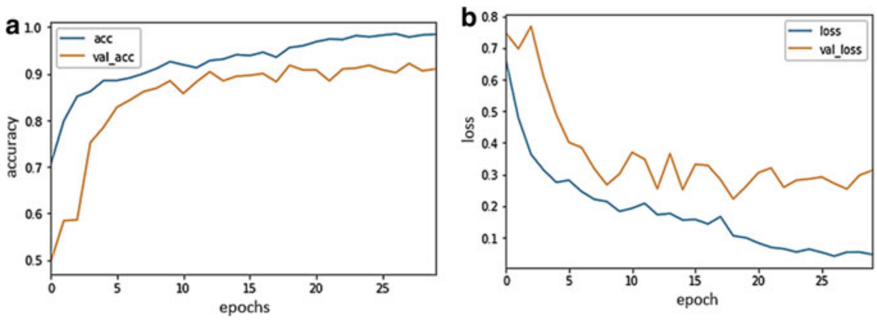

Fig. 4 **a** Training accuracy and testing accuracy graph, **b** training loss and testing loss graph of the model

the model is found out of 0.0467 is significantly very less. After testing the model with testing data, the minor difference between training and test sets are observed which suggests that the model neither overfits nor underfits. Transfer learning offers very good efficiency to deal with complex image processing problems with a massive number of the images data set.

References

1. American Cancer Society: Cancer facts and figures 2018. Available: https://www.cancer.org/content/dam/cancer-org/research/cancer-factsand-statistics/annual-cancer-facts-and-figures/2018/cancer-facts-andfigures-2018.pdf
2. Ballerini L., Fisher R., Aldridge B., Rees J.: A color and texture-based hierarchical K-NN approach to the classification of non-melanoma skin lesions. Color Medical Image Analysis, Lecture Notes in Computational Vision and Biomechanics Volume 6, Editors: (Emre Celebi M. and Gerald Schaefer). Springer, pp. 63–86 (2013)
3. Codella N., Nguyen Q., Pankanti S., Gutman D., Helba B., Halpern A., Smith J.: Deep learning ensembles for melanoma recognition in dermoscopy images. IBM J. Res. Dev. **61**(4/5), 5:1–5:15 (2017)
4. Kittler, H., Pehamberger, H., Wolff, K., Binder, M.: Diagnostic accuracy of dermoscopy. Lancet Oncol. **3**(3), 159165 (2002)
5. Mishra N., Celebi M.: An overview of melanoma detection in dermoscopy images using image processing and machine learning. (2016). Available from: arXiv:1601.07843
6. Rajpara, S.M., Botello, A.P., Townend, J., Ormerod, A.D.: Systematic review of dermoscopy and digital dermoscopy/artificial intelligence for the diagnosis of melanoma. Br. J. Dermatol. **161**(3), 591–604 (2009)
7. Masood, A., Al-Jumaily, A.A.: Computer-aided diagnostic support system for skin cancer: a review of techniques and algorithms. Int. J. Biomed. Imaging **323268**, 2013 (2013)
8. Binder, M., et al.: Epi-luminescence microscopy-based classification of pigmented skin lesions using computerized image analysis and an artificial neural network. Melanoma Res. **8**, 261–266 (1998)
9. Burroni, M., et al.: Melanoma computer-aided diagnosis: reliability and feasibility study. Clin. Cancer Res. **10**, 1881–1886 (2004)
10. Schindewolf, T., et al.: Classification of melanocytic lesions with color and texture analysis using digital image processing. Anal. Quant. Cytol. Histol. **15**, 1–11 (1993)
11. Silver, D., et al.: Mastering the game of Go with deep neural networks and tree search. Nature **529**, 484–489 (2016)
12. Codella N., Cai J., Abedini M., Garnavi R., Hapern A., Smith J.: Deep learning, sparse coding, and SVM for melanoma recognition in dermoscopy images. In: Machine Learning in Medical Imaging. Lecture Notes in Computer Science, vol. 9352, pp. 118–126. Springer (2015)
13. Barata, C., Ruela, M., Francisco, M., Mendonça, T., Marques, J.S.: Two systems for the detection of melanomas in dermoscopy images using texture and color features. IEEE Syst. J. **8**(3), 965–979 (2014)
14. Ozkan, I.A., Koklu, M.: Skin lesion classification using machine learning algorithms. Intell. Syst. Appl. Eng. **5**(4), 285–289 (2017)
15. Litjens, G., Kooi, T., Bejnordi, B., Setio, A., Ciompi, F., Ghafoorian, M., et al.: A survey on deep learning in medical image analysis. Med. Image Anal. **42**, 60–88 (2017). https://doi.org/10.1016/j.media.2017.07.005
16. Shin, H.C., Roth, H.R., Gao, M., Lu, L., Xu, Z., Nogues, I., et al.: Deep convolutional neural networks for computer-aided detection: CNN architectures, dataset characteristics and transfer learning. IEEE Trans. Med. Imaging **35**(5), 1285–1298 (2016). https://doi.org/10.1109/TMI.2016.2528162
17. Premaladha, J., Ravichandran, K.: Novel approaches for diagnosing melanoma skin lesions through supervised and deep learning algorithms. J. Med. Syst. **40**(96), 1–12 (2016)
18. Lopez, A.R., Giro-i-Nieto, X., Burdick, J., Marques, O. et al.: Skin Lesion Classification from Dermoscopic Images using Deep Learning Techniques. IASTED International Conference on Biomedical Engineering, pp. 49–54 (2017)
19. Yu, L., Chen, H., Dou, Q., Qin, J., Heng, P.A.: Automated melanoma recognition in dermoscopy images via very deep residual networks. IEEE Trans. Med. Imaging **36**(4), 994–1004 (2016)
20. LeCun, Y., Bengio, Y., Hinton, G.: Deep learning. Nature **521**, 436–444 (2015). https://doi.org/10.1038/nature14539

21. Srinivas, S., Sarvadevabhatla, R., Mopuri, K., Prabhu, N., Kruthiventi, S., Babu, R.: A taxonomy of deep convolutional neural nets for computer vision. Front. Robot. AI **2** (2016). Available from: arXiv:1601.06615
22. Simonyan, K., Zisserman, A.: Very deep convolutional networks for large-scale image recognition. arXiv preprint arXiv:1409.1556 (2014)
23. International Skin Imaging Collaboration: Melanoma Project Website. https://isic-archive.com/
24. Esteva, A., Kuprel, B., Novoa, R., Ko, J., Swetter, S., Blau, H., et al.: Dermatologist-level classification of skin cancer with deep neural networks. Nature **542**, 115–118 (2017). https://doi.org/10.1038/nature21056
25. Pham, T.C., Luong, C.M., Visani, M., Hoang, V.D.: Deep CNN and data augmentation for skin lesion classification. In: Intelligent Information and Database Systems, Lecture Notes in Computer Science, vol. 10752, pp. 573–582. Springer (2018)
26. Hosny, K.M., Kassem, M.A., Foaud, M.M.: Classification of skin lesions using transfer learning and augmentation with Alex-net. PLoSONE **14**(5), e0217293. https://doi.org/10.1371/journal.pone.0217293
27. Lopez, A.R., Giro-i-NietO, X., Burdick, J., Marques, O., et al.: Skin Lesion Classification from Dermoscopic Images using Deep Learning Techniques. In: IASTED International Conference on Biomedical Engineering, pp. 49–54 (2017)

Susceptibility Analysis of Novel Corona Virus Using Hadoop Distributed File System

Pravin Kumar Samanta, Soumyadev Mukherjee, and Nirmal Kumar Rout

Abstract The Novel Corona Virus, COVID-19 is a major setback to the progress of the nation. The year 2020 has witnessed a disappointing beginning with this deadly virus having taken away many innocent lives. The COVID-19, which happens because of the virus Corona, showcases symptoms which are mild and at times doesn't even reflect any. However, a small section falls severely ill, and some eventually perish. This proposed research work is implemented to identify who is having the highest risk of serious illness and who are more susceptible to this disease. In this proposed research, a huge amount of semi structured healthcare data is stored and processed which are collected from healthcare dataset. Hence, in the proposed work 'Hadoop' is utilized for processing the data gathered. The input data is processed using MapReduce and finally the result is loaded into the Hadoop Distributed File System (HDFS). After details analysis and justification with the help of 'Hadoop' proposed work has predicted many possible susceptible cases which can help to reduce the number of fatalities and also save human lives.

Keywords Healthcare · Hadoop · MapReduce · HDFS · Tableau · Big data · COVID-19 · Corona virus

P. K. Samanta (✉) · N. K. Rout
School of Electronics Engineering, KIIT Deemed to Be University, Bhubaneswar, India
e-mail: pravin.samantafet@kiit.ac.in

N. K. Rout
e-mail: nkrout@kiit.ac.in

S. Mukherjee
School of Computer Science Engineering, KIIT Deemed to Be University, Bhubaneswar, India
e-mail: 1705274@kiit.ac.in

S. Banerjee and J. K. Mandal (eds.), *Advances in Smart Communication Technology and Information Processing*, Lecture Notes in Networks and Systems 165,
https://doi.org/10.1007/978-981-15-9433-5_33

1 Introduction

The Novel Corona virus, COVID-19 is an immensely infectious disease resulting from a very recently found Severe Acute Respiratory Syndrome Coronavirus-2 (SARS-CoV-2) [1]. First originated in Wuhan, China in late December, 2019 it has now been characterized as a global pandemic [2]. An individual infected with the COVID-19 virus generally witnesses mild to slight respiratory issues and get well without the need of any additional medical care. The aged mass, and individuals possessing hidden health issues like heart problems, diabetes, acute respiratory illness, and cancer are more highly prone to fall severely ill [3]. Now the question may arise that who is at most risk for COVID-19? It is high time for the nation to figure out who is more prone to fall prey to this deadly virus. Preventive measures should be taken and they should be handled with intensive care to reduce the number of fatalities.

With reference to an analysis of 45,000 positive cases in China, less than 1.0% of physically fit individuals who fell prey to the COVID-19 perished as a consequence of the same. However, it is close to 6.0% for patients having cancer, high pressure or acute respiratory illness, 7.3% for people with high glucose content and 10.5% for heart patients [1]. Patients aged 80 or more are at high risk, with close to 14.8% expiring. Younger children, those aged below 9, are not prone to serious illness. Another research suggested that males are more susceptible to severe illness than females, but those are hypothetical and may showcase the fact that males smoke more than females in China [4–6]. Coming to India, the primary concern is to analyse the trend and take intensive care of the people who are more likely to fall prey to the Novel Corona Virus. The sole objective of this proposed work is identifying the one who is most susceptible and to take preventive measures to protect them using the help of healthcare dataset. This research paper follows the following pattern: Sect. 2 describes the Hadoop Distributed File System (HDFS) methodology. Related work in the application of healthcare is described in Sects. 3 and 4 presents the description of the proposed model. Section 5 describes the implementation and results; Sect. 6 offers the conclusion of the work with future scope.

2 HDFS Methodology

Hadoop offers five daemons with each daemon possessing a Java Virtual Machine-(A) DataNode, (B) NameNode, (C) JobTracker, (D) Secondary NameNode, (E) Task-Tracker. Demons which store data and metadata, i.e.; DataNode and NameNode, come under a part of Hadoop Distributed File System (HDFS). The TaskTracker and JobTracker, which keep track and actually execute the job, come under MapReduce layer. The HDFS is used in this proposed research work because of the following reasons [7].

Large Dataset: Current population of India is more than 1.3 Billion, if we want to analyze data for that amount of people then the dataset will be huge. That much huge amount of data can't be processed by normal file system. That's why to get a smooth workflow the HDFS is used for analysis [8].

Data Replication: For working with a large dataset, occurrences of unfortunate situations like hardware failure, crashing of a node are pretty common. In such situations data loss is occurred. To overcome this kind of problem HDFS is providing a feature called data replication. The data is copied across numerous nodes in the cluster by the creation of duplicates. This methodology is maintained across stipulated time intervals by HDFS and the duplication process is taken care of by the same. The moment as machine in the cluster crashes, the data should be retrieved from other machines. Loss of data is far sighted threat and almost negligible.

Scalability: Our main goal of the work is to analyze healthcare dataset using Hadoop and facilitate a smoother conduct of the fight against COVID-19. So, the proposed work is scalable in order make it a dynamic project. This is achieved by using HDFS. In HDFS the infrastructure is scaled up by adding more racks or clusters to this system.

Data Locality: In older systems, the data is brought at the application layer and then worked upon. In this proposed research work, as a consequence of the huge bulk of data, bringing data to the application layer has lowered down the overall performance.

In HDFS, the computation part is brought to the Data Nodes where data resides. Hence, with Hadoop HDFS, computation logic is not moved to the data, rather than data is moved to the computation logic.

3 Related Work

The sole aim of the 'Healthcare System' is the treatment, diagnosis of health-related problems of human beings. Recently big data analytics is playing a very important role for the development of current healthcare practices and research [9]. For the processing of huge amount of healthcare data record lots of efficient tools and methodologies are required. For the storage and processing of huge volumes of data set, Hadoop is playing a significant role for modern healthcare system [7]. Meena et al. proposed a system for the analysis of Healthcare data set against various queries using Hadoop Cluster and Pig Latin, where in that method fully distributed Hadoop Cluster mode was utilized [10]. Ashwin Belle et al. designed a model to infer fluctuations in enrolment due to the effect of carelessness using Hadoop and Hive [11]. Highly based on Market Research Sabyasachi Dash et al. proposed a prototype for the retrieval of patient information using Sqoop (SQL + Hadoop) and Hive [12]. A. S. Thanuja Nidhadi et al. utilized data-mining techniques in classification of Naive Bayesian (NB), and Back Propagation (BP) to identify patterns leading to fraud and emphasized on using Hadoop HDFS solution for storage and processing of medical data to avoid modern issues in healthcare [13]. Based on statistical summaries and data quality visuals Wullianallur Raghupathi et al. [14] suggested a proposal to use HDFS in data calibration, data wrangler in data cleansing, R in data analytics and MapReduce Tools in Architecture Testing. In this proposed method the HDFS is used for identifying the susceptibility analysis of Corona virus based on Healthcare data set.

4 Description of Proposed Model

About the dataset:
In this proposed method Healthcare data is used which is collected from publicly published dataset [15]. The dataset comprises of factual information, results of examinations and information given by the patients. ID refers to the patient identification. Age, height, weight and gender are objective features which are in days, cm, kg and categorical code respectively. Some of the subjective features like asthma count and smoking reflect binary outputs, cholesterol count which is an examination feature showcases three different scenarios wherein (1) refers to normal cholesterol, (2) refers to high cholesterol and (3) refers to way above normal cholesterol. Corona count reflects the chances of the patient being tested positive for COVID-19 provided he's suffering from one of the diseases.

The dataset is divided into smaller blocks which are primarily processed by "Map Phase" in parallel and then by "Reduce Phase". Hadoop framework has sorted out the output of the Map phase which are then given as an input to Reduce Phase to initiate parallel reduce tasks. These input and output files are stored in file system (Fig. 1).

Input dataset is adapted by MapReduce framework from HDFS. Input dataset is taken as key-value pair and broken down for effective analysis. Then, the number of positive cases is mapped to corresponding diseases and shuffled accordingly. The number of positive cases is the reduced output. The final result is sent to the authorities and hospitals for preventive measures. In this work five MapReduce key functions are used to get the desired output/outcome. The MapReduce job model is described in Fig. 2. The functionalities of each functions are as follows:

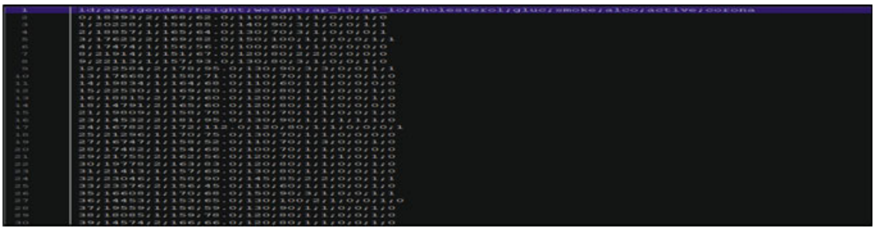

Fig. 1 Sample of input healthcare dataset. https://www.kaggle.com/iamhungundji/covid19-symptoms-checker

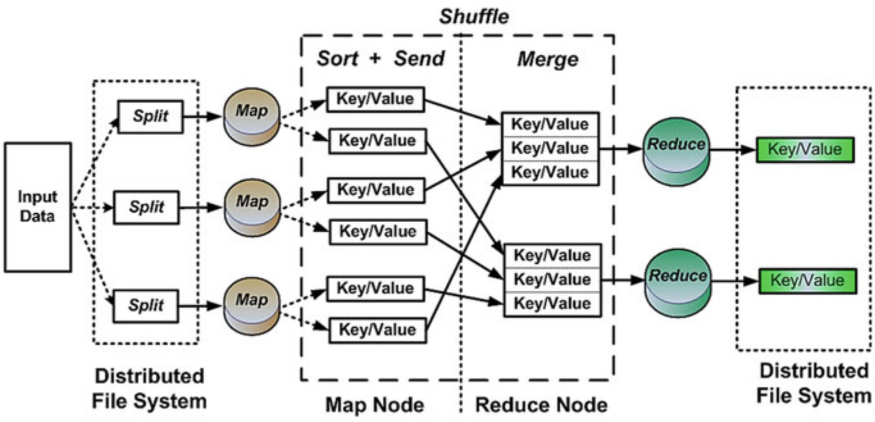

Fig. 2 Map reduce job model description (adopted from [10])

- UID_Mapper.java: Filters the header and writes to mapper output.
- UID_Reducer.java: Aggregate values for each disease and outputs positive cases.
- Sort_Mapper.java: Receive output from previous UID_Mapper-Reducer phase and shuffle (x, y1) and (x, y2) pair into (x, (y1, y2)) form.
- Sort_Comparator.java: Sorts and reduces the output in descending order.
- Sort_Reducer.java: Swap (x, y) pair into (disease, count) format and produce output.
- Driver.java: It's the main driver program for the MapReducer job.

Use case diagrams of the proposed model (which is described in Fig. 3) outlines the usefulness of a framework utilizing the on-screen characters and use cases. The actors here are the 'Users' and the 'Admin' of the system. Login, import dataset, display data, train dataset etc. are the various use cases.

5 Implementation and Results

Having done intensive analysis, the following results are found out which correspond to the dataset (which has already been discussed) anatomization using Hadoop.

Detailed description of the outcomes from the implementation results are given in Figs. 5, 6, 7, 8 and 9. In Fig. 4 gender wise height to weight distribution is represented. In Fig. 5 to Fig. 9, the number of negative cases is mapped to binary '0' as represented by blue color and the number of positive cases is mapped to binary '1' as represented by orange color (corona virus negative signifies as '0', and positive as '1'). Figure 5 shows the gender wise count of COVID-19 cases. The graph plotted reflects the fact that individuals belonging to gender 2 (male) over gender 1(female) are more prone to fall prey to COVID-19. In Fig. 6 the cholesterol versus count of COVID-19 cases are presented where 'type-1' refers to normal cholesterol, 'type-2' refers

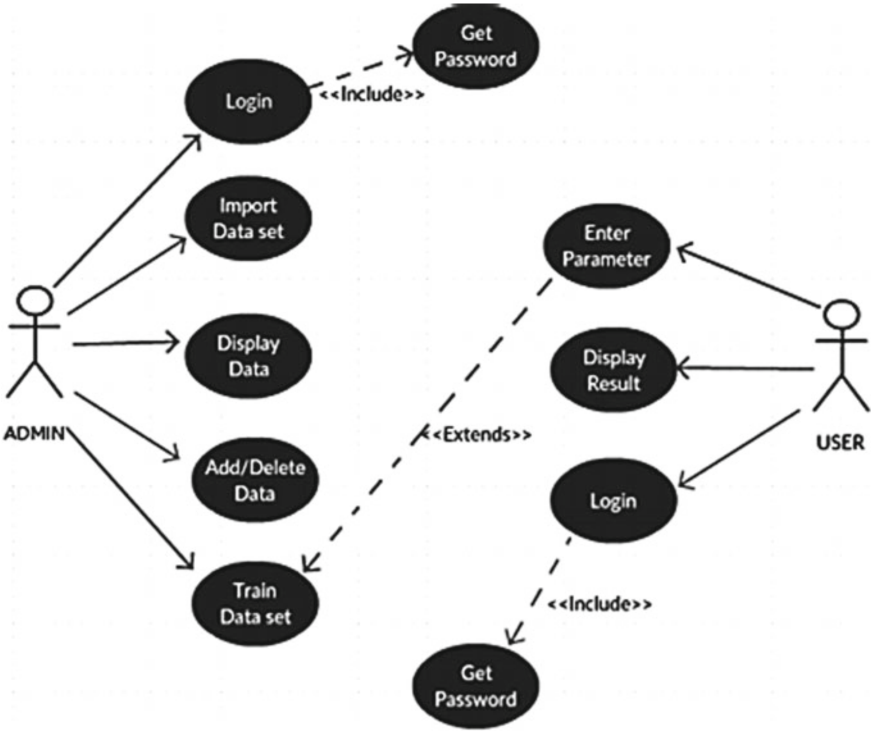

Fig. 3 Use case diagrams of the proposed model

to high cholesterol and 'type-3'refers to way above normal cholesterol. The graph plotted clearly depicts the fact that people with above normal and way above normal cholesterol are highly susceptible to the dangerous COVID-19. Figure 7 presents the Glucose content of normal (type-1), high (type-2) and very high (type-3) versus count of COVID-19 cases. The graph depicts that individuals with high or very high glucose content are more likely to fall prey to dangerous COVID-19. Figure 8, the graph of smokers versus count of COVID-19 cases gives a clear indication that (type 0) smokers or smokers are at a higher risk than non-smokers (type-1). In the plot of Fig. 9 asthma patients versus count of COVID-19 cases signifies that type-0 asthma patients are at a severe risk from COVID-19.

6 Conclusion and Future Scope

In this proposed method, after implementation of the model using Hadoop, HDFS and detailed analysis of the Healthcare dataset, it is observed that males over females and people with high glucose, cholesterol, asthma patients, smokers etc. are highly

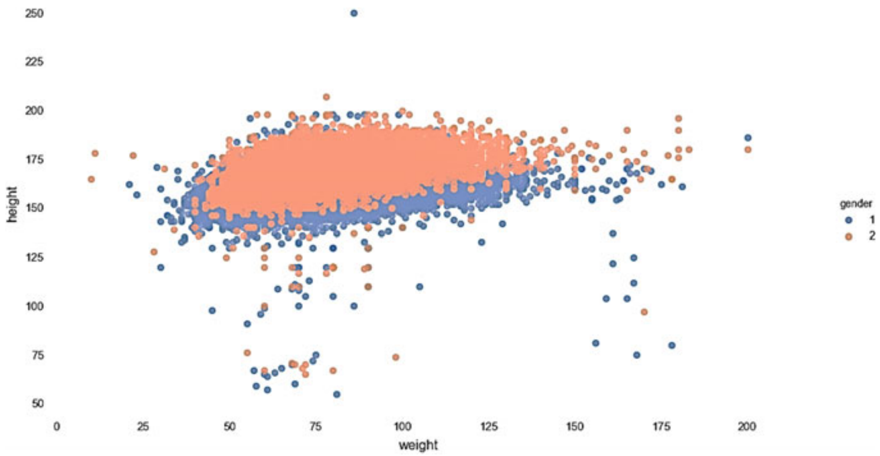

Fig. 4 Gender wise height to weight distribution

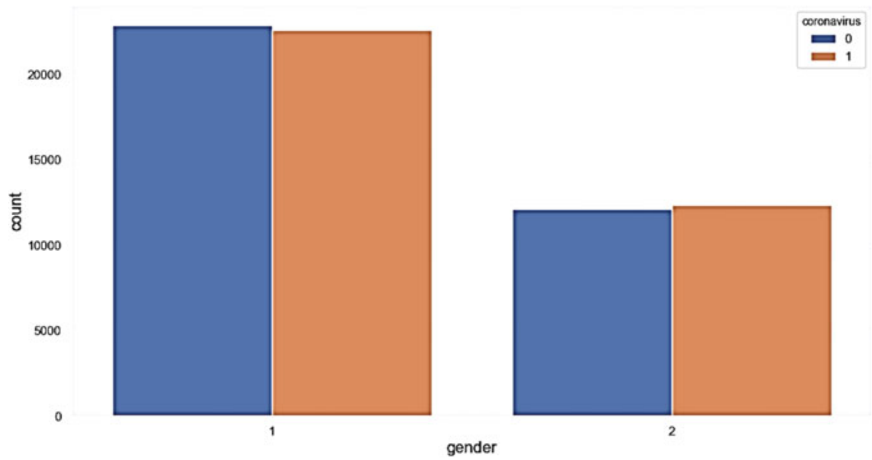

Fig. 5 Gender wise count of COVID-19 cases

susceptible to the COVID-19. This proposed research has the ability to segregate out patients with high or very high glucose content, smokers, asthma patients, people with above normal cholesterol and pay primary attention to them as they're at a higher risk of severe illness. This method has the ability to help the Government, authorities and healthcare units significantly to figure out the associated phenomenon which adds to the intensity of the dangerous COVID-19 to reduce the number of fatalities. This is also very much helpful for the healthcare units to make amendments to the existing database, to take precautionary measures and ensure a better tomorrow. The nation demands a better tomorrow and this proposed approach is a small step to bring

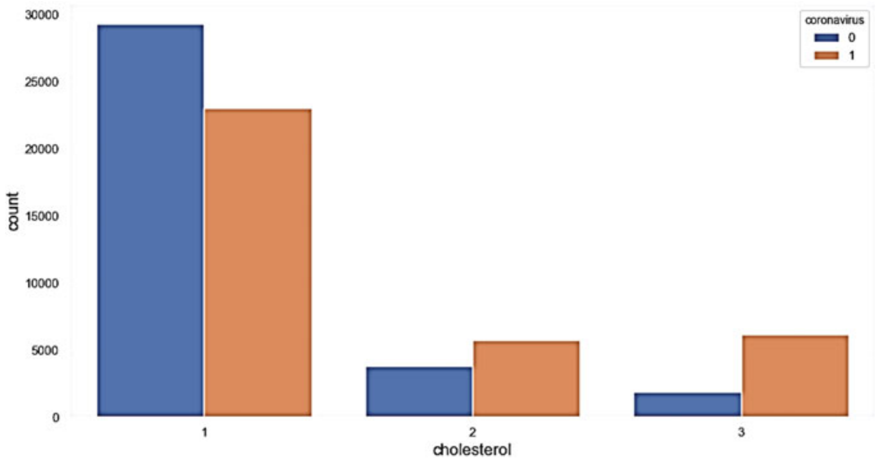

Fig. 6 Cholesterol versus count of COVID-19 case for type-1, type-2 and type-3

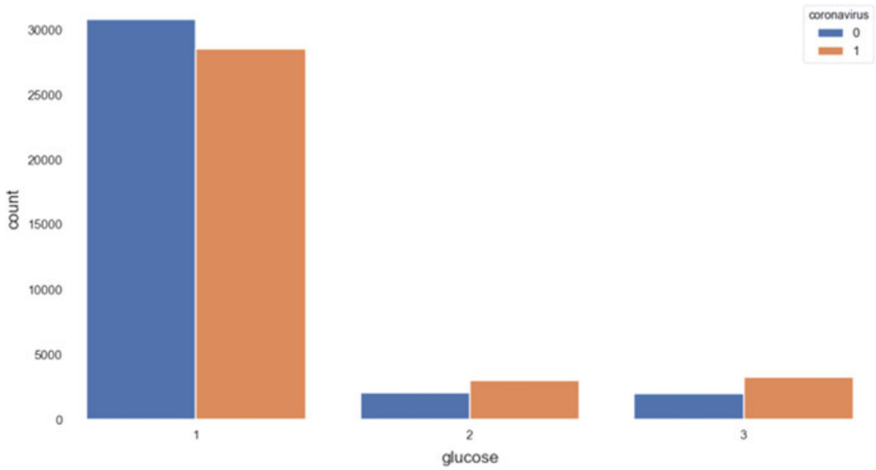

Fig. 7 Glucose versus count of COVID-19 cases for type-1, type-2 and type-3

back the lost glory. Let the innocent faces smile again and let us all say, "We shall overcome someday!"

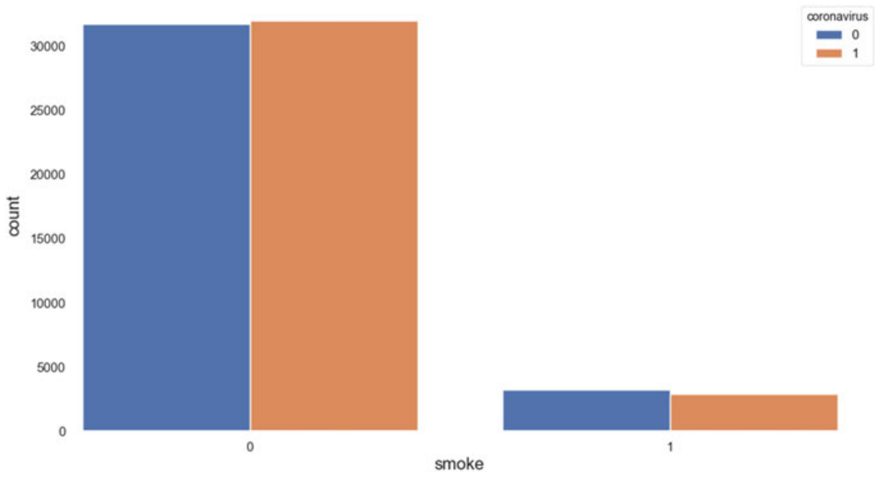

Fig. 8 Smokers versus count of COVID-19 cases

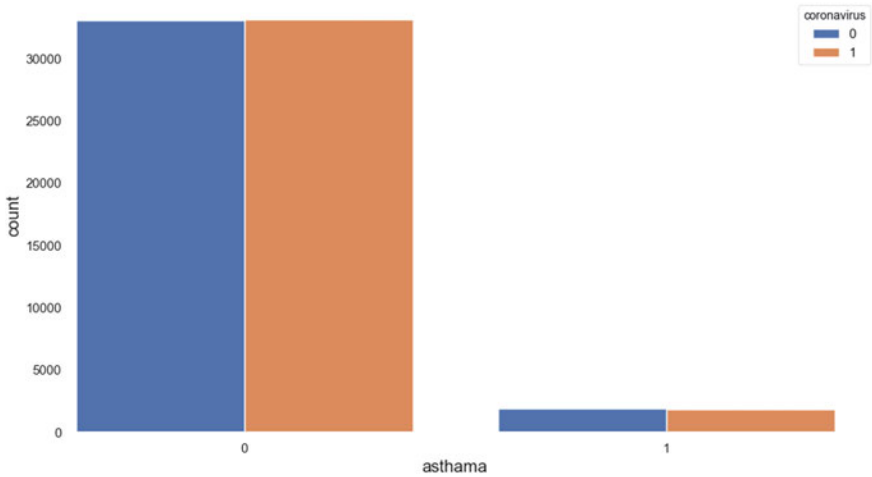

Fig. 9 Asthma patients versus count of COVID-19 cases

References

1. Zhao, S., Lin Q., Ran, J., et al.: Preliminary estimation of the basic reproduction number of novel coronavirus (2019-nCoV) in China, from 2019 to 2020: a data-driven analysis in the early phase of the outbreak. Int. J. Infect. Dis., (2020)
2. Liangjun, Chen., Weiyong, Liu., Qi, Zhang., et al.: RNA based mNGS approach identifies a novel human coronavirus from two individual pneumonia cases in 2019 Wuhan outbreak. Emerg. Microbes. Infect. **9**, 313–319 (2020)
3. Zu, Z.Y., Jiang, M.D., Xu, P.P., Chen, W., Ni, Q.Q., Lu, G.M., Zhang, L.J.: Coronavirus disease 2019 (COVID-19): a perspective from china. Radiology, (2020)

4. https://radiopaedia.org/articles/covid-19-3 and https://www.who.nt/docs/default-source/coronaviruse/situation-reports/20200413-sitrep-84-covid-19.pdf?sfvrsn=44f511ab_2
5. Liang, T.: Handbook of COVID-19 Prevention and Treatment (2020)
6. Luccioni, A., Bullock, J., Pham, K.H., Lam, C., Luengo-Oroz, M.: Mapping the landscape of artificial intelligence applications against COVID-19. arXiv:2003.11336 (2020)
7. Qin Yao, Yu., Tian, Peng-Fei Li., Tian, Li-Li., Qian, Yang-Ming, Li, Jing-Song: Design and development of a medical big data processing system based on hadoop. J. Med. Syst. **39**(3), 23 (2015)
8. Bizer, Christian., Boncz, Peter., Brodie, Michael L., Erling, Orri: The meaningful use of big data: four perspectives four challenges. ACM Sigmod Rec. **40**(4), 56–60 (2012)
9. Senthilkumar, S.A., Rai, B.K. Meshram, A.A., Gunasekaran, A., Chandrakumarmangalam, S.: Big data in healthcare management: a review of literature. Am. J. Theor. Appl. Bus. **4**(2), 57–69 (2018)
10. Meena, I., Aravind, R., Sarker, V., Sanjudharan, M.S.: Healthcare analysis using hadoop framework. IJSART**4**(14) 300–306 (2018)
11. Belle, A., Thiagarajan, R., Soroushmehr, S.M., Navidi, F., Beard, D., Najarian, K.: Big data analytics in healthcare. BioMed Res. Int. (2015)
12. Dash, S., Shakyawar, S., Sharma, M., Kaushik, S.: Big data in healthcare: management, analysis and future prospects. J. Big Data **6** (2019)
13. Thanuja Nishadi, A.S.: Healthcare big data analysis using hadoop MapReduce. Int. J. Sci. Res. Pub. **9**(3), 87104 (2019). http://doi.org/10.29322/IJSRP
14. Raghupathi, W., Raghupathi, V.: Big data analytics in healthcare: proise and potential. Health Inf. Sci. Syst. **2**(3), 7 (2014). https://doi.org/10.1186/2047-2501-2-3
15. https://www.researchgate.net/publication/333201013_Healthcare_Analysis_Using_HadoopFramework

Latest Trends in Semiconductor and Electronics Industry

Computing Photocurrent in Heterojunction Solar Cell with Gaussian Diffusion Profile

Purbasha Ray, Swarnav Mukhopadhyay, and Arpan Deyasi

Abstract The Photocurrent and corresponding net current in heterojunction solar cell is analytically computed considering variable diffusion length approximation, i.e., it is assumed that all the photogenerated carriers are not susceptible to contribute current owing to various internal scattering processes. It is also taken into account that generated minority carriers are function of depletion region widths, i.e., they have dependence on material properties. Results show variation of photocurrent on device width and incident wavelength, and are much higher when compared with homojunction device with equivalent dimensional configuration. Decrease in photocurrent with increasing wavelength suggests trapping is taken place through quantum well. Corresponding net current is computed as a function of leakage current. Findings are important for calculating figure of merit of the device.

Keywords Photocurrent · Leakage current · Heterojunction · Gaussian diffusion profile · Incident wavelength · Variable depletion width

1 Introduction

Research on solar cell is a domain of interest now-a-days due to the increased interest on renewable energy [1, 2] and the societal need. Several reputed articles are already available on bulk structure [3, 4] and also on homojunction devices [5, 6] for

P. Ray (✉) · S. Mukhopadhyay
Department of Electronics and Telecommunication Engineering, Jadavpur University, Kolkata 700032, India
e-mail: raypurbasha5@gmail.com

S. Mukhopadhyay
e-mail: swarnavhome@gmail.com

A. Deyasi
Department of Electronics and Communication Engineering, RCC Institute of Information Technology, Kolkata 700015, India
e-mail: deyasi_arpan@yahoo.co.in

S. Banerjee and J. K. Mandal (eds.), *Advances in Smart Communication Technology and Information Processing*, Lecture Notes in Networks and Systems 165,
https://doi.org/10.1007/978-981-15-9433-5_34

computing efficiency of solar cell, whereas less work is carried out on heterojunction devices. Recent literatures also exhibit works on organic solar cells [7, 8]. However, in all the works, it is assumed that all the generated photocarriers contribute to the current flow, i.e., roll of loss and scattering mechanisms are generally ignored. If that factor is taken into account, then figure of merit of the device will be changed. Since quantum efficiency of Si heterojunction solar cell is already reported [9, 10] and is relatively low, so researchers are either looking for alternative materials [11], or for change of structural layers [12]. Quantum-confined structures are also introduced for betterment of performance [13].

In order to simultaneously reduce trapping effect and increasing efficiency, heterojunction has to be formed, which is considered in this present paper. In this structure, normally all the carriers can't take part in transport, and therefore, diffusion length will not become a constant quantity, rather than it will vary with distance, and will take Gaussian profile. Incorporating this assumption, we have computed photocurrent as a function of incident wavelength and structural parameters. Effect of leakage current on net current is also estimated. Comparative study with homojunction speaks in favor of the present device.

2 Device Structure

Figure 1 shows the schematic structures of both homojunction and heterojunction devices under considerations, Fig. 1a for homo and Fig. 1b for hetero.

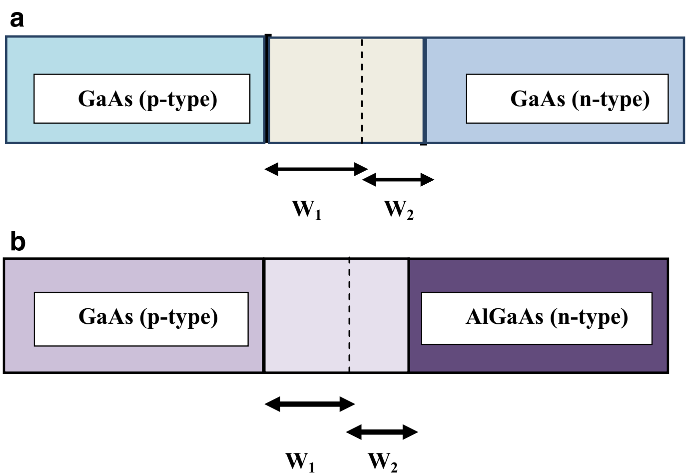

Fig. 1 **a** Schematic diagram of homojunction. **b** Schematic diagram of heterojunction

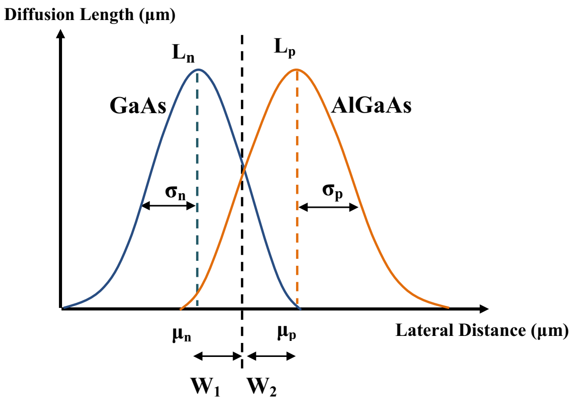

Fig. 2 Schematic Gaussian diffusion profile

As we applied forward bias on both the structures (i.e. homostructure and heterostructure) in presence of incident photons, minority carriers will be generated on both the sides of the depletion region. Minority carriers on p-side (electron) and n-side (hole) will be drifted towards positive and negative bias respectively. Due to availability of higher barrier height at GaAs-AlGaAs interface, these carriers generated inside GaAs region cannot overcome higher barrier height so they cannot recombine with the holes generated inside AlGaAs region. If the photon energy will be very high then generated minority carriers on both p and n side obtain enough kinetic energy to overcome the barrier as thermionic emission though the probability is very low. That is why net recombination rate in heterostructure solar cell is much lower than homojunction solar cell. Due to the formation of 2DEG at AlGaAs-GaAs interface, depletion region inside the GaAs region is much less than the AlGaAs side. Due to higher bandgap the refractive index of AlGaAs is lower than GaAs so the depletion region spread more inside the AlGaAs region. Corresponding diffusion profiles for both the cases are depicted in Fig. 2.

For the present structure, photon energy varies from 0.1 to 10 eV. So the surface area under which photon fall may have different energy on the different position. This phenomenon is random in nature. Taking consideration of this energy profile phenomenon the photon energy is random w.r.t the surface area. Generated electron-hole pair is also random in nature similar with the energy profile as photon. Diffusion length is also proportional with the energy of minority carrier so it follows the same energy profile. So we have modelled the diffusion length as a Gaussian curve with respect to lateral distance of the device, given in Fig. 2. σ may vary with the depletion width and doping concentration.

3 Mathematical Formulation

For mathematical formulation of current equations in heterojunction device, we have to start with one-dimensional Poisson's equation for n-side [14, 15]

$$\frac{d^2n}{dz^2} - \frac{n - n_{po}}{L_n^2} + \int\limits_{\lambda} \psi_o \cdot e^{-\alpha_1(L_1+z)} \cdot \alpha_2 \cdot e^{-\alpha_2(z-L_1)} \frac{1}{D_n} d\lambda = 0 \tag{1a}$$

Similarly we can write for p-side as

$$\frac{d^2p}{dz^2} - \frac{p - p_{no}}{L_p^2} + \int\limits_{\lambda} \psi_o \cdot e^{-\alpha_1(L_1+z)} \cdot \alpha_2 \cdot e^{-\alpha_2(z-L_1)} \frac{1}{D_p} d\lambda = 0 \tag{1b}$$

Boundary conditions are given by

$$\left.\frac{dn}{dz}\right|_{z=W_2+L} = -\frac{S_n}{D_n}\left[n(W_2+L) - n_{p0}\right] \tag{2a}$$

$$\left.\frac{dp}{dz}\right|_{z=W_1+L} = -\frac{S_p}{D_p}[p(W_1+L) - p_{n0}] \tag{2b}$$

Solution of Eqs. (1a, 1b) with appropriate boundary conditions gives the carrier concentration equations [14]

$$n_{hetero} = A_1.e^{\frac{z}{Ln}} + A_2.e^{-\frac{z}{Ln}} + n_{po} + \int (L_n^2 \cdot \psi_o \cdot \alpha_2 \cdot e^{-\alpha_1(L_1-z)} \cdot e^{-\alpha_2 \cdot L_1} \frac{\lambda}{D_{n.} \cdot (1 - \alpha_2^2 \cdot L_n^2)}) dz \tag{3a}$$

$$p_{hetero} = -A_3 \times e^{-\frac{z}{Lp}} - A_4 \times e^{\frac{z}{Lp}} + p_{no} - \int (L_p^2 \times \psi_o \times \alpha_2 \times e^{-\alpha_1(L_1+z)} \times e^{-\alpha_2 \times L_1} \frac{\lambda}{D_p \times (1 - \alpha_2^2 \times L_p^2)}) dz \tag{3b}$$

where 'L' is the length of quasi-neutral region [14, 15]. S_n and S_p are the surface recombination speed.

Solution of Eqs. (1a) and (1b) with appropriate boundary conditions gives the carrier concentration equations [14, 15]

$$Jp_{hetero} = q \times D_{p.} \times \frac{dp_{hetero}}{dz} \tag{4a}$$

$$Jn_{hetero} = q \times D_{n.} \times \frac{dn_{hetero}}{dz} \tag{4b}$$

Therefore, total photocurrent can be obtained as

$$I_L = In_{hetero} + Ip_{hetero} \tag{5}$$

Net current is

$$I_{net} = I_L + I_o.e^{(V)/(0.26 \times \eta)} \tag{6}$$

where I_L is the total photocurrent, I_0 is the leakage current, η is the ideality factor, and I_{net} is total current in presence of bias.

Variable diffusion lengths are incorporated in the calculation in flowing manner [14, 15]

$$L_n = \left(\frac{1}{\sigma_n \times \sqrt{2 \times \pi}}\right) \times e^{-\frac{(z-\mu_{Al})^2}{2(\sigma_n)^2}} \times area \tag{7a}$$

$$L_p = \left(\frac{1}{\sigma_p \times \sqrt{2 \times \pi}}\right) \times e^{-\frac{(z-\mu_{Ga})^2}{2(\sigma_p)^2}} \times area \tag{7b}$$

For homojunction device, equation for n-side is [15]

$$\frac{d^2 n}{dz^2} - \frac{n - n_{po}}{L_n^2} + \int_\lambda \psi_o \cdot e^{-\alpha(L+z)} \cdot \alpha \frac{1}{D_n} d\lambda = 0 \tag{8a}$$

and for p-side

$$\frac{d^2 p}{dz^2} - \frac{p - p_{no}}{L_p^2} + \int_\lambda \psi_o \cdot e^{-\alpha(L+z)} \cdot \alpha \frac{1}{D_p} d\lambda = 0 \tag{8b}$$

Using similar boundary conditions, concentrations are obtained as

$$n_{\hom o} = B_1.e^{\frac{z}{L_n}} + B_2.e^{-\frac{z}{L_n}} + n_{po} + \int (L_n^2 \cdot \psi_o \cdot \alpha \cdot e^{-\alpha(z+L)} \frac{\lambda}{D_{n.} \cdot (1 - \alpha^2 \cdot L_n^2)})dz \tag{9a}$$

$$p_{\hom o} = -B_3.e^{-\frac{z}{L_p}} - B_4.e^{\frac{z}{L_p}} + p_{no} - \int (L_p^2.\psi_o.\alpha.e^{-\alpha(L+z)} \frac{\lambda}{D_p \times (1 - \alpha^2 \times L_p^2)})dz \tag{9b}$$

Therefore, equation of current for the homojunction may be put in the similar format as mentioned for heterojucntion form in Eq. (5).

4 Results and Discussions

Equations (4a, 4b) and (5) are utilized to compute photocurrent and total current in heterojunction solar cell. First we have considered the variable diffusion length effect over photocurrent. Figure 3a shows the variation of photocurrent for different sets of hole and electron diffusion lengths, whereas net current profile is depicted in Fig. 3b. From the plot, it is shown that photocurrent decreases with increasing

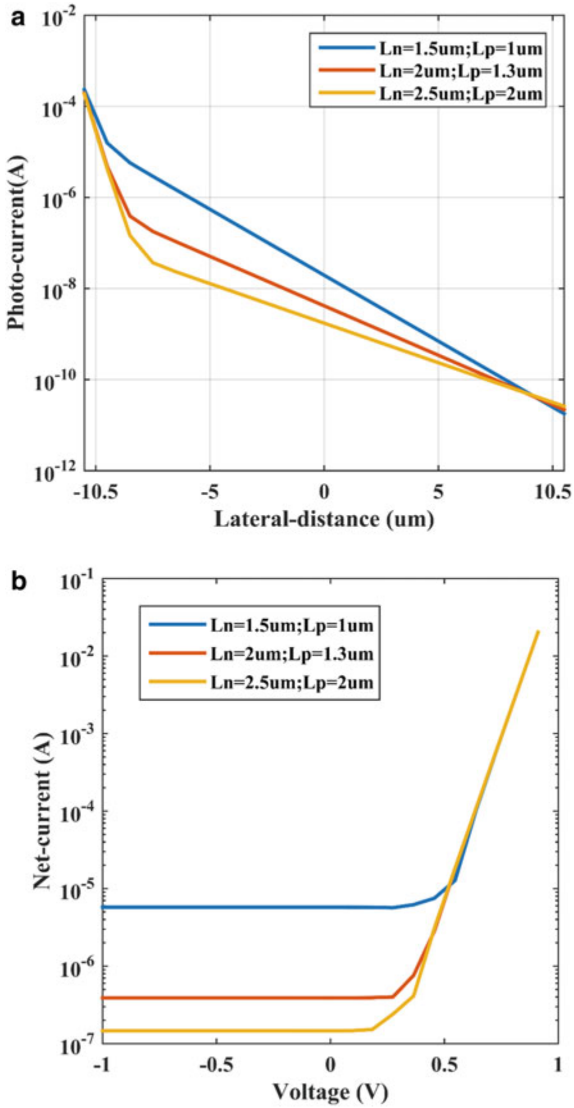

Fig. 3 **a** Photocurrent variation for different electron and hole diffusion lengths. **b** Total current variation for different electron and hole diffusion lengths

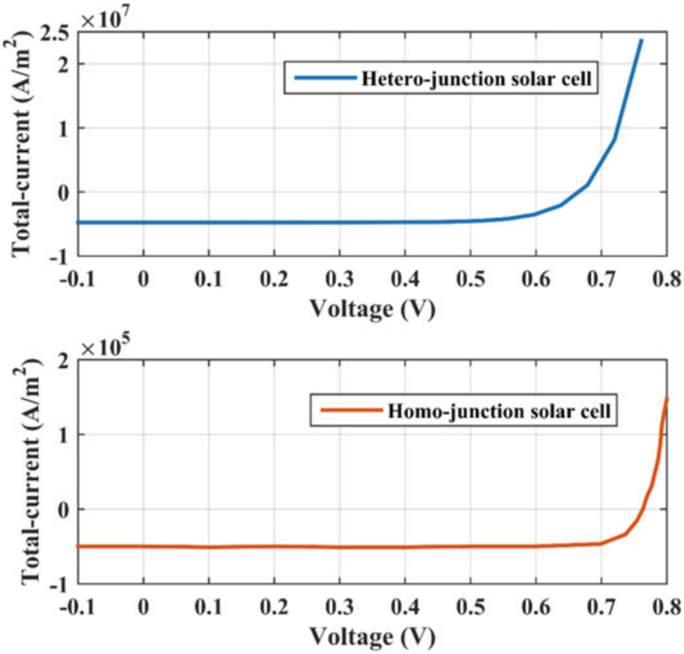

Fig. 4 Comparative study between heterojunction solar cell and homojunction solar cell [16]

distance, which is due to trapping of carriers inside the quantum well. However, net current increases as usual, represented in Fig. 3b. It may be seen that higher the diffusion lengths at both the sides, both photocurrent and net current reduce.

Figure 4 depicts the comparative study with homojunction device having same dimensional configuration under equal applied bias. It is seen from the plot that the photo-current is higher in hetero-junction solar cell than that of homo-junction solar cell.

As in hetero-structure there is a quantum well between GaAs (p-side) and AlGaAs (n-side); so the carriers can accumulate at the well, which will eventually decrease the threshold voltage of the p-n junction device. Total generated photo-current is more in hetero-junction than homo-junction, due to increased life time of generated carrier and also due to availability of quantum energy state the carriers can transit between the quantum energy state and conduction band with less amount of energy compared to electron transition from valance band to conduction band in homo-junction.

Next we have calculated photocurrent. Photons that hit the solar cell are either reflected or transmitted into the cell. Transmitted photons have the potential to give their energy, $h\upsilon$ to an electron if $h\upsilon \geq E_g$, generating an electron-hole pair. In the depletion region, the drift electric field E_{drift}, accelerates both electrons and holes towards their respective n-doped and p-doped regions (right and left, respectively). The resulting current I is called the generated photo-current. In the quasi-neutral region, the scattering electric field E_{scatt} accelerates holes (electrons) towards

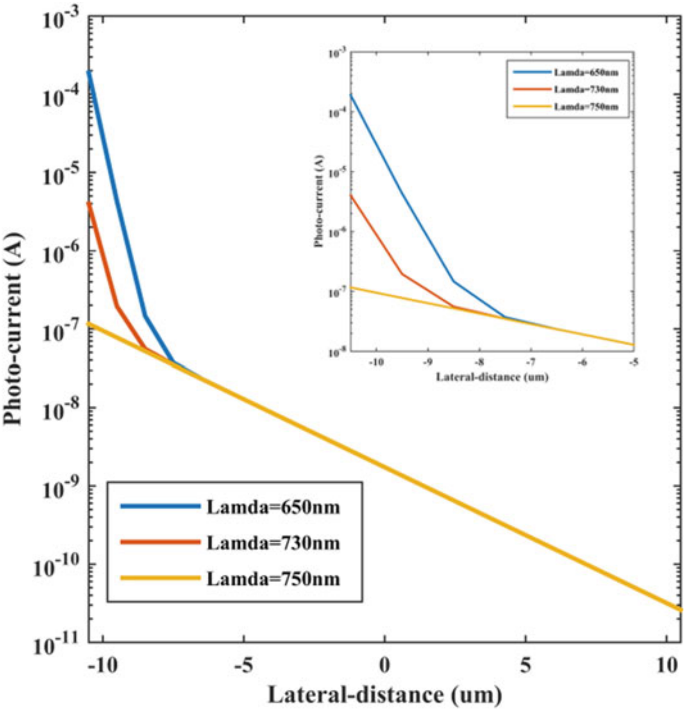

Fig. 5 Variation of photocurrent with lateral distance for different incident wavelengths

the p-doped (n-doped) region, which gives a scattering photocurrent I_{scatt} (I_{scatt}). Consequently, due to the accumulation of charge, a potential V and a photocurrent I_{ph} appear. So as the wavelength increases, energy decreases. As a consequence, photo-current decreases. This is illustrated in Fig. 5.

Figure 6 shows the variation with device width. For higher width, resistance of the device decreases, henceforth, current increases. The variation is plotted for small as well as moderate and large values of width. At a particular value of lateral distance, slope of the profile changes, this indicates that the effective diffusion takes place before the range.

Next we have computed the net current in the device. In Fig. 7, effect of net current is calculated on different leakage currents, whereas in Fig. 8, ideality factor is taken account.

Leakage current in a solar cell can be considered as undesirable current that is injected from the electrodes prior to the turn on voltage. Within the operating regime (0 V to open circuit voltage), leakage current flows opposite to the photocurrent and thereby reduces the light current. Total net current (I) therefore becomes the difference of current due to the majority carrier and Total Photocurrent (I_L). At lower light intensity photocurrent increases, which, in turn, makes higher total current. At

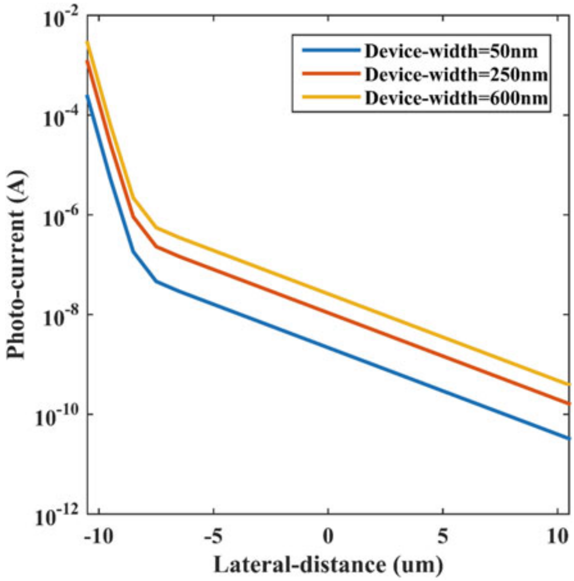

Fig. 6 Variation of photocurrent with lateral distance for different device widths

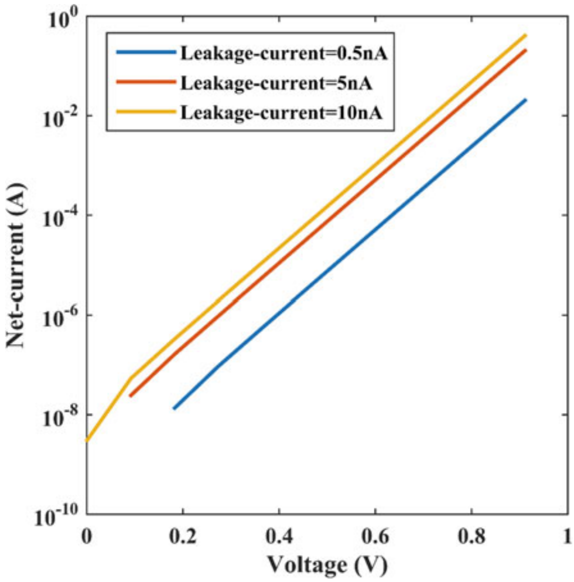

Fig. 7 Variation of total current with applied bias for different leakage currents

this point, leakage current becomes non-negligible, and the Fill-factor decreases and same for corresponding open circuit voltage (Voc).

The ideality factor (also called the emissivity factor) is a fitting parameter for any diode. It also measures how the diode follows the ideal diode equation. It is also

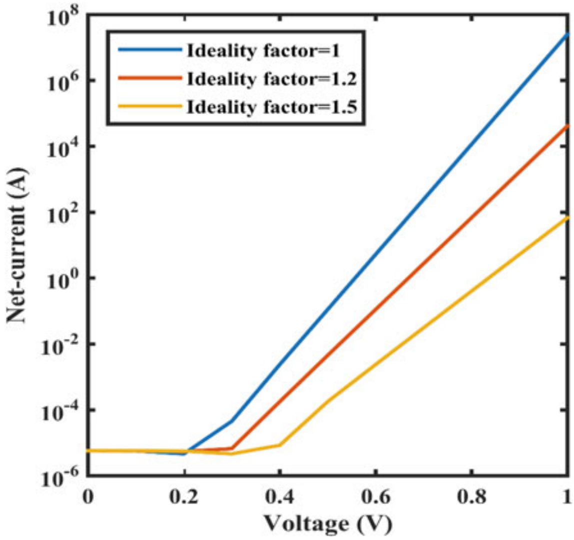

Fig. 8 Variation of total current with applied bias for different ideality factors

an indicator for the recombination process inside the diode. Now the solar cells are large compared to the diode. It affects the fill factor, and henceforth, efficiency of the solar cell in a reciprocal manner.

Now the solar cells are large compared to the diode. The operation of solar may be dominated by recombination in the space-charge region. Naturally, for higher ideality factor, net current decrease, as shown in Fig. 8. The variation is more effective at higher applied bias.

As shown in the plot, with increase of ideality factor, original diode current due to the majority carrier will decrease, that will eventually affect the net current of that cell. For $\eta = 1$ the net current is more compared to the value for 1.2 and 1.5.

5 Conclusion

Comparative study reveals that photocurrent is 100 times higher in heterojunction device than the homojunction one, which indirectly speaks for higher quantum efficiency. Ratio of net current to leakage current is extremely high (~10^6 times) at moderate bias, and also depends on device width as well as lateral distance. Gaussian diffusion profile is considered for simulation purpose, which accounts the internal losses due to scattering. Sharp decrease of photocurrent is observed with increasing diffusion length which speaks in favor of carrier trapping inside quantum well. Result speaks in favor of quantum well based heterojunction solar cell for higher electrical output.

References

1. Grisham, L.R.: Nuclear fusion. In: Letcher, T.M. (ed.) Future Energy, Improved, Sustainable and Clean Options for Our Planet, 2nd edn., pp. 291–301. Elsevier Ltd., Amsterdam (2008)
2. Bagher, A.M., Vahid, M.M.A., Mohsen, M.: Types of solar cells and application. Am J Opt Photonics **3**(5), 94–113 (2015)
3. Zin, N.S., McIntosh, K., Fong, K., Blakers, A.: High efficiency silicon solar cells. Energy Procedia **33**, 1–10 (2013)
4. Kivambe, M., Aissa, B., Tabet, N.: Emerging technologies in crystal growth of photovoltaic silicon: progress and challenges. Energy Procedia **130**, 7–13 (2017)
5. Tan, M., Zhong, S., Wang, W., Shen, W.: Silicon homo-heterojunction solar cells: a promising candidate to realize high performance more stably. AIP Adv. **7**, 085016 (2017)
6. Soley, S.S., Dwivedi, A.D.D.: Advances in high efficiency crystalline silicon homo junction solar cell technology. AIP Conf. Proc. **2104**, 030033 (2019)
7. Anagnostou, K., Stylianakis, M.M., Petridis, K., Kymakis, E.: Building an organic solar cell: fundamental procedures for device fabrication. Energies **12**(11), 2188 (2019)
8. Tang, Z., Elfwing, A., Melianas, A., Bergqvist, J., Bao, Q., Inganäs, O.: Fully-solution-processed organic solar cells with a highly efficient paper-based light trapping element. J. Mater. Chem. A **3**, 24289–24296 (2015)
9. Wolf, S.D., Descoeudres, A., Holman, Z.C., Ballif, C.: High-efficiency silicon heterojunction solarcells: a review. Green **2**, 7–24 (2012)
10. Blakers, A., Zin, N., McIntosh, K.R., Fong, K.: High efficiency silicon solar cells. Energy Procedia **33**, 1–10 (2013)
11. Benmir, A., Aida, M.S.: Analytical modeling and simulation of CIGS solar cells. Energy Procedia **36**, 618–627 (2013)
12. Yamamoto, K., Yoshikawa, K., Uzu, H., Adachi, D.: High-efficiency heterojunction crystalline Si solar cells. Jpn. J. Appl. Phys. **57**(8S3), 08RB20 (2018)
13. Chebrolu, V.T., Kim, H.J.: Recent progress in quantum dot sensitized solar cells: an inclusive review of photoanode, sensitizer, electrolyte, and the counter electrode. J. Mater. Chem. C **7**, 4911–4933 (2019)
14. Ray, P., Mukhopadhyay, S., Deyasi, A.: Computing carrier densities in heterostructure solar cell with gaussian diffusion length profile. In: IEEE National Conference on Emerging Trends on Sustainable Technology and Engineering Applications (2020)
15. Fonash, S.: Solar Cell Device Physics, 2nd edn. Academic Press (Elsevier), Burlington, USA (2010)
16. Deyasi, A., Sarkar, A.: Calculating current density and quantum efficiency of p-n junction solar cell with quasi-fermi level approximation. Int. J. Nanopart. **11**(1), 27–36 (2019)

A Low Energy and Area Efficient Switching Scheme for a Charge Redistribution SAR ADC Architecture

Pranati Ghoshal, Chanchal Dey, and Sunit Kumar Sen

Abstract An energy and area efficient switching scheme for a 4-bit charge redistribution switch capacitor (SC) successive approximation register (SAR) analog-to-digital converter (ADC) is proposed. It is based on conventional binary search algorithm. The charge redistribution type architecture implemented in the proposed scheme is fully differential in nature, hence the operation of the two sides is complementary. The proposed switching technique consumes zero energy in the first and third comparison cycles. It It is seen that the switching energy saving is as high as 99%. The method thus becomes one of the most energy efficient switching schemes recently presented by different researchers. Besides such an enormous savings in energy, it also achieves a 75% reduction in unit capacitance requirements over the conventional method. The common mode voltage variations at the comparator inputs have been studied and it is seen that the same is better than either the modified merged or hybrid method.

Keywords Symmetric switching · Monotonic switching · Unit capacitor

P. Ghoshal (✉)
Applied Electronics and Instrumentation Engineering Department, Techno Main, Salt Lake, Kolkata 700 091, India
e-mail: pranati991@gmail.com

C. Dey · S. K. Sen
Instrumentation Engineering, Department of Applied Physics, University College of Technology, 92, APC Road, Kolkata 700 009, India
e-mail: cdaphy@caluniv.ac.in

S. K. Sen
e-mail: sunitksen@yahoo.co.in

S. Banerjee and J. K. Mandal (eds.), *Advances in Smart Communication Technology and Information Processing*, Lecture Notes in Networks and Systems 165,
https://doi.org/10.1007/978-981-15-9433-5_35

1 Introduction

A successive approximation register (SAR) analog to digital converter (ADC) is a moderate speed ADC, because it needs n conversion cycles to convert an analog signal to its equivalent n bit digital equivalent. Thus, for such ADCs, time required for conversion increases with increasing resolution. With feature sizes of CMOS devices being scaled down, the SAR ADCs are gaining in speed. An SC SAR ADC basically consists of a comparator, a bootstrap switch, a capacitive DAC architecture and a SAR logic unit. The capacitor matrix of the DAC is the dominant source of power consumption. Resetting of the DAC, after all the bits of the ADC have been determined, is another major contributory factor in the overall energy consumption.

A conventional [1] SAR ADC consumes lot of power, particularly in the first few conversion steps. The differential inputs are sampled on to the bottom plates on either side of the capacitor arrays while the top plates of the same are supplied with half the reference voltage, i.e., V_r. After sampling, the inputs are disconnected from the DAC block. The MSB capacitor of the top array is charged with V_r while the other capacitors are connected to ground. The opposite is done for the bottom array. The output of the second stage will determine whether 'up' or 'down' transition would take place. An asymmetrical power consumption takes place in this—the 'up' transition consumes CV_r^2, while the 'down' transition consumes $5CV_r^2$[1]. Thus, there is an asymmetrical power consumption during the 'up' and 'down' transitions. Of late, researchers have taken lots of interests to reduce the power consumption in the first few conversion steps resulting in its suitability for situations which requires its continuous use like in environmental monitoring and implantable biomedical devices. Researchers have also ensured that both 'up' and 'down' transitions consume equal powers during evaluation of successive bits of an ADC.

A modified merged capacitor switching scheme presented by Sanyal et al. [2] resulted in a savings of 98.4% in energy and a 4 $\times$ reduction in total capacitance, while the merged capacitor switching scheme presented in [3] reduced energy requirement by 93.4% for a 10 bit ADC. In [4–6], tri-level based energy saving procedure was adopted resulting in energy savings of 98%, 97.66% and 97.26% respectively. An asymmetric monotonic switching scheme is proposed in [7] which saves up to 98.5% energy, but the digital control is complex and it requires an extra comparison cycle to complete the conversion. An energy efficient hybrid capacitor switching scheme was proposed in [8] resulting in an energy savings of98.83% in which no energy was consumed in the first three comparison cycles. Yao et al. [9] proposed a scheme based on early reset merged capacitor switching algorithm (EMCS) and monotonic capacitor switching to realize 99.6% energy saving and total area reduction by 93.75%. Osipov et al. [10] presented a novel switching scheme which resulted in energy savings to the extent of 99.21 and 99.37% for signal-independent and signal-dependent common mode voltage at the input to the comparator. Ding et al. [11] presented a technique which resulted in an energy savings of 99.9% and unit capacitance reduction of 75% compared to the conventional scheme. Liu et al. [12] presented a technique resulting in enhanced linearity and energy efficiency and also introduced a novel switching scheme (COSS) requiring less matching requirements of capacitors. In this, a novel output offset cancellation strategy was adopted asynchronously to reduce non linearity of parasitic capacitances at comparator inputs.

In [13–15], low energy and area efficient switching schemes were presented for SC SAR ADCs. In [13], the ADC was realized at the cost of multiple references. A very high energy efficient switching technique for SAR ADCs was presented by Sanyal et al. [16] which also discussed reduction in common mode voltage swings at the virtual node by having MSB capacitors starting at ground potential in the first comparison cycle.

In this paper, a 4-bit new switching technique is presented which achieves a power savings of 99% and a reduction in unit capacitor requirement by 75%. The proposed 4-bit energy efficient SAR ADC was implemented using a differential architecture with V_r,V_{cm} and $V_{cm}/2$, where V_{cm} is half the reference voltage V_r. Different voltages are applied at different stages of its implementation. The implemented architecture consumes zero energy during first and third comparison cycles, leading to a very high energy efficient design for a SC SAR ADC.

Successive sections deal with previous architectures concerning this paper, followed by the proposed scheme and its functioning. The next section deals with comparison of switching energy involving the different methods. Issues concerning common mode voltage variations are then discussed. The last section concludes with the findings of the paper.

2 Previous Architecture

2.1 Modified Merge Method [3]

A major part of the switching energy is consumed in the first few comparison cycles of conversion of the analog signal. This is consumed in the capacitive DAC which is a part of the ADC. In the modified merged method, the MSB capacitor of bottom plate is initially connected to '0' and other capacitors are connected to V_{ref} and only one capacitor is changed in each cycle, thereby drastically reducing energy consumption in these steps. Again, voltage across a capacitor is changed from V_{ref} to V_{cm} first and then from V_{cm} to 0, instead of direct transition from V_{ref} to 0. Proceeding in this way, the scheme can save switching energy by 93.4% for a 10 bit ADC and requirement of unit capacitors is reduced by 75% compared to the conventional one.

2.2 Hybrid Switching Scheme [8]

It combines two existing switching schemes: viz., tri-level switching and monotonic switching scheme to reduce even more energy consumption over the conventional.

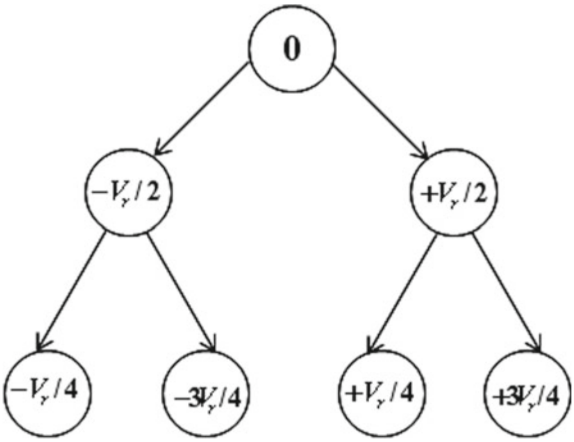

Fig. 1 Conventional binary search algorithm

Tri-level switching scheme is used for the first three switching steps for which the energy consumption is zero and for the rest of the steps, low energy monotonic switching scheme is used. Thus, the overall switching energy is reduced by 98.83% for a 4 bit ADC when compared with the conventional architecture. Moreover, it also achieves a 75% reduction in unit capacitor requirement.

2.3 The Proposed Switching Scheme

Figure 1 shows the conventional binary search algorithm which is followed in this work for realization of the energy efficient SC SAR ADC.

The flowchart of the implemented scheme is shown in Fig. 2 which is described below. Analog input voltage is split into V_{ip} and V_{in} and termed V_+ and V_- respectively. There are two ways at getting the bits of the ADC. In case, after each comparison, if V_+ is greater than V_-, the successive bits of the ADC become 1, else they are all 0's. The comparison goes on till *i* attains the value *n*—the resolution of the designed ADC.

The charge redistribution type architecture implemented in the proposed scheme is fully differential in nature, hence the operation of the two sides is complementary.

If considerable switching energy can be saved in the first few cycles—because it is where majority of power consumption takes place—then a very high energy efficient SC SAR ADC can be designed. Figure 3 shows such a proposed scheme for a 4-bit SC SAR ADC. In the sampling phase, the differential inputs are sampled onto the top plates on either side of the capacitor arrays while the bottom plates are set to $0, V_{cm}, V_{cm}$ voltages. That is, the bottom plate of the MSB capacitor (here it is 2C) is supplied with ground potential, while the other two are connected to V_{cm}. Next, the sampling switches are turned off and the first comparison cycle begins. Top plate sampling ensures that no energy is consumed in the first (which gives the MSB)

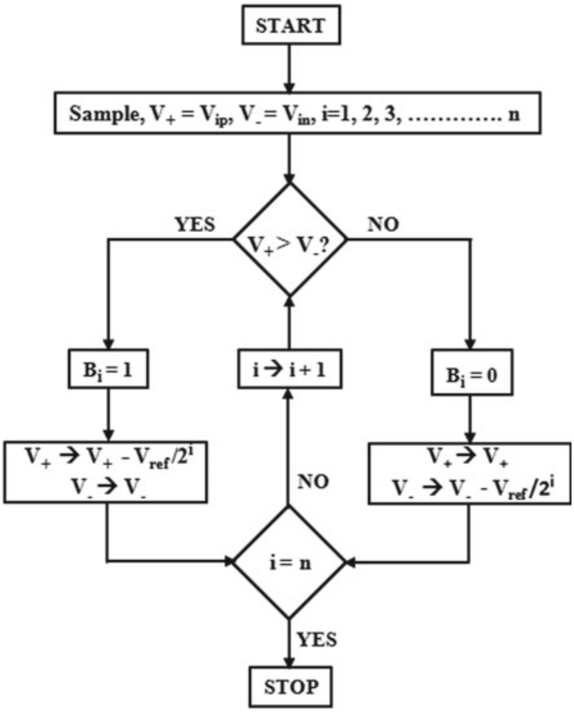

Fig. 2 Flowchart of the proposed ADC

comparison cycle, unlike the conventional one. After completion of first comparison cycle, the sequence is changed to $[0, V_{cm}, V_{cm}]$ on the bottom plates of the top array and $[V_{cm}, V_r, V_r]$ on the bottom plates of the bottom array. The second comparison cycle (which gives MSB-1) results in four possibilities: A, B, C or D and shown in Fig. 3a. The second comparison results in an average power consumption of $V_r^2/2$. In the third comparison cycle shown in Fig. 3b and c, the average power consumption is $[0 + 0 + V_r^2/16 + (-V_r^2/16) + (-V_r^2/16) + V_r^2/16 + 0 + 0] = 0$. Thus the total power consumption during third comparison cycle becomes zero. The fourth comparison cycle gives the final 4 bit pattern which is representative of the analog input.

The average switching energy for an n-bit conventional SAR ADC with equi-probable output codes is given by

$$\mathrm{E}_{\mathrm{avg,conv}} = \sum_{i=1}^{n} 2^{n+1-2i}(2^i - 1)C \tag{1}$$

While energy required for the proposed n-bit ADC, with $n \geq 4$, is found to be

$$\mathrm{E}_{\mathrm{avg,proposed}} = \sum_{i=2}^{n-2} 2^{n-3-i} C \tag{2}$$

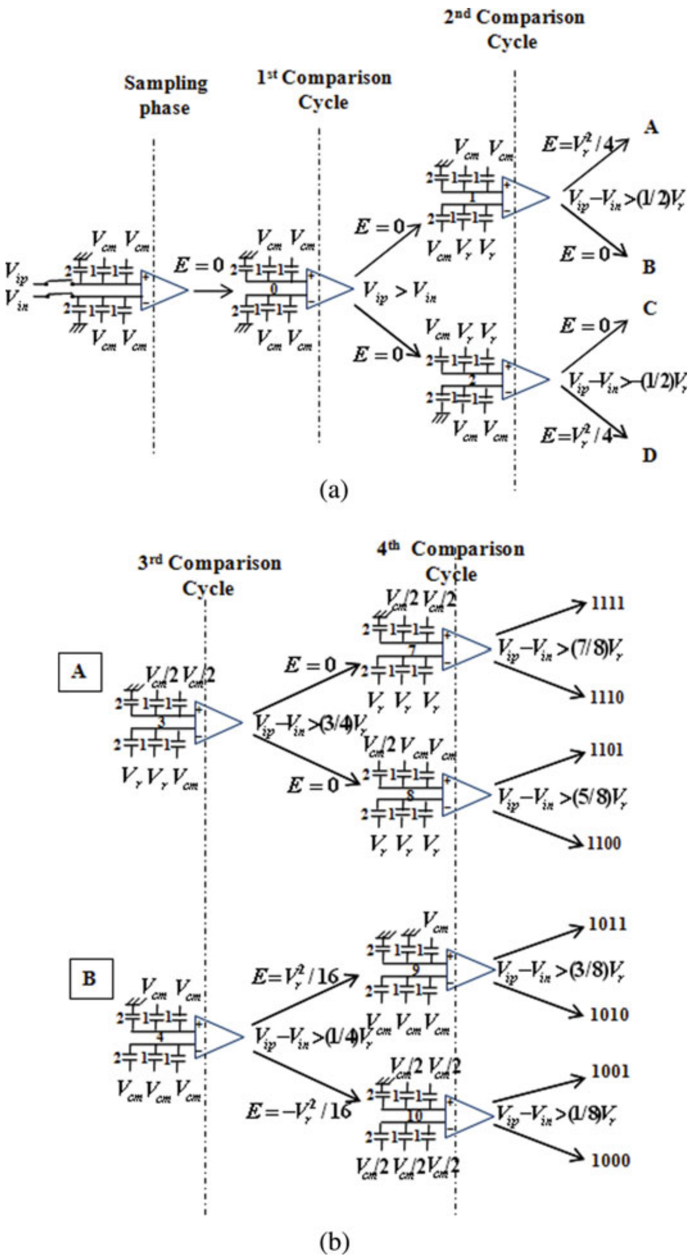

Fig. 3 Switching scheme for the proposed 4 bit ADC

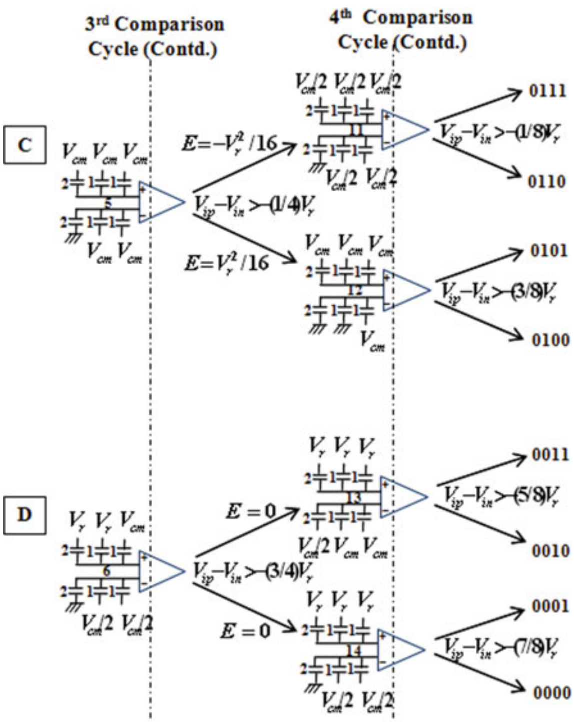

(c)

Fig. 3 (continued)

3 Comparison of Switching Energies

Average switching energy required for hybrid, modified merged and the proposed scheme are given in Table 1, while Table 2 shows the energy comparison for the aforesaid three methods.

Energy comparison for the different methods is shown in Fig. 4. While there is a power savings of 97.6% in case of hybrid compared to the conventional one, the same is 95.9% for the modified merged type. The proposed method saves energy to the extent of 99.5%. In this, the reset energy has not been considered while drawing the curves.

4 Common Mode Voltage Variation

The common mode voltage variations at the comparator inputs are shown in Fig. 5 for hybrid, modified merge and proposed methods. The first comparison cycle begins with the MSB capacitors tied to ground potential. An advantage of such a connection

Table 1 Average switching energy for proposed, modified merged and hybrid scheme: 4 bit case

Digital value	Equivalent value where 0000 = 0 and 1111 = 1000	Proposed method CV_r^2	Modified merged (3) CV_r^2	Hybrid method (8) CV_r^2
0000	0	6.25	1.5625	1.5625
0001	66.6666	6.25	1.5625	1.5625
0010	133.333	6.25	10.9375	4.6875
0011	200	6.25	10.9375	4.6875
0100	266.667	1.5625	17.1875	1.5625
0101	333.333	1.5625	17.1875	1.5625
0110	400	−1.5625	20.3125	4.6875
0111	466.667	−1.5625	20.3125	4.6875
1000	533.333	−1.5625	20.3125	4.6875
1001	600	−1.5625	20.3125	4.6875
1010	666.667	1.5625	17.1875	1.5625
1011	733.333	1.5625	17.1875	1.5625
1100	800	6.25	10.9375	4.6875
1101	866.667	6.25	10.9375	4.6875
1110	933.332	6.25	1.5625	1.5625
1111	1000	6.25	1.5625	1.5625

Table 2 Energy comparison for different methods: 4 bit case

Switching techniques	Energy consumed by different methods V_r^2	Energy saving (%)	Total no. of capacitors
Conventional	49	Reference	$2^n C_u$
Modified Merge [3]	2	95.9	$2^{n-1} C_u$
Hybrid Capacitor [8]	1	98	$2^{n-2} C_u$
Proposed	0.50	99	$2^{n-1} C_u$

is the reduction in common mode voltage swing at the virtual node [16]. In the proposed scheme, the common mode voltage at the virtual node begins at around 0.26 $V_{ref,}$, then has a zero swing for a considerable portion and then settles at around 0.55 $V_{ref.}$ This variation is better than either modified merged method or hybrid method and is evident from the figure. The reduced common mode voltage results in reduced non-linearities associated with signal dependent offset, particularly for cases where a fully differential comparator is not used.

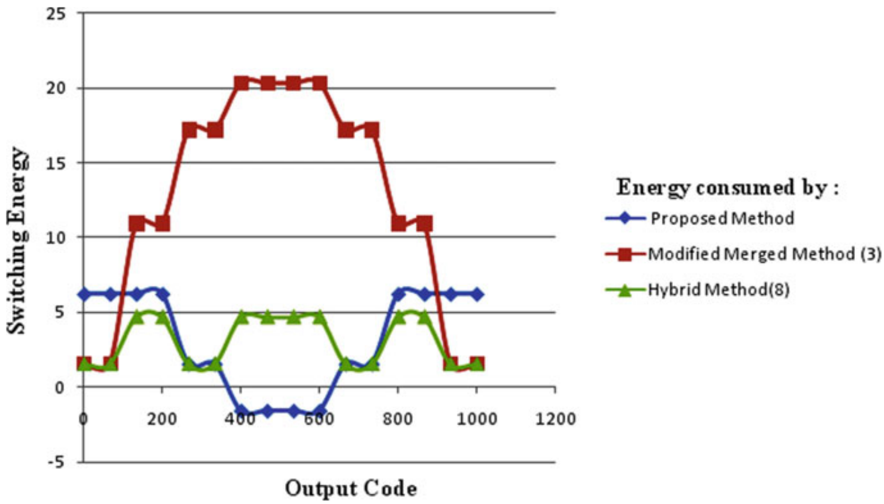

Fig. 4 Energy Comparison between hybrid, modified merged and proposed method for a 4 bit case

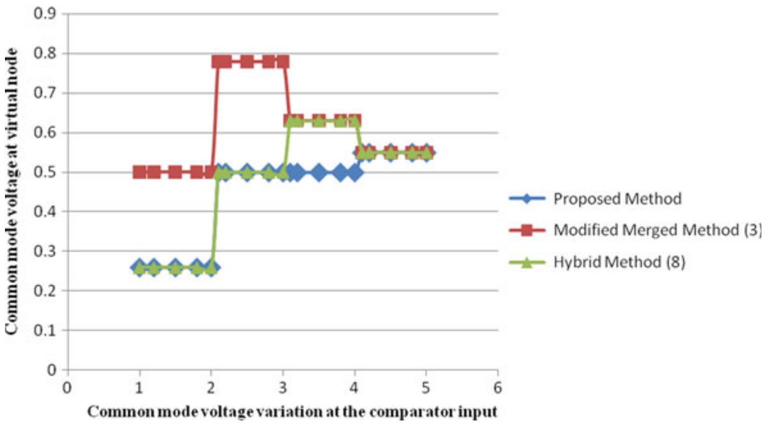

Fig. 5 Common mode voltage variation between hybrid, modified merged and proposed method

5 Conclusion

A highly energy efficient switching scheme which saves 99% energy compared to the conventional switching scheme is presented for a 4 bit ADC. Besides saving enormously on power, it also achieves a 4 $\times$ reduction in total capacitance employed in the digital to analog converter compared to the conventional DAC. The presented scheme employs voltages V_r, V_{cm} and $V_{cm}/2$ at different stages during implementation of the SAR ADC. The first and third comparison cycles consume zero power, while the second cycle consumes only $V_r^2/2$, making it one of the most energy efficient switching schemes among the existing ones.

References

1. Chang, A.H.T.: Low-power high-performance SAR ADC with redundancy and digital background calibration. Ph D Thesis, Massachusetts Institute of Technology (2013)
2. Sanyal, A., Sun, N.: SAR ADC architecture with 98% reduction in switching energy over conventional scheme. Electron. Lett. **49**(4), 248–249 (2013)
3. Hariprasath, V., Guerber, J., Lee, S.H., Moon, U.K.: Merged capacitor switching based SAR ADC with highest switching energy-efficiency. Electron. Lett. **46**(9), 620–621 (2010)
4. Sahar, S., Aain, A.K.B., Abbaszadeh, J.: High-linear, energy-efficient and area-efficient switching algorithm for high-speed SAR ADCs. Microelectron. J. **45**(3), 288–296 (2014)
5. Zhu, Z., Xiao, Y., Wang, W., Guan, Y., Liu, L., Yang, Y.: A 1.33 μW 10-bit 200KS/s SAR ADC with a tri-level based capacitor switching procedure. Microelectron. J. **44**(6), 1132–1137 (2013)
6. Shahmohammadi, M., Ashtiani, S.J., Kamarei, M.: Energy and area-efficient tri-level switching procedure based on half of the reference voltage for SAR ADC. IEICE Electron. Express **9**(17), 1397–1401 (2012)
7. Song, H., Lee, M.: Asymmetric monotonic switching scheme for energy-efficient SAR ADCs. IEICE Electron. Express **11**(12), 1–5 (2014)
8. Xie, L., Wen, G., Liu, J., Wang, Y.: Energy-efficient hybrid capacitor switching scheme for SAR ADC. Electron. Lett. **50**(1), 22–23 (2014)
9. Yao, J., Zhu, Z., Wang, Y., Yang, Y.: Variable resolution SAR ADC architecture with 99.6% reduction in switching energy over conventional scheme. IEICE Electron. Express **12**(5), 1–5 (2015)
10. Osipov, D., Paul, S.: Two advanced energy-back SAR ADC architectures with 99.21 and 99.37% reduction in switching energy. Analog Integr. Circ. Sig. Process **87**(1), 81–91 (2016)
11. Ding, R., Wu,, Q., Liang, Y., Zhu, Z.: Ultra-low energy switching scheme for SAR ADC.IEICE Electron. Express **12**(13), 1–5 (2015)
12. Liu, S., Shen, Y., Zhu, Z.: A 12-Bit 10 MS/s SAR ADC with high linearity and energy-efficient switching. IEEE Trans. Circ. Syst.-I **63**(10), 1616–1627 (2016)
13. Tong, X.Y., Zhang, W.R., Li, F.X.: Low energy and area efficient switching scheme for SAR A/D converter. Analog Integr. Circ. Sig. Process **80**(1), 153–157 (2014)
14. Liang, H., Ding, R., Liu, S.: Error! Hyperlink reference not valid. J. Circ. Syst. Comput. **27**(07) (2018)
15. Ghoshal, P., Moydudy, M., Hossain, M., Sen, S.K.: An energy and area efficient SC SAR ADC structure based on multi level capacitor switching technique. In: IEEE International Conference: Devices for Integrated Circuit (DevIC), pp. 574–577 (2017)
16. Sanyal, A., Sun, N.: A very high energy-efficiency switching technique for SAR ADCs. In: 56th International Midwest Symposium on Circuits and Systems (MWSCAS), pp. 229–232 (2013)

A Survey on Lee Filter and Its Improved Variants

Sriparna Banerjee, Sheli Sinha Chaudhuri, Raghav Mehra, and Arundhati Misra

Abstract In recent years, the high resolution, day and night and weather independent images provided by the Synthetic Aperture Radar (SAR) are widely used for various important remote sensing applications like land cover classification, crop classification, etc. These images are inherently corrupted with multiplicative speckle noise due to coherent nature of SAR which significantly influences the performance efficiencies of the classification algorithms and enhances their error rates. To mitigate this drawback, many authors have proposed various frequency domain or wavelet domain or spatial domain based non-adaptive or adaptive despeckling filters. In this work, we have performed a comprehensive review of the filtering strategies of the one of most popular existing despeckling filter, Lee filter and its improved variants which were proposed over the years in chronological order and have also highlighted their respective strengths and limitations. We have concluded our work by performing comparative qualitative and quantitative analyses of the outputs obtained by applying these filters on different sets of SAR and Polarimetric SAR images and have listed down the unexplored challenges in this field which are yet to be solved.

Keywords Lee filter · Improved variants of lee filter · Survey · Despeckling

S. Banerjee (✉) · S. Sinha Chaudhuri
Jadavpur University, Kolkata 700032, India
e-mail: sriparnatinni@yahoo.in

S. Sinha Chaudhuri
e-mail: shelism@refiffmail.com

R. Mehra · A. Misra
Indian Space Research Organization, Ahmedabad 380015, India
e-mail: raghavmehra@sac.isro.gov.in

A. Misra
e-mail: arundhati@sac.isro.gov.in

S. Banerjee and J. K. Mandal (eds.), *Advances in Smart Communication Technology and Information Processing*, Lecture Notes in Networks and Systems 165,
https://doi.org/10.1007/978-981-15-9433-5_36

1 Introduction

SAR usually provides 2D or 3D or multidimensional images of objects like landscapes which enable one to extract qualitative and quantitative information required for performing urban classification [1, 2], crop classification [3, 4], oil spill detection [5, 6] and several other crucial remote sensing applications.

SAR images are gray scale images which provide information regarding the texture, moisture content, orientation, etc. of the target regions. In these images, pixels possessing different shades of gray represent areas having different textures and moisture contents. For e.g. Smooth surfaces (like calm water bodies, flooded soil, etc.) are mostly represented by dark pixels in SAR images whereas rough surfaces (like dry soil, trees, tropical rain forests, etc.) mostly appear as bright pixels in SAR images. Backscattering coefficients of the regions which are neither too rough nor too smooth are represented by intermediate shades of gray. The day and night and weather independent nature of SAR images have significantly increased their use in performing several classification tasks. Although SAR images provide information regarding texture, orientation and moisture content of target regions of images but they do not provide any color information.

As classification of images are mostly performed using either shallow neural networks or deep neural networks which are designed to artificially replicate the behavior of human cognitive system, color information plays a very crucial role in performing image classifications as it is most sensitive to human vision system compared to other types of information.

To solve these limitations of SAR images, Polarimetric SAR (POLSAR) images are nowadays widely used for performing image classifications. These images besides providing information regarding the orientation, moisture content and texture of the target regions also provide color information. SAR provides POLSAR images by exploiting its polarimetry property. These images comprise of pixels possessing different intensities and colors which represent different polarizations of radar waves reflected by varied objects.

Both SAR and POLSAR images are inherently corrupted with multiplicative speckle noise which appears as undesirable patterns on these images and significantly influences their pixels' intensities. Hence, performing classification using information extracted from such noise-corrupted images without any pre-processing often gives erroneous results.

To mitigate these drawbacks, many authors have proposed several despeckling filters to suppress speckle noise present in images. Out of those existing filters, Lee filter [7] is one of the most popular despeckling filters proposed till date. Various improved versions of Lee filter [8–14] have also been proposed over these years.

In this work, we have performed a comprehensive review of the methodologies of the Lee filter and its improved variants in chronological order to show how their filtering strategies have evolved over the years and highlighted their respective strengths and limitations. Here, we have also conducted comparative qualitative and quantitative analyses of the outputs obtained by despeckling SAR and POLSAR images obtained from different sources using these filters. Finally, we have concluded this survey by listing down the challenges in this field which are yet to be solved.

The rest of the work is organized as: Sect. 2. Speckle Noise, Sect. 3. Lee filter and its proposed variants, Sect. 4. Qualitative and quantitative results, Sect. 5. Existing challenges and Sect. 6. Conclusion.

2 Speckle Noise

Speckle noise arises in SAR and POLSAR images mainly due to the presence of many randomly distributed elemental scatters within resolution cells. The coherent sum of these scattered signals results in strong fluctuations of the backscattering within resolution cells. They add either constructively or destructively depending upon the relative phase of each scattered waveform leading to the occurrence of black and white dots on images which are referred to as the speckle noise.

Although speckle is commonly termed as ‘noise’ but unlike other noises which mostly arise due to the undesired modification of input signals, speckle is a signal itself which fluctuates mainly due to the strong variations of the scatters within resolution cells. It is highly sensitive to the variations of the scatters in resolution cells.

Mathematically, an image corrupted with multiplicative speckle noise is represented as follows:

$$I(i, j) = R(i, j)\eta(i, j) \tag{1}$$

where, $I(i, j)$ and $R(i, j)$ represent the intensities of noisy and noise-free images at pixel position (i, j) and $\eta(i, j)$ signifies the speckle noise present at that position.

3 Lee Filter and Its Proposed Variants

In this section, we have conducted a detailed survey on Lee filter and its improved variants in chronological order to enable the researchers understand how the filtering strategy of the traditional Lee filter [7] has evolved over the years.

An ideal despeckling filter should perform noise suppression in both the heterogeneous as well as the homogeneous regions of images accurately and preserve edges, isolated points, and manmade structures satisfactorily. While conducting this survey, we have observed that although some of the shortcomings of the traditional Lee filter have been solved over the years but pointed out that some challenges are still unexplored. That is why to introduce the researchers with those unexplored challenges, here we have highlighted the limitations of each proposed version of the Lee filter and listed down the existing challenges which should be explored in future.

3.1 Lee Filter [1980]

This filter is capable of suppressing both multiplicative as well as additive noises. It performs noise removal of each center pixel, $I(i, j)$ in accordance to the mean and variance values derived from its local statistics (characteristics of the neighboring pixels lying in the local window) centered at I(i, j). Unlike most of the filters which process pixels in sequential order, Lee filter supports parallel processing of pixels. It performs noise suppression using the fundamentals of minimum mean square estimator (MMSE) in its simplest form. Mathematically, the filtering operation of the Lee filter is explained as follows:

$$\widehat{R}(i, j) = \bar{I}(i, j) + W(i, j)(\bar{I}(i, j) - I(i, j)) \tag{2}$$

where,

$$W(i.j) = 1 - \frac{C_v}{C_I}$$

$\widehat{R}$=Estimated filtered image, $C_V = \frac{\sigma_v}{\bar{v}}$=Variance coefficient of noisy image with standard deviation,σ_V, $C_I = \frac{\sigma_I}{\bar{I}}$= Variance coefficient of noise-free image with standard deviation, σ_I.

The local mean value, $\bar{I}(i, j)$ needed for filtering the center pixel, I(i, j) located at pixel position (i, j) of a local window of size $(2m + 1) \times (2n + 1)$ is computed as follows:

$$\bar{I}(i, j) = \frac{1}{(2n + 1)(2m + 1)} \sum_{k=i-n}^{n+i} \sum_{l=j-m}^{m+j} I(k, l) \tag{3}$$

:

Strength

- This filter supports parallel processing of pixels which facilitates its direct implementation in various real-time applications.

Limitation:

- As this filter performs noise suppression in the homogeneous as well as the heterogeneous regions of images identically, it often leads to undesired blurring of edges, target points and man-made structures.

3.2 Lee Sigma Filter [1983]

Like Lee filter, this filter too performs noise removal from images using MMSE as stated in (2) but in a slightly different way. It derives the mean and variance values needed for filtering each center pixel considering the local mean and variance values of neighboring pixels which lie within its two-sigma neighborhood $[I(i, j) - 2\sigma_V, I(i, j) + 2\sigma_V]$ only instead of considering the mean and variance of all the neighboring pixels as proposed in [7] assuming the noise values in images are Gaussian distributed. They have proved that in the presence of Gaussian noise, 95.5% of the neighboring pixels which possess similar properties with that of the center pixel fall within the two-sigma range while other pixels belonging to different population fall outside the range. Mathematically, $\bar{I}\ (i, j)$ is calculated in [8] using the following equation:

$$\bar{I}\ (i, j) = \sum_{k=i-n}^{n+i} \sum_{l=j-m}^{m+j} I(k, l)\delta(k, l) / \sum_{k=i-n}^{n+i} \sum_{l=j-m}^{m+j} \delta(k, l) \tag{4}$$

where,

$$\delta(k, l) = 1, if \mathrm{I(i, j)} - 2\sigma_\mathrm{V} \leq \mathrm{I(k, l)} \leq \mathrm{I(i, j)} + 2\sigma_\mathrm{V} = 0, \text{otherwise}$$

Although the use of the two-sigma neighborhood concept has improved the edge-preservation capacity of this filter compared to the Lee filter but the use of this concept disables this filter to suppress sharp spot noise present in images effectively as this type of noise mostly corrupts a cluster of one or two adjoining pixels.

To mitigate this drawback, the authors in [8] have introduced an additional step in their proposed filtering algorithm to determine the total number of pixels (M) lying within the two-sigma neighborhood range.

$\bar{I}\ (i, j) =$ two-sigma average, if M > K.

$\bar{I}\ (i, j)=$ immediate neighbor average, if M ≤ K.

Although the introduction of this additional step has enabled this filter to suppress sharp spot noise to some extent but selecting an optimum value of the threshold (K) is a very challenging task as it plays a significant role in determining the filter's performance efficiency.

The authors have manually set the value of K lesser than 4 for a local window of 7×7 dimension and lesser than 3 for a local window of 5×5 dimension.

Strength:

- This filter is designed to preserve edges of images much more effectively compared to the traditional Lee filter [7] as it performs filtering of pixels, considering only the mean and variance values of the selected neighboring pixels which possess almost similar properties.

Limitations:

- This filter performs noise removal assuming that the noise values are always Gaussian-distributed but in reality it is not so as the speckle noise mostly possesses Rayleigh and negative probability density functions which lead to the introduction of a bias in the filtered data.
- This filter performs over-smoothing of target points.
- Manual selection of the threshold (K) often leads to undesired blurring of edges and erroneous noise suppression.
- Isolated dark pixels are not filtered effectively.

3.3 Enhanced Lee Filter [1990]

Ideally, the pixels belonging to the homogenous and heterogeneous regions of images should be filtered differently in order to achieve better noise suppression and edge-preservation as the properties of the pixels belonging to homogeneous and heterogeneous regions of images vastly differ from one another.

Neither the Lee filter [7] nor the Lee Sigma filter [8] were designed considering this logic which is the main cause behind the undesired blurring of edges occurring in the outputs obtained from these filters.

Enhanced Lee filter [9] is designed incorporating this logic which has enabled it to filter pixels belonging to the homogenous and heterogeneous regions differently.

Mathematically, the noise suppression technique of this filter is described as follows:

$$\widehat{R}(i,j) = \begin{cases} \overline{I}\ (i,j) if C_I \leq C_V (homogenousregion) \\ \overline{I}\ (i,j) + W(i,j)(\overline{I}\ (i,j) - I(i,j) if C_V < C_I < C_{max}(heterogenousregion) \\ I(i,j) if C_I \leq C_{max}(Isolatedpointsor Edges) \end{cases}. \quad (5)$$

Where,

$$W(i,j) = \exp\left(\frac{-K_{damp}(C_I - C_V)}{C_{max} - C_I}\right)$$

K_{damp} and C_{max} represent damping coefficient and the maximum value of the variance coefficient of noise-affected image respectively.

Strengths:

- This filter suppresses noise present in homogenous and heterogeneous regions of images efficiently and preserves image details present in heterogeneous regions of images much more effectively compared to the Lee filter and Lee Sigma filter.
- It also efficiently preserves isolated points present in images.

Limitation:

- This filter often cannot satisfactorily suppress spot noise present in images as it often erroneously classifies spot noise as target points.

3.4 Improved Lee Sigma Filter [2009]

The filter performs noisy removal similarly as proposed in the Lee Sigma filter [8] but using redefined sigma ranges. It addresses most of the shortcomings of the Lee Sigma filter and provides solutions for each of them as discussed below:

- Lee Sigma filter performs noise removal considering the noise values are always Gaussian-distributed and the mean is always equal to the value of the center pixel in a local window which results in the introduction of bias in the filtered data as the noise values in reality are mostly Rayleigh distributed. Moreover, the means of the noise probability density functions are not equal to the center pixels' values. Improved Lee Sigma filter solves this shortcoming by computing the refined sigma ranges $[I_1 \hat{\bar{x}} \ \ I_2 \hat{\bar{x}}]$where $\hat{\bar{x}}$is the unique mean which is computed independently for each local window using a simple integration based approach.I(i, j).
- The authors in [10] have also experimentally proved that filtering dark spot noise similarly as proposed in the Lee Sigma filter but using the computed mean, $\hat{\bar{x}}$instead of $\bar{\mathrm{I}}$ (i, j) have also enabled this filter to suppress the dark spot noise much more effectively compared to the Lee Sigma filter.
- In [10], the authors have also proposed a novel target preservation approach to preserve the target points present in SAR images based on their observation that the backscattered signals obtained from the target points are mostly dominated by a small number of strong scatters. Hence, the target points are usually represented by clusters of large number of bright pixels. The authors assumed that if in any local window there are more than T_k (threshold) number of pixels whose intensities are greater than 98th percentile (Z_{98}) of the intensities of all pixels belonging to that image, then those pixels are considered to be belonging to the target points and are preserved without any processing.

The pseudo-code of the filtering operation of the Improved Lee Sigma filter is given in Fig. 1.

In [10], the authors have empirically chosen the range of T_k to be [5, 7].

Step 1: Compute 98th percentile (Z_{98}) of the intensities of all the pixels belonging to an image.
Step 2: If the number of pixels possessing intensities higher than Z_{98} are greater than T_k within any local window of size 3×3, then preserve those pixels as target points and go to Step 5. Else go to Step 3.
Step 3. Compute MMSE for a 3×3 local window and compute its refined sigma range $[I_1 \hat{\bar{x}} \ \ I_2 \hat{\bar{x}}]$.
Step 4. Performing filtering of pixels similarly as proposed in the Lee Sigma Filter but using refined sigma ranges.
Step 5. Stop.

Fig. 1 Pseudo-code of the filtering operation performed by the Improved Lee Sigma Filter

Strengths:

- This filter preserves target points and suppresses dark spot noise present in images much more effectively compared to the Lee Sigma filter.
- This filter facilitates the evaluation of unique sigma range for each local window in accordance to the probability density function of the noise distribution within that window. This eliminates any chances of the introduction of bias in the filtered data.

Limitation:

- This filter cannot preserve target points comprising of pixels lesser than T_k efficiently.

3.5 Fast Non-local Lee Filter [2011] and Non-local Lee Filter [2013]

The authors in [11, 12] have proposed hybrid filters by combining the structure similarity property of the Non-Local Means filter [13] and the homogenous similarity property of the Lee filter.

Non-Local Means filter efficiently suppresses additive noise present in the structurally similar regions of images using a weighted averaging operator.

In traditional Non-Local Means filter [13], structural similarity among different image patches are detected by measuring the Euclidean distances among them. In [12], the authors have improved the structural similarity detection procedure by replacing the Euclidean distance metric by a new distance metric which can be approximated as a Chi square distribution with $n \times n$ degrees of freedom. The use of this new distance metric facilitates the formation of a collection, S_i of similar patches whose size is generally much larger compared to the size of patches.

In order to preserve target points and the homogeneous regions of images accurately, the authors in [11] have proposed a new filtering approach by substitution the weighted average filtering operation of the Non-Local Means filter [13] with the MMSE based filtering operation of the Lee filter. Mathematically, the filtering operation of the Fast Non-Local Lee filter is explained as follows:

$$\widehat{R_i} = \bar{S_i} + \frac{(D(S_i) - \bar{S}_i^2 \sigma_s^2)}{(1 + \sigma_s^2)} (I_i - \bar{S_i}) \tag{6}$$

where, $\bar{S}_i$ is the average of the set, S_i and $D(S_i)$ is the variance of the set, S_i.

The authors in [11] have also proposed a direction projection method for performing point target preservation.

The main difference between the filters proposed in [11, 12] is that unlike [11], the authors in [12] have used Lee filter in distributive manner to perform filtering of pixels.

Strengths:

- The use of new distance metric and direction projection method in [11, 12] has decreased their computational complexities by ten folds compared to the traditional Non-Local Means filter [13].
- The use of both the structural similarity property of the Non-Local Means filter and the homogeneity property of the Lee filter in the proposed Non-Local Lee filters has enabled them to perform speckle noise suppression and edge preservation efficiently.

Limitation:

- These filters do not comprise of any additional measure to filter the dark spot noise present in images.

3.6 Refined Lee Filter [2015]

This filter performs speckle noise removal similarly as stated in (2) but instead of considering the mean and variance values of all pixels located within a local window, the authors in [14] have performed filtering of pixels considering the mean and variance values of only the $'k'$ number of pixels located within a $K \times K$ neighborhood. They have used K-Nearest Neighborhood (KNN) algorithm for selecting these $'k'$ pixels. KNN performs classification based on the assumption that similar data points should be located in close proximity and it selects $'k'$ nearest neighbors of any sample data point using the Euclidean distance metric. In [14], also KNN selects $'k'$ nearest neighbors of each center pixel using the Euclidean distance metric assuming the properties of those pixels are similar to that of $I(i, j)$.

Strength:

- The authors have experimentally proved that this filter can perform noise suppression and edge-preservation much more efficiency compared to the Lee filter when filtering is performed considering the mean and variance values of 6 nearest neighbors out of 9 neighbors located within a 3×3 neighborhood.

Limitations:

- KNN algorithm being a supervised classification algorithm requires a proper set of labeled data for training and validating the neural network designed for performing the selection of $'k'$ number of nearest neighbors. Preparing such a set of labeled data in this case is very challenging.

Table 1 Qualitative analysis of SAR images

No	SAR image	Lee filter [7]	Lee Sigma filter [8]	Enhanced Lee filter [9]	Refined Lee filter [14]
1 2 3 4				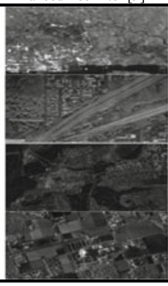	

- Optimum selection of the local window size and the value of $'k'$ depending upon the distribution of noise in images in order to achieve desired performance of the filter are also very challenging.

4 Qualitative and Quantitative Results

In this section, we have performed comparative analyses of the qualitative and quantitative results obtained by applying the filters proposed in [7–9, 14] on SAR and POLSAR images given in Tables 1, 2, 3 and 4. SAR images are acquired from freely available sources in the internet whereas POLSAR images, Image 1 is acquired from ISRO SAC and other POLSAR images (Image 2–Image 4) in Table 4.

For performing quantitative analyses, here we have chosen two quantitative parameters namely Edge preservation Index (EPI) [15] and Equivalent Number of Looks (ENL) [14]. These parameters measure edge-preservation and noise suppression capabilities of the filters respectively. Higher values of both these parameters suggest better results.

5 Existing Challenges

- While performing this survey, we have noticed that the size of the local window plays a very significant role in determining the filter's performance efficiency. Hence, proper selection of the size of the local window in accordance to the image's characteristics is very essential in order to achieve desired results. But neither Lee filter nor its' proposed variants were designed focusing on this aspect.
- The filters proposed in [7–12, 14] have used many thresholds for e.g. K [8], T_k [10], k [14], etc. at different stages of their proposed filtering algorithms to achieve better results. They have mostly set the values of these thresholds empirically, but

Table 2 Quantitative analysis of SAR images given in Table 1

Filter	Image 1		Image 2		Image 3		Image 4	
	EPI	ENL	EPI	ENL	EPI	ENL	EPI	ENL
Lee filter [7]	**0.4417**	3.4182	**0.4085**	4.3512	**0.460**	1.7504	**0.4704**	2.1293
Lee sigma filter [8]	0.3662	3.8890	0.3575	4.6846	0.3576	1.8829	0.4237	2.4125
Enhanced lee filter [9]	0.3404	**4.5163**	0.2811	**5.1980**	0.3374	1.2678	0.3410	**2.4458**
Refined lee filter [14]	0.3929	4.1371	0.3705	5.1449	0.3572	**2.3450**	0.4693	2.0618

**Note* Best quantitative results obtained for each image are highlighted in Tables 2 and 4

Table 3 Qualitative analysis of POLSAR images

No	POLSAR image	Lee filter [7]	Lee Sigma filter [8]	Enhanced Lee filter [9]	Refined Lee filter [14]
1 2 3 4		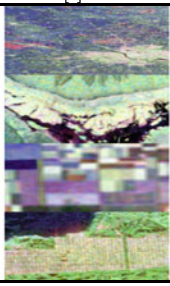	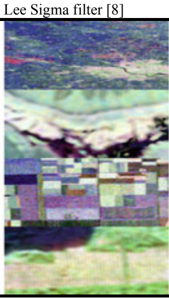	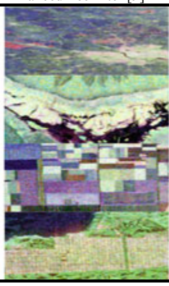	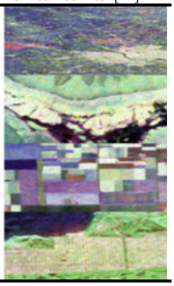

Table 4 Quantitative analysis of POLSAR images given in Table 3

Filter	Image 1		Image 2		Image 3		Image 4	
	EPI	ENL	EPI	ENL	EPI	ENL	EPI	ENL
Lee filter [7]	0.3564	14.610	0.3248	6.2575	0.3486	7.801	0.3576	6.5106
Lee sigma filter [8]	**0.3606**	6.654	**0.3396**	**7.5591**	**0.4096**	**10.098**	**0.3964**	**6.9642**
Enhanced lee filter [9]	0.3359	**17.817**	0.3359	5.8413	0.3524	7.1521	0.3846	6.1310
Refined lee filter [14]	0.3569	12.510	0.3216	6.5063	0.3421	6.8033	0.3442	6.8883

none of them proposed any technique which facilitates the automatic selection of these thresholds in accordance to the image characteristics.

6 Conclusion

In this paper, we have shown how the filtering strategy of the Lee filter has been evolved over the years. The qualitative and quantitative results obtained by applying the Lee filter and its proposed variants on both SAR and POLSAR images also depict that none of the filter gives good results consistently. Hence, there are several challenges in this field which are yet to be solved in order to acquire desired results. We have concluded our work by listing those challenges to encourage the researchers to propose optimum solutions to these challenges in future.

Acknowledgements This work is a part of the Research project titled, “Neuro-Fuzzy Synergism based POLSAR Image Classification” funded by ISRO Respond Program (No. ISRO/RES/4/673/19-20).

References

1. De, S., Bruzzone, L., Bhattacharya, A., Bovolo, F., Chaudhuri, S.: A novel technique based on deep learning and a synthetic target database for classification of urban areas in PolSAR data. IEEE J. Sel. Top. Appl. Earth Obs. Remote. Sens. **11**(1), 154–170 (2017)
2. Chen, S-W., Chen-Song, T.: PolSAR image classification using polarimetric-feature-driven deep convolutional neural network. IEEE Geosci. Remote. Sens. Lett. 15(4), 627–631 (2018)
3. Guo, J., Wei, P.L., Liu, J., Jin, B., Su, B.F., Zhou, Z.S.: Crop classification based on differential characteristics of H/α scattering parameters for multitemporal quad- and dual-polarization SAR images. IEEE Trans. Geosci. Remote Sens. **56**(10), 6111–6123 (2018)
4. Mei, X., Nie, W., Liu, J., Huang, K.: PolSAR image crop classification based on deep residual learning network. In: 7th International Conference on Agro-geoinformatics, pp. 1–6. IEEE, China (2018)
5. Xiong, Y., Zhou, H.: Oil spills identification in SAR image based on convolutional neural network. In: 14th International Conference on Computer Science & Education, pp. 667–670. IEEE, Canada (2019)
6. Solberg, A.H.S., Brekke, C., Husoy, P.V.: Oil Spill Detection in Radarsat and Envisat SAR Images. IEEE Transactions on Geoscience and Remote Sensing 45 (3), 746 – 755 (2007).
7. Lee, J.S.: Digital image enhancement and noise filtering by use of local statistics. IEEE Transactions on Pattern Analysis and Machine Intelligence, PAMI-2 (2), 165–168 (1980)
8. Lee, J.S.: Digital image smoothing and the sigma filter. Comput. Vis., Graph., Image Process. 24, 255–269 (1983)
9. Lopes, A., Touzi, R., Nezry, E.: Adaptive speckle filters and scene heterogeneity. IEEE Trans. Geosci. Remote. Sens. **28**(6), 992–1000 (1990)
10. Lee, J.S., Wen, J.H., Ainsworth, T.L., Chen, K.S., Chen, A.J.: Improved sigma filter for speckle filtering of SAR imagery. IEEE Trans. Geosci. Remote. Sens. **47**(1), 202–213 (2009)
11. Zhong, H., Lu, L., Jiao, L.: Fast non-local lee filter for SAR image despeckling using directional projection. In: Proceedings of CIE International Conference on Radar, pp. 1600–1603. IEEE, China (2011)
12. Zhong, H., Lu, L., Zhang, J., Wang, Hou, X.: Nonlocal-lee filter for SAR image despeckling based on hybrid patch similarity. In: International Geoscience and Remote Sensing Symposium, pp. 1987–1990. IEEE, Australia (2013)
13. Buades, A., Col, B., Morel, J.: A non-local algorithm for image denoising. In: Computer Society Conference on Computer Vision and Pattern Recognition, pp. 60–65. IEEE, USA (2005)
14. Yommy, A.S., Liu, R., Wu, S.: SAR Image despeckling using refined lee filter. In: 7th International Conference on Intelligent Human-Machine Systems and Cybernetics, pp. 260–265. IEEE, China (2015)
15. Sudhakar, R.: Edge preservation index. MATLAB Central File Exchange, 22 March 2020. https://www.mathworks.com/matlabcentral/fileexchange/65261-edge-preservation-index-new-file
16. https://earth.esa.int/web/polsarpro/data-sources/sample-datasets

Design and Optimization of Single Junction GaSb Solar Cell for Maximum Utilization of IR Solar Spectrum

Bubai Maji and Rik Chattopadhyay

Abstract We report the design and optimization of a n-GaSb/p-GaSb single-junction solar cell using the computer device simulator software (SILVACO ATLAS). The main objective of this paper is to optimize a single junction solar cell for maximum efficiency because of its low fabrication cost. We optimized the cell parameters such as thickness and doping concentration and to define the optimum values which allow us to reach the maximum conversion efficiency. We report a maximum conversion electrical efficiency up to 29.45% of the optimized cell under the 1.5G solar spectrum with Si substrate. The novelty of the designed cell is that it absorbed wide infrared spectrum which gives more number of carries to obtain better electrical efficiency.

Keywords Optimum solar cell structure · Thickness · Doping concentration · Efficiency

1 Introduction

Solar cell emerged as an alternative solution of green energy production reducing the environmental pollution created in conventional energy harvesting. The use of solar cells is still not widespread because of their low efficiency. Basically sunlight is an electromagnetic radiation which is divided in three spectrum i.e. ultraviolet, visible and infrared spectrum. In available commercial solar cells only the visible and half of the infrared spectrum is used [1]. The main advantage of using low bandgap material is to increase absorption of infrared spectrum. This means solar cell will absorb more number of photons from the infrared region of solar spectrum. First,

B. Maji · R. Chattopadhyay (✉)
Dept. of Electronics and Telecommunication Engineering, Indian Institute of Engineering Science and Technology, Shibpur, Howrah 711103, India
e-mail: rchattopadhyay@telecom.iiests.ac.in

B. Maji
e-mail: bubaimaji51@gmail.com

S. Banerjee and J. K. Mandal (eds.), *Advances in Smart Communication Technology and Information Processing*, Lecture Notes in Networks and Systems 165,
https://doi.org/10.1007/978-981-15-9433-5_37

GaAs-GaSb tandem solar cell were fabricated in 1989 [2]. Single-junction solar cell is relatively low cost and easily design as compare to multi-junction cell. In multi-junction solar cell defects may occur due to lattice mismatch of different materials deposited as different layers. Therefore one must choose different materials based on their lattice parameters. This increases the fabrication cost and also reduces the choice of materials in multi-junction solar cell [3]. In this work we try to improve the structure of a narrow bandgap Gallium Antimonide (GaSb) single junction solar cell which is mechanically stacked between InGap/GaSb-GaSb/Si for higher efficiency. Bandgap of GaSb is relatively smaller than silicon and other popular semiconductors used in solar cell. Due to smaller direct bandgap (0.72 eV), absorption coefficient of GaSb is very low. So active layer of the GaSb cell required to be relatively thicker [3]. Due to the narrow bandgap (0.72 eV) GaSb solar cell can absorb most of the solar spectrum (up to 1700 nm). Higher bandgap Indium Gallium Phosphide is ($In_{0.49}Ga_{0.51}P$) deposited as a window layer on the top of cell and Silicon as a substrate at the back of the cell. Finally, we optimized the cell thickness and doping concentration and found the maximum electrical efficiency around 29.45% with short circuit current (J_{sc}) of 38.99 mA/cm^2 and open circuit voltage (V_{oc}) of 0.867, fill factor of 87.08%. The maximum solar conversion efficiency is around 33.7% for a single junction photovoltaic cell. Current commercial single junction solar technology have maximum efficiency of about 25% [4].

2 Theoretical Background

A solar cell is a P-N junction diode under the light illumination with a very large surface area. When solar radiation is absorbed in a P-N junction diode electron-hole pair generates a photo current. In a P-N junction diode basically two types of current components are present, one is photon induced current and another is dark current. Figure 1 shows the effect of light on the I–V curve of the diode. The I–V curve shifts downward in the current voltage axis when light is incident on the cell.

From the Fig. 1 we can also calculate the value of fill factor that indicates the cell performance. Better values of fill factor gives more conversion efficiency.

The efficiency of the solar cell can be written as [3, 5],

$$\eta = \left(\frac{P_m}{P_{\text{In}}}\right) = \left[\frac{Voc * Isc}{P_{\text{In}}}\right] \times 100\% = \left[\frac{V_m * I_m}{P_{\text{In}}}\right] \times 100\% \quad (1)$$

Here, P_{in} = input optical power or solar radiation power.
P_m = maximum power.
And, V_m = maximum voltage at maximum power.
I_m = maximum current at maximum power.
V_{oc} = open circuit voltage.
I_{sc} = short circuit current.

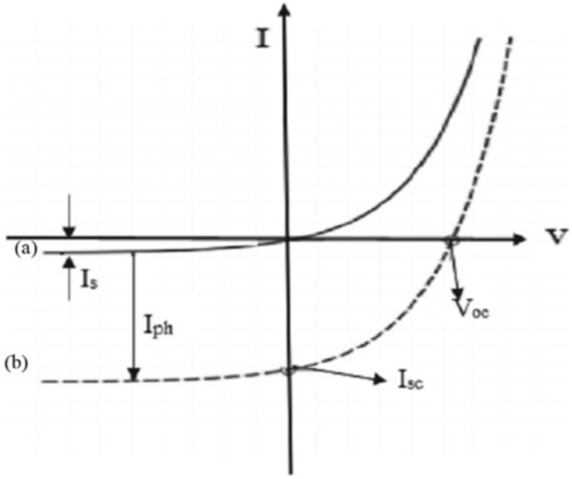

Fig. 1 Downward shifting of dark I–V curve **a** when light shines on a P-N junction **b** illuminated I–V curve

Equation (1) shows that higher current density (J_{sc}) gives high electrical efficiency of the cell. So, here we have used lower bandgap GaSb (0.72 eV) material so that it can absorb maximum range of IR spectrum which gives more number of carrier in depletion region of P-N junction. In this way short circuit current is increased in solar cell.

3 Results and Discussion

Figure 2 shows the simulated optimized structure of InGaP/GaSb-GaSb/Si. Indium gallium Phosphide (InGaP) is used at the top of the solar cell. It acts as a window layer of the solar cell to minimize the reflection of solar radiation. Lesser reflection from top surface ensures more photons to be entered in the active region and thus enhances the performance of the solar cell [6]. Si layer is used as substrate layer. It shows better perform than GaSb substrate, because some electrons of substrate layer are back reflected to the active layers due to higher potential difference between Si and GaSb.

3.1 Effect of Layer Thickness on Cell Performance

The window layer plays a very important role in the solar cell performance. Figure 3 shows the variation of cell performance with the thickness of different layers in the designed solar cell.

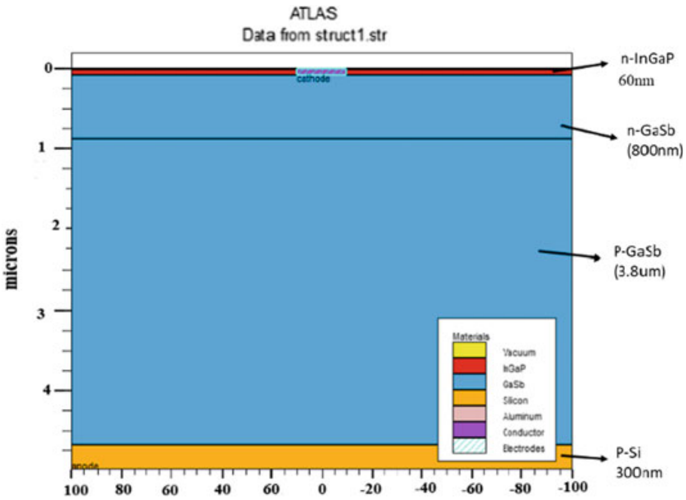

Fig. 2 Simulated structure of InGaP/GaSb-GaSb/Si

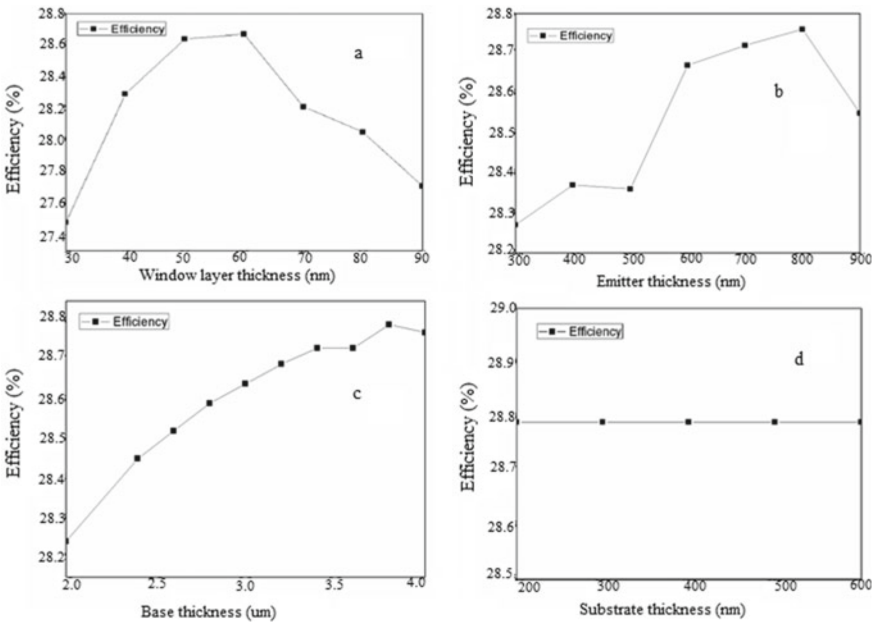

Fig. 3 Effect of thickness on cell efficiency: **a** window layer (InGaP) **b** GaSb-emitter layer **c** GaSb-base layer **d** Si- substrate layer

At first, $In_{0.49}$ $Ga_{0.51}$ P window layer thickness is varied from 30 nm to 90 nm (Fig. 3a). The maximum electrical efficiency is found for a window thickness of 60 nm. The photons having higher energy than material bandgap can get absorbed by window layer. Thus photons with lower energy cannot create electron-hole pairs and will decrease the cell performance. So decrease in the thickness value of window layer increases the cell efficiency up to 28.67% Fig. 3a for 60 nm thickness of window layer.

The GaSb layer is a part of the active layer of the solar cell. The thickness of GaSb emitter layer is varied from 300 nm to 900 nm and consequently cell performance also varies which is shown in Fig. 3b. The cell performance increases with increase in the thickness up to 0.8 μm and starts decreasing afterwords. Saturation current density is a function of emitter thickness [7]. The increase in emitter thickness leads to increment in current density as well as efficiency. Increment of emitter thickness beyond 0.8μm reduces electrical efficiency of this cell due to increase in series resistance. Optimum efficiency is obtained up to 28.72% (Fig. 3b).

The GaSb base layer play the role of an absorber layer in this solar cell. As the thickness value of base layer increases the cell efficiency also increases for the optimum value of 3.8 μm (Fig. 3c). When the thickness of GaSb base layer decreases some of the generated carriers recombine near the back contact through the substrate layer. As the layer thickness increases above the optimum value the carries also recombine because of large depth length. Maximum electrical conversion is found as 28.77% for the 3.8 μm thickness value (Fig. 3c).

After that, the thickness of substrate layer had been varied from 200 nm to 600 nm. We note that cell performance remains relatively constant around 28.79% with variation of substrate thickness as shown in Fig. 3d.

3.2 Effect of Layer Doping Concentration on Cell Performance

In this solar cell module, n-$In_{0.49}Ga_{51}P$ work as a transparent conductive oxide (TCO) layer. The donar doping concentration of this layer must be high to increase concentration of carriers due to reduced reflection of solar radiation. Doping concentration value is varied from $8 \times 10^{16}/cm^3$ to $8 \times 10^{21}/cm^3$ and other parameters are kept constant.

As the $In_{0.49}Ga_{51}P$ layer doping concentration increases the electrical conversion efficiency also increases up to $8 \times 10^{20}/cm^3$ and beyond this concentration efficiency again decreases as shown in Fig. 4a. As doping concentration increases the conductivity increases and as well as the mobility of charge carriers increases. Higher conductivity reduces the resistivity. So, higher concentration increases all electrical parameters. So higher doping concentration gives us better efficiency and it reaches of 28.79% with optimum value of doping concentration of 8×10^{20}/cm3 as shown in Fig. 4a.

After that, we varied the donor impurity of emitter layer from $2 \times 10^{18}/cm^3$ to $2 \times 10^{21}/cm^3$. Figure 4b shows that efficiency increases up to $2 \times 10^{19}/cm^3$, after that it reduces the cell performance, because increment in the GaSb emitter layer doping concentration reduces the potential barrier in the active layer, which allows

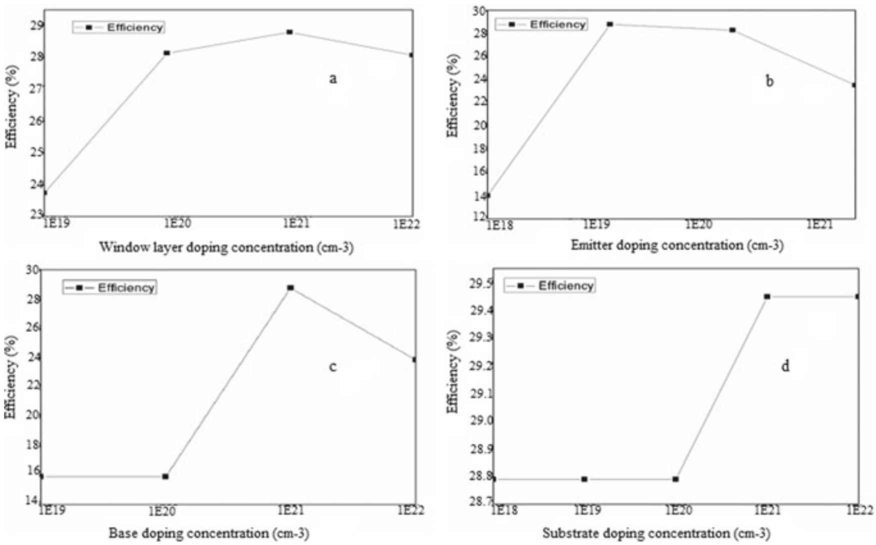

Fig. 4 Effect of doping concentration on performance: **a** InGaP window layer **b** GaSb-emitter layer **c** GaSb-base layer **d** Si-substrate layer

an enlargement of the space-charge region, which in turn reduces the short circuit current.

Improving n-GaSb layer doping actually reduce the sheet resistance and enhance conductivity or fill factor. So, Increase in the GaSb layer doping improves the collection of photo generated carriers and consequently increases the conversion efficiency. The maximum efficiency is obtained up to 28.82% for the optimum doping concentration of $2 \times 10^{19}/cm^3$ as shown in the Fig. 4b.

The significant variation in the cell efficiency is observed by varying the acceptor doping concentration of GaSb base layer. The doping concentration varied from $1 \times 10^{19}/cm^3$ to $1 \times 10^{22}/cm^3$ and other parameters are kept constant. Figure 4c shows that as the acceptor doping concentration of GaSb base layer increases the short circuit current increment becomes less because of electron losses due majority of holes. The increment of doping concentration of absorption layer also reduces the dark current or reverse saturation current [6]. Further increment is not possible as it leads to saturation in V_{oc}. Finally, 28.87% maximum efficiency is obtained for the concentration of $1 \times 10^{21}/cm^3$ (Fig. 4c).

Finally, we varied the doping concentration of silicon substrate layer from $1 \times 10^{18}/cm^3$ to $1 \times 10^{22}/cm^3$. Figure 4d shows how cell performance improves with changing doping concentration of silicon substrate layer. Basically use of higher potential or higher concentration substrate makes electron get back to the active layer and in this way surface recombination reduced and the short circuit current as well to the efficiency increases. We find optimum doping concentration of $1 \times 10^{21}/cm^3$ for maximum electrical conversion efficiency of 29.45%.

3.3 Characteristics Curve

Figure 5 shows is the I–V characteristics of this optimized solar cell with donar doping concentration of $2 \times 10^{19}/cm^3$ and acceptor doping concentration of $10^{21}/cm^3$. I–V curve is the most important curve in solar cell. From this curve we find the value of fill factor and we observed the performance of solar cell.

From the I–V curve (Fig. 5) the value of open circuit voltage comes out as 0.867 V which is defined by x-axis and it is the maximum output voltage of this solar cell. The y-axis shows the short circuit current is 38.99 mA/cm^2, which is the maximum output current from the solar cell.

Table 1 shows that in the GaSb solar cell with silicon substrate gives 4.13% better performance than GaSb substrate.

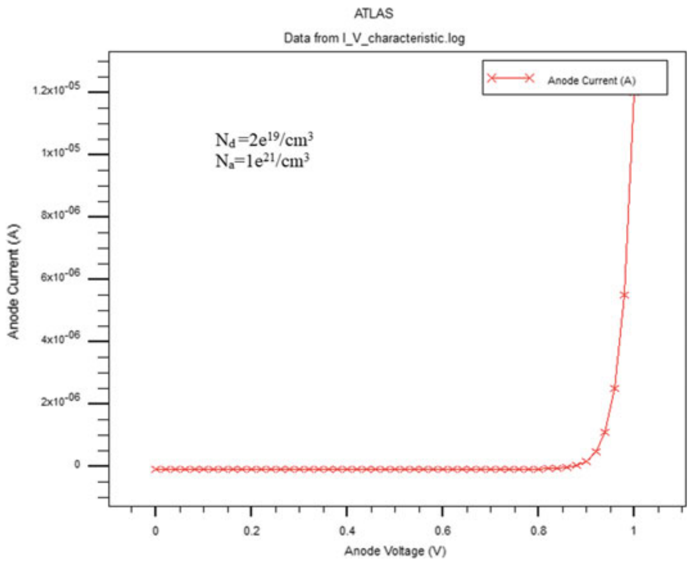

Fig. 5 I–V curve of simulated solar cell

Table 1 Simulated result of different substrate materials

Optimized solar cell	n-InGaP/n-GaSb/p-GaSb/p-GaSb	n-InGaP/n-GaSb/p-GaSb/p-Si
V_{oc} (V)	0.85	0.867
J_{sc}(mA/cm^2)	38.80 mA/cm^2	38.99 mA/cm^2
FF (%)	85.45	87.08
Efficiency (%)	28.18	29.45

4 Conclusion

The main focus of this work is to introduce an extensive performance analysis due to thickness and doping concentration of GaSb single junction solar cell. Simulation of GaSb solar cell structure was performed using computer device simulator software. The performance of GaSb solar cell is troubled by the back surface recombination, but it possible to minimize by adding a Si layer as a substrate layer. The conversion efficiency reached up to 29.45%. The addition of Si layer enhances the carrier collection which contributes in improving the performance due to higher quantum efficiency. Therefore, the doping concentration, thickness of different layers and recombination rate were upgraded and highest cell efficiency was obtained with the optimized value of thickness and doping concentration.

Acknowledgements The authors would like to acknowledge Prof. P. Chakraborty, Director, IIEST and Dept. of E&TCE, IIEST.

References

1. Gianneta, V., et.al.: High-performance crystalline Si solar cell on n-type Si with a thin emitte by Al-induced crystallization and doping. IEEE J. photovolt. **6**, 1109–1114 (2016)
2. Fraas, L.M., Girard, G.R., Avery, J.E., Arau, B.A., Sundaram, V.S., Thomson, A.G., Gee, J.M.: J. Appl. Phys. **66**(8), 3866 (1989)
3. Andreev, V.M., Sorokina, S.V., Timoshina, N.K., V.P. Khvostikov, M.S. Shvarts, 2009. Vol.43. No.5. pp. 695–699
4. Ruhle, S.: Tabulated values of the shockley-queisser limit for single junction solar cells. Sol. Energy **130**, 139–147 (2016). https://doi.org/10.1010/j.solener.2016.02.015
5. Green, M.A.: Solar Cell: Operating Principles, Technology And System Applications. Prent ice Hall Inc., EnglewoodCliffs, N.J., USA (1982)
6. Choudhury, F., Nayfeh, A.: **23**(1), 1885–1889 (2016)
7. King, R.R., Law, D.C., Edmondson, K.M., Fetzer, C.M., Yoon, H., Karam N.H.: Appl. Phys. Lett. **90**, 183516 (2007)

A Comprehensive Review of Median Filter, Hybrid Median Filter and Their Proposed Variants

Sriparna Banerjee, Sheli Sinha Chaudhuri, Raghav Mehra, and Arundhati Misra

Abstract During the last few decades, the high resolution, day and night and weather independent images provided by the Synthetic Aperture Radar (SAR) have been widely used for various important remote sensing applications like land cover classification, oil spill detection, etc. The coherent nature of SAR inherently corrupts the images provided by it with multiplicative speckle noise which significantly influences the performance efficiencies of the classification and detection algorithms and thereby enhances their error rates. To overcome these limitations, many authors have proposed various frequency domain or wavelet domain or spatial domain based non-adaptive or adaptive despeckling filters. In this work, we have performed a comprehensive review of the filtering strategies of some of the most popular despeckling filters like Median filter, Hybrid Median Filter and their proposed variants in chronological order to show how their filtering strategies have evolved over the years. Here we have also highlighted the strengths and limitations of each filter and performed comparative qualitative and quantitative analyses of the outputs obtained by applying these filters on different sets of SAR and Polarimetric SAR (POLSAR) images. Finally, we have concluded our work by listing down the unexplored challenges in this field which went unnoticed while deigning these filters.

Keywords Median filter · Hybrid median filter · Proposed variants · Survey

---

S. Banerjee (✉) · S. Sinha Chaudhuri
Jadavpur University, Kolkata 700032, India
e-mail: sriparnatinni@yahoo.in

S. Sinha Chaudhuri
e-mail: shelism@refiffmail.com

R. Mehra · A. Misra
Indian Space Research Organization, Ahmedabad 380015, India
e-mail: raghavmehra@sac.isro.gov.in

A. Misra
e-mail: arundhati@sac.isro.gov.in

S. Banerjee and J. K. Mandal (eds.), *Advances in Smart Communication Technology and Information Processing*, Lecture Notes in Networks and Systems 165,
https://doi.org/10.1007/978-981-15-9433-5_38

1 Introduction

SAR provides 2D or multidimensional images of target areas like landscapes which enable one to extract suitable qualitative and quantitative information required for performing urban classification [1, 2], crop classification [3, 4], etc.

SAR images are usually displayed as gray scale images where target areas possessing different texture and moisture contents are marked with different shades of gray. For e.g. Target areas possessing smooth surfaces (like calm water bodies, flooded soil, etc.) are mostly represented by dark pixels in SAR images whereas target areas possessing rough surfaces (like dry soil, trees, tropical rain forests, etc.) are mostly represented by bright pixels. Backscattering coefficients of areas which are neither too rough nor too smooth are represented by intermediate shades of gray [5]. The day and night and weather independent nature of images provided by SAR have significantly increased their popularity in performing several classification tasks.

SAR images undoubtedly provide crucial information regarding texture, moisture content, etc. of target regions but they do not give any color information.

Classifications of objects or images are usually performed using either shallow or deep neural networks which are designed to artificially replicate the behavior of human cognitive system. Hence, color information usually plays a very significant role in performing several classification tasks as it is most sensitive to human vision system compared to the other types of information.

To mitigate these drawbacks, SAR produces POLSAR images by exploring its polarimetry property. These images besides providing information regarding the orientation, moisture content and texture of the target regions also provide color information which has increased its use in performing several classification tasks. These images usually comprises of pixels possessing different intensities to represent different polarizations of radar waves reflected by varied objects.

SAR and POLSAR images are inherently corrupted with multiplicative speckle noise due to the coherent nature of SAR which significantly influences the information extracted from these images and thus leads to erroneous classifications.

To solve these shortcomings, proper despeckling of these images is necessary prior to extracting features from them to perform classification. For this purpose, several authors have proposed many despeckling filters to suppress speckle noise present in images effectively. Among these filters, Median filter, Hybrid Median Filter and their proposed variants are quite popular despeckling filters proposed till date.

Here, we have performed a comprehensive review of the filtering strategies of the Median filter, Hybrid Median Filter and their proposed variants in chronological order and highlighted their respective strengths and limitations. In this survey, we have also included comparative qualitative and quantitative analyses of the outputs obtained by despeckling SAR and POLSAR images using these filters. We have finally concluded this survey by listing down the unexplored challenges which were not considered while designing these filtering strategies.

The remaining work is organized as: Sect. 2. Speckle Noise, Sect. 3. Median Filter and its proposed variants, Sect. 4. Hybrid Median Filter and its proposed variants, Sect. 5. Comparative qualitative and quantitative results, Sect. 6. Unexplored challenges and Sect. 7. Conclusion.

2 Speckle Noise

The strong fluctuations between the randomly distributed scatters within each resolution cell of an image are the main reason behind the presence of multiplicative speckle noise in SAR and POLSAR images [6]. These scatters add either constructively or destructively depending upon their relative phases leading to the occurrence of black and white dots on images which are commonly referred to as the speckle noise.

An image corrupted with multiplicative speckle noise is mathematically represented as:

$$I(i, j) = R(i, j)\eta(i, j) \tag{1}$$

where, $I(i, j)$, $R(i, j)$ and $\eta(i, j)$ represent the intensity of noisy image, intensity of noise-free image and speckle noise present at pixel location, (i, j) respectively.

3 Median Filter and Its Proposed Variants

3.1 Median Filter [1970]

This filter is designed by the authors in [7] to primarily suppress the salt and pepper noise present in images. It performs filtering of the center pixel of any local window of size $(2n + 1) \times (2n + 1)$ with the median value of the intensities of all the pixels lying within that window.

Strength

- Being a non-linear filter, this filter performs edge-preservation much more efficiently compared to the linear filters like mean (average) filter.

Limitation

- This filter does not include any additional measures either to preserve target points or to suppress sharp spot noise present in images effectively.

3.2 *Local Adaptive Median Filter [2004]*

This filter [8] is designed following the noise suppression strategies proposed in the Lee Sigma Filter [9] and the Local Sigma Filter [10].

Lee Sigma Filter is a well-known variant of one of the most popular despeckling filter, Lee Filter [11]. It performs filtering of the multiplicative speckle noise present in SAR and POLSAR images using the minimum mean square estimation (MMSE) method assuming the noise values are always Gaussian distributed. It filters the center pixel, $I(i, j)$ within any local window as stated below:

$$\widehat{R}(i, j) = \bar{I}(i, j) + W(i, j)(\bar{I}(i, j) - I(i, j)) \quad (2)$$

where,

$$W(i.j) = 1 - \frac{C_v}{C_I}$$

$\widehat{R}$ = Estimated filtered image, $C_V = \frac{\sigma_v}{\bar{v}}$ = Variance coefficient of noisy image with standard deviation, σ_V, $C_I = \frac{\sigma_I}{\bar{I}}$ = Variance coefficient of noise-free image with standard deviation, σ_I.

The local mean value, $\bar{I}(i, j)$ needed for filtering the center pixel, $I(i, j)$ of any local window of size $(2n + 1) \times (2n + 1)$ is computed as follows:

$$\bar{I}(i, j) = \sum_{k=i-n}^{n+i} \sum_{l=j-n}^{n+j} I(k, l)\delta(k, l) / \sum_{k=i-n}^{n+i} \sum_{l=j-n}^{n+j} \delta(k, l)$$

where,

$$\begin{aligned} \delta(k, l) &= 1, if\ I(i, j) - 2\sigma_V \le I(k, l) \le I(i, j) + 2\sigma_V \\ &= 0, \text{otherwise} \end{aligned}$$

It filters the center pixel of any local window considering the local mean and standard deviation values of the pixels which lie within the sigma range, $[I(i, j) - 2\sigma_V, I(i, j) + 2\sigma_V]$ only, assuming that the pixels lying within this range possess almost similar properties while the pixels lying outside this range are dissimilar.

Local Sigma Filter [10] performs noise suppression similarly as proposed in [9] but instead of using a fixed sigma range, they performed similar operation using flexible sigma range by introducing a user-defined variable, M whose value is either 1 or 2. The introduction of this user-defined variable facilitates the variation of the sigma range adaptively for each local window depending upon its' noise distribution. The flexible sigma range is defined as $[I(i, j) - M\sigma_V, I(i, j) + M\sigma_V]$.

Local Adaptive Median Filter performs noise suppression similarly as proposed in [10] but unlike [9, 10], where the authors have filtered all the pixels, this filter performs noise suppression of the center pixel of any local window only when it is classified as a noisy pixel. For this purpose, prior to filtering pixels, they classified them into two classes namely, a. valid pixel and b. noisy pixel, using the following logic:

a. If the center pixel of any local window lies within the computed sigma range, then it is classified as a valid pixel and is preserved without despeckling.
b. If the center pixel of any local window lies outside the computed sigma range, then it is classified as a noisy pixel and is substituted by the median value of the pixels which lie within the sigma range, $[I(i, j) - M\sigma_V, I(i, j) + M\sigma_V]$.

Strength

- The use of adaptive sigma range and the selective pixel filtering strategy has enabled this filter to perform noise suppression much more efficiently compared to the traditional Median filter [7].

Limitation

- The performance efficiency of this filter is largely dependent on the optimum selection of M which is very challenging.
- This filter like Lee Sigma Filter often introduces bias in the filtered data as it performs despeckling of SAR and POLSAR images considering the noise values in these images are Gaussian distributed but in reality it is not so as it is stated in [12], that noise present in SAR and POLSAR images mostly follows Rayleigh distribution.

3.3 3D Median Filter with PSA [2006] and 3D Median Filter with RPSA [2007]

In [13, 14], the authors have introduced 3-D Median filter which suppresses speckle noise present in images having $N \times N \times N$ dimension using their proposed partial sort algorithm (PSA) and reverse partial sort algorithm (RPSA) respectively. The use of PSA and RPSA to sort the pixel intensities present in any local window in order to compute its median value has reduced the computational complexities of these filters largely compared to the computational complexity of a similar filter which performs sorting of pixel using the bubble sort algorithm. PSA and RPSA sort elements in a 2D array as stated in Fig. 1 and Fig. 2 respectively.

In the above figures, x_m represents the median value of the pixels lying in the local window of size 3×3 whereas min and max signify the minimum and maximum intensities of the pixels located within that window.

In [13, 14], the authors have performed despeckling of images using 3D sliding window which moves first along the x direction then along the y direction followed by the z direction as shown in the Fig. 3.

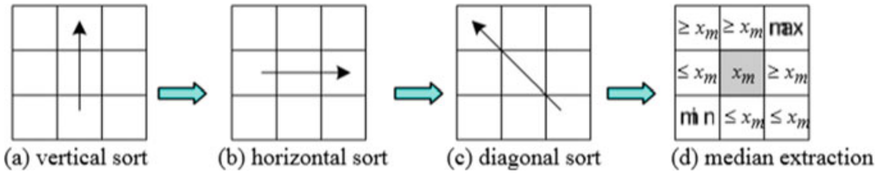

Fig. 1 Sequence following which sorting is performed by PSA algorithm [14]

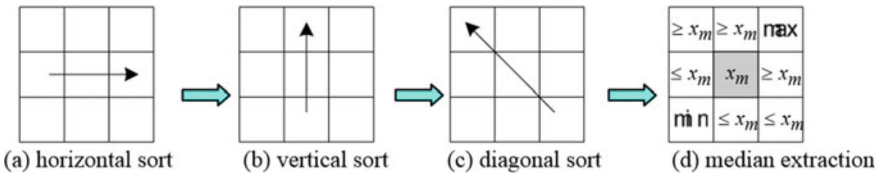

Fig. 2 Sequence following which sorting is performed by RPSA algorithm [14]

Fig. 3 3D sliding window [14]

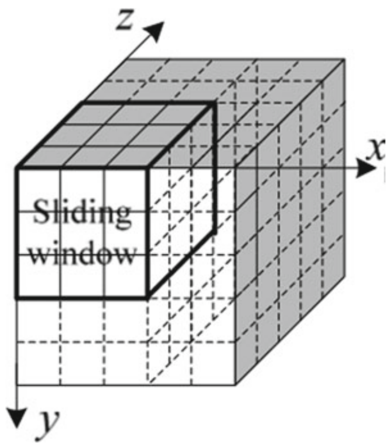

When the sliding window moves by one position N^2 samples of the old plane gets substituted by N^2 samples of new plane. The median value of a $3 \times 3 \times 3$ window is computed in [13, 14] as depicted in the Fig. 4.

Where (a, b, c) represent three 3×3 planes of an image and (h, l, m) represent median values of these planes where $h_m \geq m_m \geq l_m$.

Strength

- The use of PSA and RPSA for sorting elements has largely reduced the computational complexities of these filters as bubble sort algorithm requires 36 'compare and exchange' operations to perform sorting of 9 elements in a 3×3 matrix whereas PSA and RPSA requires only 24 and 17 'compare and exchange' operations to perform the same operation.

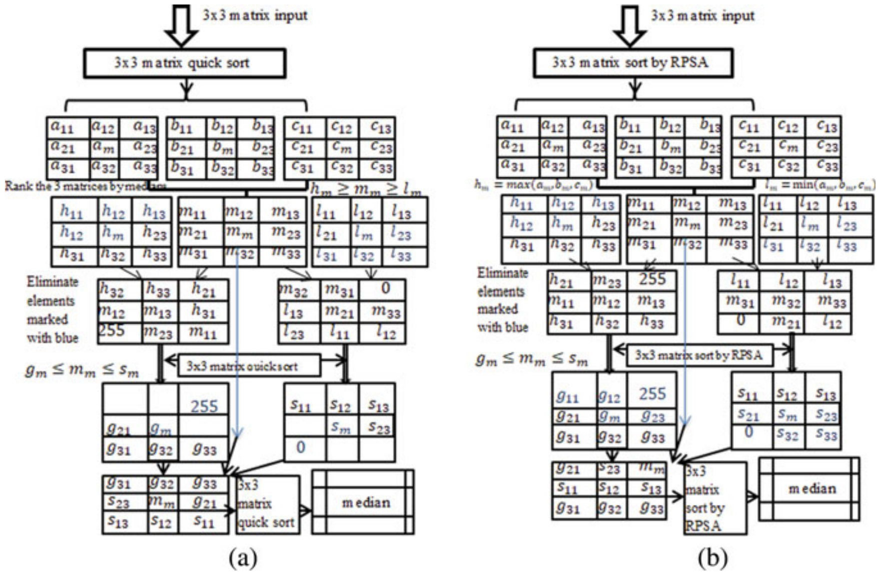

Fig. 4 **a** and **b** Median value computation techniques proposed in [13] and [14] respectively

Limitation

- These filters have not adapted any additional measures to suppress sharp spot noise or preserve target points and edges present in images.

3.4 An Improved Median Filtering Algorithm Combined with Average Filtering [2011] and an Improved Median Filtering Algorithm for Image Noise Reduction [2013]

This filter [15] is designed by combining the properties of Mean (Average) Filter and Median Filter. It filters only the noisy pixels present in images using a sliding filter window which changes its size adaptively in accordance to the local distribution of noise in images considering Peak Signal-to-Noise Ratio (PSNR) as an objective function which enhances this filter's noise suppression capability and time complexity by many folds compared to those of the traditional Median filter [7].

The authors in [15, 16] have designed these filters based on the assumption that noisy pixels differ largely from their neighboring pixels while all other pixels including the edge pixels possess almost similar properties as that of neighboring pixel. If the intensity of the center pixel of any local window is greater than the mean of all the pixels lying within that window, then it is considered as a noisy pixel and is despeckled. Else it is considered as a valid pixel and is preserved without despeckling.

In [15], the authors have proposed a novel adaptive window concept which facilitates the adjustment of the size of the local window in accordance to the local distribution of noise in images having $M \times N$ dimension as discussed below:

Step 1. If the center pixel of any local window of size $(2n + 1) \times (2n + 1)$ is detected as a noisy pixel, then it is filtered similarly as proposed in [7].

Step 2. Calculate $PSNR_n$ value as described below:

$$\text{Meansquareerror}_n(MSE_n) = \frac{1}{M \times N} \sum_{i=1}^{M} \sum_{j=1}^{N} (I_{out}(i, j) - I(i, j))^2 \tag{3}$$

$$PSNR_n = 10 \log (\frac{a_{\max}^2}{MSE}) dB \tag{4}$$

where, I_{out}: Filtered image, $a_{\max} = 2^k - 1$, k: the number of bits used for pixel representation in an image.

Step 3. Then set $n = n+2$, and filter I_{out} using the despeckling algorithm proposed in [7]. The output thus obtained is termed as $I_{out}^{'}$.

Step 4. Calculate $PSNR_{n+1}$ value similarly as stated in (3) and (4) but replacing I with I_{out} and I_{out} with $I_{out}^{'}$.

Step 5. If $PSNR_n > PSNR_{n+1}$, then consider the size of the window to be $(2n + 1) \times (2n + 1)$. Else go to Step 3 and further enlarge the size of the window.

The authors in [16] too have proposed a similar despeckling algorithm but with a different adaptive window size selection procedure which is defined as follows:

Step 1. Initialize: n = 1.

Step 2. Compute: $A1 = med - \min$ and $A2 = med - \max$. (med, max and min represent the median, maximum and minimum values of the intensities of the pixels lying within any local window).

Step 3. If $A1 > 0$ and $A2 < 0$, then go to Step 4. Else enlarge the size of the window by setting $n = n + 1$ and go to Step 2.

Step 4. Substitute $I(i, j) = med$.

Step 5. Stop.

In [16], the authors have also proposed a statistical histogram based median value computation procedure which decreases this filter's computational complexity from $O(N^2)$ to $O(N)$ where $O(N^2)$ denotes the computational complexity of the traditional Median filter [7].

Strength

- The use of adaptive window concept has increased the noise suppression capabilities of these filters compared to the Median filter [7].

Limitation

- These filters perform noise suppression in both homogeneous and heterogeneous regions identically which often leads to undesired edge-blurring.

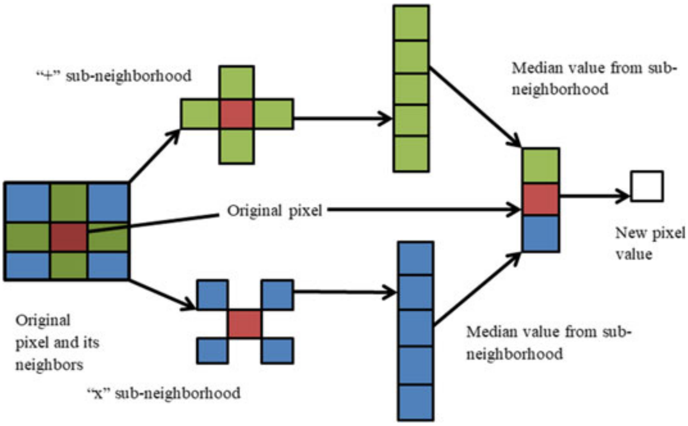

Fig. 5 Pictorial representation of the filtering algorithm proposed in [18]

4 Hybrid Median Filter and Its Proposed Variants

4.1 Hybrid Median Filter [2006]

This filter [17] performs noise suppression in each 5×5 local window of an image using the following steps:

Step 1: Pixels belonging to each 5×5 window are grouped into two groups where the first group comprises of the neighboring pixels located 45° angles to the center pixel. This group is termed as "+" sub-neighborhood while the second group comprises of the neighboring pixels located 90° angles to the center pixel. This group is termed as "x" sub-neighborhood. The median value of the first group is termed as m_+ and the median value of the second group is termed as m_x.

Step 2: The center pixel is substituted by the median of m_+, m_x and $I(i, j)$.

The filtering operation proposed in [17] is pictorially represented as follows (Fig. 5).

4.2 Modified Hybrid Median Filter [2010]

This filter [19] performs noise suppression using similar despeckling algorithm proposed in [17] but after substituting the second step as follows:

Instead of replacing the value of the center pixel with the median of m_+, m_x and $I(i, j)$, the authors have replaced it with the median of $\max_x$, m_+ and $I(i, j)$ where $\max_x$ is the maximum value of the pixels lying in the "x" sub-neighbourhood of the center pixel lying in the patch which is centered at pixel location, (i, j).

Strength of the Filters Proposed in [17] and [19]

- Time complexities of these filters are much lesser compared to that of the traditional Median filter [7].

Limitation of the Filters Proposed in [17] and [19]

- The use of sliding window of identical size to despeckle both homogeneous and heterogeneous regions of images by these filters often lead to the production of blurred images.

4.3 Adaptive Window Hybrid Median Filter [2013]

The authors in [18] have performed noise suppression similarly as proposed in [17] but with the introduction of a new adaptive window concept. They proposed that if the center pixel of any local window is detected as edge pixel, then it is filtered using the same algorithm proposed in [17] but using an local window of size 3×3. Else it is filtered using a local window of size 5×5. They have detected edge pixels using Sobel operator with the threshold value (100).

Strength

- The use of sliding windows of different sizes by this filter to suppress noise in both the homogeneous and heterogeneous regions of images has somewhat improved its edge-preservation capability compared to those of the filters proposed in [17] and [19].

Limitation

- The use of Sobel operator by this filter for performing edge detection that too using a fixed threshold often leads to the production of erroneous results as Sobel operator cannot efficiently detect edges in noisy images. This significantly influences the performance efficiency of this filter.

5 Comparative Qualitative and Quantitative Results

In this section, we have provided comparative qualitative and quantitative analyses of the results obtained by applying the filters proposed in [7, 14, 17, 19] on SAR and POLSAR images in Tables 1 and 2. SAR image which we have used here for performing the comparative analyses are acquired from freely available sources in the internet. Among the POLSAR images, Image 2 is obtained from ISRO SAC and other images (3–5) are acquired from the source mentioned in [20].

We have performed quantitative analyses using two quantitative parameters namely Edge preservation Index (EPI) [21] and Equivalent Number of Looks (ENL)

Table 1 Comparative qualitative analyses' results

No	Image	Median filter [5]	3D median filter [12]	Hybrid median filter [15]	Modified hybrid median filter [17]
1	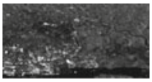	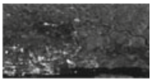	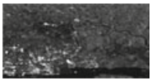	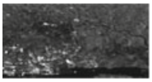	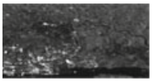
2					
3					
4					
5					

which measure the edge-preservation and noise suppression capabilities of the filters respectively. Higher values of both these parameters suggest better outcomes.

6 Unexplored Challenges

- None of these filters have adapted any additional measure to suppress sharp spot noise present in images.
- These filters do not include any target point preservation technique which is very essential to despeckle images efficiently.

7 Conclusion

In this paper, we have discussed in detail about how the filtering strategies of the Median Filter and Hybrid Median Filter and their proposed variants have evolved over the years. The qualitative and quantitative results obtained by applying the filters proposed in [5, 12, 15, 17] on both SAR and POLSAR images also depict that none of the existing filters possess strikingly better edge–preservation and noise suppression capabilities compared to the others. Most limitations of these filters arise due to several unexplored challenges which went unnoticed while designing these filters.

Table 2 Comparative quantitative analyses' results

Filter	Image 1		Image 2		Image 3		Image 4		Image 5	
	EPI	ENL	EPI	ENL	EPI	ENL	EPI	ENL	EPI	ENL
Median filter [5]	0.39	3.7	**0.38**	13.9	0.40	5.0	**0.40**	5.8	**0.42**	5.2
3D median filter [12]	**0.41**	**3.9**	0.37	5.5	0.38	**5.1**	0.39	**6.7**	0.41	**5.5**
Hybrid median filter [15]	0.39	3.8	0.36	**14.4**	**0.41**	**5.1**	0.39	5.8	0.40	5.2
Modified hybrid median filter [17]	0.38	**3.9**	0.36	13.8	0.39	**5.1**	0.38	5.8	0.41	5.2

*In this table, we have highlighted the best quantitative results obtained for each image

We have concluded our work by listing down some of those challenges which should be explored in future.

Acknowledgements This work is a part of the Research project titled, “Neuro-Fuzzy Synergism based POLSAR Image Classification” funded by ISRO Respond Program (No. ISRO/RES/4/673/19-20).

References

1. De, S., Bruzzone, L., Bhattacharya, A., Bovolo, F., Chaudhuri, S.: A novel technique based on deep learning and a synthetic target database for classification of urban areas in PolSAR data. IEEE J. Select. Topics Appl. Earth Obser. Remote Sens. **11**(1), 154–170 (2017)
2. Chen, S-W., Tao, C.-S.: PolSAR image classification using polarimetric-feature-driven deep convolutional neural network. IEEE Geosci. Remote Sens. Lett. **15**(4), 627–631 (2018)
3. Guo, J., Wei, P.L., Liu, J., Jin, B., Su, B.F., Zhou, Z.S.: Crop classification based on differential characteristics of H/α scattering parameters for multitemporal quad- and dual-polarization sar images. IEEE Trans. Geosci. Remote Sens. **56**(10), 6111–6123 (2018)
4. Mei, X., Nie, W., Liu, J., Huang, K.: PolSAR image crop classification based on deep residual learning network. In: 7th International Conference on Agro-Geoinformatics, pp. 1–6. IEEE, China (2018)
5. https://crisp.nus.edu.sg/~research/tutorial/sar_int.htm
6. Moreira, A., Prats-Iraola, P., Younis, M., Krieger, G., Hajnsek, I., Papathanassiou, K.P.: A tutorial on synthetic aperture radar. IEEE Geosci. Remote Sens. Magaz. 1–43 (2013)
7. David, H.A., Nagaraja, H.N.: Order Statistics. Wiley Series in Probability and Statistics, 3rd edn (1970)
8. Qiu, F., Berglund, J., Jensen, J.R., Thakkar, P., Ren, D.: Speckle noise reduction in SAR Imagery using a local adaptive median filter. GISci. Remote Sens. **41**(3), 244–266 (2015)
9. Lee, J.S.: Digital image smoothing and the sigma filter. Comput. Vision Graph. Image Process. **24**, 255–269 (1983)
10. Eliason, E.M., McEwen, A.S: Adaptive box filters for removal of random noise from digital images. Photogramm. Eng. Remote Sens. **56**(4), 453–458 (1990)
11. Lee, J.S: Digital image enhancement and noise filtering by use of local statistics. IEEE Trans. Pattern Anal. Mach. Intell. **PAMI-2**(2), 165–168 (1980)
12. Lee, J.S., Wen, J.H., Ainsworth, T.L., Chen, K.S., Chen, A.J.: Improved sigma filter for speckle filtering of SAR imagery. IEEE Trans. Geosci. Remote Sens. **47**(1), 202–213 (2009)
13. Jiang, M., Crookes, D.: High-performance 3D median filter architecture for medical image despeckling. IET Electron. Lett. **42**(24), 1379–1380 (2006)
14. Xiong, C., Hou, J., Gao, Z., He, X., Chen, S.: Fast algorithm of 3D median filter for medical image despeckling. In: Proceedings of Medical Imaging, Parallel Processing of Images, and Optimization Techniques, pp. 678915–1:678915–5. China (2007)
15. Youlian, Z., Cheng, H.: An improved median filtering algorithm combined with average filtering. In: 3rd, International Conference on Measuring Technology and Mechatronics Automation, pp. 420–423. IEEE, China (2011)
16. Youlian, Z., Cheng, H.: An improved median filtering algorithm for image noise reduction. Phys. Procedia **25**, 609–616 (2012)
17. Davies, E.R.: Machine Vision Theory, Algorithms, Practicalities, 3rd edn. Elsevier (2006)
18. Umamaheswari, G., Vanithamani, R.: An adaptive window hybrid median filter for despeckling of medical ultrasound images. J. Sci. Ind. Res. **73**(2), 100–102 (2014)
19. Vanithamani, R., Umamaheswari, G., Ezhilarasi, M.: Modified hybrid median filter for effective speckle reduction in ultrasound images. In: International Conference on Networking, VLSI and signal processing, pp. 166–171. ACM, United States (2010)

20. https://earth.esa.int/web/polsarpro/data-sources/sample-datasets
21. Sudhakar, R.: Edge preservation index (https://www.mathworks.com/matlabcentral/fileexchange/65261-edge-preservation-index-new-file). MATLAB Central File Exchange. Accessed 22 March 2020

Dual-Axis Solar Tracker Without Microcontroller

Sohom Chakraborty, Anusua Roy, and Sukanya Dey

Abstract Solar energy is the most abundant renewable energy source on the Earth. It is one of the best replacement of fossil fuel which is considered as a secure, lower-risk renewable energy source. Solar energy comes from the sun and can be captured by various technologies primarily Solar Panel. Solar tracking system is mainly of two types: Single-axis solar tracking system and Dual-axis solar tracking system. Although many paper has been published on sun tracking solar panel based on microcontroller, in this paper we are trying to make a dual-axis solar panel without using microcontroller. Previously published papers have shown that dual axis solar panel is 31.4% more power efficient than stationary or single axis solar panel (Amadi and Gutiérrez in Eur J Electr Comput Eng 3:1–2, 2019). Our paper is based on a dual-axis solar panel which tracks the sun using four reference panels. To make the system cheaper we are using two servomotors which will move the panel according to the sun's position in the horizontal and vertical axis using the voltage differences of the four reference panels. The main aim is to maximize the power received from the solar panel using a dual axis solar tracking system so that the energy obtained from the solar panel can be efficiently used to run the household appliances. Use of theoretical concepts has been put into use.

Keywords Dual axis solar panel · Design · Without microcontroller · Cheap

S. Chakraborty (✉) · A. Roy · S. Dey
University of Engineering and Management, Kolkata 700 156, India
e-mail: sohom.chakraborty@uem.edu.in

A. Roy
e-mail: anusua.roy1998@gmail.com

S. Dey
e-mail: jhilik2829@gmail.com

S. Banerjee and J. K. Mandal (eds.), *Advances in Smart Communication Technology and Information Processing*, Lecture Notes in Networks and Systems 165,
https://doi.org/10.1007/978-981-15-9433-5_39

1 Introduction

Solar panel works by absorbing sunlight with photovoltaic cells, generating direct current (DC) energy and then converting it to usable alternating current (AC) energy with the help of inverter technology. Solar- inverter converts the DC electricity from the solar modules to AC electricity which is used by most home appliances.

The science of generating electricity with solar panels boils down to the photovoltaic effect. Solar panel generates electricity by absorbing sunlight through photovoltaic cells applying photovoltaic effect. Photovoltaic cells mainly comprises of two silicon layers (p-type and n-type). It generates sufficient electric field required for photovoltaic effect. In this process the silicon photovoltaic solar cell absorbs solar radiation. When the sun's rays interact with the silicon cells, electrons begin to move creating a flow of electric current. Wires capture and feed this direct current (DC) electricity to a solar inverter to be converted to alternating current electricity. Solar inverter converts the DC electricity from the solar modules to AC electricity which is used by most home appliances.

Design of Solar Tracker System for PV Power Plants by Tiberiu Tudorache, Liviu Kreindler deals with the design and execution of a solar tracker system dedicated to the PV conversion panels [9]. The operation of the experimental model of the device is based on a DC motor intelligently controlled by a dedicated drive unit that moves a mini PV panel according to the signals received from two simple but efficient light sensors.

Through the course of time the solar tracking system is being improved day by day from single axis solar panel to dual axis solar panel for better efficiency. In this paper we have tried to make a dual axis solar panel which will make the system bigger as well as the four reference panels can detect the voltage differences more efficiently.

2 Literature Review

Design and Research of Dual axis solar tracking system in condition of town Almaty by Shyngys Sadyrbayey, Orynbayev Seitzhan, Amangeldi Bekbayev, Zhanibek Kaliyev describes a dual axis solar tracking system [3]. This study presents the efficiencies of energy conversion of photo module with solar tracking system and fixed photo module. The proposed sun tracking system uses 4 photo resistors, which are mounted on the sides of the photo module. By these photo resistors the solar tracking system becomes more sensitive and it allows to determining a more accurate location of the sun. A comparative analysis was performed between fixed and dual-axis tracking systems. The results showed that the dual-axis solar tracking system produced 31.4% more power compared with stationary photo module.

Dual Axis Solar Tracking System-A Comprehensive Study: Bangladesh Context by Amit Chakraborty Chhoton, Narayan Ranjan Chakraborty presents a performance analysis of dual axis solar tracking system using Arduino [4–11]. The main objective of this research is whether static solar panel is better than solar tracker or not. Result showed dual-axis solar tracking system produced extra 10.53 W power compared with fixed and single axis solar tracking system.

Energy Efficient Hybrid Dual Axis Solar Tracking System by Rashid Ahammed Ferdaus, Mahir Asif Mohammed, Sanzidur Rahman, Sayedus Salehin and Mohammad Abdul Mannan describes the design and implementation of an energy efficient solar tracking system from a normal mechanical single axis to a hybrid dual axis [5]. The power gain and system power consumption are compared with a static and continuous dual axis solar tracking system. It is found that power gain of hybrid dual axis solar tracking system is almost equal to continuous dual axis solar tracking system, whereas the power saved in system operation by the hybrid tracker is 44.44% compared to the continuous tracking system.

3 Need of Sun Tracking System

A sun tracking solar panel maximizes our solar system's electricity production by moving our panels to follow the sun throughout the day which optimizes the angle at which our panels receive solar radiation. A dual axis solar tracker allows our panels to move along two axes-horizontal and vertical. This type of system is designed to maximize our solar energy collection throughout the year. It can track seasonal variations in the height of the sun in addition to normal daily motion.

Dual-axis solar trackers can produce 45% more energy than typical static panels and can help business produce enough power to fuel their operations in a smaller space. The biggest benefit of a solar tracking system is that it offers a boost in electricity production. Solar trackers offer the greatest value proposition in high latitude locations due to yearly movements of the sun. Solar tracking systems are also often used in large commercial projects typically over 1 megawatt (MW).

When solar panels are exposed to sunlight, the angle at which the sun's rays meet the surface of the solar panel (known as angle of incidence) determines how well the panel can convert the incoming light into electricity. The narrower the angle of incidence the more energy a photovoltaic panel can produce. Solar trackers help to minimize the angle by working to orient panels so that light strikes them perpendicular to the surface [8].

4 Block Diagram

In this paper we are trying to give a basic idea of the block diagram. The block diagram of our project consists of two subtractors which are made using operational amplifier. The other components are p–n junction diode, comparator, battery and servomotors. Since, we are using a dual-axis solar panel so we have four reference

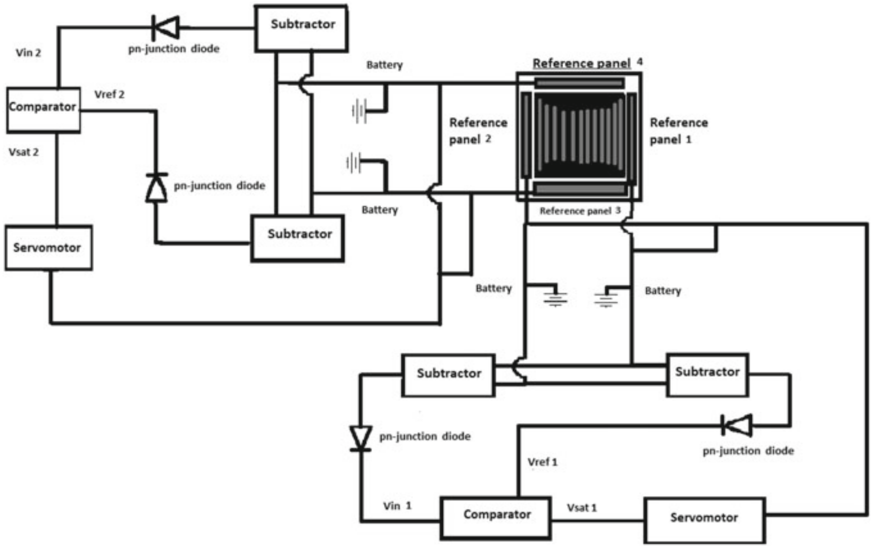

Fig. 1 Design of dual-axis solar panel without microcontroller

panels besides the main solar panel. For a single-axis solar panel we need only one servomotor but since we are using dual-axis solar panel we need two servomotors (Fig. 1).

5 Hardware Design

Since we have already discussed what components we are using in this project, through this hardware design we are going to describe each and every component.

5.1 Subtractor

Subtractor is been used to measure the difference between the voltages of the two reference panels which will provide output to the p–n junction diode. In this project we have used four subtractors. Since we are using a dual-axis solar panel the block diagram consists of two parts, one for moving the panel in the horizontal direction and the other one for moving the panel in the vertical direction.

Suppose the voltage from the reference panel 1 be V1 and that from reference panel 2 be V2, then out of the four subtractor, one is used to measure (V1–V2) and another one to measure (V2–V1) in the vertical direction. Similarly for horizontal direction, let the voltage from reference panel 3 be V3 and that from reference panel 4 be V4, then one subtractor is used to measure the (V3–V4) and other one to measure (V4–V3) and the outputs are going to their respective p–n junction diodes.

5.2 P–n Junction Diode

A p–n junction diode is a two terminal or two electrode semiconductor device, which allows the electric current in only one direction while blocks the electric current in opposite or reverse direction. If the diode is forward biased, it allows the electric current flow. On the other hand if the diode is reverse-biased, it blocks the electric current flow. Here, we are using total four p–n junction diodes [10].

5.3 Battery

In the block diagram we have shown two different parts, one for moving the panel in the horizontal direction and the other one for moving the panel in the vertical direction. In the vertical part, we are using two batteries, in which we are storing the energies from the two reference panels 1 and 2, and then utilizing that energy in the servomotor so that no other external energy source is required for working the servomotor. Similarly in the horizontal part, energy from the reference panels 3 and 4 is being stored in the respective two batteries.

5.4 Comparator

In this project, we are taking (V1–V2) as Vref 1 or reference voltage of the comparator, and (V2–V1) as Vin 1 or input voltage of the comparator for the vertical part and same concept is applied on horizontal part where (V3–V4) is Vref 2 and (V4–V3) is Vin 2. We are using total two 5 V comparators for the two parts. Comparator output of 4 reference panels can be showed as Table 1.

Table 1 Comparator output

Input voltage	Output voltage
Vin 1 > Vref 1	Vout1 = +Vsat 1
Vin 1 < Vref 1	Vout1 = −Vsat 1
Vin 1 = Vref 1	Vout 1 = 0
Vin 2 > Vref 2	Vout2 = +Vsat 2
Vin 2 < Vref 2	Vout2 = −Vsat 2
Vin 2 = Vref 2	Vout2 = 0

5.5 Servomotor

A servomotor is a rotary actuator or linear actuator that allows for precise control of angular or linear position, velocity and acceleration. It consists of a suitable motor coupled to a sensor for position feedback. Here, we are using two servomotors for two different parts. The reference panels are joined mechanically to the servomotor.

All the electronic devices can be operated using the main solar panel.

6 Working Procedure and Results

We have assumed that, reference panel 1 and 2 are east and west side of the main solar panel. At the same time, reference panel 3 and 4 are south and north side of the main solar panel. In the early morning, voltage of east-side is greater than west-side solar panel. If that reference panel's voltage is greater than p–n junction diode's cutoff voltage then only we will get reference voltage and input voltages in comparator. We have considered (V1–V2) as Vref1 and (V2–V1) as Vin1. When Vin1 is greater than V ref1, then Vout1 becomes + Vsat1. Then, servomotor will rotate towards reference panel 1 to get more sunlight. In the midday, sun directs in the south in mid-northern part of earth. Then we need to measure north and south side of reference panels which are represented as reference panel 4 and 3. Here also (V3–V4) as Vref2 and (V4–V3) as Vin2. Then Vin2 is greater than Vref2. Then Vout2 becomes + Vsat2. Then, servo motor will rotate towards reference panel 4 to get more sunlight. In this way we can track sun by using voltage difference of the solar panel.

Sun also changes its position in the south and north in the middle of the summer and winter. That's why, dual-axis solar panel is needed to get sunlight efficiently. Power generated by dual axis solar panel also changes depending on the number of cells and various factors. It is to be noted that the four reference panels working along each axis works simultaneously and never in isolation.

7 Discussion

Our paper is based on a dual-axis solar panel without microcontroller which aims at maximizing the power received from the solar panel so that the energy obtained can be efficiently used to run the household appliances. In this project we are using four reference panels. To make the system cheaper we are using two servomotors which will move the panel according to the sun's position in the horizontal and vertical axis using the voltage differences of the four reference panels. Other than this, we are using four subtractors which used to measure the difference between the voltages of the two reference panels which will provide output to the p–n junction diode. The p–n junction diode then allows the electric current in only one direction while blocks the electric current in opposite or reverse direction. If the diode is forward biased, it allows the electric current flow. On the other hand if the diode is reverse-biased, it blocks the electric current flow. Here, we are using total four p–n junction diodes. We are using four batteries two in each part i.e. vertical and horizontal. In the vertical part, we are using two batteries, in which we are storing the energies from the two reference panels 1 and 2, and then utilizing that energy in the servomotor so that no other external energy source is required for working the servomotor. Similarly in the horizontal part, energy from the reference panels 3 and 4 is being stored in the respective two batteries. We are using two 5 V comparators to compare the voltages from the two panels in two different parts and finally pass the output to the servomotor.

8 Future Scope

- We have used mechanically connected reference panels, so we should take good care of its maintenance especially in harsh weather conditions. Otherwise we have to use four different servo motors to rotate four reference panels which can be expensive so, we should think about how maintenance can be done in cheaper way.
- Voltage regulator can also be used to make the power generated by the main solar panel more stable.
- Furthermore, power generated from main solar panel also can be used with the help of different voltage regulators to run different components of solar system.
- We have used batteries to store reference panel voltages. Only drawback is that less amount of current will conduct through subtractors. Due to less voltage difference servo motor will not rotate the amount it should. Applying super capacitor can be helpful as less amount of current will flow through it, but it is minimum 10 times costlier than batteries. So, we must think of maintaining solar trackers accuracy in cheaper way.
- Servomotor creates vibration when it stops. It vibrates for one pulse. So, it may create problem in rotation. Also if something gets damaged in solar system the servomotor will become uncertain. We can also use timer circuit to control servomotor instead of controller. As the circuit size is increased, probability of breaking parts also increased. So, more secure circuits are needed.
- Solar tracker is designed for more manageable weather patterns. Fixed tracker accommodates harsher environmental conditions more easily than tracking systems. That's why solar tracker claims only 5–10 years warranty. We should think about how we can increase its longevity and efficiency after warranty period, as panel's efficiency will be reduced by 1% per year.
- We have also thought of using concave mirrors to use maximum reflected light towards the solar panel. But increased heat can easily damage the solar panel. In this case thermoelectric generator can be used to convert this heat energy to

electrical energy and some cooling system can be used if required. This will result in efficient utilization of energy that comes with an additional cost.

- In our paper we have used lots of electrical components so we should think about how we can make a compact structure of the system, at the same time maintaining low cost, stability and security of the circuit.
- We have only given the theoretical concept of the dual-axis solar panel without using microcontroller, the practical implementation has not been yet performed. So, we should think about the practical implementation for future purposes.

9 Conclusion

Through this paper we are trying to give the concept of a dual-axis sun tracking solar panel without using microcontroller which will make the system cheaper and can also produce maximum power received from the solar panel so that the energy obtained can be efficiently used to run the household appliances.

Acknowledgements We would like to give our special thanks to all those who provided us the possibility to complete this paper. We both teammates have given a lot of efforts on this project. So we both are thankful to each other and our guide teacher who have guided us and still guiding to improve this project.

References

1. Enslin, J.H.R.: Maximum power point tracking a cost-saving necessity in solar-energy systems. Renew. Energy **2**(6), 543–549 (1992)
2. Amadi, H.N., Gutiérrez, S.: Design and performance evaluation of a dual-axis solar tracking system for rural applications. Eur. J. Electr. Comput. Eng. **3**(1), 1–2 (2019)
3. Sadyrbayey, S., Seitzhan, O., Bekbayev, A., Kaliyev, Z.: Design and research of dual axis solar tracking system in condition of town Almaty. Middle-East J. Sci. Res. **17**(12), 1747–1751 (2013)
4. Chakraborty Chhoton, A., Chakraborty, N.R.: Dual axis solar tracking system-a comprehensive study: Bangladesh context. In: International Conference on Advances in Electrical Engineering, Dhaka-Bangladesh (2017)
5. Ferdaus, R.A., Mohammed, M.A., Rahman, S., Salehin, S., Mannan, M.A.: Energy efficient hybrid dual axis solar tracking system. Renew. Energy 12, (2014)
6. Mitra, D., Das, D., Brahma, D., Maiti, D., Mondal, T.: Sun Tracking Solar Panel Without Microcontroller. IEEE, Kolkata (2019)
7. Wang, F., Jou, X., Chen, J.: Research and Design of DC servo motor position control system based on lab view. ICEEE, China (2010)
8. Rizk, J., Chaiko, Y.: Solar tracking system more efficient use of solar panels. World Acad. Sci. Eng. Technol. 313–315 (2008)
9. Tudorache, T., Kreindler, L.: Design of solar tracker system for PV power plants. Acta Polytechnica Hungarica **7**(1), 23–39 (2010)

10. Cristea, M.J.: Unified model for P-N junction current-voltage characteristics. Open Eng. **1**(1), 1–3(2009)
11. Othman, N., Manan, M.I.A., Othman, Z., Junid, S.A.M.A.: Performancea analysis of dual-axis solar tracking system. IEEE 370–375 (2013)

Inter-subband Photoresponse Analysis of CdS/ZnSe QWIP

Md Aref Billaha, Biplab Bhowmick, and Santosh Kumar Choudhary

Abstract We report the study of inter-subband transition based performance of CdS/ZnSe quantum well photodetector. With the increasing well width, transition wavelength shifts to higher wavelength region and the number of quantized energy states increases. Results indicate that mid and long wavelengths of absorptions are significant. Photocurrents are calculated considering the continuity equation of the quantum well and results are observable.

Keywords CdS/ZnSe · FDM · Absorption · Photocurrent

1 Introduction

Inter-subband (ISB) transition based photonic devices (e.g. photodetectors, LEDs, etc.) are formed by quantum confinement of carriers in semiconductor nanostructures [1, 2]. In truth, ISB transitions in nanostructures give a wide range of potential applications for various optoelectronic devices [3]. These devices based on semiconductors paying much attention due to their impressive properties ranging from thermoelectric to photovoltaic effect [4, 5]. Nowadays, researchers mainly focused on the miniaturized design of quantum well infrared photodetectors (QWIP) with high sensitivity, multispectral response, high speed and admirable stability [6, 7]. InGaAs/AlGaAs and GaAs/AlGaAs QWs grown on GaAs substrate are the most widely considered materials for the detection of mid wavelength (MW) and long wavelength (LW) infrared (IR) region respectively [8, 9]. However, multiple number of quantum wells grown by InGaAs/AlGaAs is difficult due to the lattice constant

Md. A. Billaha (✉) · B. Bhowmick
Department of Electronics and Communication Engineering, Asansol Engineering College, Asansol 713305, India
e-mail: aref.ece@aecwb.edu.in

S. K. Choudhary
Department of Electronics and Communication Engineering, VNR Vignana Jyothi Institute of Engineering and Technology, Hyderabad, India

S. Banerjee and J. K. Mandal (eds.), *Advances in Smart Communication Technology and Information Processing*, Lecture Notes in Networks and Systems 165,
https://doi.org/10.1007/978-981-15-9433-5_40

mismatch between InGaAs and GaAs material and hence, absorption quantum efficiency of the QWIP is limited. Moreover, design of two-color QWIP in the mid and long wavelength IR region is mainly based on the multistacks InGaAs/AlGaAs and GaAs/AlGaAs MQWs [10–13]. Therefore, limitation applicable in the two-color QWIPs as well. Absorption quantum efficiency can be increased by the selection of large value of doping density. However, this also enhances the dark current density of the detector. In the recent development of wide bandgap II–VI low-dimension structures have opened up to explore new epoch in the design of two or multi-color IR detectors in order to overcome such situations [14–18]. For example, Lu et al. reported inter-subband transitions in $Zn_{0.46}Cd_{0.54}Se/Zn_{0.24}Cd_{0.25}Mg_{0.51}Se$ multiple quantum wells (MQWs) with 3.99 and 5.35 μm wavelengths respectively [16]. Another material system based on CdS/ZnSe/BeTe QW structure grown on the GaAs substrate has been reported by Akimoto et al. in 2005 [19].

The work aims to design an IR detector and study the performance characteristics of the QWIP based on CdS/ZnSe concerning inter-subband transition in the conduction band. Using this structure, one may obtain more than two number of quantized energy states due to the formation of a large conduction band offset. In this paper, we report a theoretical analysis of ISB transitions based type-II CdS/ZnSe quantum well photodetector. Carriers generation and recombination phenomenon are considered to calculate photocurrent and for the same, absorptions are evaluated in this article. Schrödinger equations are solved using the finite difference method (FDM) for finding the quantized energy states. The paper is prepared as follows. Physics and structure of the model and hence, calculation of the photocurrent are described in Sect. 2. Desired simulation results are discussed in Sect. 3 and the brief finding of the work is given in Sect. 4.

2 Physics and Structure of the Model

The structure of the model is shown in Fig. 1 where the formation of the quantum well is seen due to the considered materials of CdS and ZnSe. The emitter and collector are the contact layers made of heavily doped (2×10^{18} cm^{-3}) ZnSe material.

Following the basic approach given in Ref [20], the photocurrent of the proposed structure can be calculated by considering carriers capture and escape phenomenon as

$$\frac{\partial n_{q\omega}}{\partial t} = \frac{\left(1 - \beta_{cap}\right)}{q} j + I_0\left(e^{-\alpha(k-1)L_w} - e^{-\alpha k L_w}\right) - n_{q\omega} r_{es,v} - n_{q\omega} r_{es,th} - n_{q\omega} r_r \tag{1}$$

where, n_{qw} is the electron sheet concentration, $(1-\beta_{\text{cap}})$ is the carrier capture probability at the barrier-well interface, j is the current density, I_0 is the intensity of incident IR radiation, α is the absorption coefficient, $r_{es,v}$ and $r_{es,th}$ are the escape rate of electrons from the quantum well due to bias and thermionic emission, r_r

Fig. 1 Schematic layer structure of the proposed model and the corresponding conduction band diagram

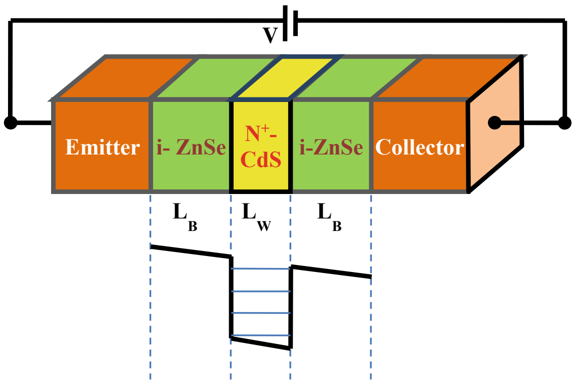

is the electron recombination rate. Now, Escape rate of electrons can be written as [20, 21]

$$r_{es,v}(V) = r_{es}(0)e^{V/V_{act}} \text{ and}$$
$$r_{es,th} = Be^{-V_{act}/K_B T} \tag{2}$$

where $r_{es}(0)$ is the emission rate of electrons at no bias, V_{act} is the effective potential barrier lowering and B is the parameter which depends on the well width and effective mass of the well layer.

Now, the estimation of absorption (α) is an important parameter of the quantum well structure since the calculation of photocurrent depends on absorption which can be observed from Eq. (1). The term, absorption is wavelength dependent and can be evaluated by the accurate finding of Eigen energy states and wave functions of carriers. Finite difference method is used to solve the Schrödinger equation (SE) to determine energy state and can be written as [20].

$$-\frac{\hbar^2}{2m_e^*}\frac{\partial^2\psi(z)}{\partial z^2} + (V(z) - q\varepsilon z)\psi(z) = E\psi(z)$$
$$\text{where, } V(z) = V_c(z) + \delta V_c + V_H(z) \tag{3}$$

where $V_c(z)$ is the conduction band offset, δV_c is the change in band energy due to strain, $V_H(z)$ is the Hartree potential, ε is the electric field and rest of the parameters have their usual meaning. The term, δV_c can be expressed as $\delta V_c = \mathrm{a}_c(2\varepsilon_{xx}+\varepsilon_{zz})$ where, $\varepsilon_{xx} = (a_{\text{mat}} - a_{\text{subs}})/a_{\text{subs}}; \varepsilon_{zz} = -2\varepsilon_{xx}(C_{12}/C_{11})$($a_{\text{subs}}$ is defined as the lattice constant of the substrate).

From Eq. (3), the Hamiltonian matrix can be expressed as

$$H = -\frac{\hbar^2}{2m_e^*}\frac{\partial^2}{\partial z^2} + (V_c(z) + \delta V_c + V_H(z) - q\varepsilon z) \tag{4}$$

Equation (4) is used to convert into a difference equation by standard finite difference technique for the solution of SE and is given by

$$\left(\frac{\partial^2\psi(z)}{\partial z^2}\right)_{z=z_m} = \frac{1}{a^2}[\psi(z_{m+1}) - 2\psi(z_m) + \psi(z_{m-1})] \tag{5}$$

where, a is the small piece of elements of equal width.

The values of the material required for the calculation are $L_W = 5.4$ nm, $L_B = 30$ nm, $N = 0.5 \times 10^{18}$ cm^{-3}, $P_{in} = 1$ mW, $A = 200 \times 200$ µm^2 and $\phi = 45°$. The above values are chosen to study the absorption and photoresponse of two different wavelength of interest in mid and long wavelength of region. These values can be tailored for obtaining efficient absorption at a given wavelength of the reader's interest and hence, adaptable response of the photodetector.

3 Results and Discussion

Performance of the CdS/ZnSe based QWIP is discussed in this section. The solution of Schrödinger equation provides four numbers of quantized energy states using FDM calculation and their possible transition wavelength variation as a function of different well width is illustrated in Fig. 2. It happens due to the selection of two different bandgap materials of CdS and ZnSe and hence, their quantum well formation comprises of large conduction band offset. It is observed that transition wavelength changes from one operating wavelength to another wavelength due to

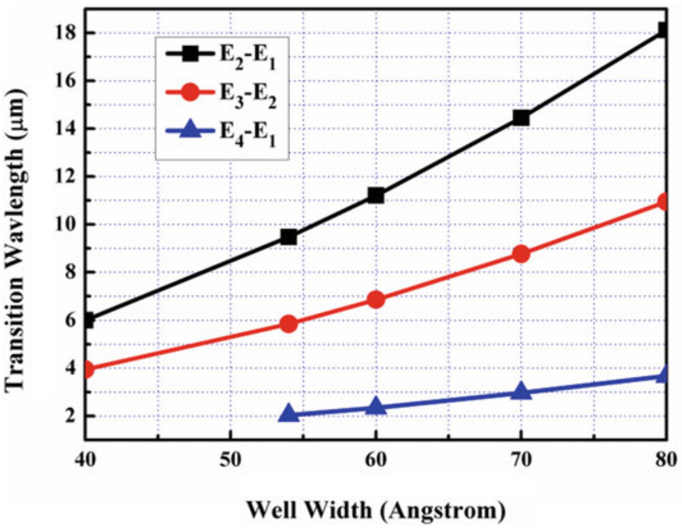

Fig. 2 Variation of transition wavelength with well width of CdS

the enhancement of CdS well width. For example, wavelength shifted from 11.21 to 14.45 μm, 6.86 to 8.77 μm and 2.34 to 2.96 μm respectively for changing well width from 6 to 7 nm. Therefore, the wavelength of operation can be altered by a suitable choice of the active well layer. For the sake of comparison, the variation is similar to the reported work in Ref. [22] where wavelength of 5.2 μm is observed at $L_W = 4$ nm whereas we observed 5.83 μm of wavelength considering same L_W. This discrepancy is observed due to the consideration of different model from our structure and the approach adopted by the author Zeiri et al. [22]. It is important to note that the lowest subband energy must be occupied with carriers which can be enhanced by proper selection of doping in the active region to observe significant inter-subband transition.

In this work, the calculation of transition wavelength is very important for the determination of the absorption coefficient. The expression of absorption can be obtained from Refs. [23, 24]. Figure 3 shows that the peak absorption coefficients arise in two different regions of interest in mid and long wavelength and the corresponding values are sufficient to estimate the photocurrent. The transition from E_4 to E_1 has also happened but this transition has a very low value of peak absorption approximately 50 cm^{-1} and is not shown in the absorption plot. The reason behind such a phenomenon is mainly due to the effect of strong overlap integral of wave functions in the mid wavelength (MW) as compared to the long wavelength (LW) of operation and the carrier confinement in ground state energy in comparison with higher energy states. The calculated absorption in mid wavelength is less as compared to absorption estimated by N. Sfina et al. [3] and it is due to the selection of lower doping concentration in well region where doping plays an important role for the calculation of absorption. Moreover, the material values are different from

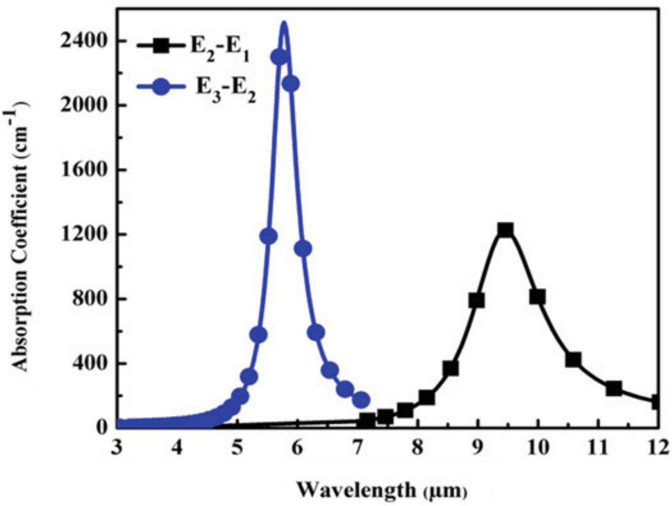

Fig. 3 Calculated absorption coefficient as a function of wavelength of our considered model

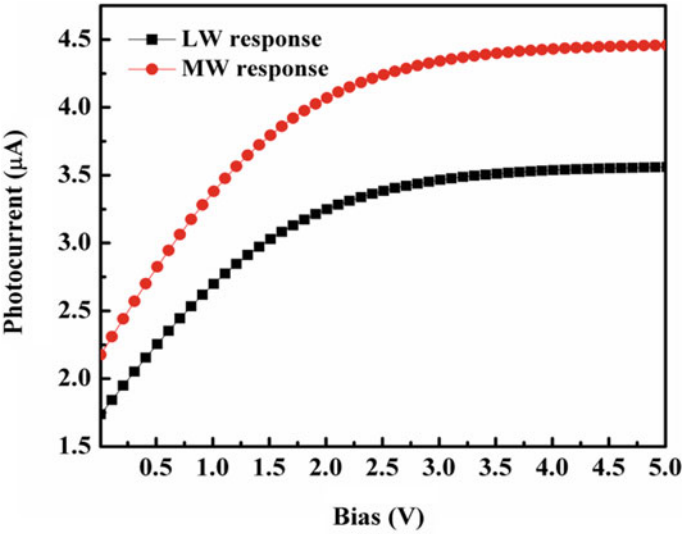

Fig. 4 Photocurrent response of the MW and LW region

our reported values in this article. But, the absorption calculation of infrared light is not sufficient to judge the performance of QWIP since carriers must be collected at the collector region after generation. During collection, carriers may be lost due to recombination, low transit time, etc. Equation (1) is solved under the steady-state condition and the calculated photocurrents are shown in Fig. 4 for two IR regions such as LW and MW region. For the calculation of current due to the incident photon, I_0 can be evaluated using the relationship [25] $I_0 = (p_{in}\cos(\phi))\big/ A\hbar\omega$. It is nice to see that photocurrent response in MW is quite larger than LW response due to the strong dependence of current on the absorption. At the same time, current not only depends on absorption, another mechanism of carrier escape and capture, effective active potential barrier due to the applied bias, etc. are also contribute their role on the calculation of photocurrent of CdS/ZnSe QWIP. Current increases with bias rapidly and after certain bias photocurrent behaves like an independent bias on the detector.

4 Conclusions

In conclusion, Inter-subband transition based analysis of CdS/ZnSe QWIP is reported. Results show the flexibility of tuning the desired peak wavelength of operation by controlling the active well width for the design of the IR detector. However, the strength of peak absorption is larger in MW than the LW region and hence, observation of photocurrent is significant.

References

1. Shen, A.: Molecular beam epitaxy-grown wide band gap II-VI semiconductors for intersubband device applications. Mol. Beam Epitaxy **15**, 327–341 (2018)
2. Lee, W.-J., Umana-Membreno, G.A., Dell, J., Faraone, L.: Effect of CdS processing conditions on the properties of CdS/Si diodes and CdS/CdTe thin-film solar cells. IEEE J. Photovolt. **5**(6), 1783–1790 (2015)
3. Sfina, N., Abdi-Ben Nasrallah, S., Mnasri, S., Said, M.: Absorption coefficient of intersubband transition at 1.55 μm in (CdS/ZnSe)/BeTe quantum wells. J. Phys. D Appl. Phys. **42**, 045101 (2009)
4. Xia, Y.N., Yang, P.D., Sun, Y.G., Wu, Y.Y., Mayers, B., Gates, B., Yin, Y.D., Kim, F., Yan, H.Q.: One- dimensional nanostructures: synthesis, characterization, and applications. Adv. Mater. **15**, 353–389 (2003)
5. Deng, K., Li, L.: CdS nanoscale photodetectors. Adv. Mater. **26**, 2619–2635 (2014)
6. Soci, C., Zhang, A., Bao, X.Y., Kim, H., Lo, Y., Wang, D.L.: Nanowire photodetectors. J. Nanosci. Nanotechnol. **10**, 1430–1449 (2010)
7. Logeeswaran, V.J., Oh, J., Nayak, A.P., Katzenmeyer, A.M., Gilchrist, K.H., Grego, S., Kobayashi, N.P., Wang, S.Y., Talin, A.A., Dhar, N.K., Islam, M.S.: A perspective on nanowire photodetectors: current status, future challenges, and opportunities. IEEE J. Sel. Top. Quant. Electron. **17**, 1002 (2011)
8. Fiore, A., Rosencher, E., Bois, P., Nagle, J., Laurent, N.: Strained InGaAs/AlGaAs quantum well infrared photodetectors at 4.5 μm. Appl. Phys. Lett. **64**, 478 (1994)
9. Lenchyshyn, L.C., Liu, H.C., Buchanan, M., Wasilewski, Z.R.: Mid-wavelength infrared detection with InGaAs/AlGaAs multiple quantum well structures. Semicond. Sci. Tech. **10**, 45 (1995)
10. Bandara, S.V., Gunapala, S.D., Liu, J.K., Rafol, S.B., Ting, D.Z., Mumolo, J.M., Chuang, R.W., Trinh, T.Q., Liu, J.H., Choi, K.K., Jhabvala, M., Fastenau, J.M., Liu, W.K.: Four-band quantum well infrared photodetector array. Infrared Phys. Technol. **44**, 369–375 (2003)
11. Sundaram, M., Wang, S.C.H.: 2-Color QWIP FPAs. Proc. SPIE **4028**, 311 (2000)
12. Wang, H., Zhang, R., Wang, F., Jiao, Z., Shao, D., Fu, Z., Zhou, T., Tan, Z., Cao, J.: Two-colour THz quantum well photodetectors. Electron. Lett. **53**(16), 1129–1130 (2017)
13. Srinivasan, S.A., Porret, C., Vissers, E., Favia, P., Coster, J.D., Bender, H., Loo, R., Thourhout, D.V., Campenhout, J.V., Pantouvaki, M.: High absorption contrast quantum confined stack effect in ultra-thin Ge/SiGe quantum well stacks grown on Si. IEEE J. Quant. Electron. **56**(1), 1–7 (2020)
14. Goppert, M., Grun, M., Maier, C., Petillon, S., Becker, R., Dinger, A., Storzum, A., Jorger, M., Klingshirn, C.: Intersubband and interminiband spectroscopy of doped and undoped CdS/ZnSe multiple quantum wells and superlattices. Phys. Rev. B **65**, 115334 (2002)
15. Kaya, Y., Ravikumar, A., Chen, G., Tamargo, M.C., Shen, A., Gmachl, C.: Two-band ZnCdSe/ZnCdMgSe quantum well infrared photodetector. AIP Adv. **8**, 075105 (2018)
16. Lu, H., Shen, A., Tamargo, M.C., Song, C.Y., Liu, H.C., Zhang, S.K., Alfano, R.R.: Optical characterization of intersubband transitions in $Zn_xCd_{1-x}Se/Zn_{x'}Cd_{y'}Mg_{1-x'-y'}Se$ multiple quantum well structures by contactless electro reflectance. Appl. Phys. Lett. **89**, 131903 (2006)
17. Dinger, A., Petillon, S., Grun, M., Hetterich, M., Klingshirn, C.: Conduction band offset of the CdS/ZnSe heterostructure. Semicond. Sci. Technol. **14**, 595–598 (1999)
18. Li, B.S., Akimoto, R., Shen, A.: Thermal annealing effects on intersubband transitions in (CdS/ZnSe)/BeTe quantum wells. Appl. Phys. Lett. **92**, 021123 (2008)
19. Akimoto, R., Li, B.S., Akita, K., Hasama, T.: Subpicosecond saturation of intersubband absorption in (CdS/ZnSe)BeTe quantum well waveguides at telecommunication wavelength. Appl. Phys. Lett. **87**, 181104 (2005)
20. Billaha, M.A., Das, M.K.: Peformance analysis of AlGaAs/GaAs/InGaAs-based asymmetric long-wavelength QWIP. Appl. Phys. A **125**, 457 (2019)
21. Das, N.R., Deen, M.J.: Effect of interface-trapping on the frequency response of a photodetector. J. Vac. Sci. Technol. A **20**(3), 1105–1110 (2002)

22. Zeiri, N., Sfina, N., Abdi-Ben Nasrallah, S., Lazzari, J.-L., Said, M.: Intersubband transitions in quatum well mid-infrared photodetectors. Infra. Phys. Technol. **60**, 137–144 (2013)
23. Billaha, A., Das, M.K.: Influence of doping on the performance of GaAs/AlGaAs QWIP for long wavelength applications. Opto-Electron. Rev. **24**(1), 25–33 (2016)
24. Davies, J.: The Physics of Low-Dimensional Semiconductors An Introduction. Cambridge University Press, Cambridge (1998)
25. Henini, M., Razeghi, M.: Handbook of Infrared Detection Technologies, first edn. Elsevier Science (2002)

Fire Extinguishing Robot Using Arduino and DTMF Controller

Susmita Chaki, Didhiti Nandi, and Juhita Das

Abstract Detecting fire and extinguishing it is a hazardous job for a fire extinguisher as it often risks the life of that person. In this paper we aim to give a technical solution to the mentioned problem.A robot is a mechanical design that is capable of carrying out a complex series of actions automatically, especially one programmable by a computer. For movement and reaching the fire, a fire extinguisher robot is controlled using a mobile phone or a remote control through DTMF tones. To detect fire and give the further signal to the extinguisher units to trigger the pump and spray the water, the flame sensor is used. The whole system is programmed in microcontroller AT328P, embedded in an Arduino UNO board.

Keywords Arduino uno board · DTMF controller · Fire sensor · Motor driver board · Ultrasonic sensor

1 Introduction

The main objective of this paper is to build a fire-extinguisher robot which will be controlled using a mobile phone or a remote control through DTMF tones for its movements and reaching the fire.The flame sensor will be then used to detect the fire, raise an alarm and give the further signal to the extinguisher units to trigger the pump and spray the water. The entire system logic is programmed in microcontroller AT328P, embedded in an Arduino UNO, which forms the brain of the system.

S. Chaki (✉) · D. Nandi · J. Das
University of Engineering & Management, Kolkata, India
e-mail: susmitachaki1991@gnail.com

D. Nandi
e-mail: didhiti.nandi@gmail.com

J. Das
e-mail: juhita302@gmail.com

S. Banerjee and J. K. Mandal (eds.), *Advances in Smart Communication Technology and Information Processing*, Lecture Notes in Networks and Systems 165,
https://doi.org/10.1007/978-981-15-9433-5_41

A firefighting rover is designed which can extinguish the fire with the help of fire fighter away from the hazardous area or a blazed area. It can also reach critical areas like damaged and demolished buildings and help to turn off fire in any scenario without the loss of human life.

It is intended to help firefighting professionals to easily find and put off the fire. since this design has caterpillar traction in the rover, it can be operated from a safe distance and it can move into rough terrains inside the building. In our proposed system, a ventilating system is equipped with water mist which is able to eliminate the smoke and reduce the temperature in the premises nominally. A fire canon is attached to the pipeline of the fire extinguishing, liquor tank, which can be raised or lowered to target the fire. Here, LED lighting is employed to get clear visual with regard to ongoing action for monitoring purpose. Georgi Hristov et al. have discussed and present two different emerging solutions for early detection of forest fires [1]. The first of these solutions involves the use of un-manned aerial vehicles (UAVs) with specialized cameras. Evgenit Krasnov et al. have dedicated to the overview of the firefighting [2] robots control systems. The main goal of that paper is to show the variety of different firefighting robots and to analyze their advantages and imperfections.

Hasam U. Zaman et al. have introduced a novel design of a multi-purpose fire-fighting [3] robot, with the help of a streaming video camera attached to it, transmits live video from its surroundings to a remote location from where the robot can be controlled. The robot is mobilized and directed to the spot of the fire and throw water at the fire. It used RF signal for communication and was capable of performing three different functions related to firefighting operation. Amit R. Bhende et al. found that when a place catches fire it is well observed fact that a large amount of time is wasted by the fire man to extinguish [4] fire due to huge distance present between the place of the fire and the water hose or water monitor. For that reason, large amount of water is wasted due to evaporation of water loss during jet impact. Robin R. Murphy et al. presented a preliminary domain theory for robot-assisted wild land fire-fighting domain [5]. The domain theory is based on a focus group hosted by the Texas Engineering Extension Service with eight subject matter experts and nine technologists. Six potential functions of a ground robot are identified by the focus group: (1) transport supplies, hoses, trunk lines and people (2) reconnoiter the fire direction, speed, and other attributes (3) direct fire suppression (4) identify hot spots under canopies using thermal imaging (5) areas for fire hazards have investigated from dead trees and level burnt remnants and (6) serve as a movable weather station determining relative humidity, wind speed and direction, fuel moisture and fuel temperature. We, in this paper have tried to give a technical solution to the problem of fire-fighting, by taking all their views.

2 Theory

2.1 Description of System Model

The block diagram of the proposed system is shown in Fig. 1.

Figure 1 shows the block representation of the proposed system. It has mainly two modules (1) Navigation module (2) Extinguishing module. The Navigation module (transmitter) is used to navigate robotic vehicle or extinguishing module.

Navigation module consists of remote control application or DTMF decoder and the motor driver board, controlling the movements of the rover. In our proposed system, extinguishing module is a whole firefighting robotic vehicle (receiver).A water sprayer is here to extinguish fire. Extinguishing module is controlled by received signals from navigation module. Flame detection is the next part of fire extinguishing module. This detects flame with respect to temperature which is nearer to the vehicle. Also the feature of control unit is used to control the whole vehicle by using Arduino UNO Microcontroller board based on the ATmega328P microcontroller. From above we can visualize the scenario surrounding the vehicle by using camera (Fig. 2).

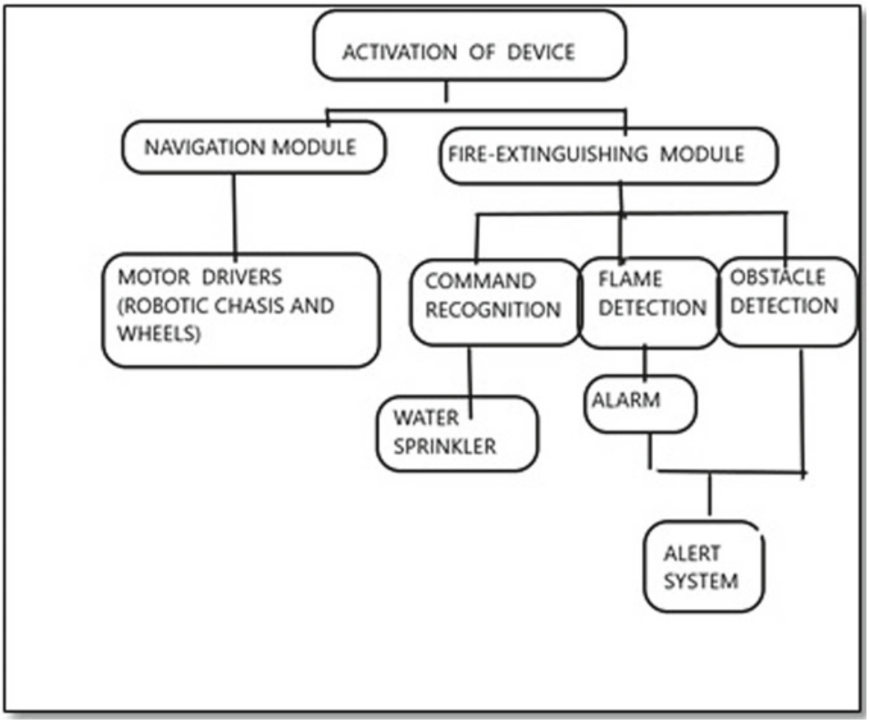

Fig. 1 Block diagram of proposed system

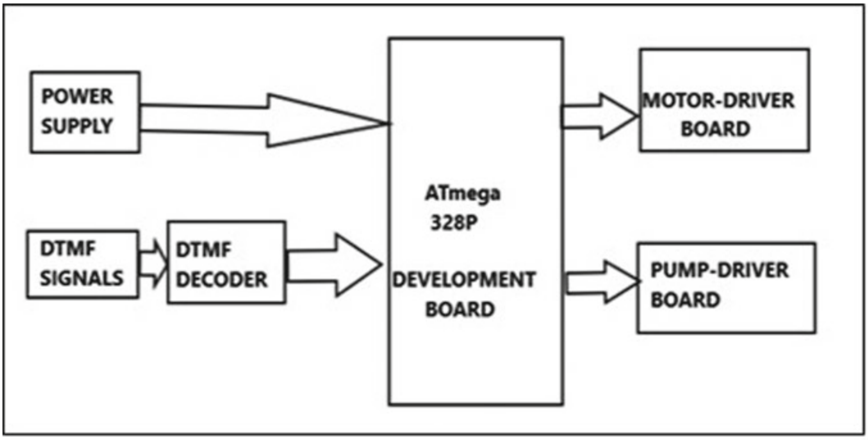

Fig. 2 Block diagram of designed system

The micro-controller in turn controls the extinguishing system. The micro-controller operates in 5 V and its clock speed is 16 MHz and the recommended input voltage 7–12 V, whereas the input voltage limits between 6 and 20 V. The Dual-tone multi- frequency signaling (DTMF) is an in-band telecommunication signaling system which use the voice-frequency band over telephone lines between telephone equipment and other communications devices and switching centers. The motor driver board described the direction of movement of the robot. The motor driver board is used to give high voltage and high current, given as an output to run the motors which are used in the project for the movement of the robot. A simple DC motor is used in our proposed system for the rotation of the wheel, which is responsible for the movement of the robot. DC motors usually convert electrical energy into mechanical energy. To extinguish the fire a pump is used to pump the water on to the flame. A simple motor is used to pump the water. The pumping motor in extinguishing system controls the flow of water coming out of pump. A fire sensor or flame detector is used to detect and respond to the presence of a flame or fire. Responses to a detected flame includes sounding an alarm, deactivating a fuel-line (such as a propane or a natural-gasoline), and activating a fires suppression system. The HC-SR04 Ultrasonic (US) sensor is used to measure distance or sense objects in its path.

The sensor has two sensors which forms the Ultrasonic transmitter and Receiver. The sensor works with the simple formula that

$$\text{Distance} = \text{Speed} \times \text{Time} \tag{1}$$

The universal speed of US wave at room condition is 330 m/s.

The flow-chart explaining the function of each module is:

DTMF (dual tone multi frequency) is used for communication. The firefighting robot flowchart is shown in Fig. 3. Fire-Extinguishing Robot is designed using Arduino. At the time, when the right, middle and front sensors are obstructed, the left engine goes backward for 15 ms and returns to the right. When the obstacle is not detected in the right, middle and front sensors and also not detected in the middle sensor but the obstacle is detected in the front sensor, the vehicle stops for 15 ms, goes back 100 ms. The left engine goes back 500 ms, the right engine goes back 400 ms, the

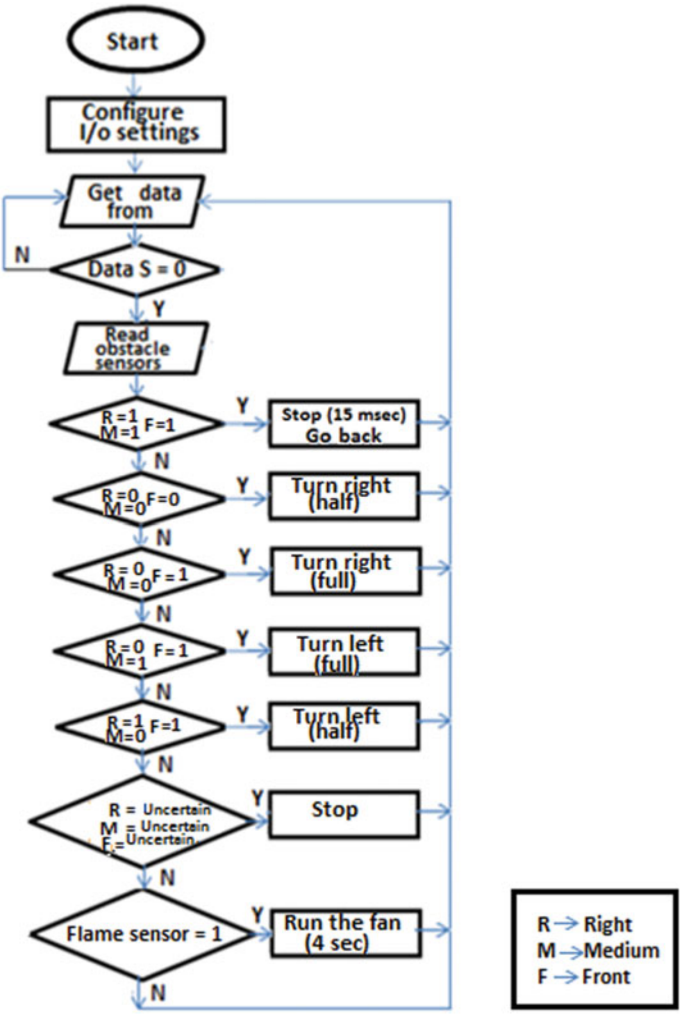

Fig. 3 The flow-chart showing the working of the designed robot

right sensor does not obstruct the center and the front sensor detects the obstacle. When the obstacle is detected in the middle sensor, the vehicle turns 15, 100 ms back, left motor 150 ms forward and right motor 50 ms backward. If anything else hap-pens, if the flame is detected by the sensor, the van will not start or the vehicle will stop.

3 Result

Flame extinguishment has been performed by the proposed firefighting system with the proposed estimation and control method. The Fig. 4 shows motion of the extinguisher in an experimental result on flame extinguishment.

Thick lines: Results. Thin lines: References.

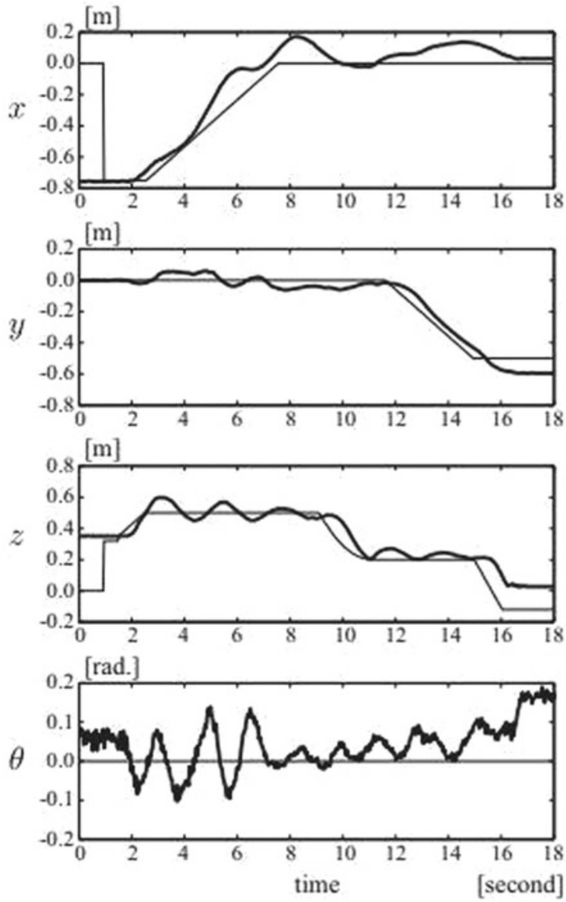

Fig. 4 The graph shows time histories of the states

The flame was extinguished at 11.1 s.

The Fire Fighting Robot that we have designed employs DTMF technology to control the directions of the robot. We have designed the fire detection system using flame sensor that is capable of sensing the flame of wavelength range 600 to 1500 nm, approximately and the sensing range depends on the sensitivity and varies from 10 cm to 1.5 feet and can also overcome any obstacle in its path. The robot can operate in the environment which is inaccessible by human in very short time; the delay employed is very minimal. The robot can finds the fire accurately and efficiently and within minimum time after the fire is detected, it is extinguished and has an efficiency of about 70%.

4 Conclusion

In the present condition the firefighting robot can extinguish fire only in the one direction and not in all direction around the rooms. It can be extended to areal fire extinguisher by replacing the fan used to cool the robotic system by a carbon-di-oxide carrier and by making it to extinguish fires of all the room using microprogramming. Also solar cells can be used to charge or power different components of the circuit in place of battery to make the robot more friendly to our environment.

5 Future Scope

In the present condition, the firefighting robot can extinguish fire only up to a certain height. It being a land rover form of model, can only extinguish and control fire on the ground level. It could be further extended if the entire robotic system can be employed on drones so that it can attain great height and reach the rooftops and namely other places of tall buildings. Also a solar cell could be used to charge or power different components or parts of the robot to reduce the dependency on battery, increase the lifespan of the robot and make our robot more friendly to our environment.

References

1. Hristov, G., Raychev, J., Kinaneva, D., Zahariev, P.: Emerging methods for early detection of forest fires using unmanned aerial vehicles and LoRaWAN sensor networks. In: 28th EAEEIE Annual Conference (EAEEIE) (2018)
2. Krasnov, E., Bagaev, D.: Conceptual analysis of fire fighting robots control systems. In: 2012 IV International Conference “Problems of Cybernetics and Informatics” (PCI)
3. Hasan U.Z., Rakibol, I.R., Shanewaze, S., Nazmul, I.S., Aowrongajab, U.: The design of a novel multi-purpose fire fighting robot with video streaming capability. In: 2019 IEEE 5th International Conference for Convergence in Technology (I2CT)

4. Amit, R.B., Prashant, S.K.: Behavioral analysis of hydraulically driven fire fighting water monitor trailer subjected to type of fire & ways of its fire protection. In: Second International Conference on Emerging Trends in Engineering and Technology, ICETET-09
5. Robin, R.M., Rachel, B., Reginald G., Clint, T.A.: Preliminary domain theory for robot-assisted wildland firefighting. In: 2009 IEEE International Workshop on Safety, Security & Rescue Robotics (SSRR 2009)

Studies on al and Mg Co-Doped ZnO Thin Films Grown by Sol-Gel Technique

Arpita Das and Sohom Chakraborty

Abstract ZnO thin films were grown by sol-gel process on glass substrates and were doped with Mg and Al by introduction of their respective salts in the solution. A series of samples were deposited by maintaining the same dopant concentration in the solution, but by varying the substrate temperature employed in the final annealling step. The concentration of dopant elements in the final ZnO film was estimated using Energy Dispersive X-ray Spectroscopy (EDS) measurements. Surface morphology was observed by using Scanning Electron Microscope (SEM). The energy band-gap was measured using optical absorption studies. Photoluminescence (PL) measurements were carried out at room temperature. Photocurrent measurements were carried out using Ag contacts by exposure to ultraviolet radiation. The results indicate that with increase of substrate temperature from 500 to 650 °C, the band gap reduced from 3.37 to 3.34 eV, along with an evolution of the PL peak. The dark and photocurrent levels were also reduced significantly with increased substrate temperature. A corresponding reduction in photocurrent switching transient times was also observed. The results indicate that higher substrate temperatures cause a precipitation or segregation of dopants into clusters thereby reducing their effectiveness.

Keywords Thin film · Co-doping · Annealing temperature · UV photodetector

1 Introduction

Oxide semiconductors, such as Zinc Oxide (ZnO), Magnesium Oxide (MgO) and Aluminum Oxide (Al_2O_3) are highly effective materials for development of optoelectronic devices. Among them ZnO is an important group II–VI semiconductor with attractive electronic and optoelectronic properties. High electron mobility, high

A. Das · S. Chakraborty (✉)
University of Engineering and Management, Kolkata 700 156, India
e-mail: sohom.chakraborty@uem.edu.in

A. Das
e-mail: arpita.das@uem.edu.in

S. Banerjee and J. K. Mandal (eds.), *Advances in Smart Communication Technology and Information Processing*, Lecture Notes in Networks and Systems 165,
https://doi.org/10.1007/978-981-15-9433-5_42

thermal conductivity, wide and direct band gap (~3.25 eV) and large exciton binding energy (60 meV) make ZnO suitable for a wide range of optoelectronic, field-emission and MEMS devices. These optoelectronic devices include photodetectors, light-emitting diodes and laser diodes [1–4]. The use of ZnO for development of UV photodetectors is a good alternative to GaN based technology [5].

In order to develop heterojunction electronic devices, doping and alloying of ZnO materials must be carried out [6]. Alloying of ZnO with small amounts of MgO leads to an increase in the band gap [7]. As the ionic radii of Mg^{2+} and Zn^{2+} are nearly equal, this results in very little lattice distortion. Challenges arise due to the difference in the crystal structures between ZnO (wurtzite) and MgO (rock-salt) which limit the alloy range and related band-gap tunability [8]. On the other hand, Al-doped ZnO (AZO) films have a significant application as Transparent Conductive Oxides (TCO) used in solar cells, liquid crystal displays, heat mirrors, gas sensors, optical position sensors and acoustic wave transducers, making it a good alternative to the more commonly used Indium Tin Oxide (ITO) [9]. Recently doping and co-doping studies on ZnO has been carried out using various elements to either achieve p-type conductivity (N, In) [10], for spintronics applications (Mn, Co) [11] or to improve electrical and optical properties in ZnO (Ga, Al etc.) [12].

While sol-gel is a relatively simple low cost technique, the process nevertheless allows effective doping of ZnO thin films with various elements by introducing their salts into the precursor solution. In this work, the effect of substrate temperature employed during thin film formation on its various electrical and optical properties have been investigated. The aim of the work is to develop thin film ultraviolet photodetectors with improved sensitivity and switching speeds.

2 Experimental Details

Sol-gel is a well-known technique used for several decades for ZnO thin film deposition on glass substrates [13]. Zinc acetate dihydrate ($Zn(CH_3COO)_2.2H_2O$) was dissolved in Isopropanol (IPA) to form a 0.5 M solution. Diethanolamine (DEA) ($HN(CH_2CH_2OH)_2$) was added at 1:1 ratio to act as a stabilizer. The solution was stirred at 60 °C for 2 h. For Al/Mg co-doping purpose, Magnesium acetate tetrahydrate [$Mg\ (CH_3COO)_2.4H_2O$], and Aluminum Nitrate Nonahydrate ($Al(NO_3)_3{\cdot}9H_2O$) were added respectively. A solution containing 3% Al and 1% Mg was prepared. A series of samples are prepared by dip coating the soda lime glass substrates in solution and preheated at 300 °C for 10 min in air. This process was repeated thrice to generate the desired thickness. During the final heat treatment process, four samples were heated at 500, 550, 600 and 650 °C for 30 min to produce co-doped ZnO thin films. For optical characterization purpose, optical transmission was carried out using an Ocean Optics Jaz Spectrometer. Photoluminescence spectroscopy was carried out using a He-Cd laser as an excitation source. The content of Al/Mg in the ZnO thin films were determined by EDS (Energy-dispersive X-ray Spectroscopy) mounted on a Zeiss EVO 18 scanning electron microscope. UV photo response and persistent photocurrent measurements were conducted using a 30 W Deuterium lamp dispersed by a Princeton Instruments monochromator for optical excitation. Electrical measurements were carried out using silver contacts [14], with the help of a Keithley 236 Source Measure Unit.

3 Results and Discussion

A series of samples were grown where the Al and Mg co-doping concentrations were kept fixed at 3% Al and 1% Mg respectively and the annealing temperature was varied from 500 to 650 °C. The samples details are given in Table 1.

3.1 Optical Transmission

Optical transmission spectroscopy was performed on the co-doped ZnO thin films in order to determine their absorption edge. Figure 1 shows the results for sample IA, and it is observed that the transparency level is above 80%. A clear and sharp optical

Table 1 Details of samples studied

Sample no.	Al, Mg concentration in solution (%)	Substrate temperature (°C)
IA	3, 1	500
IB	3, 1	550
IC	3, 1	600
ID	3, 1	650

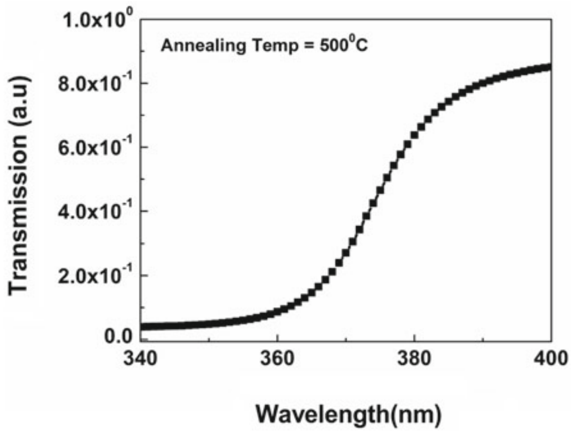

Fig. 1 Optical transmission of ZnO thin film (sample IA)

Table 2 Optical band gap obtained from absorption edge

Sample no.	Substrate temperature (°C)	Optical band gap obtained from absorption edge (eV)
IA	500	3.369
IB	550	3.367
IC	600	3.343
ID	650	3.334

absorption edge is observed. The band-gap was determined by from the peak of the derivative of the absorption coefficient with respect to energy.

The optical band gap calculated from absorption edge for various samples is listed in Table 2. It was observed that absorption edge continuously shifts to lower energy levels as the substrate temperature is increased. This is an interesting result indicating that the doping properties of the ZnO thin film are critically dependent on substrate temperature. It should be noted that while MgO alloying in the film causes a shift of the absorption edge to higher energy, the effect of Al incorporation can also do the same due to the Burstein Moss effect [15].

3.2 Photoluminescence Studies

Room temperature photoluminescence studies of samples IA and ID, grown from the same precursor solution and annealed at 500 °C and 650 °C respectively is shown in Fig. 2 a and b. An interesting result was obtained, indicating that while the optical absorption edge for the two samples showed a relative red-shift for sample ID, an opposite movement can be observed for the photoluminescence peak. The peak shifts to higher energy from 379 nm to 377 nm for the two samples. A related observation is that the peak for sample ID is significantly sharper, and while the PL from sample IA shows a prominent hump at ~420 nm, this is much reduced for sample ID.

It should be noted here that the photoluminescence from Al doped ZnO has been previously reported to be relatively broad, with increases with increased doping level, Furthermore, the transitions from various impurities and point defects introduced during the growth can be observed as shoulders or distinct peaks.

3.3 Scanning Electron Microscopy (SEM) and Energy Dispersive X-Ray Spectroscopy (EDS)

In order to resolve the differences in the optical absorption and photoluminescence results, the surface morphology of the sample ID was studied using scanning electron microcopy (SEM) and doping incorporation was examined using Energy Dispersive

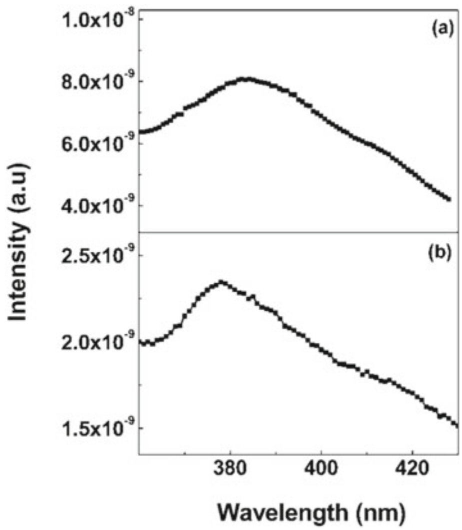

Fig. 2 **a**–**b** Room temperature PL spectra of samples IA and ID respectively

X-ray Spectroscopy (EDS). It was observed from SEM and EDS results that the surface showed crater like features, or regions of embedded particulates, as shown in Fig. 3 a and b.

EDS measurements indicate that at these features, the concentration of impurities can be significantly different from that in the solution. From the region showed in the box, the impurity in atomic % of Al and Mg was 3.7 and 2.7 respectively, which is much higher than that was expected.

We believe that for higher substrate temperatures, there is a significant amount of impurity segregation which form precipitates at such regions shown in Fig. 3 b. These impurities therefore form clusters of high concentration, thereby reducing the overall incorporation level in the rest of the film. However both optical absorption and photoluminescence measurements are dominated by the dopant incorporation of the film and not from specific clusters—unless they are very optically active.

Therefore, with the increase in substrate temperature, the incorporation of impurities falls, or at least become less important in PL and optical absorption measurements. Thus, there is red-shift of the band gap as the Mg and Al incorporation decreases. In the PL measurement, the peak position of highly doped or co-doped samples is determined by the impurity levels in the material. This leads to a red-shift as well as a broadening of the peak. With reduction of impurities, the peak sharpens and shifts to the blue. However the exact mechanism for these processes are still under study and significant work remains before any specific conclusion can be drawn.

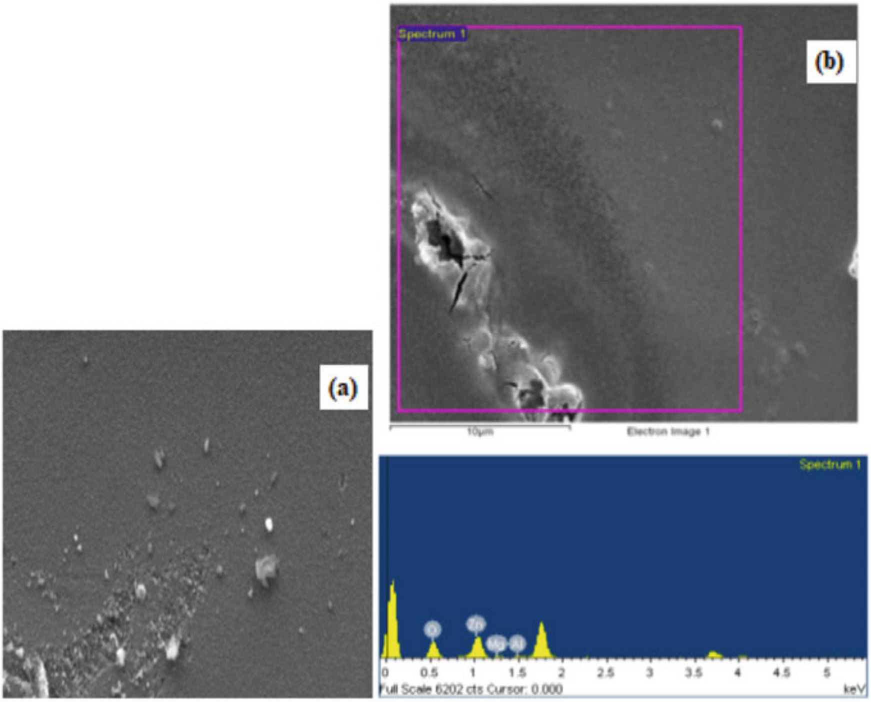

Fig. 3 **a** SEM and **b** EDS image for sample ID

3.4 Photocurrent Measurements

The I-V characteristics of the Al/Mg co-doped ZnO thin film grown on glass substrate were measured using silver contacts. Measurements were made in dark and UV illuminated conditions in air. Figure 4 a–d shows I–V measurements for samples IA, IB, IC and ID.

For sample IA dark current was ~1.7μA at 20 V bias. Upon UV excitation the photocurrent reaches to ~7μA. Figure 4 b shows I–V response of sample IB where dark response is ~19μA and reaches up to ~33μA on UV excitation thereby reducing the I_{ph}/I_{dark} ratio. For sample IC, the dark current and the photocurrent is reduced to ~13μA and ~23μA respectively, further reducing the ratio. However sample ID shows a significantly reduced dark and photo response, where both currents are in the nA range.

These results indicate overall that the effective doping level decreases with the increased substrate temperature. However the exact mechanism is difficult to determine due to the complex transport mechanisms involved as well as the presence of both impurity doping and structural imperfections such as vacancies, which also depend on growth temperature.

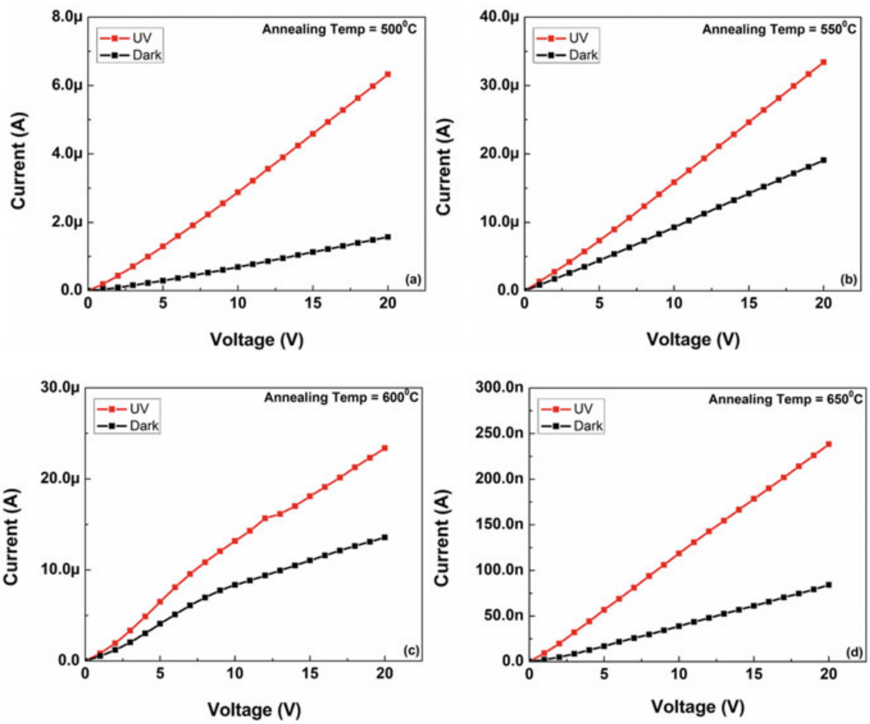

Fig. 4 **a–d** Dark and photocurrent for all samples respectively

The devices IA-ID were tested to determine their photocurrent transient response (Fig. 5 a–d). It is an important parameter, since for practical applications UV photodetectors devices have to be reasonably fast in their switching speeds, Furthermore, the measurement of turn off transients can be used to determine the nature and density of carrier traps in these materials. Since these measurements were carried out at room temperature, we have neglected the effect of oxygen emission due to UV irradiation.

For all samples, the UV light was switched on, held constant for a period of ~300 s and then turned off. For sample IA, the decay transient indicates a single exponential nature, which can be fitted to the equation given below to determine the time constant.

$$I = I_0 e^{-t/T} \tag{1}$$

As the substrate temperature in increased to 550 °C, the decay transient become slower and a second slope is apparent at the end of the transient period. This is more apparently for higher substrate temperatures, where a initial fast decay time is followed by a subsequent very slow process. In fact for 650 °C, the photocurrent appears to saturate or show a very long transient after a fast initial decay. This is presented in Table 3. A similar effect can also be observed in the turn-on transient where a fast initial rise is followed by a relatively slow one.

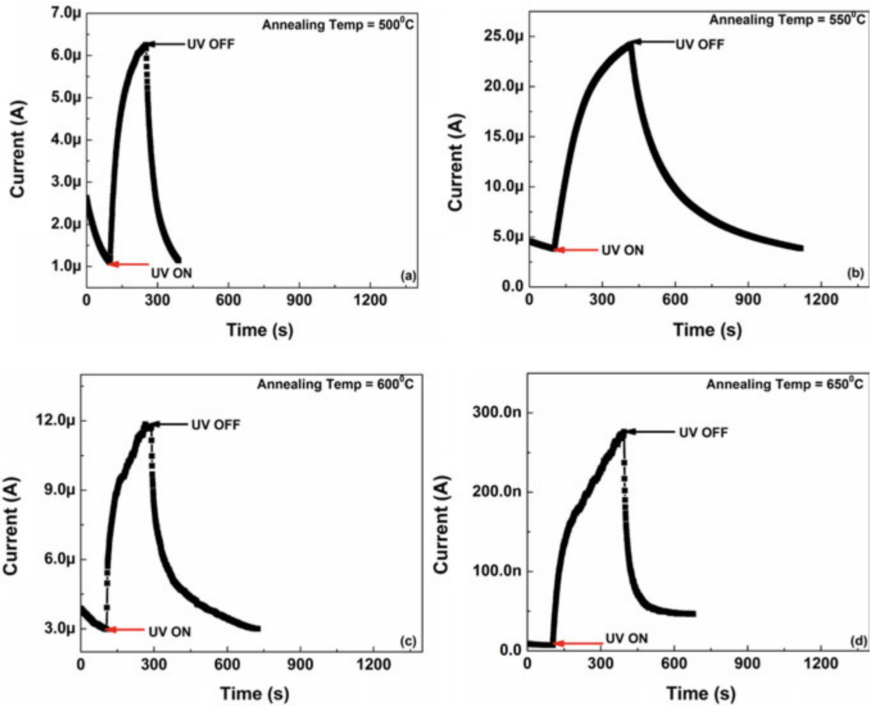

Fig. 5 **a**–**d** Dark and photocurrent transients for all samples

Table 3 Decay time calculation

Sample no.	Substrate temperature (°C)	Initial decay time constant (t_1) (s)	Final decay time constant (t_2) (s)
IA	500	46	137
IB	550	155	694
IC	600	33	746
ID	650	15	1598

It is interesting to note that as the substrate temperature is increased to 650 °C, the initial fast decay transient becomes faster, with a ~10 times reduction from the sample having annealing temperature 550 °C, but the subsequent slow decay increases significantly. The result can be attributed to the trapping de-trapping processes in these materials, which is a function of not only deliberately introduced dopants, but also oxygen and zinc vacancies, interstitials and antisite defects [16].

We believe that with increased substrate temperature, the dopants move to cluster sites, thereby making the initial transient—which is dominated by trapping at dopant sites—faster. However, the higher temperature generates more native defects, which cause the longer transients to be even more pronounced. However more studies are necessary before a clearer picture emerges.

4 Conclusion

In this paper we investigate the deposition of ZnO thin films co-doped with Al and Mg by incorporating their salts into the precursor solution. A range of substrate temperatures were employed, and its effect was studied on the optical and electrical properties of the deposited thin films.

Our results indicate that increase of substrate temperature from 500 to 650 °C reduces the optical band-gap energy from 3.369 to 3.334 eV. However, during the same period the photoluminescence peak narrows and shifts to the blue. SEM and EDS studies show that for higher substrate temperature, the surface shows crater or precipitate type regions which are very rich in dopant atoms, indicating the formation of dopant segregated regions. The result is that the rest of the film, whose properties dominates the optical measurements, is effectively doped less.

These films were studied by ultraviolet photocurrent measurements, and we see a strong increase in the sharpness of the turn off transient for co-doped samples grown at 650 °C. These results are linked to the presence of carrier-trapping and de-trapping mechanisms, which are in turn related to the presence of deliberately introduced impurities, grain size, and the presence of native interstitials and vacancies. Further studies are necessary to pinpoint the various mechanisms.

Acknowledgements This work was carried out at the Institute of Radio Physics and Electronics, University of Calcutta, and the center for Research in Nanoscience and Nanotechnology, University of Calcutta.

References

1. Jagadish, C., Pearton, S.J.: Zinc oxide bulk, thin films, and nanostructures: processing. Properties and Applications. Elsevier, New York (2006)
2. Radzimska, A.K., Jesionowski, T.: Zinc oxide-from synthesis to application: a review. Materials. **7**, 2833–2881 (2014). https://doi.org/10.3390/ma7042833
3. Ozgur, U., Hofstetter, D., Morkoc, H.: ZnO devices and applications: a review of current status and future prospects. Proc. IEEE **98**(7), 1255–1268 (2010). https://doi.org/10.1109/jproc.2010.2044550
4. Sonawane, B.K., Bhole, M.P., Patil, D.S.: Structural, optical and electrical properties of post annealed Mg doped ZnO films for optoelectronics applications. Opt. Quant. Electron. **41**, 17–26 (2009). https://doi.org/10.1007/s11082-009-9317-y
5. Janotti, A., Van de Walle, C.G.: Fundamentals of zinc oxide as a semiconductor. Rep. Prog. Phys. **72**, 126501 (2009). https://doi.org/10.1088/0034-4885/72/12/126501
6. Ellmer, K., Bikowski, A.: Intrinsic and extrinsic doping of ZnO and ZnO alloys. J. Phys. D: Appl. Phys. **49**(41), 413002 (2016). https://doi.org/10.1088/0022-3727/49/41/413002

7. Shan, F.K., Kim, B.I., Liu, G.X., Liu, Z.F., Sohn, J.Y., Lee, W.J., Shin, B.C., Yu, Y.S.: Blueshift of near band edge emission in Mg doped ZnO thin films and aging. J. Appl. Phys. **95**, 4772 (2004). https://doi.org/10.1063/1.1690091
8. Salina, M., Ahmed, R., Suriani, A.B., Rusop, M.: Bandgap alteration of transparent zinc oxide thin film with Mg dopant. Trans. Electr. Electron. Mater. **13**, 64–68 (2012). https://doi.org/10.4313/TEEM.2012.13.2.64
9. Tang, W., Cameron, D.C.: Aluminum-doped zinc oxide transparent conductors deposited by the sol-gel process. Thin Solid Films **238**, 83–87 (1994). https://doi.org/10.1016/0040-6090(94)90653-X
10. Chen, L.L., Lu, J.G., Ye, Z.Z., Lin, Y.M., Zhao, B.H., Ye, Y.M., Li, J.S., Zhu, L.P.: p-type behavior in In–N codoped ZnO thin films. Appl. Phys. Lett. **87**, 252106 (2005). https://doi.org/10.1063/1.2146309
11. Yan, L., Ong, C.K., Rao, X.S.: Magnetic order in Co-doped and (Mn, Co) codoped ZnO thin films by pulsed laser deposition. J. Appl. Phys. **96**, 508–511 (2004). https://doi.org/10.1063/1.1757652
12. Ebrahimifard, R., Golobostanfard, M.R., Abdizadeh, H.: Sol-gel derived Al and Ga co-doped ZnO thin films: an optoelectronic study. Appl. Surf. Sci. **290**, 252–259 (2014). https://doi.org/10.1016/j.apsusc.2013.11.062
13. Bandyopadhyay, S., Paul, G.K., Roy, R., Sen, S.K., Sen, S.: Study of structural and electrical properties of grain-boundary modified ZnO films prepared by sol–gel technique. Mater. Chem. Phys. **74**, 83–91 (2002). https://doi.org/10.1016/S0254-0584(01)00402-3
14. Ikhmayies, S.J., Abu El-Haija, N.M., Ahmad-Bitar, R.N.: A comparison between different ohmic contacts for ZnO thin films. J. Semiconductors **36**(3), 033005 (2015). https://doi.org/10.1088/1674-4926/36/3/033005
15. Hung-Chun Lai, H., Basheer, T., Kuznetsov, V.L., Egdell, R.G., Jacobs, R.M.J., Pepper, M., Edwards, P.P.: Dopant-induced bandgap shift in Al-doped ZnO thin films prepared by spray pyrolysis. J. Appl. Phys. **112**(8), 083708 (2012). https://doi.org/10.1063/1.4759208
16. Das, A., Roy, P.G., Dutta, A., Sen, S., Pramanik, P., Das, D., Banerjee, A., Bhattacharyya, A.: Mg and Al co-doping of ZnO thin films: effect on ultraviolet photoconductivity. Mater. Sci. Semicond. Process **54**, 36–41 (2016). http://dx.doi.org/10.1016/j.mssp.2016.06.018

Grid Connected Rooftop Solar Photo-Voltaic Power Plants Programme in India: A Review of State Solar Rooftop Policies, Net Metering Regulations, Challenges and Way Forward

Arvind Kumar, Hiren Chandra Borah, and Utpal Goswami

Abstract Ministry of New and Renewable Energy (MNRE), Government India has set a target of installing 175 GW of Renewable Energy capacity by the year 2022, which includes 100 GW from Solar, 60 GW from Wind, 10 GW from Bio-Power and 5 GW from Small Hydropower. Under 100 GW, Grid Connected Rooftop Solar share of 40 GW, catering the demand into Residential, Commercial, Industrial, Social, Institutional and Government sectors. This paper examines the development of Grid Connected Rooftop Solar Sector, Current Trends and Major Installation Achievements, Existing State Solar Policies, Metering Regulations, Goals and Challenges in better development and deployment across the county will also discussed.

Keywords Rooftop solar plants · Metering regulations · Solar policies · Central financial assistance · DISCOMs · MNRE

1 Introduction

1.1 Brief About the History

The sources of electricity production such as coal, oil, and natural gas have contributed to one-third of global greenhouse gas emissions. It is essential to raise

A. Kumar (✉)
Ernst & Young LLP, Golf View Corporate Tower B, Golf Course Road, Sector 42, Gurugram, Haryana 122002, India
e-mail: arvind2.kumar@in.ey.com

H. C. Borah
Ministry of New and Renewable Energy, Government of India, Block-14, CGO Complex, Lodhi Road, New Delhi 110003, India
e-mail: hiren.borah@nic.in

U. Goswami
West Bengal Renewable Energy Development Agency, Kolkata, West Bengal 700091, India
e-mail: utpal_cgr@rediffmail.com

S. Banerjee and J. K. Mandal (eds.), *Advances in Smart Communication Technology and Information Processing*, Lecture Notes in Networks and Systems 165,
https://doi.org/10.1007/978-981-15-9433-5_43

the standard of living by providing cleaner and more reliable electricity [1]. Under National Action Plan on Climate Change (NAPCC), the Government of India (GoI) had approved the National Solar Mission (JNNSM) in January 2010, which paved way for the growth of solar capacity in the country [2]. The Renewable Energy sector in India has progressed significantly in the last few years, with the country now home to some of the largest solar installations in the world. The sector received a major boost during 2015 following the Government's decision to revise the national Renewable Energy target. The new target redefined the scale and scope of the sector, especially for solar as the previous target was only 20 GW, over the last few years, the Government has launched a series of supportive policies, regulations and schemes to encourage and accelerate the development of renewable capacities across the country. The dramatic fall in prices of solar PV modules (by over 35% between 2015 and 2017) has further strengthen the growth of the solar. To accomplish the ambitious targets of 175 GW installation of renewable energy by Dec 2022, it is essential that the government creates 330,000 new jobs and livelihood opportunities [3, 4].

The steps taken by the Government for boosting the solar power generation in the country, inter alia, include the (i) announcement of a target of installing 175 GW of Renewable Energy capacity by December 2022, (ii) waiver of Inter State Transmission System (ISTS) charges and losses for Inter- State sale of solar and wind power for projects to be commissioned up to December 2022, (iii) permitting Foreign Direct Investment (FDI) up to 100 percent under the Automatic route, (iv) Notification of standard bidding guidelines to enable distribution licensee to procure solar and wind power at competitive rates in cost effective manner, (v) declaration of trajectory for Renewable Purchase Obligation (RPO) up to year 2022, (vi) implementation of Green Energy Corridor (GEC) project to facilitate grid interaction of large-scale Renewable Energy capacity addition, (vii) notification of standards for deployment of solar photovoltaic systems and, (viii) central Financial Assistance (CFA) and Performance based Incentives under various on-going schemes (i.e. Rooftop Solar, Kisan Urja Suraksha evam Utthaan Mahabhiyan (KUSUM), Solar Park, CPSU scheme, Distributed Grid-connected Solar PV Power Projects in Andaman & Nicobar Islands and Lakshadweep Islands, Decentralized Solar Photovoltaic Systems, Atal Jyoti Yojna (AJAY), Off-Grid and Decentralized Solar Thermal Technologies for Community Cooking, Process Heat and Cooling Applications in Industrial, Institutional and Commercial Establishments etc.).

1.2 Historical Developments of Rooftop Solar Sector in India

The Ministry of New and Renewable Energy has announced the guidelines of grid connected rooftop and small solar power plants programme in June 2014, which was later upscaled on 30.12.2015, with increase in scheme outlay of 300 MWp to 4200 MWp in the country by year 2019–20, of which 2,100 MW was through Central Financial Assistance (CFA) and balance 2,100 MW was without CFA. State Nodal Agencies (SNA's), Solar Energy Corporation of India (SECI), DISCOMs, Public

Sector Undertakings (PSUs) and other Government Agencies were the implementing agencies for this Programme. Central Financial Assistance (CFA) was provided for residential, institutional, social sectors and achievement linked incentives in various slabs have been provided for Government sectors for the sanctioned projects under this. CFA was up to 30% of MNRE benchmark cost or tender cost whichever was lower for general category states and up to 70% of MNRE benchmark cost or tender cost whichever was lower for special category States (i.e. North Eastern States including Sikkim, Uttarakhand, Himachal Pradesh, Jammu and Kashmir, Andaman and Nicobar and Lakshadweep island). Similarly, maximum incentives for Govt. sector was up to 25% of MNRE benchmark cost or tender cost whichever was lower for general category states and up to 60% of MNRE benchmark cost or tender cost whichever was lower for special category States. Majority of the RTS project under this programme was already installed and some of the RTS projects are under final stage of implementation.

The Phase-II programme [5] has two different components viz., CFA for Residential Sector and Incentives in slabs to DISCOMs on incremental RTS capacity installed by the DISCOMs in their distribution area from the installed base capacity (at the end of previous financial year) within the time line of 12 months (financial year-wise, i.e. 01.04.2019 to 31.03.2020 and so on till the duration of the programme). The key features of Phase-II programme under its Operational Guidelines are summarized in the Tables 1 and 2.

Benchmark Cost is a subject to revision on Financial Year (FY) basis. MNRE declares Benchmark Cost effective for the entire FY for various project size ranges/category of States (say Special Category States/General Category States).

To speed up installation of RTS projects in Government Sector, MNRE pursued identification of rooftop space and vacant areas in Government/PSU buildings with various Ministries/Departments. Initial survey data of various organisations of about 55 Ministries/Departments indicated cumulative solar potential of about 5900 MW in Government of India Ministries/departments. To boost the development of RTS power plants in Government/PSU sector, MNRE has kept provision of performance linked financial incentives. Major challenges in the government sector installation may be due to various reasons but not limited to the following e.g. the non-mandatory directions from parent Ministry, non-availability of vacant shadow free roof areas of some department buildings due to working of multiple departments in the same buildings owned by other Govt. Departments, varying capacity limitation as proposed

Table 1 Key features of phase-II rooftop solar programme

Component-A: (central financial assistance)	Residential sector	Setting up of 4000 MW of grid connected rooftop solar projects in residential sector with CFA
Component-B: (Incentives to DISCOMs)	For all sectors including residential, institutional, social, Government, commercial, industrial etc.	Incentives in slabs to DISCOMs based on achievement towards initial 18 GW installation of RTS plants

Table 2 CFA provisions under component-A of phase-II rooftop solar programme

Category of residential segment	Central financial assistance (CFA) provision
Residential sector (maximum up to 3 kW capacity)	40% of benchmark cost or rate discovered through competitive process whichever will be lower
Residential sector (above 3 kW capacity and up to 10 kW capacity) *	40% up to 3 KW + 20% for RTS system above 3 kW and up to 10 kW of Benchmark Cost or Rate discovered through competitive process whichever will be lower
Group housing societies/residential welfare associations (GHS/RWA) etc. for common facilities up to 500 kWp/10 kWp/house), with the upper limit being inclusive of individual rooftop plants already installed by individual residents in that premises at the time of installation of RTS for common activity	20% of benchmark cost or rate discovered through competitive process whichever will be lower

in State regulations for solar rooftop plants in terms of connected electrical load of the consumer/distribution transformer capacity, limitation of maximum capacity of 500 kW/1000 kW for net-metering, non-availability of funds with the government offices for installation under CAPEX mode and long process of signing the Power Purchase Agreement by the Government offices including its field offices with the RESCO developers, floating of individual tenders office-wise instead of tendering of cumulative capacity of the concerned departments/State-wise aggregated, non-availability of net metering for Govt. sector/RESCO projects in regulations of a few States, low feed in tariff etc.

Presently Net Metering, Gross Metering and Virtual Metering are different categories of metering mechanism to support DISCOMs to regulate the RTS generated power for accounting and settlement under billing cycle. Under the provision of net metering, consumer is billed by adjusting the units of power exported to the grid after capitive consumption from the units of power imported from the grid. For example, if an electricity consumer who has installed RTS imported "X" unit of electricity and export "Y" unit of electricity from the total solar electricity generation of Z units to the grid then he will be billed for "X-Y" units during billing cycle. If the exported units are more than these exported units are adjusted in yearly billing or lapsed or he will be paid at a predetermined rate by the DISCOM as specified by the State Electricity Regulatory Commission of the State. In case of Gross metering, all the power generated by RTS is exported to the grid and the electricity consumer is paid for the total generation by the DISCOM at a predetermined rate decided by the state regulator whereas the consumer pay the bill to the DISCOM as per the routine bill generated by the DISCOM at the pre-defined tariff rate. As the rate at which DISCOM charge the consumer for the electricity consumed by him is much higher than the tariff rate at which DISCOM pay to the consumer for the electricity generated and exported through RTS power plant in gross metering mechanism, therefore, from consumer prospective gross regulation is not benificial. Whereas, in case of net metering, concerns of the DISCOM is that they have to purchase the electricity generated by RTS power plants at that time when there is less demand and have to supply electricity when there is peak demand. To safeguard the interest of DISCOMs as well as RTS installer, it is necessary that the tariff under gross metering regulation should also be reasonable so that RTS installer gets a reasonable return on the investment made on installation of RTS power plants. MNRE has been requesting the State Governments, State/Joint Electricity Regulators and DISCOMs to take care of this aspect while fixing the tariff under gross metering regulation.

Grid Connected RTS power plants can be installed in two modes; viz. (i) CAPEX/Ownership mode where investment is made by Rooftop owner and bids are generally invited on total project cost and (ii) RESCO/PPA mode where Project investment is made by 3rd party private/public sector developer and bids are invited on tariff to be charged by developer for recovering the investment. Under this model, Power Purchase Agreement (PPA) is to be signed by the consumer with the project developer. RESCO mode is generally preferable with large size of RTS say 50 KWp and more at one site. However, this may vary depending on bid capacity allowed in the tenders. The operation and maintenance of the plant installed under RESCO mode taken care by the developers.

1.3 State Wise Tentative 40 GW RTS Target Allocation

MNRE in June 2015 has made State wise tentative breakup of 40 GW RTS target in proportion to State wise power consumption and consequent solar power requirement to meet the corresponding Renewable Energy Purchase Obligation (RPO) [6].

1.4 RTS Potential in India

There is a significant potential of small and large scale of grid connected RTS in India. In 2014, National Institute of Solar Energy (NISE) estimated rooftop SPV potential of 42.8 GW in the country.

1.5 Renewable Energy Institutional Structure in India

In addition to existing institutional structure in India, in the year of 2011, GoI has constituted Solar Energy Corporation of India (SECI) to be considered as Implementing Agency for executing the Government aided Solar Energy/Renewable Energy projects in country. SECI plays an integral role in bridging the demand and supply of Solar Energy installations.

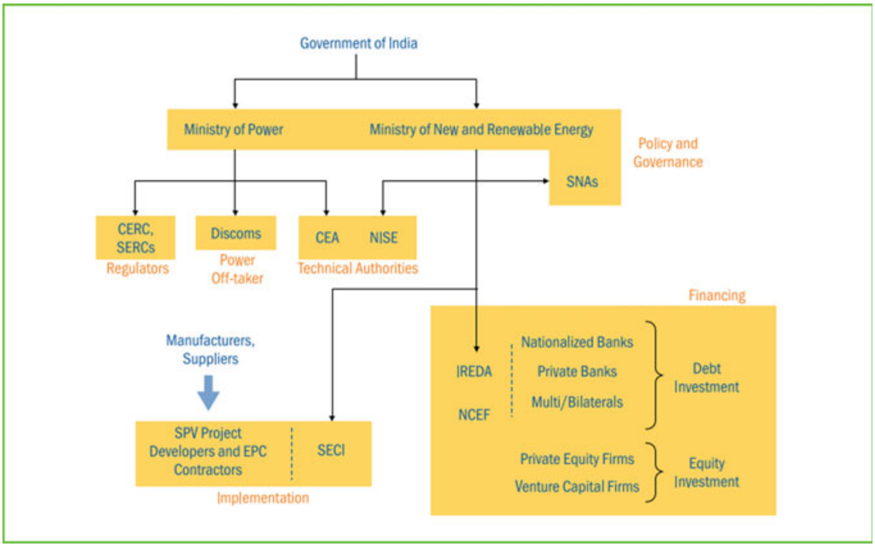

Fig. 1 Major stakeholder structures in promoting solar rooftop segment across the country

Indian Renewable Energy Development Agency (IREDA) is an a Mini Ratna Enterprise under the administrative control of MNRE. IREDA is a Public Limited Government Company established as a Non-Banking Financial Institution in 1987 engaged in promoting, developing and extending financial assistance for setting up projects relating to new and renewable sources of energy and energy efficiency/conservation with the motto: "ENERGY FOR EVER" [7] (Fig. 1).

2 Rooftop Solar Development in India

MNRE has indexed a target to attain 175 GW of renewable energy which would consist of 100 GW from solar energy, 10 GW from bio-power, 60 GW from wind power, and 5 GW from small hydropower plants by the year Dec 2022 [8]. Solar rooftop segment is slowly gaining momentum with considerable interest from various stakeholders like entrepreneurs, developers, financial institutions, development banks, Bilateral and Multilateral donor agencies, end users and government entities. On a very positive note, rooftop solar PV has already attained grid parity in commercial and industrial sectors and is becoming most attractive for residential consumers as well.

To achieve our rooftop solar targets, it is important to develop an ecosystem that ensures information symmetry, access to financing and clear market signals. MNRE in association with stakeholders has developed the State Rooftop Solar Attractiveness Index–SARAL with attempt to evaluate Indian States based on their attractiveness for rooftop solar development. SARAL is the first of its kind index to provide a comprehensive overview of state-level measures adopted to facilitate rooftop solar deployment [9].

2.1 Solar Energy Policies in India

In 1981, Government of India has constituted Commission of Alternate Source of Energy (CASE) under the aegis of Department of Science and Technology with the ambition to reform the Renewable Energy (RE) policies in the States for better development and deployment segment. In 1982, CASE had renamed as Department of Non-Conventional Energy Sources (DNES) and declared full fledged Ministry of Non-Conventional Energy Sources (MNES) in 1992 which was renamed as Ministry of New and Renewable Energy (MNRE) in 2006 [10]. MNRE's guidelines on purchase of power generated through RE sources at the rate of 2.25 per unit with 5% escalation triggered the initial stage development of RE sector. MNRE has issued several policies and guidelines to promote RE sector. Direct and Indirect tax benefit and custom duty exemption was also granted in promotion. Project Developers were also executed from all the income taxes on all the earning made through deployment of RE sources.

The Electricity Act 2003 provides a favorable environment for an overall development and growth of electricity sector in India. The Act has a provision on preferential tariffs and DISCOMs are mandated to procure RE power to fulfill their Renewable Energy Purchase Obligation (RPO) target. National Electricity Policy 2005 provides preferential tariffs on the power generated through RE sources. The Tariff Policy 2006 has kept special provisions to procure minimum amount of power generated through RE sources at a special tariff rate. National Action Plan for Climate Change (NAPCC) 2008 was set up to mitigate the Climate Change issues, with special intensification of Solar Energy [11]. Jawaharlal Nehru National Solar Mission (JNNSM) 2010 has put significance importance on Solar Energy segment. Further in this connection, a National Clean Energy Fund (NCEF) was also setup to provide the financial assistance for deployment of RE sectors with provision to aid fund up to 40% of total project cost.

In 2014, MNRE has formulated guidelines for the Central Financial Assistance up to 30% of MNRE benchmark cost or tender cost whichever was lower for general category states and up to 70% of MNRE benchmark cost or tender cost whichever was lower for special category States (i.e. North Eastern States including Sikkim, Uttarakhand, Himachal Pradesh, Jammu and Kashmir, Andaman & Nicobar and Lakshadweep island). While in 2019, MNRE has launched Phase-II Rooftop Solar Scheme, in which Central Financial Assistance (CFA) amount was again revised to 40% of project cost (for 1 kW to 3 kW) and 20% per kW (for system above 3 kW and up to 10 kW) which can be availed by the Residential Projects only in different tranches according to the capacity of power plant.

Under the umbrella of National Institute of Solar Energy (NISE), the Surya Mitra program has provisions of trainings for graduates/diploma candidates in the installation, commissioning, operations and management of solar power plants. The International Solar Alliance (ISA) headquarters in India (Gurgaon) will likely be a new commencement for solar energy improvement in India [12].

2.2 Major Achievements

In parallel with Government of India's initiative, almost all the States has come up with their own dedicated Solar Energy/Solar Rooftop Policies and Metering Regulations to promote the RTS segment.

E.g. Gujarat facilitates the RTS power plants under net metering for all Government, Commercial and Industrial installations up to 50% of their connected load, whereas in case of Residential Consumers, RTS System capacity is irrespective of their sanctioned load and also have provisions for Electricity Duty and 100% CDM benefits. Karnataka facilitates the RTS systems up to 100% of consumer sanctioned load under Gross Metering and Net Metering mechanism. The RTS systems can be installed up to 100% of Distribution Transformer (DT) capacity with yearly settlement of net energy units with the Grid. Installed RTS capacities are also exempted from mandatory inspection of Chief Electrical Inspectors (CEIs) [13]. Rajasthan Government has kept a provision of 25 GW installation in their policy by 2022. RTS systems can install up to 80% value of load with 30% DT capacity [14]. Rajasthan is one of the preferred State within the country having more than 722 numbers of registered companies for investment [15] for setting up of solar power plants amounting to a total capacity of 16,900 MW in Rajasthan. This preference is often attributed to geographical and climatic advantage of Rajasthan [16].

Further, few States has also initiated various business models (e.g. on-bill financing model of Andhra Pradesh Eastern Power Distribution Company, Utility led non-subsidized model of Kerala State Electricity Board, Group/Virtual Net Metering by BSES Rajdhani Delhi, RESCO model for residential sector project by Chandigarh Electricity Dept., Demand Aggregation model of Madhya Pradesh Urja Vikas Nigam Ltd. for Govt. sector buildings, online demand aggregation of residential sector in Gujarat etc.). In addition, a few States/UTs have started mandating rooftop system for certain category of buildings above certain plot area/connected load e.g. Haryana, Chandigarh, Chhattisgarh and Uttar Pradesh.

Further, few States were also providing State Subsidy (e.g. Gujarat, Tamil Nadu, Uttarakhand, Andhra Pradesh, Madhya Pradesh and Generation Based Incentives by Delhi in initial stages of the programme) besides the Central Government Subsidy. Further, almost all States has exempted CEIG inspection for smaller residential rooftop solar systems for less than 10 kW capacity.

3 Current Challenges and Outlook

MNRE's ambitious target of 175 GWp installation by Dec 2022 has been a driving force for RE sector and is in no small part responsible for introduction of supportive polices and regulations, market mechanism, investor confidence in RE sector in India [17]. Although India has set up 40 GWp target for Rooftop Solar segment for installation by Dec 2022, only 1.92 GWp (Table 3) has been reported as on 17.03.2020 over MNRE online SPIN portal. Further, MNRE under Phase-II Rooftop Solar Programme has already sanctioned 516 MWp capacity among 54 Power Distributing Companies (DISCOM)/electricity Departments of 27 States/UTs for further installation over Residential Sector [18]. Over the last few years, MNRE, GoI has launched a series of supportive of Policies and Guidelines for effective implementation and support RE development and deployment across the country. Dramatic fall of price of Solar Cell (over 35% from 2015–2017), supportive policies and its implementation by States/UTs, low cost financing from Banks/FIs/NBFCs, training of stakeholders and awareness of beneficiary and many more have boosted and catalysed the Renewable Energy sector, while Central Financial Assistance (CFA) and incentives has attracted developers and beneficiaries for rapid adoption. However, there is a need to discuss the major challenges, possible solutions and recommendations to tackle these challenges to attain the steady development growth of renewable sector [19, 20] (Table 4).

The Operation & Maintenance (O&M) of Rooftop solar PV is highly sophisticated in ensuring the adequate efficient output from power plants. Solar developers also offer Annual Maintenance Contract (AMC) during their work contract, in which around 64% of developers agrees that AMC is profitable with 89% or respondent indicating that they are generating additional business opportunities. The Majority of respondent (~62%) are getting less than Two (2) plant service requests in starting years, while another ~24% have indicated to receive Two (2) to Four (4) plant service requests. In plant O&M, main challenge comes into the Inverter failure and generation related issues [21]. There is also an expressed shortage and challenge of skilled and trained manpower, mostly associated with designing SPV systems and integration (Figs. 2 and 3).

Metering Mechanism, Central Financial Assistance and incentives to the State Distribution Companies (DISCOMs)/State Nodal Agencies (SNAs) are the fundamental necessity in development of Rooftop Solar segment due to initial upfront cost. Means of covering investors risk along with greater consumer awareness can be basic building Blocks. Skill Development along with dedicated regulators & utilities, maximizing suitable rooftop space and mandates to drive adoption once viability and ecosystem in place can be considered second building blocks. Nonetheless the major barriers faced during large scale deployment of RTS includes lack of consumer awareness about the benefits of the technologies along with the procedure involved for installation of RTS, involvement of multiple stakeholders (e.g. Beneficiary/Installer/State Nodal Agency/DISCOM/CEIG etc.) expected revenue loss of DISCOMs due to adoption of RTS by high tariff paying consumers, un-availability of solar power during evening peak, lack of standard operating procedure with timelines

Table 3 MNRE state-wise RTS tentative target allocation

S. no.	Name of states/UTs	Tentative target capacity (in MW) by 2022	Installed capacity as o 17.03.2020 (in MW)
1.	Andhra Pradesh	2000	88.03
2.	Bihar	1000	6.95
3.	Chhattisgarh	700	10.39
4.	Delhi	1100	119.40
5.	Gujarat	3200	297.38
6.	Haryana	1600	121.35
7.	Himanchal Pradesh	320	16.73
8.	Jammu & Kashmir	450	10.81
9.	Jharkhand	800	17.12
10.	Karnataka	2300	134.60
11.	Kerala	800	44.96
12.	Madhya Pradesh	2200	50.23
13.	Maharashtra	4700	222.11
14.	Orissa	1000	14.37
15.	Punjab	2000	67.94
16.	Rajasthan	2300	123.77
17.	Tamil Nadu	3500	155.99
18.	Telangana	2000	77.58
19.	Uttarakhand	350	77.12
20.	Uttar Pradesh	4300	142.59
21.	West Bengal	2100	44.46
22.	Arunachal Pradesh	50	0.22
23.	Assam	250	30.56
24.	Manipur	50	5.50
25.	Meghalaya	50	0.12
26.	Mizoram	50	1.43
27.	Nagaland	50	0.08
28.	Sikkim	50	0.07
29.	Tripura	50	2.96
30.	Chandigarh	100	30.15
31.	Goa	150	0.83
32.	Dadra & Nagar Haveli	200	0.48
33.	Daman & Diu	100	0.39
34.	Puducherry	100	1.92
35.	Andaman & Nicobar	20	4.59
36.	Lakshadweep	10	0.00
	Total	40,000	1923.17

Table 4 Summary of mandatory solar notifications

S. no.	Name of Issuing Authority	Date of Issue	Mandatory Solar provisions for
1.	MoHUA (as building bye law*)	Year 2016	Residential—(plotted/group housing having 50 Sqm and above shadow free rooftop area) Education/Institute/C&I/Recreational/Mercentile—having plot size of 500 sqm and above)
2.	Government of Haryana	03.09.2014	Residential—plot size of 500 sq.yard and above, Private institute/Govt. Building: Connected load 30 kW and above, Private Hospital/C&I: Connected load of 50 kW and above, New Housing complexes: plot size of 0.5 acre and above, Water lifting stations: Connected load of 100 kW and above
3.	Government of Chandigarh	12.04.2016	Govt./Semi Govt. buildings, autonomous institutions, private builder/developers (educational/institutional/business/C&I, conference/storage) having connected load of 50 kW and above
4.	Govt. of Chandigarh	18.05.2016	Residential: plot size of 500 sq. yard and above Private institute/Govt. building: connected load 30 kW and above, Private hospital/C&I: Connected load of 50 kW and above, New housing complexes: plot size of 0.5 acre and above
5.	Govt. of Uttar Pradesh	09.10.2015	Govt./Semi Govt. buildings, autonomous body, housing and commercial complex having area of 5000 sqm and above

*Advisory in nature, State may follow

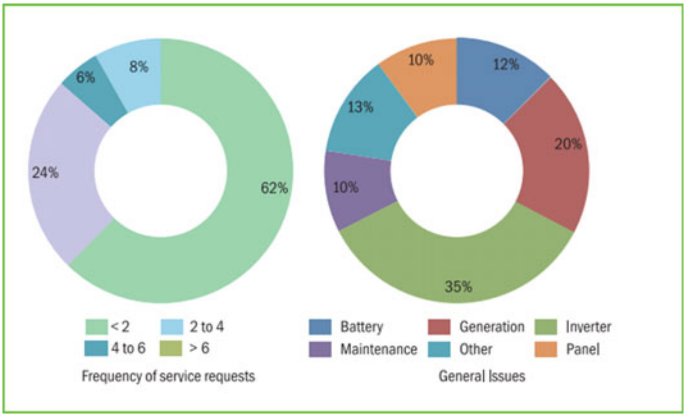

Fig. 2 Challenge on operation and maintenance requirement

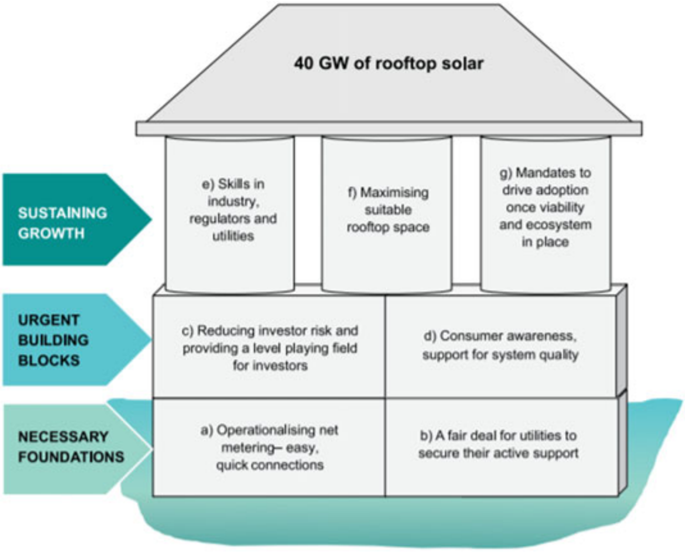

Fig. 3 Basic building block for growth of RTS segment in India (*Source* [17])

by DISCOMs along with single window clearance portal, lack of sufficient manufacturing facilities, lack of skilled workforce, high initial investment, lack of innovative business models and challenges for its implementation, Regulation and Policy challenges {e.g. State Electricity Regulatory Commissions (SERCs) as in Table 5, quoted Different values of Distribution Transformer (DT) Capacity and Connected Load}. Grid likely to become locally less resilient with massive PV deployment hence the sizing of the power transformers and connected load ought to be considered for future deployment of medium sized solar photovoltaics in buildings), multiple tenders, delay in tendering process for rate discovery/vendor empanelment, delay in signing of Power Purchase Agreement for RESCO mode etc.

Table 5 Sample comparative analysis of grid interactive metering regulations of different states

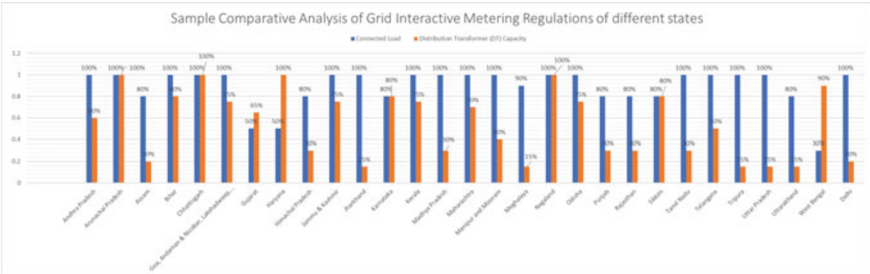

Source State electricity regulatory commission/joint electricity regulatory commission

However, the Government is taking a number of steps to promote rooftop solar in the country, these include: (i) Under phase II of the programme Electricity Distribution Companies (DISCOMs) have been made as implementing agencies and CFA is available for residential sector only. Incentives for the DISCOMs for achievement of additional capacity above baseline has also been provided for. (ii) MNRE is requesting States to notify model operating procedure for RTS/exemption from CEIG inspection for smaller plants/issue of mandatory notification/provision in building bye laws, (iii) Assisting States in development of online portal/demand aggregation, (iv) Prepared model MoU, CAPEX/RESCO Models, PPA Agreement for expeditious implementation of RTS projects in Govt. Sector, (v) Allocated Ministry-wise expert PSUs for handholding and support in implementation of RTS projects in various Ministries/Departments, (vi) Creation of SPIN-an online platform for expediting project approval, report submission and monitoring progress of implementation of RTS projects, (vii) Facilitated availability of concessional loans from World Bank and Asian Development Bank (ADB) through SBI and PNB respectively, for disbursal of loans to industrial and commercial sectors, where CFA/Incentive is not being provided by the Ministry. In addition, initiatives have also been taken for providing financing of residential sector projects through funding of World Bank and Asian Development Bank and (viii) Initiated various IEC activities.

4 Conclusion

A support of Central Government Ministries/Departments/Autonomos Bodies/PSUs along with State Government will be highly solicited in reference to formation of dedicated Solar Rooftop Polices and Regulations, which will create a favorable environment for better development of RTS segment on ground. States have kept limit on DT loading for Solar Rooftop Power Plants, which is limiting the RTS installation in distribution network area. Development of standard operating procedure guidelines and digital clearance and monitoring platform is also necessary for fast track deployment process. Both the CAPEX/RESCO mode are prevalent in India. To safeguard the interest of DISCOMs as well as developers, it is necessary that the tariff under gross metering regulation should also be reasonable so that developers can get a reasonable return on the investment made on installation of power plants. State wise ranking index for rooftop deployment will assist to low ranking States to gain best experience of high performing States to perform better in addition to creating a competitive environment among States.

A Review of State experience in RTPV installation (Table 3) indicates direct dominance of DT capacity and sanctioned load over the size of power plant installation. Post 2015, Central Financial Assistance (CFA) and Low Rates of Modules have played a very vital role in attractiveness in sector development.

Multilateral Soft Loans, Central Financial Assistance (CFA), Role of State Government and market-based approach and different business models also played effective role in encouragement of consumer behaviors towards RTS adoption.

Residential and Commercial sectors have highest number of installations due to their adoptability. Comparative analysis of State Policies and Metering Regulation (Table 3) is important in promotion of RTS in States. There is a need to address major challenges e.g. lack of consumer awareness about the benefits of the technologies and administrative procedures, involvement of multiple stakeholders (e.g. beneficiary/installer/State Nodal Agency/DISCOM/CEIG etc.) expected revenue loss of DISCOMs, lack of demand side management, lack of standard operating Guidelines and digital clearance portal, lack of sufficient manufacturing facilities and skilled workforce, high initial upfront investment, lack of innovative business models and implementation challenges, Regulatory and Policy level challenges (e.g. variable values of DT and Connected load), multiple tenders in vendor empanelment, delay in PPA signing etc. Higher deployment of RTS will likely to boost the manufacturing capability of not even Solar Modules, but also solar cell, inverter, batteries, innovative structures, wires, connectors, meters and other necessary equipments in Country.

While in other aspect, capacity building of Systems Integrators, Manufacturers, Engineers, Operation & Maintenance (O&M), Testing facilitators are another key challenge in front of Central as well as State Government departments.

An outlook, linking for State Solar Policies and Metering Regulations with current existing allocated targets, it is recommended to sensitize the existing State Solar Policies and Regulation in compliance with the Central Scheme and Guidelines and also ensure the skill development and capacity buildings of System Integrators, Manufacturer, DISCOM Engineers to create the favorable environment for developers for their healthy participation and execution of installations to accomplish 40 GWp RTS target by Dec 2022.

References

1. Chr, V.Z.: Effective use of renewable energies for greenhouse heating. Renew. Energy **5**(1–4), 479–485 (1994)
2. The Sate of Renewable Energy Index: (2019). https://shaktifoundation.in/wp-content/uploads/2019/04/State-of-Renewable-Energy-in-India.pdf
3. Harrison, T., Kostka, G.: Balancing priorities, aligning interests: developing mitigation capacity in China and India. Comp. Polit. Stud. **47**, 450–480 (2014)
4. Shukla, A.K.: Renewable energy resources in South Asian countries: challenges, policy and recommendations. Resour. Efficient Technol. **3**, 342–346 (2017)
5. The Operation Guidelines for implementation of Phase-II of Grid-connected Rooftop Solar Programme for achieving cumulative capacity of 40 GWp RTS projects by the year 2022. http://164.100.77.194/img/documents/uploads/7ccd3b4b3bb94a51af516e2ee4fdede3.pdf
6. MNRE's DO. No. 03/13/2015-16/GCRT Dated 30th June 2015 on "State-wise and Year-wise targets for installation of 40,000 MWp Grid-connected Solar Rooftop Systems" in India
7. IREDA Homepage. https://ireda.in/forms/contentpage.aspx?lid=820
8. Charles Rajesh Kumar, J., Mary Arunsi, B., Jenova, R., Majid, M.A.: Sustainable waste management through waste to energy technologies in India—opportunities and environmental impacts. Int. J. Renew. Energy Res. 9(1), 309–342 (2019)
9. PIB Press Release on Power Minister Shri RK Singh launches SARAL: State Rooftop Solar Attractiveness Index' during RPM Meeting. https://pib.gov.in/newsite/PrintRelease.aspx?relid=192752

10. Kumar, S., Meena, R.L.: Renewable energy sources—policies in India. Int. J. Appl. Environ. Sci. **12**(2), 293–297 (2017)
11. Sawhney, A.: Policy monitor: renewable energy policy in india: addressing energy poverty and climate mitigation. Rev. Environ. Econ. Policy **7**(2), 296–312 (2013)
12. Charles Rajesh Kumar, J., Majid, M.A.: Renewable energy for sustainable development in India: current status, future prospects, challenges, employment, and investment opportunities. Energy Sustain. Soc. **10**(2), (2020)
13. Karnataka Solar Policy 2014–2022: https://kredlinfo.in/solargrid/Solar%20Policy%202014-2021.pdf
14. Rajasthan Solar Energy Policy—2019: https://energy.rajasthan.gov.in/content/dam/raj/energy/rrecl/pdf/Home%20Page/Rajasthan%20Solar%20Energy%20Policy%202019.pdf
15. Sisodia, G.S., Singh, P.: The status of renewable energy research on India. Energy Procedia **95**, 416–423 (2016)
16. Pandey, S., Singh, V.S., Gangwar, N.P., Vijayvrgia, M.M., Prakash, C., Pandey, D.N.: Determinants of success for promoting solar energy in Rajasthan, India. Renew. Sustain. Energy Rev. **16**(6), 3593–3598 (2012)
17. Sawhney, A.: Policy monitor: renewable energy policy in india: addressing energy poverty and climate mitigation. Rev. Environ. Econ. Policy **7**(2), 296–312 (2013)
18. Online data from MNRE's Physical Progress Achievement: https://mnre.gov.in/the-ministry/physical-progress
19. Bhattacharyya, S.C.: Shaping a sustainable energy future for India: management challenges. Energy Policy **38**(8), 4173–4185
20. Singh, S., Boparai, K.C.: Secretary, India and renewable energy: a future challenge. Renew. Energy **15**(1–4), 16–21
21. Goel, Malti: Solar Rooftop in India: policies, challenges and outlook. Green Energy Environ. **1**, 129–137 (2016)

Design of a Microring Resonator Having High Sensitivity for Biosensing Applications

Piyali Mukherjee and N. R. Das

Abstract Sensors used for biological and chemical sensing have been active research topics because of several potential applications like medical diagnostics, environment monitoring, etc. Among the existing sensors, integrated optical waveguides based sensors making use of photonic microring resonators possess a promising performance. When light propagates through the microring, it generates an evanescent field that extends beyond the structure which is sensitive to the refractive index of the analytes adsorbed on its surface, and it modulates the resonant wavelength of light within the cavity. This sensing capability has been utilized for the detection of biological targets and facilitates label-free detection. This paper presents the design of a laterally coupled microring resonator having high sensitivity for biosensing applications. Silicon-on-Insulator (SOI) based resonator is preferred because of its small size, low cost and high sensitivity. Simulation results are done to validate with the existing design structures and propose smaller dimension structure that can still achieve high sensing efficiency of the order of 10^{-8} RIU.

Keywords Microring resonator · Biosensing · Silicon-on-insulator · Laterally coupled · High sensitivity

1 Introduction

Optical ring resonators have emerged almost a decade ago and have found their way into many applications. They can be custom-designed for diverse applications, such as lasers, amplifiers, sensors, optical filters, switches, digital logic gates, etc. [1, 2].

P. Mukherjee (✉)
University of Engineering & Management, Kolkata, India
e-mail: piyali.mukherjee@uem.edu.in

P. Mukherjee · N. R. Das
Institute of Radio Physics & Electronics, University of Calcutta, Kolkata, India
e-mail: nrd@ieee.org

S. Banerjee and J. K. Mandal (eds.), *Advances in Smart Communication Technology and Information Processing*, Lecture Notes in Networks and Systems 165,
https://doi.org/10.1007/978-981-15-9433-5_44

Medical Science outshines other areas of research. Needless to say the direct impact of medical science on our health and to the society at large. The existing system believes in treatment only after the appearance of symptoms. This leads to delayed diagnosis and prolonged duration of care. The major hindrance of the existing system is the limited number of staff which may lead to neglect of patients.

With the advancement in technology, molecular diagnosis methods have evolved that can sense abnormality before symptoms are generated [3, 4]. The commonly used diagnosis methods are Polymerase Chain Reaction (PCR), Micro-array Assay, Enzyme-Linked Immunosorbent Assay (ELISA), etc. These methods are expensive, requires skilled people to operate, and the result generation is time consuming. This leads to motivation for a simple, inexpensive, automated point-of-care system.

Silicon, a leading material in micro-optoelectronics makes SOI based devices extremely low cost and compatible with existing technology. Silicon and its oxide layer provides large refractive index difference, which allows designing of single-mode waveguide enabling large scale integration, hence making SOI a suitable choice for device design. This paper deals with the designing of laterally coupled, high refractive index contrast silicon-on-insulator (SOI) microring resonator [5] sensor for biosensing. It provides analytical derivations and simulation results to validate with the existing design structures and propose smaller dimension structure that can still achieve high sensing efficiency.

2 Working of Microring Resonators

A micro-ring resonator in the simplest form consists of a ring waveguide that channels light and serves as a resonant cavity that supports certain wavelengths of light in both longitudinal and transverse modes and is responsible for its intensity build-up. A coupling mechanism exists such that the ring waveguide couples with the straight bus waveguides that servers as input and output ports (Fig. 1).

The relation between the electric field components existing between the waveguides can be obtained by solving the electric field interactions by transfer matrix

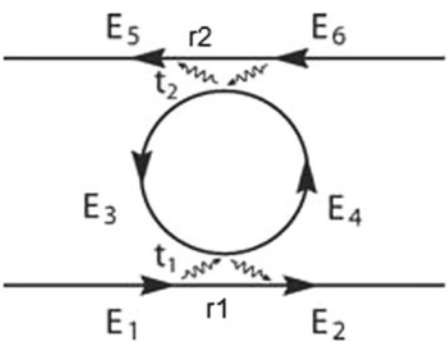

Fig. 1 Fields associated with add-drop resonator

given by [13]:

$$\begin{bmatrix} E_4(\omega) \\ E_2(\omega) \end{bmatrix} = \begin{bmatrix} r_1 r_2 & it_1 \\ it_1 & r_1 \end{bmatrix} \begin{bmatrix} E_3(\omega) \\ E_1(\omega) \end{bmatrix} \tag{1}$$

$$\begin{bmatrix} E_5(\omega) \\ E_4(\omega) \end{bmatrix} = \begin{bmatrix} r_2 & it_2 \\ it_2 & r_1 r_2 \end{bmatrix} \begin{bmatrix} E_6(\omega) \\ E_3(\omega) \end{bmatrix} \tag{2}$$

where, r_1, r_2, are the self-coupling coefficients, t_1, t_2, are the cross-coupling coefficients. Within the ring waveguide, the fields are related as:

$$E_3 = ae^{i\varphi} E_4 \tag{3}$$

where, a is the transmission amplitude that takes into account the propagation loss within the waveguide, $\varphi = \beta L$ is the phase shift with β as the propagation constant of the circulating mode and L is the round trip length.

The ring resonator acts as an add-drop filter and is coupled to two bus waveguides, the incident wavelengths which are supported by the cavity gets coupled and is transmitted through the drop port and the rest through the pass/through port. The transmission coefficient of the two ports with respect to the input port is obtained as:

$$T_{pass} = \frac{I_2}{I_1} = \frac{r_2^2 a^2 - 2r_1 r_2 a cos\varphi + r_1^2}{1 - 2r_1 r_2 a cos\varphi + (r_1 r_2 a)^2} \tag{4}$$

$$T_{drop} = \frac{I_5}{I_1} = \frac{(1 - r_1^2)(1 - r_2^2)a}{1 - 2r_1 r_2 a cos\varphi + (r_1 r_2 a)^2} \tag{5}$$

The ring will be in resonance if the wavelength of light is an integer multiple of the optical ring length. From the transmission spectrum, the resonance condition is obtained as:

$$\lambda_r \frac{n_{eff} L}{m}; m = 1, 2, 3, \ldots \tag{6}$$

with $n_{eff} = \frac{\beta}{k}$, [6] k being the wave number.

3 Design Issues

3.1 Silicon/Silicon Dioxide (SOI) Based Resonator

Silicon, a leading material in micro-optoelectronics makes SOI-based photonic devices potentially economical and compatible with existing electronic technology.

Passive silicon waveguide structures have revealed an unprecedented reduction in footprint of waveguides and especially in wavelength-selective devices [7, 8]. Silicon and its oxide layer provides large refractive index difference that allows designing of single-mode waveguide and compact integrated devices that enables large scale integration, making SOI a suitable choice for device design.

3.2 Laterally Coupled Resonator Sensor

Coupling between the ring and the straight waveguides can be achieved either vertically or laterally. Vertically coupled resonator designs proposed so far have advantages of higher modal overlap, and that waveguides are buried and remain isolated from the effects of surface treatments.

The laterally coupled ring resonators, offer several other advantages like their coplanar structure results in easy design and since they employ propagation of TE mode, these structures lead to modal confinement and lower radiation leakage loss. Due to the inherent advantages the laterally coupled ring resonators possess, they are preferred to be used for sensor design (Fig. 2).

4 Performance Parameters Evaluation for Sensor Design

The performance parameters for sensor design can be obtained from the transmission spectrum of the resonator as well as they can be obtained analytically. All the device performance parameters are governed by the structural parameter of the resonator. So, defining the ring dimensions are essential for device design.

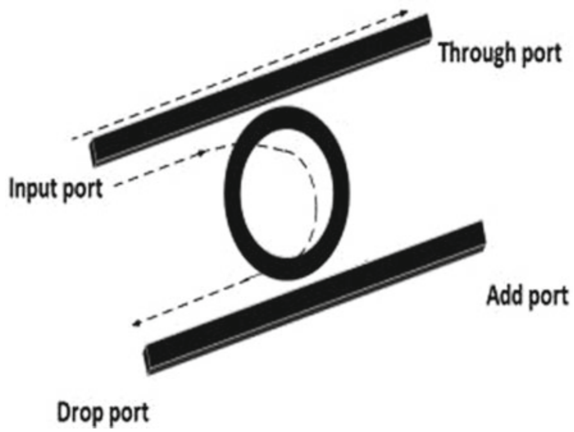

Fig. 2 Schematic of lateral coupling mechanism

4.1 Free Spectral Range (FSR)

FSR is the distance between two consecutive resonant peaks of the transmission spectrum at the drop port. This determines selectivity of the sensor. Mathematically, it is given by:

$$FSR = \frac{\lambda_{res}^2}{n_g L} \tag{7}$$

n_g is the group index. The group index takes into account the dispersion in the waveguide and is given as [9]:

$$n_g = n_{eff} - \lambda_0 \frac{dn_{eff}}{d\lambda} \tag{8}$$

4.2 Quality Factor

Quality factor of a resonator is a measure of the sharpness of the resonance relative to its center frequency.

$$Q - factor = \frac{\lambda_{res}}{FWHM} = \frac{\pi n_g L \sqrt{r_1 r_2 a}}{\lambda_{res}(1 - r_1 r_2 a)} \tag{9}$$

4.3 Resonator Sensitivity

The ring resonator is sensitive to a multitude of effects, and hence attractive for the use in sensing applications. There are two sensing mechanisms that are commonly used. They are homogeneous sensing and surface sensing [10], a schematic view of which is shown [4] (Fig. 3).

In homogeneous sensing, the waveguide core is surrounded by an analyte solution, which serves as the top cladding of the waveguide. The analyte modifies the bulk refractive index of the solution and in turn the effective index of the guided mode. In surface sensing, the device is pretreated to have binding sites on its surfaces, which selectively binds the specific analyte [11]. Accordingly, this method enables specificity as well as label-free detection in addition to high sensitivity.

To transduce the amount of analytes to a detectable signal of a microring sensor, two sensing schemes used are Resonant-wavelength-shift scheme and Intensity-variation scheme. The resonant-wavelength-shift scheme monitors the shift of a resonant wavelength caused by analytes. The intensity-variation scheme monitors the

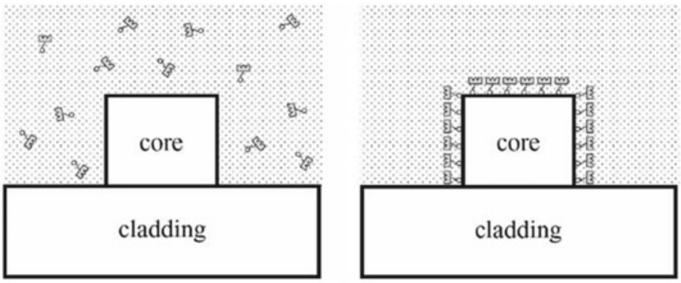

Fig. 3 Sensing mechanisms: homogeneous sensing (left) and surface sensing (right)

		Sensing Scheme	
		resonant wavelength shift	intensity variation
Sensing Mechanism	homogeneous	$S \equiv \frac{\partial \lambda_c}{\partial n_c} = \frac{\partial \lambda_c}{\partial n_{eff}} \cdot \frac{\partial n_{eff}}{\partial n_c}$	$S \equiv \frac{\partial I}{\partial n_c} = \frac{\partial I}{\partial n_{eff}} \cdot \frac{\partial n_{eff}}{\partial n_c}$
	surface	$S \equiv \frac{\partial \lambda_c}{\partial t} = \frac{\partial \lambda_c}{\partial n_{eff}} \cdot \frac{\partial n_{eff}}{\partial t}$	$S \equiv \frac{\partial I}{\partial t} = \frac{\partial I}{\partial n_{eff}} \cdot \frac{\partial n_{eff}}{\partial t}$

Fig. 4 Sensitivity for different combinations of sensing schemes and sensing mechanisms

output intensity variation at the wavelength with the highest slope in the transmission spectrum [12].

To evaluate device performance, sensitivity is defined as the ratio of the change in the measured optical parameter to the change in the waveguide parameter affected by analytes. A table of sensitivity for different combinations of sensing schemes and sensing mechanisms is stated in Fig. 4.

5 Results and Analysis of the Performance Parameters

Several performance parameters of the ring resonator are directly related to the transmission spectrum. So, evaluating and obtaining the transmission spectrum is important. The transmission spectrum of add-drop resonator at both transmission port and drop port is shown in Fig. 5.

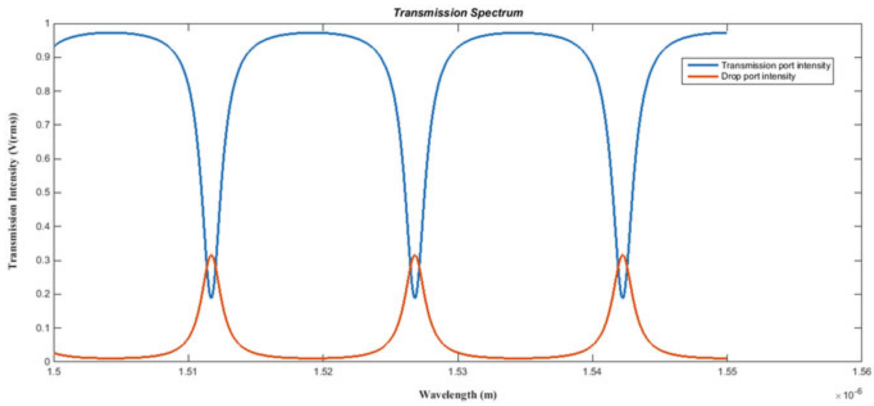

Fig. 5 Transmission spectrum for an add-drop resonator

The difference in wavelengths between the two peaks at the drop port transmission gives the free spectral range (FSR) of the sensor.

With the variation in the ring dimension, the obtained spectrum also varies. As the ring radius increases, the round trip length of the ring resonator increases [13] (Fig. 6).

The ring dimensions also affect another parameter, namely Quality factor. A plot of Q-factor for different lengths of the ring is shown in Fig. 7.

For better performance of the sensor, high Q-factor is required, this in turns leads to the requirement of large ring dimensions. The ring length cannot be increased indefinitely as it will result in a large sensor dimension. So, loss minimization (propagation loss and bend loss) within the cavity is required. The variation of Q-factor with different values of propagation loss figures has been obtained in Fig. 8 which

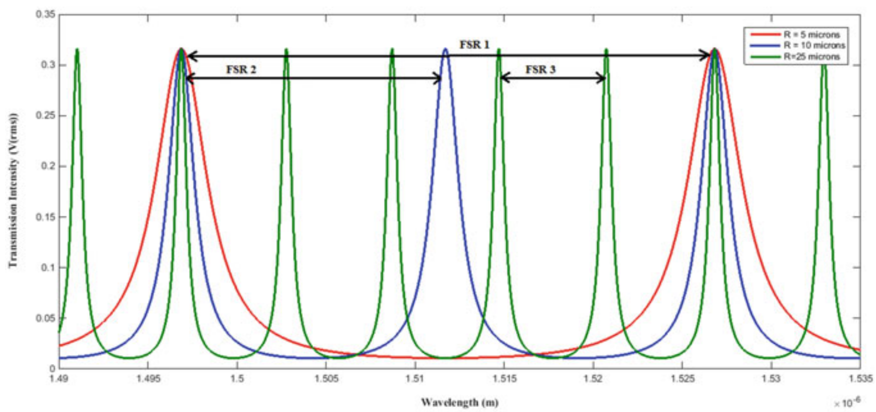

Fig. 6 Variation of FSR with resonator ring radius

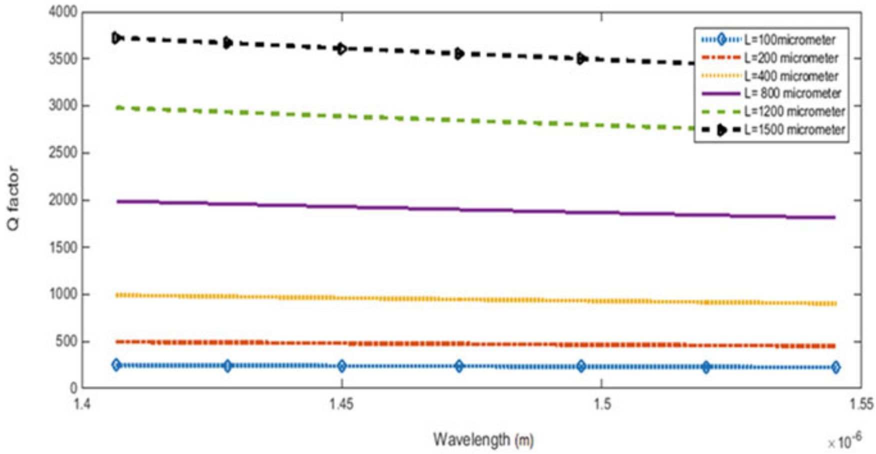

Fig. 7 Variation of Q-factor with wavelength for varying round trip lengths

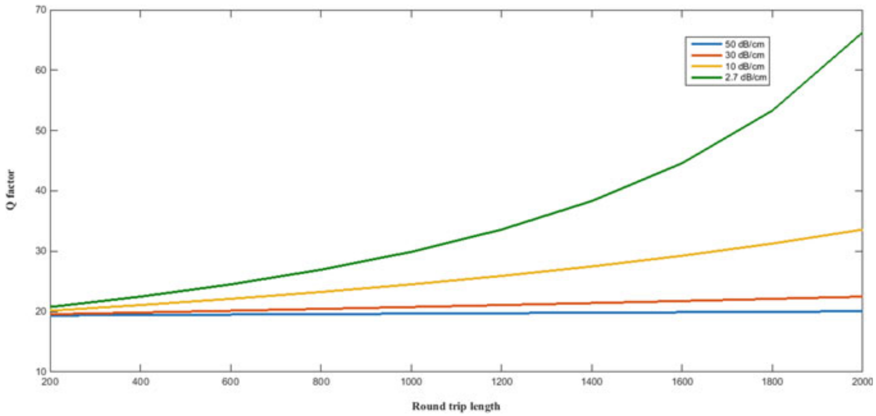

Fig. 8 Variation of Q-factor with round trip length for varying losses

implies that Q-factor improves for lower propagation loss figures.

Mode is the spatial distribution of optical energy in one or more dimensions of light propagation. The fundamental modes, i.e., the Transverse Electric (TE) and Transverse Magnetic (TM) modes have their maxima within the core and drops sinusoidally towards the edge and finally becomes exponential outside the core. TE mode leads to greater confinement than TM thus leads to designing of waveguides that confines transverse electric modes.

For critical coupling, the propagation constants in both the ring and the bus waveguide are matched and the effective index of the mode is found to be 2.3869 for a dimension of 450 nm width and 220 nm height waveguide (Fig. 9), which has been proposed so far. These waveguides offer very little modal radiations outside it which

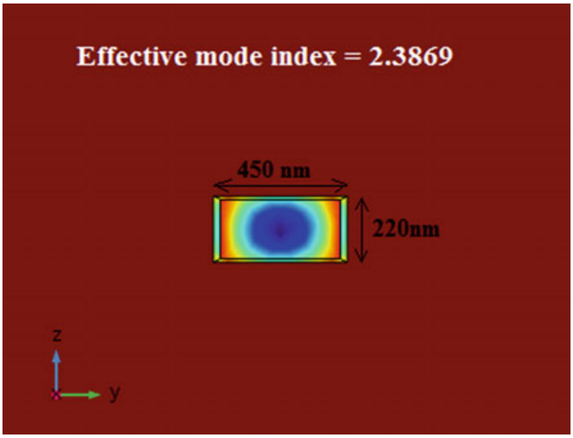

Fig. 9 TE mode for waveguide dimension of 450 × 220 nm

leads to lower evanescent coupling and hence reduces sensitivity of the resonator sensor. This possesses necessity for reduction in waveguide dimension that will result in greater evanescent fields and will not lead to excess modal radiations.

To comply with the need of reduction in waveguide dimension, the effective index of the mode is found to be 2.2445 for guide dimension of 420 nm width and 200 nm height (Fig. 10). This modal field distribution reveals that there is an increase in the evanescent field that will result in greater coupling.

Sensitivity is a crucial parameter to determine the performance of a sensor. It is because the resonator is sensitive to refractive index change of the guided mode that it is being made used as a sensor.

Here, the resonant-wavelength-shift scheme is adopted, where the resonant wavelength for the detectable analyte shifts in the transmission spectrum. This is observed in Fig. 11, where a shift in the resonant wavelength occurs when de-ionized water

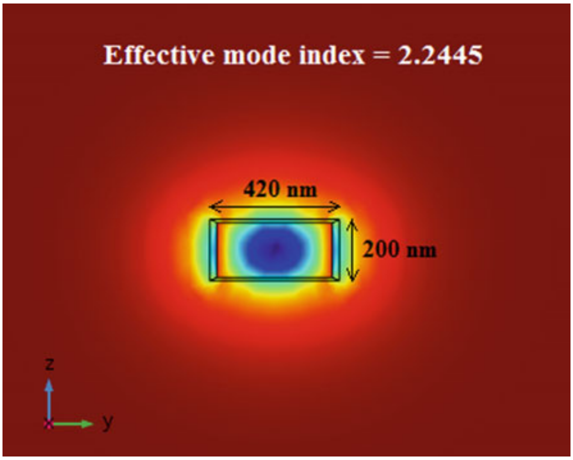

Fig. 10 TE mode for waveguide dimension of 420 × 200 nm

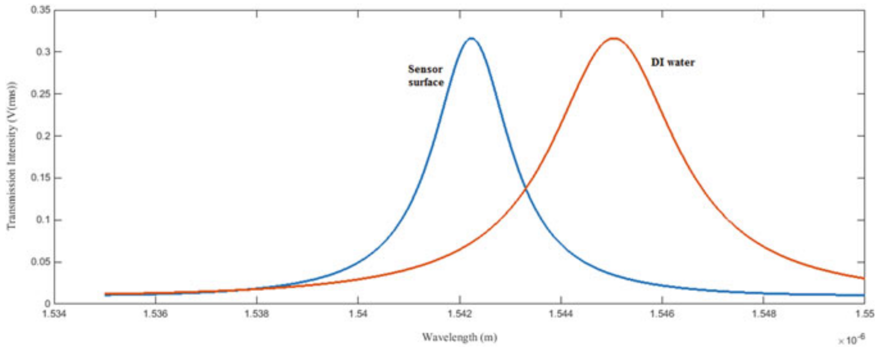

Fig. 11 Shift in resonant wavelength when deionized water is flowed across sensor's surface

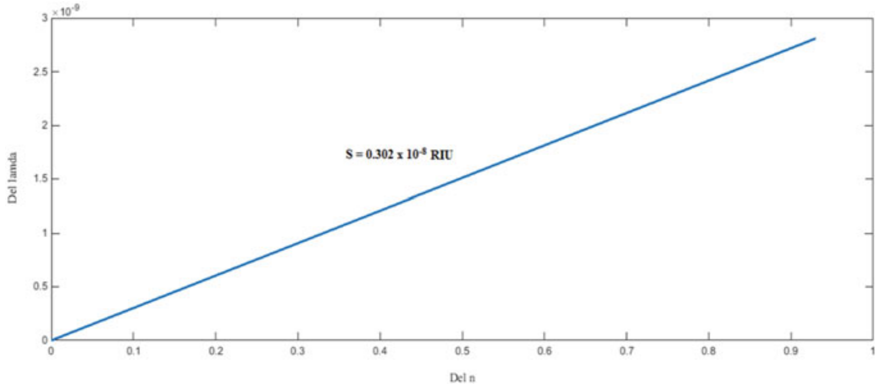

Fig. 12 Variation of change in resonant wavelength to the change in cladding index

(DI water) is made to flow over the sensor's surface.

When analytes get placed on the resonator's surface, the refractive index of the cladding changes which affects the resonant wavelength of the guided mode. The refractive index change of the resonator cladding to the change in resonant wavelength is obtained (Fig. 12). This gives the value of sensitivity which is obtained in the order of 10^{-8} RIU. Other analytes may also be sensed in a similar fashion depending on the requirement of the sensor design.

6 Conclusion and Future Scope

This work gives a comprehensive overview of silicon microring resonators. It deals with the computation of waveguide dimension and propose smaller resonator dimensions for which the performance parameters are computed through simulation as well as mathematically. There is a restriction in the resonator height of less than 250 nm so as to enable single mode operation. From the mathematical expressions, it was established that FSR and Q-factor varies differently with the resonator length and the ring radius. So, a tailoring of the structural parameters is required. Again, lowering the propagation loss improves the value of Q-factor. The computational results state that ring radius of 10 μm gives an FSR of 16 nm, which is comparatively higher and a Q of 6000 which is at a setback. Besides, the sensitivity is also computed to be in the order of 10^{-8} RIU which is quite high than reported in literature.

References

1. Heebner, J., Grover, R., Ibrahim, T.A.: Optical Microresonators: Theory, Fabrication and Applications. In: Springer Series in Optical Sciences (2008)
2. Rabus, D.G.: Integrated Ring Resonators, The Compendium. In: Springer Series in Optical Sciences (2007)
3. Kindt, J.T., Bailey, R.C.: Biomolecular analysis with microring resonators: application in multiplexed diagnostics and interaction screening. Curr. Opin. Chem. Biol. **17**(5), (2013)
4. Chao, C.Y., Guo, L.J.: Design and optimization of microring resonators in biochemical sensing applications. J. Lightwave Technol. **24**(3), 1395–1402 (2006)
5. Niehusmann, J., Vorckel, A., Bolivar, P.H., Wahlbrink, T., Henschel, W., Kurz, H.: Ultrahigh-quality-factor silicon-on-insulator microring resonator. Opt. Lett. **29**, 2861–2863, Optical Society of America (2004)
6. Hunsperger, R.G.: Optical waveguide modes. In: Integrated Optics, Theory and Technology, pp. 17–31 (2009)
7. Bogaerts, W., Dumon, P., Thourhout, D.V., Taillaert, D., Jaenen, P., Wouters, J., Beckx, S., Wiaux, V., Baets, R.G.: Compact wavelength-selective functions in silicon-on-insulator photonic wires. IEEE J. Sel. Top. Quantum Electron. **12**, (2006)
8. Bogaerts, W., Selvaraja, S.K., Dumon, P., Brouckaert, J., Vos, K.D., Thourhout, D.V., Baets, R.: Silicon-on-insulator spectral filters fabricated with CMOS technology. IEEE J. Sel. Top. Quantum Electron. **16**, (2010)
9. Bogaerts, W., et al.: Silicon microring resonators. Laser Photonics Rev. **1**, 47–73 (2012)
10. Chao, C.Y., Fung, W.: High Q-factor polymer microring resonators used in the biochemically sensing applications. IEEE J. Sel. Topics Quantum Electron **12**(1), 134–142 (2006)
11. Vollmer, F., Braun, D., Libchaber, A., Khoshsima, M., Teraoka, I., Arnold, S.: Protein detection by optical shift of a resonant microcavity. Appl. Phys. Lett. **80**(21), 4057–4059 (2002)
12. Chao, C.Y., Guo, L.J.: Biochemical sensors based on polymer microrings with sharp asymmetrical resonance. Appl. Phys. Lett. **83**(8), 1527–1529 (2003)
13. Mukherjee, P., Das, N.R.: Tailoring the parameters to increase the efficiency of a micro-ring resonator sensor for biosensing. In: Advances in Computer, Communication and Control, vol. 41, pp. 477–485. Springer (2019)

Technical Assessment for Implementation of Agricultural Solar Pump in West Bengal to Reduce AT&C Loss of Discom—A Case Study

Utpal Goswami, Arnab Ganguly, Prabir Kumar Dash, Suprava Chakraborty, and Arvind Kumar

Abstract Agriculture provides the primary source of income for majority of the rural population in India. Around 38% of the net-sown area of our country remains un-irrigated due to lack of irrigation infrastructure. Lack of access to reliable electricity supply is one of the major barriers for developing effective agricultural pumping infrastructure in the country. On the other hand, majority of the electricity distribution companies (DISCOMS) in India are reluctant to help in popularising solar pumps for agriculture, in fear of loss of their revenue. In addition, the distribution companies are suffering from very high aggregate technical and commercial losses. West Bengal State Electricity Distribution Company Limited (WBSEDCL), the largest DISCOM in West Bengal, plans to reduce the AT&C loss to 22.5% within its operational area. This paper argues that, the quantum of AT&C losses that can be reduced by providing solar agricultural pumps which could be channelized as a lucrative Feed in Tariff (FIT) to the agriculture consumers.

Keywords Agriculture · Solar pump · Solar system · DISCOM · AT&C loss

U. Goswami (✉)
West Bengal Renewable Energy Development Agency, Kolkata, India
e-mail: utpal_cgr@rediffmail.com

A. Ganguly
CUTS International, Jaipur, India

P. K. Dash
Ministry of New and Renewable Energy, New Delhi, India

S. Chakraborty
MNIT, Jaipur, India

A. Kumar
World Bank-MNRE-SBI Technical Assistance Programme, New Delhi, India

S. Banerjee and J. K. Mandal (eds.), *Advances in Smart Communication Technology and Information Processing*, Lecture Notes in Networks and Systems 165,
https://doi.org/10.1007/978-981-15-9433-5_45

1 Introduction

In India, nearly fifty percent (50%) of the population depends on agriculture for their primary source of livelihood. Easy access to dependable and adequate irrigation facility is important for growth of agricultural production which in turn will increase the revenue for Indian farmers [1–3]. India's irrigation mainly relies on high efficacy groundwater pumping. A recent study reveals that, Indian farmers currently use 19 million electric and 9 million diesel pumps for irrigation purpose. Despite using such high number of irrigation pumps, more than 53% of the net-sown area of our country remains un-irrigated. High cost of fuel, unreliable power supply and high upfront cost of installation of agricultural pumps prevent the farmers from adopting productive irrigation system [4–7].

Considering this, in March, 2018 the Ministry of New and Renewable Energy, Government of India formulated a scheme titled "Kisan Urja Suraksha Evam Utthaan Mahabhiyan" (KUSUM) for Indian farmers aimed at providing a boost to the production and increase in income from agricultural activity by adopting solar based irrigation systems. The scheme has four components [8]:

1. Installation of grid-connected solar power plants each of capacity up to 2 MW in the rural areas;
2. Installation of standalone off-grid solar water pumps to fulfil irrigation needs of farmers not connected to grid;
3. Solarization of existing grid-connected agriculture pumps to make farmers independent of grid supply and also enable them to sale surplus solar power generated to DISCOM and get extra income; and
4. Solarization of tube-wells and lift irrigation projects of Government sector.

Further, under the scheme, financial assistance of 60% of the project cost (split equally between state and central governments) 30% to be funded by banks and financial institutions in the form of loans. That leaves only 10% to be invested directly by farmers, in the form of equity.

Among others, the second and third components of the KUSUM scheme are especially significant from two counts—*first*, they would facilitate the process of solarisation of diesel run pumps; and *second*, it would discourage over exploitation of ground water as the farmers could be better off financially by selling electricity to the grid rather than indulging into flood irrigation. For the DISCOMs this would be particularly beneficial since it would help them reduce the Aggregate Technical and Commercial (AT&C) losses emanating from power theft in the agriculture sector and also help them in adhering to their renewable purchase obligations (RPO) [9–12].

In the year 2014, M/s KPMG Advisory Services, a global consulting firm carried out a feasibility analysis for solar agricultural water pump sets in India. The feasibility report argues in favour of replacing diesel pump sets with solar pump sets and extensively talks about the economic benefits that would accrue to the farmers and DISCOMs from such transition. The study reveals that, the annual diesel cost for a 2.2 kW pump would be around INR 30,000. The cost of a 2.2 kW solar pump would cost INR 320,000. The study also highlights that, farmers were found to be willing to invest the diesel cost for 2–3 years, but they are unable to provide the maximum upfront cost. The maximum upfront cost that the farmers are able to invest is in the range of INR 60,000 to INR 90,000 and balance i.e. INR 230,000 to INR 260,000 required from financial organization as loan or government subsidy (roughly 70%). The study estimated that, by providing solar irrigation pumps the DISCOMs can save an amount of INR 65,000/- per new connection coupled with an estimated cost of power delivery amounting to INR 14,000/- per annum per farmer. The study further underlines that, with reduction in price of solar pumps the internal rate of return for replacing diesel pumps with solar pumps would be 33% (with yield benefits) as against 19% in 2014; and the internal rate of return for replacing electrical pumps with solar pumps would be 30% (with yield benefits) as against 13% in 2014. The study concludes that, while the process of replacing diesel pumps with solar pumps can be technically and economically feasible but replacing grid connected pumps become feasible only when solar pumps become cheaper [13–17].

In the year 2018 CEEW (an India-based but globally engaged research think-tank) developed an economic model to calculate the annual cash flow for farmers and the government under different pump deployment scenarios. The model used background data for the Indian state of Uttar Pradesh and data collected after review of various secondary literature and farmer interviews. The study analysed cash flow to farmers and their Net Present Values (NPV) to analyse seven distinct irrigation models that include the following [18–21]

- Purchasing water from a government pumping station at a flat monthly rate;
- Irrigation by purchasing water or renting a pump from a neighbour;
- Irrigation by using own electric pump;
- Irrigation by using diesel pump;
- Irrigation by using a stand-alone solar pump;
- Irrigation by using a grid connected solar pump and sell surplus energy back to the distributor at a feed-in-tariff; and
- Irrigation by using solar pump and sell water or electricity to neighbours.

The report argues that while purchasing water from a government pumping station at a flat monthly rate (INR 500/- per month) is the cheapest available option, but such infrastructure is not always available to the farmers. The study also underlines that, while irrigation by purchasing water or renting a pump from a neighbour is the costliest option (INR 120/- per hour for a 3HP pump and a water table of six to eight meters) but small and marginal farmers prefer this arrangement owing to their lack of paying capacity to afford the upfront cost required to purchase an electric pump. The report suggests designing policies to make the solar pumps affordable to this category of farmers since it would be economical for them from a long-term perspective. The report also points out that, with government subsidy of 30% on solar pumps will make it economically attractive compared to diesel pumps and there will be possibilities of such substitution from diesel to solar pumps [22].

While discussing the findings pertaining to grid connected pumps, the report highlighted that in Uttar Pradesh, a farmer having one hectare of land and willing to install a 3HP pump would need a 3 kWp solar array. Depending on irrigation requirements, the study assumes that out of 365 days in a year, irrigation would be required for 140 days and for the rest 225 days the solar pump can generate an excess electricity of almost 2,000 kWh. With a feed-in-tariff of INR 3.50 per kWh the farmers will have an income of INR 7,000/- per year by selling excess electricity to the grid. While the farmer can make some income by selling electricity to the grid, but the system remains underutilised, which challenges the very economics of using solar pumps. The report further goes on to argue that grid connected systems will put additional burden on both the government (providing subsidies) and the state DISCOMs (since they would have to buyback the electricity) [23–26].

The above analysis underlines two distinct facts:

- Replacing diesel pumps by solar pumps are economically feasible; and
- Grid Connected solar irrigation pumps may not be a feasible choice for the consumers, DICOMs and Governments as there are issues of under utilisation of the systems and buying back power on top of subsidies provided for grid extension will put additional financial burden on the consumers.

While the argument cited in the paper was appealing but, it overlooked the component of how grid connected solar pumps can help the DISCOMs and the Government to reduce the AT&C losses in agriculture [27–32].

In this paper an analysis has been presented in the context of West Bengal's agriculture sector. Technical assessment also performed in terms of needs of solar pumps in agricultural sector in West Bengal. Since WBSEDCL caters to majority of the farmers in the state, the data for analysis has been mostly taken from filed visit and annual reports of WBSEDCL.

WBSEDCL, the largest DISCOM in West Bengal supplied, 1,433 Million kWh of electricity to 287,579 agricultural consumers (including Government run River Lift Irrigation pumps) and the total revenue collected has been INR 5.9487 million in the financial year FY 2016–17. Therefore the per capita electricity consumption in agriculture sector has been roughly 4,983 kWh at an average tariff of INR4.51 per kWh. Considering the AT&C loss of 28.96% [32], one can assume that the total revenue received from sale of electricity to the agriculture sector could have been higher than the actual figure.

Further, the Government of West Bengal plans to reduce the AT&C loss to 22.5%, and to that end the KUSUM scheme could be a game changer for reducing AT&C loss in the agriculture sector [32].

The present paper cites data related to the quantum of AT&C losses that can be reduced by providing solar pumps and argues that the savings on this account may be channelized to offer a lucrative FIT to the agriculture consumers [32–34].

2 Brief Agriculture Overview in West Bengal

2.1 Availability of Ground Water

West Bengal is located in eastern part of India beside the river Ganga. The annual average rain fall in last five years is around 1,200–2,500 mm. West Bengal also have 31 billion cubic meter of ground water resource. In 95% of villages of West Bengal, ground water available within 5–10 m below the ground level. In terms of availability of ground water per 1,000 ha of net cultivated area, West Bengal is second and in terms of availability of ground water per 100 km^2 of area the state ranks third in the country. The highest availability of ground water is observed in the Nadia district which is around 86% and the lowest at Jalpaiguri district at 5% [35–37].

2.2 Cropping Pattern in West Bengal

In West Bengal, production of rice constitutes around 68% of the total food grains produced in the state. In addition to this mustard, wheat, sugarcane jute, potato, fruits, pulses, vegetables and flowers are the other category of agricultural products cultivated in West Bengal. Intensity of cropping in this zone is around 162%. The crop production pattern in West Bengal has been depicted in Fig. 1 [38–42].

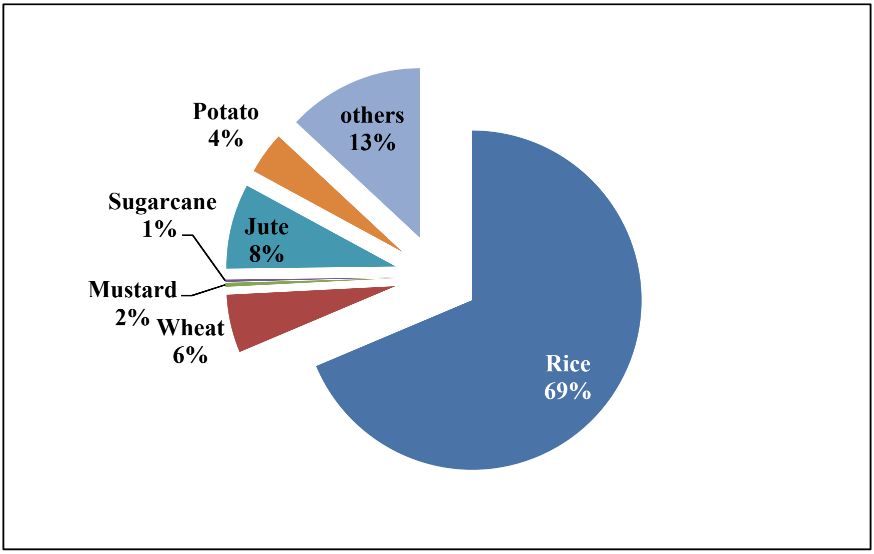

Fig. 1 The crop production pattern in West Bengal

2.3 Condition of Irrigation Activity in West Bengal

In West Bengal, irrigation activity mostly depends on availability of deep irrigation pumps. Since, only 12.5% of the agricultural pumps are electrified, rest are diesel operated pumps. The farmers of West Bengal suffer from high tariff of electricity as well as rising price of diesel. The price for 1 h of water uses of 5 HP diesel pump is around INR 70 hour. The agricultural pump owner first fulfil his or her demands and then sell surplus water to other farmers at very high price [40–42].

3 Result and Discussion

3.1 A Brief Overview of the Nature and Use of Electricity Consumption by the Agriculture Consumers of WBSEDCL

Table 1A, B, provides data on the year wise units of electricity sold by WBSEDCL for irrigation, the revenue collected and the total number of consumers of electricity for irrigation purpose. Analysis of the data shows a decline in per capita electricity

Table 1 A, B. A snapshot of key variables pertaining to electricity supplied by WBSEDCL to its consumers for irrigation purpose

(A)

Financial year (1)	Units of electricity sold (2)	Revenue (Lakhs) (3)	No. of consumers (4)	T&D loss (5)	AT&C loss (6)
2013–14	1,183,096,000.00	3,500,500,000.00	212,745	27.96	32.05
2014–15	1,491,990,000.00	5,783,100,000.00	241,250	27.60	29.96
2015–16	1,524,190,000.00	6,196,200,000.00	266,009	27.74	31.61
2016–17	1,433,540,000.00	5,948,700,000.00	287,579	27.47	28.96

(B)

Financial year (1)	Per capita electricity consumption (PCCONSM) (7) = (2)/(4)	Per capita realisation (REALPC) (8) = (3)/(4)	Per unit cost of electricity supplied (9) = (3)/(2)	Average cost of electricity supply (10)	Actual tariff (11)	Difference between (12) = (10) – (11)
2013–14	5561.10	16453.97	2.96	6.0893	3.84	3.13
2014–15	6184.41	23971.40	3.88	6.5604	4.59	2.68
2015–16	5729.84	23293.20	4.07	6.5513	4.59	2.49
2016–17	4984.86	20685.45	4.15	6.8932	4.75	2.74

consumption coupled with increase in per capita expenditure on electricity for irrigation which is shown in Fig. 2. One of the reasons has been an increase in the per unit actual cost of electricity consumed for irrigation (Column No. 09 in Table 1). Available data suggest that while WBSEDCL's actual per unit tariff realised from the agricultural consumers is less than the tariff approved by the State Regulatory Commission. The difference in 2016–17 was INR 0.60 per unit lower than 2013–14 which was INR 0.88 per unit, as shown in Fig. 3. It is important to note here that, for the sake of simplicity, we have considered the tariff charged for irrigation pumping for agriculture (metered supply from mixed HV feeder).

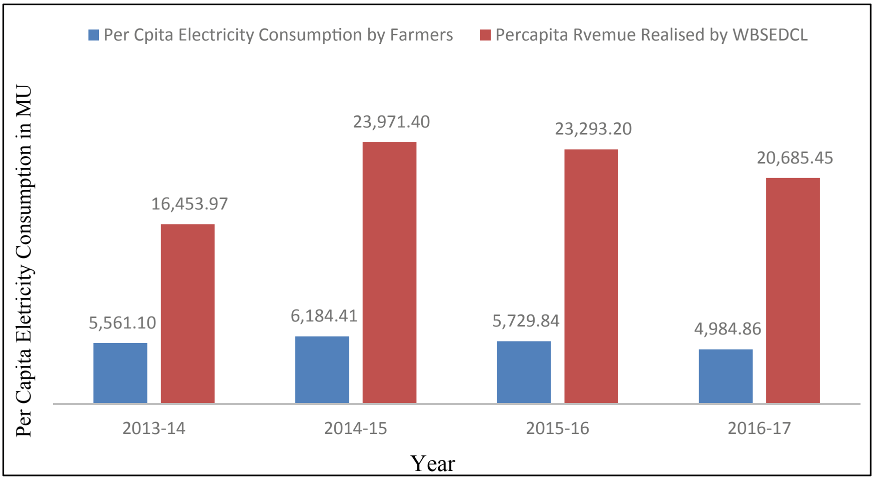

Fig. 2 Trends in per capita consumption of electricity for irrigation purpose by consumers of WBSEDCL from 2013–14 to 2016–17

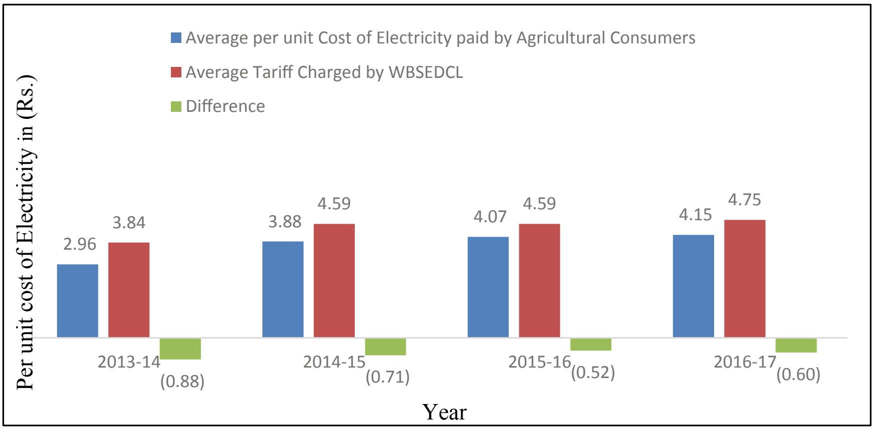

Fig. 3 Actual cost, actual tariff and their differential

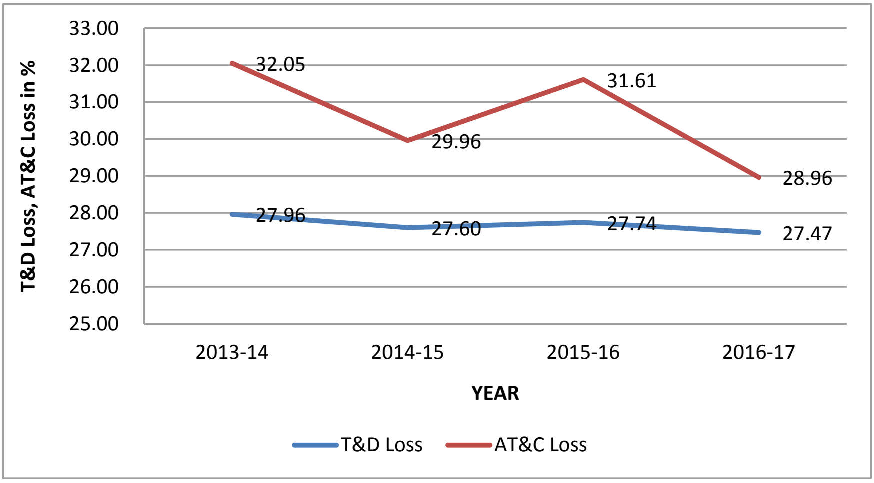

Fig. 4 T&D loss and AT&C loss suffered by WBSEDCL between 2013–14 and 2016–17

This difference as presented in Fig. 3 can be partly explained by the following three important factors:

- Transmission and Distribution Loss (T&D);
- Government Subsidy; and
- Aggregate Commercial and Technical Loss (AT&C).

Figure 4 provides a diagrammatic presentation of the figures on T&D and AT&C losses presented in Table 1. However, it is important to note here that, the data on T&D and AT&C losses, specifically for the irrigation sector is not available. Hence the data presented in Table 1A, B and Fig. 4 are aggregated figures for WBSEDCL's entire area of supply covering all category of electricity consumers. WBSEDCL reviles that, in general, the AT&C loss in the agriculture sector is higher compared to other sectors in the state, owing to issues like theft, tampering of meters, and limited reach out of WBSEDCL.

Figure 4 shows that while there has been a reduction in AT&C losses in 2016–17, but the same was still greater than 26%, the benchmark set by Ministry of Power, Government of India to be achieved in 2016–17 under the Integrated Power Development Scheme (IPDS). By 2019–20, the target is to restrict AT&C losses at 21%.

3.2 Effect of Implementation of Solar Water Pump in AT&C Loss

Consider a case where a farmer in West Bengal installs a 5HP solar pump. Going by the assumptions made in the CEEW study, the farmer would need to install a 5 kWp system. In West Bengal the average generation per kWp solar panel is 1,200 units per year. Thus, a 5 kWp system would generate 6,000 unit in one year. We further assume that a farmer irrigates the agricultural land for 145 days which would mean that the solar panel would generate 3,616.44 units for the rest 225 days. This excess unit could be sold to the grid provided grid connectivity is available. Considering an average cost of supply of INR 4.75 per unit, the amount a farmer can earn by injecting solar to the grid would be roughly INR 17,000/- per year.

Table 2 and Fig. 5 presents data comparing how much WBSEDCL could have

Table 2 Revenue that WBSEDCL could have earned had the AT&C losses be reduced by 1% from their actual values from 2013–14 to 2016–17

Financial year	Net energy supplied by WBSEDCL for running irrigation pumps	AT&C loss reduced by 1%	Units for which revenue could have been collected after reduction of AT&C loss by 1%	Average cost of supply (Rs per unit)	Revenue to WBSEDCL if AT&C loss could have been reduced by 1%
2013–14	1,183,096,000	31.05	367,351,308	6.0893	72,042,264.73
2014–15	1,491,990,000	28.96	432,080,304	6.5604	97,880,511.96
2015–16	1,524,190,000	30.61	466,554,559	6.5513	99,854,259.47
2016–17	1,433,540,000	27.96	400,817,784	6.8932	98,816,779.28

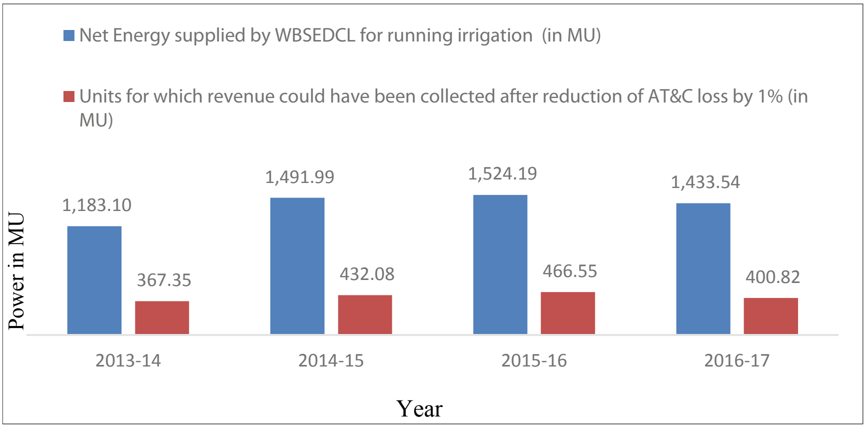

Fig. 5 The quantum of energy that could have been realised had the AT&C loss be reduced by 1%

saved had the AT&C loss be reduced by 1% from their actual values.

The data reveals that in 2016–17, WBSEDCL could have earned INR 68.09 million had the AT&C loss be reduced by 1–27.96% instead of 28.96% in 2016–17. If the DICOMs succeed in reducing the AT&C losses to 21% the revenue would be even higher for the DISCOMs and the Government need to think of ways of channelizing this savings for promoting solar pumps under KUSUM scheme.

4 Conclusion

The case study reveals that, if solar pump based irrigation infrastructure is introduced and incentivised, then the farmers will be directly benefited by reduction in their cost of production. Also, they will earn additional income by selling the surplus power to DISCOM. Simultaneously, the DISCOM will be benefited by reducing their AT&C loss in a significant manner and voltage profile of the grid will also improve by injection of power from the consumer at tail end. In addition, solar pump based irrigation infrastructure will help the DISCOM to reduce cross subsidy charges from the bulk consumer which in turn could lead to a reduction of tariff to industrial customers. In the post-COVID scenario with global economies experiencing a major recession, triggered mainly by a fall in industrial activities, a reduction in industrial tariff would be of great help to the industries. Increase in the agricultural productivity of the state will help to improve state's GDP significantly.

References

1. Abu-Aligah, M.: Design of photovoltaic water pumping system and compare it with diesel powered pump. Jordan J. Mech. Ind. Eng. **5**(3), 273–280 (2011)
2. Agrawal, S., Jain, A.: Solar Pumps for Sustainable Irrigation—A Budget Neutral Opportunity. Council on Energy, Environment and Water (CEEW), New Delhi, India (2015). http://ceew.in/publication_detail.php?id=273
3. Agrawal, S., Jain, A.: Financing Solar for Irrigation in India. Council on Energy, Environment and Water (CEEW) (2018). http://ceew.in/pdf/CEEW-FinancingSolarforIrrigation(SPIS)17Jan18.pdf
4. Ujala, A.: Panels of solar pumps stolen from state agriculture farms (2015). https://www.amarujala.com/uttar-pradesh/shahjahanpur/the-state-farm-solar-panels-stolen-pump-hindi-news
5. Assefa, G., Frostell, B.: Social sustainability and social acceptance in technology assessment: a case study of energy technologies. Technol. Soc. **29**(1), 63–78 (2007). https://doi.org/10.1016/j.techsoc.2006.10.007
6. Azimoh, L., Wallin, F., Klintenberg, P., Karlsson, B.: An assessment of unforeseen losses resulting from inappropriate use of solar home systems in South Africa. Appl. Energy **136**, 336–346 (2014). https://doi.org/10.1016/j.apenergy.2014.09.044
7. Bassi, N.: Irrigation and energy nexus solar pumps are not viable. Econ. Polit. Weekly **50**(10), 63–66 (2015)
8. Benghanem, M., Daffallah, K.O., Alamri, S.N., Joraid, A.A.: Effect of pumping head on solar water pumping system. Energy Convers. Manag. **77**, 334–339 (2014). https://doi.org/10.1016/j.enconman.2013.09.043

9. Bloomberg: Solar irrigation pumps take aim at half a billion smallholder farms. Bloomberg Briefs (Nov) **13** (2016). Boyd, O.: Africa's portable solar revolution is thwarting thieves (2016). https://www.theguardian.com/sustainable-business/2016/sep/26/africa-solar-mobile-revolution-stolen-mali-kenya-ghana
10. Brouwer, C., Heibloem, M.: Irrigation Water Management. Food and Agriculture Organisation (1986). http://www.fao.org/docrep/s2022e/s2022e00.htm#Contents
11. Burney, J., Woltering, L., Burke, M., Naylor, R., Pasternak, D.: Solar-powered drip irrigation enhances food security in the Sudano-Sahel. Proc. Natl. Acad. Sci. U.S.A. **107**(5), 1848–1853 (2010). https://doi.org/10.1073/pnas.0909678107
12. Campana, P.E.: PV Water Pumping Systems for Agricultural Applications. Malardalen University Sweden, Västerås, Sweden (2015)
13. Central Electricity Authority: Executive Summary—Power Sector December 15, pp. 1–52. Ministry of Power, Government of India (2014). http://www.cea.nic.in/reports/monthly/executive_rep/feb14.pdf
14. De Fraiture, C., Giordano, M.: Small private irrigation: a thriving but overlooked sector. Agric. Water Manag. **131**, 167–174 (2014). https://doi.org/10.1016/j.agwat.2013.07.005
15. Durga, N., Verma, S., Gupta, N., Kiran, R., Pathak, A.: Can solar pumps energize Bihar's agriculture? Water Policy Research Highlight, IWMI, vol. 3 (2016). https://www.iwmi-tata.blogspot.in
16. ECREEE: ToR technical assistant to support the implementation of the regional certification scheme for solar PV installers as well as the development of regional RE standards (2018). http://www.ecreee.org/ToR_Consultant_Regional_Certification_Scheme_and_RE_standards. Evans, A., Strezov, V., Evans, T.J.: Assessment of sustainability indicators for renewable energy technologies. Renew. Sustain. Energy Rev. **13**(5), 1082–1088 (2009). https://doi.org/10.1016/j.rser.2008.03.008. FAO: The State of the World's Land and Water Resources for Food and Agriculture—Managing Systems at Risk, pp. 308. Food and Agriculture Organization, Rome, Italy (2011). http://www.fao.org/docrep/017/i1688e/i1688e01.pdf
17. FAO & GIZ: Prospects for solar-powered irrigation systems (SPIS) in developing countries. Paper presented at the Workshop by Food and Agriculture Organization (FAO) and German Agency for International Cooperation (GIZ), pp. 1–19 (2015). http://www.royalcommission.vic.gov.au/ finaldocuments/summary/PF/VBRC_Summary_PF.pdf
18. Fthenakis, V.M.: Overview of potential hazards. In: Markvart, T., Castañer, L. (eds.) Practical Handbook of Photovoltaics: Fundamentals and Applications, p. 961. Elsevier, Oxford, United Kingdom (2003)
19. Fthenakis, V.M., Kim, H.C., Alsema, E.: Emissions from photovoltaic life cycles emissions from photovoltaic life cycles. Environ. Sci. Technol. **42**(February), 2168–2174 (2008). https://doi.org/10.1021/es071763q
20. Gebregziabher, G.: Water Lifting Irrigation Technology Adoption in Ethiopia: Challenges and Opportunities. International Water Management Institute (IWMI), Addis Ababa, Ethiopia (2012)
21. Gebregziabher, G., Hagos, F., Haileslassie, A., Getnet, K., Hoekstra, D., Gebremedhin, B., Getahun, G.: Does investment in motor pump-based smallholder irrigation lead to financially viable input intensification and production? An economic assessment (LIVES Working Paper No. 13) (2016). https://lives-ethiopia.org/2016/06/14/lives-wp13/
22. Gibson, R.B.: Sustainability assessment: basic components of a practical approach. Impact Assess. Project Apprais. **24**(3), 170–182 (2006). https://doi.org/10.3152/147154606781765147
23. Gopal, C., Mohanraj, M., Chandramohan, P., Chandrasekar, P.: Renewable energy source water pumping systems—a literature review. Renew. Sustain. Energy Rev. **25**, 351–370 (2013). https://doi.org/10.1016/j.rser.2013.04.012
24. Grand View Research: Solar pumps Market expected to reach USD 3.63 billion by 2022 (2016). grandviewresearch.com/press-release/solar-pumps-market
25. Hossain, M.A., Hassan, M.S., Mottalib, M.A., Ahmmed, S.: Technical and economic feasibility of solar pump irrigations for eco-friendly environment. Procedia Eng. **105**, 670–678 (2015). https://doi.org/10.1016/j.proeng.2015.05.047

26. Hossain, M.A., Hassan, M.S., Mottalib, M.A., Hossain, M.: Feasibility of solar pump for sustainable irrigation in Bangladesh. Int. J. Energy Environ. Eng. **6**(2), 147–155 (2015). https://doi.org/10.1007/s40095-015-0162-4
27. Hossain, M.S., Hassan, M.S., Ahmmed, S., Islam, M.S.: Solar pump irrigation system for green agriculture. Agric. Eng. Int.: CIGR J. **16**(4), 1–15 (2014)
28. Huijts, N.M.A., Molin, E.J.E., Steg, L.: Psychological factors influencing sustainable energy technology acceptance: a review-based comprehensive framework (2012)
29. Renew. Sustain. Energy Rev. **16**(1), 525–531. https://doi.org/10.1016/j.rser.2011.08.018
30. Ibrahim, S.: New solar-powered water pump poised to transform agricultural output (2017). http://sunculture.com/press/new-solar-powered-water-pump-poised-to-transform-agricultural-output
31. IFC: Market Assessments for Solar-Powered Irrigation Pumps in Morocco, South Africa and Yemen. International Finance Corporation, Rome, Italy (2015)
32. Annual Reports and Accounts, 2016–17, West Bengal Electricity Distribution Company Limited. https://www.wbsedcl.in/irj/go/km/docs/internet/new_website/Annual_Reports.html. Accessed 27 Oct 2018
33. http://www.ipds.gov.in/IPDS_Order_Guidelines/AT_And_C_Loss_Trajectory.pdf. Accessed 31 Oct 2018
34. IRENA: Solar Pumping for Irrigation: Improving Livelihoods and Sustainability. The International Renewable Energy Agency (IRENA), Abu Dhabi (2016)
35. Jain, A., Shahidi, T.: Adopting Solar for Irrigation—Farmers perspective from Uttar Pradesh. Council on Energy, Environment and Water (2018). http://ceew.in/pdf/CEEW-Adopting. Solar for Irrigation (SPIS)—Farmers' Perspectives from UP Report 17Jan18.pdf
36. Jain, R., Choudhury, P., Palakshappa, R., Ghosh, A., Padigala, B., Panwar, T.S., Worah, S.: Renewables Beyond Electricity. WWF-India, New Delhi, India. 12 of 14 Agrawal and Jain (2013)
37. Kakkar, H.: Sunny-side up: Claro energy is increasing the farmland under irrigation with its solar-powered pumps (2017). https://www.outlookbusiness.com/specials/good-businesses_2016/sunny-side-up-3003
38. Kelley, L.C., Gilbertson, E., Sheikh, A., Eppinger, S.D., Dubowsky, S.: On the feasibility of solar-powered irrigation. Renew. Sustain. Energy Rev. **14**(9), 2669–2682 (2010). https://doi.org/10.1016/j.rser.2010.07.061
39. Kishore, A., Shah, T., Tewari, N.P.: Solar irrigation pumps—farmers' experience and state policy in Rajasthan. Econ. Polit. Weekly **XLIX**(10), 55–62 (2014)
40. Kohler, F.: Spread the word on solar pumping! Supporting farmers in Bihar to adopt clean technologies to improve agricultural outputs (2014). http://igen-re-giz.blogspot.co.uk/2014/05/spread-word-on-solar-pumping-supporting.html
41. KPMG: Feasibility Analysis for Solar Agricultural Water Pumps in India. KPMG India, Gurugram, India (2014). http://shaktifoundation.in/wp-content/uploads/2014/02/feasibility-analysis-for-solar-High-Res-1.pdf
42. Kumar, H.D., Kumar, N.T., Suresh, K.R., Mitavachan, H., Shankar, G.: Advanced solar-irrigation scheduling for sustainable rural development: a case of India. In: Groh, S., van der Straeten, J., Edlefsen Lasch, B., Gershenson, D., Leal Filho, W., Kammen, D.M. (eds.) Decentralized Solutions for Developing Economies, pp. 123–131. Springer International Publishing, Cham, Switzerland (2015). https://doi.org/10.1007/978-3-319-15964-5

Author Index

A
Acharjee, Labani, 317
Ahmed, Hazim, 219

B
Bagchi, Sreejit, 219
Banerjee, Arghasree, 135, 181, 207, 229, 239, 251, 299
Banerjee, Saswata, 27
Banerjee, Soumen, 3, 59, 83, 229
Banerjee, Sriparna, 371, 393
Banik, Sayani, 37
Basak, Piyali, 111
Bera, R., 83
Bhadra, Avishek, 307
Bhattacharjee, Joy, 125
Bhattacharjee, Mayukh, 135, 181, 229, 239, 251, 299
Bhattacharjee, Soumi, 147
Bhowmick, Biplab, 417
Billaha, Md Aref, 417
Borah, Hiren Chandra, 443
Brahmachari, Aditya, 11

C
Chaki, Susmita, 425
Chakraborty, Shouvik, 251, 259, 267, 279, 289, 299, 307
Chakraborty, Sohom, 407, 433
Chakraborty, Souvik, 307
Chakraborty, Suprava, 471
Chatterjee, Anuplab, 11
Chatterjee, Diya, 19
Chatterjee, Sankhadeep, 135, 181, 207, 229, 239, 251, 259, 267
Chatterjee, Sombuddha, 59
Chattopadhyay, Rik, 385
Chaudhuri, Sheli Sinha, 147, 157, 171
Choudhary, Santosh Kumar, 417
Chowdhury, Chandreyee, 71
Chowdhury, Debkumar, 219

D
Das, Arpita, 433
Das, Asit Kumar, 229
Dash, Prabir Kumar, 471
Das, Juhita, 425
Das, N. R., 459
Das, Priyanka, 19, 27, 37
Das, Trisha, 219
Deyasi, Arpan, 125, 349
Dey, Chanchal, 361
Dey, Shubhadeep, 27
Dey, Sukanya, 407

G
Ganguly, Arnab, 471
Ganguly, Soham, 317
Ghosh, A., 83
Ghoshal, Pranati, 361
Ghosh, Kushankur, 135, 181, 207, 229, 239, 259, 279
Ghosh, Mouli, 37
Goswami, Utpal, 443, 471
Gupta, Bhaskar, 111
Gupta, Shubhojit, 317

S. Banerjee and J. K. Mandal (eds.), *Advances in Smart Communication Technology and Information Processing*, Lecture Notes in Networks and Systems 165,
https://doi.org/10.1007/978-981-15-9433-5

H

Hazarika, Biki Raj, 91

K

Kumar, Arvind, 443, 471
Kumar, Sachin, 91

M

Mahanti, G. K., 99
Maji, Bubai, 385
Mali, Kalyani, 251, 259, 267, 279, 289, 299
Mallick, Sakil, 71
Mandal, B., 83
Mandal, Chinmoy, 219
Mandal, Sujit Kumar, 91, 99
Manna, Srijita, 147
Mazumdar, Sampoorna Das, 59
Mehra, Raghav, 371, 393
Mishra, Sanjukta, 219
Misra, Arundhati, 371, 393
Mitra, Sandipan, 11
Mohanty, Abhinandan, 193
Mondal, P., 83
Mondal, Samrat, 307
Mondal, Subhodeep, 37
Mondal, Sukanto, 71
Mukherjee, Piyali, 459
Mukherjee, Pooja, 19
Mukherjee, Soumyadev, 337
Mukhopadhyay, Swarnav, 349

N

Nandi, Didhiti, 425
Navyashri, S., 19
Neogy, Sarmistha, 71

P

Pal, Srikanta, 111
Pal, Subhradeep, 47
Panja, Ayan Kumar, 71
Parui, S. K., 83
Parui, Susanta Kumar, 3, 59
Pathak, N., 99
Patra, S., 99
Paul, Hrittika, 317
Paul, Soumik, 71
Paul, Sujoy, 219
Pramanik, Sayan, 157
Prasad, Suraj, 307

R

Ray, Purbasha, 349
Ray, Reeju, 19
Rout, Nirmal Kumar, 327, 337
Roy, Anusua, 407
Roy, Deepayan, 267, 289
Roy, Kyamelia, 147, 157, 171
Roy, Mousomi, 267, 289
Roy, Priya, 71
Roy, Probhakar, 171
Roy, Rohan, 47
Roy, Sreyashi, 193

S

Saha, Abhirupa, 111
Sah, Akash, 317
Saha, Soumi, 47
Saha, Surjya Prakash, 11
Samanta, Pravin Kumar, 327, 337
Santra, Soumen, 125
Santra, Subhadip, 11
Sarkar, Arya, 181, 207, 259, 279
Sarkar, Goffar Ali, 3
Sen, Sunit Kumar, 361
Shekhar, Sudhanshu, 37
Sil, Sanjib, 111
Singh, Harshavardhan, 91
Sinha Chaudhuri, Sheli, 371, 393

T

Tarafdar, Arunabha, 317